COMPOUND CLIMATE EXTREMES IN THE PRESENT AND FUTURE CLIMATES: MACHINE LEARNING, STATISTICAL METHODS AND DYNAMICAL MODELLING

EDITED BY: Wei Zhang, Abdou Khouakhi, Ming Luo and Hiroyuki Murakami
PUBLISHED IN: Frontiers in Earth Science and Frontiers in Environmental Science

frontiers Research Topics

ISSN 1664-8714
ISBN 978-2-88974-024-6
DOI 10.3389/978-2-88974-024-6

About Frontiers

Frontiers is more than just an open-access publisher of scholarly articles: it is a pioneering approach to the world of academia, radically improving the way scholarly research is managed. The grand vision of Frontiers is a world where all people have an equal opportunity to seek, share and generate knowledge. Frontiers provides immediate and permanent online open access to all its publications, but this alone is not enough to realize our grand goals.

Frontiers Journal Series

The Frontiers Journal Series is a multi-tier and interdisciplinary set of open-access, online journals, promising a paradigm shift from the current review, selection and dissemination processes in academic publishing. All Frontiers journals are driven by researchers for researchers; therefore, they constitute a service to the scholarly community. At the same time, the Frontiers Journal Series operates on a revolutionary invention, the tiered publishing system, initially addressing specific communities of scholars, and gradually climbing up to broader public understanding, thus serving the interests of the lay society, too.

Dedication to Quality

Each Frontiers article is a landmark of the highest quality, thanks to genuinely collaborative interactions between authors and review editors, who include some of the world's best academicians. Research must be certified by peers before entering a stream of knowledge that may eventually reach the public - and shape society; therefore, Frontiers only applies the most rigorous and unbiased reviews.
Frontiers revolutionizes research publishing by freely delivering the most outstanding research, evaluated with no bias from both the academic and social point of view. By applying the most advanced information technologies, Frontiers is catapulting scholarly publishing into a new generation.

What are Frontiers Research Topics?

Frontiers Research Topics are very popular trademarks of the Frontiers Journals Series: they are collections of at least ten articles, all centered on a particular subject. With their unique mix of varied contributions from Original Research to Review Articles, Frontiers Research Topics unify the most influential researchers, the latest key findings and historical advances in a hot research area! Find out more on how to host your own Frontiers Research Topic or contribute to one as an author by contacting the Frontiers Editorial Office: frontiersin.org/about/contact

COMPOUND CLIMATE EXTREMES IN THE PRESENT AND FUTURE CLIMATES: MACHINE LEARNING, STATISTICAL METHODS AND DYNAMICAL MODELLING

Topic Editors:
Wei Zhang, Utah State University, United States
Abdou Khouakhi, Cranfield University, United Kingdom
Ming Luo, Sun Yat-sen University, China
Hiroyuki Murakami, University Corporation for Atmospheric Research (UCAR), United States

Citation: Zhang, W., Khouakhi, A., Luo, M., Murakami, H., eds. (2021). Compound Climate Extremes in the Present and Future Climates: Machine Learning, Statistical Methods and Dynamical Modelling. Lausanne: Frontiers Media SA. doi: 10.3389/978-2-88974-024-6

Table of Contents

frontiers in Earth Science

EDITORIAL
published: 19 November 2021
doi: 10.3389/feart.2021.807224

Editorial: Compound Climate Extremes in the Present and Future Climates: Machine Learning, Statistical Methods and Dynamical Modelling

Wei Zhang[1]*, *Hiroyuki Murakami*[2,3], *Abdou Khouakhi*[4] *and Ming Luo*[5,6]

[1]Department of Plants, Soils and Climate, Utah State University, Logan, UT, United States, [2]University Corporation for Atmospheric Research (UCAR), Boulder, CO, United States, [3]Geophysical Fluid Dynamics Laboratory, National Oceanic and Atmospheric Administration, Princeton, NJ, United States, [4]School of Water, Energy and Environment, Centre for Environmental and Agricultural Informatics, Cranfield University, Cranfield, United Kingdom, [5]School of Geography and Planning, Sun Yat-sen University, Guangzhou, China, [6]Guangdong Provincial Engineering Research Center for Public Security and Disaster, and Guangdong Key Laboratory for Urbanization and Geo-Simulation, Guangzhou, China

Keywords: compound extremes, machine learning, statistical methods, dynamical modeling, climate change

Editorial on the Research Topic

Compound Climate Extremes in the Present and Future Climates: Machine Learning, Statistical Methods and Dynamical Modelling

OPEN ACCESS

Edited and reviewed by:
Yuqing Wang,
University of Hawaii at Manoa,
United States

****Correspondence:***
Wei Zhang
w.zhang@usu.edu

Specialty section:
This article was submitted to
Atmospheric Science,
a section of the journal
Frontiers in Earth Science

Received: *01 November 2021*
Accepted: *04 November 2021*
Published: *19 November 2021*

Citation:
Zhang W, Murakami H, Khouakhi A and Luo M (2021) Editorial: Compound Climate Extremes in the Present and Future Climates: Machine Learning, Statistical Methods and Dynamical Modelling.
Front. Earth Sci. 9:807224.
doi: 10.3389/feart.2021.807224

Compound extremes, namely simultaneous, concurrent, or coincident extreme hydrometeorological events, may have broader impacts on human society and the environment than any individual extreme alone (Hao et al., 2018; Zscheischler et al., 2018, 2020, 2021; AghaKouchak et al., 2020; Raymond et al., 2020). There are a wide range of compound events that occur on a variety of spatial and temporal scales: typical examples include droughts coupled with heat waves, coastal flooding coupled with wind hazards, sea level rise and storm surge, or tropical cyclones followed by heat waves. However, we are yet to fully understand all types of compound extremes, the dynamical and physical processes associated with their occurrence, the framework and the methods required for their analysis, and their likelihood within the present and future climate.

This research topic aims to advance our knowledge about the processes and dynamical linkages associated with different types of compound extremes, to showcase the development of new statistical methods and machine learning techniques for efficiently examining these extremes, and to quantify the potential risks of compound extremes in the present and future climate. This Research Topic comprises 15 articles (14 research articles and 1 review article) on extreme weather events and compound extremes. These articles have visited compound hydrometeorological events, extreme temperatures, extreme weather and climate events in tropical ocean basins, climate modeling and machine learning technologies for examining extremes and their compounding effects.

Compound hydrometeorological events under present and future climates have been examined in this research topic. Giang et al. used pattern scaling along with the Generalized Extreme Value (GEV) distribution to calculate changes in multi-day extreme precipitation in North Central Vietnam in future projections under three Representative Concentration Pathways from IPCC AR5. Similarly, an attribution analysis over the mid–lower reaches of the Yangtze River of China found that anthropogenic warming has reduced the likelihood of 2019-like 14-days heavy precipitation by 20%, but increased that of 2-days extremes by 30% (Nanding et al.). Wu et al. found that the fraction of extreme precipitation events in Guangdong preceded by hot weather is even larger in more populated and urbanized areas such as the Pearl River Delta (PRD) region, and revealed significant increases in the frequency and fraction of compound extreme heat and precipitation events. Lai et al. examined the evolution of compound flood days based on global precipitation and storm surge data in observations and reported that the frequency has risen significantly on the east coast of the US and northern Europe, but decreased significantly in southern Europe and Japan. Zhang et al. reviewed the physical drivers, mechanisms and methods related to compound hydrometeorological extremes and discussed current advances in the understanding of compound heat wave and drought (hot-dry), compound heat stress and extreme precipitation (hot-wet), and cold-wet, cold-dry and compound flooding. Yang et al. investigated the responses of heat stress to temperature and humidity changes due to anthropogenic heating and urban expansion in South and North China. Using gauge-based precipitation observations, they found that heavy precipitation events were the main contributor to the increasing trend of summer precipitation over the Three-Rivers Headwater Region (Zhao et al.). Li et al. unraveled synoptic weather patterns that modulate warm-sector heavy rainfall in South China. They found that the locations of six large-scale extreme precipitation events were related to the urban agglomerations in Guangdong–Hong Kong–Macao Greater Bay Area.

Two papers in this Research Topic have advanced the understanding of extreme temperatures. Ngarukiyimana et al. examined the spatial and temporal variations of daily maximum and minimum surface air temperature (Tmin and Tmax) and diurnal temperature range. With high confidence, the results indicate a significant positive trend in both Tmin and Tmax in three study regions in Rwanda during the whole study period. Based on observations of automatic weather stations in Beijing during the summers of 2014–2020, Zong et al. studied the interaction between heat waves events and the Urban Heat Island (UHI) effect and found that latent heat flux has increased more in rural areas because of sufficient water availability and vegetation.

Studies in this Research Topic have also focused on developing machine learning technologies for examining extremes. For example, Huang et al. reported that the stacking model and the XGBoost model performed the best in predicting solar radiation. Wang et al. developed a new extreme detection method for unravelling remote compound extremes in Southeast China. Wang et al. introduced the MultiLLR ML model and found that the subseasonal prediction skill of China precipitation with 2–6 weeks lead time could be enhanced. Finally, the T-mode principal component analysis statistical approach was used to study the warm-sector heavy rainfall by unravelling large-scale circulation patterns (Li et al.).

Works in this Research Topic have also examined extreme weather and climate events in tropical ocean basins. For example, footprints of the Atlantic Multidecadal Oscillation (AMO) in the western North Pacific assessed using observations and coupled atmosphere-ocean simulations of sea surface temperature (WNP SST) and atmospheric states exert a significant impact on tropical cyclone intensity (Sun et al.). Chen et al. compared the temporal evolution of environmental conditions for Rapid Intensification (RI) and non-RI of TCs in the South China Sea (SCS) during 2000–2018, and identified key factors for RI of SCS TCs using the box difference index and stepwise regression.

Several future research directions for compound climate extremes are documented: 1) projecting the risk of compound climate extremes corresponding to future warming; 2) evaluating the impacts of the compound climate extremes on natural and built environments; 3) designing adaptation measures to the changing risk of the extremes; 4) improving subseasonal-to-seasonal prediction of these compound extremes; 5) improving the representation and evaluation of compound climate extremes in fully-coupled climate models; and 6) applying machine learning and other advanced methods to understand these extremes.

AUTHOR CONTRIBUTIONS

All authors listed have made a substantial, direct, and intellectual contribution to the work and approved it for publication.

FUNDING

WZ is supported by USDA NIFA Hatch Project (1026229), the UAES Seed Grant and the startup fund of Utah State University. ML is supported by the Pearl River Talent Recruitment Program of Guangdong Province, China (2017GC010634) and the Science and Technology Program of Guangzhou, China (202102020489).

ACKNOWLEDGMENTS

We appreciate the Editorial Board and the Editorial Office of Frontiers in Earth Science for their kind invitation to edit this Research Topic and their support throughout the entire process.

REFERENCES

AghaKouchak, A., Chiang, F., Huning, L. S., Love, C. A., Mallakpour, I., Mazdiyasni, O., et al. (2020). Climate Extremes and Compound Hazards in a Warming World. *Annu. Rev. Earth Planet. Sci.* 48, 519–548. doi:10.1146/annurev-earth-071719-055228

Hao, Z., Singh, V., and Hao, F. (2018). Compound Extremes in Hydroclimatology: A Review. *Water* 10, 718. doi:10.3390/w10060718

Raymond, C., Horton, R. M., Zscheischler, J., Martius, O., AghaKouchak, A., Balch, J., et al. (2020). Understanding and Managing Connected Extreme Events. *Nat. Clim. Chang.* 10, 611–621. doi:10.1038/s41558-020-0790-4

Zscheischler, J., Martius, O., Westra, S., Bevacqua, E., Raymond, C., Horton, R. M., et al. (2020). A Typology of Compound Weather and Climate Events. *Nat. Rev. Earth Environ.* 1, 333–347. doi:10.1038/s43017-020-0060-z

Zscheischler, J., Sillmann, J., and Alexander, L. (2021). Introduction to the Special Issue: Compound Weather and Climate Events. *Weather Clim. Extremes*, 100381. doi:10.1016/j.wace.2021.100381

Zscheischler, J., Westra, S., Van Den Hurk, B. J. J. M., Seneviratne, S. I., Ward, P. J., Pitman, A., et al. (2018). Future Climate Risk from Compound Events. *Nat. Clim Change* 8, 469–477. doi:10.1038/s41558-018-0156-3

Conflict of Interest: The authors declare that the research was conducted in the absence of any commercial or financial relationships that could be construed as a potential conflict of interest.

frontiers in Earth Science

ORIGINAL RESEARCH
published: 23 November 2020
doi: 10.3389/feart.2020.604807

The Footprint of Atlantic Multidecadal Oscillation on the Intensity of Tropical Cyclones Over the Western North Pacific

***Cheng Sun*[1]*, Yusen Liu*[1], *Zhanqiu Gong*[1], *Fred Kucharski*[2], *Jianping Li*[3,4], *Qiuyun Wang*[5] and *Xiang Li*[6]**

[1]College of Global Change and Earth System Science (GCESS), Beijing Normal University, Beijing, China, [2]The Abdus Salam International Centre for Theoretical Physics, Trieste, Italy, [3]Frontiers Science Center for Deep Ocean Multispheres and Earth System (FDOMES), Key Laboratory of Physical Oceanography, Institute for Advanced Ocean Studies, Ocean University of China, Qingdao, China, [4]Laboratory for Ocean Dynamics and Climate, Pilot National Laboratory for Marine Science and Technology (Qingdao), Qingdao, China, [5]Key Laboratory of Mesoscale Severe Weather/Ministry of Education and School of Atmospheric Sciences, Nanjing University, Nanjing, China, [6]Key Laboratory of Marine Hazards Forecasting, National Marine Environmental Forecasting Center, Ministry of Natural Resources, Beijing, China

Sea surface temperature (SST) over the western North Pacific (WNP) exhibits strong decadal to multidecadal variability and in this region, warm waters fuel the tropical cyclones (TCs). Observational records show pronounced decadal variations in WNP TC metrics during 1950–2018. Statistical analysis of the various TC metrics suggests that the annual average intensity of WNP TCs is closely linked to the AMO ($r = 0.86$ at decadal timescales, $p < 0.05$). Observations and coupled atmosphere-ocean simulations show that the decadal WNP SST variations regarded as the primary driver of TC intensity, are remotely controlled by the AMO. Corresponding to the WNP SST warming, the local SLP gets lower and the tropospheric air becomes warmer and moister, enhancing atmospheric instability and the generation of convective available potential energy. These favorable changes in the background environment provide more “fuel” to the development of deep convection and intensify the WNP TCs. The footprints of AMO in WNP SST and atmospheric states through trans-basin interaction eventually exert a significant impact on the TC intensity over the WNP region.

Keywords: Atlantic multidecadal oscillation, inter-basin interaction, teleconnection, extreme weather and climate, tropical cyclone

Edited by:
Wei Zhang,
The University of Iowa, United States

Reviewed by:
Si Gao,
Sun Yat-sen University, China
Chao Wang,
Nanjing University of Information Science and Technology, China

Correspondence:
Cheng Sun
scheng@bnu.edu.cn

Specialty section:
This article was submitted to Atmospheric Science, a section of the journal Frontiers in Earth Science

Received: *10 September 2020*
Accepted: *28 October 2020*
Published: *23 November 2020*

Citation:
Sun C, Liu Y, Gong Z, Kucharski F, Li J, Wang Q and Li X (2020) The Footprint of Atlantic Multidecadal Oscillation on the Intensity of Tropical Cyclones Over the Western North Pacific. Front. Earth Sci. 8:604807. doi: 10.3389/feart.2020.604807

INTRODUCTION

Tropical cyclone (TC) is one of the most destructive natural disasters. Almost 30% of all TCs over the globe take place in the western North Pacific (WNP; 100°–180°E, 0°–40°N). As the surface temperature has warmed notably, observed changes in the WNP TC activity during the recent decades are metric dependent, showing a strengthening trend in the intensity but decreasing trends in the frequency and duration (Emanuel, 2005; Liu and Chan, 2013). In addition to the effects of climate change (Knutson et al., 2019; Knutson et al., 2020), internal climate variability can also influence TC activity. For example, WNP TC activity shows pronounced interannual variability and most studies have identified ENSO as an important contributor to the interannual variations (Chan 1985; Camargo and Sobel 2005; Wang et al., 2014; Liu and Chen 2018; Patricola et al., 2018).

Madden-Julian oscillation (MJO), Pacific–Japan (PJ) teleconnection and other atmospheric variabilities also play roles in influencing the WNP TC activity (Nakazawa 1986; Maloney and Hartmann 2001; Li et al., 2014; Wu et al., 2020; Zhou et al., 2019). Some other studies highlighted the remote effects of SST variability in Indian and Atlantic Oceans on WNP TCs but mostly focused on the frequency and genesis of TCs (Liu and Chan, 2008; Liu and Chan, 2013; Huo et al., 2015; Zhang et al., 2017; Gao et al., 2018; Zhang et al., 2018; Zhang and Villarini, 2019; Gao et al., 2020). Besides the interannual variability, some studies have suggested a significant multidecadal change in the WNP TC activity (Leung et al., 2005; Chan, 2006; Li and Zhou, 2014; Wang et al., 2015). However, there have been much fewer studies focusing on the decadal variations (or fluctuations) of the WNP TC activity, and the decadal variability of WNP TC intensity and the driving mechanism remain unclear.

It is widely recognized that sea surface temperature (SST) is an important environmental condition for TC activity (Gray and Brody, 1967; Landsea, 2005). The global SSTs show pronounced interdecadal variabilities and one of the most well-known patterns is the Atlantic Multidecadal Oscillation (AMO) (Kerr, 2000). Previous studies indicated that the AMO plays a crucial role in climate around the Atlantic region (Enfield et al., 2001; McCabe et al., 2004; Sutton and Hodson, 2005; Wang and Lee, 2009; Sutton and Dong, 2012), together with the remote regions (Lu et al., 2006; Li and Bates, 2007; Sun et al., 2015; Sun et al., 2017b). Hurricane activity over the North Atlantic basin has been linked to the AMO (Zhang and Delworth, 2007), indicating the effects of local SST variability. Meanwhile, inter-basin SST interactions at decadal time scales have received considerable attention in recent years as many studies have suggested a strong SST teleconnection from North Atlantic to Pacific (Li and Zhou, 2014; McGregor et al., 2014; Lopez et al., 2016; Ruprich-Robert et al., 2017). Particularly, some previous studies based on both modeling and observational analysis have suggested that the multidecadal variations in the SST and atmospheric circulation aloft over the western tropical Pacific and North Pacific are significantly influenced by the AMO signal (Sun et al., 2017a; Gong et al., 2020). Zhang et al. (2018) have linked the multidecadal variations of WNP TC genesis frequency since 1980 to the AMO, but the potential influence of AMO on the WNP TC intensity remains to be studied. Previous studies have reported that there are decadal variations in the WNP basin-wide TC intensity, showing an increasing trend since the mid-1970s (Wu et al., 2008; Wu and Zhao, 2012). Thus, it is of interest to examine the relationship between the AMO and TC intensity at decadal timescales.

Our analysis will focus on the decadal variations of the WNP TC activity. In this study, the accumulated cyclone energy (ACE) proposed by Bell et al. (2001) is used to represent the activity of TCs. In addition to the ACE index, the number of TCs (frequency), TC days, and average intensity are defined to distinguish the characteristics of TC activity. Detailed information can be found in the Methods. We also perform statistical analysis on a suite of Atlantic Pacemaker experiments to investigate the AMO effects on the WNP TC activity, and a strong connection at decadal time scales can be found. A mechanism is then proposed to explain the teleconnection between the AMO and WNP TC activity which connects the WNP climate to the North Atlantic Ocean. Our results highlight the remote influence of AMO on WNP TC activity. This may also have implications for better understanding the decadal variability and predictability of the WNP TC activity.

DATA AND METHODOLOGY

Data

The global observational SST data set used in this study is the Extended Reconstruction SST version 3 (ERSST v3b) data set (Smith et al., 2008). The atmospheric data set derives from the NOAA ESRL 20th Century Reanalysis, version 2 (20CRv2) (Compo et al., 2011) which includes air temperature, specific humidity and sea level pressure (SLP).

The data sets of the WNP TC metrics (the number of Named TCs, the Named TC days, and the Accumulated Cyclone Energy) we used are available online from the Department of Atmospheric Science at Colorado State University (http://tropical.atmos.colostate.edu/Realtime/). And the statistics are calculated from National Hurricane Center, the Central Pacific Hurricane Center and the Joint Typhoon Warning Center best tracks as archived in the International Best Track Archive for Climate Stewardship (IBTrACS) (Knapp et al., 2010; Knapp et al., 2018). The code for calculating the maximum potential intensity is publicly available (ftp://texmex.mit.edu/pub/emanuel/TCMAX/).

The AMO index is defined as the area-weighted average of SST anomalies over the North Atlantic region (0°–60°N, 80°W–0°). And the index used in this study comes from the NOAA ESRL Climate Timeseries, which is calculated from the Kaplan SST dataset (Enfield et al., 2001). Other indices of climate modes are obtained from the following websites: NPGO index: http://www.o3d.org/npgo/, IPO index: https://psl.noaa.gov/data/timeseries/IPOTPI/ and PDO index: https://cmdp.ncc-cma.net/pred/cn_enso.php?product=cn_enso_pdo.

Statistics of Western North Pacific Tropical Cyclone Activity

The Accumulated Cyclone Energy (ACE) index is a well-known statistic that uses the maximum wind speed over time to quantify cyclone activity (Bell, 2001). It is proposed to describe the total TC activity (Waple et al., 2002) and is calculated by integrating the squares of the maximum sustained surface wind every 6 h for named cyclones (greater than 34 knots).

$$\sum_{n=1}^{N} \int_{0}^{D(n)} V_{\max}^{2}(n,t)dt = \text{ACE} \tag{1}$$

where the $V_{\max}$ is the maximum sustained surface wind. As shown in **Eq. 1**, for a specific year the ACE of WNP TCs equals the sum of the square of maximum sustained wind of TCs ($V_{\max}$) over all named TCs (denoted as N in the **Eq. 1**) and the corresponding TC durations (denoted as D in the **Eq. 1**). This definition takes three key factors into account: the TC count, intensity, and duration of all the TCs in the active season of a year and indicates that the annual ACE is the numerical integral of a time series.

According to **Eq. 1**, ACE is a function of the TC intensity, duration and total count, describing the annual TC activity in a basin. To distinguish the individual contributions from the TC intensity, duration and total count to the annual TC activity from the ACE, Wu et al., (2008) defined a parameter of the annual average intensity of TCs for a specific basin. Following the method, the average intensity of WNP TCs for a specific year (denoted as V_a in the **Eq. 2**) is obtained by averaging the Vmax over the duration of each TC and then for all of the TCs in that year.

$$\sum_{n=1}^{N} \int_{0}^{D(n)} V_{\max}(n,t)dt = V_a \cdot \sum_{n=1}^{N} D(n) \tag{2}$$

Therefore, in addition to the parameter of annual ACE index, the annual TC activity in the WNP basin can be characterized by the TC average intensity and the annual accumulated TC duration (total TC days, $\sum_{n=1}^{N} \mathrm{D}(\mathrm{n})$ in **Eq. 2**), and the latter can be further decomposed into TC total count and average duration (Wu et al., 2008; Zhao et al., 2011; Wu and Zhao, 2012).

Statistical Methods

We use a two-tailed Student's t-test to determine the statistical significance of the linear regression and correlation between two autocorrelated time series. The effective number of degrees of freedom is N^{eff}, which is given by the following approximation:

$$\frac{1}{N^{eff}} = \frac{1}{N} + \frac{2}{N} \sum_{j=1}^{N} \frac{N-j}{N} \rho_{XX}(j) \rho_{YY}(j)$$

where N is the sample size, and $\rho_{XX}(j)$ and $\rho_{YY}(j)$ are the autocorrelations of two sampled time series X and Y, respectively, at time lag j (Li et al., 2013; Sun et al., 2015).

Model and Experiments

We use the International Center for Theoretical Physics AGCM (ICTPAGCM, version 41) (Kucharski et al., 2016) developed from the general circulation model (GCM) with a coupled slab ocean thermodynamic mixed-layer model to perform an Atlantic Pacemaker experiment (partially coupled experiment, referred to as ATL_VARMIX). The code of ICTPAGCM is available through the URL: https://www.ictp.it/research/esp/models/speedy.aspx. The mixed-layer model includes spatially varying annual mean mixed-layer depths (varying from 40 m in tropics to 60 m in the extra-tropics). To investigate the WNP SST and atmospheric circulation responses to the Atlantic SST forcing, the SSTs over the Atlantic basin (60°S–60°N, 70°W–10°E) are prescribed using the observational monthly-varying SSTs from the Hadley Center Sea Ice and Sea Surface Temperature (HadISST) data set (Rayner et al., 2003). In the Indo-Pacific basins, the ocean is allowed to integrate the atmospheric heat fluxes and to interact with the atmosphere. Thus, the simulated SSTs in the Indo-Pacific basins are interactively generated by coupling with the slab ocean. The simulated variations in atmospheric circulation are the responses to the combined effects of Atlantic SST forcing and atmosphere-ocean coupling out of the Atlantic region. The large-scale environmental conditions for WNP TC activity in ATL_VARMIX (e.g., MPI and VWS) are further calculated based on the simulation results of SST and atmospheric variables.

The simulations of the ATL_VARMIX experiment are integrated from 1872 to 2013 and an ensemble of five members is generated to reduce the uncertainties due to different initial conditions. The ensemble mean of the five integrations is analyzed and displayed in the figures unless stated otherwise. More details about the ATL_VARMIX simulations can be found in the **Supplementary Material**.

RESULTS

Western North Pacific Tropical Cyclone Average Intensity and Climate Modes

In order to better understand the characteristics of WNP TC time series at decadal time scales, in this study, we mainly focus on the decadal variations of the four annual mean TC metrics, including annual accumulated cyclone energy (ACE), number of TCs (or frequency), total TC days and average intensity between 1950 and 2018, which are calculated using Joint Typhoon Warning Center (JTWC) best track dataset. The detailed definitions of these quantities are given in the *Methods* section. The index of each TC metric in WNP manifests significant decadal variability and two peaks can be found in this time series (**Figure 1**). More specifically, the time series of the TC days index (**Figure 1C**) shows a similar variation to that of ACE (**Figure 1A**) which reaches its maximum in the mid-1990s and exhibits a decreasing trend in the following 15 years. However, the frequency index (**Figure 1B**) reaches its maximum in the mid-1960s, earlier than the ACE and TC days. Here, the average intensity of TCs is defined as the mean intensity of all named cyclones in a year, and the product of the average intensity and the total number of TC days in that year equals the annual ACE index (see *Statistics of Western North Pacific Tropical Cyclone Activity* for details). Moreover, decadal variability in TC average intensity over WNP (**Figure 1D**) is also evident and manifests a decadal trend for about 20 to 30 years. There are two turning signs appearing in the 1970s and around 2000s which resemble the AMO index (Kerr, 2000), further implying the potential linkage between them. More evidence will be discussed in the following sections.

Then, the comparison between the AMO index and annual mean average intensity further supports our speculations based on the consistency of their turning signs. The time series of the AMO index (**Figure 2**) has approximately 50–60 years variation, with changes of sign in reverse polarity in the 1920s, 1960s and around 2000s (Schlesinger and Ramankutty, 1994; Enfield et al., 2001), demonstrating that the AMO and WNP TC average intensity are closely connected and share a similar decadal fluctuation. This result indicates that the variation of WNP

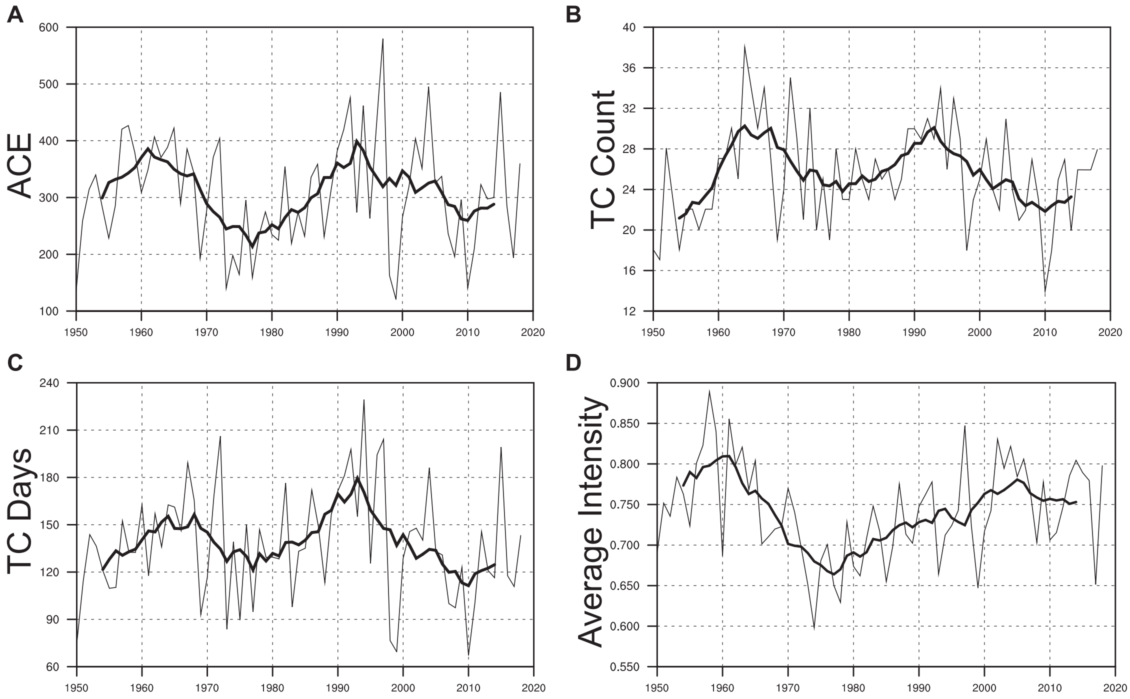

FIGURE 1 | Interannual-to-decadal variability of various TC metrics. Time series of annual mean **(A)** ACE index (unit: $10^4 \cdot$ *knot*^{2}), **(B)** frequency, **(C)** TC days (unit: days) and **(D)** average intensity (unit: $10^2\cdot$ *knot*) of TCs in the western North Pacific as a function of time for 1950–2018 (thin solid black curve). The thick black curve in each panel shows the 9-year running averages. The long-term linear trends were removed.

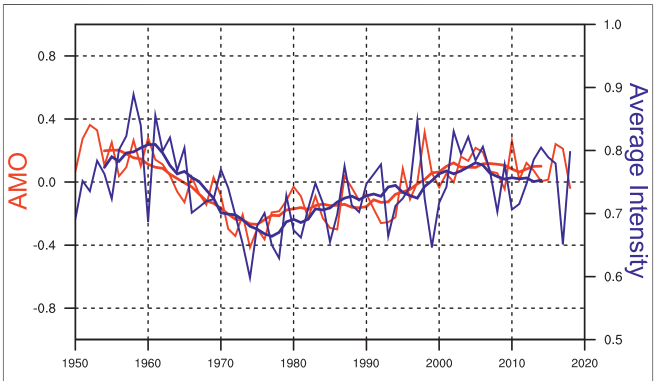

FIGURE 2 | Time series of annual mean average intensity (thin blue curve; unit: $10^2\cdot$ *knot*) and the AMO index (thin red curve; unit: K) for 1950–2018. The thick curves show the 9-year running averages. The long-term linear trends were removed.

TABLE 1 | Correlations Between Four WNP TC Metrics and AMO, PDO, IPO, and NPGO for 1950–2018.

Correlation coefficients	TC days	Frequency	ACE	Average intensity
AMO (1950–2018)	0.36 (13)	−0.35 (10)	0.36 (10)	**0.86** (4)
PDO (1950–2018)	**0.58** (11)	0.41 (9)	0.20 (7)	-0.29 (4)
IPO (1950–2018)	**0.65** (10)	0.46 (9)	0.24 (8)	-0.30 (5)
NPGO (1950–2018)	−**0.72** (12)	−**0.59** (11)	-0.43 (10)	0.10 (6)

The long-term linear trends were removed before analysis. Correlations significant at the 95% level based on the estimated effective degrees of freedom are underlined (in bold). The effective degrees of freedom are included in parentheses next to the correlation coefficient. The calculation of the effective degrees of freedom is given in the Methods.

TC average intensity is highly correlated to the remote AMO signal at decadal time scales and it might be affected by the North Atlantic basin.

As the Pacific Decadal Oscillation (PDO/IPO) (Mantua et al., 1997; Zhang et al., 1997) and North Pacific Gyre Oscillation (NPGO) have been recognized for playing a dominant role in modulating North Pacific SST at decadal time scales, it is essential to examine the correlations of Pacific SST variability with each of the four WNP TC metrics. Several studies have implied the possible effects of PDO, IPO and NPGO on WNP TC activity (Chan, 2008; Liu and Chan, 2008; Goh and Chan, 2010; Zhang et al., 2013). Thus, we further calculate the correlation coefficients between those four TC metrics and these decadal and multidecadal oceanic modes (the time series are shown in **Supplementary Figure S1** and the correlations are listed in **Table 1**), in order to clarify whether Pacific decadal SST variability has such correlations with WNP TC as AMO does and to highlight the relative roles of AMO and Pacific decadal SST variability on WNP TC activity. In general, the variations of the IPO and NPGO index are different from those of the AMO and the WNP TC average intensity, and the correlations of the TC intensity with the IPO and NPGO are low and insignificant. Nevertheless, the NPGO show significant correlations with the WNP TC days and genesis frequency. This is consistent with the previous study which suggests a significant impact of NPGO on TC frequency. Meanwhile, the PDO/IPO might correlate to the total TC days but the correlation coefficient is relatively small. Such findings are consistent with the previous studies which indicated that the PDO plays a minor role in the decadal variations of WNP TC characteristics (i.e., frequency and intensity) and it can barely explain the regional-scale features of WNP climate variability (Zhang et al., 2013; Sun et al., 2017a; Gong et al., 2020). Another interesting thing is that the correlation coefficient between WNP TC average intensity and the AMO index reaches 0.86 ($p < 0.05$), further confirming the strong connection between them as is inferred from **Figure 2**. We can then conclude that the linkage between AMO and WNP TC intensity is robust at decadal time scales, while other TC metrics such as ACE, frequency and TC days show weaker correlations with the AMO.

Previous studies have suggested that the TC intensity records may be less reliable before the mid-1970s (Dvorak 1975; Chu et al., 2002; Ackerman et al., 2018). We repeat the above analysis but for a more recent period 1975–2018. As shown in **Supplementary Table S1**, the average intensity of WNP TCs is mostly correlated with the AMO for 1975–2018, while the effects of other SST modes are relatively insignificant. This is in good agreement with the results for the longer analysis period 1950–2018. The decadal-scale variation in average intensity during 1975–2018 is characterized by an increasing trend before 2000 and a flattening trend afterward. These variations are best matched with the AMO variability, leading to a highly positive correlation (r = 0.89, significant at the 95% confidence level). For the WNP TC days and frequency, the effects of Pacific SST modes (PDO, IPO, and NPGO) are stronger, with strong positive correlations observed for the PDO/IPO and negative correlations for the NPGO during 1975–2018. Similar negative correlations are also observed for the AMO, which shows a general warming trend during 1975–2018, coincident with the decreasing trend in the TC days and frequency. Zhang et al. (2018) have also suggested that the warming trend in AMO may lead to the decreasing of WNP TC frequency during the period 1980–2014. Nevertheless, consistent with the results for the longer period, the correlation of the AMO with the TC average intensity (0.89) is higher than that with the TC days and frequency (−0.71 and −0.68, respectively), indicating a more profound influence of AMO on the WNP TC intensity. **Supplementary Figure S2** further shows the correlation map between WNP TC average intensity and Northern Hemisphere SST at decadal timescales for the period 1975–2018. The SST correlations over the North Atlantic show a basin-wide coherent pattern with significant positive values that resembles the AMO. Therefore, both the analyses of temporal variations and the spatial pattern of SST correlations confirm the close relationship between the AMO and WNP TC average intensity for the more recent period 1975–2018, indicating that the finding of AMO footprint in WNP TC average intensity is insensitive to the analysis period.

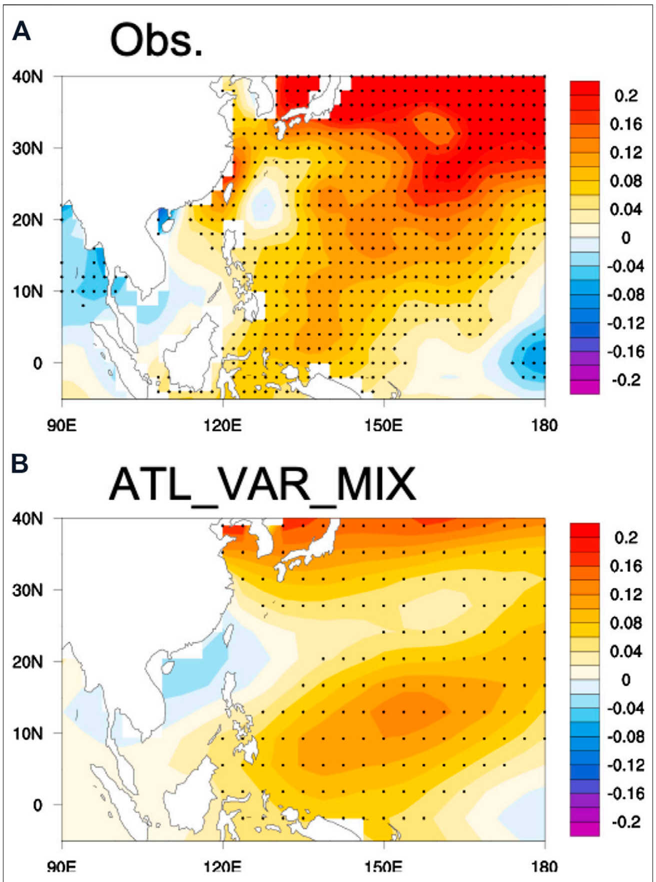

FIGURE 3 | (A) The regression map of SST anomalies (unit: K) onto the normalized AMO index based on the data from the ERSST data for 1950–2010. **(B)** As in **(A)**, but in the ATL_VARMIX experiment. The long-term linear trends in the SST data set were removed before the regression analysis, and dots indicate the regression coefficients significant at the 95% confidence level.

Western North Pacific Tropical Cyclone Average Intensity and TC Activity

The average intensity of TCs over the WNP basin is a basin-wide metric, and it is necessary to examine the relationships between this basin-wide metric and variations in TC characteristics (i.e., genesis location and track distributions). Observed TC data are obtained from the International Best Track Archive for Climate Stewardship (IBTrACS) including the Joint Typhoon Warning Center (JTWC), Japan Meteorological Agency (JMA), and Chinese Meteorological Administration (CMA) best track data. **Supplementary Figure S3** shows the regression map of the annual genesis density of WNP TCs on the basin-wide average intensity. The genesis density is calculated by counting the number of tropical cyclones with genesis (first position) in each 2.5° × 2.5° latitude and longitude square (Camargo et al., 2007). The regression map shows that the increase (decrease) of the TC average intensity corresponds to more TC genesis over the western WNP basin and less TC genesis over the eastern WNP basin. The results based on the data sets from the three agencies are similar. We also analyze the relationship between average TC intensity and track distributions. The time series of WNP TC average intensity shows a period of weak intensity during 1970–1990 and two periods of strong intensity during 1950–1964 and 1996–2015. As shown in **Supplementary Figure S4**, the average TC genesis location during the strong intensity period (1950–1964 and 1996–2015) is to the west of that during the weak intensity period (1970–1990). This is consistent with the results of TC genesis density shown in **Supplementary Figure S3**. For the average TC track distributions, the TCs during the strong intensity period show a more north-oriented track compared with the weak intensity period, and the average TC track during the strong intensity period extends farther northward than the weak intensity period. Therefore, during the high TC intensity period, the TCs in the WNP basin tend to travel a relatively long distance. In addition, the intensity-related variations in TC genesis locations and track distributions for the TC active season (JJASO, **Supplementary Figure S5**) are generally consistent with the annual ones (**Supplementary Figures S3**, **S4**). Overall, the increase of WNP average TC intensity is associated with the westward shift of the TC genesis locations and the more northward extension of TC tracks.

Previous studies (Byers, 1944; Palmen, 1948; Malkus and Riehl, 1960; Chan et al., 2001) have illustrated the fundamental physical basis between TC average intensity and the ocean boundary and confirmed that the warm SST is favorable to the intensification of TCs over the Northern Hemisphere Oceans. Here, regression analyses are used to quantify the relationships between those factors associated with TC intensity and AMO index and to reveal the underlying mechanism. The regression map of 9-year running mean observational SST anomalies onto the normalized AMO index (**Figure 3A**) exhibits significant positive SST anomalies over the most area of the WNP region despite a slight northward shift of the maximum. The warm SST anomalies are strong and statistically significant over the western WNP basin, while over the eastern WNP, the SST anomalies are relatively weak and nearly opposite to the western WNP. We further calculate the latitudinal average of SST anomalies between the equator and 20°N (**Supplementary Figure S6**), which also shows a peak of warm SST anomalies between 110°E and 150°E, and east of 150°E, the SST anomalies decrease rapidly and become weak. This feature of WNP SST anomalies may explain the changes in the average genesis location of TCs revealed in the above analysis, and hence the average intensity of TCs formed in the WNP basin.

We can further infer that the AMO indeed affects WNP TC through modifying SST at decadal time scales, but the causality cannot be suggested only by statistical analysis. We then perform model simulations to further verify the remote effects of AMO on the WNP SST. Similar results can be found in the ATL_VARMIX experiment (Atlantic Pacemaker experiment, see *Methods*). The simulated regression pattern of WNP SST onto the AMO index is consistent with the observed one, and the regression coefficients are significant over the WNP region. Overall, the experiment does indicate the existence of warming responses of WNP SST to the AMO and the results are consistent with previous studies that explain the underlying mechanism of such phenomenon (Sun et al., 2017a; Gong et al., 2020; Wu et al., 2020). The warm AMO phase could induce anomalous surface high pressures over the northern and eastern Pacific which generate diverging flow toward the WNP, leading to anomalous convergence and low pressures there. The warm SST anomaly further develops due to the SST–sea level pressure–cloud–longwave radiation positive feedback. For the TC active season (June to October, JJASO), both observations and ATL_VARMIX simulations suggest a significant inter-basin SST teleconnection from North Atlantic to the WNP (**Supplementary Figure S7**), consistent with the annual mean data (**Figure 3**). The AMO-induced atmospheric teleconnection pattern is also similar to that based on annual mean data, showing anomalous high pressures in the northern and eastern Pacific accompanied by diverging flow toward the WNP. The WNP is dominated by anomalous convergence and low-pressure anomaly (**Supplementary Figure S7**), and the warm SST anomaly can be further developed and maintained through the local air-sea interaction. We can infer that the AMO may influence WNP TC average intensity by modifying SSTs in association with the inter-basin teleconnection. As shown in **Figure 3B**, the model shows the capability to reproduce the strong warm SST anomalies over the western WNP and rather weak SST anomalies in the eastern WNP, and the simulated latitudinal average of SST anomalies between the equator and 20°N also shows a peak of warm SST anomalies over the western WNP basin. It should be also noted that there is a discrepancy of SST anomaly center between observations and model simulations, indicating that the model experiment shows limitations in simulating the centers of maximum SST anomalies in the WNP associated with the AMO. Nevertheless, the model experiment reasonably reproduces the basin-wide SST warming in the WNP in response to the warm AMO phase, and the main structure of the observed SST anomaly pattern in the tropical WNP and the amplitude are fairly well reproduced by the model.

The effects of local SST changes on the WNP TC intensity at decadal timescales have also been highlighted in the previous studies (Wu and Zhao, 2012; Mei et al., 2015). Wu and Zhao (2012) compared the individual contributions of changes in local SST, vertical wind shear, and prevailing tracks to the increasing trend in WNP TC intensity over the period 1975–2007. They found that while the individual changes in vertical shear and prevailing tracks played an insignificant role in TC intensity, the warming SST over the period 1975–2007 significantly contributed to the multidecadal increasing trend in TC intensity. This is consistent with our present study that we also find the TC average intensity in WNP is closely related to the local SST at decadal timescales, and the increasing trend of TC average intensity is coincident with the SST warming during the period 1975–2018 (**Supplementary Figure S2**).

The relationship between local SST and TC intensity may be timescale dependent. The interannual component of TC average intensity is shown in **Supplementary Figure S8** by using a 2–9-

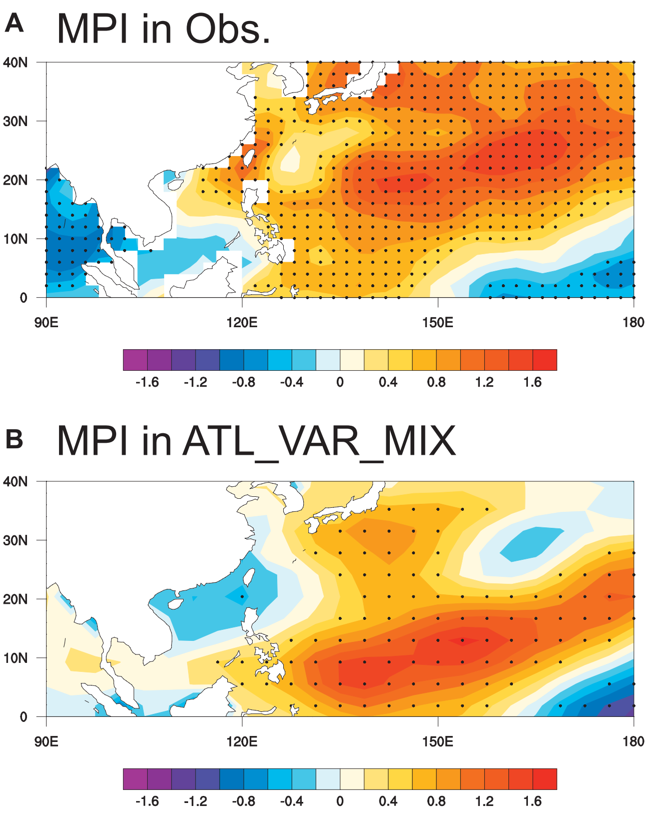

FIGURE 4 | The regression map of maximum potential intensity anomalies (m/s) onto the normalized AMO index based on the observational SST and 20CR atmospheric data for 1950–2010. **(B)** As in **(A)**, but in the ATL_VARMIX experiment. The long-term linear trends in the data were removed before the regression analysis, and dots indicate the regression coefficients significant at the 95% confidence level.

year band-pass filter. The correlation map of SST with interannual TC intensity is further shown in **Supplementary Figure S8**. The SST correlations clearly indicate an ENSO-like pattern, with positive correlations over the tropical central and eastern Pacific while negative correlations over the WNP region. This suggests that the ENSO significantly influences the WNP TC intensity at interannual timescales as previous studies suggested (Zhao et al., 2011). On the other hand, the negative SST correlations in WNP indicate that the dynamical large-scale parameters may play a more important role than the WNP local SST in the linkage between ENSO and WNP TC intensity (Zhao et al., 2011).

Roles of Large-Scale Environmental Factors

Relationships between the AMO index and other factors influencing WNP TC intensity are also examined. The moist convection associated with those factors plays a dominant role in the development of TCs and their average intensity (Raymond and Sessions, 2007). The maximum potential intensity is a direct quantity to represent the effects of large-scale environmental conditions on the TC intensity. Using the maximum potential intensity (MPI) theory (Bister and Emanuel 2002; Emanuel 2018), the estimated TC MPI anomalies in the WNP basin related to the AMO are shown in **Figure 4A**. The anomaly pattern suggests that the AMO-induced changes in SST and atmospheric conditions could result in significant variations in the MPI of TCs over the WNP, namely, the warm (cold) AMO phase could cause an overall significant increase (decrease) in the TC MPI. Particularly, at the lower latitudes (south of 10°N), the MPI anomaly pattern shows significant positive anomalies over the western WNP, and in the eastern WNP, the anomalies are relatively weak and nearly of opposite sign. This pattern of the MPI is consistent with the SST anomalies, further suggesting a key role of SST anomalies in modulating, the intensity of TCs in WNP. In this study, the MPI is used as a proxy to represent the effects of large-scale environmental conditions on the TC intensity. At decadal timescales, the variability of WNP MPI is closely related to the TC average intensity, indicating a significant impact of large-scale environmental conditions over the WNP (**Supplementary Figure S9**). In **Figure 5B**, lower tropospheric air temperature over the WNP region exhibits a uniformly warming response to the AMO. The sea level pressure (SLP) field is first examined, and the regression between AMO and SLP (**Figure 5A**) shows prominent consistency with that in SST. The warming in the ocean surface related to the AMO would further decrease the sea surface pressure over the entire WNP region. Thus, it supports that the WNP SSTs interact with the AMO and favor more intense TCs to develop. Corresponding to the responses of WNP SST to the AMO, it could be induced by the ocean-atmosphere interaction, with more heat fluxes released from a warmer ocean surface. The pattern of air temperature over 300 hPa shows similar results, but more significant warming can be found over the WNP region. Despite the differences in distributions of maximum centers between upper and lower troposphere, it still indicates tropospheric warming in WNP associated with the AMO. As for specific humidity (**Figures 5C,D**), positive moisture anomalies are most pronounced in WNP, especially near the tropics. Unlike the air temperature, the lower-level specific humidity shows more significantly increased responses to the AMO than the upper level, which is probably due to more water vapor content at the lower level and thus is more sensitive to the temperature changes.

By calculating the regressions of each factor onto the AMO index, potential linkages between them can be addressed as follow. All the variables exhibit significant responses to the AMO. In the WNP region, the SST warming induced by the AMO would reduce the sea surface pressure and increase the low-level air temperature, further intensifying the ascending motion and increasing the water vapor content. As a result, more water vapor could be pumped into the upper troposphere and release the latent heat above the lifting condensation level (LCL), heating the air over upper levels. Previous studies have pointed out that the increased low-level specific humidity and warm air temperature anomalies would intensify convective activity, such as TC (Gettelman et al., 2002; Chen et al., 2019). Low-level specific humidity can intensify positive buoyancy and more latent heat release, and in this case, the decrease in SLP provides

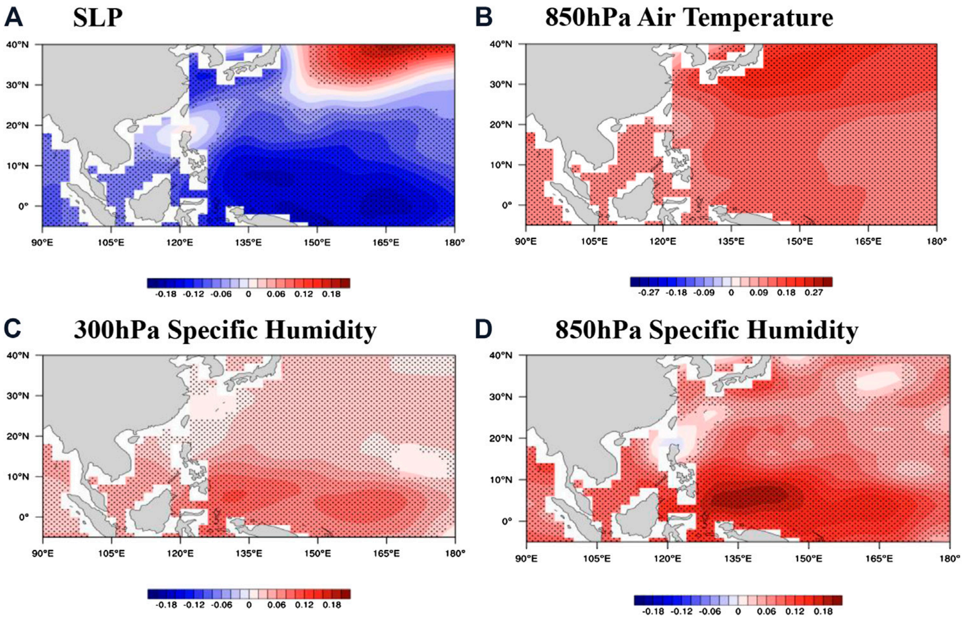

FIGURE 5 | The regression maps of **(A)** sea level pressure (unit: hPa), **(B)** 850 hPa air temperature anomalies (unit: K), **(C)** 300 hPa specific humidity anomalies (unit: $g \cdot kg^{-1}$), and **(D)** 850 hPa specific humidity anomalies (unit: $g \cdot kg^{-1}$) onto the normalized AMO index for 1950–2010 in 20CR reanalysis data. Dotted shading in **(A–D)** represents the regression coefficients significant at the 95% confidence level. The long-term linear trends for 1950–2010 in all variables were removed before the regression analysis.

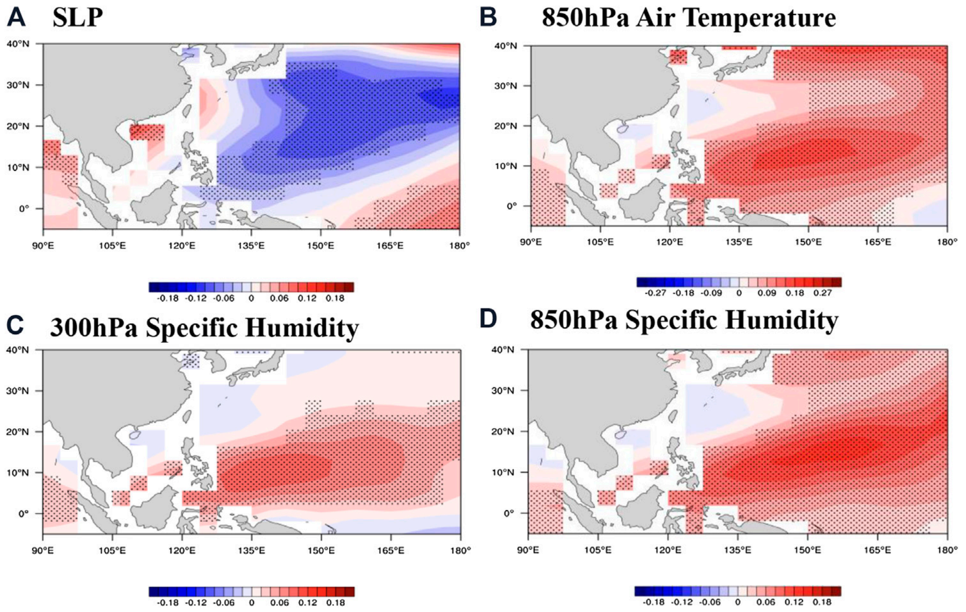

FIGURE 6 | The regression maps of **(A)** sea level pressure (unit: hPa), **(B)** 850 hPa air temperature anomalies (unit: K), **(C)** 300 hPa specific humidity anomalies (unit: $g \cdot kg^{-1}$), and **(D)** 850 hPa specific humidity anomalies (unit: $g \cdot kg^{-1}$) onto the normalized AMO index for 1950–2010 in the ATL_VARMIX experiment. Dotted shading represents the regression coefficients significant at the 95% confidence level. The long-term linear trends were removed.

favorable initial perturbation for the air parcel being easily lifted and passes the level of free condensation (LFC) to derive convective energy from the atmosphere and be able to ascend automatically. The WNP convective available potential energy (CAPE) anomalies in response to the remote AMO SST forcing correspond to the local SST warming and exhibit significantly increased responses over most of the WNP region (**Supplementary Figure S10**). Thus, more CAPE will be produced with more latent heat released, and stronger warming and moistening at the lower level further amplifies this effect. Previous studies have also pointed out that the increased low-level specific humidity and warm air temperature anomalies would contribute to more CAPE genesis, which plays an important role in the rapid intensification of the WNP TCs (Gao et al., 2017), and the enhanced CAPE further acts as a crucial bridge linking the WNP SST warming and increase TC intensity. Meanwhile, other variables, especially to air temperature and specific humidity which are favorable to the increased MPI, also exhibit physically consistent responses to the AMO. Based on the observation and the ATL_VARMIX simulations, we can so far conclude that WNP atmospheric variables are closely linked to the remote AMO and shows significantly increased responses.

Model simulation is then carried out to highlight the role of AMO in the anomalies of atmospheric variables related to the WNP TC intensity, and the same calculations performed in **Figure 4A** and **Figure 5** are also applied to the ATL_VARMIX experiment. The Atlantic pacemaker experiment (ATL_VARMIX) captures the main structure of the MPI anomalies in the observation (**Figure 4B**), further indicating that the AMO signal could induce an overall increase/decrease in the MPI of TCs over the WNP. The SLP response to the AMO (**Figure 6A**) is similar to that in the observation, as the decrease in SLP induced by the AMO can be seen in the WNP region. In addition, the distribution of significant regression coefficients, corresponding to the SST warming, shows prominent consistency with the observation. It should be noted that the physical connections between MPI and other variables (SLP, air temperature and water vapor) are well captured by the model, as the variables in WNP show consistent anomalies in response to the North Atlantic SST forcing. Nevertheless, the vertical structure of air temperature in response to the AMO exhibits different quantitative relationships between the upper and lower level. In the ATL_VARMIX, the lower-level air temperature shows stronger warming responses to the AMO, compared with the upper level. The simulated distribution of the maximum responses of 850 hPa air temperature to the AMO (**Figure 6B**) is located over the WNP region, which is consistent with the simulated SST anomalies as more heat is released from a warmer ocean surface (**Figure 3B**). The distributions of upper-level and low-level specific humidity anomalies under the AMO forcing (**Figures 6C,D**) are similar to the observational results (**Figure 5C and 5D**). In the ATL_VARMIX experiment, WNP atmospheric factors exhibit significant responses to the AMO, which is also consistent with the observation. This result provides model evidence for the conclusion emphasized above, that both troposphere air warming and moistening are favorable for the TC average intensity under the AMO forcing in the WNP region.

Given the significant relationships between AMO, MPI and those associated factors have been discussed above (the correlation maps are also shown in Supplementary Material), how do they influence the TC intensity and connect it to the remote AMO? First of all, SST has long been recognized as the primary factor that modifies the TC intensity. Model evidence suggests that when other environmental factors are fixed, the varied SST still contributes to the variations in TC intensity. In the WNP region, strong responses can be found in local SST to the AMO forcing (Sun et al., 2017a; Wu et al., 2020). The warmed SST related to the AMO would lower the minimum central pressure around the core and provide favorable backgrounds, such as large-scale convergence and SLP decrease for the ascending motion (**Figures 5A**, **6A**). Thus, more energy can be released from the ocean to the atmosphere and directly contributes to the intensification of TC activities. In addition, SST warming would increase the water vapor content and enhance the moist instability over the lower troposphere (**Figures 5D**, **6D**). As mentioned above, the WNP SST warming induced by the AMO through the inter-basin SST teleconnection (Sun et al., 2017a; Gong et al., 2020) can partially explain such correlation between WNP TC intensity and the AMO. Moreover, WNP SST warming also induces significant changes in the vertical stability of the atmospheric column that may regulate the development of TCs. The TC intensity is closely linked to the ascending motion in the eyewall that the air parcel must extract energy from the ocean

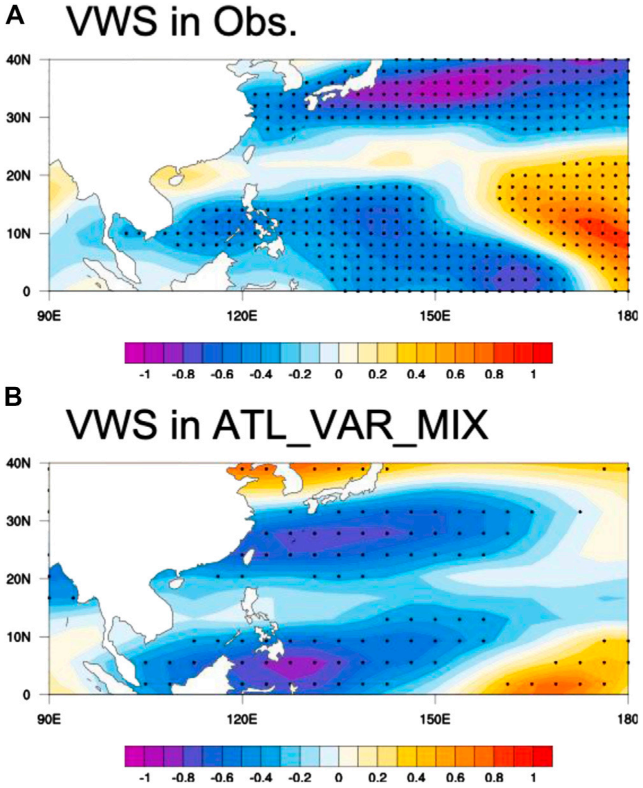

FIGURE 7 | The regression map of vertical wind shear (wind differences between 850 hPa and 200 hPa levels, m/s) anomalies onto the normalized AMO index based on the data from the 20CRv2 for 1950–2010. **(B)** As in **(A)**, but in the ATL_VARMIX experiment. The long-term linear trends in the data were removed before the regression analysis, and dots indicate the regression coefficients significant at the 95% confidence level.

and atmosphere to fight against gravity for elevation. In association with the WNP SST warming, the local SLP decrease and tropospheric warming and moistening lead to the increase of MPI over the WNP region (**Figures 4A,B**) and hence provide a favorable environment for TC intensification. Therefore, the interaction between lower-boundary SST and atmospheric factors intensifies the deep convection and provides energy to drive the development of TCs. Based on that, the strong connection between AMO and WNP TC intensity can be explained by the inter-basin footprints of AMO on the WNP SST and the associated atmospheric states.

We finally investigate the role of vertical wind shear (VWS) in the modulation of the WNP TC variations. The regression maps of WNP VWS anomalies on the AMO index are shown in **Figure 7**. In association with the warm AMO phase, the VWS anomalies over the WNP show an overall reduction over the WNP region, corresponding to the overall increase of average TC intensity. This suggests that the VWS indeed plays an important role in the connection between AMO and average TC intensity in the WNP. In addition, the zonal structure of the VWS at the lower latitudes shows a nearly dipole structure, with significantly reduced VWS over the western WNP and stronger VWS over the eastern WNP. The weakened-VWS region extends eastward to about 170°E, but the intensified-VWS region is limited to the east of 170°E. This pattern of VWS anomalies is consistent with the previous study (Zhang et al., 2018). The SST warming in WNP induces strong lower-level convergence, accompanied by lower-level westerly anomalies in the western WNP and easterly anomalies to the east (Sun et al., 2017a). Given the climatological easterlies in the lower levels over the WNP region, the intensified easterlies induce stronger VWS over the eastern WNP and westerly anomalies tend to weaken the VWS (Zhang et al., 2018), leading to the anomaly pattern of VWS shown in **Figure 7**. Moreover, the pattern of VWS is also consistent with the changes in genesis locations of WNP TCs, leading to the westward shift of TC genesis locations (Zhang et al., 2018). The overall reduction of WNP VWS and its spatial pattern are reproduced in the ATL_VARMIX simulations, providing further modeling evidence to support the influence of AMO on the WNP VWS, which could further affect the TC intensity.

SUMMARY AND DISCUSSION

In this study, we find a significant decadal variability of TC activity in the WNP region, based on the observational data set from 1950 to 2018. Statistical analysis of the various TC metrics suggests that the average intensity of WNP TCs is strongly connected with the AMO ($r = 0.86$ at decadal timescales, $p < 0.05$), showing a much closer relationship than other TC statistics (i.e., frequency and TC days). Observations and coupled atmosphere-ocean simulations show significant decadal SST warming over the WNP region in response to the AMO warm phase, which acts as a primary driver of the increase in TC intensity. The associated atmospheric changes also provide a favorable background environment. Corresponding to the SST warming, the local SLP decrease and the tropospheric air warming and moistening would enhance the atmospheric instability, which provides more energy to the development of deep convection and intensify the WNP TCs. In conclusion, the AMO-induced changes in SST and atmospheric states in WNP through trans-basin interaction eventually exert a significant impact on the TC intensity over the WNP region.

This study reveals a close relationship between AMO and WNP TC average intensity. The connections of AMO with other TC metrics, like the genesis frequency, are relatively weak. A possible explanation for this may lie in the distribution of the anomalous genesis density (**Supplementary Figure S3**). The genesis density anomaly pattern associated with the AMO indicates a westward/eastward shift of the WNP TC genesis rather than a basin-wide increase/decrease of the TC genesis over the entire WNP region. This anomalous pattern of WNP TC genesis density can be explained by the VWS anomalies (**Figure 7**). During the warm AMO phase, the VWS shows weakened VWS in the western WNP and intensified VWS in the eastern WNP, leading to the westward shift of TC genesis locations.

Our findings may help us better understand the impacts of AMO on the WNP climate, especially to the TC activity, which causes large damage to the adjacent countries. Thus, it could be a useful indicator for TC intensity prediction, when we take the North Atlantic signal into consideration. The main findings in the present study are based on the available records of WNP TC data since 1950, and future research is warranted as more observational records accumulate. Although the fundamental linkage between WNP TC intensity and the AMO can be reasonably well reproduced by the model, some biases can still be found, possibly due to the simplified and idealized physics of the coupled model. Thus, state-of-the-art coupled models with more comprehensive physics would be needed to better reproduce such mechanisms and reduce model uncertainties. The mixed layer ocean model shows the capability to reproduce the roles of SST and large-scale environment conditions in connecting the AMO to WNP TC intensity. Despite this, further modeling studies are required to understand the possible role of ocean dynamics in shaping the AMO-TC intensity linkage. A shortcoming of the simulations in the current study is low resolution, and TCs cannot be directly simulated by the model. Nevertheless, the main findings here indicate that statistical insights into the variations of TC metrics may be gained from these simulations.

DATA AVAILABILITY STATEMENT

The original contributions presented in the study are included in the article/**Supplementary Material**, further inquiries can be directed to the corresponding author.

AUTHOR CONTRIBUTIONS

CS designed the research. CS, ZG, and YL performed the data analysis, prepared all figures and led the writing of the manuscript. All the authors discussed the results and commented on the manuscript.

FUNDING

This work was jointly supported by the National Natural Science Foundation of China (41775038, 41790474, and 41975082), National Key Research and Development Program of China (2016YFA0601801), and the National Program on Global Change and Air–Sea Interaction (GASI-IPOVAI-06 and GASI-IPOVAI-03).

SUPPLEMENTARY MATERIALS

The Supplementary Material for this article can be found online at: https://www.frontiersin.org/articles/10.3389/feart.2020.604807/full#supplementary-material

REFERENCES

Ackerman, S., Platnick, S., Bhartia, P., Duncan, B., L'ecuyer, T., Heidinger, A., et al. (2018). Satellites see the world's atmosphere. *Meteorol. Monogr.* 59, 4.1–4.53. doi:10.1175/AMSMONOGRAPHS-D-18-0009.1

Bell, W. (2001). Report 10. ESCAP Ii: estimation of correlation bias in 2000 ace estimates using revised demographic analysis results executive steering committee for ACE policy II.

Bister, M., and Emanuel, K. A. (2002). Low frequency variability of tropical cyclone potential intensity 1. Interannual to interdecadal variability. *J. Geophys. Res.: Atmosphere* 107 (D24), ACL 26-1–ACL 26-15. doi:10.1029/2001jd000776

Byers, H. R. (1944). "Atmospheric turbulence and the wind structure near the surface of the earth," in *General meteorology* (New York: McGraw-Hill Book Co., Inc.), ch. XXIV.

Camargo, S. J., and Sobel, A. H. (2005). Western North pacific tropical cyclone intensity and enso. *J. Clim.* 18 (15), 2996–3006. doi:10.1175/jcli4282.1

Camargo, S. J., Emanuel, K. A., and Sobel, A. H. (2007). Use of a genesis potential index to diagnose enso effects on tropical cyclone genesis. *J. Clim.* 20 (19), 4819–4834. doi:10.1175/jcli3457.1

Chan, J. C. L., Shi, J.-E., and Liu, K. S. (2001). Improvements in the seasonal forecasting of tropical cyclone activity over the western North pacific. *Weather Forecast.* 16 (4), 491–499. doi:10.6057/2012TCRR03.07

Chan, J. C. L. (1985). Tropical cyclone activity in the northwest pacific in relation to the el niño/southern oscillation phenomenon. *Mon. Weather Rev.* 113 (4), 599–606. doi:10.1175/1520-0493(1985)113<0599:TCAITN>2.0.CO;2

Chan, J. C. (2006). Comment on" changes in tropical cyclone number, duration, and intensity in a warming environment. *Science* 311 (5768), 1713. doi:10.1126/science.1121522

Chan, J. C. L. (2008). Decadal variations of intense typhoon occurrence in the western North pacific. *Proc. Math. Phys. Eng. Sci.* 464, 249–272.

Chen, X., Zhang, J. A., and Marks, F. D. (2019). A thermodynamic pathway leading to rapid intensification of tropical cyclones in shear. *Geophys. Res. Lett.* 46 (15), 9241–9251. doi:10.1029/2019gl083667

Chu, J.-H., Sampson, C. R., Levine, A. S., and Fukada, E. (2002). The joint typhoon warning center tropical cyclone best-tracks, 1945–2000. Ref. NRL/MR/7540-02 16

Compo, G. P., Whitaker, J. S., Sardeshmukh, P. D., Matsui, N., Allan, R. J., Yin, X., et al., (2011). The Twentieth Century reanalysis project. *Q. J. R. Meteorol. Soc.* 137 (654), 1–28. doi:10.1002/qj.776

Dvorak, V. F. (1975). Tropical cyclone intensity analysis and forecasting from satellite imagery. *Mon. Weather Rev.* 103, 420–430. doi:10.1175/1520-0493(1975)103<0420:TCIAAF>2.0.CO;2

Emanuel, K. (2005). Increasing destructiveness of tropical cyclones over the past 30 years. *Nature* 436 (7051), 686–688. doi:10.1038/nature03906

Emanuel, K. (2018). 100 years of progress in tropical cyclone research. *Meteorol. Monogr.* 59, 15.1–15.68. doi:10.1175/AMSMONOGRAPHS-D-18-0016.1

Enfield, D. B., Mestas-Nuñez, A. M., and Paul, J. T. (2001). The Atlantic multidecadal oscillation and its relation to rainfall and river flows in the continental us. *Geophys. Res. Lett.* 28 (10), 2077–2080. doi:10.1029/2000gl012745

Gao, S., Chen, Z., and Zhang, W. (2018). Impacts of tropical North Atlantic SST on western North Pacific landfalling tropical cyclones. *J. Clim.* 31, 853–862. doi:10.1175/jcli-d-17-0325.1

Gao, S., Chen, Z., Zhang, W., and Shen, X. (2020). Effects of tropical North Atlantic sea surface temperature on intense tropical cyclones landfalling in China. *Int. J. Climatol.* doi:10.1002/joc.6732

Gao, S., Zhai, S. N., Chen, B. Q., and Li, T. (2017). Water budget and intensity change of tropical cyclones over the western North pacific. *Mon. Weather Rev.* 145, 3009–3023. doi:10.1175/mwr-d-17-0033.1

Gettelman, A., Seidel, D. J., Wheeler, M. C., and Ross, R. J. (2002). Multidecadal trends in tropical convective available potential energy. *J. Geophys. Res. Atmosphere* 107 (D21), 4606. doi:10.1029/2001jd001082

Goh, A. Z.-C., and Chan, J. C. L. (2010). Interannual and interdecadal variations of tropical cyclone activity in the south China sea. *Int. J. Climatol.* 30 (6), 827–843. doi:10.1002/joc.1943

Gong, Z., Sun, C., Li, J., Feng, J., Xie, F., Ding, R., et al. (2020). An inter-basin teleconnection from the north Atlantic to the subarctic North Pacific at multidecadal time scales. *Clim. Dynam.* 54 (1-2), 807–822. doi:10.1007/s00382-019-05031-5

Gray, W. M., and Brody, L. (1967). Global view of the origin of tropical disturbances and storms: citeseer.

Huo, L., Guo, P., Hameed, S. N., and Jin, D. (2015). The role of tropical Atlantic sst anomalies in modulating western North pacific tropical cyclone genesis. *Geophys. Res. Lett.* 42 (7), 2378–2384. doi:10.1002/2015gl063184

Kerr, R. A. (2000). A North Atlantic climate pacemaker for the centuries. *Science* 288 (5473), 1984–1985. doi:10.1126/science.288.5473.1984

Knapp, K. R., Kruk, M. C., Levinson, D. H., Diamond, H. J., and Neumann, C. J. (2010). The international best track archive for climate stewardship (ibtracs) unifying tropical cyclone data. *Bull. Am. Meteorol. Soc.* 91 (3), 363–376. doi:10.1175/2009bams2755.1

Knapp, K. R., Velden, C. S., and Wimmers, A. J. (2018). A global climatology of tropical cyclone eyes. *Mon. Weather Rev.* 146 (7), 2089–2101. doi:10.1175/mwr-d-17-0343.1

Knutson, T, Camargo, S. J., Chan, J. C. L., Emanuel, K., Ho, C.-H., Kossin, J., et al. (2020). Tropical cyclones and climate change Assessment: Part II: projected response to Anthropogenic warming. *Bull. Am. Meteorol. Soc.* 101 (3), E303–E322. doi:10.1175/BAMS-D-18-0194.1

Knutson, T., Camargo, S. J., Johnny, C. L., Emanuel, K., Ho, C.-H., James, K., et al. (2019). Tropical cyclones and climate change Assessment: Part I: detection and attribution. *Bull. Am. Meteorol. Soc.* 100 (10), 1987–2007. doi:10.1175/BAMS-D-18-0189.1

Kucharski, F., Parvin, A., Rodriguez-Fonseca, B., Farneti, R., Martin-Rey, M., Polo, I., et al. (2016). The teleconnection of the tropical Atlantic to indo-pacific sea surface temperatures on inter-annual to centennial time scales: a review of recent findings. *Atmosphere* 7 (2), 29. doi:10.3390/atmos7020029

Landsea, C. W. (2005). Hurricanes and global warming. *Nature* 438 (7071), E11–E12. doi:10.1038/nature04477

Leung, Y. K., Wu, M. C., and Chang, W. L. (2005). Variations of tropical cyclone activity in the south China sea. *ESCAP/WMO Typhoon Committ. Ann. Rev.* 1, 277–292. doi:10.6057/2012TCRR02.01

Li, J., Sun, C., and Jin, F.-F. (2013). NAO implicated as a predictor of northern Hemisphere mean temperature multidecadal variability. *Geophys. Res. Lett.* 40 (20), 5497–5502. doi:10.1002/2013GL057877

Li, R. C. Y., and Zhou, W. (2014). Interdecadal change in south China sea tropical cyclone frequency in association with zonal sea surface temperature gradient. *J. Clim.* 27 (14), 5468–5480. doi:10.1175/jcli-d-13-00744.1

Li, R. C. Y., Zhou, W., and Li, T. (2014). Influences of the pacific–Japan teleconnection pattern on synoptic-scale variability in the western North pacific. *J. Clim.* 27 (1), 140–154. doi:10.1175/jcli-d-13-00183.1

Li, S., and Bates, G. T. (2007). Influence of the Atlantic multidecadal oscillation on the winter climate of east China. *Adv. Atmos. Sci.* 24 (1), 126–135. doi:10.1007/s00376-007-0126-6

Liu, K. S., and Chan, J. C. L. (2008). Interdecadal variability of western North pacific tropical cyclone tracks. *J. Clim.* 21 (17), 4464–4476. doi:10.1175/2008jcli2207.1

Liu, K. S., and Chan, J. C. L. (2013). Inactive period of western North pacific tropical cyclone activity in 1998–2011. *J. Clim.* 26 (8), 2614–2630. doi:10.1175/JCLI-D-12-00053.1

Liu, Y., and Chen, G. (2018). Intensified influence of the enso modoki on boreal summer tropical cyclone genesis over the western North pacific since the early 1990s. *Int. J. Climatol.* 38, e1258–e1265. doi:10.1002/joc.5347

Lopez, H., Dong, S., Lee, S.-K., and Goni, G. (2016). Decadal modulations of interhemispheric global atmospheric circulations and monsoons by the south Atlantic meridional overturning circulation. *J. Clim.* 29 (5), 1831–1851. doi:10.1175/JCLI-D-15-0491.1

Lu, R., Dong, B., and Ding, H. (2006). Impact of the Atlantic multidecadal oscillation on the Asian summer monsoon. *Geophys. Res. Lett.* 33 (24), L24701. doi:10.1029/2006gl027655.

Malkus, J. S., and Riehl, H. (1960). On the dynamics and energy transformations in steady-state hurricanes. *Tellus* 12 (1), 1–20. doi:10.1111/j.2153-3490.1960.tb01279.x

Maloney, E. D., and Hartmann, D. L. (2001). The madden–julian oscillation, barotropic dynamics, and North pacific tropical cyclone formation. Part I: observations. *J. Atmos. Sci.* 58 (17), 2545–2558. doi:10.1175/1520-0469(2001)058<2545:tmjobd>2.0.co;2

Mantua, N. J., Hare, S. R., Zhang, Y., Wallace, J. M., and Francis, R. C. (1997). A pacific interdecadal climate oscillation with impacts on salmon production. *Bull. Am. Meteorol. Soc.* 78 (6), 1069–1080. doi:10.1175/1520-0477(1997)078<1069:apicow>2.0.co;2

McCabe, G. J., Palecki, M. A., and Betancourt, J. L. (2004). Pacific and Atlantic Ocean influences on multidecadal drought frequency in the United States. *Proc. Natl. Acad. Sci. U.S.A.* 101 (12), 4136–4141. doi:10.1073/pnas.0306738101

McGregor, S., Timmermann, A., Stuecker, M. F., England, M. H., Merrifield, M., Jin, F.-F., et al. (2014). Recent walker circulation strengthening and pacific cooling amplified by Atlantic warming. *Nat. Clim. Change* 4 (10), 888–892. doi:10.1038/nclimate2330

Mei, W., Xie, S.-P., Primeau, F., Mcwilliams, J. C., and Pasquero, C. (2015). Northwestern Pacific typhoon intensity controlled by changes in ocean temperatures. *Sci. Adv.* 1, e1500014. doi:10.1126/sciadv.1500014

Nakazawa, T. (1986). Intraseasonal variations of olr in the tropics during the fgge year. *J. Meteorolog. Soc. Japan. Ser. II* 64 (1), 17–34. doi:10.2151/jmsj1965.64.1_17

Palmen, E. (1948). On the formation and structure of tropical hurricanes. *Geophysica* 3 (1), 26–38.

Patricola, C. M., Camargo, S. J., Klotzbach, P. J., Saravanan, R., and Chang, P. (2018). The influence of enso flavors on western North pacific tropical cyclone activity. *J. Clim.* 31 (14), 5395–5416. doi:10.1175/jcli-d-17-0678.1

Raymond, D. J., and Sessions, S. L. (2007). Evolution of convection during tropical cyclogenesis. *Geophys. Res. Lett.* 34 (6), L06811. doi:10.1029/2006gl028607

Rayner, N. A. A., Parker, D. E., Horton, E. B., Folland, C. K., Alexander, L. V., Rowell, D. P., et al. (2003). Global analyses of sea surface temperature, Sea Ice, and night marine air temperature since the late nineteenth Century. *J. Geophys. Res. Atmosphere* 108 (D14), 4407. doi:10.1029/2002JD002670

Ruprich-Robert, Y., Msadek, R., Castruccio, F., Yeager, S., Delworth, T., and Danabasoglu, G. (2017). Assessing the climate impacts of the observed Atlantic multidecadal variability using the gfdl Cm2. 1 and ncar Cesm1 global coupled models. *J. Clim.* 30 (8), 2785–2810. doi:10.1175/jcli-d-16-0127.1

Schlesinger, M. E., and Ramankutty, N. (1994). An oscillation in the global climate system of period 65–70 years. *Nature* 367 (6465), 723–726. doi:10.1038/367723a0

Smith, T. M., Reynolds, R. W., Peterson, T. C., and Lawrimore, J. (2008). Improvements to noaa's historical merged land–ocean surface temperature analysis (1880–2006). *J. Clim.* 21 (10), 2283–2296. doi:10.1175/2007jcli2100.1

Sun, C., Kucharski, F., Li, J., Jin, F.-F., Kang, I.-S., and Ding, R. (2017a). Western tropical pacific multidecadal variability forced by the Atlantic multidecadal oscillation. *Nat. Commun.* 8 (1), 1–10. doi:10.1038/ncomms15998

Sun, C., Li, J., Ding, R., and Jin, Z. (2017b). Cold season Africa–Asia multidecadal teleconnection pattern and its relation to the Atlantic multidecadal variability. *Clim. Dynam.* 48 (11-12), 3903–3918. doi:10.1007/s00382-016-3309-y

Sun, C., Li, J., and Zhao, S. (2015). Remote influence of Atlantic multidecadal variability on siberian warm season precipitation. *Sci. Rep.* 5, 16853. doi:10.1038/srep16853

Sutton, R. T., and Dong, B. (2012). Atlantic Ocean influence on a shift in European climate in the 1990s. *Nat. Geosci.* 5 (11), 788–792. doi:10.1038/ngeo1595

Sutton, R. T., and Hodson, D. L. R. (2005). Atlantic Ocean forcing of north American and European summer climate. *Science* 309 (5731), 115–118. doi:10.1126/science.1109496

Wang, C., and Lee, S. K. (2009). Co-variability of tropical cyclones in the North Atlantic and the eastern North Pacific. *Geophys. Res. Lett.* 36, L24702. doi:10.1029/2009gl041469

Wang, X., Wang, C., Zhang, L., and Wang, X. (2015). Multidecadal variability of tropical cyclone rapid intensification in the western North Pacific. *J. Clim.* 28, 3806–3820. doi:10.1175/jcli-d-14-00400.1

Wang, X., Zhou, W., Li, C., and Wang, D. (2014). Comparison of the impact of two types of El Niño on tropical cyclone genesis over the South China Sea. *Int. J. Climatol.* 34, 2651–2660. doi:10.1002/joc.3865

Waple, A. M., Lawrimore, J. H., Halpert, M. S., Bell, G. D., Higgins, W., Lyon, B., et al. (2002). Climate Assessment for 2001. *Bull. Am. Meteorol. Soc.* 83 (6), S1–S62. doi:10.1175/1520-0477(2002)083<0938:caf>2.3.co;2

Wu, L., Wang, B., and Braun, S. A. (2008). Implications of tropical cyclone power dissipation index. *Int. J. Climatol.* 28, 727–731. doi:10.1002/joc.1573

Wu, L., and Zhao, H. (2012). Dynamically derived tropical cyclone intensity changes over the western North Pacific. *J. Clim.* 25, 89–98. doi:10.1175/2011jcli4139.1

Wu, Q., Wang, X., and Tao, L. (2020). Interannual and interdecadal impact of western North pacific subtropical high on tropical cyclone activity. *Clim. Dynam.* 54 (3-4), 2237–2248. doi:10.1007/s00382-019-05110-7

Zhang, R., and Delworth, T. L. (2007). Impact of the Atlantic multidecadal oscillation on North Pacific climate variability. *Geophys. Res. Lett.* 34 (23), L23708. doi:10.1029/2007gl031601.

Zhang, W., Leung, Y., and Min, J. (2013). North Pacific gyre oscillation and the occurrence of western North pacific tropical cyclones. *Geophys. Res. Lett.* 40 (19), 5205–5211. doi:10.1002/grl.50955

Zhang, W., Vecchi, G. A., Murakami, H., Villarini, G., Delworth, T. L., Yang, X., et al. (2018). Dominant role of Atlantic multidecadal oscillation in the recent decadal changes in western North pacific tropical cyclone activity. *Geophys. Res. Lett.* 45 (1), 354–362. doi:10.1002/2017gl076397

Zhang, W., and Villarini, G. (2019). Seasonal forecasting of western North pacific tropical cyclone frequency using the north American multi-model ensemble. *Clim. Dynam.* 52 (9-10), 5985–5997. doi:10.1007/s00382-018-4490-y

Zhang, W., Vecchi, G. A., Villarini, G., Murakami, H., Rosati, A., Yang, X., et al. (2017). Modulation of western North pacific tropical cyclone activity by the Atlantic meridional mode. *Clim. Dynam.* 48 (1-2), 631–647. doi:10.1007/s00382-016-3099-2

Zhang, Y., Wallace, J. M., and Battisti, D. S. (1997). ENSO-Like interdecadal variability: 1900–93. *J. Clim.* 10 (5), 1004–1020. doi:10.1175/1520-0442(1997)010<1004:eliv>2.0.co;2

Zhao, H., Wu, L., and Zhou, W. (2011). Interannual changes of tropical cyclone intensity in the western North Pacific. *J. Meteorolog. Soc. Japan Ser. II* 89, 243–253. doi:10.2151/jmsj.2011-305

Zhou, Q., Wei, L., and Zhang, R. (2019). Influence of Indian ocean dipole on tropical cyclone activity over western North pacific in Boreal Autumn. *J. Ocean Univ. China* 18 (4), 795–802. doi:10.1007/s11802-019-3965-8

Conflict of Interest: The authors declare that the research was conducted in the absence of any commercial or financial relationships that could be construed as a potential conflict of interest.

frontiers
in Environmental Science

BRIEF RESEARCH REPORT
published: 25 November 2020
doi: 10.3389/fenvs.2020.603061

Anthropogenic Influences on 2019 July Precipitation Extremes Over the Mid–Lower Reaches of the Yangtze River

Nergui Nanding[1], Yang Chen[2], Huan Wu[1]*, Buwen Dong[3], Fangxing Tian[3], Fraser C. Lott[4], Simon F. B. Tett[5], Miguel Angel Rico-Ramirez[6], Yiheng Chen[6], Zhijun Huang[1], Yan Yan[1], Delei Li[7], Rouke Li[8], Xuan Wang[9] and Xuewei Fan[10]

[1] Guangdong Province Key Laboratory for Climate Change and Natural Disaster Studies, School of Atmospheric Sciences, Sun Yat-sen University, Guangzhou, China, [2] State Key Laboratory of Severe Weather, Chinese Academy of Meteorological Sciences, Beijing, China, [3] National Centre for Atmospheric Science, Department of Meteorology, University of Reading, Reading, United Kingdom, [4] Met Office Hadley Centre, Exeter, United Kingdom, [5] School of Geosciences, The University of Edinburgh, Edinburgh, United Kingdom, [6] Department of Civil Engineering, University of Bristol, Bristol, United Kingdom, [7] CAS Key Laboratory of Ocean Circulation and Waves, Institute of Oceanology, Chinese Academy of Sciences, Qingdao, China, [8] SKLLQG, Institute of Earth Environment, Chinese Academy of Sciences, Xi'an, China, [9] Key Laboratory of Mesoscale Severe Weather, School of Atmospheric Sciences, Nanjing University, Nanjing, China, [10] State Key Laboratory of Earth Surface Processes and Resource Ecology, Faculty of Geographical Science, Beijing Normal University, Beijing, China

OPEN ACCESS

Edited by:
Wei Zhang,
The University of Iowa, United States

Reviewed by:
Tao Gao,
Institute of Atmospheric Physics (CAS), China
Maofeng Liu,
University of Miami, United States

****Correspondence:***
Huan Wu
wuhuan3@mail.sysu.edu.cn

Specialty section:
This article was submitted to Atmospheric Science, a section of the journal Frontiers in Environmental Science

Received: *05 September 2020*
Accepted: *26 October 2020*
Published: *25 November 2020*

Citation:
Nanding N, Chen Y, Wu H, Dong B, Tian F, Lott FC, Tett SFB, Rico-Ramirez MA, Chen Y, Huang Z, Yan Y, Li D, Li R, Wang X and Fan X (2020) Anthropogenic Influences on 2019 July Precipitation Extremes Over the Mid–Lower Reaches of the Yangtze River.
Front. Environ. Sci. 8:603061.
doi: 10.3389/fenvs.2020.603061

Understanding the driving factors for precipitation extremes matters for adaptation and mitigation measures against the changing hydrometeorological hazards in Yangtze River basin, a habitable area that provides water resources for domestic, farming, and industrial needs. However, the region is naturally subject to major floods linked to monsoonal heavy precipitation during May–September. This study aims to quantify anthropogenic influences on the changing risk of 2-week-long precipitation extremes such as the July 2019 extreme cases, as well as events of shorter durations, over the middle and lower reaches of Yangtze River basin (MLYRB). Precipitation extremes with different durations ranging from 1-day to 14-days maximum precipitation accumulations are investigated. Gridded daily precipitations based on nearly 2,400 meteorological stations across China are used to define maximum accumulated precipitation extremes over the MLYRB in July during 1961–2019. Attribution analysis is conducted by using the Met Office HadGEM3-GA6 modeling system, which comprises two sets of 525-member ensembles for 2019. One is forced with observed sea-surface temperatures (SSTs), sea-ice and all forcings, and the other is forced with preindustrialized SSTs and natural forcings only. The risk ratio between the exceedance probabilities estimated from all-forcing and natural-forcing simulations is calculated to quantify the anthropogenic contribution to the changing risks of the July 2019–like precipitation extremes. The results reveal that anthropogenic warming has reduced the likelihood of 2019-like 14-days heavy precipitation over the mid–lower reaches of the Yangtze River by 20%, but increased that of 2-days extremes by 30%.

Keywords: precipitation extreme events, climate change, Yangtze (Changjiang) catchment, attribution studies, anthropogenic influence

INTRODUCTION

During July 3–16, 2019, the mid–lower reaches of the Yangtze River basin (MLYRB) suffered from prolonged heavy precipitation, with regional-mean record-breaking precipitation total of 232 mm (90% higher) against the 1961–2010 July climatology of maximum 14-days accumulated rainfall of 122 mm. This event endangered the main stream of the Yangtze River, including Poyang Lake (China's largest freshwater lake) and Dongting Lake, by producing severe floods. Heavy rain and floods killed 37 people, affected 10.3 millions of residents, and damaged 776,900 hectares of farmland across four provinces (China Ministry of Emergency Management, 2020). The direct economic loss is estimated to be at least 32 billion RMB (equivalent to US $4.6 billion).

Tens of millions of people live in the floodplain of the MLYRB, a habitable area that provides water resources for domestic, farming, and industrial needs. However, the MLYRB is naturally subject to major floods linked to monsoonal heavy precipitation during May–September (Jiang et al., 2008). In this region, water level rises and soils get saturated gradually because of the accumulation of earlier-stage (April–June) monsoon rainfall. When compounded with subsequent heavy precipitation in the following months, persistent events, in particular, catastrophic floods and landslides, can occur.

Understanding the driving factors for precipitation extremes matters for adaptation and mitigation measures against the changing hydrometeorological hazards in this vulnerable region. This study aims to address this scientific question by quantifying anthropogenic influences on the changing risk of 2-week-long precipitation extremes such as the July 2019 case, as well as events of shorter durations, over the MLYRB.

DATA AND METHODS

Precipitation extremes during July 3–16, 2019, in the Yangtze River basin (YRB), severely hit widespread regions (566,357 sq km) within the study basin (**Figure 1A**). Gridded daily rainfall observations (0.56° × 0.83°) for 1961–2019 from ~2,400 quality-controlled meteorological stations (Shen et al., 2010) are used. This data set is provided by the China National Meteorological Information Center.

The Met Office HadGEM3-GA6 attribution model at a spatial resolution of 0.56° × 0.83° was applied in this study. The model outputs include 525 members of all forced simulations (Historical2019) conditioned on the observed 2019 sea surface temperature (SST) and sea ice from the HadISST data set (Rayner et al., 2003), and simulations of the natural climate (Natural2019) with anthropogenic signals removed from 2019 SST patterns and with preindustrial levels. Additional 15-member ensembles (Historical) spanning from 1960 to 2013 were ran using SST boundary conditions and historical forcing conditions to provide a baseline climatology. More details for the design of HadGEM3-GA6 attribution model are provided in Christidis et al. (2013) and Ciavarella et al. (2018).

The multimodel ensembles from the Coupled Model Intercomparison Project Phase 5 (CMIP5) were also employed to further corroborate the attribution results. Climate simulation experiments of historical, historicalNat, and the Representative Concentration Pathway projection scenario 8.5 (RCP8.5) are used in this study. Specifically, historical runs reflect observed atmospheric composition changes due to both anthropogenic and natural forcings, whereas historicalNat only considers the forcings of natural factors including solar irradiance and volcanic aerosols (Van Vuuren et al., 2011). Only model runs that provide daily-scale simulations in historical, historicalNat, and RCP8.5 experiments (the latter are needed for extending historical simulations) were used. This criterion leaves us 36 members from 16 models (**Table 1**). Then, two 36-member ensemble simulations were constructed for the attribution analysis. CMIP5 historicalNat runs for 1996–2005 were used as natural-forcing runs (NAT), and RCP8.5 runs for 2016–2025 were used to represent the 2019 state driven by all forcings (ALL). The selection of time periods for both CMIP5 ALL and NAT simulations is to avoid impacts from major volcano activates such as the 1991 eruption of Mount Pinatubo. Since the historical runs terminate at the end of 2005, CMIP5 historical (1961–2005) and RCP8.5 simulations (2006–2010) were combined to provide a baseline climatology. This is because the projected greenhouse gas forcings of RCP8.5 are more consistent with the present realization than other scenarios (Peters et al., 2013). Note that, unlike HadGEM3-GA6 simulations based on 2019 SSTs, CMIP5 simulations encompass a wide range of ocean states. Consequently, the event probabilities estimated hereafter are differently conditioned, such that the results from the two model sets will not be directly comparable.

Extreme precipitation events of varying durations (RxNday, N = 2, 3, 7, 14) are defined based on the regional-mean maximum accumulated rainfall during July. These RxNday extreme events were expressed as the precipitation anomaly (mm/day) with respect to the 1961–2010 climatology, serving to remove the mean bias in model climatology. The exceedance probability values of the 2019-like RxNday extreme events were estimated from the generalized extreme value (GEV) (Jenkinson, 1955; Ailliot et al., 2011) fitted probability distribution function (PDF) of precipitation anomalies. The risk ratios ($\mathrm{RR} = P_{\mathrm{ALL}}/P_{\mathrm{NAT}}$) between the exceedance probabilities of the RxNday precipitation anomalies estimated from all forcings (P_{ALL}) and natural-only forcing simulations (P_{NAT}) were calculated to quantify the changing risk of the 2019-like precipitation extremes due to anthropogenic influences. RR uncertainty with 90% confidence interval (90% CI) was estimated by identifying the empirical 5th and 95th percentiles among 1,000-times resampling of model ensemble members by using Monte Carlo bootstrapping procedure (Christidis et al., 2013). Doing each bootstrap, model ensemble simulations are randomly resampled with replacement to get a set of new data with the same length as the original. A two-sample Kolmogorov–Smirnoff (K-S) test (Hodges, 1958) with a significance level of 0.05 was applied to test whether the distributions of observed and simulated precipitation anomalies during 1961–2010 are from the same population. Note that precipitation

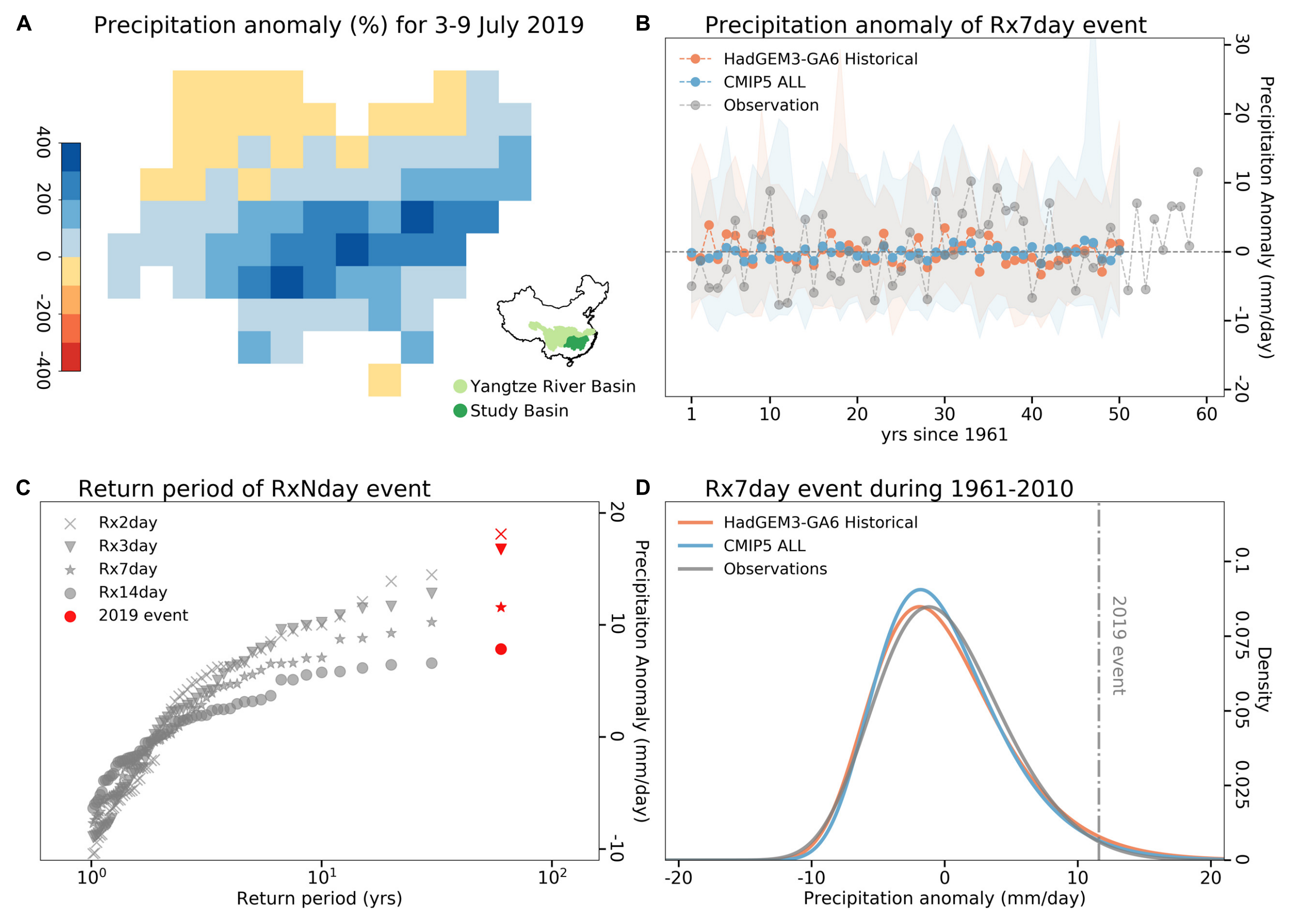

FIGURE 1 | (A) Normalized observed anomalies (%) in precipitation accumulations for 3–9 July 2019 with respect to the Rx7day July precipitation anomalies during 1961–2010 climatology. The study basin (dark green) was located at the mid-lower reaches of the Yangtze River Basin; **(B)** Time series of observed and simulated Rx7day July precipitation anomalies with respect to the 1961–2010 climatology. The shaded areas indicate the spread of 15 and 36 members of HadGEM3-GA6 Historical and CMIP5 ALL simulations, respectively, whereas the dotted lines show their ensemble means; **(C)** The empirical return periods of RxNday July events estimated from the observations during 1961–2019; **(D)** PDFs of Rx7day July precipitation anomalies for the observations, HadGEM3-GA6 Historical and CMIP5 ALL ensemble simulations during 1961–2010 climatology.

anomalies estimated from each model were calculated with their own 1961–2010 climatology, serving to remove the model climatological mean bias.

RESULTS AND DISCUSSION

During July 3–16, 2019, the mid–lower reaches of the Yangtze River were continuously hit by heavy rainfall, of which from July 3–9, precipitation totals more than doubled in 70% of the grids and even tripled in 40% of the grids with respect to the 1961–2010 climatological counterparts during July (**Figure 1A**). From the perspective of regional mean, the observed 2-, 3-, 7-, and 14-days events are all the wettest case on record since 1961 (**Figure 1C**).

Model performances are evaluated against the 1961–2010 climatology. It is clear that the observations were enveloped in their 90% CI uncertainty range for Rx7day event. The probability distributions of simulations and observations are not distinguishable based on visual inspection (**Figure 1D**) and K-S test (Pval=0.97 for HadGEM3-GA6 and Pval=0.63 for CMIP5, **Table 2**). Note that while precipitation anomalies are reasonably simulated by HadGEM3-GA6 and CMIP5, residual errors (systematic and random) remain in both models in terms of actual precipitation values.

To quantify the anthropogenic influences on the changing risk of precipitation extremes, the distributions of all forcings and natural-only forcing simulations are compared. For Rx2day event, the PDFs of all forcing simulations for both HadGEM3-GA6 and CMIP5 models shift toward the larger precipitation anomalies (**Figure 2A**), which indicates the increased probability of daily extreme event when anthropogenic influences are included. Specifically, the exceedance probability of HadGEM3-GA6 Natural2019 increases from 0.008 (90% CI, 0.004–0.013) to HadGEM3-GA6 Historical2019 of 0.011 (90% CI, 0.006–0.016), giving an RR of 1.36 (90% CI, 0.63–3.08) for the 2019-like Rx2day event. While P_{NAT} of CMIP5 NAT increases from 0.016 (90% CI, 0.007–0.024) to P_{ALL} of 0.020 (90% CI, 0.011–0.029) for CMIP5 ALL, which gives the empirical RR of 1.27

TABLE 1 | List of 36 ensemble members from 16 CMIP5 models used in this study.

Models	Resolution (lat × lon)	No. of members
ACCESS1.3	1.25 × 1.875	1
BNU-ESM	2.7906 × 2.8125	1
CCSM4	0.94 × 1.25	3
CESM1-CAM5	0.94 × 1.25	1
CSIRO-Mk3.6.0	1.865 × 1.875	10
CanESM2	2.7906 × 2.8	5
GFDL-CM3	2.0 × 2.5	1
GFDL-ESM2M	2.0225 × 2.5	1
HadGEM2-ES	1.25 × 1.875	4
IPSL-CM5A-LR	1.8947 × 3.75	3
IPSL-CM5A-MR	1.2676 × 2.5	1
MIROC-ESM-CHEM	2.7906 × 2.8125	1
MIROC-ESM	2.7906 × 2.8125	1
MRI-CGCM3	1.1215 × 1.125	1
NorESM1-M	1.8947 × 2.5	1
BCC-CSM1	2.7906 × 2.8125	1

(90% CI, 0.60–2.94). That is, the likelihood of 2019-like Rx2day precipitation extreme has increased by about 30% over the study basin because of the anthropogenic influences. Return periods of simulations also confirm that 2019-like daily precipitation extreme happens more frequently because of anthropogenic influences (**Figure 2B**).

For the Rx14day event, however, the PDFs shift toward the smaller anomalies in all forcing simulations compared to those in natural-only forcing simulations, particularly for HadGEM3-GA6 simulations (**Figure 2C**). Specifically, anthropogenic influences reduce the exceedance probability of the 2019-like Rx14day event from 0.006 (90% CI, 0.002–0.010) of P_{NAT} to 0.003 (90% CI, 0.001–0.006) of P_{ALL} for HadGEM3-GA6 simulations, which gives an empirical RR of 0.50 (90% CI, 0.14–1.42). The CMIP5 multimodel attribution system provides similar results, i.e., RR of 0.82 (90% CI, 0.49–2.12). Thus, the likelihood of 2019-like Rx14day persistent heavy precipitation is reduced by about 20% at least over the study basin because of anthropogenic forcings. Return periods of simulations also confirm that the persistent heavy precipitation became less frequent in July because of anthropogenic influences (**Figure 2D**).

The intensification of daily precipitation extremes could be largely related to atmospheric moistening as temperature rises due to anthropogenic forcings (Allen and Ingram, 2002), while the reduced probability of 14-days extreme rainfall due to anthropogenic forcings might be largely induced by aerosols. By scattering and absorbing solar radiation, increased aerosols over East Asia lead to the weakening of the East Asian summer monsoon (EASM) and reduced summer seasonal mean precipitation over monsoon regions (Song et al., 2014; Tian et al., 2018; Dong et al., 2019; Zhou et al., 2020). These changes induced by aerosols can overwhelm the greenhouse gasses–induced intensification of EASM and precipitation (Song et al., 2014; Tian et al., 2018; Zhou et al., 2020), leading to weakening of EASM, reduced summer mean, and summer persistent (e.g., 14-days) heavy rainfall. Further disentangling the contributions from greenhouse gasses and aerosols on extreme precipitation on different time scales would improve understanding of the attribution outcome.

These findings are consistent with the attribution outcomes in Li et al. (2018, 2021) and Zhang et al. (2020), which all reported anthropogenic influences reduced the likelihood of warm-season persistent precipitation extremes but focused on subregion at the lower reaches of YRB, central-western China, and southern China, respectively. As the other side of the coin, Lu et al. (2021) found that the anthropogenic influences increased the 2019 May–June like droughts over southern China [Figure 2D in Lu et al. (2021)].

Similar attribution analysis was also conducted with respect to the RxNday ($\mathrm{N} = 2,\ 3,\ 7,\ 14$) precipitation extremes during summertime from June to August. These supplementary analyses serve to test the sensitivity of attribution conclusions on timing (entire summer vs. July) of cases considered. It was found that anthropogenic influences have reduced the likelihood of similar summertime Rx14day precipitation extremes by about 20% in HadGEM3-GA6 and 10% in CMIP5, whereas the likelihood of 2019 July-like Rx2day precipitation extremes has increased about 35% and 50% in HadGEM3-GA6 and CMIP5, respectively (**Supplementary Figure S2**). The attribution analysis was also repeated based on percentage anomaly thresholds (precipitation anomaly divided by summer/July climatology) for events of various durations (figures omitted). The qualitative statement that anthropogenic forcings have made short-duration precipitation

TABLE 2 | Attribution results for July RxNday events with risk ratio, exceedance probability from all forcings, and natural-only forcing simulations.

Model	Event	RR (90% CI)	P_{ALL} (90% CI)	P_{NAT} (90% CI)	K-S test (Pval)
HadGEM3-GA6	Rx2day	1.36 (0.63–3.08)	0.011 (0.006–0.016)	0.008 (0.004–0.013)	0.46
	Rx3day	1.45 (0.60–3.77)	0.008 (0.004–0.013)	0.006 (0.003–0.010)	0.53
	Rx7day	1.19 (0.52–2.98)	0.007 (0.004–0.012)	0.006 (0.003–1.010)	0.97
	Rx14day	0.50 (0.14–1.42)	0.003 (0.001–0.006)	0.006 (0.002–0.010)	0.86
CMIP5	Rx2day	1.27 (0.60–2.94)	0.020 (0.011–0.029)	0.016 (0.007–0.024)	0.32
	Rx3day	1.21 (0.50–3.47)	0.012 (0.006–0.019)	0.010 (0.004–0.016)	0.43
	Rx7day	1.60 (0.67–3.96)	0.012 (0.006–0.019)	0.007 (0.003–0.012)	0.63
	Rx14day	0.82 (0.49–2.12)	0.025 (0.016–0.035)	0.031 (0.012–0.042)	0.66

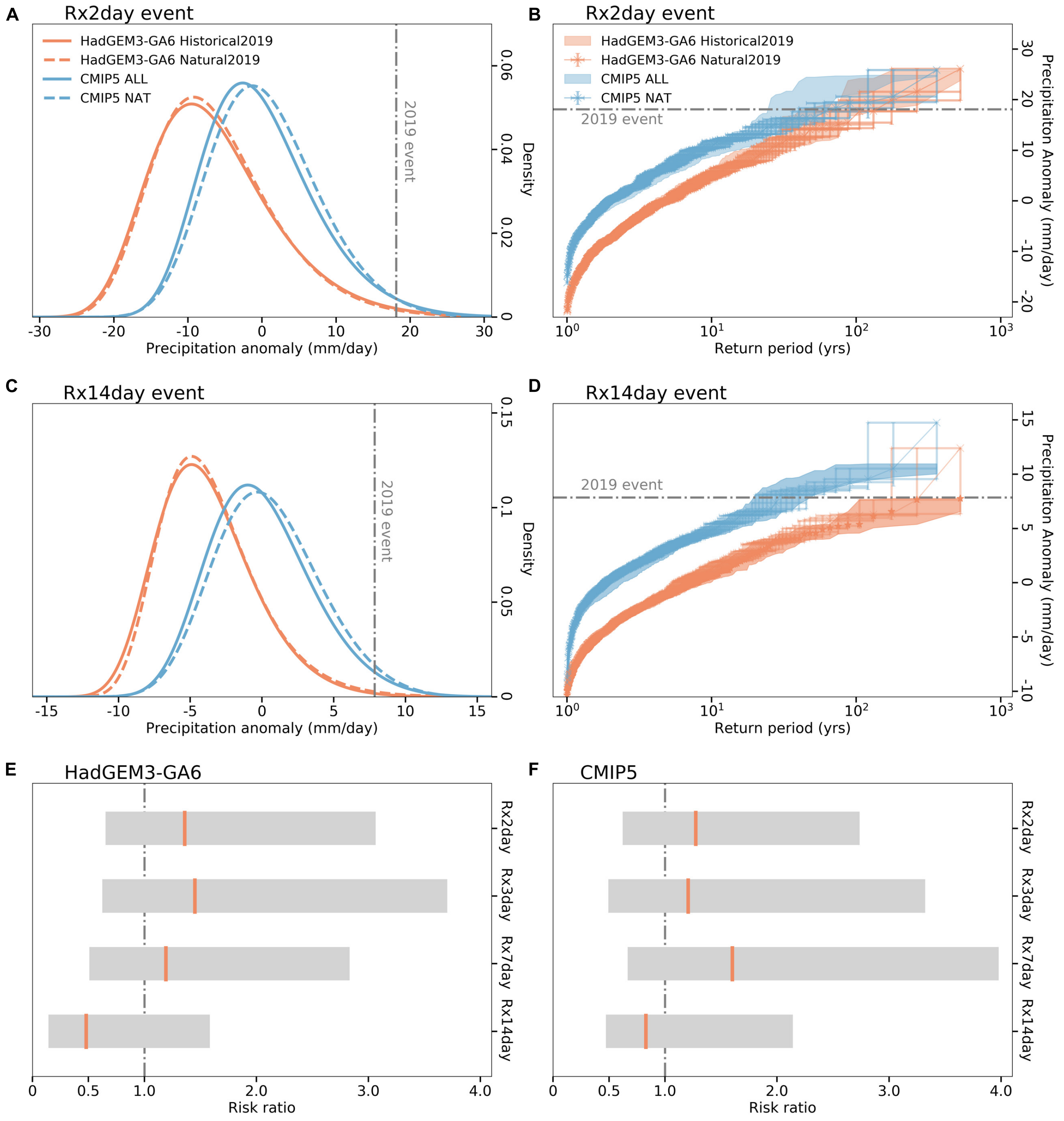

FIGURE 2 | PDFs of precipitation anomalies for the HadGEM3-GA6 and CMIP5 model ensembles with all-forcings (orange) and natural-only forcings (blue) simulations for **(A)** Rx2day and **(C)** Rx14day extreme events; Return periods of **(B)** Rx2day and **(D)** Rx14day extreme events estimated from the HadGEM3-GA6 and CMIP5 model ensembles; Empirical risk ratios (vertical line) with 90% confidence interval (shaded) for RxNday extreme events estimated from the **(E)** HadGEM3-GA6 and **(F)** CMIP5 multimodel ensembles.

extremes more frequent but long-lived events less frequent robustly holds.

CONCLUSION

This attribution analysis reveals that anthropogenic forcings reduce the likelihood of 2019 July-like persistent heavy precipitation event (Rx14day) by about 20% at least, but increase those of daily precipitation extremes (Rx2day) by about 30% over mid–lower reaches of the YRB. The findings are robust against attribution models, timing, and the form of thresholds (absolute anomalies or percentage anomalies) considered. This study highlights that despite reduced risks from long-lasting precipitation extremes, anthropogenic forcings pose the populous and highly urbanized YRB at higher risks of flash floods and resultant hydrometeorological hazards due to the increase of shorter-duration precipitation extremes.

DATA AVAILABILITY STATEMENT

The original contributions presented in the study are included in the article/**Supplementary Material**, further inquiries can be directed to the corresponding author.

AUTHOR CONTRIBUTIONS

BD, ST, FL, HW, YC, and NN conceived and planned the experiments. NN, YC, and HW carried out the experiments. YHC, DL, RL, XF, XW, ZH, and YY contributed to data preparation. NN took the lead in writing the manuscript. All authors provided critical feedback and helped to shape the research, analysis, and manuscript.

FUNDING

This study was conducted during the Operational Attribution Workshop at Sun Yat-sen University, jointly sponsored by the National Key R&D Program (2018YFC1507700), the UK-China Research and Innovation Partnership Fund through the Met Office Climate Science for Service Partnership (CSSP) China as part of the Newton Fund, and the Natural Science Foundation (NSF) of China (41975105). NN was funded by the NSF of China (41905101 and U1811464) and the Fundamental Research Funds for the Central Universities (20lgpy25). HW was funded by the NSF of China (41861144014, 41775106, and U1811464). RL was funded by the National Key R&D Program (2017YFA0605004) and the NSF of China (41991254). DL was funded by the NSF of China (41706019) and the Strategic Priority Research Program of the Chinese Academy of Sciences (XDB42000000). ST, BD, and FL were supported by the UK-China Research and Innovation Partnership Fund through the Met Office Climate Science for Service Partnership (CSSP) China as part of the Newton Fund.

SUPPLEMENTARY MATERIAL

The Supplementary Material for this article can be found online at: https://www.frontiersin.org/articles/10.3389/fenvs.2020.603061/full#supplementary-material

REFERENCES

Ailliot, P., Thompson, C., and Thomson, P. (2011). Mixed methods for fitting the GEV distribution. *Water Resour. Res.* 47, 1–14.

Allen, M. R., and Ingram, W. J. (2002). Constraints on future changes in climate and the hydrologic cycle. *Nature* 419, 228–232. doi: 10.1038/nature01092

China Ministry of Emergency Management (2020). *2019 Top 10 Natural Disasters in China*. Available online at: https://www.mem.gov.cn/xw/bndt/202001/t20200116_343570.shtml (accessed April 13, 2020).

Christidis, N., Stott, P. A., Scaife, A. A., Arribas, A., Jones, G. S., Copsey, D., et al. (2013). A new HadGEM3-A-based system for attribution of weather-and climate-related extreme events. *J. Clim.* 26, 2756–2783. doi: 10.1175/jcli-d-12-00169.1

Ciavarella, A., Christidis, N., Andrews, M., Groenendijk, M., Rostron, J., Elkington, M., et al. (2018). Upgrade of the HadGEM3-A based attribution system to high resolution and a new validation framework for probabilistic event attribution. *Weather Clim. Extremes* 20, 9–32. doi: 10.1016/j.wace.2018.03.003

Dong, B., Wilcox, L. J., Highwood, E. J., and Sutton, R. T. (2019). Impacts of recent decadal changes in Asian aerosols on the East Asian summer monsoon: roles of aerosol–radiation and aerosol–cloud interactions. *Clim. Dyn.* 53, 3235–3256. doi: 10.1007/s00382-019-04698-0

Hodges, J. (1958). The significance probability of the Smirnov two-sample test. *Arkiv för Matematik* 3, 469–486. doi: 10.1007/bf02589501

Jenkinson, A. F. (1955). The frequency distribution of the annual maximum (or minimum) values of meteorological elements. *Q. J. R. Meteorol. Soc.* 81, 158–171. doi: 10.1002/qj.49708134804

Jiang, T., Kundzewicz, Z. W., and Su, B. (2008). Changes in monthly precipitation and flood hazard in the Yangtze River Basin, China. *Int. J. Climatol.* 28, 1471–1481. doi: 10.1002/joc.1635

Li, C., Tian, Q., Yu, R., Zhou, B., Xia, J., Burke, C., et al. (2018). Attribution of extreme precipitation in the lower reaches of the Yangtze River during May 2016. *Environ. Res. Lett.* 13:014015. doi: 10.1088/1748-9326/aa9691

Li, R., Li, D., Nanding, N., Wang, X., Fan, X., Chen, Y., et al. (2021). Anthropogenic influences on heavy precipitation during the 2019 extremely wet rainy season in Southern China. *Bull. Am. Meteorol. Soc.* 102, S103–S109.

Lu, C., Jiang, J., Chen, R., Ullah, S., Yu, R., Lott, F. C., et al. (2021). Anthropogenic influence on 2019 May–June extremely low precipitation in Southwestern China. *Bull. Am. Meteorol. Soc.* 102, S97–S102.

Peters, G. P., Andrew, R. M., Boden, T., Canadell, J. G., Ciais, P., Le Quéré, C., et al. (2013). The challenge to keep global warming below 2 °C. *Nat. Clim. Change* 3, 4–6. doi: 10.1038/nclimate1783

Rayner, N. A., Parker, D. E., Horton, E. B., Folland, C. K., Alexander, L. V., Rowell, D. P., et al. (2003). Global analyses of sea surface temperature, sea ice, and night marine air temperature since the late nineteenth century. *J. Geophys. Res. Atmos.* 108, 4407–4437. doi: 10.1029/2002jd002670

Shen, Y., Xiong, A., Wang, Y., and Xie, P. (2010). Performance of high-resolution satellite precipitation products over China. *J. Geophys. Res. Atmos.* 115:JD012097. doi: 10.1029/2009jd012097

Song, F., Zhou, T., and Qian, Y. (2014). Responses of East Asian summer monsoon to natural and anthropogenic forcings in the 17 latest CMIP5 models. *Geophys. Res. Lett.* 41, 596–603. doi: 10.1002/2013gl058705

Tian, F., Dong, B., Robson, J., and Sutton, R. (2018). Forced decadal changes in the East Asian summer monsoon: the roles of greenhouse gases and anthropogenic aerosols. *Clim. Dyn.* 51, 3699–3715. doi: 10.1007/s00382-018-4105-7

Van Vuuren, D. P., Edmonds, J., Kainuma, M., Riahi, K., Thomson, A., Hibbard, K., et al. (2011). The representative concentration pathways: an overview. *Clim. Change* 109:5. doi: 10.1007/s10584-011-0148-z

Zhang, W., Li, W., Zhu, L., Ma, Y., Yang, L., Lott, F. C., et al. (2020). Anthropogenic influence on 2018 summer persistent heavy rainfall in Central Western China. *Bull. Am. Meteorol. Soc.* 101, S65–S70.

Zhou, T., Zhang, W., Zhang, L., Zhang, X., Qian, Y., Peng, D., et al. (2020). The dynamic and thermodynamic processes dominating the reduction of global land monsoon precipitation driven by anthropogenic aerosols emission. *Sci. China Earth Sci.* 63, 919–933. doi: 10.1007/s11430-019-9613-9

Conflict of Interest: The authors declare that the research was conducted in the absence of any commercial or financial relationships that could be construed as a potential conflict of interest.

frontiers in Earth Science

ORIGINAL RESEARCH
published: 29 January 2021
doi: 10.3389/feart.2020.609727

Key Environmental Factors for Rapid Intensification of the South China Sea Tropical Cyclones

Yao Chen[1,2], *Si Gao*[3,4]*, *Xun Li*[2] and *Xinyong Shen*[1,4]*

[1]Key Laboratory of Meteorological Disaster, Ministry of Education, and Collaborative Innovation Centre on Forecast and Evaluation of Meteorological Disaster, Nanjing University of Information Science and Technology, Nanjing, China, [2]Key Laboratory of South China Sea Meteorological Disaster Prevention and Mitigation of Hainan Province, China Meteorological Administration, Haikou, China, [3]School of Atmospheric Sciences, and Key Laboratory of Tropical Atmosphere-Ocean System, Ministry of Education, Sun Yat-sen University, Zhuhai, China, [4]Southern Marine Science and Engineering Guangdong Laboratory (Zhuhai), Zhuhai, China

Edited by:
Hiroyuki Murakami,
University Corporation for Atmospheric Research (UCAR), United States

Reviewed by:
Jiuwei Zhao,
Pohang University of Science and Technology, South Korea
Xidong Wang,
Hohai University, China

***Correspondence:**
Si Gao
gaosi5@mail.sysu.edu.cn
Xinyong Shen
shenxy@nuist.edu.cn

Specialty section:
This article was submitted to Atmospheric Science, a section of the journal Frontiers in Earth Science

Received: *24 September 2020*
Accepted: *22 December 2020*
Published: *29 January 2021*

Citation:
Chen Y, Gao S, Li X and Shen X (2021) Key Environmental Factors for Rapid Intensification of the South China Sea Tropical Cyclones. Front. Earth Sci. 8:609727. doi: 10.3389/feart.2020.609727

Forecasting rapid intensification (RI) of the South China Sea (SCS) tropical cyclones (TCs) remains an operational challenge, mainly owing to the incomplete understanding of its physical mechanisms. Based on TC best-track data, atmospheric analysis data, and sea surface temperature data, this study compares temporal evolution characteristics of environmental conditions from the previous 24 h to the onset time for RI and non-RI TCs in the SCS during 2000–2018, and then identifies key factors for RI of the SCS TCs using the box difference index and stepwise regression. A combination of strong divergence in the upper troposphere and strong convergence in the boundary layer, weak deep-layer vertical wind shear, fast storm translation speed, and high TC intensification potential (i.e., maximum potential intensity minus current intensity) north of the storm center at the previous 24 h are favorable for RI of the SCS TCs, and their importance for RI is in descending order. The results may shed light on operational forecasting of rapid intensification of the SCS TCs.

Keywords: tropical cyclone, South China Sea, rapid intensification, environmental factors, box difference index

INTRODUCTION

The South China Sea (SCS) is the largest semi-closed sea in the tropical western Pacific. Its basin is small and is surrounded by densely populated Asian countries. The SCS tropical cyclones (TCs) include the TCs generated in the SCS and the TCs moving into SCS from the sea to the east of the Philippines. They are usually featured by short duration and variable path and intensity. The SCS TCs often make landfall in the coastal areas of South China and Vietnam and then bring severe rainfalls, gales and storm surges, often leading to serious losses of life and property near the landing sites. For example, super typhoon Rammasun (1409) made landfall in Wenchang, Hainan Province, causing direct economic losses of nearly 27 billion yuan in the three provinces of South China. Rammasun experienced rapid intensification (RI) twice when it was near shore, which caused large errors in the TC intensity forecast, seriously affecting the strategy making on preventing typhoons and reducing disasters. Therefore, the in-depth research on the influencing factors of TC RI in the SCS has great practical significance for improving the operational forecast of TC intensity and reducing the typhoon disaster losses.

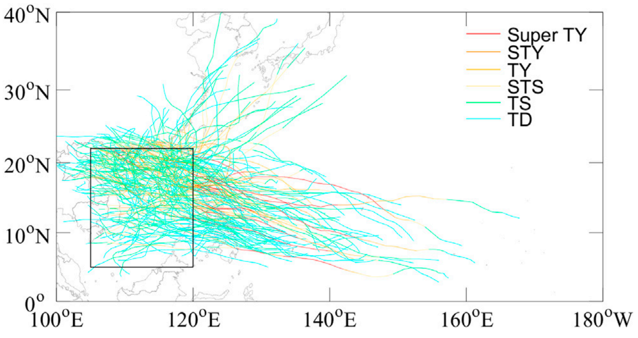

FIGURE 1 | Tracks of the SCS TCs during 2000–2018. Black box denotes the SCS region defined in this study. Colors of the track represents different TC intensity (TD, tropical depression; TS, tropical storm; STS, severe tropical storm; TY, typhoon; STY, severe typhoon; Super TY, super typhoon).

The evolution of TC intensity involves complex physical processes, and the factors affecting TC intensity change are mainly from three aspects. The first is the influence of the underlying surface, such as the ocean. The ocean heat is the dominant factor affecting the formation and development of TCs, which can be expressed by two related factors: ocean heat content and sea surface temperature (SST). The SST, which can affect the latent heat, sensible heat and water vapor fluxes transported from the ocean into TCs (e.g., Emanuel, 1986; Holland, 1997; Gao and Chiu, 2010; Gao et al., 2016), is a key factor determining the maximum potential intensity (MPI; Emanuel, 1988) of TCs. Large ocean heat content can provide the energy for TC development and offset the cooling effect of ocean upwelling (e.g., Shay et al., 2000). The second aspect is the internal dynamics of TCs. For example, the asymmetry of the TC inner core can limit the development of TCs (Yang et al., 2007). When the TC eyewall starts to replace, the intensity would usually increase; later, when the inner-core structure becomes a concentric ring, the intensity would decrease; when the wind speed of the outer eyewall exceeds that of the inner eyewall, the TC would intensify again and could often reach its maximum intensity in its lift cycle (Sitkowski et al., 2011), and meanwhile the radius of maximum wind significantly decreases (Yang et al., 2017). The third aspect is the effect of the large-scale environment field, such as the upper-level trough. When the warm outflow of TC is close to the cold trough, the increase of the temperature gradient leads to the strengthening of the upper-level jet. If the TC center is exactly located at the right of the jet entrance, the secondary circulation related to this jet is conducive to the development of the ascending motion and TC (Hanley et al., 2001). The environmental vertical wind shear (VWS) could also affect the TC intensity. The weak VWS is often considered to be conducive to TC RI (e.g., Merrill, 1988; Zeng et al., 2007; Bai and Wang, 2016), but the mechanisms are different, mainly including the theory of ventilation flow (Gray, 1968), the secondary circulation effect (Tuleya and Kurihara, 1981), the tilt and stability effect (Demaria, 1996), and the Rossby penetration theory (Jone, 1995), and so on.

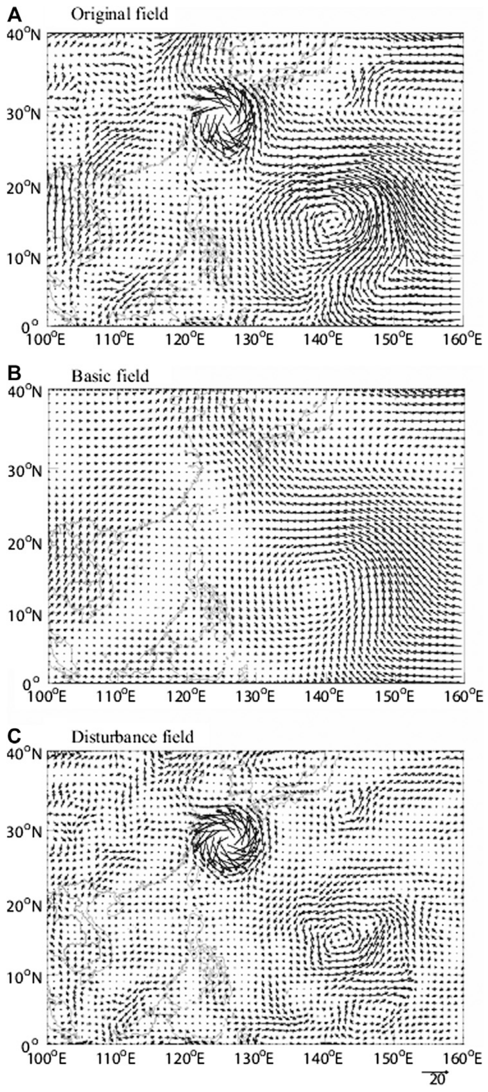

FIGURE 2 | (A) Original total wind (m s^{-1}) field, and the corresponding **(B)** environmental wind field and **(C)** disturbance wind field at 850 hPa at 0000 UTC August 9, 2000.

Previous studies on the RI of the SCS TCs show that RI occurs further south, and is associated with weaker VWS, weaker easterly wind at 200 hPa, and smaller radius of 15.4 m s^{-1} winds compared to non-RI TCs (Li et al., 2011). The VWS and low-level water vapor convergence are the main factors affecting TC RI in the SCS (Hu and Duan, 2016). TC RI in the SCS mostly occurs after the monsoon season when the middle-latitude trough invades the SCS and the southwesterly wind in the southern SCS is still strong (Chen et al., 2015). The anomalous warmer SST, the stronger low-level jet, the stronger cross-equatorial air flow, the weaker environmental VWS and the stronger upper-level outflow play important roles in RI of the super typhoon Ramason (Cheng et al., 2017). The specific location and timing of the nearshore RI of TCs in the SCS are related to the adjustment of the East Asian summer monsoon

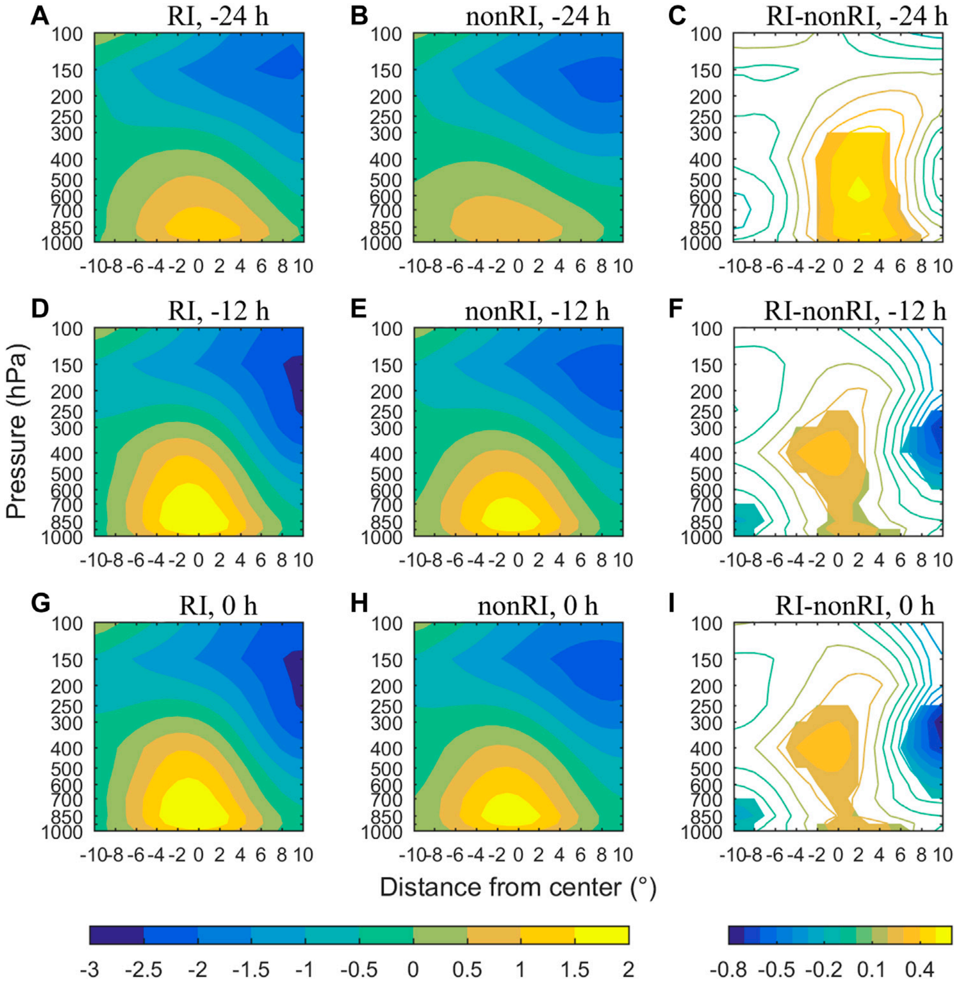

FIGURE 3 | Meridional cross sections of environmental relative vorticity (10^{-5} s^{-1}). **(A,D,G)** are the composites for RI TCs at −24, −12, and 0 h, respectively; **(B,C,H)** are the composites for non-RI TCs at −24, −12, and 0 h, respectively; **(C,F,I)** are the differences between RI and non-RI TCs at −24, −12, and 0 h, respectively, shadings denote significant differences above the 90% confidence level.

when the Meiyu period in the Yangtze River Basin ends. The adjustment of the East Asian summer monsoon can not only strengthen the interactions between TCs and the upper-level trough, but also make the water vapor flux accompanied by the monsoon surge enter the TC circulation, preventing the dry air accompanied by the western Pacific subtropical high (WPSH) from intruding into the TC circulation. Thus, it is conducive to the occurrence of the nearshore RI of the SCS TCs (Qiu et al., 2020).

The above researches on RI of the SCS TCs only list some favorable environmental factors, and fail to comprehensively compare the importance of those factors and to analyze the evolution of the factors before the onset of RI. In this paper, we investigate the temporal evolution characteristics of potential environmental factors during a 24 h period before the onset of TC RI in the SCS, so as to find the indicative precursors and the key influence areas of significant factors by composite analyses. Furthermore, based on the box difference index (BDI; Fu et al., 2012) of each factor calculated in the key influence area, the key environmental factors for RI of the SCS TCs will be identified. This research is expected to provide some references for the operational intensity prediction of the SCS TCs.

DATA AND METHOD

Data

The TC information at a 6 h interval (latitude and longitude of the TC center and the maximum sustained wind speed) is obtained from the TC best-track dataset (Ying et al., 2014) released by the Shanghai Typhoon Institute of the China Meteorological Administration (CMA). The atmospheric environment fields are obtained from the FNL data released by the United States National Centers for Environmental Prediction (NCEP), with an interval of 6 h and a spatial

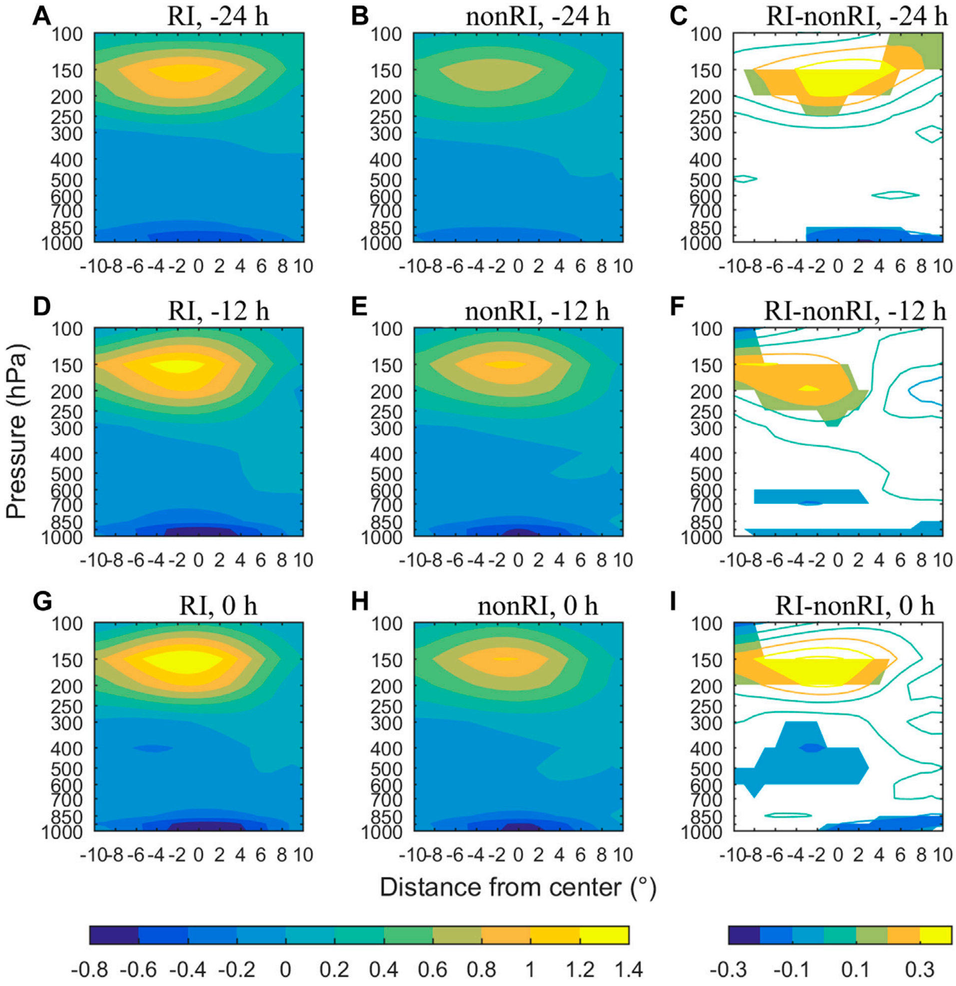

FIGURE 4 | Same as **Figure 3**, but for environmental divergence (10^{-5} s^{-1}).

resolution of 1°. The daily SST data (OISST V2; Reynolds et al., 2007) is released by the United States National Oceanic and Atmospheric Administration (NOAA), with a spatial resolution of 0.25°. We use the above datasets during our study period 2000–2018.

Method

To exclude the influence of land, the TCs located over the SCS (5–22°N, 105–120°E) are selected as the research objects. The tracks of the SCS TCs from 2000 to 2018 are shown in **Figure 1**. In previous studies, the 95th percentile of all the samples of 24-h changes in maximum sustained wind speed ($\Delta V_{24} = V_{+24h} - V_{0h}$) for TCs in an ocean basin was often used as the threshold to define RI (e.g., Kaplan and DeMaria, 2003). In this paper the 95th percentile of all ΔV_{24} samples of TCs in the SCS during the study period is 12 m s^{-1} (**Supplementary Figure S1**), so $\Delta V_{24} \geq 12$ m s^{-1} is defined as an RI event, and $\Delta V_{24} < 12$ m s^{-1} is defined as a non-RI event.

The RI/non-RI onset time is recorded as 0, 12, and 24 h before the onset are recorded as −12 and −24 h, respectively. For the horizontal two-dimensional physical quantity field, an area of 20° × 20° outside the TC center is used as the analysis area. For the three-dimensional physical quantity field, a longitude/latitude-height cross section with a horizontal span of 20° is used, and composite analyses are performed for the RI and non-RI events of the SCS TCs at three times (i.e., −12, −24, and 0 h), and the Student's *t* test is used to judge the significance of the difference in physical quantity between the two groups of samples at the same time. There are 34 RI samples and 463 non-RI samples at −24 h. For −12 and 0 h, the numbers of RI samples are both 37, and the numbers of non-RI samples are both 511.

The environmental divergence, relative vorticity, VWS and relative humidity are all obtained from the large-scale environmental field in which the TC vortexes have been filtered from the original field. This vortex-removing algorithm (Kurihara et al., 1993) can completely eliminate the disturbances with the wavelength less than 1,000 km. The 850-hPa wind field at 0000 UTC on August 9, 2000 is used as an example to verify the vortex-removing algorithm (**Figure 2**). At

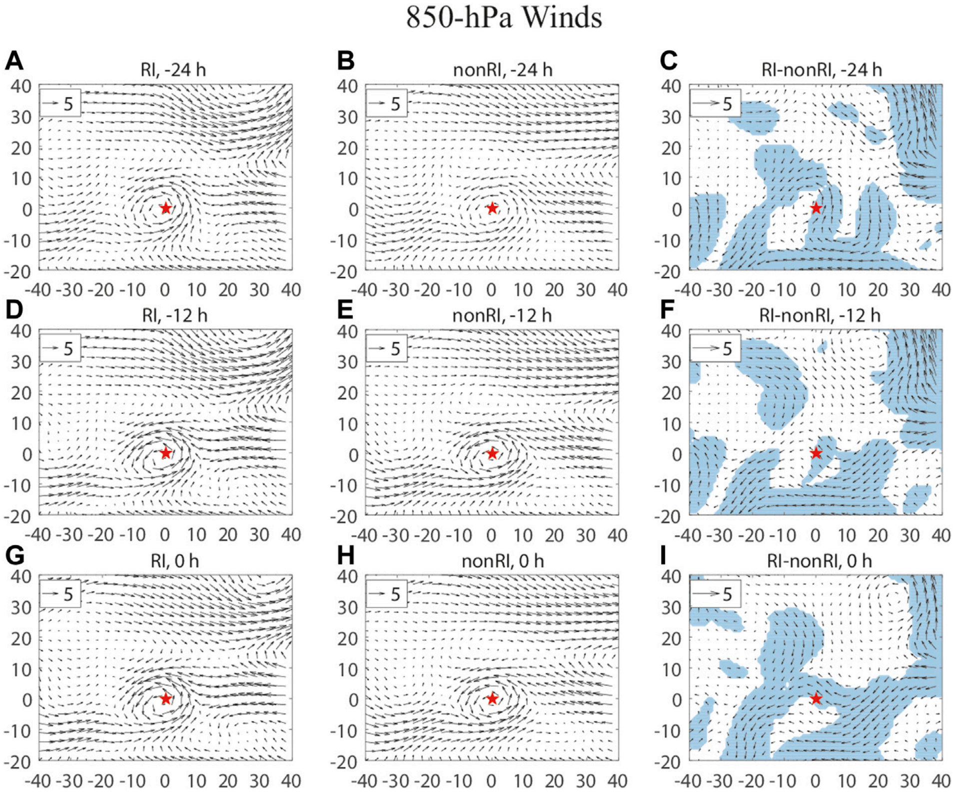

FIGURE 5 | Composite 850-hPa environmental wind fields (m s^{-1}) for RI and non-RI TCs and their differences. **(A,D,G)** are the composites for RI TCs at −24, −12, and 0 h, respectively; **(B,C,H)** are the composites for non-RI TCs at −24, −12, and 0 h, respectively; Shadings in **(C,F,I)** denote significant differences above the 90% confidence level.

that time there were two TCs (**Figure 2A**) in the western North Pacific (WNP), and the algorithm can completely remove the two TC vortexes (**Figure 2C**). The large-scale monsoon gyre still exists (**Figure 2B**) after the vortex removal, indicating good performance of the algorithm.

Following Wang et al. (2015), the environmental VWS is defined as the difference in environmental wind vector between each level and 850 hPa:

$$VWS_{lev-850} = \sqrt{(u_{lev} - u_{850})^2 + (v_{lev} - v_{850})^2} \tag{1}$$

where u and v are the zonal and meridional wind speed after removing the vortexes, respectively, and the subscript represents the level.

The area with significant difference between RI and non-RI events for each factor is identified, and the areal average is calculated. Following Fu et al. (2012), the BDI is then calculated as

$$BDI = \frac{M_{RI} - M_{nonRI}}{\sigma_{RI} + \sigma_{nonRI}} \tag{2}$$

where M_{RI} and σ_{RI} (M_{nonRI} and σ_{nonRI}) represent the average and standard deviation of the physical quantity for the RI (non-RI) samples, respectively.

COMPOSITE ANALYSES OF POTENTIAL ENVIRONMENT FACTORS FOR RI

Relative Vorticity

The temporal evolutions of the meridional cross sections of environmental relative vorticity are shown in **Figure 3**. At −24 h, there is a broad region of positive relative vorticity near the RI TC center at the middle and lower levels, and the negative relative vorticity is dominant at the upper levels. The relative vorticity to the north of the TC center is smaller than that to the south, and the vorticity distribution of non-RI TCs is similar. At −12 h, the middle- and lower-level relative vorticity of RI and non-RI TCs increases significantly, and the maximum positive vorticity at lower troposphere reaches 2×10^{-5} s^{-1}. From −12 to 0 h, the relative vorticity variations of the two TC types are small. The temporal evolutions of the zonal cross sections of the relative vorticity are similar to those of the meridional cross sections, except that the zonal distribution is more symmetrical (figure not shown). The relative vorticity at the three times (−24, −12, and 0 h) near the RI TC center is larger than that near the non-RI TC center, and the difference is the most significant at the middle and lower levels (1,000–300 hPa) at −24 h, which has certain indicative meaning for RI. The larger relative vorticity at lower levels usually corresponds to a stronger Ekman

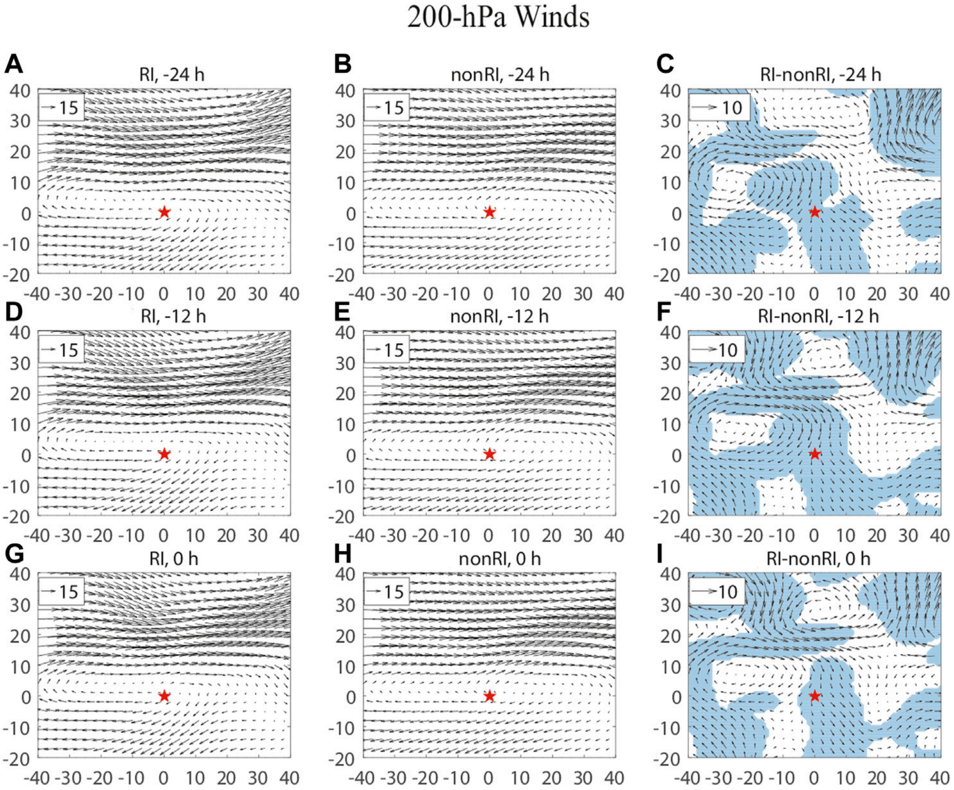

FIGURE 6 | Same as **Figure 5**, but for the composite 200-hPa environmental wind fields (m s^{-1}).

pumping, that is, the stronger lower-level convergent inflow, which is conducive to the maintenance and development of the TC vorticity (Xu et al., 2017). The strong cumulus convection near the TC center transports the lower-level positive vorticity upward, thus there is also large cyclonic vorticity at middle levels.

Divergence

Figure 4 shows the temporal evolutions of the meridional cross sections of environmental divergence. At −24 h, there is strong divergence at 200–150 hPa near the RI TC center, and weak convergence in the boundary layer. Non-RI TCs have a similar configuration, but the upper-level divergence and boundary-layer convergence of RI TCs are both significantly stronger than those of non-RI TCs, which can be used as a precursory signal for RI. At −12 h, the upper-level divergence and boundary-layer convergence near the RI TC center significantly enhance, and the evolution for non-RI TCs is similar. At 0 h, the upper-level divergent area of RI TCs expands, with the maximum divergence exceeding 1.4×10^{-5} s^{-1}, while the upper-level divergence of non-RI TCs weakens slightly. The temporal evolutions of the zonal cross sections of divergence are similar (figure not shown). The upper-level divergence and boundary-layer convergence of RI TCs at the three times (−24, −12, 0 h) are significantly stronger than those of non-RI TCs. The strong upper-level divergent environment provides a favorable "pumping" effect. Together with the convergence in the boundary layer, the "pumping" effect is reinforced, which is conducive to the occurrence of TC RI (Mei and Yu, 2016).

Wind Field

The composite environmental wind fields at upper, middle and low levels are plotted to analyze the synoptic patterns for the two types of SCS TCs. **Figure 5** shows the composite environmental wind fields at 850 hPa. The common feature of the low-level wind fields for RI and non-RI TCs is that, the easterly airflow southwest of the WPSH and the southwest monsoon from the Bay of Bengal merge into a cyclonic gyre near the TC center. At −24 h, the cyclonic wind field near the RI TC center is significantly stronger than that near the non-RI TC center, which is consistent with the stronger boundary-layer convergence for RI TCs. From −12 to 0 h, the anomalous easterly wind of RI TCs is stronger than that of non-RI TCs. There are westerly troughs on the northeast side of RI TCs at the three times, which is consistent with Chen et al. (2015).

The composite environmental wind field at 500 hPa is shown in **Supplementary Figure S2**. The westerly trough is located to the north, the continental high is located to the west, and the WPSH is located to the east of the two types of TCs.

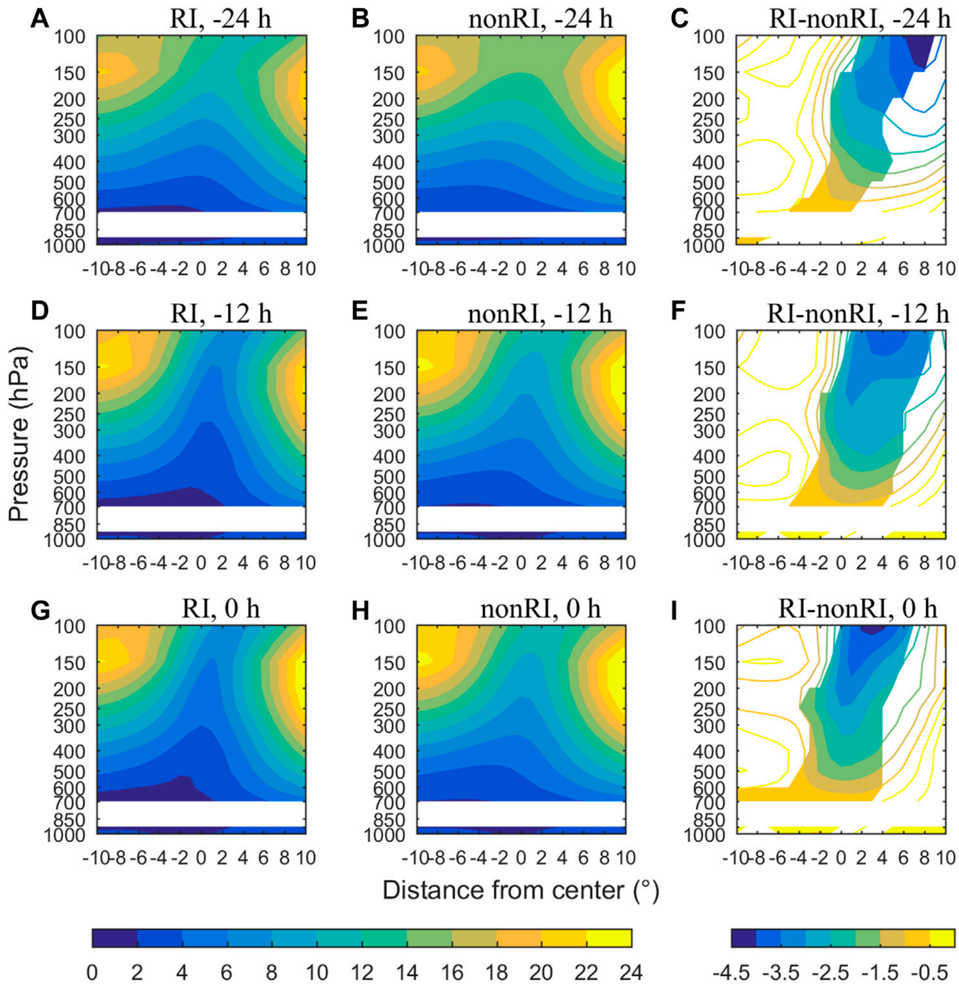

FIGURE 7 | Same as **Figure 3**, but for environmental VWS (m s^{-1}).

These systems for RI TCs are significantly stronger at the three times (−24, −12, 0 h) than those for non-RI TCs. The cold air mass behind the westerly trough invades southward into the TC, and triggers baroclinic deep convection and produces potential vorticity (PV) anomalies outside the TC inner-core area. The inward transport of PV anomalies and the subsequent symmetrization of the TC circulation are conducive to RI of TCs (May and Holland, 1999; Moller and Montgomery, 2000; Nolan et al., 2007). Besides, the continental high accompanied by the westerly trough can strengthen the cyclonic horizontal shear and convergence, which is also conducive to TC intensification (Chen et al., 2015).

Figure 6 shows the composite environmental wind field at 200 hPa. Both types of TCs are located to the south of the upper-level westerly jet. RI TCs are located in the easterly flow on the equator side of the upper-level anticyclonic ridge. The southwestward outflow in the south and the northeastward outflow in the northeast are significantly stronger than those associated with non-RI TCs, which is consistent with the stronger upper-level divergence of RI TCs mentioned above. The more favorable upper-level outflow channels of RI TCs can strengthen the TC secondary circulation, which is conducive to the spin-up of the TC primary circulation.

VWS

The temporal evolutions of the meridional and zonal cross sections of environmental VWS are shown in **Figures 7**, **8**, respectively. The spatial distributions of VWS for the RI and non-RI TCs are similar. The VWS gradually increases from the lower to upper troposphere. The VWS near the TC center is notably weaker than that north and south of the center, and the VWS to the north is stronger than that to the south. However, the zonal distribution of VWS is more uniform. The VWS evolutions of the two types of events are somewhat different. During the 24-h period, the VWS around the RI TC center shows a decreasing tendency while the VWS of non-RI TCs changes little; the VuWS of RI TCs are always weaker than that

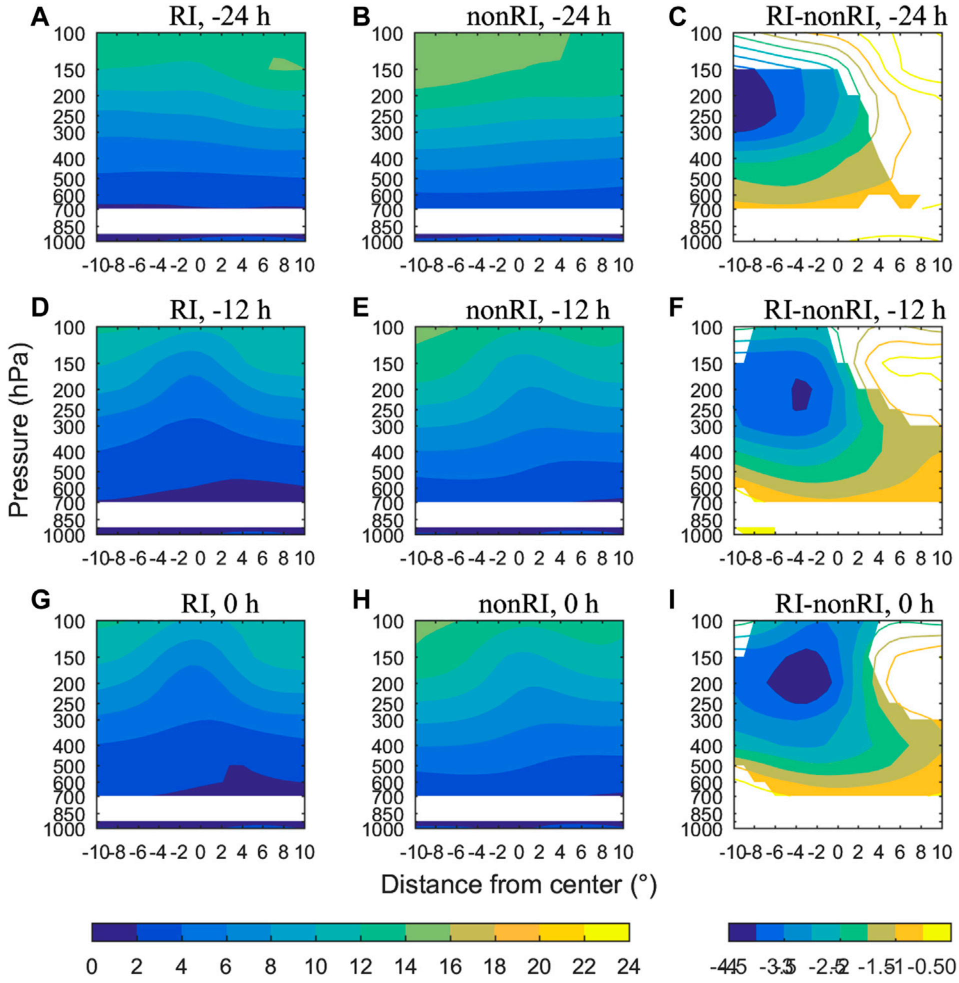

FIGURE 8 | Same as **Figure 7**, but for zonal cross sections.

of non-RI TCs, and the deep-layer shear between the upper levels and 850 hPa around the RI TC center is always less than 10 m s^{-1}. The deep-layer shear northwest of the TC center at 0 h shows the most significant difference between RI and non-RI TCs (**Figures** 7, **8**). However, Wang et al. (2015) pointed out that the low-level shear between 850 and 1,000 hPa was more negatively correlated with intensity change of the WNP TCs than deep-layer shear. This inconsistency suggests that the relative importance of VWS in different layers for TC intensity change may depend on large-scale circulations over the specific ocean basin.

Relative Humidity

The temporal evolutions of the meridional and zonal cross sections of environmental relative humidity are indicated in **Figures 9**, **10**, respectively. At the three times (−24, −12, and 0 h), the spatial distributions of relative humidity of RI and non-RI TCs are similar, featuring wet upper and lower troposphere and dry middle troposphere, with the driest middle-level air located northwest of the TC center. At −24 h, there is a significant difference in relative humidity southeast of the TC center at the middle and upper levels, which can be used as a precursor to RI. Over time, the middle- and upper-level air southeast of the TC center humidifies to a certain extent, and the significant difference in relative humidity southeast of the TC center at the middle and upper levels is still maintained. This may be related to the continuous water vapor transport by the southeasterly wind southwest of the WPSH.

The intrusion of middle-level dry air from the northwest to the TC inner core can suppress the development of cumulus convection and the release of latent heat of condensation, which is not conducive to TC intensification (Braun et al., 2012; Ge et al., 2013). We notice that the middle-level humidity near the RI TC center is significantly higher than that of non-RI TCs, so it can effectively resist the intrusion of middle-level dry air from the northwest (Gao et al., 2017). In addition, moist air is

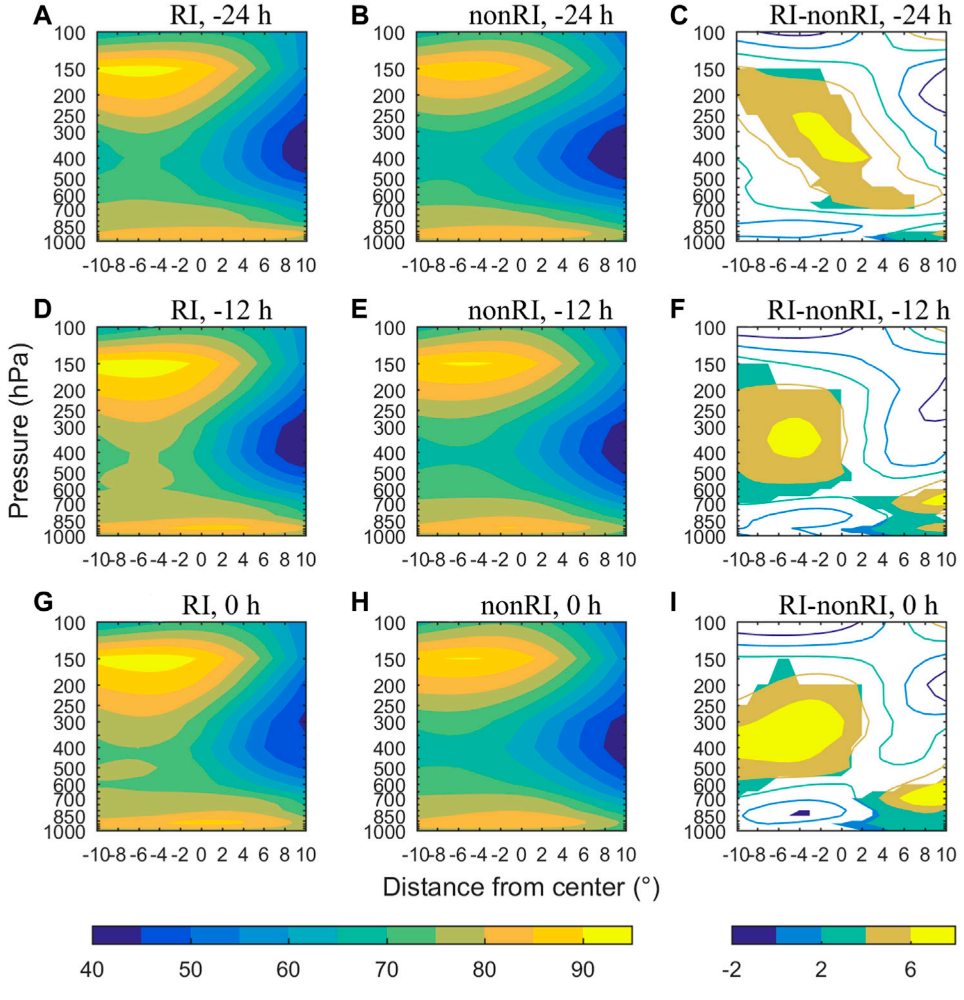

FIGURE 9 | Same as **Figure 3**, but for environmental relative humidity (%).

transported from the southeast to the inner core of RI TCs. Both are conducive to the development of moist convection, thus leading to TC RI.

SST

The temporal evolution of the composite SST is shown in **Figure 11**. The spatial patterns for two types of TCs are both characterized by cold SST in the north and warm SST in the south, and SST near the TC center exceeds 28°C, which meets the necessary SST condition for RI (Holliday and Thompson, 1979). SST of RI TCs around the storm center is significantly higher than that of non-RI TCs at the three times. This result is consistent with previous studies (e.g., Wang et al., 2015; Gao et al., 2016). TCs tend to intensify at a higher rate under higher SST because of a larger supply of surface latent and sensible heat fluxes (e.g., Emanuel, 1986; Gao and Chiu, 2010). The meridional SST gradient does not show meaningful differences between RI and non-RI SCS TCs (figure not shown).

Intensification Potential (POT)

MPI is the theoretically-estimated maximum intensity that a TC can achieve under current atmospheric and ocean conditions (Emanuel, 1988). POT is the difference between MPI and current intensity, representing the intensification potential of TCs. The temporal evolution of the composite POT is shown in **Figure 12**. The POT of RI and non-RI TCs decreases from the south to the north, and gradually reduces with time. At −24 h, the POT west and north of RI TCs is significantly greater than that of non-RI TCs. Since most of TCs move westward or northward (dsl), the POT over 40 m s^{-1} in the west and north at −24 h is conducive to the occurrence of RI. Therefore, the POT north of TCs in the SCS at −24 h has a good predictive significance for RI.

Key Factors for RI

According to the above composite results, the time with the most significant difference in each factor between RI and non-RI TCs and the area with significant difference are given in **Table 1**, and the corresponding areal average for each factor is calculated.

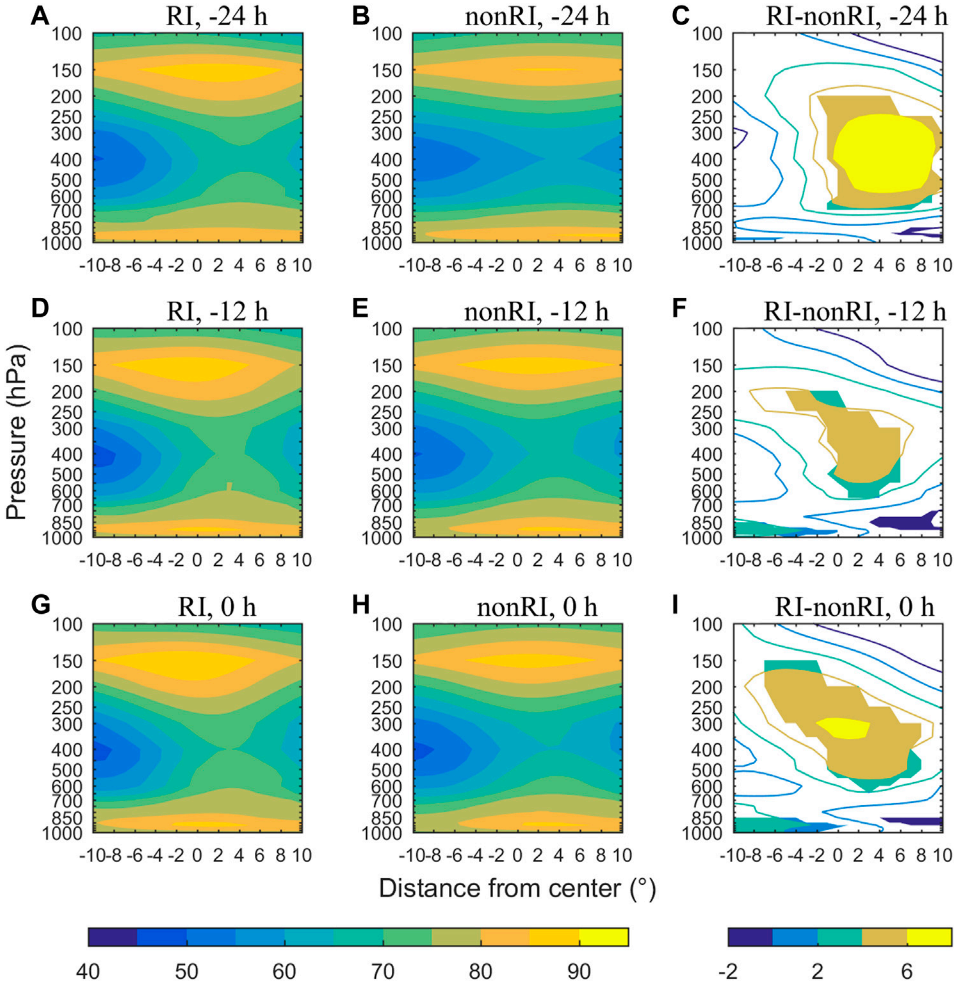

FIGURE 10 | Same as **Figure 9**, but for zonal cross sections.

Figure 13 shows the BDI values of their areal averages and TC translation speed as well as the *t*-test results. The difference in environmental divergence between the upper and lower levels at −24 h, the deep-layer environmental VWS at 0 h, SST around the TC center, the POT north of the TC center at −24 h, the middle- and upper-level environmental relative humidity southeast of the TC center at −24 h, and TC translation speed from 0 to 24 h pass the significance test at the 95% confidence level, indicating that they are important factors for RI of the SCS TCs.

To further clarify the importance of different factors for RI, stepwise regression is applied on the normalized variables including the predictand ΔV_{24} and the potential predictors listed in **Table 1**. The regression equation trained with the 95% confidence level is

$$\Delta V_{24} = 1.06 + 1.39 * DIV - 0.62 * VWS + 0.31 * SPD + 0.10 * POT \tag{3}$$

The regression equation confirms that the difference in environmental divergence between the upper and lower levels at −24 h, the deep-layer environmental VWS at 0 h, TC translation speed from 0 to 24 h, and the POT north of the TC center at −24 h are key factors for RI of the SCS TCs. Their decreasing absolute values of regression coefficients suggest their importance in that order.

Figure 14 shows the boxplots for six factors of RI and non-RI TCs. The RI samples are more concentrated than the non-RI samples. Although all factors passing the 95% significance test, the boxes of RI and non-RI TCs partly overlap. Therefore, it is difficult to forecast RI by using an individual factor. In general, such conditions, including strong divergence in the upper troposphere and strong convergence in the lower troposphere, weak deep-layer VWS, large POT north of the TC center at −24 h, and fast TC translation speed, are favorable for RI of the SCS TCs.

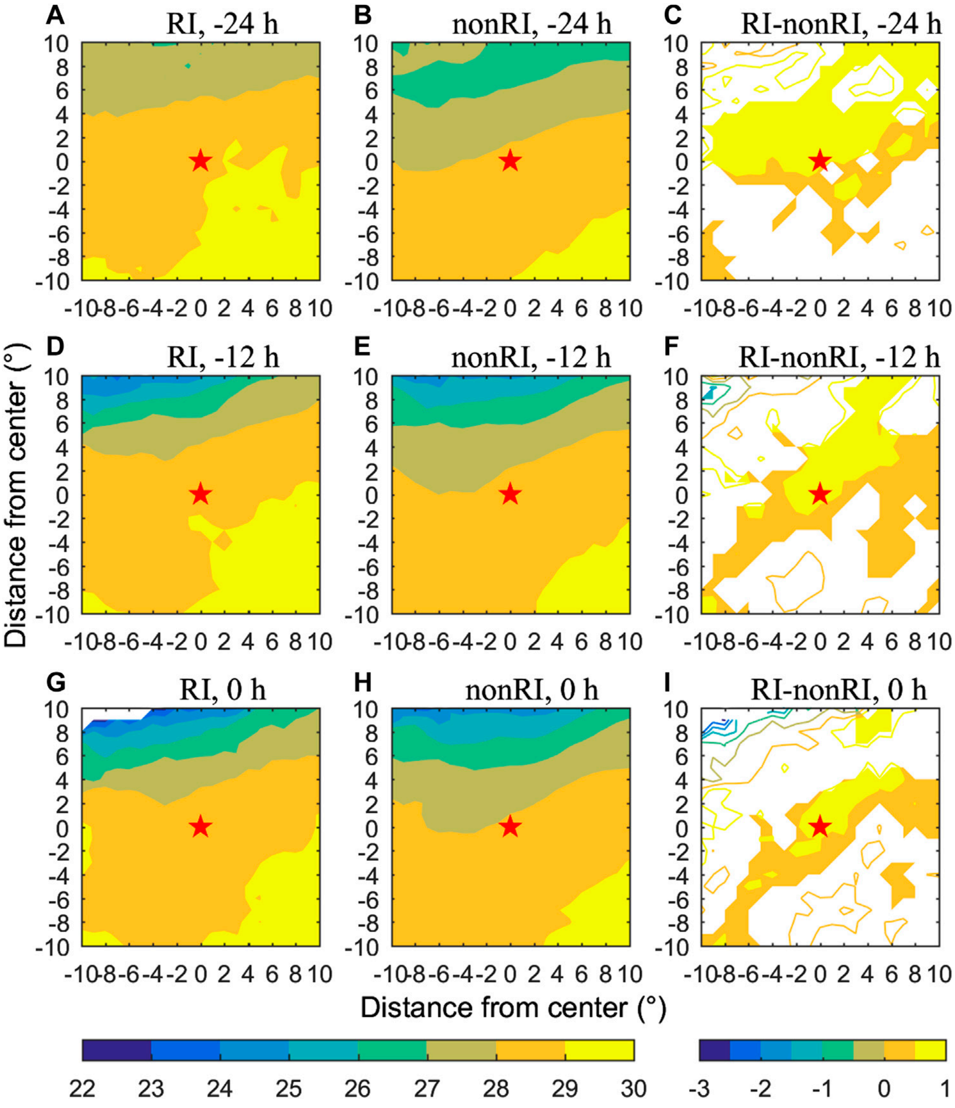

FIGURE 11 | Same as **Figure 5**, but for SST (°C) in 20° × 20° areas around the TC center.

CONCLUSION AND DISCUSSION

The temporal evolution characteristics of the environmental fields of RI and non-RI TCs in the SCS during 2000–2018 have been compared in this paper, and the following characteristics of RI TCs have been found. From −24 to 0 h, the positive vorticity at 1,000–300 hPa, the divergence at 200–150 hPa, and boundary-layer convergence continues to increase. The deep-layer shear between the upper levels and 850 hPa around the TC center is always less than 10 m s^{-1}. The environmental moist layer is thick. The underlying SST is high. The POT north of the TC center is larger than 40 m s^{-1} at −24 h. Then, the average environmental factors are calculated over the areas with significant difference between the two types of TCs. Combined with the BDI and *t*-test method as well as stepwise regression, it has been found that the configuration of strong upper-level divergence and strong boundary-layer convergence, weak deep-layer VWS, fast TC translation speed, and large POT north of the TC center are the key factors for RI of the SCS TCs, and their importance to the RI decreases in that order.

Compared with TCs in the entire WNP basin, the environmental fields conducive to the occurrence of TC RI in the SCS are somewhat different. First, RI TCs in the SCS are accompanied by higher environmental relative humidity at middle and upper levels, while RI TCs in the WNP is accompanied by higher low-level relative humidity (Shu et al., 2012). Secondly, RI TCs in the SCS have weaker deep-layer VWS, while RI TCs in the WNP

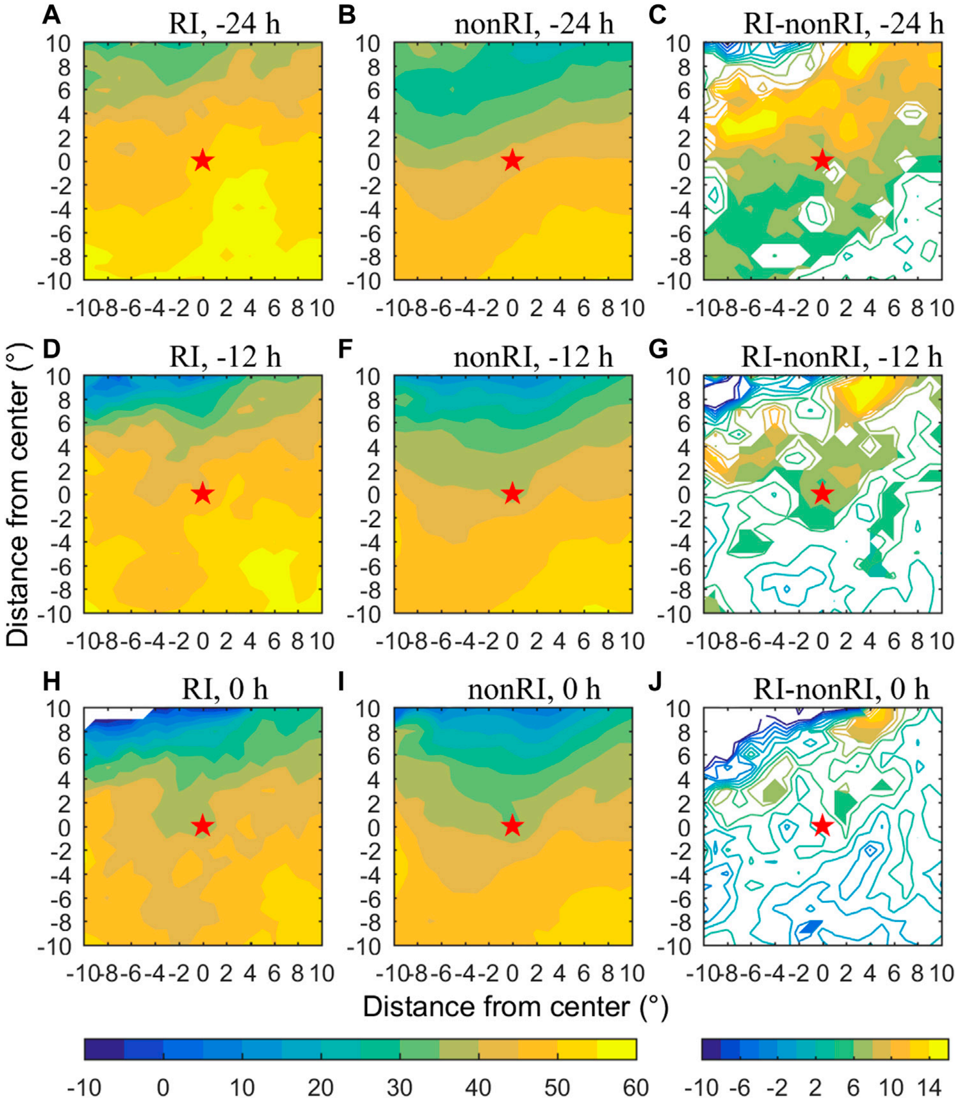

FIGURE 12 | Same as **Figure 11**, but for POT (m s^{-1}).

TABLE 1 | The selected time and range for calculating the areal average of each environmental factor.

Variable	Description	Time (h)	Vertical and horizontal ranges for areal average
DIV	Difference between upper-level and lower-level divergence	−24	200–150 hPa, −6 to 6° in both zonal and meridional directions; 1,000–850 hPa, −3 to 6° in meridional direction, and −6 to 4° in zonal direction
VWS	Wind shear between the upper levels and 850 hPa	0	400–100 hPa, 0–4° in meridional direction, and −8 to 0° in zonal direction
SST	Sea surface temperature	0	−2 to 2° in meridional direction, and −2 to 2° in zonal direction
POT	MPI minus current intensity	−24	0–6° in meridional direction, and −8 to 6° in zonal direction
RH	Middle–upper-tropospheric relative humidity	−24	500–200 hPa, −4 to 1° in meridional direction, and 0–8° in zonal direction
VOR	Middle–lower-tropospheric relative vorticity	−24	1,000–300 hPa, −2 to 5° in meridional direction, and −4 to 2° in zonal direction
SPD	TC translation speed	0 to +24	N/A

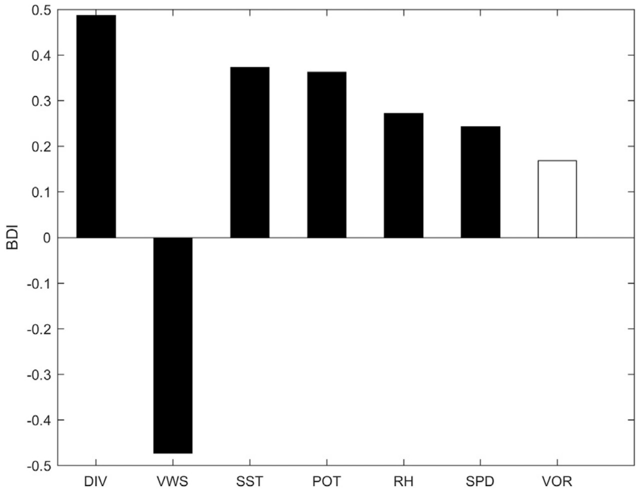

FIGURE 13 | BDI values of the environmental factors listed in **Table 1**. Filled boxes denote those factors significant above the 95% confidence level.

have weaker low-level VWS (Wang et al., 2015). Thirdly, RI TCs move significantly faster than non-RI TCs in the SCS, while there is no significant difference in translation speed between RI and non-RI TCs in the WNP (Shu et al., 2012). In addition, the areas with significant differences in these key factors are also quite different from the areas for calculation of the related predictors in operational statistical intensity prediction schemes of the WNP TCs (e.g., Knaff et al., 2005; Gao and Chiu, 2012), indicating that the environmental factors affecting intensity change of TCs in the SCS and WNP are somewhat different. Thus, we should deal with the predictors separately when establishing the statistical intensity prediction models for the SCS TCs.

In this study, some key environmental factors for RI of the SCS TCs have been identified through statistical methods. However, some samples of these factors overlap in the boxplots of RI and non-RI TCs, hence it is difficult to effectively forecast RI by using an individual factor. In the near future, combined with a variety of techniques, we will use these key factors to establish TC intensity prediction models, aiming to make more accurate forecasts for RI of the SCS TCs. Due to the limitation of data availability, some factors such as ocean heat content and mixed layer depth, which could also contribute to RI, are not analyzed in this study. The importance of these factors in intensity change of the SCS TCs would be examined when the data over a long period of time are available.

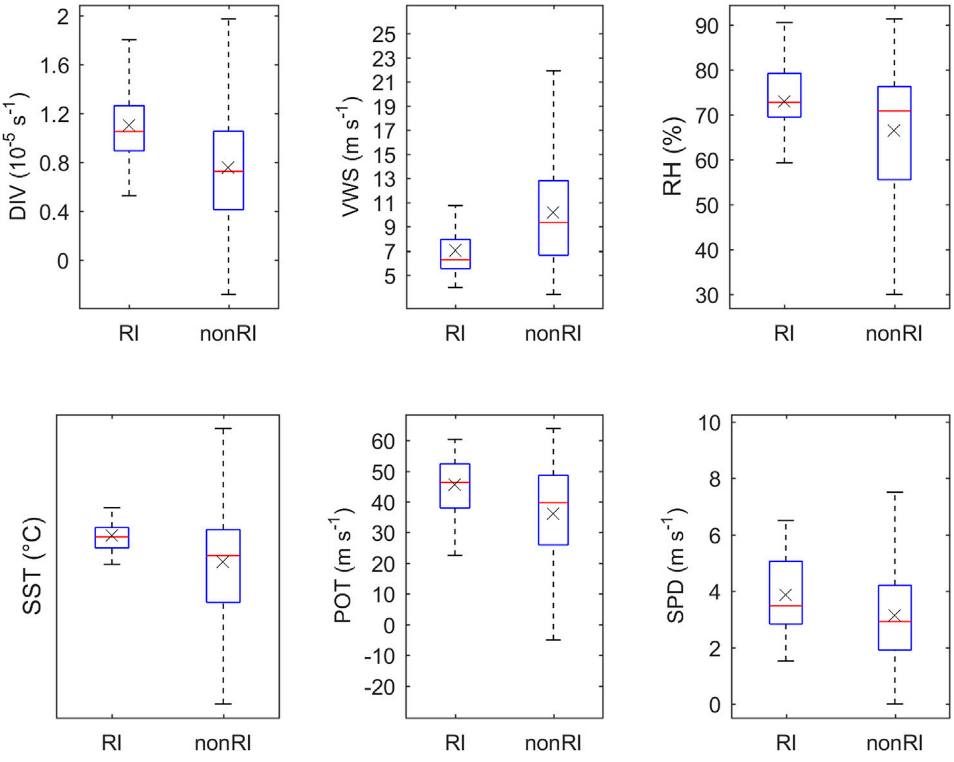

FIGURE 14 | Boxplots of the environmental factors for RI and non-RI TCs. The top (bottom) of each dashed line corresponds to the maximum (minimum) value. The upper (lower) boundary of each box denotes the 75th (25th) percentile, and the red line (black cross sign) inside the box denotes the median (mean).

DATA AVAILABILITY STATEMENT

The TC best track dataset is provided by the CMA Shanghai Typhoon Institute at http://tcdata.typhoon.org.cn/en/. The NCEP FNL analysis data are provided by the U.S. NCAR Research Data Archive at https://rda.ucar.edu/datasets/ds083.2. The OISST V2 data are provided by the NOAA/OAR/ESRL PSL, Boulder, Colorado, USA, from their Web site at https://psl.noaa.gov/.

AUTHOR CONTRIBUTIONS

SG designed the research. YC performed data analyses and prepared the figures. YC and SG wrote the manuscript. XL and XS discussed the results and commented on the manuscript.

FUNDING

This work was supported by the National Natural Science Foundation of China (Grant Nos. 41930967 and 41975054), the Strategic Priority Research Program of the Chinese Academy of Sciences (Grant No. XDA20100304), and Key Laboratory of South China Sea Meteorological Disaster Prevention and Mitigation of Hainan Province (Grant No. SCSF201901).

SUPPLEMENTARY MATERIAL

The Supplementary Material for this article can be found online at: https://www.frontiersin.org/articles/10.3389/feart.2020.609727/full#supplementary-material.

REFERENCES

Bai, L., and Wang, Y. (2016). Effects of vertical wind shear on tropical cyclone intensity change. *J. Trop. Meteorol.* 22, 11–18. doi:10.16555/j.1006-8775.2016.01.002

Braun, S. A., Sippel, J. A., and Nolan, D. S. (2012). The impact of dry midlevel air on hurricane intensity in idealized simulations with no mean flow. *J. Atmos. Sci.* 69, 236–257. doi:10.1175/jas-d-10-05007.1

Chen, X., Wang, Y., and Zhao, K. (2015). Synoptic flow patterns and large-scale characteristics associated with rapidly intensifying tropical cyclones in the South China Sea. *Mon. Weather Rev.* 143, 64–87. doi:10.1175/mwr-d-13-00338.1

Cheng, Z., Lin, L., Yang, G., and Sha, T. (2017). Rapid intensification and associated large-scale circulation of super typhoon Rammasun in 2014. *J. Appl. Meteorol. Sci.* 28, 318–326 [in Chinese, with English abstract]. doi:10.11898/1001-7313.20170306

Demaria, M. (1996). The effect of vertical shear on tropical cyclone intensity change. *J. Atmos. Sci.* 53, 2076–2088. doi:10.1175/1520-0469(1996)053<2076:teovso>2.0.co;2

Emanuel, K. A. (1986). An air-Sea interaction theory for tropical cyclones. Part I: steady-state maintenance. *J. Atmos. Sci.* 43, 585–605. doi:10.1175/1520-0469(1986)043<0585:aasitf>2.0.co;2

Emanuel, K. A. (1988). The maximum intensity of hurricanes. *J. Atmos. Sci.* 45, 1143–1155. doi:10.1175/1520-0469(1988)045<1143:tmioh>2.0.co;2

Fu, B., Peng, M. S., Li, T., and Stevens, D. E. (2012). Developing versus nondeveloping disturbances for tropical cyclone formation. Part II: Western North Pacific. *Mon. Weather Rev.* 140, 1067–1080. doi:10.1175/2011mwr3618.1

Gao, S., and Chiu, L. S. (2010). Surface latent heat flux and rainfall associated with rapidly intensifying tropical cyclones over the western North Pacific. *Int. J. Rem. Sens.* 31, 4699–4710. doi:10.1080/01431161.2010.485149

Gao, S., and Chiu, L. S. (2012). Development of statistical typhoon intensity prediction: application to satellite-observed surface evaporation and rain rate (STIPER). *Weather Forecast* 27, 240–250. doi:10.1175/waf-d-11-00034.1

Gao, S., Zhai, S., Chen, B., and Li, T. (2017). Water budget and intensity change of tropical cyclones over the western North Pacific. *Mon. Weather Rev.* 145, 3009–3023. doi:10.1175/mwr-d-17-0033.1

Gao, S., Zhai, S., Chiu, L. S., and Xia, D. (2016). Satellite air-sea enthalpy flux and intensity change of tropical cyclones over the western North Pacific. *J. Appl. Meteorol. Clim.* 55, 425–444. doi:10.1175/jamc-d-15-0171.1

Ge, X., Li, T., and Peng, M. (2013). Effects of vertical shears and midlevel dry air on tropical cyclone developments*. *J. Atmos. Sci.* 70, 3859–3875. doi:10.1175/jas-d-13-066.1

Gray, W. M. (1968). Global view of the origin of tropical disturbances and storms. *Mon. Weather Rev.* 96, 669–700. doi:10.1175/1520-0493(1968)096<0669:gvotoo>2.0.co;2

Hanley, D., Molinari, J., and Keyser, D. (2001). A composite study of the interactions between tropical cyclones and upper-tropospheric troughs. *Mon. Weather Rev.* 129, 2570–2584. doi:10.1175/1520-0493(2001)129<2570:acsoti>2.0.co;2

Holland, G. J. (1997). The maximum potential intensity of tropical cyclones. *J. Atmos. Sci.* 54, 2519–2541. doi:10.1175/1520-0469(1997)054<2519:tmpiot>2.0.co;2

Holliday, C. R., and Thompson, A. H. (1979). Climatological characteristics of rapidly intensifying typhoons. *Mon. Weather Rev.* 107, 1022–1034. doi:10.1175/1520-0493(1979)107<1022:ccorit>2.0.co;2

Hu, H., and Duan, Y. (2016). Analysis of environmental variables of rapidly intensifying tropical cyclones in the South China Sea. *J. Trop. Meteorol.* 32, 299–310 [in Chinese, with English abstract]. doi:10.16032/j.issn.1004-4965.2016.03.002

Jone, S. C. (1995). The evolution of vortices in vertical shear. I: initially barotropic vortices. *Q. J. Roy. Meteorol. Soc.* 121, 821–851. doi:10.1002/qj.49712152406

Kaplan, J., and DeMaria, M. (2003). Large-scale characteristics of rapidly intensifying tropical cyclones in the North Atlantic basin. *Weather Forecast.* 18, 1093–1108. doi:10.1175/1520-0434(2003)018<1093:lcorit>2.0.co;2

Knaff, J. A., Sampson, C. R., and DeMaria, M. (2005). An operational statistical typhoon intensity prediction scheme for the Western North Pacific. *Weather Forecast* 20, 688–699. doi:10.1175/waf863.1

Kurihara, Y., Bender, M. A., and Ross, R. J. (1993). An initialization scheme of hurricane models by vortex specification. *Mon. Weather Rev.* 121, 2030–2045. doi:10.1175/1520-0493(1993)121<2030:aisohm>2.0.co;2

Li, X., Zhao, S., Li, Z., Li, Y., and Wang, Y. (2011). Characteristics of intensity change in tropical cyclones affecting the South China Sea from 1977 to 2007. *J. Trop. Meteorol.* 17, 156–165 [in Chinese, with English abstract]. doi:10.3969/j.issn.1006-8775.2011.02.008

May, P. T., and Holland, G. J. (1999). The role of potential vorticity generation in tropical cyclone rainbands. *J. Atmos. Sci.* 56, 1224–1228. doi:10.1175/1520-0469(1999)056<1224:tropvg>2.0.co;2

Mei, Y., and Yu, J. (2016). Effect of environment field on rapid intensification process of tropical cyclones over the western North Pacific. *J. Appl. Meteorol. Sci.* 36, 770–778 [in Chinese, with English abstract]. doi:10.3969/2016jms.0006

Merrill, R. T. (1988). Environmental influences on hurricane intensification. *J. Atmos. Sci.* 45, 1678–1687. doi:10.1175/1520-0469(1988)045<1678:eiohi>2.0.co;2

Möller, J. D., and Montgomery, M. T. (2000). Tropical cyclone evolution via potential vorticity anomalies in a three-dimensional balance model. *J. Atmos. Sci.* 57, 3366–3387. doi:10.1175/1520-0469(2000)057<3366:tcevpv>2.0.co;2

Nolan, D. S., Moon, Y., and Stern, D. P. (2007). Tropical cyclone intensification from asymmetric convection: energetics and efficiency. *J. Atmos. Sci.* 64, 3377–3405. doi:10.1175/jas3988.1

Qiu, W., Wu, L., and Ren, F. (2020). Monsoonal influences on offshore rapid intensification of landfalling typhoons in a sheared environment over the South China Sea. *Weather Forecast* 35, 623–634. doi:10.1175/waf-d-19-0134.1

Reynolds, R. W., Smith, T. M., Liu, C., Chelton, D. B., Casey, K. S., and Schlax, M. G. (2007). Daily high-resolution-blended analyses for sea surface temperature. *J. Clim.* 20, 5473–5496. doi:10.1175/2007jcli1824.1

Shay, L. K., Goni, G. J., and Black, P. G. (2000). Effects of a warm oceanic feature on Hurricane Opal. *Mon. Weather Rev.* 128, 1366–1383. doi:10.1175/1520-0493(2000)128<1366:eoawof>2.0.co;2

Shu, S., Ming, J., and Chi, P. (2012). Large-scale characteristics and probability of rapidly intensifying tropical cyclones in the western North Pacific Basin. *Weather Forecast* 27, 411–423. doi:10.1175/waf-d-11-00042.1

Sitkowski, M., Kossin, J. P., and Rozoff, C. M. (2011). Intensity and structure changes during hurricane eyewall replacement cycles. *Mon. Weather Rev.* 139, 3829–3847. doi:10.1175/mwr-d-11-00034.1

Tuleya, R. E., and Kurihara, Y. (1981). A numerical study on the effects of environmental flow on tropical storm genesis. *Mon. Weather Rev.* 109, 2487–2506. doi:10.1175/1520-0493(1981)109<2487:ansote>2.0.co;2

Wang, Y., Rao, Y., Tan, Z.-M., and Schönemann, D. (2015). A statistical analysis of the effects of vertical wind shear on tropical cyclone intensity change over the western North Pacific. *Mon. Weather Rev.* 143, 3434–3453. doi:10.1175/mwr-d-15-0049.1

Xu, W., Zhou, S., Ge, X., and Ma, Y. (2017). Wind speed distribution features of rapidly intensifying tropical cyclones in Northwest Pacific. *J. Trop. Meteorol.* 33, 259–266 [in Chinese, with English abstract]. doi:10.16032/j.issn.1004-4965.2017.02.012

Yang, B., Wang, Y., and Wang, B. (2007). The effect of internally generated inner-core asymmetries on tropical cyclone potential intensity*. *J. Atmos. Sci.* 64, 1165–1188. doi:10.1175/jas3971.1

Yang, S., Li, Y., and Chen, L. (2017). The characteristics of tropical cyclone intensity change in western North Pacific. *J. Trop. Meteorol.* 33, 666–674 [in Chinese, with English abstract]. doi:10.16032/j.issn.1004-4965.2017.05.010

Ying, M., Zhang, W., Yu, H., Lu, X., Feng, J., Fan, Y., et al. (2014). An overview of the China Meteorological Administration tropical cyclone database. *J. Atmos. Ocean. Technol.* 31, 287–301. doi:10.1175/jtech-d-12-00119.1

Zeng, Z., Wang, Y., and Wu, C.-C. (2007). Environmental dynamical control of tropical cyclone intensity-an observational study. *Mon. Weather Rev.* 135, 38–59. doi:10.1175/mwr3278.1

Conflict of Interest: The authors declare that the research was conducted in the absence of any commercial or financial relationships that could be construed as a potential conflict of interest.

frontiers in Earth Science

ORIGINAL RESEARCH
published: 02 February 2021
doi: 10.3389/feart.2020.601666

Prediction of the Variability of Changes in the Intensity and Frequency of Climate Change Reinforced Multi-Day Extreme Precipitation in the North-Central Vietnam Using General Circulation Models and Generalized Extreme Value Distribution Method

Pham Quy Giang *

Faculty of Environment, Ha Long University, Quang Ninh, Vietnam

OPEN ACCESS

Edited by:
Ming Luo,
Sun Yat-Sen University, China

Reviewed by:
Zhen Liu,
University of Edinburgh,
United Kingdom
Yuan Shi,
The Chinese University of Hong Kong,
China

***Correspondence:**
Pham Quy Giang
phamquygiang@daihochalong.edu.vn

Specialty section:
This article was submitted to
Interdisciplinary Climate Studies,
a section of the journal
Frontiers in Earth Science

Received: *01 September 2020*
Accepted: *16 December 2020*
Published: *02 February 2021*

Citation:
Giang PQ (2021) Prediction of the Variability of Changes in the Intensity and Frequency of Climate Change Reinforced Multi-Day Extreme Precipitation in the North-Central Vietnam Using General Circulation Models and Generalized Extreme Value Distribution Method.
Front. Earth Sci. 8:601666.
doi: 10.3389/feart.2020.601666

Flooding of downstream agricultural fields and cities is normally caused by consecutive days of extreme precipitation in upstream areas. As climate change is widely projected to accelerate the hydrological cycle, concerns about the increase in frequency and intensity of extreme precipitation arise. The present study used Pattern Scaling coupled with Generalized Extreme Value (GEV) distribution to calculate changes in multi-day extreme precipitation in the North Central Vietnam in 2050, 2070, and 2090 under three AR5's Representative Concentration Pathways RCP2.6, RCP6.0 and RCP8.5. Twenty long-term historical observation stations in the study area with daily data mostly date back to more than 50 years were employed and 5-day maximum total precipitation was analyzed. The results reveal an agreement among the employed GCMs on an increase in the intensity and a shortening of the return periods of extreme precipitation, with the most reinforced trend occurring under RCP8.5, followed by RCP6.0 and then RCP2.6. This indicates that the risk of associated floods is likely to increase, especially under higher RCPs. Therefore, planning and decision making of durable infrastructure along with flood mitigation strategies to cope with such events are recommended.

Keywords: climate change, extreme precipitation, GEV, pattern scaling, frequency, intensity

INTRODUCTION

Extreme precipitation (EP) is the major cause of floods, erosion and landslides, which result in severe damages to agriculture and infrastructures. It has been reported that during the past century, there has been a significant increase in extreme precipitation events; and more notably, in many regions, especially mid-latitude regions, increases in annual heavy precipitation events were disproportionate compared to changes in mean values (IPCC, 2013). For instance, in the United States, the frequency of extreme precipitation events since the 1920s/1930s was found to sizably increase (Kunkel, 2003). In Germany, an analysis of precipitation observed during 1901–2000 shows that climate was getting more extreme in the winter during this period (Tromel and Schonwiese, 2007). A similar finding was reported by Zolina et al. (2008), and that a positive linear trend in heavy precipitation was found not only for winter but also for spring and autumn since 1950. Significant increases in Evapotranspiration (ET) were also observed in different regions of China in the second half of the 20th century, including its western part, the middle and lower Yangtze River basin, and its southeast coastal part (Zhao et al., 2014).

Although observations have shown significant increases in extreme precipitation and it is widely acknowledged that extreme climate events in general and ET in particular potentially produce greater impacts on the society and environment than a shift in average values (IPCC, 2007), less attention has been paid to their future changes, especially at regional and local scales. This may be due to the lack of an effective method. To date, General Circulation Model (GCM) is still the most common tool for the simulation and prediction of climate change in large scales. However, because the spatial resolution of GCMs is generally low so that it is not appropriate to directly use their output for local scale, especially for extreme precipitation because extreme precipitation is a much localized phenomenon (Ye and Li, 2011). In order to overcome the shortcoming of coarse spatial resolution of GCMs, the downscaling approaches, including dynamical downscaling and statistical downscaling have been introduced and have become widely used in research (IPCC, 2001). The dynamic method refers to the use of Regional Climate Models which utilize large scale and lateral boundary conditions of GCMs to generate finer spatial resolution outputs; while in the statistical method, a statistical relationship between the observations of large scale variables and that of a local variable is used for the calculation of the local variable in the future from the GCM output (Trzaska and Schnarr, 2014). The use of downscaling in climate research became widespread in the early 1990s (Wilby and Wigley, 1997). In Europe during the 1990s, the Dutch Meteorological institute (KNMI) and the Danish Meteorological institute (DMI) built the Regional Atmospheric Climate Model (RACMO) based on the High Resolution Limited Area Model (HIRLAM). Another related regional climate model called HIRHAM established in 1992 (Christensen et al., 1996), which was based on a subset of the regional HIRLAM and global ECHAM models (Roeckner et al., 2003), combining the dynamics of the former with the parameterization schemes of the latter. Other regional models include Weather Research and Forecasting (WRF) and the HadRCM3 at the United Kingdom. Hadley Centre, and RCA from the Swedish Rossby Centre. In North America, the North American Regional Climate Change Assessment Program (NARCCAP) was established with the efforts to produce high-resolution climate change simulations for the North American region, and in 2004, it launched experiment 0.0 and 0.1 to compare (among other things) temperature and precipitation from the models with observations. In Asia, the Regional Climate Model Intercomparison Project (RMIP) (Fu et al., 2005) was established to examine and compare different climatological drivers to those of its American and European counterparts. The drivers in question included the Asian monsoon and the effect of the Tibetan Plateau on the large-scale flows crossing the Eurasian continent. In recent years, numerous studies applied downscaling was conducted (such as Rummukainen, 2010; Maraun et al., 2010; Gutiérrez et al., 2013; Trzaska and Schnarr, 2014). For extremes, most of the past work on extremes and their dependency on climate change has involved RCMs or empirical-statistical downscaling (ESD), using some index representing extremes (e.g., STARDEX). ESD-based approaches can involve a number of different methods and may be set up to estimate parameters of the probability distribution function describing the local climate. However, some methods may not be well suited for downscaling extremes because they are unable to prescribe values outside the historical sample on which it is trained. According to Deser et al. (2012), from an analytics perspective, it will become possible to derive better information about extreme events, especially if ensembles of GCMs increase in size, their resolution is improved, the range of natural variability is better represented, and improved tools use the latest statistical methods, and hence attribute probabilities. In short, although downscaling methods are able to provide outputs which can be used for a local scale, they require either extensive computational power or a huge number of observations.

The present study predicts changes in future multi-day extreme precipitation using both the result of climate models through the application of Simple Climate Model so-called pattern scaling method and the trend of historical extreme precipitation using Generalized Extreme Value (GEV) distribution. Pattern scaling method was first introduced by Santer et al. (1990) with the assumption that the local response of a climate variable is linearly related to the global mean temperature change, with the geographical pattern of change independent of the forcing. Spatial features of the externally forced change, standardized by global average temperature warming, were estimated on the basis of 2xCO2 equilibrium simulations by mixed-layer ocean GCMs. These patterns were assumed to remain stable also during a transient simulation where the main external forcing is an increase in well-mixed greenhouse gases. These common features explain a large portion of the variability of the externally forced changes in temperature and precipitation over time and across scenarios within a given model. Pattern scaling has been widely used, its application therefore has a rich literature. Ruosteenoja et al. (2007), Watterson (2008), Giorgi (2008), Harris et al. (2010), Cabre et al. (2010), and Watterson and Whetton (2011) used pattern scaling to produce regional climate change projections, and Dessai et al. (2005) and Fowler et al. (2007) used pattern scaling for impact studies. Although limitations of this method have been found, such as it was less accurate for strongly mitigated stabilization scenarios (May, 2012) or it needs to be modified if future scenarios include significant changes over time in the strength of regional sources of pollution (May, 2008), many model experiments have shown that precipitation patterns scale linearly with global average temperature to a good degree of accuracy (Neelin et al., 2006; Shiogama et al., 2010), and that pattern scaling method is accurately applicable for climate change projection in general and precipitation projection in particular.

Meanwhile, GEV distribution is a continuous probability distribution evolved within extreme value theory and is used as an approximation to model the maxima of long or finite sequences of random variables. The use of GEV distribution in extreme precipitation analysis and prediction is well documented. For instance, Rahmani et al. (2014) used GEV (Weibull type) distribution to calculate the extreme precipitation frequency in Kansas and the adjacent states in the United States. Xia et al. (2012) and Du et al. (2014) used (GEV) and Generalized Pareto distribution (GPD) to study the historical extreme precipitation frequency and its spatio-temporal variations in Haihe and Huaihe river basins of China. Benyahya et al. (2014) compared GEV with other four probability distributions (Generalized Logistic, Weibull, Gamma, and Lognormal) to identify the appropriate methods providing the most accurate seasonal maximum precipitation in southern Quebec of Canada. Rahman et al. (2013) investigated the suitability of GEV and other different probability distributions based on large Australian annual maximum flood datasets. In the Netherlands, most previous studies applied the GEV model to climatological statistics to describe the monthly and annual distribution of precipitation maxima (such as Buishand et al., 2009; https://www.sciencedirect.com/science/article/pii/S2212094716300433, Hanel and Buishand, 2010; Overeem and Buishand, 2012). It was found that the monthly variation generated by the GEV distribution model contains information about return levels (Rust et al., 2009). Previous studies have shown that GEV distribution is appropriate for extreme precipitation prediction, especially for the greatest values. According to Kharin et al. (2007) because it is impossible to collect observations for future climate conditions, using the GEV is a step to verify if a particular climate model can be used to assess potential effects of climate change on future extreme weather events.

In Vietnam, extreme precipitation is a serious concern due to its direct and indirect effects (through flooding, erosion and landslides) on agriculture, socio-economic activities and human life. Efforts have been made in analysis and prediction of extreme precipitation locally and nationally. Ho et al. (2011) studied extreme climatic events, including hot days, cold nights and heavy rainfall days in seven climatic sub-regions in Vietnam, based on historical observed data (1961–2007) and climate projections of the International Center for Theoretical Physics regional climate model version 3 (RegCM3). Extremes of each sub-region detected from the simulation of RegCM3 for the baseline period 1980–1999 were applied to the projection in the years 2001–2050, based on the IPCC SRES A1B and A2 scenarios, to reveal the changing trend of extremes in the future. The RegCM3 projections indicate that, the rainy season heavy rainfall events tend to decrease for allsub-regions except for two, in northwest and south-central Vietnam. Strong opposite projected changes in precipitation extremes over the southern half of Vietnam seem to be linked to changes in southwesterly air flow from the Bay of Bengal and the number of strong tropical cyclones coming from the South China Sea and the NW Pacific. Raghavan et al. (2017) applied a systematic ensemble high resolution climate modeling to study extreme precipitation over Vietnam using the PRECIS model developed by the Hadley Center in United Kingdom. The PRECIS model simulations were conducted at a horizontal resolution of 25 km for the baseline period 1961–1990 and a future climate period 2061–2090 under scenario A1B. The annual cycles and seasonal averages of precipitation over different sub-regions of Vietnam show the ability of the model in reproducing the observed peak and magnitude of monthly rainfall. The climate extremes of precipitation were also fairly well captured. Projections of future climate show both increases and decreases in the mean climate over different regions of Vietnam. The analyses of future extreme rainfall using the STARDEX precipitation indices show an increase in 90th percentile precipitation (P90p) over the northern provinces (15–25%) and central highland (5–10%) and over southern Vietnam (up to 5%). The total number of wet days (Prcp) indicates a decrease of about 5–10% all over Vietnam. Consequently, an increase in the wet day rainfall intensity (SDII), is likely inferring that the projected rainfall would be much more severe and intense which have the potential to cause flooding in some regions. Risks due to extreme drought also exist in other regions where the number of wet days decreases. In addition, the maximum 5 days consecutive rainfall (R5d) increases by 20–25% over northern Vietnam but decreases in a similar range over the central and southern Vietnam. Nam et al. (2015) assessed the near future (2,026–2,035) changes in extreme rainfall over Vietnam using projections by four high resolution multi-model belonging to the Coupled Model Intercomparison Project phase five, as compared to the baseline period (1979–2003). Results (ensemble mean) show that the highest precipitation amount in 3-day period and total precipitation on very wet days will greatly increase in the near future climate with larger increases in the northwest and southwest. Meanwhile, the highest precipitation amounts in one-and consecutive 5-day tend to be slightly increasing.

The application of GEV distribution and pattern scaling method in the present study for the North Central Region of Vietnam is a new method applied in Vietnam, and its result is expected to present another outlook of the future precipitation extreme in the studied region.

MATERIALS AND METHODS

The Study Area and Data

The area selected for this study is the Lower Ca River Basin (LCRB) (17°50'N-20°50'N, 103°14'E-106°10'E), which is one of the largest river basins in Vietnam. The LCRB is situated in the North Central Region with a basin area of 17,730 km^2, covering the entire Provinces of Nghe An and Ha Tinh and a part of Nhu Xuan District of Thanh Hoa Province. The North Central Region in general and the LCRB in particular is well-known as a hotspot of flooding in Vietnam due to high frequency and severity of floods in the region. Geographic location of the LCRB is shown in **Figure 1**.

Located in a tropical monsoon region, climate of the LCRB is characterized by two distinct seasons: rainy season (May to October) and dry season (November to April of the next year). The rainy season is hot and humid with temperature up to more than 42°C and humidity up to 95% around June and July,

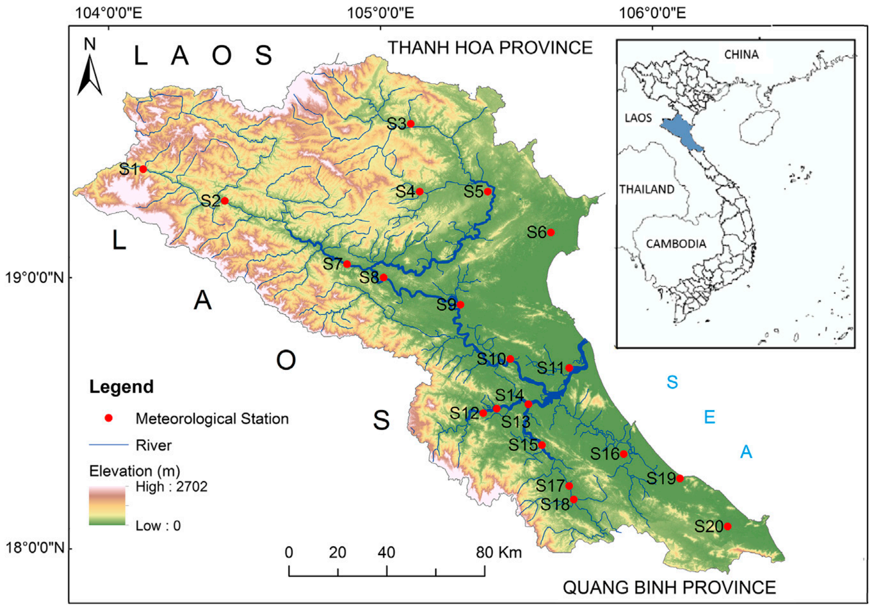

FIGURE 1 | Geographic location of the LCRB and meteorological stations in the basin.

while the dry season is cold and dry with the lowest temperature dropping to 0°C around January. Precipitation in the LCRB is abundant, but is seasonally and spatially uneven distributed (Giang et al., 2014; OECD, 2020). According to data of 20 gauges recorded from the 1960s to date, annual precipitation in the basin was mostly more than 1,000 mm, and exceeded 4,000 mm in some wet years. Mean annual precipitation for the observation period (mostly 1960–2018) varies from 1,200 mm to 2,800 mm depending on the weather station, with an average of approximately 2,000 mm. Precipitation was found to have an increasing trend from north-west to south-east direction, with all of 10 gauges in the North of Vinh (S11) having mean annual precipitation below 2,000 mm and eight of nine gauges in the South of Vinh having mean annual precipitation above 2,000 mm (Except for S14, which has mean annual precipitation of 1,974 mm) (**Table 1**). During the observation period, there were some very wet years, of which historic extreme precipitations and historic floods were recorded; they are 1978, 1988, 1989, 1991, and 2010. The highest annual precipitation in the basin was 4,391 mm (in 1988 at S16) and the highest daily precipitation was 788.4 mm, recorded on September 27, 1978 at S9. Although the basin receives a high amount of precipitation annually, more than 80% of precipitation is in the wet season, and 80% of this amount fall in the flood months which typically lasts from August to October. This seasonal uneven distribution of precipitation is the main factor causing annual floods and droughts in the basin.

An analysis of historical rainfall and flood data shows that in the study area, on average, the number of days from it starts raining till floods reach the peak level is 5 days. The present study therefore calculated the change of the maximum consecutive 5-days precipitation, which is defined as five-day extreme precipitation in this study.

In this study, twenty long-term historical observation stations in the LCRB with daily data mostly date back to more than 50 years were employed. The observed daily station data was firstly aggregated for every five consecutive days to construct a five days total precipitation time series and five-days maximum total precipitation was analyzed. The volume resolution of 24-h precipitation is 0.1 mm and there is missing data at three stations: S10 (missing June- December, 1981), S12 (missing 1967) and S19 (missing 1967 and 1968).

Methods

The present study applied Generalized Extreme Value (GEV) distribution for extreme precipitation analysis. GEV distribution is a continuous probability distribution evolved within extreme value theory and is used as an approximation to model the maxima of long or finite sequences of random variables. It is parameterized with the three parameters: Shape parameter (γ), location parameter (μ) and scale parameter (σ), and is presented by the following functions:

$$F_{\sigma,\gamma,\mu}(x) = exp\left[-\left(1+\gamma\frac{x-\mu}{\sigma}\right)^{-1/\gamma}\right] \quad with \quad 1+\gamma\left(\frac{x-\mu}{\sigma}\right)>0, \quad \gamma\neq 0 \tag{1}$$

and

$$F_{\sigma,\gamma,\mu}(x) = exp\left(-e^{-\frac{x-\mu}{\sigma}}\right) \qquad with \quad \gamma = 0 \tag{2}$$

where $\mu \in$ R and $\sigma > 0$. The shape parameter γ determines the type of GEV distribution. There are three types of distribution called Fréchet, Gumbel, and Weibull corresponding to $\gamma < 0$, $\gamma = 0$, and $\gamma > 0$, respectively.

TABLE 1 | List of meteorological stations used in this study.

Station ID	Station name	Long (°E)	Lat (°N)	Elevation (m)	Mean annual (mm)	Annual max (mm)	24 h max (mm)	Data availability	Missing
S1	Muong Xen	104.133	19.400	335.0	1,198	1,960 (1973)	193.2 (25/6/11)	1967–2018	1968
S2	Tuong Duong	104.433	19.283	97.0	1,283	1,888 (2005)	192 (31/8/80)	1961–2018	
S3	Quy Chau	105.117	19.567	87.0	1,673	2,492 (1978)	304.1 (18/8/91)	1961–2018	
S4	Quy Hop	105.150	19.317	76.2	1,612	2,346 (1978)	272.4 (23/10/86)	1968–2018	
S5	Tay Hieu	105.400	19.317	72.0	1,592	2,744 (1978)	344.6 (4/10/07)	1960–2018	
S6	Quynh Luu	105.633	19.167	3.0	1,608	3,101 (1978)	710.1 (8/9/93)	1961–2018	
S7	Con Cuong	104.883	19.050	32.0	1730	2,901 (1978)	449.5 (27/9/78)	1961–2018	
S8	Dua	105.017	19.00	27.7	1761	3,089 (1978)	683.7 (27/9/78)	1960–2018	
S9	Do Luong	105.300	18.900	14.0	1842	3,539 (1978)	788.4 (27/9/78)	1960–2018	
S10	Nam Dan	105.483	18.700	10.4	1725	2,939 (1978)	419 (27/9/78)	1960–2018	Jun–Dec 1981
S11	Vinh	105.700	18.667	6.0	2055	3,521 (1989)	596.7 (11/10/89)	1960–2018	
S12	Son Diem	105.383	18.500	18.1	2071	3,160 (1989)	364 (10/10/92)	1961–2018	1967
S13	Huong Son	105.433	18.517	11.0	2,193	3,344 (1989)	518.8 (11/10/83)	1963–2018	
S14	Linh Cam	105.550	18.533	22.6	1974	3,279 (1989)	429.9 (16/10/13)	1971–2018	
S15	Hoa Duyet	105.600	18.383	10.0	2,372	3,682 (1989)	681.5 (3/10/83)	1961–2018	
S16	Ha Tinh	105.900	18.350	3.0	2,622	4,391 (1988)	546 (23/10/86)	1961–2018	
S17	Chu Le	105.700	18.233	8.8	2,288	3,357 (2010)	548.2 (16/10/10)	1970–2018	
S18	Huong Khe	105.717	18.183	17.0	2,389	3,774 (1989)	492.6 (4/10/83)	1961–2018	
S19	Cam Nhuong	106.107	18.260	5.0	2,688	4,064 (1991)	583.6 (1/10/86)	1959–2018	1967, 1968
S20	Ky Anh	106.283	18.083	3.0	2,809	3,839 (1989)	573.1 (7/8/07)	1961–2018	

The three parameters of GEV distribution (i.e. σ, μ, and γ) can be estimated by different approaches depending on the object investigated. In hydrology and climatology, an approach known as Probability Weighted Moments (PWM) (Greenwood et al., 1979; Landwehr et al., 1979; Hosking et al., 1985) is widely used. Thus, in this study, GEV function parameters for the GCM baseline and future periods were estimated using the PWM method for each GCM grid (x,y). The change of extreme precipitation in a future period compared to the baseline period corresponding to a specific return period (the estimated time interval between precipitation events of a similar intensity) T is determined as:

$$\Delta P_{TFR\,(xy)} = P_{TFR\,(xy)} - P_{T\,(xy)} \tag{3}$$

Where $P_{T(xy)}$ is baseline extreme precipitation value for the grid (xy) attainted from applying GEV function to GCM simulation for the baseline period. In IPCC AR5, the baseline period is 1986–2005, centered by 1995 (Collins et al., 2013). $P_{TFR(xy)}$ is projected precipitation value for the future year F under Representative Concentration Pathway R for the same grid. The future year F is the central year of a projected period (20 years in principle).

As global warming is driven by increased radiative forcing, the Pattern Scaling method applied in this study can be described as: for a given P_T, its anomaly ΔP^{*}_{T} in future year (F) under Representative Concentration Pathway R for grid (x,y) can be derived as:

$$\Delta P^{*}_{TFR\,(xy)} = \Delta C_F \cdot P'_{T\,(xy)} \tag{4}$$

where ΔC_F is the difference between annual global mean temperature in future year F and that of the baseline period derived from applying the Model for the Assessment of Greenhouse-gas Induced Climate Change (MAGICC) (Wigley, 2008); and $\Delta P'_{T(xy)}$ is the change rate of P_T at grid (x,y) in response to that change of annual global mean temperature.

Pattern scaling method assumes that, for a given GCM, $\Delta P'_{T(xy)}$ can be obtained from any simulation run of that GCM. Practically, however, such a homogeneous result seldom happens for given available GCM data. This may be due to the GCM simulation period of 20 years is not long enough to obtain $\Delta P'_{T(xy)}$ with sufficient statistical significance. Another possible reason would be that the change rate of precipitation P_T does not have a linear relationship with the annual global temperature change in nature. In fact, in order to obtain more accurate predictions of future climate, deeper studies of the relationships between the change rate of climate variables and the global mean temperature changes are in need. However, such further studies require extensive experiments with purposely designed input and outputs of GCM simulation, which cannot be obtained by current technologies. Nevertheless, according to Ruosteenoja et al. (2007), error of pattern-scaling method in constructing regional climate projections for extreme events seems to be not very large. Thus, if pattern scaling method is applied for calculating $\Delta P'_{T(xy)}$ for a given GCM, in order to reduce the effects of the GCM internal variability from different RCPs and time periods when calculating $\Delta P'_{T(xy)}$, it is desirable to take into the calculation all available GCM outputs. Mitchell (2003) and Ruosteenoja et al. (2007) recommended a least squares regression method as follows:

$$\Delta \boldsymbol{P}'_{\boldsymbol{T}\,(xy)} = \frac{\sum\limits_{F=1}^{m}\sum\limits_{R=1}^{n} \Delta \boldsymbol{C}_{\boldsymbol{FR}} \cdot \Delta \boldsymbol{P}_{\boldsymbol{TFR}\,(xy)}}{\sum\limits_{F=1}^{m}\sum\limits_{R=1}^{n} \left(\Delta \boldsymbol{C}_{\boldsymbol{FR}}\right)^2} \tag{5}$$

where m is the number of simulation periods from a GCM and n is the number of Representative Concentration Pathway. For a given baseline extreme precipitation value P_T, a spatial $\Delta P'_T$ was calculated by applying **Eq. 5** to each GCM grid (x,y). After that, ΔP^*_T can be determined from **Eq. 4** with a given ΔC_F, and the future extreme precipitation value for grid (xy) can be determined by the following equation:

$$\boldsymbol{P}_{\boldsymbol{TFR}\,(xy)} = \boldsymbol{P}_{\boldsymbol{OT}\,(xy)} + \Delta \boldsymbol{P}^{*}_{\boldsymbol{TFR}\,(xy)} \tag{6}$$

where $P_{OT(xy)}$ is the observed extreme value with return period T.

To establish the GEV function for a future year F, $\Delta P_{T(xy)}$ was calculated for seven different return period (i.e., 2, 5, 10, 20, 50, and 100 years) based on **Eq. 6**. Then, the Levenberg-Marquardt algorithm developed by Press et al. (1997) was applied to fit the seven extreme values to GEV function in order to calculate the GEV function parameters. It should be noted that although the same GEV function parameters were applied to all selected GCMs, the change pattern of extreme precipitation for the same region (or more precisely for the same GCM grid) may vary among GCM simulations due to inter-model uncertainty. To quantify the widest possible range of uncertainties, large ensembles of GCM predictions are needed. The quantified uncertainty range is helpful information for proposing proper countermeasure for tackling future climate change impact.

In the present study, fourteen GCMs from the Coupled Model Intercomparison Project phase five (CMIP5) archive (which is also the data source for IPCC AR5 climate change projections) were employed. The selection of GCMs was principally based on the spatial resolution of the GCMs. In each GCM family, only one GCM with highest resolution was selected. In the case there were two or more GCMs with the same resolution, the latest GCM was selected. A list of GCMs employed is presented in **Table 2**.

RESULTS AND DISCUSSION

Change in the Intensity of Extreme Precipitation Events

To investigate the spatial variation of change of extreme precipitation, ensemble median of all fourteen GCMs listed in **Table 1** was carried out for all twenty local stations in the studied basin. Employing multiple ensemble members helps to reduce bias prediction of each single member GCM. Results reveal increases in precipitation extremes in the future time periods (2050, 2070, and 2090) relative to the baseline scenario (1986–2005) under all the three RCP pathways, but with a divergent pattern depending on the RCP and the return period (**Figure 2**). Among the three scenarios, extreme precipitation increases the most under RCP8.5, followed by RCP6.0 and increases the least under RCP2.6 for all return periods. Both RCP6.0 and RCP8.5 show an upward trend throughout the projection period but the increment is steadier under the higher RCP. The low RCP2.6 pathway shows a downward trend in the increase of the extreme precipitation from 2050 forward. The trend is steady from 2050 to 2070 but becoming almost balance at around 1.0% from 2070 to 2090. Overall, it can be seen that the predictions of the three RCP pathways diverge with time, with smaller differences in 2050 and largest differences in 2090. The projections discussed above correspond with the characteristics of the RCP pathways, which show similar levels of greenhouse gas emission in early 21st century, and then the emission becomes to diverge: RCP8.5 drives a sharp increase overtime, RCP6.0 drives a moderate increase till the end of the 21st century while RCP2.6 drives a moderate increase till halfway through the century, peaks around 2050 and declines thereafter. The correspondence between predicted future mean monthly/annual temperature and precipitation to emission scenarios has been reported by a number of studies applying Special Report on Emissions Scenarios (SRES) scenarios (IPCC, 2000) for different regions in the world such as United States (Liu et al., 2012), Spain (Ribalaygua et al., 2013), and Southeast Asia (Giang et al., 2014). For RCP pathways, because these scenarios were very recently adopted by the IPCC (Collins et al., 2013), little research applying them for extreme climates in general and extreme precipitation in particular has been published. However, the characteristic of extreme precipitation change under RCP scenarios may vary. Ahn et al. (2016) found that future extreme precipitation over South Korea, neither the mean value nor frequency had a significant trend such as temperature response to radiative forcing under RCP4.5 and RCP8.5. In contrast, findings of Saeed et al. (2013) show that future extreme precipitation over the greater Congo region in Africa could change prominently, led by RCP8.5, then RCP4.5 and then RCP2.6. Similar

TABLE 2 | List of GCMs used in this study.

No	CMIP5 models	Developer	Resolution (long*lat)		Vintage	References
			Atmospheric variable	**Ocean variable**		
1	ACCESS1-3	CSIRO and Bureau of Meteorology, Australia	192*145	360*300	2011	Dix et al. (2013)
2	CanESM2	Canadian Center for Climate Modeling and Analysis	128*64	256*192	2010	Von Salzen et al. (2013)
3	CESM1-BGC	NSF-DOE-NCAR, United States	288*192	320*384	2010	Long et al. (2013)
4	CMCC-CM	Centro Euro-Mediterraneo Per I Cambiamenti Climatici, Italy	480*240	182*149	2009	Fogli et al. (2009)
5	CNRM-CM5	CNRM and CERFACS, France	256*128	362*292	2010	Voldoire et al. (2013)
6	CSIRO-Mk-3–6	QCCCE and CSIRO, Australia	192*96	192*189	2009	Rotstayn et al. (2012)
7	GFDL-ESM2G	NOAA Geophysical Fluid Dynamics Laboratory, USA	144*90	360*210	2012	Dunne et al. (2012)
8	HadGEM2-ES	Met Office Hadley Center, United Kingdom	192*145	360*216	2009	Collins et al. (2011)
9	INMCM4	Institute for Numerical Mathematics, Russia	180*120	360*340	2009	Volodin et al. (2010)
10	IPSL-CM5A-MR	Institut Pierre Simon Laplace, France	144*142	182*149	2009	Dufresne et al. (2013)
11	MIROC5	UTokyo, NIES, and JAMSTEC, Japan	256*128	256*224	2010	Watanabe et al. 2010
12	MPI-ESM-MR	Max Planck Institute for Meteorology, Germany	192*96	802*404	2009	Stevens et al. (2013)
13	MRI-CGCM3	Meteorological Research Institute, Japan	320*160	360*368	2011	Yukimoto et al. (2011)
14	NorESM1-M	Norwegian Climate Center, Norway	144*96	320*384	2011	Iversen et al. (2013)

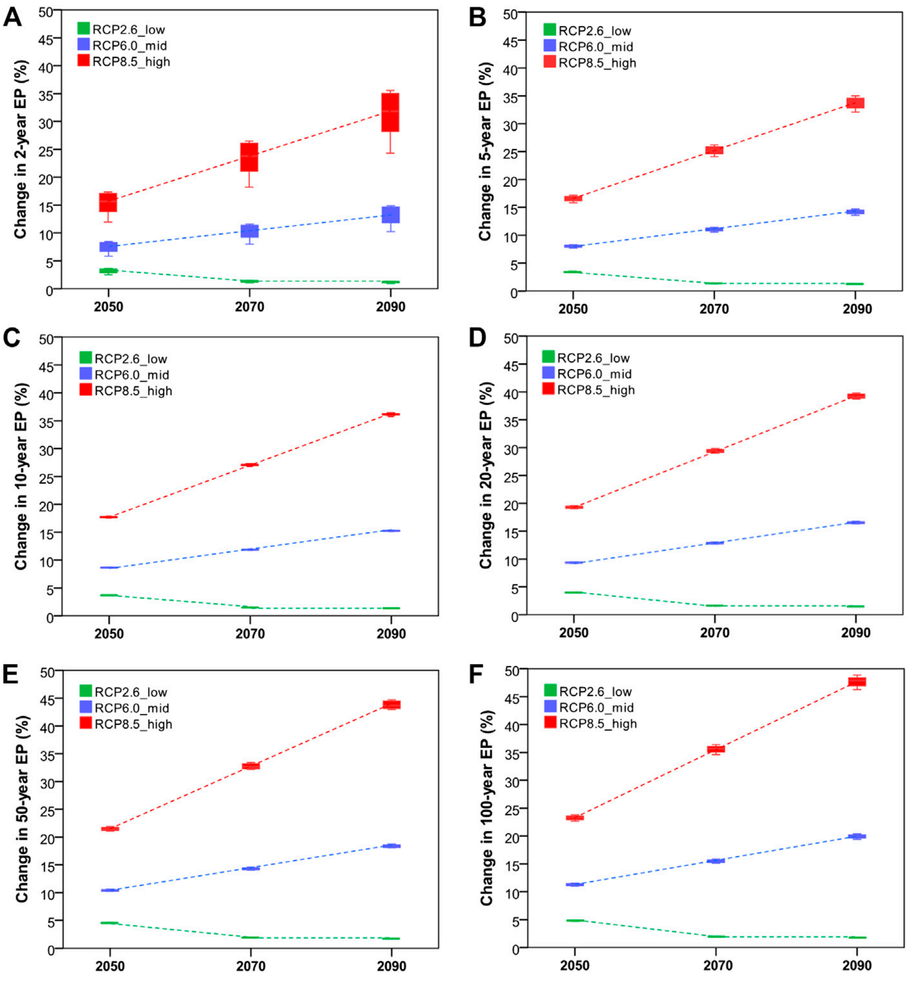

FIGURE 2 | Spatial variability of change in future 5-day extreme precipitation under the ensemble scenario corresponding to different return periods: T = 2 years **(A)**, T = 5 years **(B)**, T = 10 years **(C)**, T = 20 years **(D)**, T = 50 years **(E)**, and T = 100 years **(F)**. Figure presents data of 20 stations.

behavior was found by Janssen (2013) for precipitation in the United States under RCP4.5 and RCP8.5: the higher the RCP, the more prominent change is expected for both intensity and frequency.

These findings point to the fact that a region may differ from another in the sensitivity to the radiative forcing which varies in the RCPs, as indicated in Shindell et al. (2012). To our knowledge, however, no

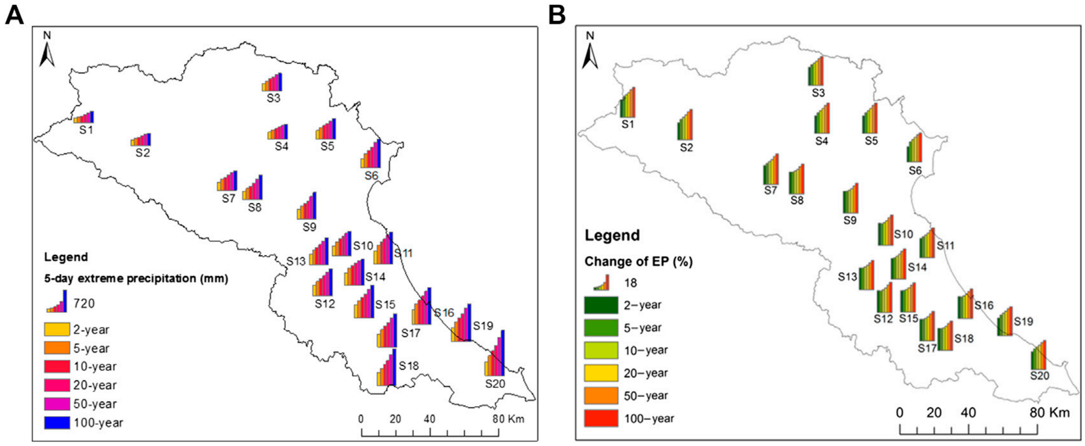

FIGURE 3 | Spatial variability of baseline 5-days extreme precipitation **(A)** and its change in 2070 according to RCP8.5 scenario **(B)**.

research has been published for multi-day extreme precipitation, which is focused in the present study.

It is noticeable that spatial variability of extreme precipitation also consistent with the temporal change: The variability increases with time under RCP8.5 and RCP6.0 but decreases with time under RCP2.6, although the variability under RCP2.6 is very small. In addition, the higher the RCP, the greater the spatial variability it produces. For instance, the increase of the total 5-days precipitation with $T = 2$ ranges between 11.96 and 17.35% (standard deviation S_{td} = 1.72%) in 2050, 18.21–26.47% (S_{td} = 2.65%) in 2070, and 24.32–35.55% (S_{td} = 3.59%) in 2090 under RCP8.5. Under RCP6.0 it ranges between 5.82 and 8.46% (S_{td} = 0.84%) in 2050, 7.99–11.59% (S_{td} = 1.15%) in 2070, and 10.25–14.87 (S_{td} = 1.47%) in 2090, meanwhile under RCP2.6 it ranges between 2.49–3.63% (S_{td} = 0.36%), 1.02–1.49% (S_{td} = 0.15%), and 0.92–1.34% (S_{td} = 0.15) in 2050, 2070, and 2090, respectively.

Interestingly, comparison among the return periods, it is clear that spatial variability of smaller extremes (closer to the lower tail) and greater extremes (closer to the upper tail) is greater than medium extremes. More specifically, the variability starts highest for $T = 2$, but then reduces for $T = 5$, and reduces more for $T = 10$. However, after $T = 10$ it starts to rise for $T = 20$, rise more for $T = 50$, and then more so for $T = 100$. This characteristic occurs under all the three pathways, although under RCP2.6, the difference among the return periods is very small. This characteristic can be explained by the characteristic of GEV distribution. When fitting data to GEV distribution, the uncertainty is often largest at its tails, in other words, medium extremes are usually most fitted to the distribution while small extremes and large extremes are often lie farther from the GEV curve. This leads to variability in GEV values among local datasets.

Most noticeable in **Figure 2** is that extreme precipitation in the LCRB with a return period of two years has large spatial variability, especially in the end of the 21st century under the highest RCP pathway (range between 24.32 and 35.55%); despite the moderate basin size. Review from literature shows that large spatial variability in the change of precipitation at local scale driven by a warmer climate was also abundantly reported. For instance, research by Mahmood et al. (2015) for the Jhelum river basin of Pakistan and India, which has similar basin size as the LCRB in the present study, reveals that precipitation change in the studied basin spatially varies from a decrease of 12% to an increase of 12% in the 2050s, and from a decrease of 11% to an increase of 16% in the 2080s under SRES scenario A2. Research by Keuser (2012) for Milwaukee County of the United State (3,082 km^2) and 24 km buffer around it shows that spatial variation of precipitation increases relative to the current climate is likely to be large, ranging from 15.8 to 39.6% in 2050s and from 21.3 to 46% in 2080s, also under SRES scenario A2. Note that both studies used downscaled GCMs output together with trends in observed precipitation for the predictions, which is similar to the method used in the present study. According to Ye and Li (2011) and Li et al. (2011), precipitation in general and extreme precipitation in particular is a much localized phenomenon and not always strongly influenced by large-scale dynamics. This means that although a large-scale GCM gives homogenous prediction for future precipitation change for the region within its particular grid, more detailed approach such as downscaling or pattern scaling may result in large spatial variability of the precipitation change. Spatial distribution of 5-days extreme precipitations for different return periods and their increase in 2070 under the highest RCP (RCP8.5) compared to the baseline period is shown in **Figure 3**.

Comparison among the predictions of the employed GCMs for 2050, 2070, and 2090 under the three pathways is presented in **Figure 4** wherein data for Vinh (S11), which is considered as the most central station in the LCRB, is shown. Prediction of the selected GCMs is very divergent, but can be divided into two groups:

- Five GCMs including ACCESS1-3, CanESM2, CMCC-CM, GFDL-ESM2G, and MPI-ESM-MR predict greater increases to smaller extremes and smaller increases to greater extremes. This is represented by downward lines in **Figure 4** with CanESM2 being the steepest, representing the most typical for this tendency. For example, this model predicts that under RCP8.5 in 2070 5-days extreme precipitation increases 50.60% for $T = 2$, 30.27% for $T = 5$, 20.87% for $T = 10$, 13.48% for $T = 20$, 5.51% for $T = 50$, and 0.39% for $T = 100$ compared to the baseline period. This rate then decreases from 62.18% ($T = 2$) to 0.37% ($T = 100$) in 2090. More noticeably

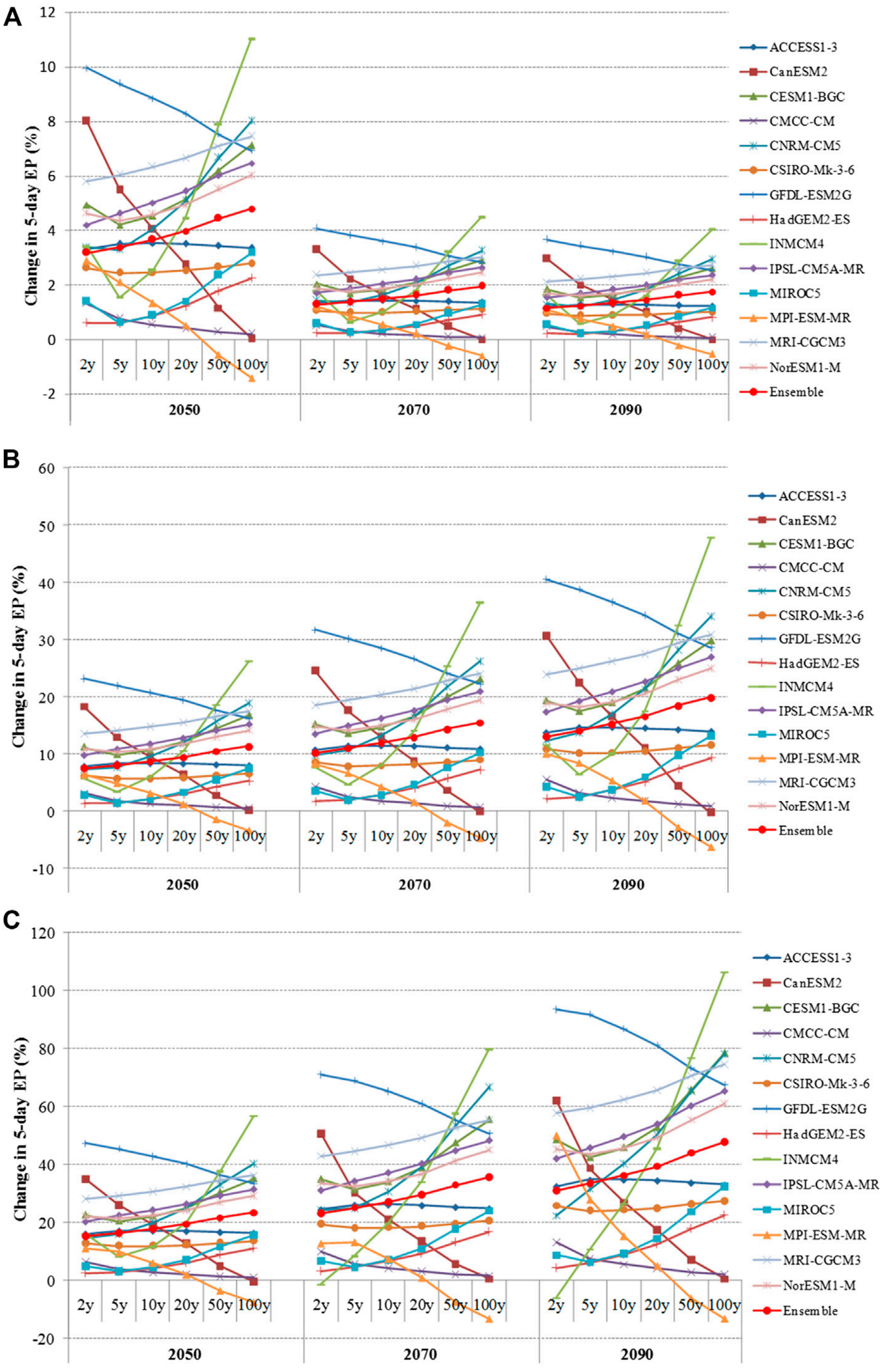

FIGURE 4 | Change in 5-day extreme precipitation under 14GCMs and their ensemble at Vinh Station corresponding to RCP2.6 **(A)**, RCP6.0 **(B)**, and RCP8.5 **(C)**.

among this group is that the downward line of MPI-ESM-MR passes through the X-axis after the return period $T = 20$, meaning that the change of extreme precipitation relative to the baseline period turns from an increase for $T = 2$, 5, 10, and 20 to a decrease for $T = 50$ and $T = 100$. In general, prediction of this model shows that by the end of 21st century 5-days extreme precipitation is expected to change from +2.89 to −1.40% under RCP2.6, from +10.04 to −6.26% under RCP6.0, and from +50.09 to −13.24% under RCP8.5.

- The other nine GCMs including CESM1-BGC, CNRM-CM5, CSIRO-Mk-three to six, HadGEM2-ES, INMCM4, IPSL-CM5A-MR, MIROC5, MRI-CGCM3, and NorESM1-M predict smaller increases to smaller extremes and greater increases to greater

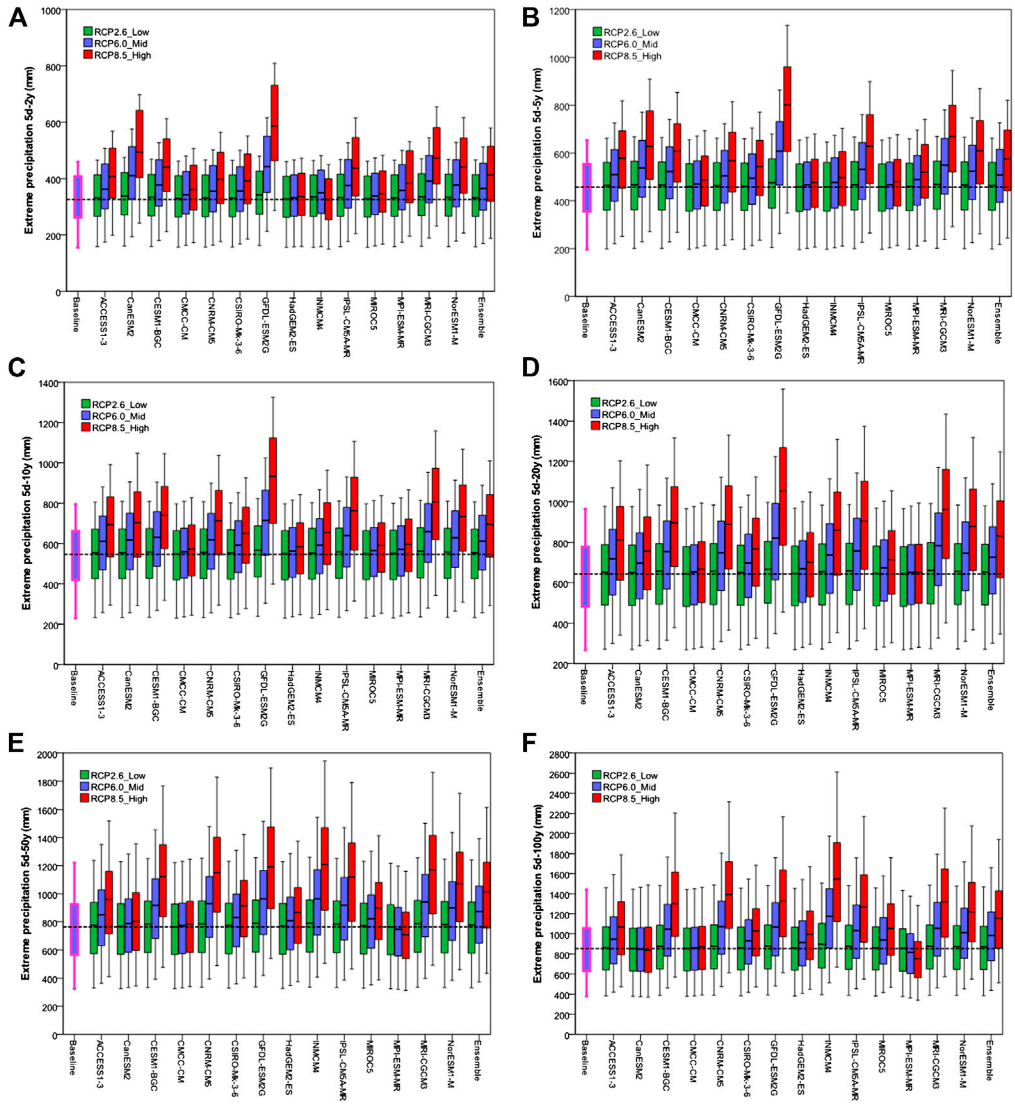

FIGURE 5 | Variation of projected 5-day extreme precipitation under 14GCMs and their ensemble in 2070 corresponding to different return periods: T = 2 years **(A)**, T = 5 years **(B)**, T = 10 years **(C)**, T = 20 years **(D)**, T = 50 years **(E)**, and T = 100 years **(F)**. Figure presents data of 20 monitoring stations

extremes. This is represented by the upward lines in **Figure 4**. Among these models, INMCM4 shows the most dramatically upward trend toward more extreme precipitation, except for a short down from *T* = 2 to *T* = 5 for all three future time periods under RCP2.6 and RCP6.0 and for 2050 under RCP8.5. The largest range of 5-days extreme precipitation change relative to the baseline period according to this model is in 2090 under RCP8.5 when it rises from a decrease of 5.93% for *T* = 2 to an increase of 106.28% for *T* = 100.

Prediction of the ensemble median of the 14 selected GCMs is in line with the later group: smaller increases for smaller extremes and greater increases for greater extremes. Under this ensemble scenario, in mid-21st century, 5-days extreme precipitation at S11 with return period ranging from *T* = 2 years to *T* = 100 years is expected to rise between 3.19% (T = 2 years) and 4.81% (T = 100 years) under RCP2.6, between 7.43 and 11.28% under RCP6.0, and between 15.19 and 23.28% under RCP8.5. Meanwhile, by the end of the 21st century, it would rise between 1.17 and 1.78%, 13.03–19.93%, and 30.90–47.90% under RCP2.6, RCP6.0 and RCP8.5 respectively.

Considering the prediction of each individual GCM relative to the three RCPs, it is obvious that the magnitude of change produced by each individual GCM under RCP2.6 is smaller than RCP6.0, and smaller still than RCP8.5. The change under RCP2.6 becomes smaller while the change under RCP6.0 and RCP8.5 becomes greater toward the end of this century. These behaviors of prediction are consistent with the characteristics of RCP pathways as discussed earlier in this paper. An overview of the predictions of the employed GCMs for 20 monitoring stations in the study area under the three pathways is presented in **Figure 5**.

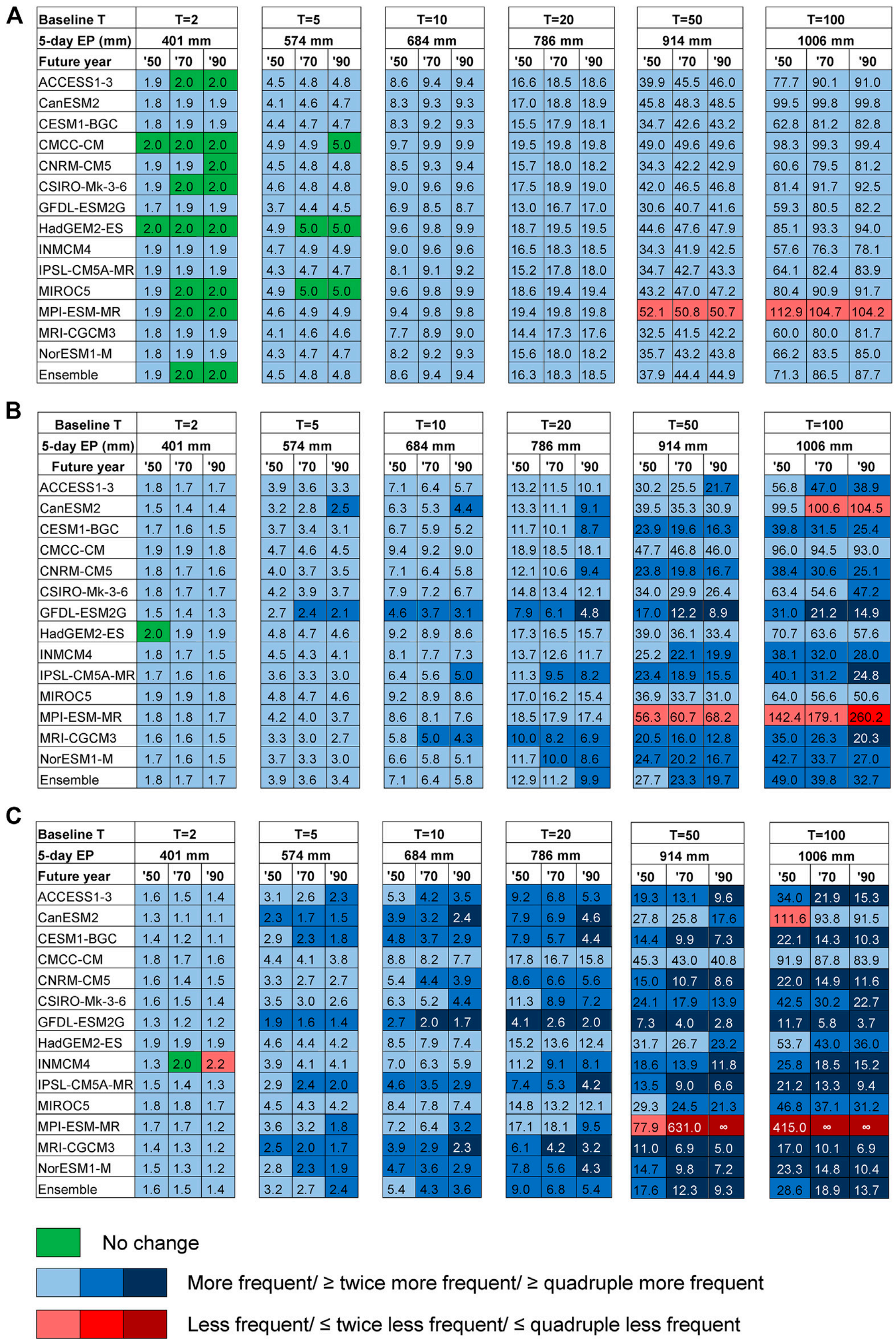

A

Baseline T	T=2			T=5			T=10			T=20			T=50			T=100		
5-day EP (mm)	401 mm			574 mm			684 mm			786 mm			914 mm			1006 mm		
Future year	'50	'70	'90	'50	'70	'90	'50	'70	'90	'50	'70	'90	'50	'70	'90	'50	'70	'90
ACCESS1-3	1.9	2.0	2.0	4.5	4.8	4.8	8.6	9.4	9.4	16.6	18.5	18.6	39.9	45.5	46.0	77.7	90.1	91.0
CanESM2	1.8	1.9	1.9	4.1	4.6	4.7	8.3	9.3	9.3	17.0	18.8	18.9	45.8	48.3	48.5	99.5	99.8	99.8
CESM1-BGC	1.8	1.9	1.9	4.4	4.7	4.7	8.3	9.2	9.3	15.5	17.9	18.1	34.7	42.6	43.2	62.8	81.2	82.8
CMCC-CM	2.0	2.0	2.0	4.9	4.9	5.0	9.7	9.9	9.9	19.5	19.8	19.8	49.0	49.6	49.6	98.3	99.3	99.4
CNRM-CM5	1.9	1.9	2.0	4.5	4.8	4.8	8.5	9.3	9.4	15.7	18.0	18.2	34.3	42.2	42.9	60.6	79.5	81.2
CSIRO-Mk-3-6	1.9	2.0	2.0	4.6	4.8	4.8	9.0	9.6	9.6	17.5	18.9	19.0	42.0	46.5	46.8	81.4	91.7	92.5
GFDL-ESM2G	1.7	1.9	1.9	3.7	4.4	4.5	6.9	8.5	8.7	13.0	16.7	17.0	30.6	40.7	41.6	59.3	80.5	82.2
HadGEM2-ES	2.0	2.0	2.0	4.9	5.0	5.0	9.6	9.8	9.9	18.7	19.5	19.5	44.6	47.6	47.9	85.1	93.3	94.0
INMCM4	1.9	1.9	1.9	4.7	4.9	4.9	9.0	9.6	9.6	16.5	18.3	18.5	34.3	41.9	42.5	57.6	76.3	78.1
IPSL-CM5A-MR	1.9	1.9	1.9	4.3	4.7	4.7	8.1	9.1	9.2	15.2	17.8	18.0	34.7	42.7	43.3	64.1	82.4	83.9
MIROC5	1.9	2.0	2.0	4.9	5.0	5.0	9.6	9.8	9.9	18.6	19.4	19.4	43.2	47.0	47.2	80.4	90.9	91.7
MPI-ESM-MR	1.9	2.0	2.0	4.6	4.9	4.9	9.4	9.8	9.8	19.4	19.8	19.8	52.1	50.8	50.7	112.9	104.7	104.2
MRI-CGCM3	1.8	1.9	1.9	4.1	4.6	4.6	7.7	8.9	9.0	14.4	17.3	17.6	32.5	41.5	42.2	60.0	80.0	81.7
NorESM1-M	1.8	1.9	1.9	4.3	4.7	4.7	8.2	9.2	9.3	15.6	18.0	18.2	35.7	43.2	43.8	66.2	83.5	85.0
Ensemble	1.9	2.0	2.0	4.5	4.8	4.8	8.6	9.4	9.4	16.3	18.3	18.5	37.9	44.4	44.9	71.3	86.5	87.7

B

Baseline T	T=2			T=5			T=10			T=20			T=50			T=100		
5-day EP (mm)	401 mm			574 mm			684 mm			786 mm			914 mm			1006 mm		
Future year	'50	'70	'90	'50	'70	'90	'50	'70	'90	'50	'70	'90	'50	'70	'90	'50	'70	'90
ACCESS1-3	1.8	1.7	1.7	3.9	3.6	3.3	7.1	6.4	5.7	13.2	11.5	10.1	30.2	25.5	21.7	56.8	47.0	38.9
CanESM2	1.5	1.4	1.4	3.2	2.8	2.5	6.3	5.3	4.4	13.3	11.1	9.1	39.5	35.3	30.9	99.5	100.6	104.5
CESM1-BGC	1.7	1.6	1.5	3.7	3.4	3.1	6.7	5.9	5.2	11.7	10.1	8.7	23.9	19.6	16.3	39.8	31.5	25.4
CMCC-CM	1.9	1.9	1.8	4.7	4.6	4.5	9.4	9.2	9.0	18.9	18.5	18.1	47.7	46.8	46.0	96.0	94.5	93.0
CNRM-CM5	1.8	1.7	1.6	4.0	3.7	3.5	7.1	6.4	5.8	12.1	10.6	9.4	23.8	19.8	16.7	38.4	30.6	25.1
CSIRO-Mk-3-6	1.8	1.7	1.7	4.2	3.9	3.7	7.9	7.2	6.7	14.8	13.4	12.1	34.0	29.9	26.4	63.4	54.6	47.2
GFDL-ESM2G	1.5	1.4	1.3	2.7	2.4	2.1	4.6	3.7	3.1	7.9	6.1	4.8	17.0	12.2	8.9	31.0	21.2	14.9
HadGEM2-ES	2.0	1.9	1.9	4.8	4.7	4.6	9.2	8.9	8.6	17.3	16.5	15.7	39.0	36.1	33.4	70.7	63.6	57.6
INMCM4	1.8	1.7	1.5	4.5	4.3	4.1	8.1	7.7	7.3	13.7	12.6	11.7	25.2	22.1	19.9	38.1	32.0	28.0
IPSL-CM5A-MR	1.7	1.6	1.6	3.6	3.3	3.0	6.4	5.6	5.0	11.3	9.5	8.2	23.4	18.9	15.5	40.1	31.2	24.8
MIROC5	1.9	1.9	1.8	4.8	4.7	4.6	9.2	8.9	8.6	17.0	16.2	15.4	36.9	33.7	31.0	64.0	56.6	50.6
MPI-ESM-MR	1.8	1.8	1.7	4.2	4.0	3.7	8.6	8.1	7.6	18.5	17.9	17.4	56.3	60.7	68.2	142.4	179.1	260.2
MRI-CGCM3	1.6	1.6	1.5	3.3	3.0	2.7	5.8	5.0	4.3	10.0	8.2	6.9	20.5	16.0	12.8	35.0	26.3	20.3
NorESM1-M	1.7	1.6	1.5	3.7	3.3	3.0	6.6	5.8	5.1	11.7	10.0	8.6	24.7	20.2	16.7	42.7	33.7	27.0
Ensemble	1.8	1.7	1.7	3.9	3.6	3.4	7.1	6.4	5.8	12.9	11.2	9.9	27.7	23.3	19.7	49.0	39.8	32.7

C

Baseline T	T=2			T=5			T=10			T=20			T=50			T=100		
5-day EP	401 mm			574 mm			684 mm			786 mm			914 mm			1006 mm		
Future year	'50	'70	'90	'50	'70	'90	'50	'70	'90	'50	'70	'90	'50	'70	'90	'50	'70	'90
ACCESS1-3	1.6	1.5	1.4	3.1	2.6	2.3	5.3	4.2	3.5	9.2	6.8	5.3	19.3	13.1	9.6	34.0	21.9	15.3
CanESM2	1.3	1.1	1.1	2.3	1.7	1.5	3.9	3.2	2.4	7.9	6.9	4.6	27.8	25.8	17.6	111.6	93.8	91.5
CESM1-BGC	1.4	1.2	1.1	2.9	2.3	1.8	4.8	3.7	2.9	7.9	5.7	4.4	14.4	9.9	7.3	22.1	14.3	10.3
CMCC-CM	1.8	1.7	1.6	4.4	4.1	3.8	8.8	8.2	7.7	17.8	16.7	15.8	45.3	43.0	40.8	91.9	87.8	83.9
CNRM-CM5	1.6	1.4	1.5	3.3	2.7	2.7	5.4	4.4	3.9	8.6	6.6	5.6	15.0	10.7	8.6	22.0	14.9	11.6
CSIRO-Mk-3-6	1.6	1.5	1.4	3.5	3.0	2.6	6.3	5.2	4.4	11.3	8.9	7.2	24.1	17.9	13.9	42.5	30.2	22.7
GFDL-ESM2G	1.3	1.2	1.2	1.9	1.6	1.4	2.7	2.0	1.7	4.1	2.6	2.0	7.3	4.0	2.8	11.7	5.8	3.7
HadGEM2-ES	1.9	1.9	1.9	4.6	4.4	4.2	8.5	7.9	7.4	15.2	13.6	12.4	31.7	26.7	23.2	53.7	43.0	36.0
INMCM4	1.3	2.0	2.2	3.9	4.1	4.1	7.0	6.3	5.9	11.2	9.1	8.1	18.6	13.9	11.8	25.8	18.5	15.2
IPSL-CM5A-MR	1.5	1.4	1.3	2.9	2.4	2.0	4.6	3.5	2.9	7.4	5.3	4.2	13.5	9.0	6.6	21.2	13.3	9.4
MIROC5	1.8	1.8	1.7	4.5	4.3	4.2	8.4	7.8	7.4	14.8	13.2	12.1	29.3	24.5	21.3	46.8	37.1	31.2
MPI-ESM-MR	1.7	1.7	1.2	3.6	3.2	1.8	7.2	6.4	3.2	17.1	18.1	9.5	77.9	631.0	∞	415.0	∞	∞
MRI-CGCM3	1.4	1.3	1.2	2.5	2.0	1.7	3.9	2.9	2.3	6.1	4.2	3.2	11.0	6.9	5.0	17.0	10.1	6.9
NorESM1-M	1.5	1.3	1.2	2.8	2.3	1.9	4.7	3.6	2.9	7.8	5.6	4.3	14.7	9.8	7.2	23.3	14.8	10.4
Ensemble	1.6	1.5	1.4	3.2	2.7	2.4	5.4	4.3	3.6	9.0	6.8	5.4	17.6	12.3	9.3	28.6	18.9	13.7

🟩 No change

🟦🟦🟦 More frequent/ ≥ twice more frequent/ ≥ quadruple more frequent

🟥🟥🟥 Less frequent/ ≤ twice less frequent/ ≤ quadruple less frequent

FIGURE 6 | Change in frequency of extreme precipitation according to RCP 2.6 **(A)**, RCP 6.0 **(B)**, and RCP 8.5 **(C)**. Number in each block presents the future return period of current return level.

Change in the Frequency of Extreme Precipitation Events

Frequency of extreme precipitation, represented by its return period provides important information for assessing its impact to the environment and society as well as for decision making. For instance, a return period of T-years represents an extreme precipitation event that has a 1/T probability of occurring in any given year. Stationary climate assumes that the frequency of extreme climates does not change over time (Klein et al., 2009). However, according to IPCC (2007), the frequency of extreme climates in general and extreme precipitations in particular has been changing and more so in the future. In this study, we examined the changes in the frequency of future extreme precipitations which presently have return periods of 2, 5, 10, 20, 50 and 100 years.

Figure 6 presents the change for five-days extreme precipitation at Vinh (S11) in 2050, 2070, 2090 relative to the baseline period. It can be seen that for all return levels, extreme precipitation is likely to be more frequent (as their return periods shorten) in the future, except for a few cases wherein it remains unchanged or becomes less frequent. In general, the uncertainty in the frequency is smallest for present return levels with $T = 2$ years and largest for present return levels with $T = 100$ years in all three RCPs. The uncertainty also increases consistently with the order of the RCPs (RCP8.5 > RCP6.0 > RCP2.6) and increases with time.

Specifically, under RCP2.6 extreme precipitation is projected to remain unchanged in frequency in many cases for $T = 2$ years, but only in 7 cases for $T = 5$ years (in 2090 under CMCC-CM, and in 2070 and 2090 under HadGEM2-ES and MIROC5), and in no cases for the other greater return periods. The frequency is also projected to decrease but only in six cases (for return level with current return period $T = 50$ and $T = 100$ years in 2050, 2070, and 2090. All are under MPI-ESM-MR). The other majority of cases show an increase in frequency. However, it should be noted that all of the increases or decreases in frequency under RCP2.6 are within twice less frequent to twice more frequent.

Under RCP6.0, only one case exhibits an unchanged frequency, meanwhile many cases exhibit double frequency (twice more frequent) or beyond and a few cases exhibit quadruple frequency or beyond. In comparison with RCP2.6, the decrease in frequency was also projected for larger extremes (with current return period $T = 50$ and $T = 100$ years), but for eight cases under CanESM2 and MPI-ESM-MR in which one case show a double decrease in frequency (return level with current return period T = 100 in 2090 under MPI-ESM-MR).

Under RCP8.5, many cases show a double (or more) increase in frequency, even for lower return levels, meanwhile the number of cases with a quadruple (or more) increase has become more dominant in larger return levels. The number of cases which show a balance frequency and a decreased frequency remains the same compared with RCP6.0 although they are not exactly the same cases. Most noticeable among the cases with decreased frequency is that three of these cases are likely not to happen in the future as their predicted frequency is infinitive. These cases include the return levels with current return period $T = 50$ in 2090 and $T = 100$ in 2070 and 2090, all are under MPI-ESM-MR.

CONCLUSION AND RECOMMENDATION

This study investigated the variability in the intensity and frequency of future multi-day extreme precipitation using pattern scaling method coupled with Generalized Extreme Value Analysis with the case study of the LCRB in the Northcentral Vietnam of Vietnam. The results exhibit different uncertainties following the characteristics of RCP scenarios and depending on each GCM employed. In general, the uncertainty in both intensity and frequency is in line with the order of the RCP scenarios and increase with time. In the future, multi-day precipitation is likely to become more extreme and more frequent in most cases. The increase in extreme precipitation found in this study was in line with findings of previous studies on climate change in Vietnam including the Northcentral region, however, the pattern of change was different due to the difference in methodologies and the GCMs used. It is also valuable to note that the present study provided more details of the pattern of changes in both intensity and frequency of extreme precipitation. The shortening of return periods for extreme precipitation events and greater intensity of such events has potential consequences for the increase in flood magnitude and frequency, which could ultimately produce large impacts on the environment and society. Therefore, planning and decision making of durable infrastructure along with flood mitigation strategies to cope with such events are recommended.

DATA AVAILABILITY STATEMENT

The original contributions presented in the study are included in the article/Supplementary Material, further inquiries can be directed to the corresponding author.

AUTHOR CONTRIBUTIONS

PQG performed the design of study, data collection and analysis, model simulation, and manuscript writing and edition. People whole gave comments and advice for the improvement of the manuscript have been acknowledged in the Acknowledgment section.

FUNDING

This research was supported by Japan Society for the Promotion of Science (JSPS).

ACKNOWLEDGMENTS

The author wishes to thank Vietnam Institute of Meteorology-Hydrology and Climate Change, Hydro-Meteorological Data Center for providing data for this research. Appreciation is also given to researchers at The University of Tokyo, Vietnam National University of Agriculture, and Ha Long University for their useful comments and suggestions for the improvement of the article.

REFERENCES

Ahn, J. B., Jo, S., Suh, M. S., Cha, D. H., Lee, D. K., Hong, S. Y., et al. (2016). Changes of precipitation extremes over South Korea projected by the 5 RCMs under RCP scenarios. *Asia Pac. J. Atmos. Sci.* 52, 223–236. doi:10.1007/s13143-016-0021-0

Benyahya, L., Gachon, P., St-Hilaire, A., and Laprise, R. (2014). Frequency analysis of seasonal extreme precipitation in Southern Quebec (Canada): an evaluation of regional climate model simulation with respect to two gridded datasets. *Nord. Hydrol. Res.* 45 (1), 115–133. doi:10.2166/nh.2013.066

Buishand, T. A., Jilderda, R., and Wijngaard, J. B. (2009). Regionale verschillen in extreme neerslag. Available at:https://edepot.wur.nl/191834https://edepot.wur.nl/191834.

Cabre, M. F., Solman, S. A., and Nunez, M. N. (2010). Creating regional climate change scenarios over Southern South America for the 2020's and 2050's using the pattern scaling technique: validity and limitations. *Clim. Change* 98 (3–4), 449–469. doi:10.1007/s10584-009-9737-5

Christensen, J. H., Christensen, O. B., Lopez, P., van Meijgaardand Botzet, M. (1996). Research Report, 96–4. The HIRHAM4 regional atmospheric climate model. Danish Meteorological Institute.

Collins, M., Knutti, R., Arblaster, J., Dufresne, J. L., Fichefet, T., Friedlingstein, P., et al. (2013). "Long-term climate change: projections, commitments and irreversibility," in *Climate change 2013: the physical science basis. Contribution of working group I to the fifth assessment Report of the intergovernmental panel on climate change*. Editors T. F. Stocker, D. Qin, G. K. Plattner, M. Tignor, S. K. Allen, J. Boschung, et al. (Cambridge, United Kingdom and New York, NY: Cambridge University Press), 1029–1136.

Collins, W. J., Bellouin, N., Doutriaux-Boucher, M., Gedney, N., Halloran, P., Hinton, T., et al. (2011). Development and evaluation of an Earth-System modelHadGEM2. *Geosci. Model Dev. (GMD).* 4, 1051–1075. doi:10.5194/gmdd-4-997-2011

Deser, C., Knutti, R., Solomon, S., and Phillips, A. S. (2012). Communication of the role of natural variability in future North American climate. *Nat. Clim. Change* (11), 775–779. doi:10.1038/NCLIMATE1562

Dessai, S., Lu, X. F., and Hulme, M. (2005). Limited sensitivity analysis of regional climate change probabilities for the21st century. *J. Geophys. Res. Atmos.* 110 (D19), D19108. doi:10.1029/2005JD005919

Dix, M., Vohralik, P., Bi, D., Rashid, H., Marsland, S., O'Farrell, S., et al. (2013). The Access coupled model: documentation of core CMIP5 simulations and initial results. *Aust. Meteorol. Oceanogr. J.* 63, 83–99. doi:10.22499/2.6301.004

Du, H., Xia, J., Zeng, S., She, D., and Liu, J. (2014). Variations and statistical probability characteristic analysis of extreme precipitation events under climate change in Haihe River Basin, China. *Hydrol. Process* 28 (3), 913–925. doi:10.1002/hyp.9606

Dufresne, J. L., Foujols, M. A., Denvil, S., Caubel, A., Marti, O., Olivier, A., et al. (2013). Climate change projections using the IPSL-CM5 Earth system model: from CMIP3 to CMIP5. *Clim. Dynam.* 40, 2123–2165. doi:10.1007/s00382-012-1636-1

Dunne, J. P., John, J. G., Adcroft, A. J., Griffies, S. M., Hallberg, R. W., Shevliakova, E., et al. (2012). GFDL's ESM2 Global coupled climate-carbon earth system models. part I: physical formulation and baseline simulation characteristics. *J. Clim.* 25, 6646–6665. doi:10.1175/JCLI-D-11-00560.1

Fogli, P. G., Manzini, E., Vichi, M., Alessandri, A., Patara, L., Gualdi, S., et al. (2009). INGV-CMCC carbon (ICC): a carbon cycle earth system model. *CMCC Res. Pap.-Euro-Mediterranean Center Clim. Change*, 31. Available at: https://www.cmcc.it/wp-content/uploads/2012/05/rp0061-ns-04-2009.pdf. doi:10.2139/SSRN.1517282

Fowler, H. J., Blenkinsop, S., and Tebaldi, C. (2007). Linking climate change modelling to impacts studies: recent advances in downscaling techniques for hydrological modelling. *Int. J. Climatol.* 27 (12), 1547–1578. doi:10.1002/joc.1556

Fu, C., Wang, S., Xiong, Z., Gutowski, W. J., Lee, D.-K., McGregor, J. L., et al. (2005). Regional climate model intercomparison project for Asia. *Bull. Am. Meteorol. Soc.* 86, 257–266. doi:10.1175/BAMS-86-2-257

Giang, P. Q., Toshiki, K., Sakata, M., Kunikane, S., and Vinh, T. Q. (2014). Modelling climate change impacts on the seasonality of water resources in the upper Ca river watershed in Southeast Asia. *Sci. World J.* 2014, 279135. doi:10.1155/2014/279135

Giorgi, F. (2008). A simple equation for regional climate change and associated uncertainty. *J. Clim.* 21 (7), 1589–1604. doi:10.1175/2007jcli1763.1

Greenwood, J. A., Landwehr, J. M., Matalas, N. C., and Wallis, J. R. (1979). Probability-weighted moments: definition and relation to parameters of several distributions expressable in inverse form. *Water Resour. Res.* 15, 1049–1054. doi:10.1029/WR015i005p01049

Gutiérrez, J. M., San-Martín, D., Brands, S., Manzanas, R., and Herrera, S. (2013). Reassessing statistical downscaling techniques for their robust application under climate change conditions. *J. Clim.* 26 (1), 171–188. doi:10.1175/JCLI-D-11-00687.1

Hanel, M., and Buishand, T. A. (2010). On the value of hourly precipitation extremes in regional climate model simulations. *J. Hydrol.* 393, 265–273. doi:10.1016/j.jhydrol.2010.08.024

Harris, G. R., Collins, M., Sexton, D. M. H., Murphy, J. M., and Booth, B. B. B. (2010). Probabilistic projections for 21st century European climate. *Nat. Hazards Earth Syst. Sci.* 10 (9), 2009–2020. doi:10.5194/nhess-10-2009-2010

Ho, T. M. H., Phan, V. T., Le, N. Q., and Nguyen, Q. T. (2011). Extreme climatic events over Vietnam from observational data and RegCM3 projections. *Clim. Res.* 49 (2), 87–100. doi:10.3354/cr01021

Hosking, J. R. M., Wallis, J. R., and Wood, E. F. (1985). Estimation of the generalized extreme-value distribution by the method of probability-weighted moments. *Technometrics* 27, 251–261. doi:10.2307/1269706

IPCC (2000). *Special Report on emissions scenarios: a special report of working group III of the intergovernmental panel on climate change*. Cambridge, United Kingdom: Cambridge University Press.

IPCC (2001). *IPCC climate change 2001: impact, Adaptation and Vulnerability.Contribution of working group II to the third assessment report of the intergovernmental panel on climate change*. Cambridge, United Kingdom: Cambridge University Press.

IPCC (2007). *Climate change 2007: synthesis report. Contribution of working groups I, II and III to the fourth assessment report of the intergovernmental panel on climate change*. Geneva, Switzerland: IPCC, 104.

IPCC (2013). "Climate Change 2013: the physical science basis," in *The working group I contribution of working group I to the fifth assessment report of the intergovernmental panel on climate change*. Editors T. F. Stocker, D. Qin, G. K. Plattner, M. Tignor, S. K. Allen, J. Boschung, et al. (Cambridge, United Kingdom and New York, NY: Cambridge University Press), 1535.

Iversen, T., Bentsen, M., Bethke, I., Debernard, J. B., Kirkevåg, A., Seland, O., et al. (2013). The Norwegian Earth system model, NorESM1–M. Part 2: climate response and scenario projections. *Geosci. Model Dev.* 6, 1–27. doi:10.5194/gmd-6-389-2013

Janssen, E. (2013). Trends and projections of extreme precipitation over the contiguous United States. Master's thesis. Urbana (IL): University of Illinois at Urbana-Champaign.

Keuser, A. P. M. (2012). Decadal changes and future projections of precipitation in the metropolitan area of Milwaukee. Master's thesis. Milwaukee (WI): The University of Wisconsin-Milwaukee.

Kharin, V. V., Zhang, X., and Hegerl, G. C. (2007). Changes in temperature and precipitation extremes in the IPCC ensenble of global coupled model simulations. *J. Clim.* 20, 1419–1444. doi:10.1175/JCLI4066.1

Klein, T., Zwiers, F. W., and Zhang, X. (2009). "Guidelines on Analysis of extremes in a changing climate in support of informed decisionsfor adaptation," in *World meteorological organization collection(s) and series*. (Geneva, Switzerland: World Meteorological Organization), Vol 1500, 56.

Kunkel, K. E. (2003). North American trends in extreme precipitation. *Nat. Hazards* 29, 291–305. doi:10.1023/A:1023694115864

Landwehr, J., Matalas, N., and Wallis, J. (1979). Probability weighted moments comparedwith some traditional techniques in estimating gumbel parameters and quantiles. *Water Resour. Res.* 15, 1055–1064. doi:10.1029/WR015i005p01055

Li, F., Collins, W. D., Wehner, M. F., Williamson, D. L., and Olson, J. G. (2001). Response of precipitation extremes to idealized global warming in an aqua-planet climate model: towards a robust projection across different horizontal resolutions. *Tellus* 63A, 876–883. doi:10.1111/j.1600-0870.2011.00543.x

Liu, L., Hong, Y., Hocker, J. E., Shafer, M. A., Carter, L. M., Gourley, J. J., et al. (2012). Analyzing projected changes and trends of temperature and precipitation in the southern USA from 16 downscaled global climate models. *Theor. Appl. Climatol.* 109, 345–360. doi:10.1007/s00704-011-0567-9

Long, M. C., Lindsay, K., Peacock, S., Moore, J. K., and Doney, S. C. (2013). Twentieth century oceanic carbon uptake and storage in CESM1(BGC). *J. Clim.* 26, 6775–6800. doi:10.1175/JCLI-D-12-00184.1

Mahmood, R., Babel, S. M., and Shaofeng, J. (2015). Assessment of temporal and spatial changes of future climate in theJhelum river basin, Pakistan and India. *Weather Clim. Extremes.* 10, 40–55. doi:10.1016/j.wace.2015.07.002

Maraun, D., Wetterhall, F., Ireson, A. M., Chandler, R. E., Kendon, E. J., Widmann, M., et al. (2010). Precipitation downscaling under climate change: recent developments to bridge the gap between dynamical models and the end user. *Rev. Geophys.* 48 (3), 219. doi:10.1029/2009RG000314

May, W. (2008). Climatic changes associated with a global"2 °C-stabilization"scenario simulated by the ECHAM5/MPI-OM coupled climate model. *Clim. Dynam.* 31 (2–3), 283–313. doi:10.1007/s00382-007-0352-8

May, W. (2012). Assessing the strength of regional changes in near-surface climate associated with a globalwarming of 2°C. *Clim. Change.* 110 (3–4), 619–644. doi:10.1007/s10584-011-0076-y

Mitchell, T. D. (2003). Pattern scaling: an examination of the accuracy of the technique for describing future climates. *Clim. Change.* 60, 217–242. doi:10.1023/A:1026035305597

Nam, D. H., Dung, N. Q., Duong, P. C., Mai, D. T., and Thuan, D. H. (2015). "Near future changes in extreme rainfall over Vietnam projected by CMIP5 high resolution climate models," in Vietnam-Japan Workshop on Estuaries, Coasts and Rivers 2015, Hoi An, Vietnam, September 7–8, 2015.

Neelin, J. D., Münnich, M., Su, H., Meyerson, J. E., and Holloway, C. E. (2006). Tropical drying trends in global warming models and observations. *Proc. Natl. Acad. Sci. USA.* 103 (16), 6110–6115. doi:10.1073/pnas.0601798103

OECD (2020). "Multi-dimensional review of Viet Nam towards an integrated, transparent and sustainable economy," in *OECD Development Pathways*. (Paris, France: OECD Publishing). doi:10.1787/367b58c-en

Overeem, A., and Buishand, A. (2012). Statistiek van extreme gebiedsneerslag in Nederland (RPRT). KNMI. Available at: https://library.wur.nl/WebQuery/wurpubs/427690.

Press, W. H., Teukolsky, S. A., Vetterling, W. T., and Flannery, B. P. (1997). *Numerical recipes in C.* New York, NY: Cambridge University Press.

Raghavan, S. V., Vu, M. T., and Liong, S. Y. (2017). Ensemble climate projections of mean and extreme rainfall over Vietnam. *Global Planet. Change* 148, 96–104. doi:10.1016/j.gloplacha.2016.12.003

Rahman, A. S., Rahman, A., Zaman, M. A., Haddad, M., Ahsan, A., and Imteaz, M. A. (2013). A study on selection of probability distributions for at-site flood frequency analysis in Australia. *Nat. Hazards* 69 (3), 1803–1813. doi:10.1007/s11069-013-0775-y

Rahmani, V., Hutchinson, S. L., Hutchinson, J. M. S., Aavudai, A., et al. (2014). Extreme daily rainfall event distribution patterns in Kansas. *J. Hydrol. Eng.* 19 (4), 707–716. doi:10.1061/(ASCE)HE.1943-5584.0000839

Ribalaygua, J., Pino, M. R., Pórtoles, J., Roldán, E., Gaitán, E., Chinarro, D., et al. (2013). Climate change scenarios for temperature and precipitation in Aragón (Spain). *Sci. Total Environ.* 463-464, 1015–1030. doi:10.1016/j.scitotenv.2013.06.089

Roeckner, E., Bäuml, G., Bonaventura, L., Brokopf, R., Esch, M., Giorgetta, M., et al. (2003). Report No.: 349. The atmospheric general circulation model ECHAM 5. PART I: model description. Hamburg, Germany: Max Planck Institute for Meteorology.

Rotstayn, L. D., Jeffrey, S. J., Collier, M. A., Dravitzki, S. M., Hirst, A. C., Syktus, J. I., et al. (2012). Aerosol- and greenhouse gas-induced changes in summer rainfall and circulation in the Australasian region: a study using single-forcing climate simulations. *Atmos. Chem. Phys.* 12, 6377–6404. doi:10.5194/acp-12-6377-2012

Rummukainen, M. (2010). State-of-the-art with regional climate models. *Wiley Interdiscip. Rev. Clim. Change* 1 (1), 82–96. doi:10.1002/wcc.8

Ruosteenoja, K., Tuomenvirta, H., and Jylhä, K. (2007). GCM-based regional temperature and precipitation change estimates for Europe under four SRES scenarios applying a super-ensemble pattern-scaling method. *Clim. Change* 81, 193–208. doi:10.1007/s10584-006-9222-3

Rust, H. W., Maraun, D., and Osborn, T. J. (2009). Modelling seasonality in extreme precipitation: a UK case study. *Eur. Phys. J. Spec. Top.* 174, 99–111. doi:10.1140/epjst/e2009-01093-7

Saeed, F., Haensler, A., Weber, T., Hagemann, S., and Jacob, D. (2013). Representation of extreme precipitation events leading to opposite climate change signals over the Congo basin. *Atmosphere* 4, 254–271. doi:10.3390/atmos4030254

Santer, B. D., Wigley, T. M. L., Schlesinger, M. E., and Mitchell, J. F. B. (1990). Report No.: 47. Developing climate scenarios from equilibrium GCM results. Available at: https://pure.mpg.de/rest/items/item_2566446/component/file_2566445/content

Shindell, D. T., Voulgarakis, A., Faluvegi, G., and Milly, G. (2012). Precipitation response to regional radiative forcing. *Atmos. Chem. Phys.* 12, 6969–6982. doi:10.5194/acp-12-6969-2012

Shiogama, H., Hanasaki, N., Masutomi, Y., Nagashima, T., Ogura, T., Takahashi, K., et al. (2010). Emission scenario dependencies in climate change assessments of the hydrological cycle. *Clim. Change* 99 (1–2), 321–329. 10.1007/s10584-009-9765-1

Stevens, B., Giorgetta, M., Esch, M., Mauritsen, T., Crueger, T., Rast, S., et al. (2013). Atmospheric component of the MPI-M Earth system model: ECHAM6. *J. Adv. Model. Earth Syst.* 5, 146–172. doi:10.1002/jame.20015

Tromel, S., and Schonwiese, C. D. (2007). Probability change of extreme precipitation observed from 1901 to 2000 in Germany. *Theor. Appl. Climatol.* 87, 29–39. doi:10.1007/s00704-005-0230-4

Trzaska, S., and Schnarr, E. (2014). *A review of downscaling methods for climate change projections*. Burlington, Vermont: United States Agency for International Development Tetra Tech ARD.

Voldoire, A., Sanchez-Gomez, E., Salas y Mélia, D., Decharme, B., Cassou, C., Sénési, S., et al. (2013). The CNRM-CM5.1 global climate model: description and basic evaluation. *Clim. Dynam.* 40, 2091–2121. doi:10.1007/s00382-011-1259-y

Volodin, E. M., Dianskii, N. A., and Gusev, A. V. (2010). Simulating present-day climate with the INMCM4.0 coupled model of the atmospheric and oceanic general circulations. *Izvestiya Atmos. Ocean. Phys.* 46, 414–431. doi:10.1134/S000143381004002X

Von Salzen, K., Scinocca, J. F., McFarlane, N. A., Li, J., Cole, J. N. S., Plummer, D., et al. (2013). The Canadian fourth generation atmospheric global climate model (CanAM4). Part I: representation of physical processes. *Atmos. Ocean.* 51, 104–125. doi:10.1080/07055900.2012.755610

Watanabe, M., Suzuki, T., O'ishi, R., Komuro, Y., Watanabe, S., Emori, S., et al. (2010). Improved climate simulation by MIROC5: mean states, variability, and climate sensitivity. *J. Clim.* 23, 6312–6335. doi:10.1175/2010JCLI3679.1

Watterson, I. G. (2008). Calculation of probability density functions for temperature and precipitation change under global warming. *J. Geophys. Res. Atmos.* 113 (D12), D12106. doi:10.1029/2007JD009254

Watterson, I. G., and Whetton, P. H. (2011). Joint PDFs for Australian climate in future decades and an idealized application to wheat crop yield. *Aust. Meteorol. Oceanogr. J.* 61, 221–223. doi:10.22499/2.6104.003

Wigley, T. M. L. (2008). MAGICC/SCENGEN 5.3: user manual version 2. Available at: http://www.cgd.ucar.edu/cas/wigley/magicc/UserMan5.3.v2.pdf (Accessed February 10, 2020).

Wilby, R. L., and Wigley, T. M. L. (1997). Downscaling general circulation model output: a review of methods and limitations. *Prog. Phys. Geogr.* 21, 530–548. doi:10.1177/030913339702100403

Xia, J., Du, H., Zeng, S., She, D., Zhang, Y., Yan, Z., et al. (2012). Temporal and spatial variations and statistical models of extreme runoff in Huaihe River Basin during 1956–2010. *J. Geogr. Sci.* 22 (6), 1045–1060. doi:10.1007/s11442-012-0982-6

Ye, W., and Li, Y. (2011). "A method of applying daily GCM outputs in assessing climate change impact on multiple day extreme precipitation for Brisbane River catchment." in 19th International Congress on Modelling and Simulation, Perth, Australia, December, 12–16, 2011

Yukimoto, S., Yoshimura, H., Hosaka, M., Sakami, T., Tsujino, H., Hirabara, M., et al. (2011). *Meteorological research institute-earth system model v1(MRI-ESM1)-model description*. Ibaraki, Japan: Technical Report of MRI, 88.

Zhao, Y., Zou, X., Cao, L., and Xu, X. (2014). Changes in precipitation extremes over the Pearl River Basin, Southern China, during 1960–2012. *Quat. Int.* 333, 26–39. doi:10.1016/j.quaint.2014.03.060

Zolina, O., Simmer, C., Kapala, A., Bachner, S., Gulev, S., and Maechel, H. (2008). Seasonally dependent changes of precipitation extremes over Germany since 1950 from a very dense observational network. *J. Geophys. Res. Atmos.* 113, D06110. doi:10.1029/2007JD008393

Conflict of Interest: The author declares that the research was conducted in the absence of any commercial or financial relationships that could be construed as a potential conflict of interest.

frontiers in Earth Science

ORIGINAL RESEARCH
published: 23 March 2021
doi: 10.3389/feart.2021.619512

Climate Change in Rwanda: The Observed Changes in Daily Maximum and Minimum Surface Air Temperatures during 1961–2014

Jean Paul Ngarukiyimana[1], *Yunfei Fu*[1]*, *Celestin Sindikubwabo*[2], *Idrissa Fabien Nkurunziza*[1,3], *Faustin Katchele Ogou*[2], *Floribert Vuguziga*[4], *Bob Alex Ogwang*[5] *and Yuanjian Yang*[4,6]*

[1]School of Earth and Space Sciences, University of Science and Technology of China, Hefei, China, [2]University of Chinese Academy of Science, Beijing, China, [3]University of Rwanda, Kigali, Rwanda, [4]School of Atmospheric Physics, Nanjing University of Information Science and Technology, Nanjing, China, [5]Uganda National Meteorological Authority, Kampala, Uganda, [6]State Key Laboratory of Loess and Quaternary Geology, Institute of Earth Environment, Chinese Academy of Sciences, Xian China

Edited by:
Ming Luo,
Sun Yat-Sen University, China

Reviewed by:
Asher Siebert,
International Research Institute for Climate and Society (IRI), Palisades, NY, United States
Jianyu Liu,
China University of Geosciences Wuhan, China

***Correspondence:**
Yunfei Fu
fyf@ustc.edu.cn
Yuanjian Yang
yyj1985@nuist.edu.cn

Specialty section:
This article was submitted to Interdisciplinary Climate Studies, a section of the journal Frontiers in Earth Science

Received: 20 October 2020
Accepted: 08 February 2021
Published: 23 March 2021

Citation:
Ngarukiyimana JP, Fu Y, Sindikubwabo C, Nkurunziza IF, Ogou FK, Vuguziga F, Ogwang BA and Yang Y (2021) Climate Change in Rwanda: The Observed Changes in Daily Maximum and Minimum Surface Air Temperatures during 1961–2014. Front. Earth Sci. 9:619512. doi: 10.3389/feart.2021.619512

Rwanda has experienced high temperature rising phenomena over the last decades and hence, highly vulnerable to climate change. This paper examined the spatial and temporal variations of daily maximum and minimum surface air temperature (Tmin and Tmax) and diurnal temperature range (DTR). It studied variables at monthly, seasonal and annual time-scales from 1961 to 2014. The study applied various statistical methods such as ordinary least-square fitting, Mann-Kendall, Sen' slope and Sequential Mann-Kendall statistical test to the new reconstructed ENACTS dataset that cover the period from 1983 to 2014 while pre-1983s recorded data from 24 meteorological stations have been added to complete the lengthiness of ENACTS data. The January to February season did not show a significant trend at seasonal time-scales. The authors decided only to consider March-to-May, June-to-August and October-to-December seasons for further analyses. Topography impacts on temperature classified stations into three regions: region one (R1) (1,000–1,500 m), region two (R2) (1,500–2,000 m) and region three (R3) (≥2,000 m). With high confidence, the results indicate a significant positive trend in both Tmin and Tmax in all three regions during the whole study period. However, the magnitude rate of temperatures change is different in three regions and it varies in seasonal and annual scale. The spatial distributions of Tmax and Tmin represent a siginificant warming trend over the whole country notably since the early 1980s. Surprisingly, Tmin increased at a faster rate than Tmax in R3 (0.27 vs. 0.07°C/decade in March-to-May) and (0.29 vs. 0.04°C/decade in October-to-December), resulting in a significant decrease in the DTR. This is another confirmation of warming in Rwanda. The mutation test application exhibited most of the abrupt changes in the seasonal and annual Tmax and Tmin trends between 1984 and 1990. The present work mainly focus on the spatial and temporal variability of Tmin, Tmax and DTR in Rwanda and their relationship with elevation change, leaving a gap in other potential cause factors explored in the future.

Keywords: minimum temperature (Tmin), maximum temperature (Tmax), warming, Rwanda, climate change

INTRODUCTION

The harmful impacts of climate change on human life, infrastructure and ecosystem have led to increased studies on the subject globally (IPCC, 2001a; Alexander et al., 2006; Myoung et al., 2013). Temperature is one of the most critical climate factors that affect human, agriculture, and to a significant extent, thermal comfort (Walther et al., 2002; Diaz et al., 2005). Global warming and climate variability have remained a hot topic of debate worldwide (Morak et al., 2013; Otto and Friederike, 2016; Easterling et al., 2000; Penuelas and Flella, 2001; IPCC, 2001b). Globally, the temperature has been characterized by warming in minimum and maximum temperature (Vose et al., 2005; Brown et al., 2008; Donat et al., 2013).

The fifth assessment report (AR5) of the Intergovernmental Panel on Climate Change (IPCC) approximated an average increase of global temperature in 1951–2012 to be 0.72°C. Furthermore, The IPCC (2013) revealed that the hottest 30-year period in the last 1,400 years might have been between 1983 and 2012. The report suggested that the trend in Tmean may be due to changes in either Tmax or Tmin, or relative changes in both (IPCC, 2013). Considering that the changes in mean temperature (Tmean) were broadly an essential indicator of climate change, but changes in maximum and minimum temperatures (hereafter Tmax and Tmin) provide more valuable information than the Tmean alone (Safeeq et al., 2013; Iqbal et al., 2016; Yang et al., 2013; 2020a). Several authors noted that the minimum temperatures are warming more rapidly than maximum temperatures (IPCC, 2007; Christy et al., 2009; Stern et al., 2011; Nicholson et al., 2013). Consequently, the assessment of fluctuations of observed and simulated Tmax and Tmin has captured many researchers' attention (Revadekar et al., 2013; Sayemuzzaman et al., 2015; Easterling et al., 1997; Lobell et al., 2007; Tingley and Huybers, 2013). It is likely agreed that Tmax and Tmin trends and variability play an essential role in detecting climate change impacts on human health such as vector-borne disease (Ren et al., 2016; Sun et al., 2017). The impacts of extreme temperature on mortality have been confirmed in a number of other studies (Barreca et al., 2016; Heal and Park, 2016; Ndenga et al., 2006) revealed that unusual high maximum temperatures positively correlate with many malaria cases. For instance, according to the findings from Rwanyiziri and Rugema (2013), the rise in temperature and changes in the amount of rainfall and its distribution have altered water resources availability, consequently affecting rice productivity across Bugesera District. Moreover, studies have indicated that spatiotemporal changes of Tmax and Tmin significantly affect the intensity, duration and extent of temperature extremes worldwide (Salman et al., 2017; Sun et al., 2017). Furthermore, food production, biodiversity, and ecosystems are highly affected by Tmax and Tmin changes (Qasim et al., 2016; Walther et al., 2002; Smith et al., 1999). Similarly, Parmesan et al. (2003) found that climate change is already affecting living systems. Other studies indicate that the changes in Tmax and Tmin has a significant impact on agriculture, health, food security (Iqbal et al., 2016). Thus, the assessment of Tmax and Tmin's long-term changes is to better understand impacts of climate change to a country with economy depending on agriculture like Rwanda (Minitere, 2006). Moreover, such information is useful for proper climate adaptation plan in future at the local level (Berardy and Chester, 2017).

Rwanda has experienced a significant increase in temperatures in recent years and hence, highly vulnerable to climate change. Previous studies have reported dynamic changes in Tmax and Tmin over different parts of Rwanda (Henninger, 2009; Minitere, 2006; Eriksen and Rosentrater, 2008; Safari, 2012). An increase in temperature of approximately 0.7–0.9°C over Rwanda in the last century were reported (Eriksen and Rosentrater, 2008). Similarly, Henninger (2009) reported an average of 1.5°K increase in temperature with air pollution increase in Kigali city. The detected temperatures fluctuation in Kigali city was attributed to the growing population urbanization and industrialization experienced in that area. By analyzing precipitation and air temperature records from 6 sites in Rwanda for the period 1964–2010, a warming pattern over past 40 years at the average of 0.35°C per decade has been noted by Mohammed et al., 2016.

Moreover, a significant warming trend for the period after 1977–1979 has been detected where the capital Kigali recorded a slope of 0.0455°C/year (Safari, 2012). The studies mentioned above have reported significant results in terms of dynamic variability of Tmax and Tmin over some regions of Rwanda. However, most of those previous studies were limited to a specific area, which may fail to cover country's general representation. Furthermore, none of those previous studies did consider the impact of topography and seasonal variation factors, which are very important in detecting and attributing climate change in Rwanda's regional difference. Previous studies have almost agreed that topography regulates temperatures distribution in many regions where Tmin changes has been recorded to be significantly related to the elevation (Revadekar et al., 2013; Sun et al., 2017). Therefore, it is of great importance to have appropriate knowledge of previous Tmax and Tmin variability to reduce the impact caused by their changes in the future.

The present study's objective is to examine the long-term variations and trends of the surface air temperature based on a perspective of Tmax and Tmin, and diurnal temperature range (DTR) series over Rwanda on monthly, seasonal and annual time-scales. Thus, this study improves terms of changes in Tmax and Tmin with the extended time scale, stations and additional statistical analysis. Furthermore, no comprehensive research made to assess the spatial and temporal changes in Tmax and Tmin over the whole country. Rwanda recorded significant economic development over last years. The government aims to achieve more in its vision 2050 (Punam and Manka, 2011; U.N Economic Commission for Africa, 2016). However, climate change and its related risks could become potential threats to achieving these goals. Therefore, it is vital to assess the spatial and temporal changes in Tmax, and Tmin in the study area.

This study focus on observed changes in Tmax and Tmin over Rwanda for the period 1961–2014. It is also the first of its kind to detect abrupt changes in seasonal and annual time series of Tmax

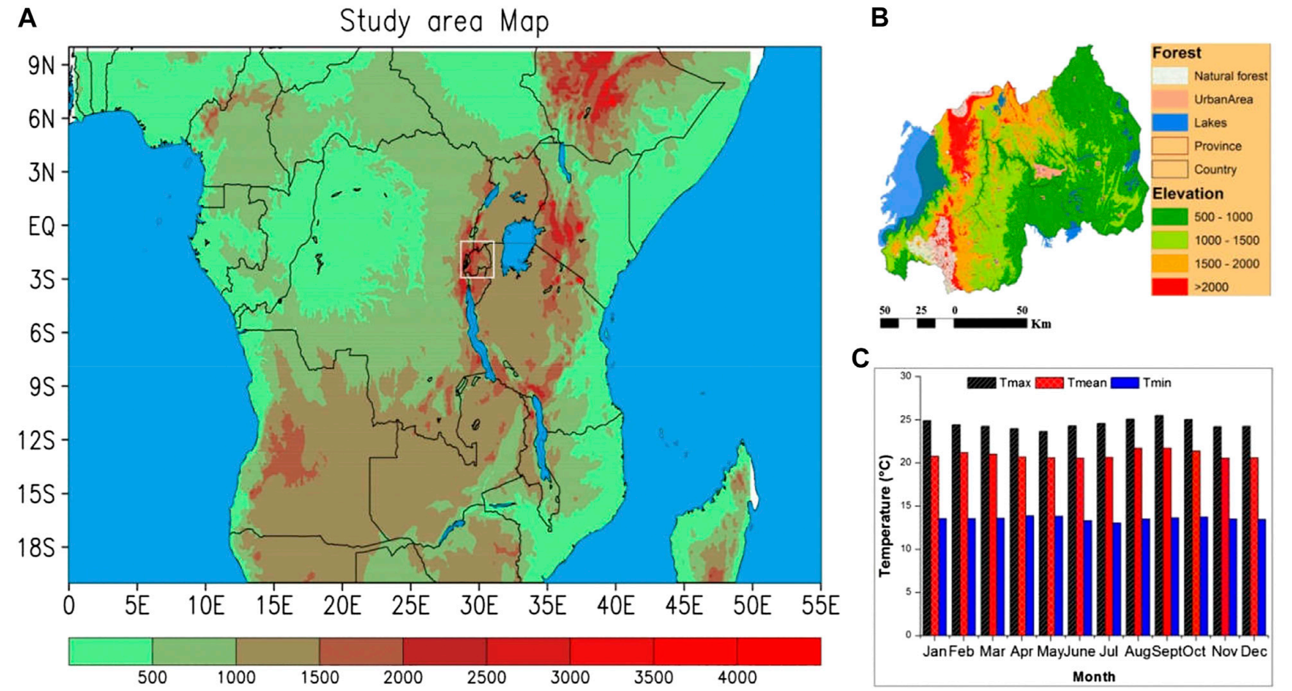

FIGURE 1 | Study area: **(A)** Location of Rwanda in Middle Africa, **(B)** Topography of Rwanda, **(C)** Climatological monthly means of Tmax, Tmean and Tmin over Rwanda during 1961–2014.

and Tmin in the target area and to combine the new reconstructed ENACTS (the Enhancing National Climate Services) data with the previous observed stations data for analysis.

STUDY AREA, DATA AND METHODOLOGY

Rwanda with equatorial climate lies within latitude 1°4′–2°51′S and longitude 28°53′–30°53′E (**Figure 1A**). It is positioned near the equator in between central and East Africa. Rwanda is bounded with Uganda in the north, Tanzanian East, the Democratic Republic of the Congo in West and Burundi in South. The high elevation influence leads the country to enjoy temperate climate varying with topography (**Figure 1A**). Its topography dominated by mountains in the volcanic highland areas of north and north-western region with abundant rainfall (>1,200 mm) and savannah region to the east and southeast with less rainfall (<900 mm) through the year (**Figure 1B**). Rwanda has two rainy seasons separated by two dry seasons with March-May being the 'long rains' season. The monthly averaged maximum temperature occurs in August. The monthly averaged sub-maximum monthly averaged temperature occurs in February. There are two minima for monthly averaged temperature in May and November (**Figure 1C**). The average, maximum and minimum temperature for Rwanda varies with the topography. For example, the warmest annual average temperatures are in the eastern plateau (20–21°C), and the southwestern in the valley of Rusizi (23–24°C), and cooler temperatures are in higher elevations of the central plateau (17.5–19°C) and high-lands (<17°C) (**Figures 2A–C**).

The data used in this study were obtained from Rwanda Meteorology Agency (RMA). Due to the existing gap in observed stations data of mid-1990s during the Genocide to 2010, the ENACTS project supported by the International research Institute for Climate and Society (IRI) and its partners was initiated and aimed to fill that gap. The reconstructs temperature data were obtained by combining station data with reanalysis data and the merged final product is spatiotemporally complete from the early 1983s to present. The ENACTS data used in this study cover the period from 1983 to 2014. The quality control of station data was performed during the generation of new data set. The same ENACTS data were used by Siebert et al. (2019) to analysis the temperature climatology for the period between 1981 and 2016. Detailed information on ENACTS data can be freely accessed online via http://maproom.meteorwanda.gov.rw. In order to cover the whole study period of 54 years, a monthly temperature was calculated from observed daily data from 24 weather stations covering the period from 1961 to 1983. The selected stations from observed data are the same stations used in ENACTS data. Data quality was checked and only stations with length records completeness are used. The selected stations from observed data are the same stations used in ENACTS data. It is very important to mention that before 1990s, there is no significant gap in reported data from meteorological stations. Safari, 2012 used the same observed data to examine the trend of mean annual temperature from five observatories during 1958–2010. While those previous studies have used stations observed data and

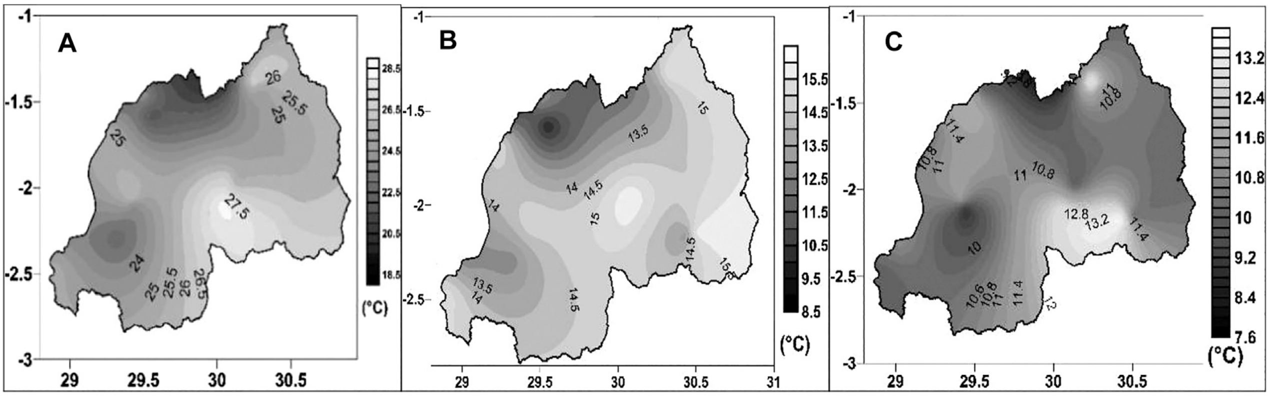

FIGURE 2 | Distribution of **(A)** Minimum, **(B)** Maximum and **(C)** diurnal temperature over Rwanda for the period of 1961–2014. Unit (°C) (Note: *X*-axis refers to longitude while *Y*-axis stand for latitude).

TABLE 1 | Selected Stations and their respective location based on their elevation in three various regions (region one, region two and region three).

Region	Observatory	Lat (°S)	Lon (°E)	Altitude (m)	Tmin (°C)	Tmax (°C)
REGION one (R1) (1,000–1,500 m)	KANOMBE	1.965	30.13	1,490	15.2	26.8
	GITEGA	1.95	30.07	1,474	14.7	26.6
	KAWANGIRE	1.82	30.45	1,473	14.3	27.2
	GABIRO	1.38	30.24	1,472	13.3	26.9
	RUSOMO	2.16	30.44	1,450	13.2	26.8
	NYAMATA	2.09	30.05	1,428	15.4	28.3
	KARAMA P	2.17	30.16	1,403	14.7	27.8
	NYAGATARE	1.3	30.33	1,377	13.8	26.3
REGION two (R2) (1,500–2,000 m)	RULINDO	1.43	29.55	1,800	12.6	22.9
	RWANKUBA	1.45	29.5	1,750	12.7	24.3
	BYIMANA	2.11	29.44	1,750	12.8	23.7
	RUTONGO	1.43	30.3	1,700	13.6	24.7
	RUBENGERA	2.06	29.42	1,700	14.8	26.1
	KIBUNGO	2.15	30.5	1,680	15.7	26.2
	KAMEMBE	2.47	28.92	1,591	15.2	25.2
	GISENYI	1.67	29.25	1,554	14.9	25.5
REGION three (R3) ≥2,000 m	RWERERE	1.32	29.53	2,312	11.8	21.7
	KABAYA	1.44	29.32	2,250	9.6	21.3
	RWANKERI	1.35	29.32	2,250	8.9	18.2
	GICUMBI	1.35	30.04	2,235	11.9	19.5
	BIGUTU	2.3	29.02	2,025	12.7	23.7
	KINIGI	1.27	29.35	2,200	9.5	18.9
	BUSOGO	1.58	29.55	2,100	9.9	21.6
	KIGEME	2.29	29.32	2,000	12.7	22.6

ENACTS data separately, the current study combine both datasets to give more information on Rwanda's climate. Due to the strong influence of topography those stations were classified into three different regions; region one (R1), region two (R2) and region three (R3) with the elevation ranging 1,000–1,500 m, 1,500–2,000 m, and ≥2,000 m respectively (**Table 1**), to provide a proper spatial coverage over the entire country.

Table 1 shows the details of the weather stations used in this study to complete the ENACTS dataset. For each region, stations with elevation in the same range are combined together and monthly values were averaged for the temperature to get seasonal and annual averages. Although the calculation of data from each station can provide an insight into climatic trends for those particular regions, it is not appropriate to use a single station to represent the entire region. Homogeneity of the regional series was checked before in-depth analysis and confirmed by applying the Kruskal-Wallis test (Theodorsson-Norheim, 1986). The three seasons considered were long rains season "March to May" (MAM), the dry season "June to August" (JJA), and short rains season "October to December" (OND). Those chosen three seasons have a very significant impact on crop production and hence people's life. During preliminary results, the JF season temperatures did not show a significant change, therefore JF was removed from further analysis.

The magnitude of the trends was derived from the regression line's slop using the least-squares method. Simultaneously, the statistical significance was determined by Mann-Kendall and

Student *t*-test (Sneyers, 1990). The Sneyers' research, in temperature and precipitation studies, the moving average is a conventional procedure used to reduce the intra-annual variability of series. A 5-years running average was employed in this study. For each element X_i ($i = 1, \ldots, n$), the number of lower elements X_j ($X_j < X_i$) preceding i_t ($j < i$) is calculated and the statistical parameter t is given by:

$$t_i = \sum n_i \tag{1}$$

The distribution of the test statistic t under the null hypothesis has an expected value $E_{(t)}$ and variance $\varphi_{(t)}$ such that:

$$\begin{aligned} E_{(t)} &= n(n-1)/4 \\ \phi^2 &= n(n-1)(2n-5)/72 \end{aligned} \tag{2}$$

The hypothesis is rejected for $|u|_{(t)} > 1.96$ with a statistical significance of 5% and with:

$$u_{(t)} = t - E_{(t)} \Big/ \left(\phi^2_{(t)}\right)^{1/2} \tag{3}$$

Mann-Kendall (MK) Test

The Mann-Kendall (Mann 1945; Kendall 1975) test is applied in trend analysis to detect the type of trend in temperatures and its significance. The MK test is a nonparametric test widely known for its flexibility and simplicity f in estimating trends. This test is commonly used in meteorological studies (Asfaw et al., 2018; Weldegerima et al., 2018; Praveen et al., 2020). It is based on null and alternative hypotheses (H_0 and H_1). In the assessment, the null hypothesis (H_0) assuming no trend in the data is rejected if standard normal test statistics $Z > 1.96$. Alternative hypothesis H1 suggests a monotonic trend. The computation of the MK test is shown below:

$$S = \sum_{k=1}^{n-1} \sum_{j=k+1}^{n} \operatorname{sgn}\left(x_j - x_k\right) \tag{4}$$

where,

$$\operatorname{sgn}\left(x_j - x_k\right) = \begin{cases} 1 & \text{if} \quad x_j - x_k > 0 \\ 0 & \text{if} \quad x_j - x_k = 0 \\ -1 & \text{if} \quad x_j - x_k < 0 \end{cases}$$

The components x_j and x_k are seasonal mean temperature values in years *j* and *k* with $k > j$.

S represents the Kendall test statistics and is assumed to be normal distributed. A positive (negative) value of *S* indicates an increasing (decreasing) trend. Thus, for the selected sample with $n \geq 10$, the $E(S) = 0$, and the variance is calculated as follows:

$$Var(S) = \left[\frac{n(n-1)(2n-5) - \sum_{t=1}^{m} t_i(t_i - 1)(2t_i + 5)}{18}\right] \tag{5}$$

n is the number of observation and variables *m* and t_i stand for the number of ties and sample points in the sample *i*, respectively.

The statistical test *Z* is obtained from **Eqs (2)** and **(3)** as follow:

$$Z_\alpha = \begin{cases} \dfrac{S-1,}{\sqrt{Var(S)}} & \text{if} \quad S > 0 \\ 0, & \text{if} \quad S = 0 \\ \dfrac{S+1}{\sqrt{Var(S)}} & \text{if} \quad S < 0 \end{cases} \tag{6}$$

The positive or negative *Z* value depict trends directions (upward or downward). In case $Z = 0$, the data series is assumed to be normally distributed. The standard test statistic $Z\alpha$ is used to measure the trend significance. In case $|Z\alpha|$ is greater than $Z\alpha/2$, the trend is significant. Here α represents the chosen significance level (e.g., 5% with Z 0.025 = 1.96).

Theil Sen's Slope Estimator

The magnitude of seasonal temperature trends is based on Theil sen's slope method (Sen, 1968). Senvs slope estimator is another nonparametric method widely used to detect the magnitude of time series data. It frequently used to estimate an intercept of a linear regression equation.

For a given time series *x*, the computation of slope Q between two random values use equation below:

$$T_i = \frac{x_j - x_k}{k - j} \tag{7}$$

x_k and x_j are the data values at times *k* and *j* ($j > k$).

The Median of *N* Values of Qi is Computed as

$$Q_{\text{med}} = \begin{cases} T_{(N+2)/2}, & N \text{ is odd} \\ \frac{1}{2}T_{N/2} + T_{(N+2)/2}, & N \text{ is even} \end{cases} \tag{8}$$

The positive or negative Q_{med} indicates an increasing or decreasing trend.

Sequential Mann-Kendall (SMK) test is employed to show a change in trend with time. Forward sequential statistic $[u(t)]$ and backward sequential statistic $[u'(t)]$ from progressive analysis of the MK test help in the analysis of change in trend with time (Sneyers, 1990). Hence, trend analyses on monthly, seasonal and annual time-scales were performed in order to capture changes in temperature series for Rwanda. The progressive MK values $u(t)$ and $u'(t)$ were calculated using the appropriate MK test for each dataset, from the beginning to the end of the study period. In the analysis of SMK, the confidence limits of the standard normal *z* values at α = 5%. The lower and upper confidence limits, thus, correspond to −1.96 and +1.96, respectively. The method has been used in related studies in East Africa (Nsubuga et al., 2014; Ongoma and Chen 2017) as well as over Rwanda by Safari (2012).

RESULTS

Using available temperatures data for the period 1961–2014, the distribution of Tmin, Tmax and DTR is displayed in **Figure 2** (Temperature unit (Degree Celsius). Over Rwanda,

TABLE 2 | Annual and Seasonal Trends (°C/decade) from 1961 to 2014 for minimum, maximum and DTR for R1, R2 and R3 at 95% confidence level.

Region	Temp	Period	Mean	Trend	Z score	Sen's slope	P Value
R1	Tmax	MAM	25.95994	Increasing	5.759	0.061*	0
R1	Tmax	JJA	26.84309	Increasing	6.162	0.063*	0
R1	Tmax	OND	26.49632	Increasing	6.132	0.058*	0
R1	Tmax	ANN	26.5335	Increasing	6.401	0.063*	0
R1	Tmin	MAM	14.67805	Increasing	5.804	0.03*	0
R1	Tmin	JJA	13.96235	Increasing	5.215	0.032*	0
R1	Tmin	OND	14.49871	Increasing	7.147	0.037*	0
R1	Tmin	ANN	14.39297	Increasing	6.326	0.033*	0
R1	DTR	MAM	11.24416	Increasing	4.118	0.035*	0
R1	DTR	JJA	12.76529	Increasing	4.521	0.038*	0
R1	DTR	OND	12.02416	Increasing	3.297	0.027*	0.001
R1	DTR	ANN	12.10011	Increasing	4.894	0.035*	0
R2	Tmax	MAM	24.47446	Increasing	5.386	0.031*	0
R2	Tmax	JJA	25.01556	Increasing	5.476	0.04*	0
R2	Tmax	OND	24.84689	Increasing	5.013	0.026*	0
R2	Tmax	ANN	24.86244	Increasing	6.118	0.033*	0
R2	Tmin	MAM	13.78974	Increasing	6.147	0.03*	0
R2	Tmin	JJA	13.07773	Increasing	5.536	0.031*	0
R2	Tmin	OND	13.63125	Increasing	6.759	0.035*	0
R2	Tmin	ANN	13.51054	Increasing	6.446	0.032*	0
R2	DTR	MAM	10.68472	No trend	0.179	0.001	0.858
R2	DTR	JJA	11.93783	No trend	1.895	0.012	0.058
R2	DTR	OND	11.21565	Decreasing	-2.283	-0.014	0.022
R2	DTR	ANN	11.3519	No trend	0.791	0.003	0.429
R3	Tmax	MAM	20.5834	No trend	1.41	0.007	0.159
R3	Tmax	JJA	20.6977	Increasing	2.79	0.017*	0.005
R3	Tmax	OND	21.09731	No trend	0.776	0.004	0.438
R3	Tmax	ANN	20.91214	Increasing	2.387	0.01*	0.017
R3	Tmin	MAM	11.14877	Increasing	4.931	0.028*	0
R3	Tmin	JJA	10.52238	Increasing	5.044	0.027*	0
R3	Tmin	OND	10.7277	Increasing	6.088	0.029*	0
R3	Tmin	ANN	10.78338	Increasing	6.147	0.027*	0
R3	DTR	MAM	9.434,634	Decreasing	-2.447	-0.018*	0.014
R3	DTR	JJA	10.17532	No trend	-1.156	-0.008	0.248
R3	DTR	OND	10.36961	Decreasing	-4.133	-0.022*	0
R3	DTR	ANN	10.12876	Decreasing	-2.641	-0.013*	0.008

Significant test (p ≤0.05) trend at a 95% confidence level.
The symbols (*) stand for significant.

the distribution of temperature increase eastwards, from region of high altitude in north and south west to the low land in east part of the country (**Figures 2A–C**). Topography regulates the temperatures distribution over the country. The maximum and minimum data were analyzed for the period 1961–2014. In general, maximum and minimum temperature increase through most of the period whereas the STR is basically trendless.

Long-Term Trends in Daily Minimum and Maximum Temperature

Tmin, Tmax and DTR trends in R1, R2 and R3, are presented in **Table 2** with significant trends at a 95% confidence level. The seasons' MAM, JJA and OND are considered along with the annual trend for further analysis. **Figure 3A** shows seasonal and annual temperatures trends from the observatories over the period 1961–2014 using a linear regression model. The slope of the regression line describes the rate of change. The Tmin, Tmax and DTR were analyzed separately. **Table 2** shows that the region one (R1) made up by all stations with altitude ranging between 1,000 and 1,500 m has experienced a considerable increase of 0.3°C/decade of Tmin during MAM season while 0.32°C/decade Tmin is noted during the JJA season and 0.37°C/decade of Tmin during OND season. The rate of increase of Tmin is higher in OND season compared to the two remaining seasons. On the annual scale, a positive trend at the rate of 0.33°C/decade of Tmin is noted. On the other hand, Tmax has significantly increased at the rate of 0.61°C/decade in MAM season and 0.63 °C/decade in JJA in R1 while 0.58°C/decade for OND season is registered. In contrast to Tmin, the highest rate of increase for Tmax is observed in JJA season as well as in annual scale with a rising rate of 0.63°C/decade. Thus, the region one (R1) has experienced increase in both minimum and maximum temperature. The Tmax has increased more rapidly than Tmin in R1 during MAM, JJA and at annual scale which leads to the observed positive trend of diurnal temperature in that region (**Figure 3A**,**B**, left column and **Table 2**).

Same as the analysis above, the situation in region two (R2) which is composed by all stations between 1,500 and 2,000 m of altitude was examined. Results show that both Tmin and Tmax have increased with Tmin raising more rapidly in OND season. An increased rate of 0.3°C/decade Tmin in MAM and 0.31°C/decade in JJA while the rate of increase of 0.35 and 0.32°C/decade are observed in OND season and Annual, respectively. There is no observed trend of diurnal temperature in R2 and this is because the rate of Tmin increase is greater particularly in OND season. Authors also note a Tmax moderate positive trend rate of 0.31°C/decade in MAM and 0.4°C/decade in JJA while 0.26 and 0.33°C/decade are noted in OND season and annual scales in R2 (**Figure 3A**,**B**, middle column and **Table 2**).

Further investigation on the temperatures trend was conducted in the region three (R3) formed by all observatories with an altitude greater than 2,000 m. This high mountains region is commonly known to have low temperatures compared to the previous two regions. Surprisingly, the results show a positive increase of both Tmin and Tmax with a very rapid increase of Tmin in all seasons and at annual scale. The rate of increase is recorded to be 0.07°C/decade for Tmax in comparison to 0.28°C/decade of Tmin during MAM and 0.17°C/decade of Tmax along with 0.27°C/decade of Tmin during JJA (**Table 2**). Similarly, the rate of rising of Tmin in OND season was higher than that of Tmax at the rate of 0.28 and 0.04°C/decade, respectively in R3 (**Figure 3A**,**B**, right column and **Table 2**).

Generally, an increase of maximum temperature and minimum temperature is revealed for the whole study period at different rate on seasonal and annual scale. Surprisinly, Tmin increase rate is also noted to be higher than that of Tmax in R3. **Figure 3A**,**B** depicts the MAM, JJA and OND seasonal along with annual time series for each variable. Results show that both Tmax and Tmin increase from later 1970s to present, with decreasing in DTR in region three. The DTR is not decreasing in R1 as both Tmin and Tmax increase with rapid increase in Tmax. However, a slightly decreases in R2 is noted during the study period, with a notable decrease in R3. From 1961 to 2014, the Tmax trend during OND season in R1, R2 and R3 is 0.58, 0.26, 0.04°C/decade respectively. The Tmin trend in the same seasons is 0.37, 0.35, and 0.28°C/decade for R1, R2 and R3 and DTR trend is 0.27, −0.07 and −0.22°C/decade in R1, R2 and R3, respectively (the trends were computed using least-squares regression). DTR trend decreases, which likely reflects the

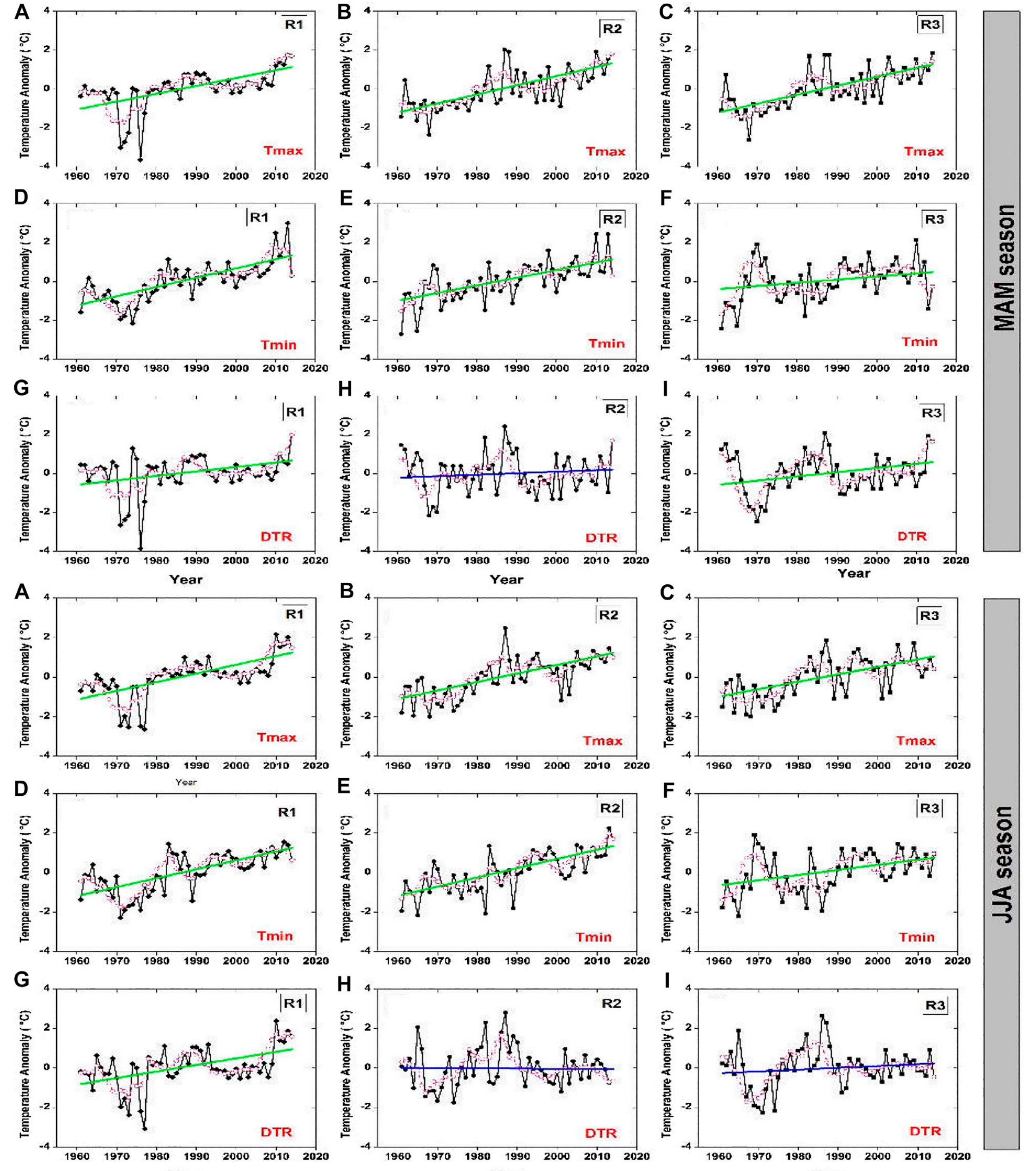

FIGURE 3a | Five-year moving average of monthly, seasonal (MAM and JJA) Maximum, Minimum and Diurnal Temperature and their linear Trends for three regions (R1: 500 ≤ stations ≤1,500 m; R2:1,500 m ≤ stations ≤2,000 m; R3: stations ≥2,000 m) over the period of 1961–2014. Green line indicates significant raising while the blue line indicates a neutral or decreasing trend.

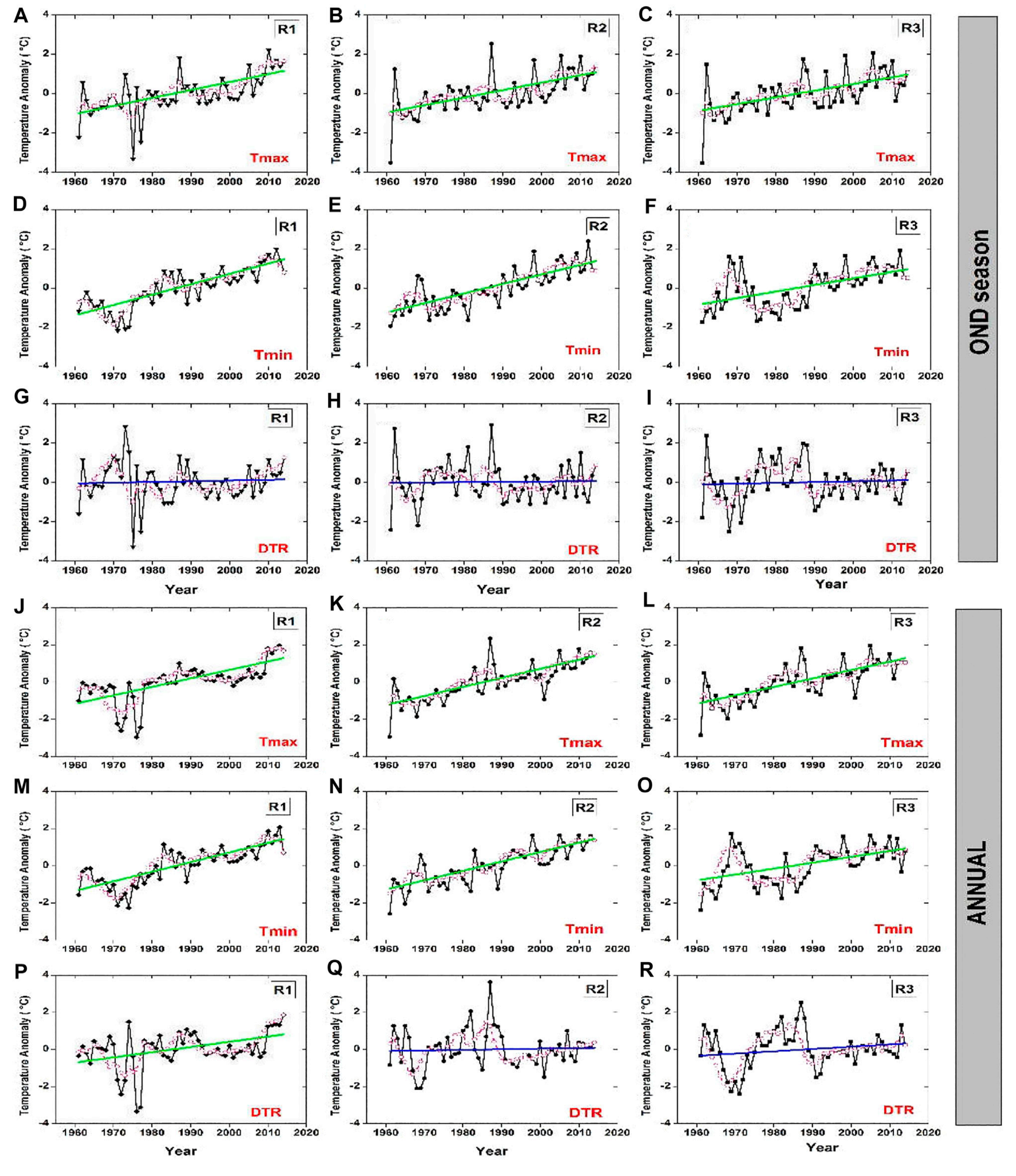

FIGURE 3b | The same analysis for OND and Annual.

accelerated rate of warming in the Tmin. Considering the rate of annual trend from 1961 to 2014, the Tmax trend rate in R1, R2 and R3 is recorded to be 0.63, 0.33 and 0.1°C/decade. On the other side, the rates of 0.33, 0.32, 0.27°C/decade, in R1, R2 and R3 for Tmin are registered with DTR trend rate of 0.35, 0.03, and −0.134°C/decade. Thus, temperatures in R3 (normally cold region) exhibit notable increases in all seasons while OND season experiences many variations in all regions.

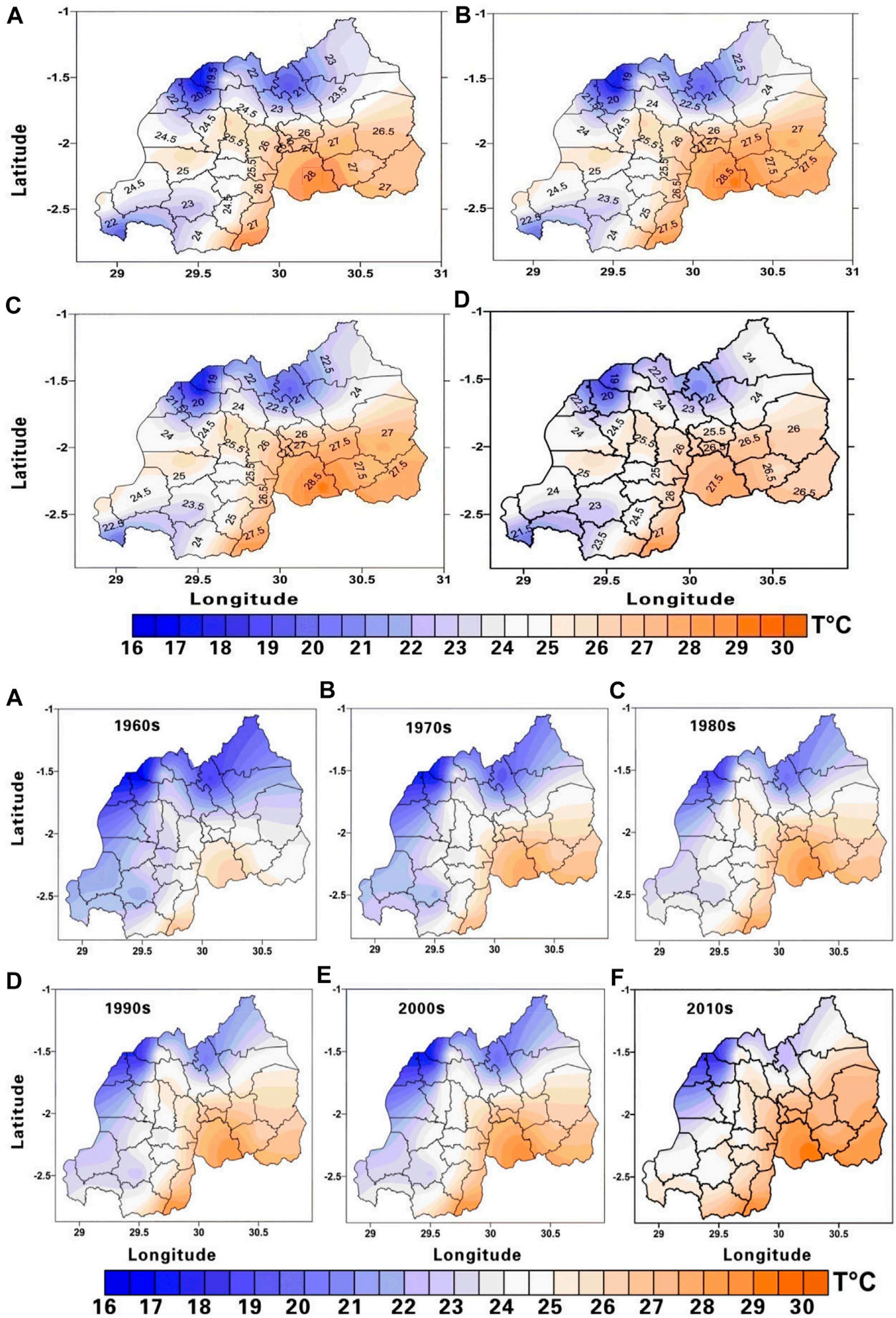

FIGURE 4a | Spatial distribution of seasonal and annual Tmax over Rwanda during 1961–2014; **(A)** Annual, **(B)** MAM, **(C)** JJA, **(D)** OND and Spatial distribution of Decadal Tmax over Rwanda during 1961–2014; **(A)** 1961, **(B)** 1970, **(C)** 1980, **(D)** 1990, **(E)** 2000, **(F)** 2010. T stands for temperature.

Generally, the analysis of temporal variations of seasonal and annual Tmax and Tmin over Rwanda (**Figure 3A**,**B**) indicates that both Tmax and Tmin have increased in all seasons and annual scales. a sharp increase is observed in October to December season and annual scales. The results agreed with the previous study by Safari, 2012 who also reported a significant

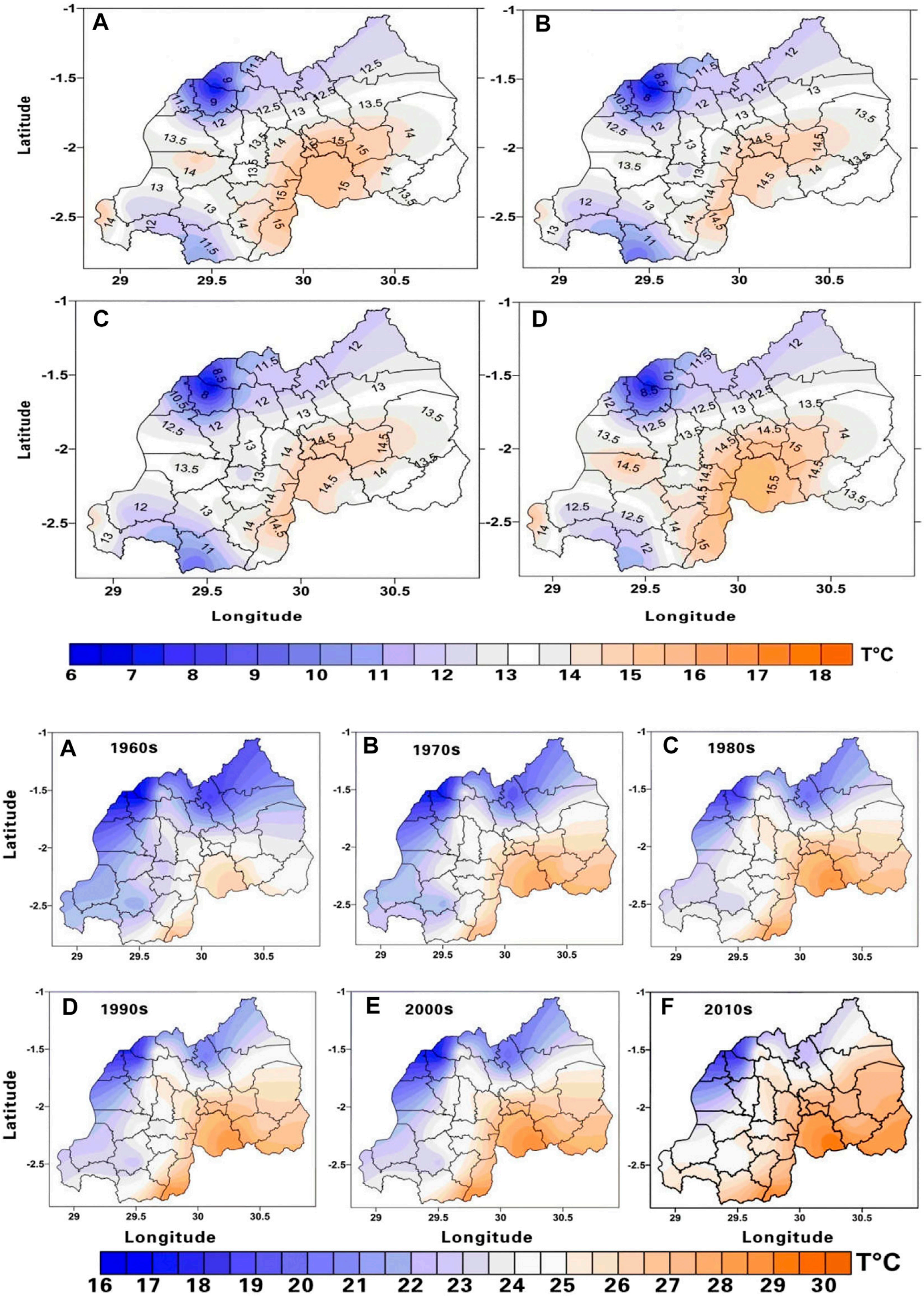

FIGURE 4b | The same analysis for Tmin.

warming trend for the period after 1977–1979 where Kigali, The capital city presented the highest value of 0.0455°C/year (i.e., 0.45°C per decadal). Furthermore, the results show that Tmax increasing rate was four times (around 0.61°C/decade) the rate of global average increase of 0.15°C/decade in R1, two times in R2.

TABLE 3 | Occurrence of abnormal temperatures (above, normal and below) in R1, R2 and R3 based on observed data during 1961–2014.

Location	Grades	Years	Condition	Occurrence (%)
R1	Above normalYears	2014, 2013, 2012, 2011, 2010, 2009, 2008, 2007 2006, 2005, 2004, 2003, 2000, 1999, 1998, 1997, 1995, 1994, 1993, 1992, 1991, 1990, 1988, 1987, 1985	Xh = (Ti > Tv +0.3°C)	47.86
	Normal years	2002, 2001, 1996, 1989, 1986, 1984, 1983, 1982, 1982, 1980, 1963, 1962	Xn = (Ti ≥ Tv–0.3°C and Ti ≤ Tv +0.3°C)	21.55
	Below normalYears	1979, 1978, 1977, 1976, 1975, 1974, 1973, 1972, 1971, 1970, 1969, 1968,1967, 1966, 1965, 1964, 1961	Xc = Ti < Tv +0.3°C	30.58
R2	Above normalYears	2014, 2013, 2012, 2011, 2010, 2009, 2008, 2007, 2006, 2005,2004,1999, 1998, 1997, 1993, 1987, 1993	Xh = Ti > Tv +0.3°C	31.50
	Normal years	1962, 1969, 1977, 1978, 1979, 1980, 1984, 1985, 1986, 1990, 1991, 1992, 1994, 1995, 1996, 2000, 2001, 2002, 2003	Xn = (Ti ≥ Tv–0.3°Cand Ti ≤ Tv +0.3°C)	35.20
	Below normalYears	1961, 1963, 1964, 1965, 1966, 1967, 1968, 1970, 1971, 1972, 1973, 1974, 1975, 1976, 1981, 1982, 1988, 1989	Xc = Ti < Tv +0.3°C	33.30
R3	Above normalYears	2014, 2013, 2012, 2011, 2010, 2009, 2007, 2005, 1993, 1992, 1991, 1990, 1984, 1982, 1981, 1980, 1979	Xh = Ti > Tv +0.3°C	31.50
	Normal years	2008, 2006, 2004, 2003, 2002, 2000, 1998, 1997, 1996, 1995, 1994, 1989, 1988, 1987, 1986, 1985, 1978, 1974, 1973, 1972, 1971, 1969, 1966, 1965, 1964, 1963, 1962	Xn = (Ti ≥ Tv–0.3°C and Ti ≤ Tv +0.3°C)	50
	Below normalYears	2001, 1999, 1983, 1977, 1976, 1975, 1970, 1968, 1967, 1961	Xc = Ti < Tv +0.3°C	18.50

Whereby; Xh: Above normal Year, Xn: Normal Year, Xc: Below normal Year While Ti: Yearly mean temperature &Tv: 54Years temperature average and Tv+0.3°C as threshold temperature.

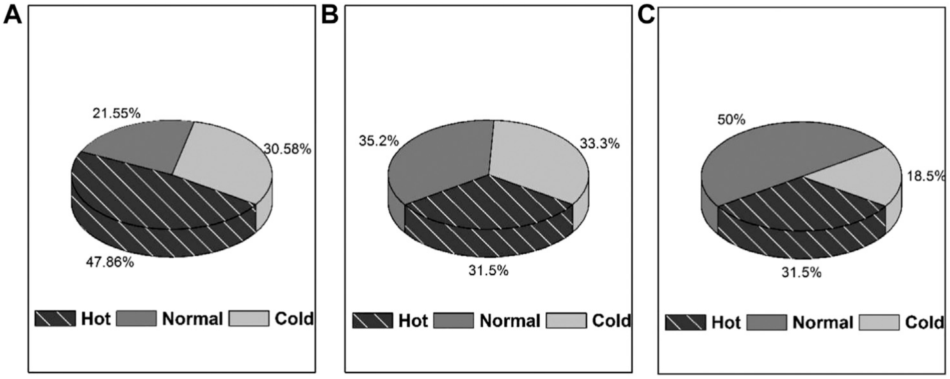

FIGURE 5 | Temperature variation (Hot condition) (Normal condition) and (Cold condition) in **(A)** R1, **(B)** R2 and **(C)** R3 based on the period of 1961–2014.

The Spatial Variations of Annual and Seasonal and Decadal Tmax

The country has 30 districts and each district is represented at least by one station. In order to have a complete coverage of the whole nation the linear interpolation from the station data was employed. **Figure 4A** depicts the spatial distribution of seasonal and annual of Tmax over Rwanda during 1961–2014. Low temperatures are observed in northern part in all seasons with average Tmax of 20°C while high temperatures are observed in the eastern and south eastern region with average of 28°C. In comparison to seasonal Tmax distribution over the study period, more warming is observed in JJA as compared to MAM and OND season. The distribution of temperatures at decadal series shows that the country has generally experienced an extended warming in all regions since 1961 which is clearly noted in latter 1980s. The decadal Tmax for MAM, JJA, OND season and annual are displayed in **Figure 4A**. In agreement with the observed standardized anomaly (**Figure 3A**), the highest warming was observed in last decade of 2010s covering almost the whole study area. The early 1960s period is dominated by lower temperatures in all regions. The highest warming is recorded in the eastern and southern parts of the country.

The Spatial Variations of Annual and Seasonal and Decadal Tmin

Same as for Tmax analysis, the Tmin spatial variations at annual, seasonal and decadal scale over Rwanda are showing in **Figure 4B**. The analysis indicates that the whole country has experienced warming during the study period. Similar toTmax, decadal Tmin and for MAM, JJA, OND and annual are also displayed in **Figure 4B**. In agreement with the observed standardized anomaly (**Figure 3B**), the highest warming was observed in last decade covering almost the whole study area. The early 1960s period is dominated by lower

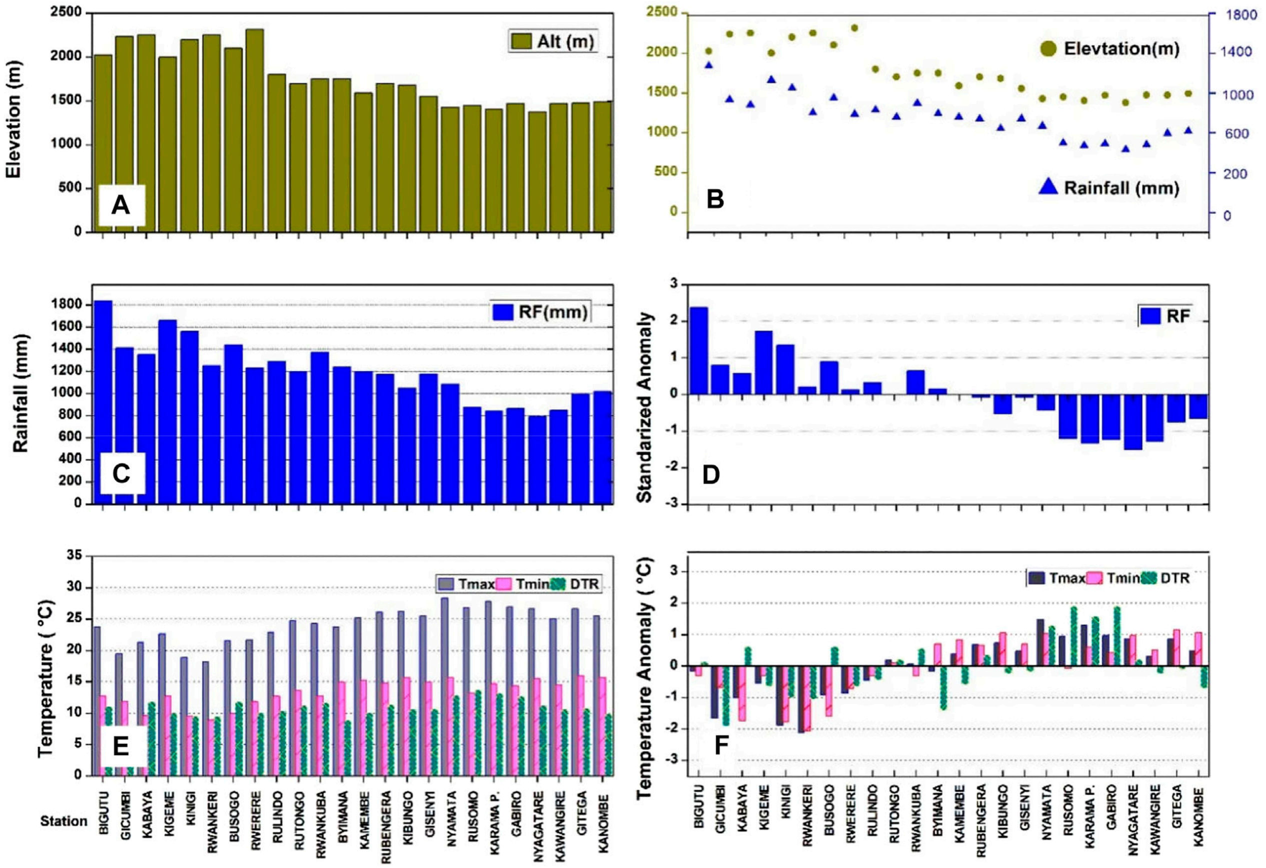

FIGURE 6 | (A) Topography distribution, **(B)** relationship between temperature and topography, **(C)** Maximum, Minimum and DTR trend, **(D)** maximum, minimum and DTR anomalies at every station selected for the period of 1961–2014.

temperatures in all three regions. The higest Tmin is recorded in the easten and southern parts of the country with average of 15° celcius while the lowest Tmin is observed in the northern part with average of 8.5° celcius. In comparison to seasonal Tmin distribution over the study period, more above normal minimum temperatures are observed in OND as compared to MAM and JJA seasons.

Abnormal Maximum and Minimum Temperatures

The above normal temperatures affect the comfort of the human body and agriculture production and many other socio economic activities. In this study, we used the 54 years temperature average plus 0.3°C as the threshold temperature (Tv + 0.3°C). A year with abnormal Tmax was consireded as above normal temperature (Xh) while a year with abnormal Tmin was connected with below normal temperature (Xn). The 54 years temperature average is noted as Tv. On the other hand, any yearly mean temperature that was found to be in the range between the temperature greater or equal to Tv minus 0.3°C and Tv plus 0.3°C, was considered as a year with normal temperature (see **Table 3**). Although, the temperature trend analysis is very important to understand the rate of the variable increase or decrease over a period of time, yet, a deeper analysis of abnormal temperatures (above, normal and below) can give a more information on the impact of that variability (**Figure 5**). The results from **Table 3** indicate that the region one (R1) has been dominated by above normal temperature years (hot condition) representing 47.86% (highest) of the total 54 years study period while 21.55 and 30.58% were recorded for normal temperature years (normal condition) and below temperature years (cold condition), respectively. Region two (R2) has less temperature fluctuations condition with 31.5% of above normal temperature years (hot condition), 35.2% of normal temperature years (normal condition) and 33.3% of below temperature years (cold condition). On the other hand, above normal temperature years (hot condition) at the rate of 31.5% is recorded in the region three (R3) which is another affirmation of warming in that high elevated area. Based on the present study findings, we encourage future studies to investigate the causes of the observed high rate of hot condition in the whole regions especially in region three (R3).

Impact of Topography on Temperature Variability

Without the consideration of the topography, it can be very hard to understand Rwanda's climate. In order to examine further,

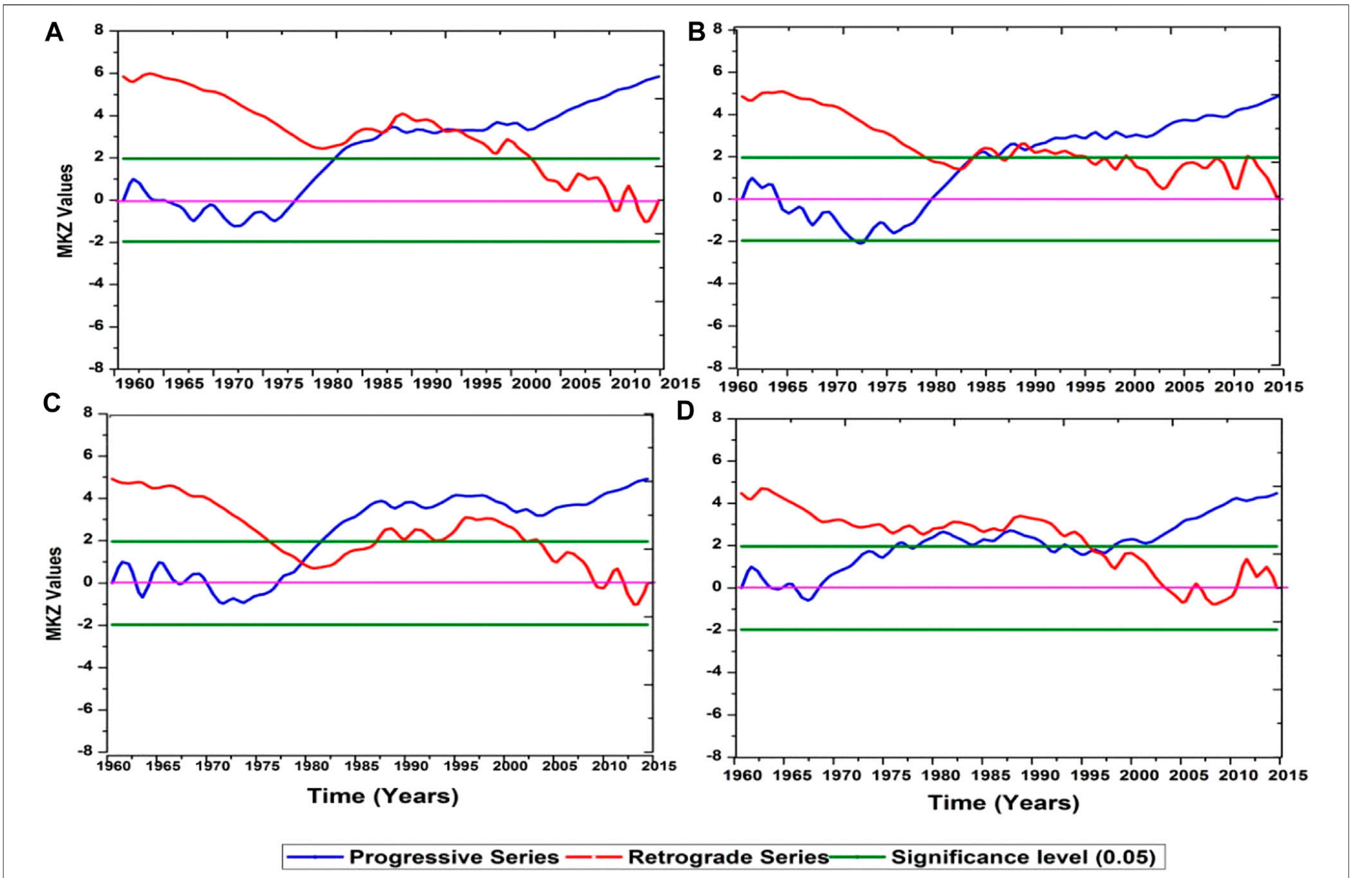

FIGURE 7a | Abrupt change of annual and seasonal Tmax over Rwanda during the period of 1961–2014; **(A)** Annual, **(B)** March–May season, **(C)** June–August, **(D)** October–December.

whether the topography features has a significant influence on the distribution of temperatures; two variables, topography and temperatures were analyzed to understand their relationship. The results reveal a very significant positive correlation between temperature distribution and elevation with a coefficient of determination value of 0.79 (**Figure 6B**).

Every single selected station in three regions is displayed and each of the represnted histogram columns in **Figure 6** refers to an individual station. The stations are arranged in the same order and each station has three variables (elevation, rainfall and temperature). The lowest minimum and maximum temperature were noted in R3 at Rwankeri station located in the northern part of the country with 8.9 and 23.7°C while the highest minimum and maximum temperature were localized in R1 at Nyamata station situated in eastern region with 13.2 and 28.3°C, respectively. This indicates that topography in Rwanda decreases eastwards with an increase in temperature (**Figures 6A,E**), which also influences the distribution of rainfall which decreases eastwards (**Figures 6A–D**). This information is helpful for agricultural activities plans. **Figures 6C,D** indicate the exisiting relationship between temperature and elevation where it is widely known that the higher elevation the lower the temperature. However, the temperatures' temporal distribution show an unusual abnormal temperature in the early 1990s (**Figure 6F**). This led us to test an existence of abrupt change in the Rwanda temperatures. According to the mutation (SQMK) test, most of the abrupt changes in seasonal and annual Tmin and Tmax time series have occurred during 1984 and 1990. Furthermore, the results show that the country has experienced a significant abrupt changes in Tmax in the period between 1980–1985 for MAM and JJA season while the change in OND season was recorded in early 1990s. This period is remarkably followed by frequent above normal in temperatures revealed by the temporal temperatures variability in **Figure 7A**. On the other hand, the significant abrupt change in annual and seasonal Tmin was noted in the early 1990s followed by an increase in minimum temperature **Figure 7B**.

To further understand the changes and trends, a temporal series was displayed. The time series shows the minimum and maximum temperature records from 1961 to 2014 (**Figure 8**). The mean maximum temperature (Tmax mean) was noted to be 24.41°C for the whole period. The warmest year of the entire series was 2010 with a maximum temperature of 1.16°C above 1961–2014 mean. This year was followed by 2005 (0.95°C above 1961–2014 mean), 2013 (0.91°C above 1961–2014 mean) and 1998 (0.77°C above 1961–2014 mean). The coldest year of the whole period was 1961 (1.5°C below 1961–2014 mean). From the year 1980–2014 the temperature was above the mean of

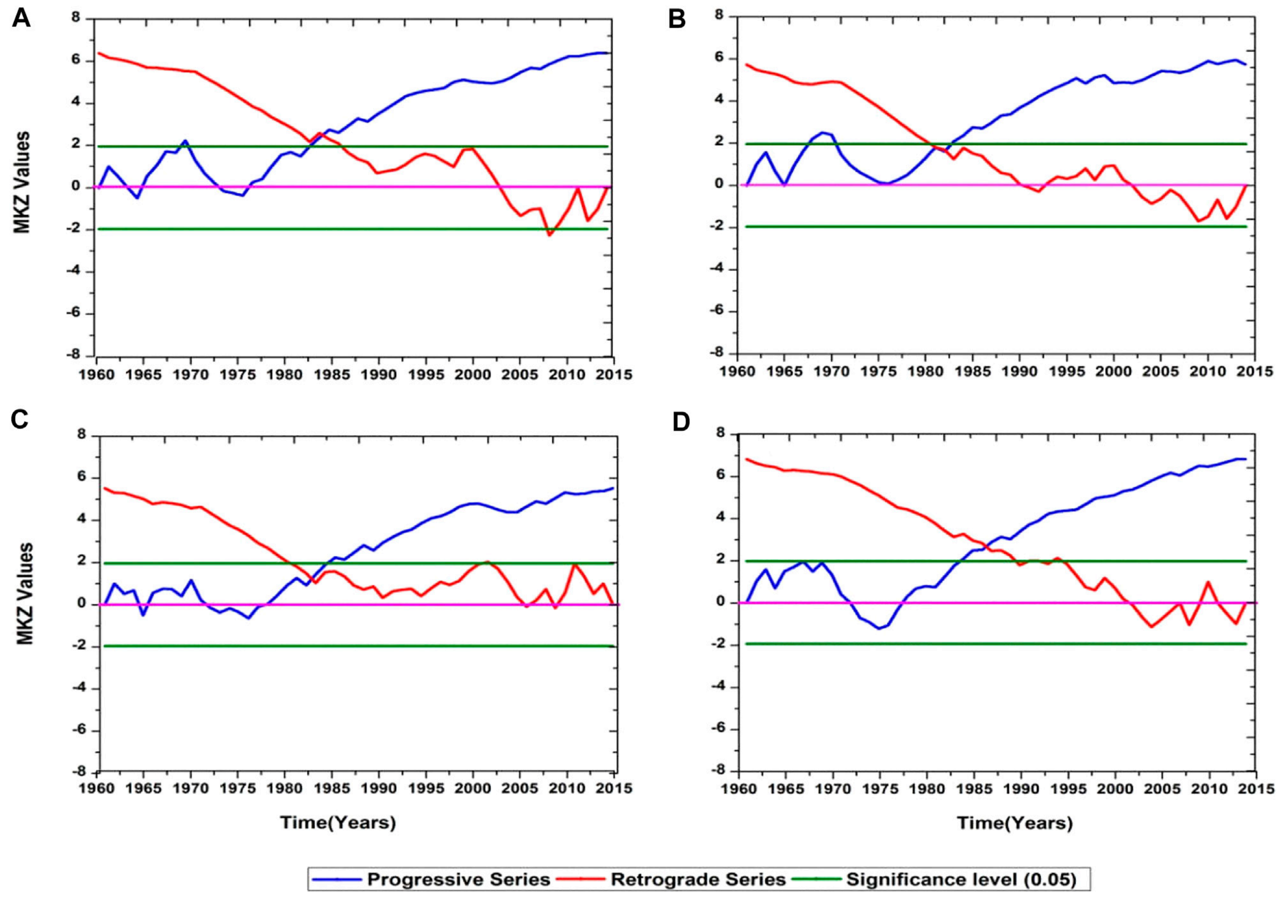

FIGURE 7b | Same analysis for Tmin.

1961–2014 except 1989, 1991, 1992 and 2001. Our future investigation will focus on revaling the causes of the observed above normal temperature after the 1980s and the causes of rapid minimum temperature in R3. This result is in agreement with Morice et al., 2012 who concluded that the decade 2001–2010 was warmer than that of 1991–2000. On the other hand, the data analysis indicate that the temperature of 1961–1979, was below the average of 1961–2014 except for the year 1962, 1978 and 1979 (**Figures 8A–D**).

DISCUSSIONS

Generally, Tmax and Tmin have increase over Rwanda at different rates in three considered regions. The variations are also different on seasonal and annual scale. The area averaged trend analysis for Tmax and Tmin is presented in **Table 2**. The *Z* scores in Tmin, Tmax and DTR are dominantly positive, an indication of an upward trend. Only the DTR in R2 during OND season and DTR of R3 recorded downward trend. For Tmin and Tmax, the scores exceed the significant value at $\alpha = 5\%$, the evidence against the null hypothesis (*Ho*). Contrarily, hypothesis (*Ha*) was accepted proving the existence of trend in series. Sen's slope estimator is displayed to explain the magnitude of change in Tmax, Tmin and DTR. The Sen's values for Tmax and Tmin are positive in all seasons and at annual series. On the other hand, absence of slope and insignificant trend are noted in DTR in R3 (**Table 2**). This shows that Tmax and Tmin in R3 are almost similar in magnitude. Decadal Tmin and Tmax for MAM, JJA, OND and annual are also displayed in **Figures 4A**,**B**, respectively. In agreement with the observed standardized anomaly (**Figures 3A**,**B**), the highest warming was observed in last decade covering almost the whole study area. The early 1960s period is dominated by lower temperatures in all three regions. The highest warming is recorded in the eastern and southern parts of the country. In comparison to seasonal anomalies over the study period, more warming is observed in JJA as compared to OND in all regions. The noted significant positive trend of both Tmax and Tmin is in agreement with a study by Safari (2012) who reported the trend analysis of Rwanda's mean annual temperature during the period 1958–2010 using five observatories. Safari 2012 recorded a significant warming trend for the period after 1977–1979 with a slope of 0.0455°C/year in Kigali city. The results from **Figure 6** shows how important it is to consider the topography effect for a better analysis of temperature distribution. The observed absence of slope and insignificant trend in DTR in R3 indicate that Tmax

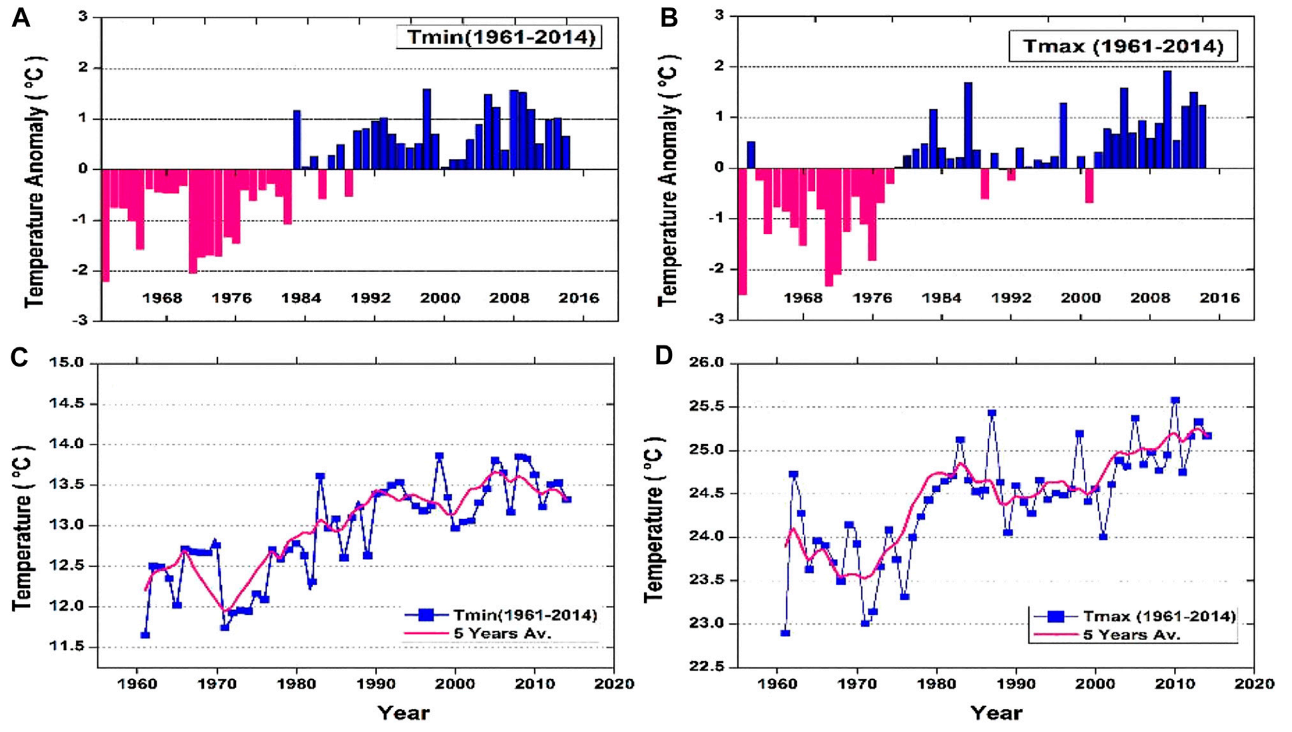

FIGURE 8 | Standardized anomalies of **(A)** minimum temperature, **(B)** maximum temperature and **(C)** minimum temperature trend, **(D)** maximum temperature trend over Rwanda for the period of 1961–2014. The pink line represents the 5-years running.

and Tmin in R3 are almost similar in magnitude. This affirms that initially cool (high elevation) zones in R3 are getting warm faster than the warm (low elevation) areas. A summary of temperature tendency is presented in **Table 2**. The spatial distributions of Tmax and Tmin represent a siginificant warming trend over the whole country notably since the early 1980s. Generally, this study classified all stations in three regions based on elevation distribution. This subdivision method is very helpful in having a deeper analysis of those weather variables in a certain specific region.

Based on observed temperature, the Inter-governmental Panel on Climate Change reported that equatorial and southern parts of eastern Africa (where Rwanda lies) had experienced a significant increase in temperature since the early 1980s (IPCC, 2014). Over Rwanda, the average temperature increase for the period 1961–2014 is 0.45°C per decade for the whole country. In their study on projections of precipitation, air temperature and potential evapotranspiration in Rwanda under changing climate conditions, Mohamed et al. (2016) also suggested an average of 0.35°C per decade from 1964 to 2014 over Rwanda. Although, Rwanda's government has made remarkable effort to increase agriculture production through many programs such as crop intensification program introduced in 2007, scaling up the consolidated land among many others. The observed increase of temperature will definitely harm agricultural production and food security over Rwanda with small-scale farmers being the most affected. This call for more measures and new adaption strategies to ensure future capacity to cope with the challenges caused by the temperature increases. In the same logic, many scholars have concluded that temperature plays a big role on spatial and temporal distribution of disease vectors (Sun et al., 2017). The policymakers have to be well aware to take the necessary measures in their national planning program for sustainable development.

In general, the present study aims mainly to have a better understanding of maximum, minimum and diurnal temperature variability and their trends over Rwanda for the period 1961 to 2014 based on new ENACTS data. The new reconstructed data could not cover the whole study period hence stations data are added for the period 1961–1983. Previous studies have focused on temperature trend variability but the importance of topography as a regulator of Rwanda climate has not been well recognized. In addition, those previous studies focus mainly on annual and intra-annual series and used few observatories, which may fail to capture the true image of trend behavior from each season. The present work mainly focus on the spatial and temporal variability of Tmax and Tmin in Rwanda and their relationship with elevation change, leaving a gap in other potential casue factors, e.g., urbanization, air pollution, sunshine duration and so on (Vose et al., 2005; Henninger, 2009; Yang et al., 2013; Yang et al., 2020a; 2020b), which should be explored in the futue.

CONCLUSION

In the present study, the long-term temporal analysis indicates that both Tmax and Tmin ere significantly increased on seasonal and annual scale. However, the minimum temperature increased at a faster rate than maximum temperature in the highest altitude region (R3) (0.27 vs. 0.07°C/decade in March-to-May) and (0.29 vs. 0.04°C/decade in October-to-December). Similarly, the spatial distribution of Tmin and Tmax shows that the warming trend in seeason and annual temperatures was noticeable over the three regions. Region one (R1) which lies mostly in east part show high rate in above normal temperature condition at the level of 47.85% while region two (R2) and three (R3) almost recorded the same rate of 31.5% above normal temperature during the study period.

The reported minimum temperature increased at a faster rate was observed during the early 1980s, resulting in a significant decrease in the DTR during OND and MAM seasons. According to the mutation (SQMK) test, most of the abrupt changes in seasonal and annual Tmin and Tmax time series have occurred during 1984 and 1990. However, the June-August season of Tmax and Tmin showed an abrupt positive changes in the early 1980s. In Tmin trends, most of rapid changes are detected during the early 1990s while in Tmax, sharpt positive changes are noticable during 1980–1985. Our findings recommend that future studies should focus on elaborating the factors that caused the observed Tmax and Tmin changes in the targeted regions. The knowledge of seasonal patterns of temperature is very important in understanding changes in land uses, crop yields, water resources and ecosystems. From the current study, it is crucial to consider local factors such as topography to better understand possible climate change for any specific area.

DATA AVAILABILITY STATEMENT

The original contributions presented in the study are included in the article/Supplementary Material, further inquiries can be directed to the corresponding authors.

AUTHOR CONTRIBUTIONS

Conceptualization, YF and YY; Methodology, JN; Software, JN; Data curation, JN; Validation, JN and YY; Formal analysis, JN and YY; Writing—original draft preparation, JN; Draft editing, JN, YF, BO, VF, CS, IN, FO, YY.

ACKNOWLEDGMENTS

The authors would like to express their appreciation to the University of Science and Technology of China (USTC) for creating a research enabling environment. Special appreciation goes to Rwanda Meteorology Agency (RMA). This study was supported by NSFC Project (Grant Nos. 91837310, 41675041, and 41620104009), the National Key R&D Program of China (Grant Nos. 2018YFC1507200 and 2017YFC1501402), The Second Tibetan Plateau Scientific Expedition and Research (STEP) program (Grant Nos. 2019QZKK0104), the Key research and development projects in Anhui province (Grant Nos. 201904a07020099), CLIMATE-TPE (ID 32070) in the framework of the ESA-MOST Dragon 4 program, and open funding of the State Key Laboratory of Loess and Quaternary Geology (SKLLQG2010).

REFERENCES

Alexander, L. V., Zhang, X., Peterson, T. C., Caesar, J., Gleason, B., Klein Tank, A. M. G., et al. (2006). Global observed changes in daily climate extremes of temperature and precipitation. *J. Geophys. Res.* 111 (5), 1–22. doi:10.1029/2005JD006290

Asfaw, A., Simane, B., Hassen, A., and Bantider, A. (2018). Variability and time series trend analysis of rainfall and temperature in northcentral Ethiopia: a case study in Woleka sub-basin. *Weather Clim. Extremes* 19, 29–41. doi:10.1016/j.wace.2017.12.002

Barreca, A., Clay, K., Deschenes, O., Greenstone, M., and Shapiro, J. S. (2016). Adapting to climate change: the remarkable decline in the US temperature-mortality relationship over the Twentieth Century. *J. Polit. Econ.* 124 (1), 105–159. doi:10.1086/684582

Berardy, A., and Chester, M. V. (2017). Climate change vulnerability in the food, energy, and water nexus: concerns for agricultural production in Arizona and its urban export supply. *Environ. Res. Lett.* 12, 113.

Brown, S. J., Caesar, J., and Ferro, C. A. T. (2008). Global changes in extreme daily temperature since 1950. *J. Geophys. Res. Atmos.* 113, D05115. doi:10.1029/2006JD008091

Christy, J. R., Norris, W. B., and McNider, R. T. (2009). Surface temperature variations in East Africa and possible causes. *J. Clim.* 22 (12), 3342–3356. doi:10.1175/2008jcli2726.1

Diaz, J., Garcia, R., and Lopez, C. (2005). Mortality impact of extreme winter temperatures. *Int. J. Biometeor.* 49, 179183.

Donat, M. G., Alexander, L. V., Yang, H., Durre, I., Vose, R., Dunn, R. J. H., et al. (2013). Updated analyses of temperature and precipitation extreme indices since the beginning of the twentieth century: the HadEX2 dataset. *J. Geophys. Res.* 118 (5), 2098–2118.

Easterling, D. R., Meehl, G. A., Parmesan, C., Changnon, S. A., Karl, T. R., and Mearns, L. O. (2000). Climate extremes: observations, modeling, and impacts. *Science* 289 (5487), 2068–2074. doi:10.1126/science.289.5487.2068

Easterling, D. R., Horton, B., Jones, P. D., Peterson, T. C., Karl, T. R., Parker, D.,E., et al. (1997). Maximum and minimum temperature trends for the globe. *Science* 277, 364–367. doi:10.1126/science.277.5324.364

Eriksen, S., and Rosentrater, L. (2008). *Climate change in eastern and southern Africa impacts, vulnerability and adaptation climate change in eastern and southern Africa impacts , vulnerability and adaptation*. New York: Global Environmental Change and Human Security.

Heal, G., and Park, J. (2016). Reflections-temperature stress and the direct impact of climate change: a review of an emerging literature. *Rev. Environ. Econ. Pol.* 10 (2), 347–362. doi:10.1093/reep/rew007

Henninger, S. (2009). “Urban climate and air pollution in Kigali , Rwanda,” in The seventh international conference on urban climate, July, 3–6.

IPCC. (2014). *Chapter 22: Africa. ClimateChange 2014: impacts, adaptation and Vulnerability,Contribution of working group II to the FifthAssessment report of the intergovernmental panelon climate change*. Cambridge and New York: Cambridge University Press.

IPCC. (2001a). *Climate change 2001: impacts, adaptation and vulnerability, contribution of working group II to the third assessment report of the intergovernmental Panel on climate change*. Cambridge, United Kingdom and New York, NY, USA: Cambridge University Press.

IPCC. (2001b). *Climate change 2001: the scientific basis. Contribution of working group I to the third assessment report of the intergovernmental Panel on climate* *change*. Cambridge, United Kingdom and New York, NY, USA: Cambridge University Press.

IPCC. (2007). *Climate change 2007: the physical basis. Contributions of working group 1 to the fourth assessment report of the intergovernmental Panel on climate change*. Cambridge, United Kingdom and New York, NY, USA: Cambridge University Press.

IPCC. (2013). *Climate change 2013: the physical science basis. Contribution of working group I to the fifth assessment report of the intergovernmental Panel on climate change*. Cambridge, United Kingdom and New York, NY, USA: Cambridge University Press.

Iqbal, M. A., Penas, A., Cano-Ortiz, A., Kersebaum, K. C., Herrero, L., and del Río, S. (2016). Analysis of recent changes in maximum and minimum temperatures in Pakistan. *Atmos. Res.* 168, 234249.

Kendall, M. G. (1975). *Rank correlation methods*. 4th edn. London: Griffin, 202.

Lobell, D. B., Bonfils, C., Duffy, P. B., and Philip, B. (2007). Climate change uncertainty for daily minimum and maximum temperatures: a model intercomparison. *Geophys. Res. Lett.* 34 (5), 1407. doi:10.1029/2006GL028726

Mann, H. B. (1945). Nonparametric tests against trend. *Econometrica* 13, 245–259. doi:10.2307/1907187

Minitere. (2006). *National adaptation programmes of action (NAPA) to climate change*. Kigali, Rwanda: Ministry of lands, environment, forestry, water and mines (MINITERE).

IPPC (2007). "Assessment of observed changes and responses in natural and managed systems," in *Climate change 2007: impacts, adaptation and vulnerability. Contribution of working group II to the fourth assessment report of the intergovernmental Panel on climate change*, Editors Parry, M. L., Canziani, O. F., Palutikof, J. P., van der Linden, P. J., and Hanson, C. E. (Cambridge, UK: Cambridge University Press), 79–131.

Mohammed, H., Jean, C. K., and Ahmad, W. A. (2016). Projections of precipitation, air temperature and potential evapotranspiration in Rwanda under changing climate conditions. *Afr. J. Environ. Sci. Technol.* 10 (1), 18–33. doi:10.5897/ajest2015.1997

Morak, S., Hegerl, G. C., Christidis, N., and Nikolaos (2013). Detectable changes in the frequency of temperature extremes. *J. Cl.* 26 (5), 1561–1574. doi:10.1175/jcli-d-11-00678.1

Myoung, B., Choi, Y.-S., Hong, S., and Park, S. K. (2013). Inter- and intra-annual variability of vegetation in the northern hemisphere and its association with precursory meteorological factors. *Glob. Biogeochem. Cycles* 27, 31–42. doi:10.1002/gbc.20017

Ndenga, B., Githeko, A., Omukunda, E., Munyekenye, G., Atieli, H., Wamai, P., et al. (2006). Population dynamics of malaria vectors in western Kenya highlands. *J. Med. Entomol.* 43 (2), 200. doi:10.1603/0022-2585(2006)043[0200:PDOMVI]2.0.CO2

Nicholson, S. E., Nash, D. J., Chase, B. M., Grab, S. W., Shanahan, T. M., Verschuren, D., et al. (2013). Temperature variability over Africa during the last 2000 years. *The Holocene* 23 (8), 1085–1094. doi:10.1177/0959683613483618

Nsubuga, F. W., Olwoch, J. M., and Rautenbach, H. (2014). Variability properties of daily and monthly observed near-surface temperatures in Uganda: 1960-2008. *Int. J. Climatol.* 34, 303–314. doi:10.1002/joc.3686

Ongoma, V., and Chen, H. (2017). Temporal and spatial variability of temperature and precipitation over East Africa from 1951 to 2010. *Meteorol. Atmos. Phys.* 129, 131–144. doi:10.1007/s00703-016-0462-0

Otto, F. E. L., and Friederike, E. L. (2016). The art of attribution. *Nat. Clim Change* 6 (4), 342–343. doi:10.1038/nclimate2971

Parmesan, C., Yohe, G., and Gary (2003). A globally coherent fingerprint of climate change impacts across natural systems. *Nature* 421 (6918), 37–42. doi:10.1038/nature01286

Penuelas, J., and Flella, I. (2001). A globally coherent fingerprint of climate change impacts across natural systems. *Science* 294, 793795.

Praveen, B., Talukdar, S., Shahfahad, M. S., Mahato, S., Mondal, J., Sharma, P., et al. (2020). Analyzing trend and forecasting of rainfall changes in India using non-parametrical and machine learning approaches. *Sci. Rep.* 10 (1), 10342. doi:10.1038/s41598-020-67228-7

Punam, C-P., and Manka, A. (2011). *Yes Africa can : success stories from a dynamic continent. The World Bank number 2335*. (Singapore: World Bank Publications).

Qasim, M., Khlaid, S., and Shams, D. F. (2016). Spatiotemporal variations and trends in minimum and maximum temperatures of Pakistan. *J. Appl. Environ. Biol. Sci.* 4, 8593.

Ren, Z., Wang, D., Ma, A., Hwang, J., Bennett, A., Sturrock, H. J., et al. (2016). Predicting malaria vector distribution under climate change scenarios in China: challenges for malaria elimination. *Sci. Rep.* 6, 20604. doi:10.1038/srep20604

Revadekar, J. V, Hameed, S., Collins, D., Manton, M., Sheikh, M., Borgaonkar, H. P., et al. (2013). Impact of altitude and latitude on changes in temperature extremes over South Asia during 1971–2000. *Int. J. Climatol.* 33, 199209.

Rwanyiziri, G., and Rugema, J. (2013). Climate change effects on food security in Rwanda: case study of wetland rice production in Bugesera district. *Rwanda J.* 1 (1), 35–51. doi:10.4314/rj.v1i1.3E

Safari, B. (2012). Trend analysis of the mean annual temperature in Rwanda during the last fifty two years. *Jep* 03 (6), 538–551. doi:10.4236/jep.2012.36065

Safeeq, M., Mair, A., and Fares, A. (2013). Temporal and spatial trends in air temperature on the Island of Oahu, Hawaii. *Int. J. Climatol.* 33, 28162835.

Salman, S. A., Shahid, S., Ismail, T., Chung, E. S., and Al-Abadi, A. M. (2017). Long-term trends in daily temperature extremes in Iraq. *Atmos. Res.* 198, 97107.

Sayemuzzaman, M., Mekonnen, A., and Jha, M. K. (2015). Diurnal temperature range trend over North Carolina and the associated mechanisms. *Atmos. Res.* 160, 99108.

Sen, P. K. (1968). Estimates of the regression coefficient based on kendall's tau. *J. Am. Stat. Assoc.* 63 (324), 1379–1389. doi:10.1080/01621459.1968.10480934

Siebert, A., Dinku, T., Vuguziga, F., Twahirwa, A., Kagabo, D. M., Delcorral, J., et al. (2019). Evaluation of ENACTS-Rwanda: a new multi-decade, high-resolution rainfall and temperature data set-Climatology. *Int. J. Climatol* 39 (6), 3104–3120. doi:10.1002/joc.6010

Smith, R. C., Ainley, D., Baker, K., Domack, E., Emslie, S., Fraser, B., et al. (1999). Marine ecosystem sensitivity to climate change. *Biol. Sci.* 49, 393–404. doi:10.2307/1313632

Sneyers, R. (1990). *On the statistical analysis of series of observations. In WMO technical note, 192*. Geneva: World Meteorology Organization.

Stern, D. I., Gething, P. W., Kabaria, C. W., Temperley, W. H., Noor, A. M., Okiro, E. A., et al. (2011). Temperature and malaria trends in highland East Africa. *PLoS ONE* 6 (9), e24524. doi:10.1371/journal.pone.0024524

Sun, X.-B., Ren, G.-Y., Shrestha, A. B., Ren, Y.-Y., You, Q.-L., Zhan, Y.-J., et al. (2017). Changes in extreme temperature events over the hindu kush himalaya during 1961-2015. *Adv. Clim. Change Res.* 8 (3), 157–165. doi:10.1016/j.accre.2017.07.001

Theodorsson-Norheim, E. (1986). Kruskal-Wallis test: BASIC computer program to perform nonparametric one-way analysis of variance and multiple comparisons on ranks of several independent samples. *Comput. Methods Programs Biomed.* 23, 57.

Tingley, M. P., and Huybers, P. (2013). Recent temperature extremes at high northern latitudes unprecedented in the past 600 years. *Nature* 496 (7444), 201–205. doi:10.1038/nature11969

UN Economic Commission for Africa & United Nations Development Programme Regional Bureau for Africa & African Union & African Development Bank (2016). "*MDGs to Agenda 2063/SDGs Transition Report 2016: 2016 towards an integrated and coherent approach to sustainable development in Africa*,". UNDP Africa Reports 267640, United Nations Development Programme (UNDP). Addis Ababa: Publications Section Economic Commission for Africa.

Vose, R. S., Easterling, D. R., Gleason, B., and Byron (2005). Maximum and minimum temperature trends for the globe: an update through 2004. *Geophys. Res. Lett.* 32 (23), 2430. doi:10.1029/2005GL024379

Walther, G. R., Post, E., Convey, P., Menzel, A., Parmesan, C., Beebee, T. J., et al. (2002). Ecological responses to recent climate change. *Nature* 416 (6879), 389–395. doi:10.1038/416389a

Weldegerima, T. M., Zeleke, T. T., Birhanu, B. S., Zaitchik, B. F., and Fetene, Z. A. (2018). Analysis of rainfall trends and its relationship with SST signals in the lake tana basin, Ethiopia. *Adv. Meteorol.* 14, 111. doi:10.1155/2018/5869010

Yang, Y., Wu, B., and Shi, C. (2013). Impacts of urbanization and station-relocation on surface air temperature series in Anhui province, China. *Pure Appl. Geophys.* 170 (11), 1969–1984. doi:10.1007/s00024-012-0619-9

Yang, Y., Zhang, Manyu., Li, Qingxiang., Chen, Bing., Gao, Zhiqiu., Ning, Guicai., et al. (2020a). Modulations of surface thermal environment and agricultural activity on intraseasonal variations of summer diurnal temperature range in the Yangtze River Delta of China. *Sci. Total Environ.* 13, 39. doi:10.1016/j.scitotenv.2020.139445

Yang, Y., Zheng, Z., Yim, S. H. L., Roth, M., Ren, G., Gao, Z., et al. (2020b). PM2.5 pollution modulates wintertime urban-heat-island intensity in the beijing-tianjin-hebei megalopolis, China. *Geophys. Res. Lett.* 47 (1). doi:10.1029/2019gl084288

Conflict of Interest: The authors declare that the research was conducted in the absence of any commercial or financial relationships that could be construed as a potential conflict of interest.

frontiers in Earth Science

ORIGINAL RESEARCH
published: 15 April 2021
doi: 10.3389/feart.2021.630192

A New Extreme Detection Method for Remote Compound Extremes in Southeast China

Luqing Wang [1], Qinglin Zhao [1], Si Gao [2,3], Wei Zhang [4,5] and Li Feng [1]*

[1] Faculty of Information Technology, Macau University of Science and Technology, Macau, China, [2] School of Atmospheric Sciences, and Key Laboratory of Tropical Atmosphere-Ocean System, Ministry of Education, Sun Yat-sen University, Zhuhai, China, [3] Southern Marine Science and Engineering Guangdong Laboratory (Zhuhai), Zhuhai, China, [4] IIHR–Hydroscience & Engineering, The University of Iowa, Iowa City, IA, United States, [5] Department of Plants, Soils and Climate, Utah State University, Logan, UT, United States

The compound heat wave and extreme precipitation events are responsible for severe damages to the environment and human societies. Although major advances have been made in understanding the compound extremes (e.g., drought and heat wave), little is known about two types of extremes synchronized/connected in different regions in China. Here we identify a new type of compound extreme termed as "remote compound extreme" with the aid of a new extreme value detection method that combines isolated forest and quantile statistics. The new compound extremes are reflected by a statistically significant correlation (i.e., 0.52) between heat wave in the Pearl River Delta and extreme precipitation in the Yangtze River Delta. The remote compound extreme may be tied to the western Pacific subtropical high that modulates typhoons, surface temperature in the Pearl River Delta and extreme precipitation in the middle and lower reaches of the Yangtze River.

Keywords: compound extremes, heat wave, extreme precipitation, extreme detection, isolation forest

Edited by:
Jing-Jia Luo,
Bureau of Meteorology, Australia

Reviewed by:
Xiaojing Jia,
Zhejiang University, China
Eduardo Zorita,
Helmholtz Center for Materials and Coastal Research (HZG), Germany

****Correspondence:***
Qinglin Zhao
zqlict@hotmail.com

Specialty section:
This article was submitted to Atmospheric Science, a section of the journal Frontiers in Earth Science

Received: *16 November 2020*
Accepted: *23 March 2021*
Published: *15 April 2021*

Citation:
Wang L, Zhao Q, Gao S, Zhang W and Feng L (2021) A New Extreme Detection Method for Remote Compound Extremes in Southeast China. Front. Earth Sci. 9:630192. doi: 10.3389/feart.2021.630192

1. INTRODUCTION

Extreme weather and climate events have devastating effects, which have been projected to intensify under climate change (Murray and Ebi, 2012; National Academies of Sciences and Medicine, 2016; Stott, 2016). Extreme events like heat waves may claim thousands of lives every year and destroy ecological systems (Gasparrini and Armstrong, 2011; Peng et al., 2011; Ma et al., 2015). This is also true for extreme precipitation related to tropical cyclones, atmospheric rivers, monsoonal systems associated with flash floods across the globe (Christensen and Christensen, 2003; Teegavarapu, 2012; Yin et al., 2018; Zhang et al., 2018).

Mounting evidence has shown that extreme weather events are connected, rather than independent or isolated (Leonard et al., 2014; Zscheischler and Seneviratne, 2017; AghaKouchak et al., 2020; Raymond et al., 2020; Zscheischler et al., 2020). Over the past years, a new type of extreme events, so-called compound extreme, has been identified (Leonard et al., 2014; Zscheischler and Seneviratne, 2017; AghaKouchak et al., 2020; Raymond et al., 2020; Zscheischler et al., 2020), leading to cascading effects on human and the environment (AghaKouchak et al., 2018). Therefore, a better understanding of this new type of extreme climate events can pave the road for projecting future climate risk assessment.

Recent studies have documented compound extreme including concurrent drought and heat wave (Fischer et al., 2007), tropical cyclone and heat waves in the future climate (Matthews et al., 2019), concurrent wind and precipitation extremes (Martius et al., 2016), concurrent heat and air pollution (Zhong et al., 2017), heat stress followed by floods in the central United States (Zhang and Villarini, 2020), and precipitation and storm surge (Wahl et al., 2015; Lentz et al., 2016). Because these extremes have been identified in the same spatial region/domain, it is still unclear regarding whether compound extremes could be connected and located in different regions.

The Pearl River Delta in South China has been frequently attacked by heat waves (Sun et al., 2017; You et al., 2017; Liu et al., 2018; Deng et al., 2020). Moreover, the Yangtze River Delta is affected by the Meiyu belt that may lead to fluvial flooding (Ge et al., 2008; Han et al., 2015; Wang and Gu, 2016; Yin et al., 2016), with the 2020 summer flooding that has wreaked havoc in China (Guo et al., 2020; Wei et al., 2020). We are yet to understand whether the heat wave (extreme heat) in the former region relates to the extreme precipitation in the later region. We will examine whether, the extent to which and how the heat wave events in the Pearl River Delta are connected to extreme precipitation in the middle and lower reaches of the Yangtze River.

Moreover, the definition of extreme events (e.g., what precipitation is extreme) may lead to large uncertainties in analysis results (Rivas et al., 2008; Stephenson et al., 2008; Pendergrass, 2018). Here we propose a new extreme value detection method that combines machine learning (i.e., isolated forest) and statistical methods. The extreme detection method is an advanced machine learning algorithm, that identifies the outlier set, followed by using the quantile function to determine the critical point of the extreme value from the outlier set (Liu et al., 2008, 2012). Therefore, the main objective of this study is to identify and investigate a new type of compound extreme (termed as "remote compound extreme") in China using machine learning technologies (i.e., isolated forest).

In what follows, the study area and data source, methods are introduced in section 2. In section 3, we give the analysis results and their interpretations. The paper is then concluded by a summary and discussion in section 4.

2. DATA AND METHODOLOGY

2.1. Study Area and Data Source

The present study focuses on extreme weather events that are connected across two regions (i.e., the Pearl River Delta and the Yangtze River Delta). The study area of this research thus covers the middle and lower reaches of the Yangtze River and the Pearl River Delta. We select daily temperature data in the Pearl River Delta region and daily precipitation data in the middle and lower reaches of the Yangtze River region, during June and July from 1979 to 2020.

We obtain daily precipitation and temperature data from the European Center for Medium-Range Weather Forecasts (ECMWF) ERA-5 reanalysis data with a spatial resolution of 0.25°. The 500-hPa geopotential height, 850 hPa winds and 500 hPa vertical velocity (omega) are also used to diagnose large-scale circulation that is conducive to extreme precipitation and temperature events across the study regions. Typhoon information is obtained from the Shanghai Typhoon Institute best track data.

2.2. A New Extreme Detection Method

This paper combines the isolated forest method and the quantile statistical method to propose a new extreme detection method.

2.2.1. Isolation Forest

In this paper, we use the isolated forest algorithm (Liu et al., 2008, 2012) to find and detect outliers. The term isolation means "separating an instance from the rest of the instances." Note that the isolated forest algorithm is different from "decision tree" and "random forest," which are also commonly used machine learning methods. Since anomalies are "few and different" and therefore they are more susceptible to isolation. The method exploits two particularities of anomalies: they represent fewer instances in the observed set, and, compared to healthy instances, they have discrepant attribute-values.

Anomaly detection using iForest is a two-stage process. The first (training) stage builds isolation trees using subsamples of the training set. The second (testing) stage passes the test instances through isolation trees to obtain an anomaly score for each instance (Liu et al., 2008, 2012).

In the training stage, *i*Trees are constructed by recursively partitioning a subsample X' until all instances are isolated. Details of the training stage can be found in Algorithms 1 and 2. Each *i*Tree is constructed using a sub-sample X' randomly selected without replacement from X, $X' \subset X$.

Algorithm 1: *i*Forest(X, t, ψ)

```
Input:
    $X$ - input data,
    $t$ - number of trees,
    $\psi$ - subsampling size
Output:
    a set of $t$ iTrees
Initialize Forest
for $i = 1$ to $t$ do
    $X' \leftarrow sample(X, \psi)$;
    $Forest \leftarrow Forest \cup iTree(X')$;
end for
return Forest;
```

There are two hyperparameters to the *i*Forest algorithm in Algorithm 1: the subsampling size ψ and the number of trees t. The subsampling size ψ controls the training data size and the number of trees t controls the ensemble size.

The normal points tend to be isolated at the deeper end of the tree, whereas anomalies are closer to the tree root, due to their singularity nature. The shorter the average path length, the higher the chances to be anomalies. Hence, the anomaly score s is then defined by:

$$s(x, n) = 2^{-\frac{E(h(x))}{c(n)}} \tag{1}$$

Algorithm 2: $i\mathrm{Tree}(X')$

```
Input:
    $X'$ - input data
Output:
    an $i$Tree
Initialize Forest
if $X'$ cannot be divided then
    return $exNode\{Size = |X'|\}$
else
    let $Q$ be a list of attributes in $X'$
    randomly select an attributes $q \in Q$
    randomly select a split point $p$ between the $max$ and $min$ values of attribute $q$ in $X'$
    $X_l \leftarrow filter(X', q < p)$
    $X_r \leftarrow filter(X', q \geq p)$
    return $inNode\{Left \leftarrow iTree(X_l), Right \leftarrow iTree(X_r), SplitAtt \leftarrow q, SplitVale \leftarrow p\}$
end if
```

where n is the number of samples in the dataset, $E(h(x))$ is the average of path length $h(x)$from a group of isolation tree, and $c(n)$ is the average of $h(x)$ given n, used for normalizing the path length.

Details of the testing stage can be found in Algorithm 3.

Algorithm 3: $PathLength(x, T, hlim, e)$

```
Input:
    $x$ - an instance, $T$ - an $i$Tree, $hlim$ - height limit, $e$ - current path length;
    to be initialized to zero when first called
Output:
    path length of x
if $T$ is an external node or $e \geq hlim$ then
    return $e + \mathrm{c}(T.size)$
end if
$a \leftarrow T.splitAtt$
if $x_a < T.splitValue$ then
    return $PathLength(x, T.left, hlim, e + 1)$
else
    return $PathLength(x, T.right, hlim, e + 1)$
end if
```

2.2.2. Quantile Statistical Methods

In probability and statistics, the quantile function, associated with a probability distribution of a random variable, specifies the value of the random variable such that the probability of the variable is less than or equal to the given probability. It is also called the percent-point function or inverse cumulative distribution function.

With reference to a continuous and strictly monotonic distribution function, for example the cumulative distribution function of a random variable X, the quantile function Q returns a threshold value x below which random draws from the given c.d.f would fall p percent of the time (Parzen, 2004).

In terms of the distribution function F, the quantile function Q is then defined by:

$$Q(p) = inf\{x \in R : p <= F(x)\}. \tag{2}$$

2.2.3. A New Extreme Detection Method

Definition of extreme values: In this paper, we treat extreme values as a subset of outliers. Therefore, we first use the isolated forest algorithm to identify and label the outliers of temperature or precipitation at each spatial grid, and then for the outliers of each grid point, the 95-quantile method is used to determine the critical point of the extreme value, and the value greater than the critical point is defined as the extreme value.

We use "isolated forest," which is an advanced machine learning algorithm, to detect the outlier set, followed by using the quantile function in statistics to determine the critical point of the extreme value from the outlier set. We finally identify values greater than the critical point as extreme values. We apply this extreme identification methodology to precipitation and temperature data over the Pearl River Delta and the middle and lower reaches of the Yangtze River in China.

In this paper, we propose a new extreme value detection algorithm as shown in Algorithm 4. The return value label of the isolated forest model uses −1 to denote the outlier. After that, the percentile function is used to obtain the critical value of the pth percentile, and finally record the points greater than the critical value in the original vector as extreme values to realize the discovery and identification of extreme values.

Algorithm 4: A new extreme detection method

```
Input:
    $x$ - an vector
Output:
    the extreme label corresponding to the vector value
    0 means non-extreme value, 1 means extreme value
Use the isolated forest algorithm to identify outliers on $x$
Use quantile statistics to obtain the critical point $\theta$ of extreme values in the outlier vector
if $x > \theta$ then
    return $1(extremevalue)$
else
    return $0(non - extremevalue)$
end if
```

Based on the assumption that extreme values are outliers, we propose a new extreme value detection method introduced in this paper. Compared with other algorithms, the isolated forest algorithm (Liu et al., 2012) has better generalization ability and robustness in the detection and recognition of outliers. It can be applied to univariate or multivariate outlier detection and identification problems, and absorbs the advantages of ensemble learning ideas.

This new extreme value detection method, on the one hand, absorbs the advantages of the isolated forest algorithm in the

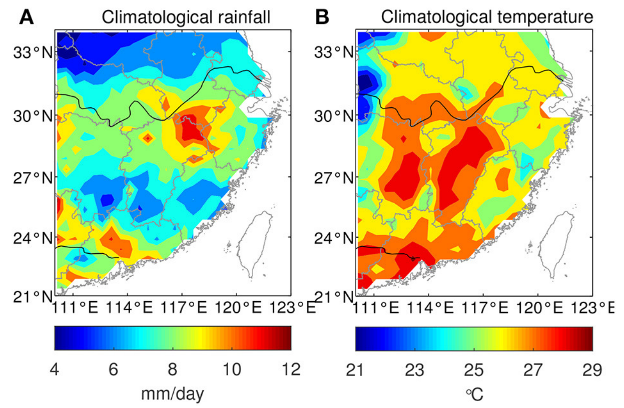

FIGURE 1 | Spatial distribution of climatological mean **(A)** precipitation (mm/day) and **(B)** temperature (°C) during June and July of 1979–2020 in Southeast China.

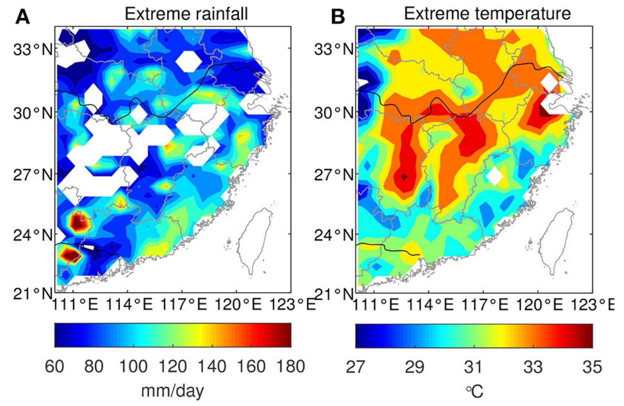

FIGURE 2 | Spatial distribution of composite **(A)** extreme precipitation (mm/day) and **(B)** extreme temperature (°C) for the date of compound precipitation and temperature extremes in Southeast China during June and July of 1979–2020.

detection and identification of outliers, on the other hand, it also incorporates the method of using statistics to determine extreme values in related papers. It belongs to a comprehensive method of extreme value discovery and recognition, and uses advanced machine learning technology and traditional statistical methods. Compared with using a single method, it has a stronger learning ability and recognition.

3. ANALYSIS RESULTS AND INTERPRETATION

We start with analyzing the climatology of temperature and precipitation across the study area: the Pearl River Delta and the middle and lower reaches of the Yangtze River (**Figure 1**). The middle and lower reaches of the Yangtze River exhibit higher climatological precipitation (e.g., 10 mm/day) than the other regions in South China during June and July (**Figure 1**, left panel). Meanwhile, a high climatological surface temperature is observed in the Pearl River Delta, suggesting a high risk of heat wave events (**Figure 1**, right panel). It is noted that the climatological surface temperature in Hunan and Jiangxi provinces is also high during June and July (**Figure 1**, right panel). In order to detect extreme temperature and precipitation, we apply the new extreme value detection method to detect extreme precipitation and extreme temperature in June and July in the Pearl River Delta and the middle and lower reaches of the Yangtze River. The spatial pattern of extreme precipitation and extreme temperature (**Figure 2**) is different from that for climatological precipitation and temperature (**Figure 1**). Because the extreme precipitation date and extreme temperature date occurred simultaneously for 169 days, accounting for 30.8% of the extreme temperature date, based on the extreme precipitation and extreme temperature at each grid point under the coincident date, we found that **Figure 2A** has more blank areas (missing values) than **Figure 2B**. Specifically, the regions with extreme temperature are shifted poleward compared with climatological temperature (**Figures 1**, **2**). The high-low-high tripolar pattern of climatological precipitation (**Figure 1**) cannot be identified for extreme precipitation (**Figure 2**). Extreme precipitation exhibits high values in eastern Guangdong Providence and a large portion of the middle and lower reaches of the Yangtze River.

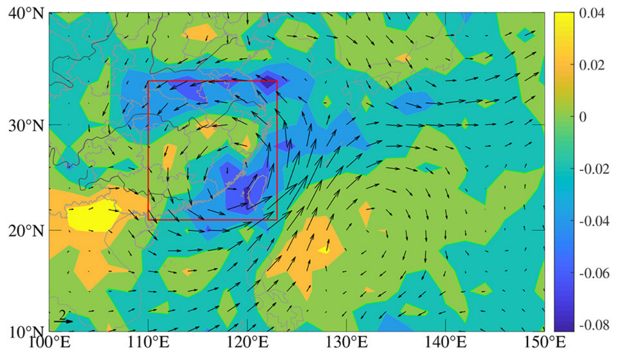

FIGURE 3 | Composite winds at 850 hPa (vector, m/s) and vertical velocity (omega) at 500 hPa (shading, Pa/s) for the date of compound precipitation and temperature extremes in Southeast China during June and July of 1979–2020. Red rectangular denotes the study area.

Figure 3 displays composite winds at 850 and 500 hPa vertical velocity during the days with compound precipitation and temperature extremes in Southeast China. The updraft (negative omega) is consistent with regions in the middle and lower reaches of the Yangtze River with extreme precipitation (**Figure 2**). Meanwhile, the downdraft associated with high temperature is located in the western part of the Pearl River Delta (**Figure 3**). The composite 500-hPa circulation pattern during days of the compound extreme features teleconnections that propagate from the east of the Philippines to South China (**Figure 3**). This 500-hPa circulation pattern, together with the pattern of 500-hPa omega, serves to interpret the compound extreme (**Figures 2**, **3**). The easterly winds along the north flank of the cyclonic system (**Figure 3**) can transport water vapor from the Pacific Ocean to the continent and may also contribute to the precipitation over Yangtze River (Yu et al., 2020). The circulation patterns are similar to the circulations related to tropical cyclones (known as typhoons in the western North Pacific) because previous studies have suggested some potential connections between tropical cyclones and heat waves (Parker et al., 2013; Lin, 2019; Matthews et al., 2019; Zhong et al., 2019). During the days with compound extremes, tropical cyclones are located close to or inside the study region (**Figure 4**), in agree with previous studies showing that tropical cyclones may be associated with heat waves (Parker et al., 2013; Lin, 2019; Matthews et al., 2019; Zhong et al., 2019). During 1979–2019, we identify 157 days of compound extremes, 85 of which are accompanied by typhoons located west of 130°E.

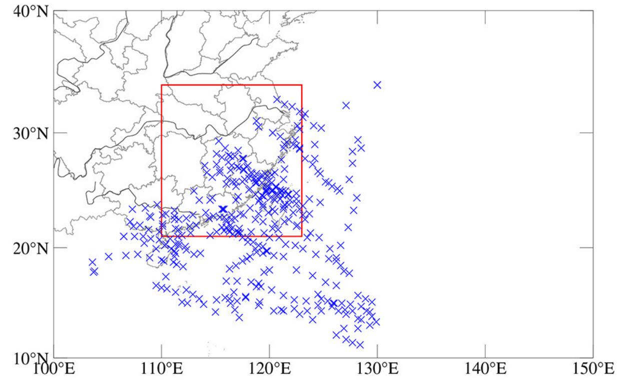

FIGURE 4 | Six-hourly tropical cyclone positions (blue crosses) west of 130°E for the date of compound precipitation and temperature extremes in Southeast China during June and July of 1979–2019. Note that tropical cyclone positions in 2020 are not shown because the tropical cyclone best-track data in 2020 are not yet available. Red rectangular denotes the study area.

Therefore, 54% of compound extremes coincide with typhoon activities, indicating an association between the compound extreme and typhoons. While tropical cyclones are influenced by large-scale circulation in terms of steering flow (tracks), genesis and intensity, these storms can also modulate the climatology of the background large-scale circulation (Arakane and Hsu, 2020). Although typhoons may modulate the circulations conducive to the compound extreme, typhoon tracks are overall controlled by the subtropical high. Therefore, the major driver of the compound extreme is the subtropical high with typhoons playing a certain role.

Based on the new extreme value identification method, we find the date of extreme temperature and the date of extreme precipitation in the middle and lower reaches of the Pearl River and the Yangtze River Delta. We use the date of extreme temperature as the reference point, and analyze the date of extreme precipitation lags 0–60 in sequence. When the date of extreme precipitation lags behind the date obtained after 18 days, 49.18% of the date is included in the date of extreme temperature. This relationship is shown in **Figure 5**.

To examine whether there is an association between extreme temperature in the Pearl River Delta and extreme precipitation in the Yangtze River Delta, we calculate the Pearson correlation coefficient between the median value of extreme temperature in the former region and the median value of extreme precipitation in the later region (**Figure 6**). There is a statistically significant Pearson correlation (0.52) between the median value of extreme temperature and the median value of extreme precipitation during the 26 years when we can detect extreme temperature and precipitation (**Figure 6A**). The Kendall's tau (0.35) between the median value of extreme temperature and the median value of extreme precipitation is also statistically significant at the 0.05 level. The significant association between the two types of extremes suggests the compound nature of this event (remote

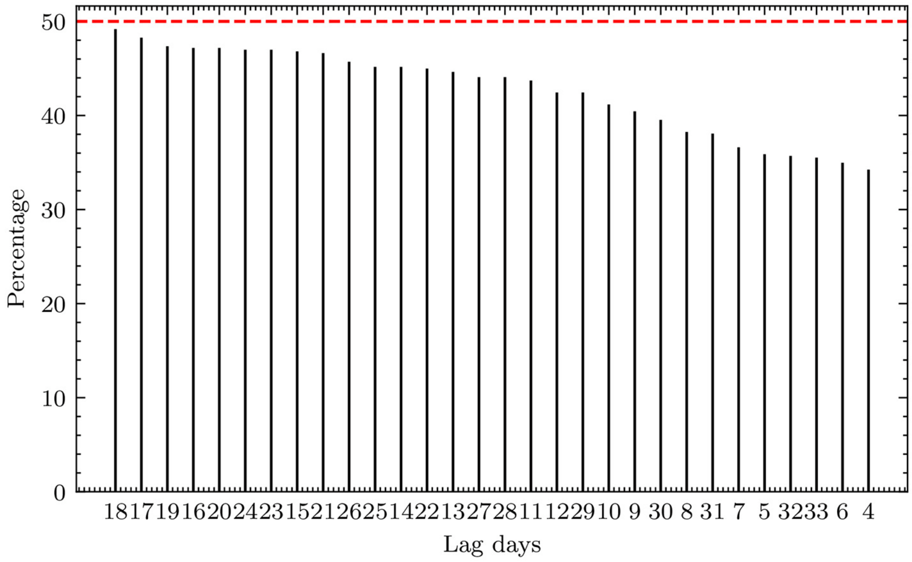

FIGURE 5 | Probability distribution of different days after extreme precipitation date lagging extreme temperature date.

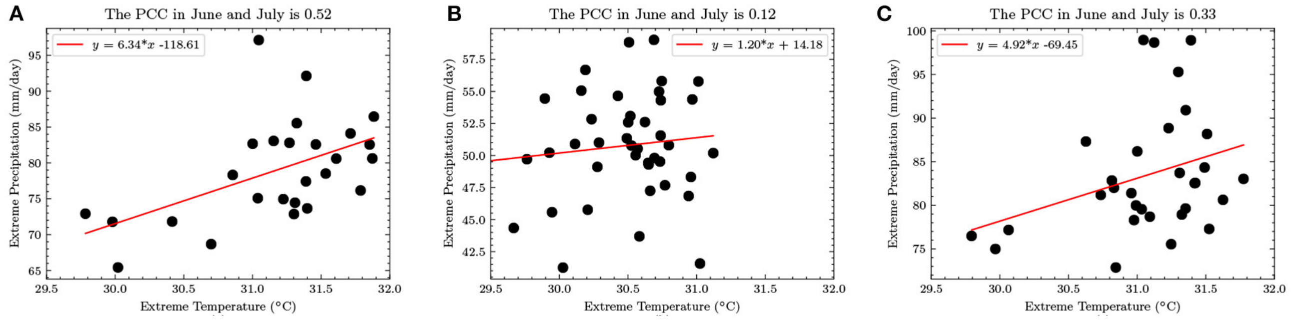

FIGURE 6 | The scatter plot of extreme temperature in the Pearl River Delta and extreme precipitation in the Yangtze River Delta during June and July using **(A)** a new extreme detection method, **(B)** the traditional 95th quantile method, **(C)** the traditional 99th quantile method.

compound extremes). That is, heat wave characterized by extreme temperature in the Pearl River Delta may be concurrent and connected with extreme precipitation events in the Yangtze River Delta (**Figure 6**). At the same time, we compared and analyzed the use of the 95% quantile method to identify extreme values, and found that the correlation between the annual median value of extreme temperature in the Pearl River Delta and extreme precipitation in the Yangtze River Delta is weak (0.12), which does not meet statistical significance (**Figure 6B**). The results by using the 99th percentile lead to a correlation of 0.33, which is not statistically significant (**Figure 6C**).

In addition to potential impacts of typhoons on the compound extremes, the physical mechanisms underlying the remote compound extremes may be tied to the subtropical high that modulates weather and climate in China, responsible for extreme temperature and precipitation. **Figure 7** exhibits the 5,880-gpm contour of 500-hPa geopotential height when extreme temperature and precipitation events occurred. The subtropical high during extreme temperature is quite consistent with that during extreme precipitation (**Figure 7**). When the subtropical high shift westward and sits on the Pearl River Delta, there tends to excite heat waves. Meanwhile, this subtropical high setting is also conducive to extreme precipitation in the Yangtze River Delta because strong moisture transport to this region is prevalent along the western flank of the subtropical high (**Figure 7**). Subtropical high also modulates the steering flow, which determines typhoon tracks (Gao et al., 2020). Therefore, the subtropical high plays a dominant role with typhoons playing secondary roles.

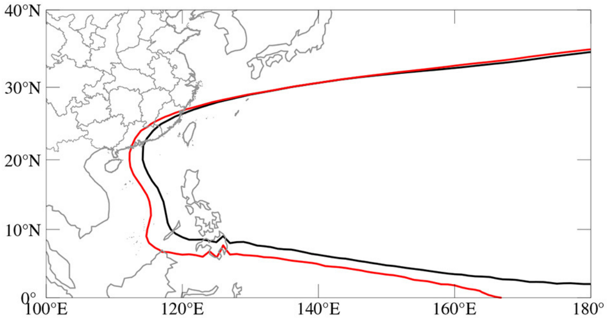

FIGURE 7 | The 5,880-gpm contour (red) of 500-hPa geopotential height for the 26 years with extreme temperature in the Pearl River Delta and extreme precipitation in the Yangtze River Delta during June and July, and the climatological mean 5,880-gpm contour (black) during June and July of 1979–2020.

4. CONCLUSIONS AND DISCUSSION

Although major advances have been made in understanding the compound extremes (e.g., drought and heat wave), little is known about two types of extremes synchronized/connected in different regions. Here we have identified a new type of compound extremes termed as "remote compound extremes" with the aid of a new extreme value detection method that combines isolated forest and quantile statistics. The main findings of this paper are summarized as follows.

1. We apply a new extreme detection method that combines isolated forest and quantile methods to identify the extreme temperature and precipitation, thereby leading to the new compound extremes.
2. We have found a statistically significant correlation (i.e., 0.52) between the heat waves in the Pearl River Delta and extreme precipitation in the Yangtze River Delta, suggesting the existence of the remote compound extremes.
3. The remote compound extreme may be tied to the western Pacific subtropical high that modulate typhoons, surface temperature in the Pearl River Delta and extreme precipitation in the middle and lower reaches of the Yangtze River.

This study for the first time quantifies the occurrence of this type of compound extreme using machine learning technologies and attempts to understand this compound. Efforts are still required to dissect the exact mechanisms underlying this compound extreme. Our future work will focus on three aspects of the new compound extreme. First, we will evaluate this new type of compound extremes across different regions. Second, we will examine the capability of climate models in simulating and reproducing this compound extreme. Last but not least, further study will focus on the predictability of this new type of extremes among the seasonal forecasting systems [e.g., The North American Multi-Model Ensemble (Kirtman et al., 2014)].

DATA AVAILABILITY STATEMENT

Publicly available datasets were analyzed in this study. This data can be found at: https://climexp.knmi.nl/ERA5/era5_t2m_daily.nc, https://climexp.knmi.nl/ERA5/era5_tp_daily.nc.

AUTHOR CONTRIBUTIONS

LW: conceptualization, methodology, formal analysis, figure, and writing—original draft. QZ: writing—review and editing. SG: figure, review, and editing. WZ: conceptualization, writing—review and editing. LF: review and editing. All authors contributed to the article and approved the submitted version.

FUNDING

This study was jointly supported by the National Key R&D Program of China (2019YFC1510400), the National Natural Science Foundation of China (File nos. 61872451 and 61872452), the Science and Technology Development Fund, Macau SAR (File nos. 0098/2018/A3, 0076/2019/A2, and 0037/2020/A1), and the Macao Science and Technology Development Fund under Macao Funding Scheme for Key R&D Projects (0025/2019/AKP).

REFERENCES

AghaKouchak, A., Chiang, F., Huning, L. S., Love, C. A., Mallakpour, I., Mazdiyasni, O., et al. (2020). Climate extremes and compound hazards in a warming world. *Annu. Rev. Earth Planet. Sci.* 48, 519–548. doi: 10.1146/annurev-earth-071719-055228

AghaKouchak, A., Huning, L. S., Chiang, F., Sadegh, M., Vahedifard, F., Mazdiyasni, O., et al. (2018). How do natural hazards cascade to cause disasters? *Nature* 561, 458–460. doi: 10.1038/d41586-018-06783-6

Arakane, S., and Hsu, H. H. (2020). A tropical cyclone removal technique based on potential vorticity inversion to better quantify tropical cyclone contribution to the background circulation. *Clim. Dyn.* 54, 3201–3226. doi: 10.1007/s00382-020-05165-x

Christensen, J. H., and Christensen, O. B. (2003). Severe summertime flooding in Europe. *Nature* 421, 805–806. doi: 10.1038/421805a

Deng, K., Yang, S., Gu, D., Lin, A., and Li, C. (2020). Record-breaking heat wave in southern china and delayed onset of South China sea summer monsoon driven by the pacific subtropical high. *Clim. Dyn.* 54, 3751–3764. doi: 10.1007/s00382-020-05203-8

Fischer, E. M., Seneviratne, S. I., Lüthi, D., and Schär, C. (2007). Contribution of land–atmosphere coupling to recent European summer heat waves. *Geophys. Res. Lett.* 34. doi: 10.1029/2006GL029068

Gao, S., Zhu, L., Zhang, W., and Shen, X. (2020). Impact of the pacific meridional mode on landfalling tropical cyclone frequency in China. *Q. J. R. Meteorol. Soc.* 146, 2410–2420. doi: 10.1002/qj.3799

Gasparrini, A., and Armstrong, B. (2011). The impact of heat waves on mortality. *Epidemiology* 22:68. doi: 10.1097/EDE.0b013e3181fdcd99

Ge, Q., Guo, X., Zheng, J., and Hao, Z. (2008). Meiyu in the middle and lower reaches of the Yangtze river since 1736. *Chin. Sci. Bull.* 53, 107–114. doi: 10.1007/s11434-007-0440-5

Guo, Y., Wu, Y., Wen, B., Huang, W., Ju, K., Gao, Y., et al. (2020). Floods in China, covid-19, and climate change. *Lancet Planet. Health* 4, e443–e444. doi: 10.1016/S2542-5196(20)30203-5

Han, L., Xu, Y., Pan, G., Deng, X., Hu, C., Xu, H., et al. (2015). Changing properties of precipitation extremes in the urban areas, Yangtze river delta, China, during 1957–2013. *Nat. Hazards* 79, 437–454. doi: 10.1007/s11069-015-1850-3

Kirtman, B. P., Min, D., Infanti, J. M., Kinter, James L., I., Paolino, D. A., et al. (2014). The North American multimodel ensemble: phase-1 seasonal-to-interannual prediction; phase-2 toward developing intraseasonal prediction. *Bull. Am. Meteorol. Soc.* 95, 585–601. doi: 10.1175/BAMS-D-12-00050.1

Lentz, E. E., Thieler, E. R., Plant, N. G., Stippa, S. R., Horton, R. M., and Gesch, D. B. (2016). Evaluation of dynamic coastal response to sea-level rise modifies inundation likelihood. *Nat. Clim. Change* 6, 696–700. doi: 10.1038/nclimate2957

Leonard, M., Westra, S., Phatak, A., Lambert, M., van den Hurk, B., McInnes, K., et al. (2014). A compound event framework for understanding extreme impacts. *Wiley Interdiscipl. Rev. Clim. Change* 5, 113–128. doi: 10.1002/wcc.252

Lin, N. (2019). Tropical cyclones and heatwaves. *Nat. Clim. Change* 9, 579–580. doi: 10.1038/s41558-019-0537-2

Liu, F. T., Ting, K. M., and Zhou, Z. H. (2008). "Isolation forest," in *2008 Eighth IEEE International Conference on Data Mining* (Pisa: IEEE), 413–422. doi: 10.1109/ICDM.2008.17

Liu, F. T., Ting, K. M., and Zhou, Z. H. (2012). Isolation-based anomaly detection. *ACM Trans. Knowl. Discov. Data* 6, 1–39. doi: 10.1145/2133360.2133363

Liu, X., Tang, Q., Zhang, X., and Sun, S. (2018). Projected changes in extreme high temperature and heat stress in China. *J. Meteorol. Res.* 32, 351–366. doi: 10.1007/s13351-018-7120-z

Ma, W., Zeng, W., Zhou, M., Wang, L., Rutherford, S., Lin, H., et al. (2015). The short-term effect of heat waves on mortality and its modifiers in china: an analysis from 66 communities. *Environ. Int.* 75, 103–109. doi: 10.1016/j.envint.2014.11.004

Martius, O., Pfahl, S., and Chevalier, C. (2016). A global quantification of compound precipitation and wind extremes. *Geophys. Res. Lett.* 43, 7709–7717. doi: 10.1002/2016GL070017

Matthews, T., Wilby, R. L., and Murphy, C. (2019). An emerging tropical cyclone–deadly heat compound hazard. *Nat. Clim. Change* 9, 602–606. doi: 10.1038/s41558-019-0525-6

Murray, V., and Ebi, K. L. (2012). *IPCC Special Report on Managing the Risks of Extreme Events and Disasters to Advance Climate Change Adaptation (SREX)*. Cambridge: Cambridge University Press, 582.

National Academies of Sciences, Engineering, and Medicine (2016). *Attribution of Extreme Weather Events in the Context of Climate Change*. Washington, DC: National Academies Press.

Parker, T. J., Berry, G. J., and Reeder, M. J. (2013). The influence of tropical cyclones on heat waves in southeastern Australia. *Geophys. Res. Lett.* 40, 6264–6270. doi: 10.1002/2013GL058257

Parzen, E. (2004). Quantile probability and statistical data modeling. *Stat. Sci.* 19, 652–662. doi: 10.1214/088342304000000387

Pendergrass, A. G. (2018). What precipitation is extreme? *Science* 360, 1072–1073. doi: 10.1126/science.aat1871

Peng, R. D., Bobb, J. F., Tebaldi, C., McDaniel, L., Bell, M. L., and Dominici, F. (2011). Toward a quantitative estimate of future heat wave mortality under global climate change. *Environ. Health Perspect.* 119, 701–706. doi: 10.1289/ehp.1002430

Raymond, C., Horton, R. M., Zscheischler, J., Martius, O., AghaKouchak, A., Balch, J., et al. (2020). Understanding and managing connected extreme events. *Nat. Clim. Change* 10, 611–621. doi: 10.1038/s41558-020-0790-4

Rivas, D., Caleyo, F., Valor, A., and Hallen, J. M. (2008). Extreme value analysis applied to pitting corrosion experiments in low carbon steel: Comparison of block maxima and peak over threshold approaches. *Corros. Sci.* 50, 3193–3204. doi: 10.1016/j.corsci.2008.08.002

Stephenson, D. B., Diaz, H., and Murnane, R. (2008). Definition, diagnosis, and origin of extreme weather and climate events. *Clim. Extremes Soc.* 340, 11–23. doi: 10.1017/CBO9780511535840.004

Stott, P. (2016). How climate change affects extreme weather events. *Science* 352, 1517–1518. doi: 10.1126/science.aaf7271

Sun, Q., Miao, C., AghaKouchak, A., and Duan, Q. (2017). Unraveling anthropogenic influence on the changing risk of heat waves in China. *Geophys. Res. Lett.* 44, 5078–5085. doi: 10.1002/2017GL073531

Teegavarapu, R. S. (2012). *Floods in a Changing Climate: Extreme Precipitation*. Cambridge: Cambridge University Press.

Wahl, T., Jain, S., Bender, J., Meyers, S. D., and Luther, M. E. (2015). Increasing risk of compound flooding from storm surge and rainfall for major us cities. *Nat. Clim. Change* 5, 1093–1097. doi: 10.1038/nclimate2736

Wang, L., and Gu, W. (2016). The eastern China flood of June 2015 and its causes. *Sci. Bull.* 61, 178–184. doi: 10.1007/s11434-015-0967-9

Wei, K., Ouyang, C., Duan, H., Li, Y., Chen, M., Ma, J., et al. (2020). Reflections on the catastrophic 2020 Yangtze river basin flooding in southern China. *Innovation* 1:100038. doi: 10.1016/j.xinn.2020.100038

Yin, J., Gentine, P., Zhou, S., Sullivan, S. C., Wang, R., Zhang, Y., et al. (2018). Large increase in global storm runoff extremes driven by climate and anthropogenic changes. *Nat. Commun.* 9:4389. doi: 10.1038/s41467-018-06765-2

Yin, Y., Chen, H., Xu, C. Y., Xu, W., Chen, C., and Sun, S. (2016). Spatio-temporal characteristics of the extreme precipitation by L-moment-based index-flood method in the Yangtze river delta region, China. *Theor. Appl. Climatol.* 124, 1005–1022. doi: 10.1007/s00704-015-1478-y

You, Q., Jiang, Z., Kong, L., Wu, Z., Bao, Y., Kang, S., et al. (2017). A comparison of heat wave climatologies and trends in China based on multiple definitions. *Clim. Dyn.* 48, 3975–3989. doi: 10.1007/s00382-016-3315-0

Yu, J., Gao, S., Zhang, L., Shen, X., and Guo, L. (2020). Analysis of a remote rainstorm in the Yangtze river delta region caused by typhoon Mangkhut (2018). *J. Mar. Sci. Eng.* 8:345. doi: 10.3390/jmse8050345

Zhang, W., and Villarini, G. (2020). Deadly compound heat stress-flooding hazard across the central United States. *Geophys. Res. Lett.* 47:e2020GL089185. doi: 10.1029/2020GL089185

Zhang, W., Villarini, G., Vecchi, G. A., and Smith, J. A. (2018). Urbanization exacerbated the rainfall and flooding caused by hurricane Harvey in Houston. *Nature* 563, 384–388. doi: 10.1038/s41586-018-0676-z

Zhong, S., Qian, Y., Zhao, C., Leung, R., Wang, H., Yang, B., et al. (2017). Urbanization-induced urban heat island and aerosol effects on climate extremes in the Yangtze river delta region of China. *Atmos. Chem. Phys.* 17. doi: 10.5194/acp-17-5439-2017

Zhong, Z., Chen, X., Yang, X. Q., Ha, Y., and Sun, Y. (2019). The relationship of frequent tropical cyclone activities over the western north Pacific and hot summer days in central-eastern China. *Theor. Appl. Climatol.* 138, 1395–1404. doi: 10.1007/s00704-019-02908-7

Zscheischler, J., Martius, O., Westra, S., Bevacqua, E., Raymond, C., Horton, R. M., et al. (2020). A typology of compound weather and climate events. *Nat. Rev. Earth Environ.* 1, 333–347. doi: 10.5194/egusphere-egu2020-8572

Zscheischler, J., and Seneviratne, S. I. (2017). Dependence of drivers affects risks associated with compound events. *Sci. Adv.* 3:e1700263. doi: 10.1126/sciadv.1700263

Conflict of Interest: The authors declare that the research was conducted in the absence of any commercial or financial relationships that could be construed as a potential conflict of interest.

frontiers
in Earth Science

ORIGINAL RESEARCH
published: 30 April 2021
doi: 10.3389/feart.2021.596860

Solar Radiation Prediction Using Different Machine Learning Algorithms and Implications for Extreme Climate Events

Liexing Huang[1,2†], *Junfeng Kang*[2,4*], *Mengxue Wan*[5,6], *Lei Fang*[7], *Chunyan Zhang*[8] *and Zhaoliang Zeng*[3*†]

[1] Ganzhou National Territory Spactial Investigation and Planning Research Center, Ganzhou, China, [2] School of Civil and Surveying and Mapping, Jiangxi University of Science and Technology, Ganzhou, China, [3] Chinese Antarctic Center of Surveying and Mapping, Wuhan University, Wuhan, China, [4] Department of Geography, University of Connecticut, Storrs, CT, United States, [5] State Key Laboratory of Environmental Criteria and Risk Assessment, Chinese Research Academy of Environmental Sciences, Beijing, China, [6] National Joint Research Center for Yangtze River Conservation, Beijing, China, [7] Department of Environmental Science and Engineering, Fudan University, Shanghai, China, [8] Chongqing Wanzhou District Planning and Design Institute, Chongqing, China

OPEN ACCESS

Edited by:
Hiroyuki Murakami,
University Corporation
for Atmospheric Research (UCAR),
United States

Reviewed by:
Yuanjian Yang,
Nanjing University of Information
Science and Technology, China
Yong Xu,
Guangzhou University, China
S. Shamshirband,
Ton Duc Thang University, Vietnam

***Correspondence:**
Junfeng Kang
junfeng.kang@jxust.edu.cn
Zhaoliang Zeng
zhaoliang.zeng@whu.edu.cn

† These authors have contributed equally to this work

Specialty section:
This article was submitted to
Environmental Informatics
and Remote Sensing,
a section of the journal
Frontiers in Earth Science

Received: *21 August 2020*
Accepted: *04 March 2021*
Published: *30 April 2021*

Citation:
Huang L, Kang J, Wan M, Fang L, Zhang C and Zeng Z (2021) Solar Radiation Prediction Using Different Machine Learning Algorithms and Implications for Extreme Climate Events. Front. Earth Sci. 9:596860. doi: 10.3389/feart.2021.596860

Solar radiation is the Earth's primary source of energy and has an important role in the surface radiation balance, hydrological cycles, vegetation photosynthesis, and weather and climate extremes. The accurate prediction of solar radiation is therefore very important in both the solar industry and climate research. We constructed 12 machine learning models to predict and compare daily and monthly values of solar radiation and a stacking model using the best of these algorithms were developed to predict solar radiation. The results show that meteorological factors (such as sunshine duration, land surface temperature, and visibility) are crucial in the machine learning models. Trend analysis between extreme land surface temperatures and the amount of solar radiation showed the importance of solar radiation in compound extreme climate events. The gradient boosting regression tree (GBRT), extreme gradient lifting (XGBoost), Gaussian process regression (GPR), and random forest models performed better (poor) prediction capabilities of daily and monthly solar radiation. The stacking model, which included the GBRT, XGBoost, GPR, and random forest models, performed better than the single models in the prediction of daily solar radiation but showed no advantage over the XGBoost model in the prediction of the monthly solar radiation. We conclude that the stacking model and the XGBoost model are the best models to predict solar radiation.

Keywords: solar radiation prediction, meteorological factors, machine learning, stacking model, climate extremes model comparison

INTRODUCTION

Solar radiation is the Earth's main source of energy and the amount of solar radiation reaching the Earth's surface is affected by the atmosphere, hydrosphere and biosphere (Budyko, 1969; Islam et al., 2009). Solar radiation also has a vital role in the global climate, and even small changes in the output of energy from the Sun will cause considerable changes in the Earth's climate (Beer et al., 2010; Siingh et al., 2011). Variations in solar radiation affect global temperatures, global mean sea-level, and compound extreme climate events (Bhargawa and Singh, 2019). Accurate observations and analyses of the temporal and spatial variability of solar radiation are therefore essential in research on solar energy, building materials, and extreme weather and climate events (Garland et al., 1990; Cline et al., 1998; Hoogenboom, 2000; Grant and Tuohimaa, 2004; Wild, 2009; Beer et al., 2010; Besharat et al., 2013; Ohunakin et al., 2015). Many methods have been developed to predict solar radiation, including theoretical parameter models, empirical models, artificial intelligence models, and satellite retrieval data (Iziomon and Mayer, 2002; Mellit, 2008; Lu et al., 2011; Li et al., 2012; Halabi et al., 2018; Makade et al., 2019). Angstrom (1924) and Prescott (1940) first proposed the A–P model, which is widely used to predict solar radiation. Bristow and Campbell (1984) constructed the BCM model by analyzing the relationship between solar radiation and daily maximum and minimum temperatures. Yang et al. (2001) developed a hybrid model (YHM), improving the A–P model by exploring the effects of meteorological parameters and then validating the model's accuracy in Japan. Salazar (2011) compared the YHM and a climatological solar radiation model to estimate the horizontal direct and diffuse components of solar radiation to generate a corrected version of the YHM (CYHM). Gueymard, 2003 selected 19 solar radiation models to investigate solar irradiance predictions, concluding that detailed transmittance models perform better than bulk models. The development of machine learning has inspired many researchers to use machine learning algorithms to develop solar radiation prediction models (Azadeh et al., 2009; Jiang, 2009; Chen et al., 2011; Voyant et al., 2012). Fadare (2009) and Linares-Rodríguez et al. (2011) adopted artificial neural network (ANN) technology to construct solar radiation prediction models to test their predictive ability. Xue (2017) used a back-propagation algorithm to develop a solar radiation prediction model and showed that the predictive accuracy depended on the combination and configuration of the input parameters. Chen et al. (2011) used the support vector machine (SVM) method to construct a solar radiation prediction model and showed that the SVM-based algorithm had a differential predictive accuracy when using different kernel functions. Olatomiwa et al. (2015) and Shamshirband et al. (2016) both optimized the SVM algorithm and achieved good prediction results. Tree algorithms, such as the random forest algorithm and the gradient boosting regression tree (GBRT) algorithm, have been used to construct solar radiation prediction models with encouraging results (Sun et al., 2016; Persson et al., 2017; Fan et al., 2018; Zeng et al., 2020). In recent years, some scholars have carried out the comparative analysis of a variety of machine learning algorithms (Meenal and Selvakumar, 2018; Pang et al., 2020; Shamshirband et al., 2020), and all these works show that the ANN algorithm does not realize

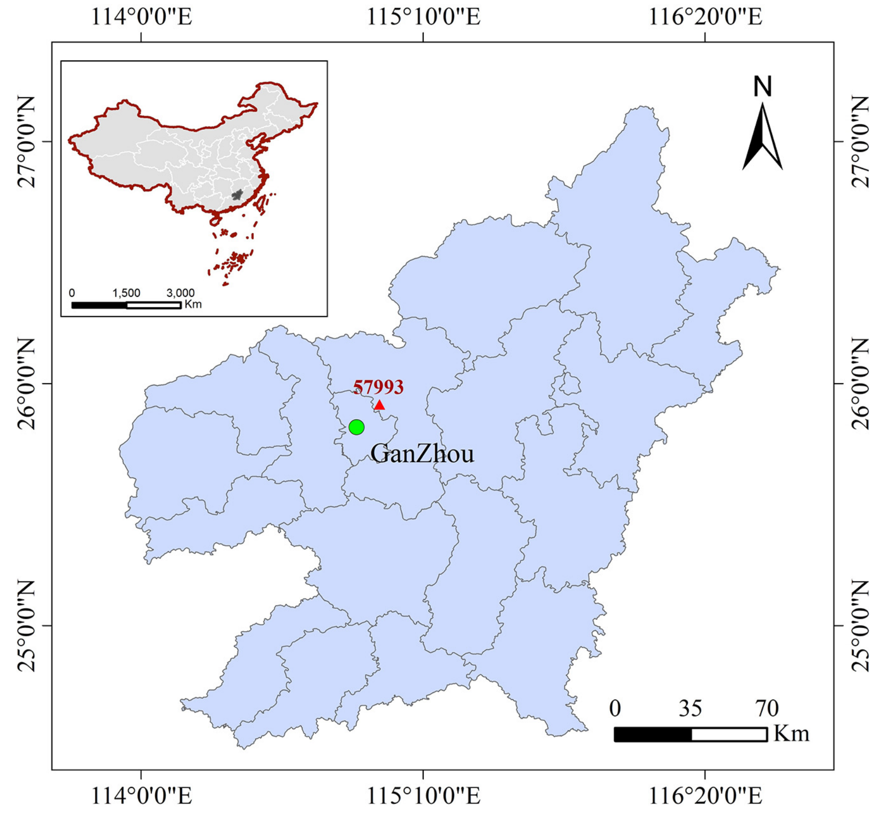

FIGURE 1 | The geographical location of solar radiation monitoring station in Ganzhou County (red triangle).

good prediction results but provides a direction for algorithm improvement. Some studies use deep learning techniques to predict solar radiation. For example, Shamshirband et al. (2019) discuss different types of deep learning algorithms applied in the field of solar, and results show hybrid networks have better performance compared with single networks. Mishra et al. (2020) proposed a short-term solar radiation prediction model using WT-LSTM and achieved good results, showing that deep learning technology has great potential in solar radiation. A CEEMDAN–CNN–LSTM model is proposed by Gao et al. (2020) for hourly multi-region solar irradiance forecasting, and the results present that the model can achieve more accurate prediction performance than other models.

As an investigative technique, machine learning has achieved noteworthy success in many areas, including natural language processing and image recognition (Angra and Ahuja, 2017).

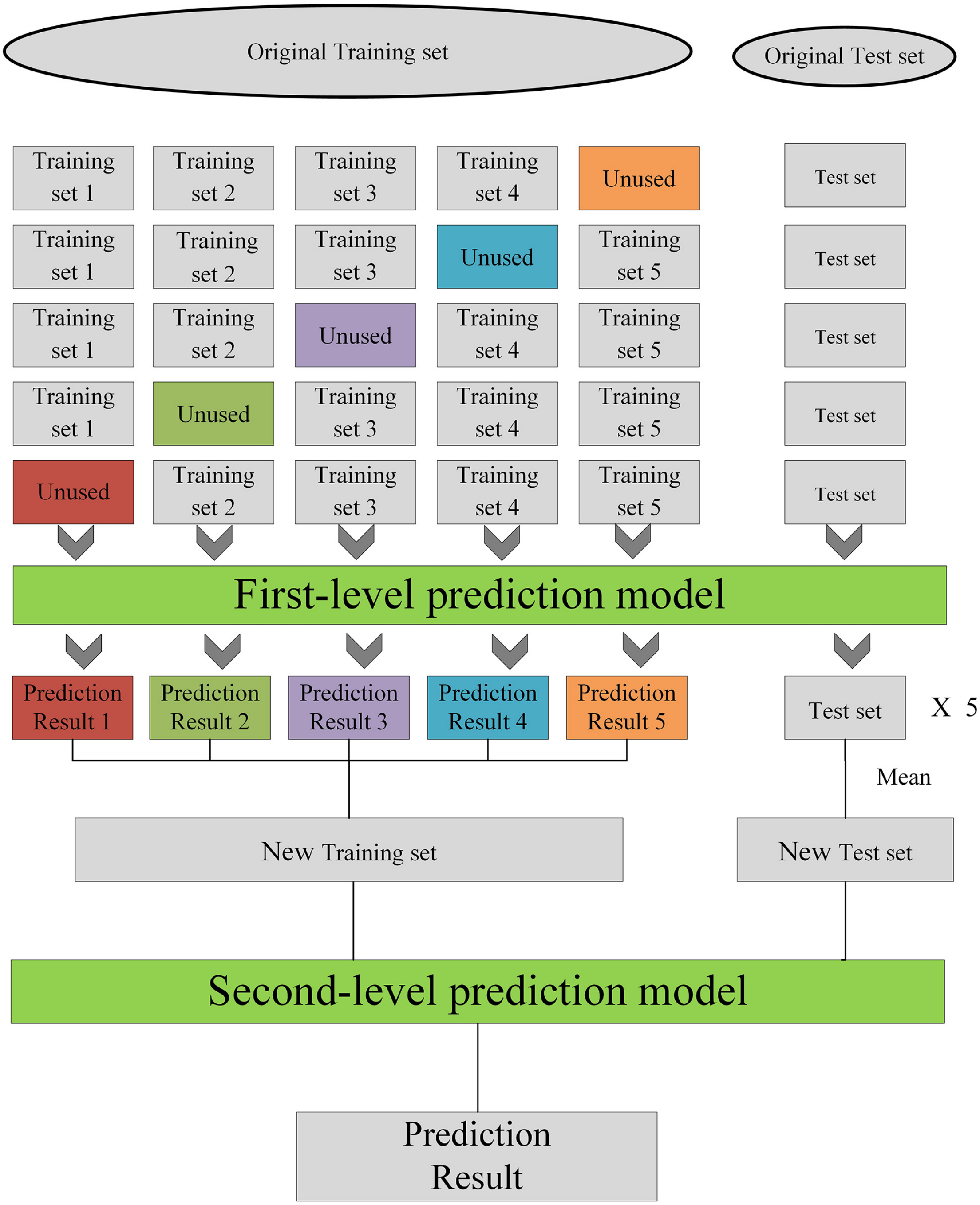

FIGURE 2 | The framework of the stacking model.

The use of machine learning has come to the forefront of the construction of solar radiation models and is a popular direction of research. However, many researchers have focused on the construction of one or several machine learning methods, and there are few in-depth considerations of the differences among these models. Therefore, we used a daily dataset of meteorological elements and basic radiation elements for Ganzhou, China, for the time period 1980–2016 to explore the differences between models of solar radiation prediction. After data processing, we applied the random forest algorithm to selected variables

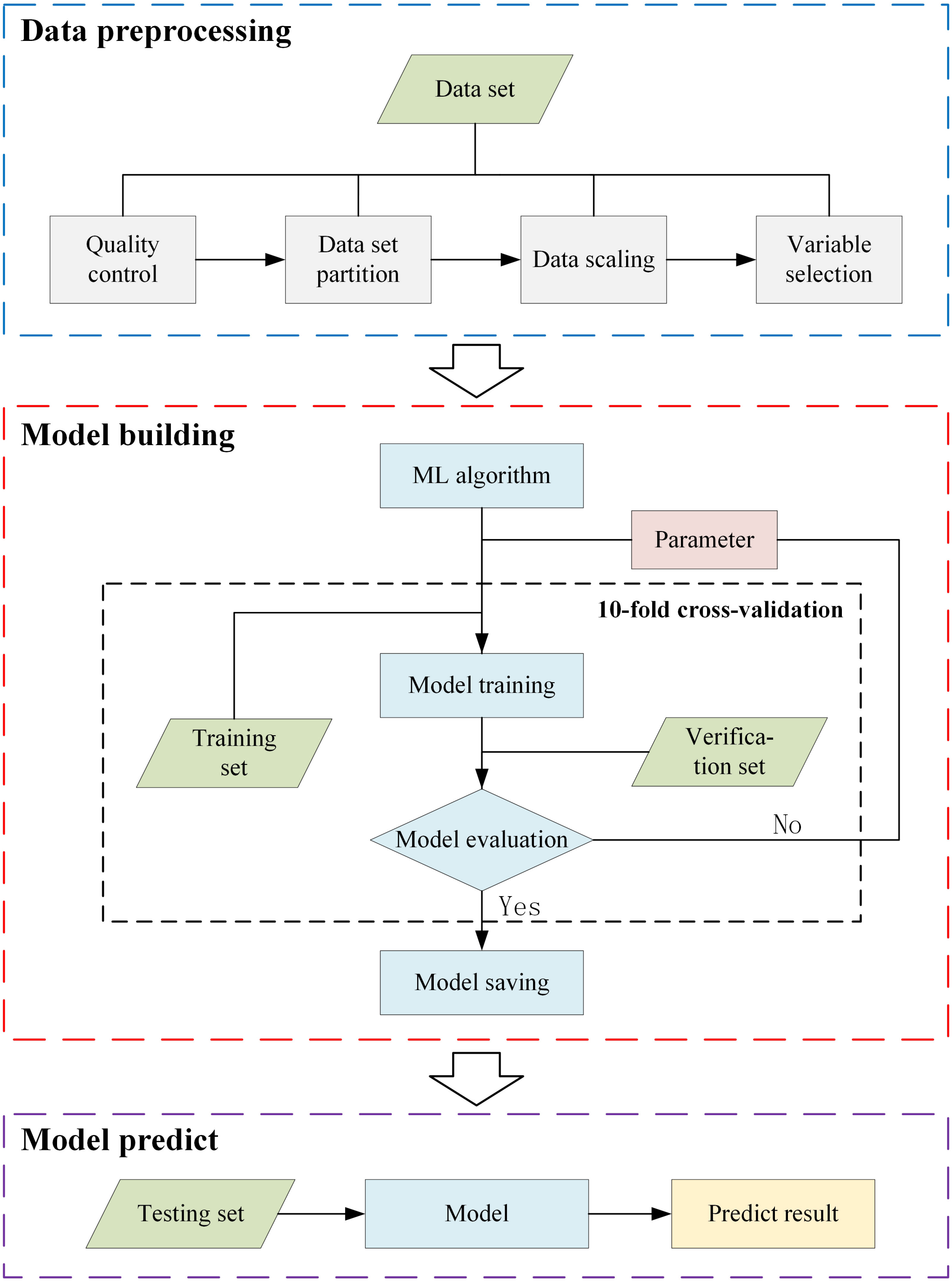

FIGURE 3 | Flow chart of the machine learning models used to estimate solar radiation.

and extracted a monthly dataset based on the daily dataset. We selected 12 machine learning methods to construct a solar radiation prediction model. By comparing the prediction results of these 12 machine learning models, we found the solar radiation prediction models with the best prediction ability. The models with the best prediction ability were then stacked in a linear model. A stacking model was obtained and the predicted results were analyzed.

DATA AND MACHINE LEARNING ALGORITHMS

Study Area and Datasets

Ganzhou city (24.48–30.06° N, 113.57–118.46° E) lies in the south of Jiangxi province in the southern subtropical zone of China and is characterized by a subtropical monsoon climate. It is bordered to the south by Guangdong province, to the east by Fujian province, and to the west by Hunan province. Ganzhou has a mild climate with four distinct seasons and both winter and summer monsoons, with precipitation concentrated in the spring and summer seasons. The annual average temperature is 19.1–20.8°C and the annual rainfall is 1152.2–1554.9 mm. There is a solar radiation monitoring station (No. 57993) in Ganxian County (25.51° N, 114.57° E, 137.5 m above sea-level) (**Figure 1**).

Experimental data were gathered from the China Meteorological Information Center website, including a dataset (V3.0) of daily climate data (temperature, precipitation, air pressure, humidity, temperature, visibility, wind speed, and sunshine duration) from surface stations in China and a daily radiation dataset from Ganzhou's surface solar radiation monitoring station. After referring to relevant research (Will et al., 2013; Mohammadi et al., 2016) and analyzing the quality of the collected data, we selected the data from 1980 to 2016 to estimate solar radiation. The data were selected including the visibility (VIS), the mean relative humidity (RHU-mean), the minimum relative humidity (RHU-min), the mean wind speed (WIN-mean), the mean precipitation (PRE-mean), the mean pressure (PRS-mean), the maximum pressure (PRS-max), the minimum pressure (PRS-min), the sunshine duration (SSD), the mean temperature (TEM-mean), the maximum temperature (TEM-max), the minimum temperature (TEM-min), the mean ground temperature (GST-mean), and the total solar radiation (RAD).

Quality control of the data was essential considering the length of the study period and the inherent errors in the instrument-based observations. We excluded missing and abnormal values in the meteorological data from the final dataset and then applied the requirements for solar radiation data quality control proposed by Younes et al. (2005). In total, 13,100 daily data records and 432 monthly average data records were obtained. The dataset was further divided into training and test sets and then normalized, with the training set

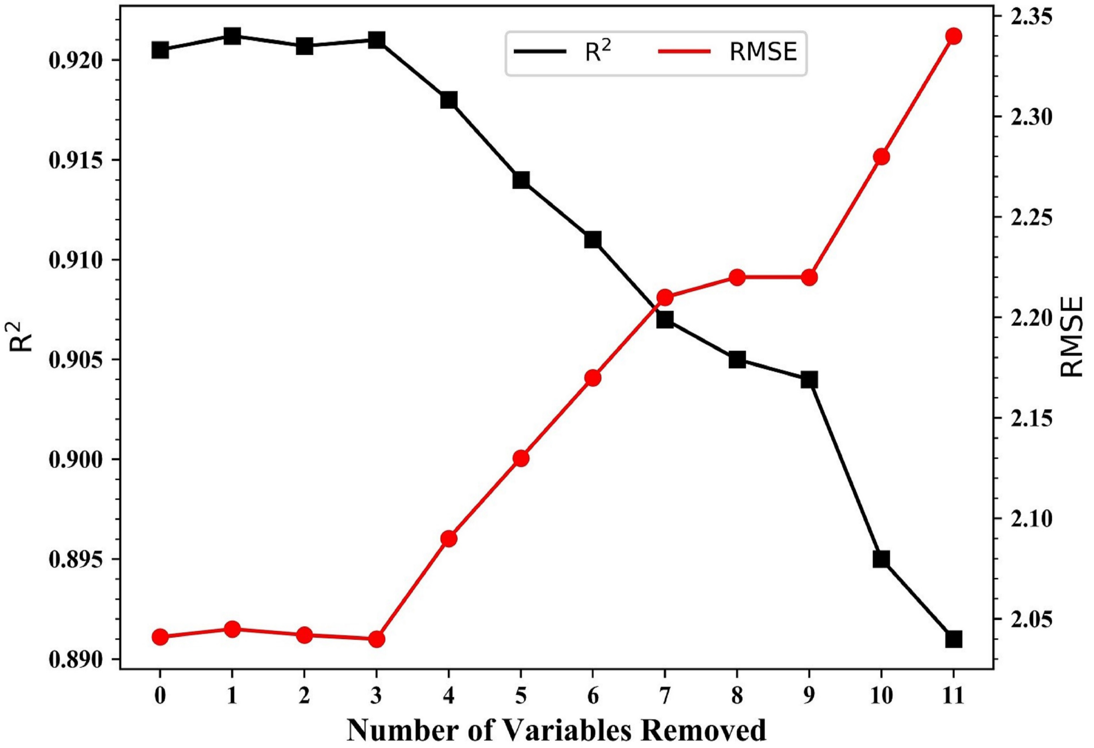

FIGURE 4 | Predictive performance (R^2 and RMSE) of the random forest model during variable selection. Variables were removed in the order PRS-min, PRS-max, RHU-min, PRE-mean, TEM-mean, WIN-mean, TEM-max, TEM-min, RHU-mean, PRS-mean, and VIS.

accounting for 90% and the test set accounting for 10% of all data. Our final sample consisted of 11,790 daily training sets, 1,310 daily test sets, 388 monthly training sets, and 44 monthly test sets.

Machine Learning Predictive Algorithms and Stacking Techniques

Machine Learning Algorithms

With the development of machine learning technology, an increasing number of researchers are using machine learning to predict solar radiation. We investigated 12 different machine learning predictive algorithms: multiple linear regression (Baczek et al., 2005; Nathans et al., 2012), the radial basis function neural network (Mahanty and Dutta Gupta, 2004; Li M. et al., 2008), the K-nearest neighbor model (Shen and Chou, 2005; Deng et al., 2016), the decision tree (Brodley and Friedl, 1997; Quinlan, 1999), the back-propagation neural network (Van Ooyen and Nienhuis, 1992; Trappey et al., 2006), the extreme learning machine (Deng et al., 2015; Huang G. et al., 2015), SVM regression (Burges, 1998; Shamshirband et al., 2016), Gaussian process regression (GPR) (Nguyen-Tuong et al., 2009; Ebden, 2015), the GBRT (Zhang and Haghani, 2015; Johnson et al., 2018), adaptive boosting (Adaboost) (Zhu et al., 2006; Li X. et al., 2008; Wang, 2012), extreme gradient lifting (XGBoost) (Nielsen, 2016; Torlay et al., 2017), and random forest (Kapwata and Gebreslasie, 2016; Sun et al., 2016) algorithms. A detailed description of machine learning methods can be found in **Supplementary Text S1**.

Stacking Model

Stacking technology is a general integration algorithm that integrates advanced learners by using multiple lower-level learners to achieve higher performance (Agarwal and Chowdary, 2020). In general, the K-fold cross-validation method is used to train and test these models and then output the prediction results. The prediction results output by each model is then combined into a stacking model, which is built to reduce the generalization errors. The stacking model usually consists of two layers. The first layer is the base learner, and the input is the initial training set. The second layer is trained with the output data from the first layer as the input data and gives the final results.

The steps of the stacking model construction are as **Figure 2**. Each model is trained using five-fold cross-validation. The training set is divided into five parts, and four parts are selected as the training data and one set as the test data. The test data in each of the four training sets is predicted to obtain a prediction result (**a**) and the test set data are predicted by the trained model to obtain the test set prediction result (**b**). After five training runs, the prediction result **a** of each of the five runs is combined into one column as **A** and the prediction result **b** is averaged as **B**. The new datasets **A** and **B** are obtained, in which the number in **A** is the same as the number of training sets, but **A** is one-dimensional data. After constructing **N** single models, **N A** and **N B** are generated, then the **N A** and **N B** data are combined into a new training set and a new test set. A simple linear model is used as the second layer to train using the new training set and test with the new test set.

TABLE 1 | Descriptive statistics of the modeling variables in the training dataset.

	Spring				Summer				Fall				Winter				Year			
	Mean	**Std**	**Max**	**Min**	**Mean**	**Std**	**Max**	**Min**	**Mean**	**Std**	**Max**	**Min**	**Mean**	**Std**	**Max**	**Min**	**Mean**	**Std**	**Max**	**Min**
VIS	14.69	5.64	50.00	1.78	22.97	10.58	65.75	4.90	14.21	5.09	51.75	4.05	12.19	3.23	35.75	2.70	16.02	6.21	65.75	1.78
RHU-mean	78.13	11.00	100.00	34.25	72.41	10.00	97.75	43.00	72.70	10.74	99.00	31.25	74.58	12.42	98.75	27.25	74.46	11.04	100.00	27.25
WIN-mean	1.41	0.80	5.25	0.00	1.62	0.75	5.00	0.00	1.39	0.76	46.00	0.00	1.39	0.81	4.75	0.00	1.45	0.78	5.25	0.00
PRE-mean	62.1	121.8	1067.0	0.00	49.3	130.0	1497.0	0.00	22.8	77.8	1184.0	0.00	23.9	66.0	1010.0	0.00	39.5	98.9	1497.0	0.00
PRS-mean	998.57	5.61	1018.80	994.80	990.42	3.17	1001.00	975.50	1001.10	5.63	1019.10	982.60	1007.96	5.04	1024.40	987.20	999.51	4.86	1024.00	975.50
TEM-mean	19.34	5.87	31.90	2.50	28.64	2.36	34.00	18.10	21.10	5.26	31.90	1.60	9.54	4.33	25.20	−0.90	19.66	4.46	34.00	−0.90
TEM-max	23.75	6.84	36.50	4.80	33.49	3.10	40.00	20.30	25.93	59.10	38.50	2.70	13.95	5.97	31.40	−0.20	24.28	5.46	40.00	−0.20
TEM-min	16.22	5.49	27.40	−0.30	25.16	1.85	30.00	15.60	17.64	5.31	27.80	0.40	6.53	4.13	22.50	−3.90	16.39	4.20	30.00	−3.90
GST-mean	21.31	6.74	39.20	3.60	33.07	4.57	43.20	20.60	24.02	6.50	40.60	3.00	10.77	4.44	27.30	0.10	22.29	5.56	43.20	0.00
SSD	3.47	3.91	126.00	0.00	71.50	4.03	13.00	0.00	5.26	4.02	11.60	0.00	3.26	3.70	10.40	0.00	4.79	3.92	13.00	0.00
RAD	10.90	7.41	28.46	2.00	17.70	6.42	30.48	5.00	12.05	6.14	26.80	3.00	7.36	4.96	20.15	1.00	12.02	6.28	30.48	1.00

Spring: March, April, May; Summer: June, July, August; Fall: September, October, November; Winter: December, January, February. Std, standard deviation; Max, maximum; Min, minimum.

MATERIALS AND METHODS

Prediction of the Flow of Solar Radiation

Our experiment consisted of three parts (**Figure 3**): data preprocessing, model building, and model prediction. The data preprocessing involved four steps: data quality control, dataset partitioning, data scaling, and variable selection. Among them, data quality control, dataset partitioning, and data scaling are described in Section "Study Area and Datasets," and variable selection is described in Section "Variable Selection." The main processes of the model building were as follows: the selection of the machine learning algorithm, parameter selection, model construction, and model saving. We used the 10-fold cross-validation method (Jiang and Wang, 2017) in the parameter selection step. We can get a detailed description of the model building in Section "Model Building." In the model prediction step, the saved model from the model building step was used to predict the solar radiation using the test dataset. Then, we save the predicted results and analysis. The specific experimental steps proceeded as follows:

(1) data collection and data preprocessing;
(2) choose a machine learning algorithm from the 12 algorithms to predict solar radiation;
(3) compare solar radiation predictive ability based on different parameters;
(4) if the best predictive ability is achieved, save the model;
(5) return to step (2) and choose another machine learning algorithm until all 12 algorithms have been subjected to machine learning model building;
(6) input the preprocessing dataset (we prepared datasets on two timescales—daily and monthly—to estimate the solar radiation predictive performance of the 12 machine learning models) and use the 12 saved machine learning models to predict solar radiation and obtain the predicted results;
(7) save predicted results and analyze.

Variable Selection

The variable selection step is important in constructing machine learning models. The current mainstream variable selection algorithms include the genetic algorithm (Huang and Chiu, 2006), the Tabu search (Corazza et al., 2013), particle swarm optimization (Khatibi Bardsiri et al., 2013), and the random forest algorithm (Kapwata and Gebreslasie, 2016). We used the random forest algorithm to select data variables (Zeng et al., 2020). Normalized daily data were used to construct and train the random forest model and to calculate the model's importance. The data preprocessing experiment was intended to verify the importance of variables in a given model and to analyze the impact of changes in the variables on the model's predictive performance. The experiment proceeded as follows:

(1) divide the dataset into a training set and test set after completing the data quality control process;
(2) use the training set to train and save the model, then calculate the correlation coefficient (R^2) and the root mean square error (RMSE) of the saved model;
(3) based on the order of importance of the variables in the model, eliminate the least important variable;
(4) repeat steps (2) and (3) until only two variables remain (the minimum required for calculation).

Figure 4 shows that when the model contained <10 variables, R^2 tended to decrease and the RMSE tended to increase. Between 12 and 10 variables, R^2 reached 0.921 and the RMSE was 2.042 MJ/m^2. With four variables, R^2 decreased sharply from 0.904 to 0.895 and the RMSE decreased from 2.19 to 2.28 MJ/m^2. Therefore, the prediction of solar radiation can achieve the best performance when using 10 variables, then the subsequent model experiments were trained with these 10 variables.

Model Building

Experiments were performed in Python 3.6 using third-party libraries such as Pandas, NumPy, the scikit-learn machine learning library (Sklearn), and the Xgb library. Twelve machine learning algorithms were chosen to build the models. The initial parameter settings of each algorithm were determined according to the algorithm's characteristics. For example, for a neural network model, the number of hidden layers and the number of neurons were determined based on empirical formulas and neural network design principles (Basheer and Hajmeer, 2000). The respective selection ranges of the adjustment parameters and other parameters were then set according to the parameter adjustment methods for different machine learning algorithms. We used Sklearn's GridSearchCV method to select parameters for each of the 12 machine learning models, ultimately saving the best model. The first layer of the stacking model consists of those multiple models with excellent predictive power. The parameters of the first layer model are the parameters selected previously and the second layer is constructed by multiple linear regression. After obtaining the best parameters, the train set was used to train the model and the final model was saved. The time spent training the model is the model construction time, and the final model size is the model memory. When the model was constructed, input the test set was input to get the prediction result.

Statistical Metrics

The models were evaluated using four indicators: R^2, RMSE, MAE, and BIAS:

$$R^2 = \frac{\left(\sum_{t=1}^{n}\left(yo_t - y\bar{o}\right)\left(ym_t - y\bar{m}\right)\right)^2}{\sum_{t=1}^{n}\left(yo_t - y\bar{o}\right)^2 \cdot \sum_{t=1}^{n}\left(ym_t - y\bar{m}\right)^2} \tag{1}$$

$$RMSE = \sqrt{\frac{1}{n}\sum_{t=1}^{n}\left(yo_t - ym_t\right)^2} \tag{2}$$

$$MAE = \frac{1}{n}\sum_{t=1}^{n}\left|\left|\left(yo_t - ym_t\right)\right|\right| \tag{3}$$

$$BIAS = \left(yo_t - ym_t\right) \tag{4}$$

where n indicates the amount of data, ym_t is the predicted solar radiation, yo_t is the observed solar radiation, and $\bar{ym}$ and $\bar{yo}$ represent the average of the predicted and observed results, respectively.

If R^2 is close to 1, then the observed and predicted values are closely correlated. The closer the RMSE/MAE values are to 0, the better the predicted value fits the observed value. A combination of metrics, including, but not limited to, the RMSE and MAE, are often required to assess the performance of the model.

RESULTS

Description and Selection of Variables

The average annual range of the RAD was 1–30.48 MJ/m^2, with a mean value of 12.02 MJ/m^2 and a standard deviation of 6.28 MJ/m^2 (**Table 1**). The annual mean (standard deviation) values were VIS 16.02 (6.21) km, RHU-mean 74.46 (11.04)%, WIN-mean 1.45 (0.78) m/s, PRE-mean 39.5 (98.9) mm, PRS-mean 999.51 (4.86) hPa, TEM-mean 19.66 (4.46)°C, TEM-max 24.28 (5.46)°C, TEM-min 16.39 (4.2)°C, GST-mean 22.29 (5.56)°C, and SSD 4.79 (3.92) h. Apart from the RHU-mean, PRE-mean, and PRS-mean, the mean values of the variables were highest in summer, followed by spring and autumn, and were lowest in winter. **Supplementary Figure 1** shows the annual maximum GST-mean and the corresponding solar radiation from 1980 to 2016. The trend of GTS-max and the corresponding solar radiation values were generally consistent and increased with the solar radiation, confirming the importance of solar radiation in compound climate extreme events (Ohunakin et al., 2015).

Figure 5 shows the importance of the input variables as predictors in the final random forest model. SSD was identified as the most critical variable, followed in descending order by GST-mean, VIS, PRS-mean, RHU-mean, TEM-min, TEM-max, WIN-mean, TEM-mean, PRE-mean, RHU-min, PRS-max, and PRS-min. The importance of SSD was 85%, which agrees with the results of earlier studies (Chen et al., 2013; Suehrcke et al., 2013; Zeng et al., 2020). The importance of GST-mean was 6% and the importance of all other variables was <5%.

Predictive Performance for Daily Solar Radiation

Figure 6 shows the performance of the 12 machine learning models in predicting solar radiation for the given daily dataset. The statistical results show that most of the machine learning models used to predict solar radiation yielded satisfactory results. The R^2 values of the 12 machine learning models ranged from 0.838 to 0.925. The GBRT, GPR, XGBoost, and random forest models were the best machine learning models to predict solar radiation with R^2 values of 0.925, 0.923, 0.922, and 0.921,

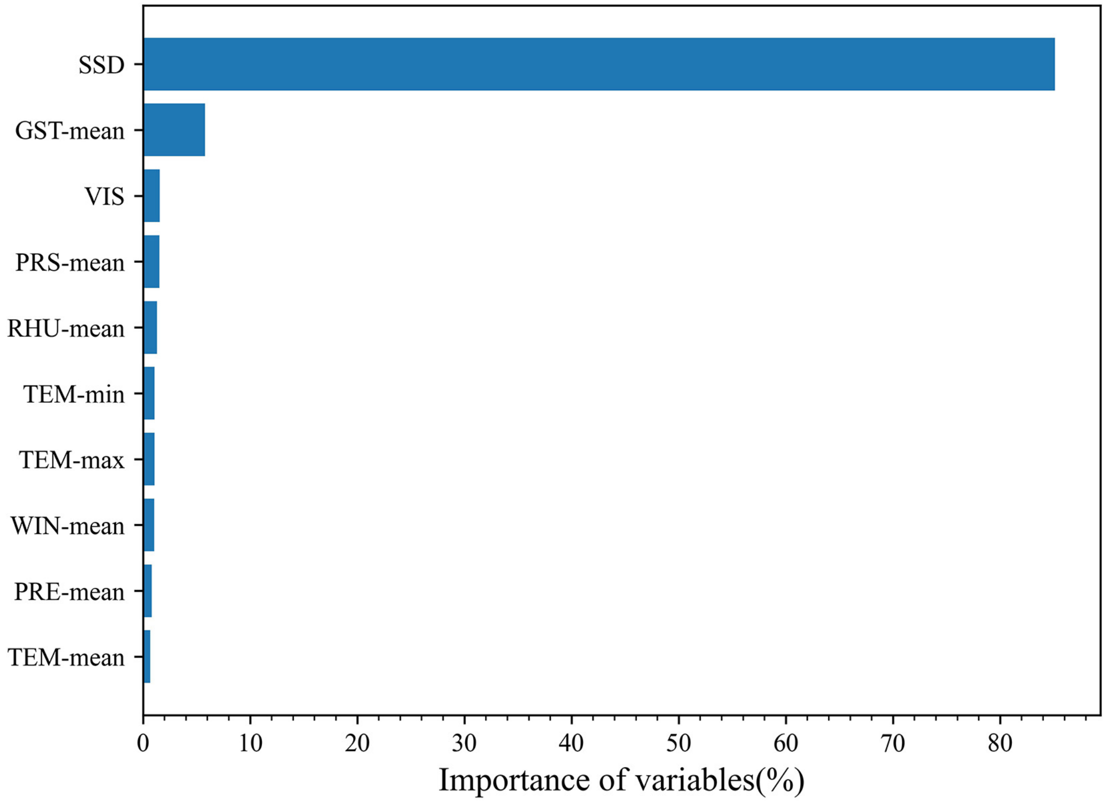

FIGURE 5 | Importance of variables in predicting solar radiation using the random forest model.

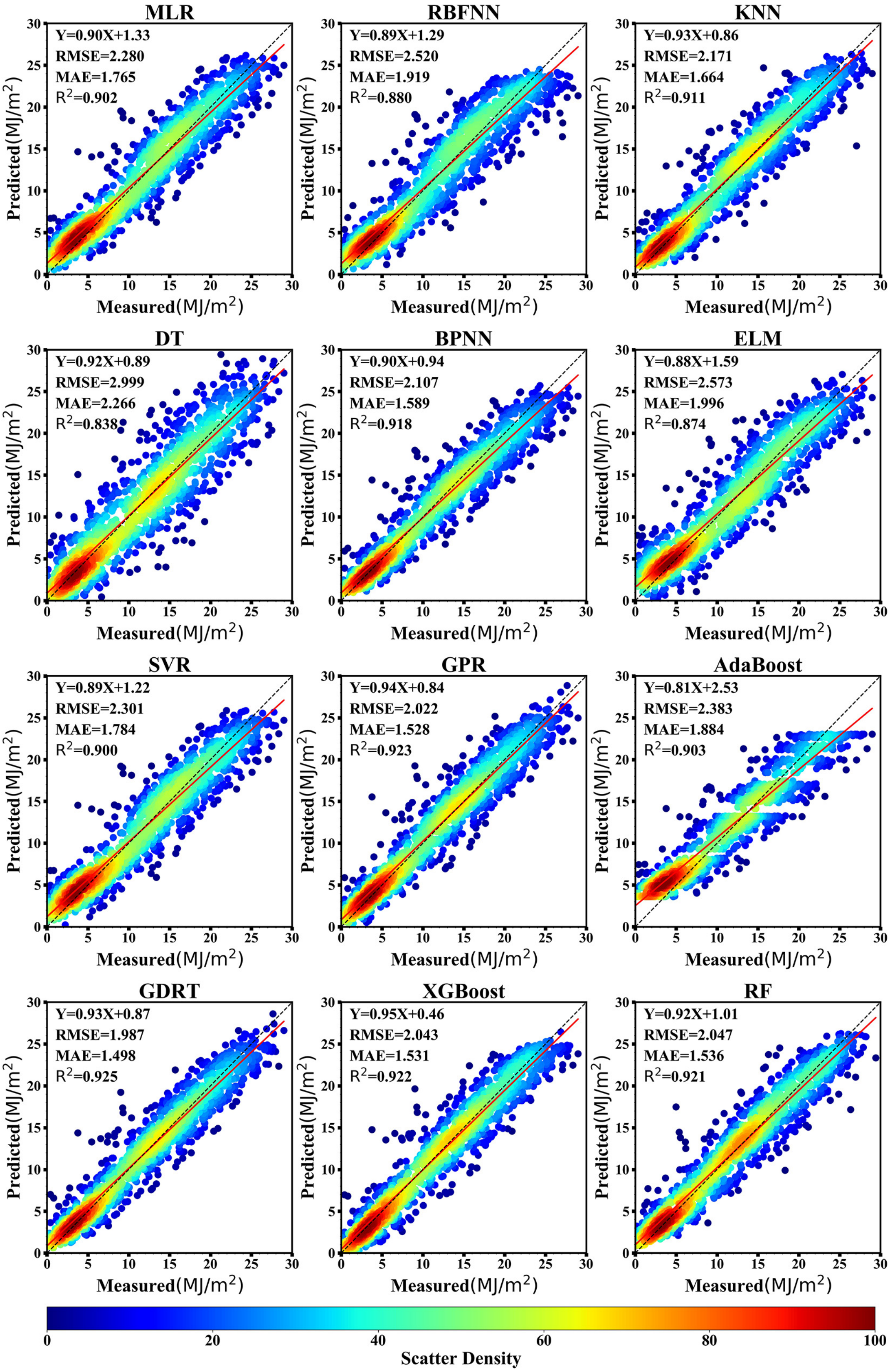

FIGURE 6 | Scatter plots of the cross-validation results for 12 machine learning models in predicting daily solar radiation at Ganzhou from 1980 to 2016.

respectively. The R^2 values of the extreme learning machine and decision tree models were 0.874 and 0.838, respectively, which indicated that these models had the poorest precision for the prediction of solar radiation. The RMSE values of the 12 machine learning models were in the range 1.987–2.999 MJ/m^2. The RMSE value of the GBRT model was the lowest (1.987 MJ/m^2),

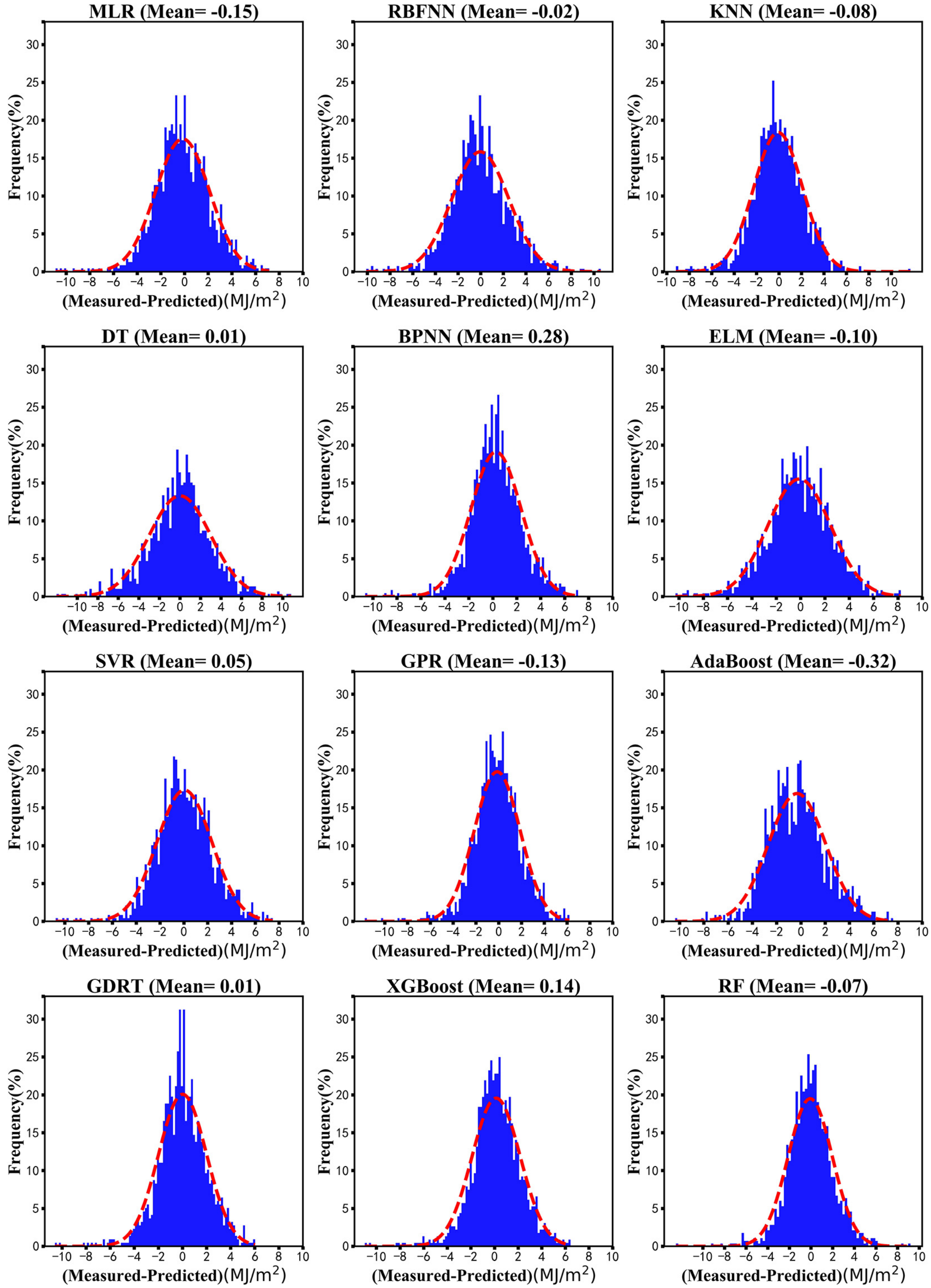

FIGURE 7 | Deviation distribution of machine learning models in predicting daily solar radiation at Ganzhou from 1980 to 2016.

indicating that this model was the best for predicting solar radiation. By contrast, the RMSE value of the decision tree model was the largest (2.999 MJ/m^2), suggesting that this model was the poorest predictor of solar radiation. The MAE values of the 12 machine learning models ranged from 1.498 to 2.266 MJ/m^2, with the GBRT model returning the smallest value (MAE = 1.498 MJ/m^2), meaning that the deviation between the predicted and measured values was also the smallest. The MAE value of the decision tree model was the largest (MAE = 2.266 MJ/m^2), demonstrating that this model had the largest prediction bias. The MAE values of the other machine learning models were both <2.0 MJ/m^2.

Figure 7 shows distribution maps of the daily deviation probability to further explore the distribution of the deviation of solar radiation prediction for the 12 machine learning models. The results showed that the bias of the GBRT and the decision tree models both were 0.01 MJ/m^2, followed by the RBNN model (−0.02 MJ/m^2). The bias of the AdaBoost model for solar radiation prediction was −0.32 MJ/m^2. The deviation values of most models were mainly distributed between −6 and +6 MJ/m^2, whereas those of the decision tree and extreme learning machine models were mainly distributed between −8 and +8 MJ/m^2. **Table 2** shows the number of deviation values that fell within the range ±2 MJ/m^2 in the prediction of solar radiation for the 12 models. The deviation in solar radiation prediction for the GBRT, GPR, XGBoost, and random forest models each exceeded 940, compared with only 734 for the decision tree model.

The prediction results from the daily value data indicate that the GBRT, XGBoost, GPR, and random forest models had a relatively good predictive ability, whereas the extreme learning machine and decision tree models performed poorly. The random forest model had the longest construction time, followed by the GBRT and the GPR models; the XGBoost model had the shortest construction time. This is related to the model principle—for example, to obtain better training results, the random forest model needs more CART-based models, which increases the training time. By contrast, XGBoost uses parallel processing to increase the operational speed and therefore requires less time.

TABLE 2 | Statistics for the amount of daily data for each model deviation within ±2 8 MJ/m^2.

Model	Number of data points	Percentage
Multiple linear regression	861	65.7
Radial basis function neural network	804	61.4
K-nearest neighbor	894	68.2
Decision tree	734	56.0
Back-propagation neural network	935	71.4
Extreme learning machine	768	58.6
Support vector machine regression	846	64.5
Gaussian process regression	941	71.8
AdaBoost	794	60.6
Gradient boosting regression tree	956	73
XGBoost	950	72.5
Random forest	945	72.1

Predictive Performance for Monthly Solar Radiation

Figure 8 presents a scatter plot of the monthly predicted and measured values for different models. The R^2 values for the 12 machine learning models ranged from 0.900 to 0.944 and were > 0.9 for all models. The XGBoost model gave the best prediction result, with an R^2 value of 0.944; the GPR (R^2 = 0.941), GBRT (R^2 = 0.938), and random forest (R^2 = 0.936) models also demonstrated a good prediction performance. The K-nearest neighbor (R^2 = 0.900) and decision tree (R^2 = 0.901) models gave relatively poor prediction results. The RMSE of each model fell between 1.131 and 1.580 MJ/m^2. The XGBoost model returned the lowest RMSE of 1.131 MJ/m^2, reflecting the highest precision of all the models. The decision tree model had the lowest precision (RMSE = 1.580 MJ/m^2). The MAE values for all models ranged from 0.870 to 1.174 MJ/m^2. The MAE of the XGBoost model was the smallest (MAE = 0.870 MJ/m^2), indicating that the predicted value was close to the observed value.

For the monthly average data, **Figure 9** shows the largest deviation in the RBNN model (bias 0.88 MJ/m^2), followed by random forest (bias −0.02 MJ/m^2) and SVM regression (bias 0.08 MJ/m^2) models and the lowest deviation in the GBRT model (bias −0.01 MJ/m^2). In contrast with the deviation in the daily data, the monthly average prediction bias of most models was positive, although the decision tree, GBRT, and random forest models showed a negative deviation. According to the monthly mean deviation probability distribution, the main distribution interval of the model deviation was within ±4. **Table 3** gives the statistical results for the monthly data with a predicted deviation between −2 and +2 MJ/m^2, with 37 data points in the random forest model and 40 data points in the GBR model.

The XGBoost, GPR, GBRT, and random forest models showed better predictive ability on the monthly average data, whereas the K-nearest neighbor and decision tree models performed poorly. When the amount of data is small, the XGBoost, GPR, GBRT, and random forest models are all built very quickly, but the XGBoost model is the fastest with the highest prediction accuracy. Besides, XGBoost has strong anti-overfitting and generalization abilities. This is advantageous for the construction of the monthly radiation value in models with a small number of data points, which is an advantage over the other machine learning models. The XGBoost model is therefore recommended when there is only a small number of data points.

Predictive Performance of the Stacking Model

The XGBoost, GPR, GBRT, and random forest single models showed excellent prediction capabilities. These four models were therefore used as the first layer model and multiple linear regression was used as the second layer model to build a stacking model. **Figures 10A,B** show the predicted results and bias probability distributions. **Figure 10A** shows that the R^2 of the stacking model is 0.929, the RMSE is 1.940 MJ/m^2, and the MAE is 1.457 MJ/m^2. Compared with the 12 single models, the stacking model has the highest R^2 value, but the lowest RMSE

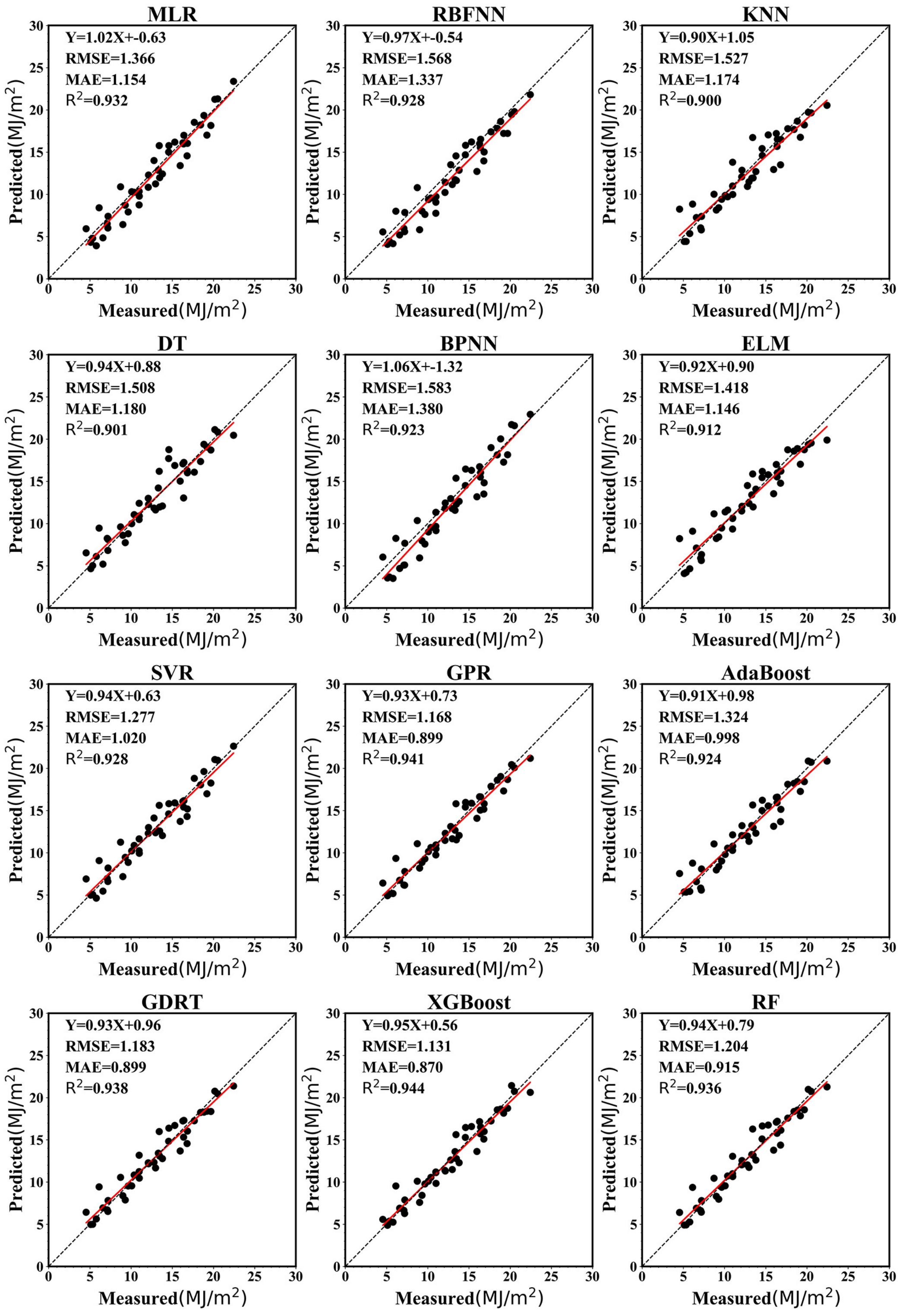

FIGURE 8 | Scatter plots of the results of machine learning models in predicting monthly average solar radiation at Ganzhou from 1980 to 2016.

and MAE. **Figure 10B** shows that the average deviation of the stacking model is 0 MJ/m^2 and the deviation of the distribution is more uniform than that of the single models. The stacking model predicts 74.8% of the data with a bias distribution in [−2, 2]. The stacking model has a better prediction ability for the daily data than the single models. **Figure 10C** shows that

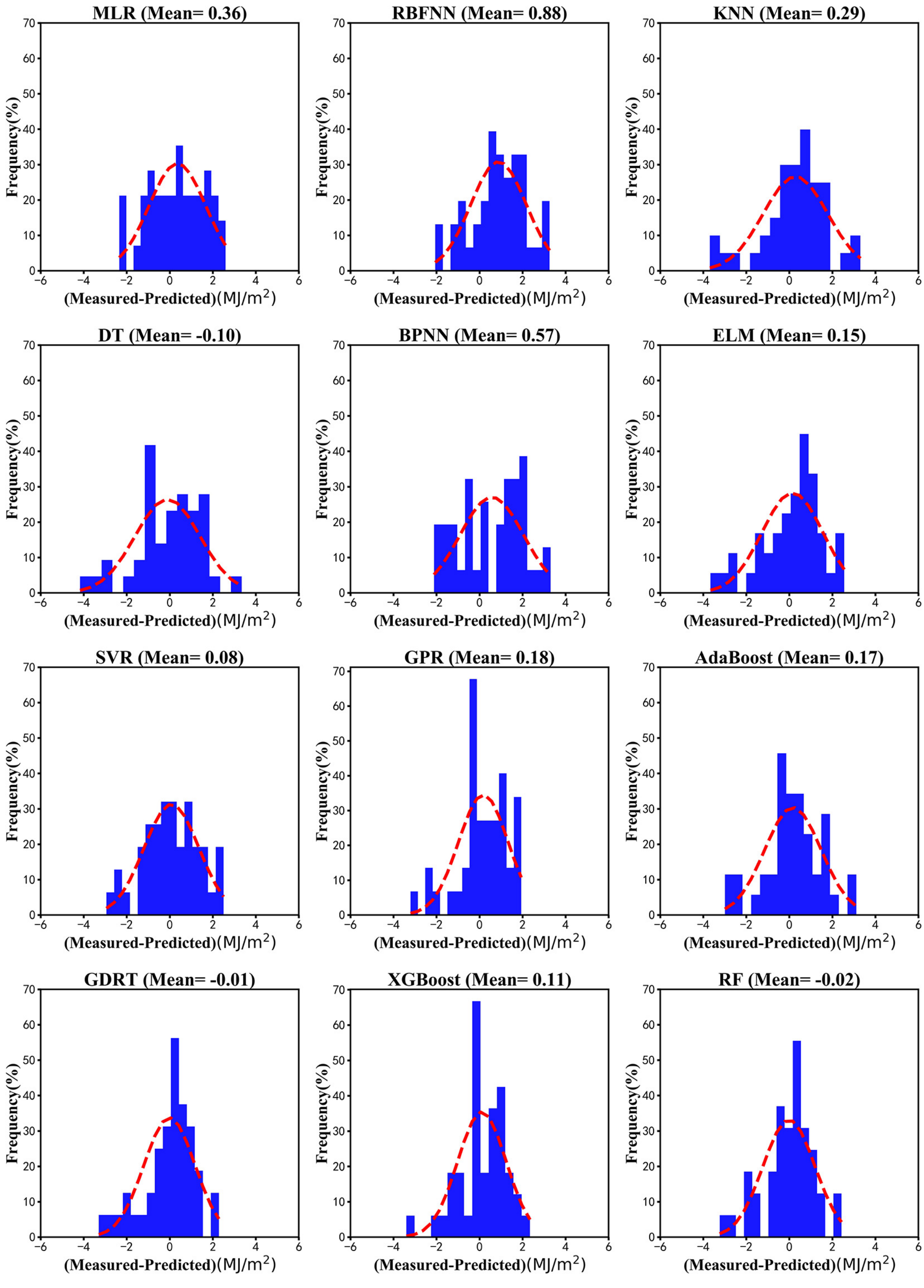

FIGURE 9 | Deviation distribution of machine learning models in predicting the monthly average solar radiation at Ganzhou from 1980 to 2016.

the R^2 value of the stacking fusion model is 0.943, the RMSE is 1.142 MJ/m^2, and the MAE is 0.884 MJ/m^2, all lower than the XGBoost model (R^2 0.944, RMSE 1.131 MJ/m^2, and MAE 0.870 MJ/m^2). **Figure 10D** shows that the average value of the stacking deviation of the stacking model is 0.13 MJ/m^2 and there are only 39 deviations between [2, −2]. The stacking model has no advantage over the XGBoost model in terms of construction time.

TABLE 3 | Statistics for the amount of monthly data in each model deviation within ±2.

Model	Number of data points	Percentage
Multiple linear regression	35	79.5
Radial basis function neural network	36	82
K-nearest neighbor	36	82
Decision tree	38	86.4
Back-propagation neural network	34	77.3
Extreme learning machine	35	79.5
Support vector machine regression	36	82
Gaussian process regression	40	90.9
AdaBoost	37	84.1
Gradient boosting regression tree	38	77.3
XGBoost	40	90.9
Random forest	37	84.1

DISCUSSION

Many studies have compared the ability of machine learning algorithms to predict solar radiation (**Supplementary Table 1**). Moreno et al. (2011) used an ANN and generalized regression to build models separately, positing that an ANN has the same predictive power as generalized regression. Yang et al. (2014) applied ANN-SVM, SVM, and ANN to construct separate models, giving a model performance in the order ANN-SVM > SVM > ANN. Wang et al. (2016) compared the MLP, RBNN, and GRNN models and noted RBNN > GRNN > MLP in terms of performance. We used daily and monthly data to predict the performance of 12 machine learning models and showed that the GBRT, GPR, XGBoost, and random forest models had better prediction capabilities than the other models. We also combined the XGBoost, GBRT, GPR, and random forest models using stacking technology. The performance of the stacking model in predicting the daily solar radiation set was better than that of the 12 single models, but the performance using the monthly dataset gave no advantage over the XGBoost model.

We found that the input of a small measured value of solar radiation returned a large predicted output value, whereas the input of a large value of solar radiation returned a small predicted output value after machine learning processing. This phenomenon may be linked to data that were relatively concentrated and contained fewer, but higher, measured values. The data scaling method greatly influences the performance of machine learning models (Huang J. et al., 2015; García et al., 2016). Normal processing methods include no processing, normalization, standardization, and regularization. We adopted four different data processing methods to build 12 different machine learning models with daily or monthly data. The results are shown in **Supplementary Tables 2, 3**.

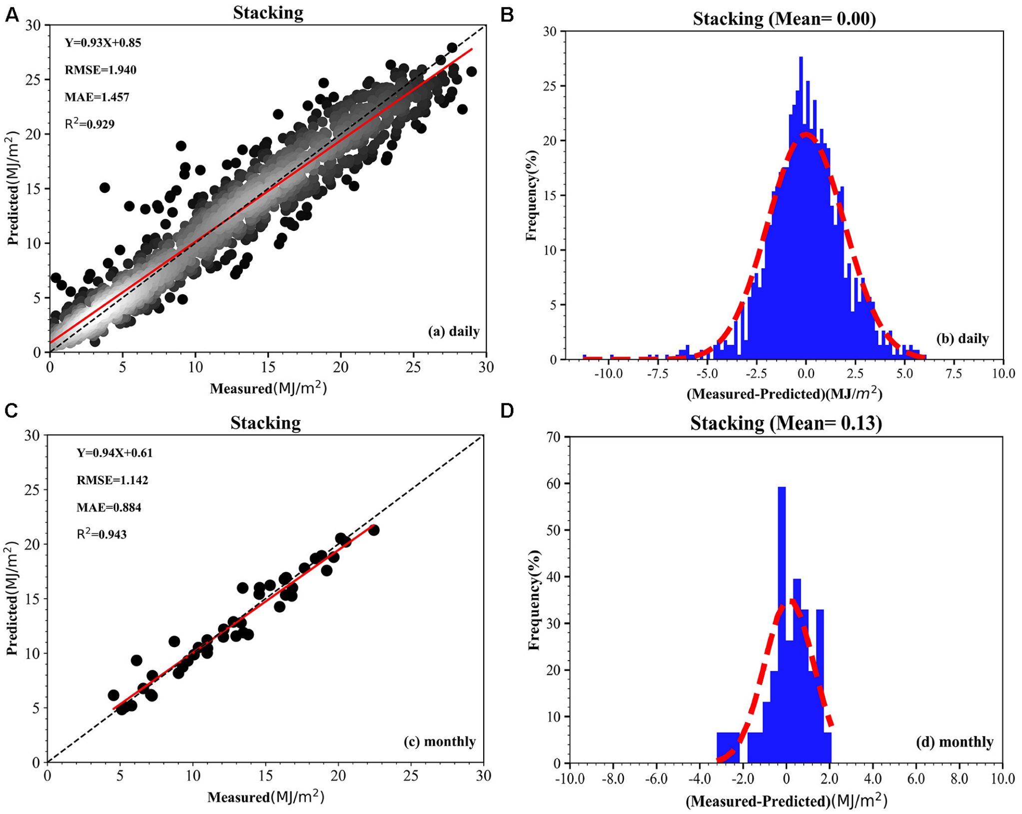

FIGURE 10 | (A–D) Scatter plot and distribution of deviation of the prediction results of the stacking model.

CONCLUSION

We performed data preprocessing and variable selection based on meteorological elements and solar radiation data from 1980 to 2016 for Ganzhou station, China. Then, 12 machine learning models were developed using Sklearn and the Xgb library. By comparing and evaluating the predictive ability of the 12 machine learning models using R^2, the RMSE, the MAE and BIAS indices, the XGBoost, GPR, GBRT, and random forest models were selected as the first layer, and multiple linear regression was selected as the second layer to construct a stacking model to predict solar radiation.

Using the random forest algorithm to select the variables, the SSD was identified as the most important variable. The time series of the annual maximum GST-mean and the corresponding solar radiation value from 1980 to 2016 showed that the maximum GTS-max increases with the solar radiation, which confirms the importance of solar radiation in compound extreme climate events. The GBRT, XGBoost, random forest, and GPR models performed better than the other models for the daily and monthly datasets. The GBRT model had the best predictive ability for the daily datasets, whereas the XGBoost model had the best predictive ability for the monthly datasets. The random forest model had the longest construction time, followed by the GBRT and GPR models, whereas the XGBoost model had the shortest construction time. This phenomenon is related to the principles of the models.

The prediction ability of the stacking model was improved in the daily solar radiation prediction model, but the monthly model performed poorly, which may be related to too little monthly training data. We concluded that the XGBoost model is the best solar radiation value prediction model, although when the amount of data is large, we suggest using the stacking fusion or XGBoost model to build the model.

DATA AVAILABILITY STATEMENT

All meteorological data were obtained from the China Meteorological Data Service Center (CMDC, http://data.cma.cn/en/?r=data/index&cid=6d1b5efbdcbf9a58), which requires an authorized log-in or via off-line data processing and product tailoring services. Specifically, daily observations are found at http://data.cma.cn/en/?r=data/detail&dataCode=SURF_CLI_CHN_MUL_DAY_CES_V3.0.

AUTHOR CONTRIBUTIONS

JK and ZZ conceived the idea of the study. LH analyzed the data and wrote the initial draft of the manuscript. The remaining authors contributed to refining the ideas, carrying out additional analyses, and finalizing this manuscript. All authors contributed to the article and approved the submitted version.

FUNDING

This work was supported by the National Key Research and Development Program of China (Grant No. 2016YFC0803105), National Natural Science Foundation of China (Grant No. 41301423), China Postdoctoral Science Foundation (Grant No. 2018M641926), Projects supported by the National Fund for Study Abroad (Grant No. 201808360065), and Jiangxi Provincial Department of Education Science and Technology Research Projects (Grant No. GJJ150661).

SUPPLEMENTARY MATERIAL

The Supplementary Material for this article can be found online at: https://www.frontiersin.org/articles/10.3389/feart.2021.596860/full#supplementary-material

REFERENCES

Agarwal, S., and Chowdary, C. R. (2020). A-stacking and A-bagging: adaptive versions of ensemble learning algorithms for spoof fingerprint detection. *Expert Syst. Appl.* 146:113160. doi: 10.1016/j.eswa.2019.113160

Angra, S., and Ahuja, S. (2017). "Machine learning and its applications: a review," in *Proceedings of the 2017 International Conference On Big Data Analytics and Computational Intelligence, ICBDACI 2017*, (Piscataway, NJ: IEEE), 57–60. doi: 10.1109/ICBDACI.2017.8070809

Angstrom, A. (1924). Solar and terrestrial radiation. Report to the international commission for solar research on actinometric investigations of solar and atmospheric radiation. *Q. J. R. Meteorol. Soc.* 50, 121–126. doi: 10.1002/qj.49705021008

Azadeh, A., Maghsoudi, A., and Sohrabkhani, S. (2009). An integrated artificial neural networks approach for predicting global radiation. *Energy Convers. Manag.* 50, 1497–1505. doi: 10.1016/j.enconman.2009.02.019

Baczek, T., Wiczling, P., Marszałł, M., Heyden, Y. V., and Kaliszan, R. (2005). Prediction of peptide retention at different HPLC conditions from multiple linear regression models. *J. Proteome Res.* 4, 555–563. doi: 10.1021/pr049780r

Basheer, I. A., and Hajmeer, M. (2000). Artificial neural networks: fundamentals, computing, design, and application. *J. Microbiol. Methods* 43, 3–31. doi: 10.1016/S0167-7012(00)00201-3

Beer, C., Reichstein, M., Tomelleri, E., Ciais, P., Jung, M., Carvalhais, N., et al. (2010). Terrestrial gross carbon dioxide uptake: Global distribution and covariation with climate. *Science* 329, 834–838. doi: 10.1126/science.1184984

Besharat, F., Dehghan, A. A., and Faghih, A. R. (2013). Empirical models for estimating global solar radiation: a review and case study. *Renew. Sustain. Energy Rev.* 21, 798–821. doi: 10.1016/j.rser.2012.12.043

Bhargawa, A., and Singh, A. K. (2019). Solar irradiance, climatic indicators and climate change – An empirical analysis. *Adv. Space Res.* 64, 271–277. doi: 10.1016/j.asr.2019.03.018

Bristow, K. L., and Campbell, G. S. (1984). On the relationship between incoming solar radiation and daily maximum and minimum temperature. *Agric. For. Meteorol.* 31, 159–166. doi: 10.1016/0168-1923(84)90017-0

Brodley, C. E., and Friedl, M. A. (1997). Decision tree classification of land cover from remotely sensed data. *Rem. Sens. Environ.* 61, 399–409. doi: 10.1016/S0034-4257(97)00049-7

Budyko, M. I. (1969). The effect of solar radiation variations on the climate of the Earth. *Tellus* 21, 611–619. doi: 10.3402/tellusa.v21i5.10109

Burges, C. J. C. (1998). A tutorial on support vector machines for pattern recognition. *Discov. Data Min. Knowl. Discov.* 2, 121–167.

Chen, J. L., Li, G. S., and Wu, S. J. (2013). Assessing the potential of support vector machine for estimating daily solar radiation using sunshine duration. *Energy Convers. Manag.* 75, 311–318. doi: 10.1016/j.enconman.2013.06.034

Chen, J. L., Liu, H. B., Wu, W., and Xie, D. T. (2011). Estimation of monthly solar radiation from measured temperatures using support vector machines – A case study. *Renew. Energy* 36, 413–420. doi: 10.1016/j.renene.2010.06.024

Cline, D. W., Bales, R. C., and Dozier, J. (1998). Estimating the spatial distribution of snow in mountain basins using remote sensing and energy balance modeling. *Water Resour. Res.* 34, 1275–1285. doi: 10.1029/97WR03755

Corazza, A., Di Martino, S., Ferrucci, F., Gravino, C., Sarro, F., and Mendes, E. (2013). Using tabu search to configure support vector regression for effort estimation. *Empir. Softw. Eng.* 18, 506–546. doi: 10.1007/s10664-011-9187-3

Deng, C. W., Huang, G. B., Xu, J., and Tang, J. X. (2015). Extreme learning machines: new trends and applications. *Sci. China Inf. Sci.* 58, 1–16. doi: 10.1007/s11432-014-5269-3

Deng, Z., Zhu, X., Cheng, D., Zong, M., and Zhang, S. (2016). Efficient kNN classification algorithm for big data. *Neurocomputing* 195, 143–148. doi: 10.1016/j.neucom.2015.08.112

Ebden, M. (2015). Gaussian processes: a quick introduction. *arXiv* [Preprint] arXiv:1505.02965,

Fadare, D. A. (2009). Modelling of solar energy potential in Nigeria using an artificial neural network model. *Appl. Energy* 86, 1410–1422. doi: 10.1016/j.apenergy.2008.12.005

Fan, J., Wang, X., Wu, L., Zhou, H., Zhang, F., Yu, X., et al. (2018). Comparison of support vector machine and extreme gradient boosting for predicting daily global solar radiation using temperature and precipitation in humid subtropical climates: a case study in China. *Energy Convers. Manag.* 164, 102–111. doi: 10.1016/j.enconman.2018.02.087

Gao, B., Huang, X., Shi, J., Tai, Y., and Zhang, J. (2020). Hourly forecasting of solar irradiance based on CEEMDAN and multi-strategy CNN-LSTM neural networks. *Renew. Energy* 162, 1665–1683. doi: 10.1016/j.renene.2020.09.141

García, S., Luengo, J., and Herrera, F. (2016). Tutorial on practical tips of the most influential data preprocessing algorithms in data mining. *Knowledge Based Syst.* 98, 1–29. doi: 10.1016/j.knosys.2015.12.006

Garland, F. C., Garland, C. F., Gorham, E. D., and Young, J. F. (1990). Geographic variation in breast cancer mortality in the United States: a hypothesis involving exposure to solar radiation. *Prev. Med. (Baltim).* 19, 614–622. doi: 10.1016/0091-7435(90)90058-R

Grant, W. B., and Tuohimaa, P. (2004). Geographic variation of prostate cancer mortality rates in the United States: Implications for prostate cancer risk related to vitamin D [3] (multiple letters). *Int. J. Cancer* 111, 470–471. doi: 10.1002/ijc.20220

Gueymard, C. A. (2003). Direct solar transmittance and irradiance predictions with broadband models. Part I: detailed theoretical performance assessment. *Sol. Energy* 74, 355–379. doi: 10.1016/S0038-092X(03)00195-6

Halabi, L. M., Mekhilef, S., and Hossain, M. (2018). Performance evaluation of hybrid adaptive neuro-fuzzy inference system models for predicting monthly global solar radiation. *Appl. Energy* 213, 247–261. doi: 10.1016/j.apenergy.2018.01.035

Hoogenboom, G. (2000). Contribution of agrometeorology to the simulation of crop production and its applications. *Agric. Forest Meteorol.* 103, 137–157. doi: 10.1016/S0168-1923(00)00108-8

Huang, G., Huang, G. B., Song, S., and You, K. (2015). Trends in extreme learning machines: a review. *Neural Netw.* 61, 32–48. doi: 10.1016/j.neunet.2014.10.001

Huang, J., Li, Y. F., and Xie, M. (2015). An empirical analysis of data preprocessing for machine learning-based software cost estimation. *Inf. Softw. Technol.* 67, 108–127. doi: 10.1016/j.infsof.2015.07.004

Huang, S. J., and Chiu, N. H. (2006). Optimization of analogy weights by genetic algorithm for software effort estimation. *Inf. Softw. Technol.* 48, 1034–1045. doi: 10.1016/j.infsof.2005.12.020

Islam, M. D., Kubo, I., Ohadi, M., and Alili, A. A. (2009). Measurement of solar energy radiation in Abu Dhabi, UAE. *Appl. Energy* 86, 511–515. doi: 10.1016/j.apenergy.2008.07.012

Iziomon, M. G., and Mayer, H. (2002). Assessment of some global solar radiation parameterizations. *J. Atmos. Solar Terrestrial Phys.* 64, 1631–1643. doi: 10.1016/S1364-6826(02)00131-1

Jiang, G., and Wang, W. (2017). Error estimation based on variance analysis of k-fold cross-validation. *Pattern Recognit.* 69, 94–106. doi: 10.1016/j.patcog.2017.03.025

Jiang, Y. (2009). Computation of monthly mean daily global solar radiation in China using artificial neural networks and comparison with other empirical models. *Energy* 34, 1276–1283. doi: 10.1016/j.energy.2009.05.009

Johnson, N. E., Bonczak, B., and Kontokosta, C. E. (2018). Using a gradient boosting model to improve the performance of low-cost aerosol monitors in a dense, heterogeneous urban environment. *Atmos. Environ.* 184, 9–16. doi: 10.1016/j.atmosenv.2018.04.019

Kapwata, T., and Gebreslasie, M. T. (2016). Random forest variable selection in spatial malaria transmission modelling in Mpumalanga Province,South Africa. *Geospat. Health* 11, 251–262. doi: 10.4081/gh.2016.434

Khatibi Bardsiri, V., Jawawi, D. N. A., Hashim, S. Z. M., and Khatibi, E. (2013). A PSO-based model to increase the accuracy of software development effort estimation. *Softw. Qual. J.* 21, 501–526. doi: 10.1007/s11219-012-9183-x

Li, M., Tian, J., and Chen, F. (2008). Improving multiclass pattern recognition with a co-evolutionary RBFNN. *Pattern Recognit. Lett.* 29, 392–406. doi: 10.1016/j.patrec.2007.10.019

Li, M. F., Fan, L., Liu, H. B., Wu, W., and Chen, J. L. (2012). Impact of time interval on the ångström-Prescott coefficients and their interchangeability in estimating radiation. *Renew. Energy* 44, 431–438. doi: 10.1016/j.renene.2012.01.107

Li, X., Wang, L., and Sung, E. (2008). AdaBoost with SVM-based component classifiers. *Eng. Appl. Artif. Intell.* 21, 785–795. doi: 10.1016/j.engappai.2007.07.001

Linares-Rodríguez, A., Ruiz-Arias, J. A., Pozo-Vázquez, D., and Tovar-Pescador, J. (2011). Generation of synthetic daily global solar radiation data based on ERA-Interim reanalysis and artificial neural networks. *Energy* 36, 5356–5365. doi: 10.1016/j.energy.2011.06.044

Lu, N., Qin, J., Yang, K., and Sun, J. (2011). A simple and efficient algorithm to estimate daily global solar radiation from geostationary satellite data. *Energy* 36, 3179–3188. doi: 10.1016/j.energy.2011.03.007

Mahanty, R. N., and Dutta Gupta, P. B. (2004). Application of RBF neural network to fault classification and location in transmission lines. *IEE Proc. Gener. Transm. Distrib.* 151, 201–212. doi: 10.1049/ip-gtd:20040098

Makade, R. G., Chakrabarti, S., and Jamil, B. (2019). Prediction of global solar radiation using a single empirical model for diversified locations across India. *Urban Clim.* 29:100492. doi: 10.1016/j.uclim.2019.100492

Meenal, R., and Selvakumar, A. I. (2018). Assessment of SVM, empirical and ANN based solar radiation prediction models with most influencing input parameters. *Renew. Energy* 121, 324–343. doi: 10.1016/j.renene.2017.12.005

Mellit, A. (2008). Artificial Intelligence technique for modelling and forecasting of solar radiation data: a review. *Int. J. Artif. Intell. Soft Comput.* 1:52. doi: 10.1504/ijaisc.2008.021264

Mishra, M., Byomakesha Dash, P., Nayak, J., Naik, B., and Kumar Swain, S. (2020). Deep learning and wavelet transform integrated approach for short-term solar PV power prediction. *Meas. J. Int. Meas. Confed.* 166:108250. doi: 10.1016/j.measurement.2020.108250

Mohammadi, K., Shamshirband, S., Petkoviæ, D., and Khorasanizadeh, H. (2016). Determining the most important variables for diffuse solar radiation prediction using adaptive neuro-fuzzy methodology; Case study: city of Kerman, Iran. *Renew. Sustain. Energy Rev.* 53, 1570–1579. doi: 10.1016/j.rser.2015.09.028

Moreno, A., Gilabert, M. A., and Martínez, B. (2011). Mapping daily global solar irradiation over Spain: a comparative study of selected approaches. *Sol. Energy* 85, 2072–2084. doi: 10.1016/j.solener.2011.05.017

Nathans, L., Oswald, F. L., and Nimon, K. (2012). Interpreting multiple linear regression: a guidebook of variable importance. *Pract. Assesment Res. Eval.* 17, 1–19. doi: 10.3102/00346543074004525

Nguyen-Tuong, D., Seeger, M., and Peters, J. (2009). Model learning with local Gaussian process regression. *Adv. Robot.* 23, 2015–2034. doi: 10.1163/016918609X12529286896877

Nielsen, D. (2016). *Tree Boosting With XGBoost: Why Does XGBoost Win Every Machine Learning Competition?* Ph. D. Thesis. Trondheim: Norwegian University of Science and Technology. doi: 10.1111/j.1758-5899.2011.00096.x

Ohunakin, O. S., Adaramola, M. S., Oyewola, O. M., Matthew, O. J., and Fagbenle, R. O. (2015). The effect of climate change on solar radiation in Nigeria. *Sol. Energy* 116, 272–286. doi: 10.1016/j.solener.2015.03.027

Olatomiwa, L., Mekhilef, S., Shamshirband, S., Mohammadi, K., Petkoviæ, D., and Sudheer, C. (2015). A support vector machine-firefly algorithm-based model for global solar radiation prediction. *Sol. Energy* 115, 632–644. doi: 10.1016/j.solener.2015.03.015

Pang, Z., Niu, F., and O'Neill, Z. (2020). Solar radiation prediction using recurrent neural network and artificial neural network: a case study with comparisons. *Renew. Energy* 156, 279–289. doi: 10.1016/j.renene.2020.04.042

Persson, C., Bacher, P., Shiga, T., and Madsen, H. (2017). Multi-site solar power forecasting using gradient boosted regression trees. *Sol. Energy* 150, 423–436. doi: 10.1016/j.solener.2017.04.066

Prescott, J. A. (1940). Evaporation from a water surface in relation to solar radiation. *Trans. R. Soc. South Aust.* 61, 114–118. Available online at: https://ci.nii.ac.jp/naid/10025613338/en/

Quinlan, J. R. (1999). Simplifying decision trees. *Int. J. Hum. Comput. Stud.* 51, 497–510. doi: 10.1006/ijhc.1987.0321

Salazar, G. A. (2011). Estimation of monthly values of atmospheric turbidity using measured values of global irradiation and estimated values from CSR and Yang Hybrid models. *Study case: Argentina. Atmos. Environ.* 45, 2465–2472. doi: 10.1016/j.atmosenv.2011.02.048

Shamshirband, S., Mohammadi, K., Tong, C. W., Zamani, M., Motamedi, S., and Ch, S. (2016). A hybrid SVM-FFA method for prediction of monthly mean global solar radiation. *Theor. Appl. Climatol.* 125, 53–65. doi: 10.1007/s00704-015-1482-2

Shamshirband, S., Mosavi, A., Rabczuk, T., Nabipour, N., and Chau, K. W. (2020). Prediction of significant wave height; comparison between nested grid numerical model, and machine learning models of artificial neural networks, extreme learning and support vector machines. *Eng. Appl. Comput. Fluid Mech.* 14, 805–817. doi: 10.1080/19942060.2020.1773932

Shamshirband, S., Rabczuk, T., and Chau, K. W. (2019). A survey of deep learning techniques: application in wind and solar energy resources. *IEEE Access.* 7, 164650–164666. doi: 10.1109/ACCESS.2019.2951750

Shen, H., and Chou, K. C. (2005). Using optimized evidence-theoretic K-nearest neighbor classifier and pseudo-amino acid composition to predict membrane protein types. *Biochem. Biophys. Res. Commun.* 334, 288–292. doi: 10.1016/j.bbrc.2005.06.087

Siingh, D., Singh, R. P., Singh, A. K., Kulkarni, M. N., Gautam, A. S., and Singh, A. K. (2011). Solar activity, lightning and climate. *Surv. Geophys.* 32, 659–703. doi: 10.1007/s10712-011-9127-1

Suehrcke, H., Bowden, R. S., and Hollands, K. G. T. (2013). Relationship between sunshine duration and solar radiation. *Sol. Energy* 92, 160–171. doi: 10.1016/j.solener.2013.02.026

Sun, H., Gui, D., Yan, B., Liu, Y., Liao, W., Zhu, Y., et al. (2016). Assessing the potential of random forest method for estimating solar radiation using air pollution index. *Energy Convers. Manag.* 119, 121–129. doi: 10.1016/j.enconman.2016.04.051

Torlay, L., Perrone-Bertolotti, M., Thomas, E., and Baciu, M. (2017). Machine learning–XGBoost analysis of language networks to classify patients with epilepsy. *Brain Inform.* 4, 159–169. doi: 10.1007/s40708-017-0065-7

Trappey, A. J. C., Hsu, F. C., Trappey, C. V., and Lin, C. I. (2006). Development of a patent document classification and search platform using a back-propagation network. *Expert Syst. Appl.* 31, 755–765. doi: 10.1016/j.eswa.2006.01.013

Van Ooyen, A., and Nienhuis, B. (1992). Improving the convergence of the back-propagation algorithm. *Neural Netw.* 5, 465–471. doi: 10.1016/0893-6080(92)90008-7

Voyant, C., Muselli, M., Paoli, C., and Nivet, M. L. (2012). Numerical weather prediction (NWP) and hybrid ARMA/ANN model to predict global radiation. *Energy* 39, 341–355. doi: 10.1016/j.energy.2012.01.006

Wang, L., Kisi, O., Zounemat-Kermani, M., Salazar, G. A., Zhu, Z., and Gong, W. (2016). Solar radiation prediction using different techniques: model evaluation and comparison. *Renew. Sustain. Energy Rev.* 61, 384–397. doi: 10.1016/j.rser.2016.04.024

Wang, R. (2012). AdaBoost for feature selection, classification and its relation with SVM, a review. *Phys. Proc.* 25, 800–807. doi: 10.1016/j.phpro.2012.03.160

Wild, M. (2009). Global dimming and brightening: a review. *J. Geophys. Res. Atmos.* 114:D00D16. doi: 10.1029/2008JD011470

Will, A., Bustos, J., Bocco, M., Gotay, J., and Lamelas, C. (2013). On the use of niching genetic algorithms for variable selection in solar radiation estimation. *Renew. Energy* 50, 168–176. doi: 10.1016/j.renene.2012.06.039

Xue, X. (2017). Prediction of daily diffuse solar radiation using artificial neural networks. *Int. J. Hydrogen Energy* 42, 28214–28221. doi: 10.1016/j.ijhydene.2017.09.150

Yang, H. T., Huang, C. M., Huang, Y. C., and Pai, Y. S. (2014). A weather-based hybrid method for 1-day ahead hourly forecasting of PV power output. *IEEE Trans. Sustain. Energy* 5, 917–926. doi: 10.1109/TSTE.2014.2313600

Yang, K., Huang, G. W., and Tamai, N. (2001). Hybrid model for estimating global solar radiation. *Sol. Energy* 70, 13–22. doi: 10.1016/S0038-092X(00)00121-3

Younes, S., Claywell, R., and Muneer, T. (2005). Quality control of solar radiation data: present status and proposed new approaches. *Energy* 30, 1533–1549. doi: 10.1016/j.energy.2004.04.031

Zeng, Z., Wang, Z., Gui, K., Yan, X., Gao, M., Luo, M., et al. (2020). Daily global solar radiation in China estimated from high-density meteorological observations: a random forest model framework. *Earth Space Sci.* 7:e2019EA001058. doi: 10.1029/2019EA001058

Zhang, Y., and Haghani, A. (2015). A gradient boosting method to improve travel time prediction. *Transp. Res. Part C Emerg. Technol.* 58, 308–324. doi: 10.1016/j.trc.2015.02.019

Zhu, J., Zou, H., Rosset, S., and Hastie, T. (2006). Multi-class AdaBoost. *Stat. Interface* 2, 349–360. doi: 10.4310/SII.2009.v2.n3.a8

Conflict of Interest: The authors declare that the research was conducted in the absence of any commercial or financial relationships that could be construed as a potential conflict of interest.

The reviewer YY declared a past co-authorship with one of the authors ZZ to the handling editor.

ORIGINAL RESEARCH
published: 03 May 2021
doi: 10.3389/feart.2021.678230

Modulations of Synoptic Weather Patterns on Warm-Sector Heavy Rainfall in South China: Insights From High-Density Observations With Principal Component Analysis

Wanju Li[1,2], Xueyan Bi[2]*, Lifang Sheng[1], Yali Luo[3] and Jianhua Sun[4]

[1] College of Oceanic and Atmospheric Sciences, Ocean University of China, Qingdao, China, [2] Guangzhou Institute of Tropical and Marine Meteorology, China Meteorological Administration, Guangzhou, China, [3] State Key Laboratory of Severe Weather, Chinese Academy of Meteorological Sciences, Beijing, China, [4] Key Laboratory of Cloud-Precipitation Physics and Severe Storms, Institute of Atmospheric Physics, Chinese Academy of Sciences, Beijing, China

OPEN ACCESS

Edited by:
Ming Luo,
Sun Yat-sen University, China

Reviewed by:
Xiaoming Shi,
Hong Kong University of Science and Technology, Hong Kong
Guicai Ning,
The Chinese University of Hong Kong, China

***Correspondence:**
Xueyan Bi
xybi@gd121.cn

Specialty section:
This article was submitted to Atmospheric Science, a section of the journal Frontiers in Earth Science

Received: 09 March 2021
Accepted: 13 April 2021
Published: 03 May 2021

Citation:
Li W, Bi X, Sheng L, Luo Y and Sun J (2021) Modulations of Synoptic Weather Patterns on Warm-Sector Heavy Rainfall in South China: Insights From High-Density Observations With Principal Component Analysis. Front. Earth Sci. 9:678230. doi: 10.3389/feart.2021.678230

Based on hourly high-density precipitation data in Guangdong Province, China, 134 warm-sector heavy rainfall (WSHR) events were selected from 2016 to 2018. The synoptic weather patterns of these WSHR events were objectively classified using T-mode principal component analysis. Six WSHR weather patterns were identified, as follows: Type 1-southwest (T1-SW), Type 2-southeast (T2-SE), Type 3-coastal jets I (T3-CJI), Type 4-coastal jets II (T4-CJ II), Type 5-western low vortex (T5-WL), and Type 6-high-pressure (T6-HP). Three high-occurrence WSHR centers were finally extracted: the areas of Yangjiang and Shanwei, and the urban agglomeration of Guangdong–Hong Kong–Macao Greater Bay Area (GBA). Compared with the other five patterns, T6-HP is a newly identified WSHR weather pattern, which is related to a local/small-scale weather system in the context of anomalous northward movement of the western Pacific subtropical high. Notably, the precipitation area of the T6-HP type of WSHR event is smaller, which can only be captured by high-density observations. In addition, the occurrence locations of six large-scale extreme precipitation events were closely associated with the urban agglomerations in GBA, implying that urbanization plays an important role in extreme magnitudes of large-scale WSHR events and their occurrence centers.

Keywords: warm-sector heavy rainfall, objective weather classification, T-mode principal component analysis, South China, high-density observations

INTRODUCTION

South China has the most abundant rainfall in China. Rainstorms in South China usually occur not only in front and behind the front, but also in the warm sector south of the front. Due to the effect of the inconspicuous baroclinicity of the environment, sufficient atmospheric water vapor, strong instability, complex topography, and underlying surface, the warm-sector heavy rainfall (WSHR) often happens suddenly, with significant regional characteristics, and frequent activities of micro and meso-scale systems, which is difficult to forecast (He et al., 2016; Sun et al., 2019).

Previous studies have shown that there are many factors influencing WSHR events in South China, including large-scale circulation, weather systems, the underlying surface, topography, and cloud microphysical processes (Zhao and Wang, 2009). The atmospheric circulations in the middle and high latitudes of Eurasia, the West Pacific subtropical high, the South Asian high, and the subtropical westerly jet are the main weather systems that lead to WSHR in South China. The weather system plays an important role in the configuration and adjustment of the conditions of the convective environment, such as vertical shear, convective stability, and water vapor distribution (Wang et al., 2018). The typical weather systems of WSHR events have been classified and summarized based on different criteria. For example, the large-scale circulation patterns can be divided into the Eurasian circulation type, subtropical high type, and tropospheric divergence type (Li et al., 1981; Zhao and Wang, 2009). According to the weather situation of the low-level troposphere, Huang (1986) summarized four types of WSHR: warm wind shear line, the Low Level Jet (LLJ) along coastlines, the prefrontal LLJ, and cold fronts or quasi-stationary fronts. Lin (2006) classified WSHR in the pre-rainy season into three types: (1) high-altitude trough, which means heavy rain caused by the convergence of southerly winds in the boundary layer and forced uplift of the terrain; (2) strong southwest monsoon, which is a type of heavy rain caused by strengthening of the monsoon and formation of low-level jets; and (3) backflow heavy rainfall, which is where the cold air flows back after moving out to sea, and the easterly and southwesterly winds converge. This last type is relatively rare compared with the other two. Chen et al. (2012) used reanalysis data and 77 meteorological stations to count the WSHR events from 2000 to 2009 in May and June, and divided them into three types: shear linear, low vortex, and southerly wind. He et al. (2016) summarized three WSHR weather system configuration models – namely, boundary layer convergence line type, southerly wind speed convergence type, and strong southwest jet type. Based on the data of 124 national stations in the South China region, Liu et al. (2019) identified 177 WSHR events from 1982 to 2015 and summarized their spatial and temporal distribution characteristics. They suggested that the weather patterns of WSHR in South China mainly include wind shear, a low vortex, southerly wind, and backflow. However, despite these efforts, due to differences in case selection, classification, data selection, and study period, no unified conclusion has yet been reached on classifying the weather situation that affects WSHR.

The main influencing factors of WSHR are the southerly wind, jet stream, low vortex, and shear line, which play key roles in determining the location, time, and intensify of WSHR. Based on statistical analysis of operational practice and experience, and by using precipitation data from national basic stations along with reanalysis data, previous studies mainly classified the WSHR events before 2016, and the statistical results were mostly the typical circulation characteristics. However, WSHR is sometimes caused by abnormal weather patterns, which tend to be small in scope, and the width of some extremely heavy rains are only 20–30 km (Lin, 2006).

To date, there have been few examples of applying objective weather classification methods to studying the weather pattern statistics of WSHR. With this in mind, the present paper uses an objective classification method to classify the weather situation affecting WSHR. Not only can it identify the typical circulation situation when the rainstorm occurs, but it can also distinguish the abnormal circulation, so as to better reflect the temporal and spatial characteristics of precipitation in different types of WSHR events.

Guangdong Province has a high spatiotemporal density of automatic weather stations (Wu et al., 2020), As the increased station density, more extreme precipitation events can be recorded by automatic weather stations. For example, a persistent torrential rain event associated with monsoon depression occurred in Guangdong from 27 August to 1 September 2018 resulting in a 24 h rainfall amount of 1056.7 mm recorded by automatic weather station, which refreshed the historical record of Guangdong Province (Cai et al., 2019). Hence, we employed the data of this dense observation station network, which is conducive to capturing small-scale processes, to explore WSHR events. The rest of the paper is organized as follows: The data and methods are introduced in section 2. The WSHR selection and classification results are presented in sections 3 and 4, respectively. The temporal and spatial distribution characteristics of WSHR under different weather types are analyzed in section 5. The possible reasons for abnormal weather are discussed in section 6, and conclusions are given in section 7.

DATA AND METHODS

Data

The rainfall cases were selected by using the hourly precipitation data of Guangdong regional automatic stations from 1 April 2016 to 30 September 2018. Considering the continuity of the data, the proportion of effective hourly precipitation data was required to be no less than 85% of the total data, meaning a total of 2,667 stations were selected. To identify the synoptic patterns, we used ERA5 [the fifth major global reanalysis produced by the European Center for Medium-Range Weather Forecasts (ECMWF)]. Severe precipitation events in southern China caused by typhoons were excluded (Ying et al., 2014).

Classification Method

T-mode principal component analysis (PCT) in COST733 software (Philipp et al., 2014) were used to objectively classify the weather system when the rainstorm occurred in WSHR events. COST733 is a weather classification software developed by the EU COST (European Cooperation in Science and Technology) 733 program. PCT is the most widely used objective classification method at present. Huth (1996) pointed out that the principal component analysis (PCA) method is more stable in time and space, less dependent on preset parameters, and can better retain the information of the original field, making it a more promising objective classification method. PCT is based on the PCA, and further improved by Huth (2000); and Huth et al. (2008). T-mode means daily patterns form the columns in the input data matrix, whereas the grid-point values form its rows. The PCT method has been widely used in classifying weather patterns in research on precipitation, ozone, and haze, amongst others (Dong et al., 2020; Ning et al., 2020; Yang et al., 2021; Zong et al., 2021).

In this study, daily mean GH at 850 hPa level is chosen to identify synoptic patterns of WSHR, as the water vapor flux is closely related to 850 hPa synoptic systems (Yang et al., 2021). More detailed information about the objective classification and the PCT method is provided in the supplementary document. To assess the performance of synoptic classification and determine the number of classes, the explained cluster variance (ECV) is selected in this study (Hoffmann and Schlünzen, 2013; Philipp et al., 2014; Ning et al., 2019, 2020). The detailed information about the ECV is also provided in the supplementary document.

DEFINITION AND SELECTION OF WSHR EVENTS

Due to the complexity and variability of WSHR, there is no uniform definition of the WSHR in South China. According to Liu et al. (2019), heavy precipitation events were selected first, as follows: (1) the precipitation affected by typhoons was eliminated; (2) the daily precipitation of three or more stations

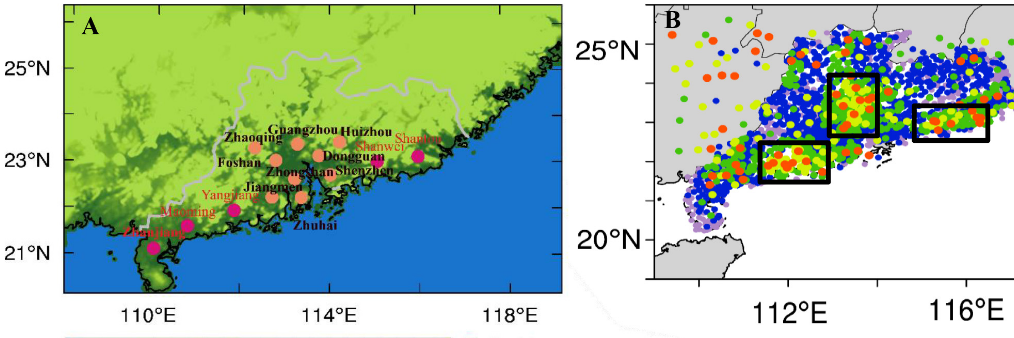

FIGURE 1 | (A) the spatial distribution of major cities mentioned below in Guangdong Province **(B)** Average daily precipitation during WSHR events recorded by meteorological stations from April to June 2016–2018 (units: mm/d). The black boxes indicate the locations of the three heavy rainfall centers.

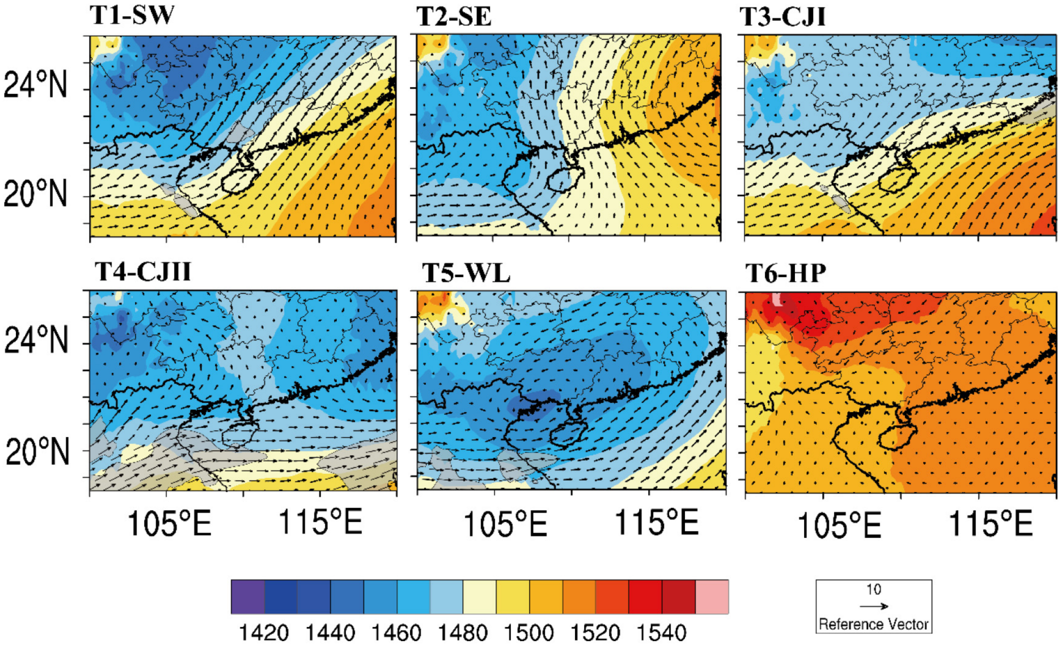

FIGURE 2 | Mean 850-hPa geopotential height and wind vector in six types of WSHR. The gray shading indicates areas where the wind speed is greater than 10 m/s.

whose distance was less than 100 km was greater than or equal to 50 mm; (3) the total precipitation of a single station in three consecutive hours was greater than or equal to 30 mm, and the hourly precipitation of each of these 3 h was greater than or equal to 5 mm (Wang et al., 2014). In these heavy precipitation events, the criteria for selecting the WSHR events were as follows: (1) According to the distribution of the daily precipitation of the selected cases, sites were selected that met the requirements of three consecutive hours of precipitation greater than or equal to 30 mm and a single hour greater than or equal to 5 mm. In the precipitation area, the station with the largest amount of precipitation that met the above conditions was the representative station (if there were multiple precipitation areas at the same time, a representative station for each precipitation area was chosen). (2) Along the longitude of each representative station, a vertical profile of the relevant physical quantities was drawn (potential pseudo-equivalent temperature (θ_{se}), temperature advection, station precipitation) (the figure is omitted), and the location of the front (with dense θ_{se} profiles), cold advection, and precipitation determined. (3) If there was no obvious front in the profile, the middle and low altitudes of the precipitation area featured southerly wind and the distance from the surface northerly wind was greater than 200 km. (4) If there was an obvious frontal system in the profile, the distance between the precipitation area and the front was greater than 200 km.

Based on the data of 2,667 automatic stations in Guangdong, 134 cases of WSHR events were selected from April to September 2016 to 2018. By counting the average rainfall of each station in all WSHR events (**Figure 1**), it can be seen that the average precipitation of WSHR events in Guangdong is more in the coastal area and less in the inland area. There are three WSHR centers. In addition to the two WSHR centers on the western coast of Guangdong near Yangjiang and the eastern coast of Guangdong near Shanwei mentioned by Wu et al. (2019), a precipitation center over the urban agglomeration near Guangzhou is also apparent.

OBJECTIVE WEATHER CLASSIFICATION OF WSHR

Classification Results

PCT objective typing was performed on the 850 hPa geopotential height field, and six circulation types were obtained (**Figure 2**). These patterns exhibit distinct spatial characteristics, as follows: (1) Type1-southwest wind (T1-SW), in which Guangdong is mainly controlled by southwesterly wind. This kind of weather situation is similar to the southerly wind pattern described in previous study (Chen et al., 2012). The rainstorm of T1-SW is mostly caused by the convergent shear of the southwesterly wind. It is a common type of rainstorm in WSHR (Chen et al., 2012), and accounts for nearly half of the total (**Table 1**). (2) Type2-southeast wind (T2-SE), in which the southeasterly wind is perpendicular to the coastline, which is similar to the southerly

TABLE 1 | Number and percentage of WSHR events for six synoptic weather types.

	WSHR events	Percentage
T1-SW	66	49.20%
T2-SE	32	23.80%
T3-CJI	16	11.90%
T4-CJII	2	1.50%
T5-WL	13	9.70%
T6-HP	5	3.70%

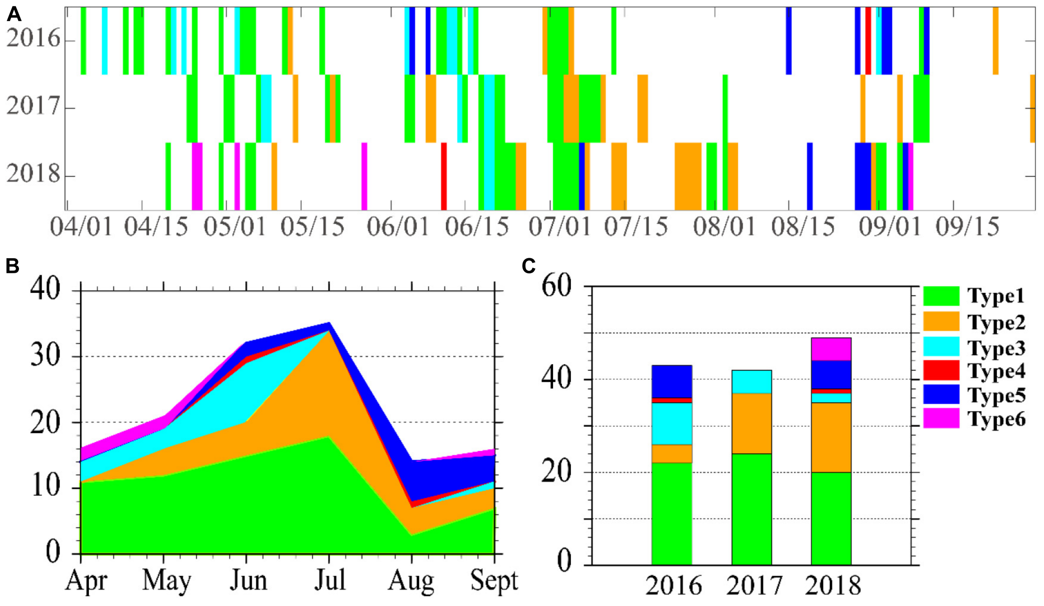

FIGURE 3 | Distributions of WSHR during six synoptic weather types: **(A)** daily, **(B)** monthly, and **(C)** annual.

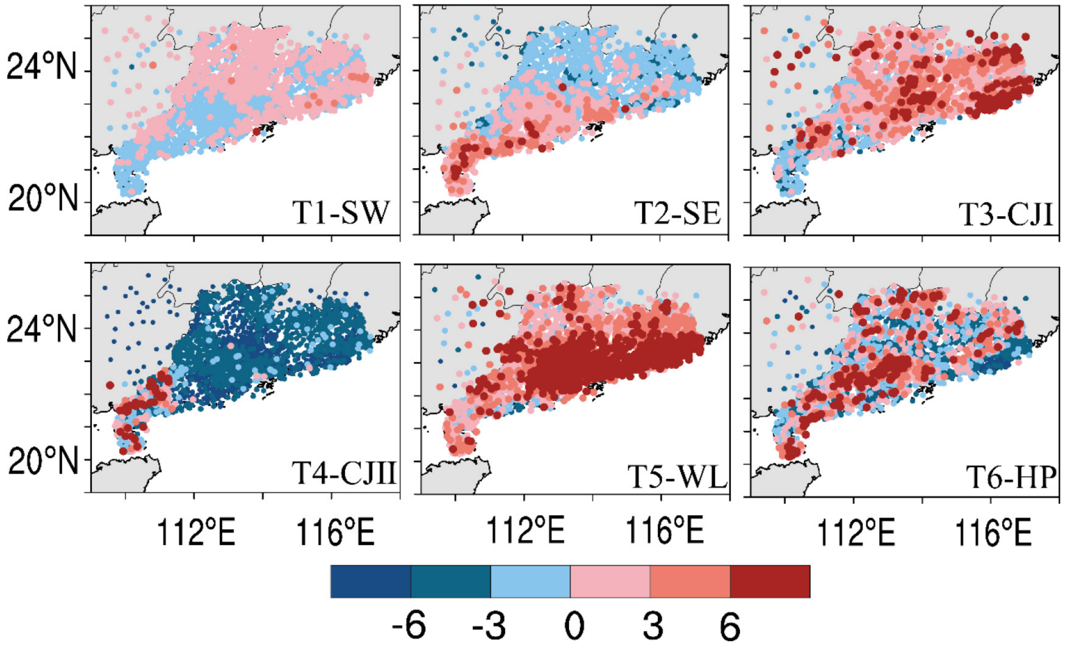

FIGURE 4 | Average daily precipitation anomaly of WSHR for six synoptic weather types (units: mm/d).

TABLE 2 | Comparison of the precipitation area with previous studies.

	Precipitation area in previous research	Precipitation area in this research
T1-SW	Around Yangjiang (Chen et al., 2012)	Yangjiang, Guangzhou, and Shanwei
T2-SE	Yangjiang and Jiangmen area (Miao et al., 2018)	Yangjiang, Jiangmen, and Zhanjiang
T3-CJI	Pearl River Estuary to East Coast of Guangdong (Miao et al., 2018)	GBA and the Shantou area
T4-CJII	/	Zhanjiang
T5-WL	Shantou (Chen et al., 2012; Liu et al., 2019)	The GBA and the coastal areas of Shantou
T6-HP	/	The GBA

wind pattern in previous study (Miao et al., 2018). In the pre-rainy season, heavy rain, local heavy rain, and extreme heavy rain that forms along the coast of South China – especially to the west of the Pearl River Estuary in Guangdong – are mostly caused by this circulation (Miao et al., 2018). (3) Type3- coastal jets I (T3-CJI) and (4) Type4- coastal jets II (T4-CJII), which are both accompanied by coastal jets (gray shaded area in **Figure 2**), but differ in that the T3-CJI jet is located to the north and Guangdong is in the jet stream, which is similar to the southwest jet stream (Miao et al., 2018) and the strong southwest jet stream (He et al., 2016). This type of WSHR is mainly triggered by the low-level jet stream axis or the high-wind core, as well as by boundary layer wind speed pulsation and topographic uplift. Compared with previous studies, the T4-CJII jet stream is slightly southerly, and wind speeds converge in Guangdong. (5) Type5-western low vortex (T5-WL), in which there is a low vortex in the western part of Guangdong, and Guangdong is in the front part of the low vortex, which is consistent with the low vortex type obtained in previous studies (Chen et al., 2012; Liu et al., 2019). The precipitation corresponding to this type is large, and the WSHR event occurs in the low vortex circulation area – close to the center of the low vortex (Chen et al., 2012). (6) Type6-high pressure (T6-HP), in which the wind speed in Guangdong is relatively low, and the entire area is under the control of high pressure. This is a new type of weather circulation that cannot be classified into previous weather types. The number of cases and their percentages of the six weather types are shown in **Table 1**. T6-HP has a relatively lower frequency of occurrence, which is different from the typical weather circulation in previous studies and belongs to abnormal weather types.

Temporal and Spatial Characteristics of Different WSHR Types

Figure 3 shows the daily, monthly, and annual distributions of the six synoptic weather types. It can be seen that the six types of circulation have obvious monthly and intra-year changes. The incidence of WSHR is high in June and July, with 32 and 35 occurrences. After August, the frequency of WSHR decreases significantly, with only 14 occurrences. This shows that WSHR occurs not only in the pre-rainy season, but also in the post-rainy season, which should be paid more attention.

As the main circulation type, T1-SW appears throughout almost the whole of the rainy season. T2-SE, T3-CJI, T5-WL, and T6-HP have obvious temporal distributions. The pre-rainy season mainly consists of T3-CJI; the post-rainy season is mainly T5-WL; and T6-HP occurs before the onset of the South China

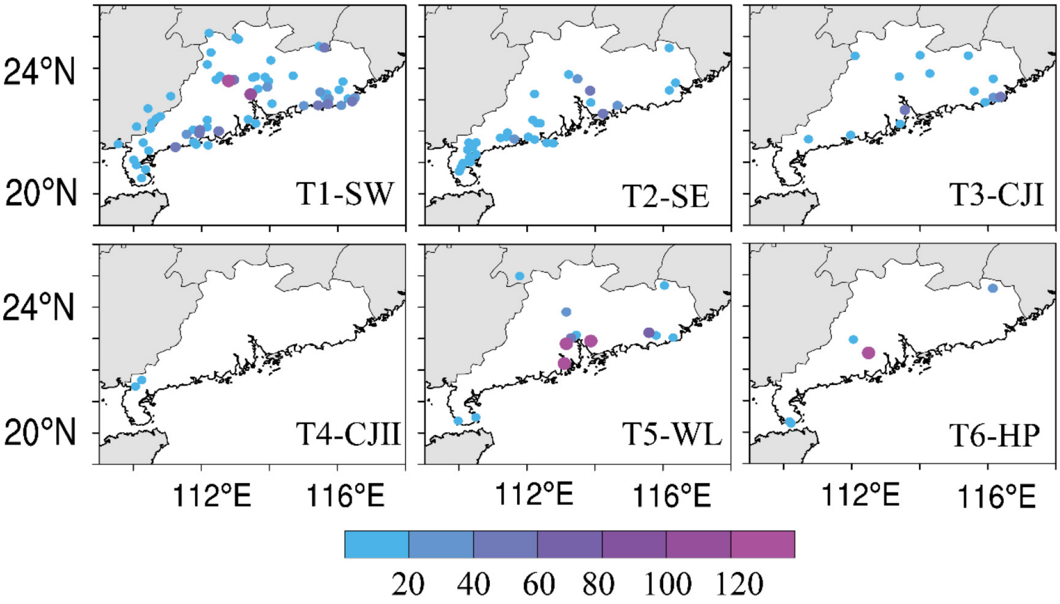

FIGURE 5 | Number of stations with heavy rain (daily precipitation >50 mm/d) around the central station for six weather types.

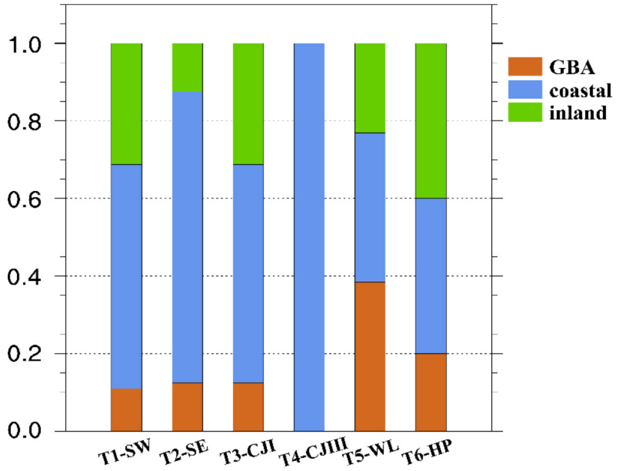

FIGURE 6 | Regional distribution characteristics of six WSHR types.

Sea summer monsoon. Afterward, T6-HP almost disappears, while the frequency of T2-SE increases significantly. T4-CJII only occurs twice, on 30 August 2016 and 11 June 2018, respectively. It is worth mentioning that T6-HP has not been seen in previous studies and only appears in 2018 during the 3 years of statistics (**Figure 3C**), which is discussed in detail below.

Figure 4 shows the anomaly distributions of the corresponding warm rainstorms under six synoptic weather patterns, and mean values of daily precipitation of WSHR are provided in the supplementary document. The spatial patterns of the average precipitation are highly consistent with the anomalies of precipitation, indicating that the results for precipitation spatial patterns of WSHR associated with six synoptic patterns are robust. The precipitation of the T1-SW type is concentrated in the areas of Yangjiang, Guangzhou and Shanwei, while that of a similar weather type in previous work was in Yangjiang area (Chen et al., 2012). The precipitation of the T2-SE type is concentrated in Yangjiang, Jiangmen and Zhanjiang areas, which is similar to previously reported (Miao et al., 2018), but with Zhanjiang added. In previous studies, T3-CJI and T4-CJII were not distinguished owing to their similar weather conditions, but because of the different locations of the jet stream, the precipitation area also differs. The T3-CJI type is concentrated over the urban agglomerations of the Guangdong – Hong Kong – Macao Greater Bay Area (GBA) urban agglomeration and Shantou, which is basically consistent with the conclusion of Miao et al. (2018). T4-CJII concentrates in the area of Zhanjiang. The rainfall of T5-WL is relatively large, concentrated over urban agglomerations and coastal areas of Shantou. Compared with the conclusion in previous studies that the precipitation center is concentrated in Shantou (Chen et al., 2012; Liu et al., 2019), urban agglomerations have been added in the present study. The high T6-HP precipitation areas are concentrated in urban agglomerations.

Comparing the results of previous studies (**Table 2**), the T1-SW type adds two high precipitation areas – namely, Guangzhou and Shanwei. For the T2-SE type, Zhanjiang also becomes a high precipitation area. For T3-CJI, T4-CJII, T5-WL, and T6-HP, GBA becomes a high precipitation area. It is found that the precipitation centers of the same type are roughly similar, but the newly discovered urban agglomerations have become precipitation centers under multiple types, indicating that it too is an area with a high incidence of WSHR.

In order to explore the scope and intensity of the WSHR events, station with the maximum amount of precipitation among all stations during an extreme precipitation event

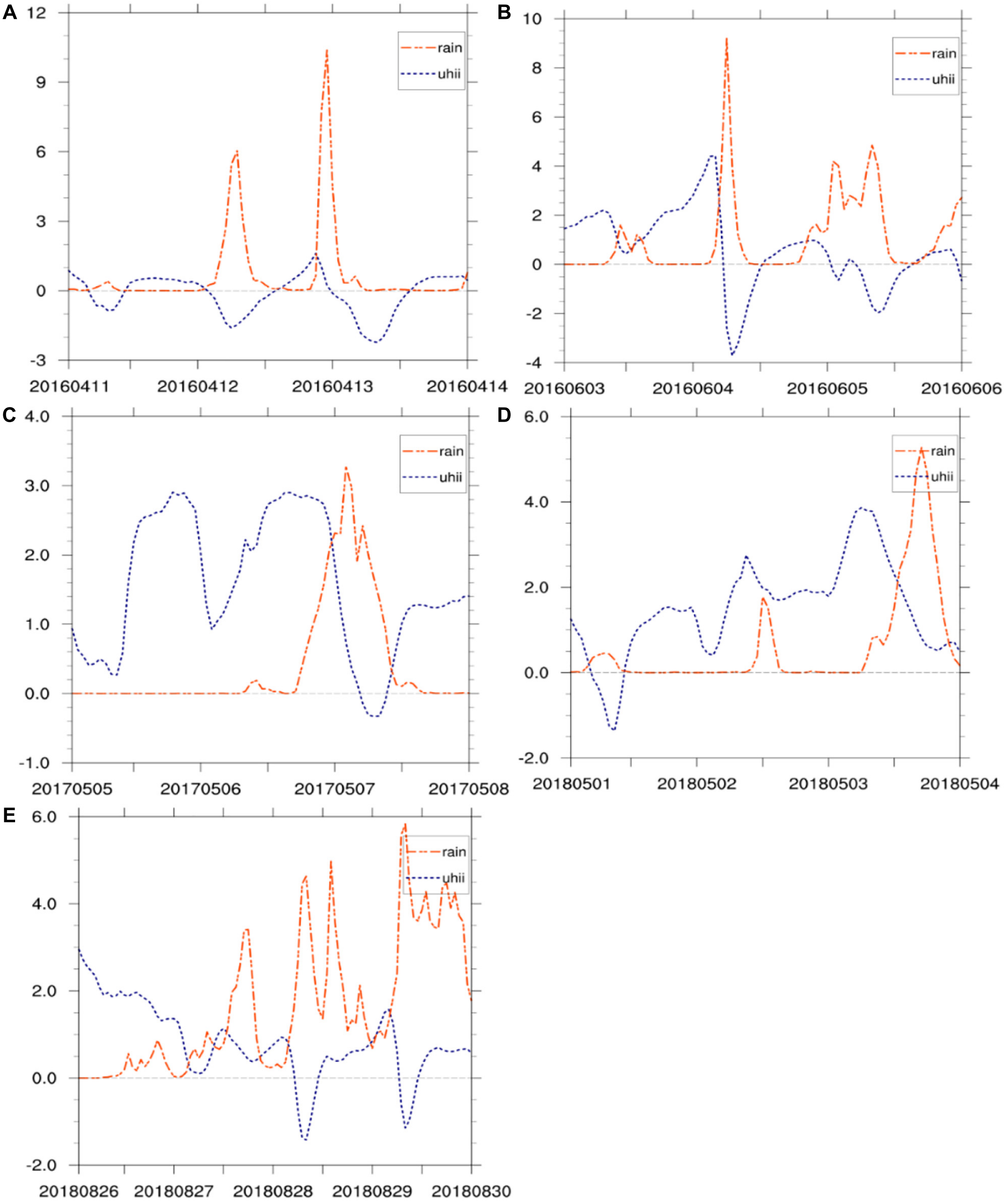

FIGURE 7 | Hourly precipitation (unit: mm) and UHII (unit:°C) change with time on **(A)** 12 April 2016, **(B)** 5 June 2016, **(C)** 7 May 2017, **(D)** 3 May 2018, **(E)** 28 August 2018 and 29 August 2018.

was set as central station, and the number of stations with daily precipitation exceeding 50 mm within 100 km were counted (**Figure 5**). It can be seen that the number of stations with precipitation exceeding 50 mm around the central station generally does not exceed 20, and the diameter of the precipitation area is less than 60 km. However, there are also extreme precipitation events. There are more than 100 stations with precipitation exceeding 50 mm around the central station. The estimated diameter of the precipitation area is greater than 134 km, indicating that these WSHR events have strong precipitation and large scope. Six large-scale heavy rainfall events were counted, among which T1-SW occurs twice (on 12 April 2016 in Foshan and on 7 May 2017 in Guangzhou), T5-WL occurs three times (on 5 June 2016 in Zhongshan, on 28 August 2018 in Guangzhou, and on 29 August 2018 in Zhongshan), and T6-HP occurs once (on 3 May 2018 in Jiangmen). These large-scale WSHR events are mostly located closer to the urban agglomeration, which may be related to the heat island effect of the city. Wu et al. (2019) showed that most of the stations in the Pearl River Delta region have

TABLE 3 | WSHR events associated with UHII in GBA.

Date	Precipitation area	UHII	Date	Precipitation area	UHII
20160404	Jiangmen	**1.81**	20170905	Dongguan	**1.58**
20160503	Jiangmen	0.49*	20170908	Dongguan	0.34*
20160605	Zhongshan	−0.18	20170909	Zhongshan	**0.74**
20160610	Guangzhou	**1.79**	20180503	Jiangmen	**3.18**
20160614	Guangzhou	**2.06**	20180705	Zhongshan	**1.07**
20160616	Zhuhai	**1.34**	20180706	Guangzhou	**0.88**
20160902	Guangzhou	0.39*	20180801	Huizhou	**2.42**
20170507	Guangzhou	**1.82**	20188028	Guangzhou	0.28*
20170711	Dongguan	−0.10	20188029	Zhongshan	**2.15**
20170718	Shenzhen	−0.72	20188031	Huizhou	**1.55**
			20180906	Guangzhou	**1.61**

*The bold values means strong UHI events, *means weak UHI events.*

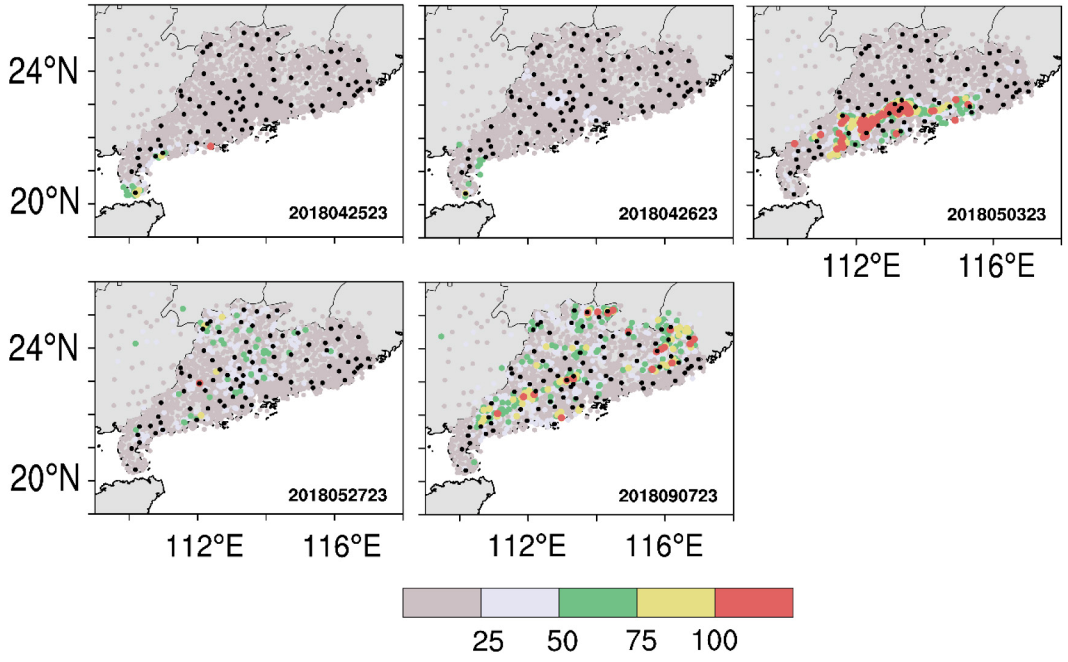

FIGURE 8 | The locations of national basic stations (black dots) and regional automatic stations (colored dots), for which the color refers to the daily precipitation (units: mm/d).

experienced a trend of extreme hourly rainfall and increased frequency caused by urbanization in the past few decades. Su et al. (2019) analyzed the variation in presummer precipitation in South China from 1979 to 2015 and its relationship with urbanization, the results also revealed that the intensity of precipitation and the occurrence of extreme precipitation events during the presummer season in South China have increased significantly, and the upward trend is much more significant in urban areas than in non-urban areas. This is because the release of anthropogenic heat and the aerosols produced by urbanization have changed the radiation budget in urban areas, which is conducive to enhanced water vapor transport and upward convergence movement, leading to more frequent extreme precipitation events (Lin et al., 2020).

The percentages of precipitation centers of the six types of WSHR are shown in **Figure 6**. According to the location of the precipitation center, the WSHR events of South China can be divided into three areas – namely, the coast of Guangdong (coastal), inland of Guangdong (inland), and GBA. It can be seen that in different types the distribution characteristics are also different. Among the six types, coastal precipitation accounts for a large proportion (38.5–100%). T2-SE also accounts for a high percentage of coastal precipitation, reaching 75%. The T4-CJI type of precipitation only occurs along the coast. In addition, T5-WL has the most significant effect on GBA, reaching 38.5%. Under the circulation of T6-HP, the proportion of precipitation in warm areas in inland Guangdong has increased compared with other types, reaching 40%.

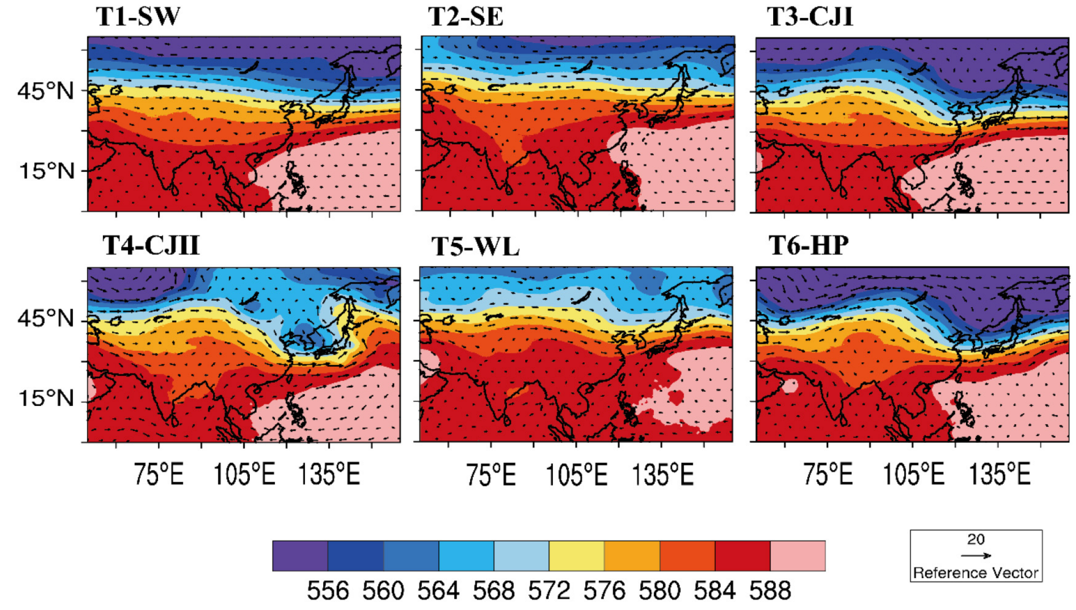

FIGURE 9 | The 500-hPa geopotential height (colorbar; unit: dagpm) and wind field (arrows; units: m/s) in WSHR of six weather types.

POTENTIAL ASSOCIATION BETWEEN EXTREME PRECIPITATION AND URBANIZATION

Previous studies have revealed urban areas are more exposed to extreme precipitation than non-urban areas, due to changed land cover, enhanced urban heat island (UHI) and resultant specific local circulation in urban areas (Su et al., 2019; Wu et al., 2019; Lin et al., 2020; Zheng et al., 2020). For example, when there are sufficient water vapors in the lower-level atmosphere, UHI can induce strong updrafts to easily trigger moist convection, enhancing precipitating convective systems with extreme precipitation (Han and Baik, 2008; Su et al., 2019; Lin et al., 2020). To explore the relationship between the six extreme precipitation events mentioned above and UHI effect, the urban heat island intensity (UHII) is introduced (Wu, 2019), which is defined as:

$$UHII = T_u - T_r \tag{1}$$

Where $T_u$and T_r are the hourly average temperatures of urban agglomeration stations and non-urban agglomeration stations, respectively. When there is at least 2 h of UHII > 0.53°C, the event is regarded as a strong UHI event; otherwise, it is regarded as a weak UHI event (Wu, 2019).

Figure 7 shows changes of UHII before and after six extreme precipitation near urban agglomerations. It can be seen that within a few hours before precipitation, the UHII increased in varying degrees, and decreased rapidly due to the cooling effect after precipitation. According to the statistics of UHIIs in 3 h before the occurrence of WSHR events in GBA from 2016 to 2018, a total of 21 WSHR events occurred, and the UHII is shown in **Table 3**. There are 14 strong UHI events (bold), four weak UHI events (*), and three weak urban cold island events, showing that most extreme precipitation events occurred under the strong UHI situation before precipitation. This implies that urban heat island effect has a potential role in promoting the occurrences of local extreme precipitation events in warm sector, which is coincide with previous studies over south China (Su et al., 2019; Wu et al., 2020; Lin et al., 2020).

ABNORMAL WEATHER TYPE

Previous studies failed to mention that WSHR can occur under the control of high-pressure weather systems, possibly because of the absence of capturing these processes. **Figure 8** shows the daily precipitation distributions of five WSHR events under T6-HP circulation. It can be seen from the figure that the WSHR events under this type are mostly small in scale and strong in locality. Many high-value areas lack the distribution of basic stations. According to the criteria for judging WSHR, this may lead to the this process not being identified when quantifying the WSHR, thereby omitting this type of weather.

In addition to the objective limitation of station density, the circulation in this year was also different from the previous 2 years. Comparing the location of the 500-hPa subtropical high of the six types (**Figure 9**) and four related indexes (**Figure 10**), it can be seen that the subtropical high area of T4-CJII and T6-HP is relatively small, the ridge point is westward, and the intensity is weak. The ridge line in T2-SE and T5-WL is also northward, but the location is eastward. The reason for this phenomenon may be attributable to interannual changes. By observing the variation of the Niño3.4 index (**Figure 11**), the anomaly is lower than 0.5°C for six consecutive months from 2017 to 2018, and it is judged that a La Niña event occurred in that year (Trenberth, 1997).

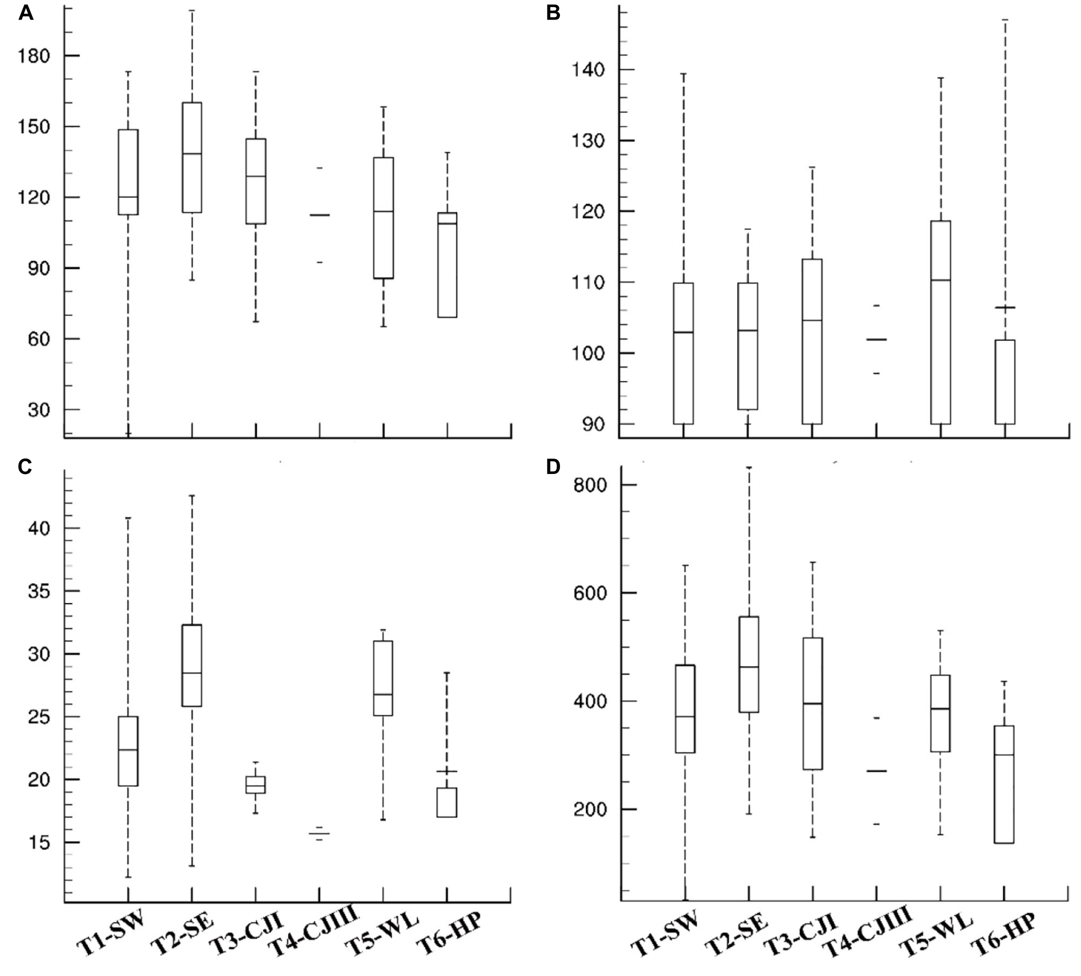

FIGURE 10 | Indices for the **(A)** western Pacific subtropical high area, **(B)** western Pacific subtropical high western ridge point, **(C)** western Pacific subtropical high ridge line, and **(D)** western Pacific subtropical high intensity.

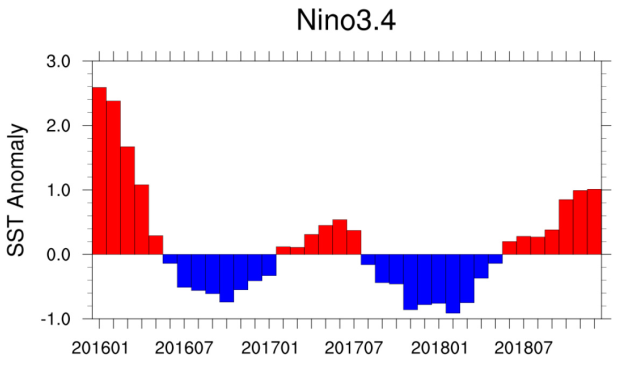

FIGURE 11 | Monthly Niño3.4 index from 2016 to 2018.

According to the research of Ai and Chen (2000), La Niña will affect the position of the subtropical high, leading to a northward displacement of the subtropical high in the following summer. Other studies have shown that when the tropical western Pacific is cooling in spring, the subtropical high moves westward (Hung et al., 2006). In summary, the subtropical high is northward and westward, and Guangdong is under the control of the subtropical high. The wind direction is a weak southerly wind, but the overall strength of the subtropical high is relatively weak. The southern branch trough is active, cold air is prone to intrusion in the lower layer, and a convection system can develop. Under this condition, the T6-HP circulation situation appears.

CONCLUSION AND DISCUSSION

Based on high-density station data, 134 WSHR events from April to September 2016 to 2018 were identified, and the typical weather patterns that caused WSHR objectively classified by using the PCT method. Our conclusions are as follows:

(1) On average, WSHR rainfall occurs more in coastal areas and less in inland areas. There are three heavy rain centers: Yangjiang, Shanwei, and the GBA urban agglomeration. The weather types of WSHR in Guangdong can be divided

into six types: T1-SW, T2-SE, T3-CJI, T4-CJ II, T5-WL, and T6-HP. T1-SW is the main weather system, which mainly appears from April to July. T2-SE is obvious after the onset of the monsoon; T3-CJI mainly occurs in the pre-rainy season; and T5-WL occurs in the post-rainy season.

(2) Different weather types have different precipitation locations. T1-SW and T3-CJI are concentrated in the GBA urban agglomeration and the areas of Shantou and Shanwei; T2-SE is concentrated along the coast, especially in the area of Yangjiang. There were two cases of precipitation for T4-CJII, both of which occurred along the southwest coast (Zhanjiang and Maoming). GBA is most affected by T5-WL, and three of six extreme precipitation events occurred under this type. Therefore, for the T5-WL type, attention should be paid to the possibility of large-scale extreme precipitation in urban agglomerations. Precipitation for the T6-HP type is also concentrated in urban agglomerations, and the inland proportion of WSHR has increased compared with other types, reaching 40%. So, we can conclude that urbanization plays an important role in extreme magnitudes of large-scale WSHR events and their occurrence centers.

(3) T6-HP is a new weather type, and its appearance may be related to ENSO. During the La Niña period, the subtropical high moved northward but the overall strength was weaker, the southern branch trough was active, and cold air intruded at the lower level. In such weather conditions, the scale of precipitation is often small. Previous low-resolution observations have been unable to capture these small-scale events, thus omitting local/small-scale rainfall under this weather situation. In contrast, the high-density observations employed in the present work were able to capture T6-HP WSHR events with their smaller coverage areas.

Previous research found that weather patterns of WSHR over the southern of middle and lower reaches of the Yangtze River include subtropical high pattern, which is similar to T6-HP (Chen et al., 2016; Wang et al., 2018). The mechanism is that the area where the heavy rain occurs has been under high temperature control for a long time and has accumulated considerable energy and water vapor, and with the role of mesoscale convergence line, atmospheric stratification becomes unstable, causing convective instability condition development. Our findings provide new insight into the cause of WSHR events over South China, but the formation mechanism of T6-HP type WSHR events needs to be further studied to improve the accuracy of WSHR forecasts.

DATA AVAILABILITY STATEMENT

Publicly available datasets were analyzed in this study. This data can be found here: The TC best track dataset is provided by the CMA Shanghai Typhoon Institute at http://tcdata.typhoon.org.cn/en/. The ERA5 reanalysis data are provided by the ECMWF at https://cds.climate.copernicus.eu/cdsapp#!/dataset/reanalysis-era5-pressure-levels?tab=overview.

AUTHOR CONTRIBUTIONS

XB designed the research. WL performed the data analyses and prepared the figures. XB and WL wrote the manuscript. LS took part in manuscript discussion. YL and JS commented on the manuscript and give some useful suggestions. All authors contributed to the article and approved the submitted version.

FUNDING

This work was jointly supported by National Key R&D Program of China (Grant Nos. 2018YFC1507404 and 2018YFC1507402); National Natural Science foundation of China (Grant No. 41975008); and National Natural Science Foundation of China (Grant No. 41875021).

SUPPLEMENTARY MATERIAL

The Supplementary Material for this article can be found online at: https://www.frontiersin.org/articles/10.3389/feart.2021.678230/full#supplementary-material

REFERENCES

Ai, Y., and Chen, X. (2000). Analysis of the correlation between the subtropical high over western pacific in summer and SST. *J. Trop. Meteorol.* 1. doi: 10.16032/j.issn.1004-4965.2000.01.001

Cai, J., Wu, Z., Chen, X., Lan, Y., Guo, Z., and Guo, C. (2019). Cause analysis of persistent torrential rain associated with monsoon depression occurred in Guangdong on August 2018. *Torrential Rain Disasters* 38, 576–586.

Chen, X., Ding, Z., Liu, C., Chang, Y., and Zhu, C. (2012). Statistic analysis on the formation system of warm-sector heavy rainfall in May and June from 2000–2009. *J. Trop. Meteorol.* 28, 707–718. doi: 10.1016/s0713-2743(00)80080-x

Chen, Y., Chen, Y., Chen, T., and He, H. (2016). Characteristics analysis of warm-sector rainstorms over the middle-lower reaches of the yangtze river. *Meteorol. Mon.* 42, 724–731. doi: 10.7519/j.issn.1000-0526.2016.06.008

Dong, Y., Li, J., Guo, J., Jiang, Z., Chu, Y., Chang, L., et al. (2020). The impact of synoptic patterns on summertime ozone pollution in the North China Plain. *Sci. Total Environ.* 735:139559. doi: 10.1016/j.scitotenv.2020.139559

Han, J. Y., and Baik, J. J. (2008). A theoretical and numerical study of urban heat island–induced circulation and convection. *J. Atmos. Sci.* 65, 1859–1877. doi: 10.1175/2007jas2326.1

He, L., Chen, T., and Kong, Q. (2016). A review of studies on prefrontal torrential rain in South China. *J. Appl. Meteorol. Sci.* 27, 559–569.

Hoffmann, P., and Schlünzen, K. H. (2013). Weather pattern classification to represent the urban heat island in present and future climate. *J. Appl. Meteorol. Climatol.* 52, 2699–2714. doi: 10.1175/jamc-d-12-065.1

Huang, S. H. (1986). *South China Rainstorm in the First Flood Season*. Guangdong: Science & Technology Press.

Hung, R., Gu, L., Zhou, L., and Wu, S. (2006). Impact of the thermal state of the tropical western Pacific on onset date and process of the South China Sea summer monsoon. *Adv. Atmos. Sci.* 23, 909–924. doi: 10.1007/s00376-006-0909-1

Huth, R. (1996). An intercomparison of computer-assisted circulation classification methods. *Int. J. Climatol.* 16, 893–922. doi: 10.1002/(sici)1097-0088(199608)16:8<893::aid-joc51>3.0.co;2-q

Huth, R. (2000). A circulation classification scheme applicable in GCM studies. *Theor. Appl. Climatol.* 67, 1–18. doi: 10.1007/s007040070012

Huth, R., Beck, C., Philipp, A., Demuzere, M., Ustrnul, Z., Cahynová, M., et al. (2008). Classifications of atmospheric circulation patterns: recent advances and applications. *Ann. N. Y. Acad. Sci.* 1146, 105–152. doi: 10.1196/annals.1446.019

Li, Z. H., Liang, B., and Bao, C. (1981). *The Causes and Forecast of the Heavy Rain in the First Flood Season in South China*. Beijing: China Meteorological Press.

Lin, L. (2006). *Guangdong Weather Forecast Technical Manual*. Beijing: China Meteorological Press.

Lin, L., Gao, T., Luo, M., Ge, E., Yang, Y., Liu, Z., et al. (2020). Contribution of urbanization to the changes in extreme climate events in urban agglomerations across China. *Sci. Total Environ.* 744:140264. doi: 10.1016/j.scitotenv.2020.140264

Liu, R., Sun, J., and Chen, B. (2019). Selection and classification of warm-sector heavy rainfall events over South China. *Chin. J. Atmos. Sci.* 43, 119–130.

Miao, C. S., Yang, Y. Y., Wang, J. H., and Li, P. (2018). A comparative study on characteristics and thermo-dynamic development mechanisms of two types of warm-sector heavy rainfall along the South China coast. *J. Trop. Meteorol.* 24, 494–507.

Ning, G., Yim, S. H. L., Wang, S., Duan, B., Nie, C., Yang, X., et al. (2019). Synergistic effects of synoptic weather patterns and topography on air quality: a case of the Sichuan Basin of China. *Clim. Dynam.* 53, 6729–6744. doi: 10.1007/s00382-019-04954-3

Ning, G., Yim, S. H. L., Yang, Y., Gu, Y., and Dong, G. (2020). Modulations of synoptic and climatic changes on ozone pollution and its health risks in mountain-basin areas. *Atmos. Environ.* 240:117808. doi: 10.1016/j.atmosenv.2020.117808

Philipp, A., Beck, C., Esteban, P., Kreienkamp, F., Krennert, T., Lochbihler, K. U., et al. (2014). *Cost733class-1.2 User Guide*. Augsburg Germany.

Su, L., Li, J., Shi, X., and Fung, J. C. (2019). Spatiotemporal variation in presummer precipitation over south China from 1979 to 2015 and its relationship with urbanization. *J. Geophys. Res. Atmos.* 124, 6737–6749.

Sun, J., Zhang, Y., Liu, R., Fu, S., and Tian, F. (2019). A review of research on warm-sector heavy rainfall in China. *Adv. Atmos. Sci.* 36, 1299–1307. doi: 10.1007/s00376-019-9021-1

Trenberth, K. E. (1997). The definition of el nino. *Bull. Am. Meteorol. Soc.* 78, 2771–2778. doi: 10.1175/1520-0477(1997)078<2771:tdoeno>2.0.co;2

Wang, L., Chen, Y., Xiao, T., Li, S., and Ge, L. (2018). Statistical analysis of warm-sector rainstorm characteristics over the Southern of middle and lower reaches of the Yangtze River in summer. *Meteorol. Mon.* 44, 771–780.

Wang, H., Sun, J., Wei, J., and Zhao, S. (2014). Classification of persistent heavy rainfall events over Southern China during recent 30 years. *Climatic and Environmental Research* 19, 713–725. doi: 10.3878/j.issn.1006-9585.2013.13143

Wu, H. Y., Li, Z., Li, W., and Zheng, J. (2020). Characteristics analysis of extremly severe precipitation based on regional automatic weather stations in guangdong. *Meteorol. Mon* 46, 801–812.

Wu, M. (2019). *A Dissertation Submitted to University of Chinese Academy of Sciences in Partial Fulfillment of the Requirement for the Degree of Doctor of Meteorology*. [dissertation/doctor's thesis]. Chennai: Chinese Academy of Meteorological Sciences.

Wu, M., Luo, Y., Chen, F., and Wong, W. K. (2019). Observed link of extreme hourly precipitation changes to urbanization over coastal South China. *J. Appl. Meteorol. Climatol.* 58, 1799–1819. doi: 10.1175/jamc-d-18-0284.1

Wu, N., Ding, X., Wen, Z., Chen, G., Meng, Z., Lin, L., et al. (2020). Contrasting frontal and warm-sector heavy rainfalls over South China during the early-summer rainy season. *Atmos. Res.* 235:104693. doi: 10.1016/j.atmosres.2019.104693

Yang, Y., Wang, R., Chen, F., Liu, C., Bi, X., and Huang, M. (2021). Synoptic weather patterns modulate the frequency, type and vertical structure of summer precipitation over Eastern China: a perspective from GPM observations. *Atmos. Res.* 249:105342. doi: 10.1016/j.atmosres.2020.105342

Ying, M., Zhang, W., Yu, H., Lu, X., Feng, J., Fan, Y., et al. (2014). An overview of the China meteorological administration tropical cyclone database. *J. Atmos. Oceanic Technol.* 31, 287–301. doi: 10.1175/jtech-d-12-00119.1

Zhao, Y. C., and Wang, Y. H. (2009). A review of studies on torrential rain during pre-summer flood season in South China since the 1980's. *Torrential Rain Disasters* 28, 3–38.

Zheng, Z., Zhao, C., Lolli, S., Wang, X., Wang, Y., and Ma, X. (2020). Diurnal variation of summer precipitation modulated by air pollution: observational evidences in the beijing metropolitan area. *Environ. Res. Lett.* 15:094053. doi: 10.1088/1748-9326/ab99fc

Zong, L., Yang, Y., Wang, H., Ning, G., Li, Y., and Gao, Z. (2021). Synoptic drivers of co-occurring surface ozone and PM2.5 pollution during summertime in eastern China. *Atmos. Chem. Phys. Discuss*. doi: 10.5194/acp-2020-596

Conflict of Interest: The authors declare that the research was conducted in the absence of any commercial or financial relationships that could be construed as a potential conflict of interest.

frontiers in Earth Science

ORIGINAL RESEARCH
published: 12 May 2021
doi: 10.3389/feart.2021.659310

Improving the Accuracy of Subseasonal Forecasting of China Precipitation With a Machine Learning Approach

Cen Wang[1], *Zhaoying Jia*[2], *Zhaohui Yin*[3]*, *Fei Liu*[4,5]*, *Gaopeng Lu*[1] *and Jianqiu Zheng*[1]

[1] School of Earth and Space Sciences, University of Science and Technology of China, Hefei, China, [2] School of Atmospheric Science, Nanjing University of Information Science and Technology, Nanjing, China, [3] Baidu Inc., Beijing, China, [4] School of Atmospheric Sciences, Sun Yat-sen University, Key Laboratory of Tropical Atmosphere-Ocean System Ministry of Education, and Southern Marine Science and Engineering Guangdong Laboratory, Zhuhai, China, [5] State Key Laboratory of Numerical Modeling for Atmospheric Sciences and Geophysical Fluid Dynamics, Institute of Atmospheric Physics, Chinese Academy of Sciences, Beijing, China

Edited by:
Wei Zhang,
Utah State University, United States

Reviewed by:
June-Yi Lee,
Pusan National University,
South Korea
Xiaojing Jia,
Zhejiang University, China

***Correspondence:**
Zhaohui Yin
yinzhaohui01@baidu.com
Fei Liu
liufei26@mail.sysu.edu.cn

Specialty section:
This article was submitted to
Atmospheric Science,
a section of the journal
Frontiers in Earth Science

Received: *27 January 2021*
Accepted: *16 April 2021*
Published: *12 May 2021*

Citation:
Wang C, Jia Z, Yin Z, Liu F, Lu G and Zheng J (2021) Improving the Accuracy of Subseasonal Forecasting of China Precipitation With a Machine Learning Approach.
Front. Earth Sci. 9:659310.
doi: 10.3389/feart.2021.659310

Precipitation change, which is closely related to drought and flood disasters in China, affects billions of people every year, and the demand for subseasonal forecasting of precipitation is even more urgent. Subseasonal forecasting, which is more difficult than weather forecasting, however, has remained as a blank area in meteorological service for a long period of time. To improve the accuracy of subseasonal forecasting of China precipitation, this work introduces the machine learning method proposed by Hwang et al. in 2019 to predict the precipitation in China 2–6 weeks in advance. The authors used a non-linear regression model called local linear regression together with multitask feature election (MultiLLR) model and chosen 21 meteorological elements as candidate predictors to integrate diverse meteorological observation data. This method automatically eliminates irrelevant predictors so as to establish the forecast equations using multitask feature selection process. The experiments demonstrate that the pressure and Madden–Julian Oscillation (MJO) are the most important physical factors. The average prediction skill is 0.11 during 2011–2016, and there are seasonal differences in forecasting skills, evidenced by higher forecast skills of winter and spring seasons than summer and autumn seasons. The proposed method can provide effective and indicative guidance for the subseasonal prediction of precipitation in China. By adding another three factors, Arctic Oscillation (AO) index, Western North Pacific Monsoon (WNPM) index and Western North Pacific Subtropical High (WNPSH) index into the MultiLLR model, the authors find that AO can improve the forecast skill of China precipitation to the maximum extent from 0.11 to 0.13, followed by WNPSH. Moreover, the ensemble skill of our model and CFSv2 is 0.16. This work shows that our subseasonal prediction of China precipitation should be benefited from the MultiLLR model.

Keywords: subseasonal forecasting, machine learning, MultiLLR, China precipitation, intraseasonal variability, seasonal cycle

INTRODUCTION

Against the backdrop of global warming, relatively frequent extreme floods and droughts can not only cause heavy economic damages but also life of threaten people, especially in China who has the largest population in the world (Cai et al., 2017; Matthews et al., 2017). Subseasonal prediction of 2-weekly to 2-monthly time scale with good skill of China precipitation is associated with crop-planting choice, disaster reduction, and life safety. Furthermore, subseasonal prediction will fill the gap between weather forecasting and climate prediction (Vitart et al., 2012). Although the statistical method and dynamic models, two mainstream methods for subseasonal prediction, have shown a higher forecast skill (Li and Robertson, 2015; Zhu and Li, 2017), subseasonal prediction that depends on both local weather and global atmospheric circulations (Robertson et al., 2015; Vitart et al., 2017) is called "predictability desert" (Vitart et al., 2012) and still remains full of challenges. It is encouraging that previous research has found certain processes in the land, ocean, and atmosphere that would increase the possibility of subseasonal prediction. Sea surface temperature (SST), which affects the atmospheric circulation through air-sea heat flux and convection, can improve the intraseasonal variability forecast skill (Woolnough et al., 2007; Liang and Lin, 2018). Arctic Oscillation (AO) and the Madden–Julian Oscillation, which modulate the teleconnection patterns in Northern Hemisphere (NH) and the tropic convective activity, are two important sources of subseasonal predictability in the atmosphere process (Baldwin, 2003; Waliser et al., 2003; Black et al., 2017). Sea ice (Holland et al., 2011), snow cover (Sobolowski et al., 2010), and soil moisture (Koster et al., 2010) are the key factors of prediction on intraseasonal time scales. Besides, the summer precipitation intraseasonal variability (ISV) in China also serves as an important factor (Liu et al., 2020).

With the development of machine learning (ML) in meteorology, ML, as a new statistical technique, has been used in various forecast systems and helps to improve the forecast skill on different time scales (McGovern et al., 2014; Liu et al., 2016). ML improves the decadal climate predictions (Strobach and Bel, 2016). As for the subseasonal to seasonal (S2S) forecast, statistical techniques are noticed again due to the ML method (Cohen et al., 2019). ML makes precipitation nowcasting no longer be limited to two existing methods, radar echo extrapolation and numerical weather prediction (NWP) (Shi et al., 2015; Qiu et al., 2017). Besides, ML techniques are also able to improve the prediction and detection of severe weather events (McGovern et al., 2014; Liu et al., 2016).

Hwang et al. (2019) developed a forecasting system, which was a combination of two non-linear regression models based on ML, to improve the subseasonal prediction skills. To improve the accuracy of subseasonal prediction of China precipitation, the authors explore the effects of Hwang's forecasting system on them. The article is presented as follows. In the "Data and Methodology" section, the data and methodology are introduced. In the "Results" section, we provide the conclusions of the effects of Hwang's forecasting system on subseasonal forecasting of China precipitation. Finally, the last section offers the summary of the study.

DATA AND METHODOLOGY

Data

This study uses the newly released CN 05.1 daily precipitation dataset in China from 1961 to 2017, which is provided by the observing stations of the China National Climate Center (Wu and Gao, 2013). The daily precipitation is converted to a sum of ensuing 2 weeks. The authors choose daily reanalysis data from NCEP/NCAR Reanalysis dataset (Kalnay et al., 1996), and obtain temperature data at 2 m, relative humidity at the sigma level 0.995, pressure at the surface, and geopotential height at 10 hPa. By projecting the daily geopotential height anomalies into the leading EOF mode at 1,000 hPa, the daily AO index has been obtained from the Climate Prediction Center (CPC). Besides, the Madden–Julian Oscillation (MJO) and the Multivariate ENSO index (MEI) are obtained from the NOAA/Earth System Research Laboratory and the Australian Government Bureau of Meteorology. Phase and amplitude are extracted from the daily MJO data starting from 1974 on the target forecast date to characterize tropical convection (Hwang et al., 2019). MEI values combine six variables associated with ENSO from 1949, including SST, sea-level pressure, surface air temperature, zonal and meridional surface wind components, and sky cloudiness.

The sea ice concentration and the sea surface temperature (SST) are obtained from the optimum interpolation sea surface temperature (OISST) analysis of NOAA, and the top three principal components (PCs) over the Pacific (20°S–65°N, 150°E–90°W) from 1981 to 2017 are also used.

The Western North Pacific Monsoon (WNPM) index is defined as the difference of zonal wind between a southern region of 5°–15°N, 100°–130°E and a northern region of 20°–30°N, 110°–140°E at the level of 850 hPa, and U850 represents the zonal wind at 850 hPa (Wang and Fan, 1999; Wang et al., 2001). WNPM index is defined as follows:

$$\begin{aligned}\text{WNPM Index} &= \text{U850}(100^\circ\text{E} - 130^\circ\text{E}, 5^\circ\text{N} - 15^\circ\text{N})\\ &\quad - \text{U850}(110^\circ\text{E} - 140^\circ\text{E}, 20^\circ\text{N} - 30^\circ\text{N})\end{aligned}$$

Following the results of Lu (2002), this research selected two indexes to describe the location of Western North Pacific Subtropical High (WNPSH) by averaging the geopotential height anomalies at 850 hPa over two regions. WNPSH1 is meridional index, over the area of 120°–150°E, 30°–40°N, and WNPSH2 is zonal index, over the area of 110°–150°E, 10°–30°N. The authors select the two WNPSH indexes because of considering the advantages in well describing the precipitation pattern (Lu, 2002), and WNPSH stands for WNPSH1 and WNPSH2 below.

According to the forecast date of the local linear regression together with multitask feature election (MultiLLR) model, we

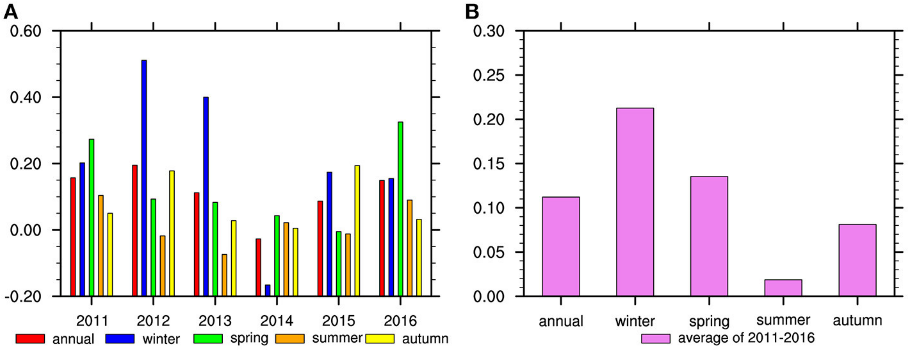

FIGURE 1 | The prediction skill of **(A)** annual average (red bar), winter (blue bar), spring (green bar), summer (orange bar), and autumn (yellow bar) for each year of 2011–2016. **(B)** 2011–2016 averaged skills for annual mean and four seasons.

got the forecast results for the total precipitation of CFSv2 Operational Forecasts 6-Hourly Products from 2011 to 2016.

The three-dimensional predictors, i.e., temperature data at 2 m, relative humidity at the sigma level 0.995, pressure at the surface, and total precipitation of CFSv2, were interpolated with a resolution of 1° by 1° and extracted over the forecast China region (14.75°N to 55.75°N, 69.75°E to 139.75°E). The top three principal components (PCs) of geopotential height at 10 hPa for all grid points globally, sea ice concentration, and sea surface temperature over the Pacific (20°S—65°N, 150°E—90°W) are also used. Except for MJO, which has the property of weekly time scales, all predictors used in this study were converted into the average of ensuing 2 weeks to be consistent with the sum precipitation of ensuing 2 weeks. The total precipitation of CFSv2 averaged during the next 14 days for each forecast date is also used.

MultiLLR Model

The authors take reference from the method of Hwang's MultiLLR model (Hwang et al., 2019) and put forward the physical factors mentioned earlier, which lagged on the basis of the frequency of the dataset, so as to provide the latest data and the temporal resolution and to add "ones" as a candidate regressor to represent intercept term that equals 1 for all data points in the total 21 candidate regression factors into the model, which is shown in the Y-axis of **Figure 3**. As shown in the Y-axis of **Figure 3**, the suffix anom of some candidate regression factors means that candidate regression factors are the anomalies based on daily climatology over the period of 1980–2010, and the "shift x" has a hysteresis characteristic from the measurement of the previous x days based on the data update time and the temporal resolution of measurement.

The MultiLLR model includes two parts, one part named local linear regression (LLR), by which we get regression coefficients for each grid point separately, and the other part called multitask backward stepwise feature selection, by which the relevant predictors are obtained from the candidate regressors through the performance forecast based on the spatial cosine similarity automatically. More algorithm details of the MultiLLR model can be referred from Hwang et al. (2019). Twenty-six forecast target dates for each year from 2011 to 2016 were made by the MultiLLR model, with a total of 156 times. For a forecast target date, the range of training data is from the first year when all the selected predictor data are commonly available to the year of the target date.

The authors choose spatial cosine similarity as the forecast skill, which is defined as:

$$\textit{forecast skil}\,(Y,\hat{Y}) = \frac{<Y,\hat{Y}>}{\|Y\|_2 * \|\hat{Y}\|_2}$$

where Y represents observed anomalies and $\hat{Y}$ represents predicted anomalies; the anomalies were obtained by removing the climatological annual cycle during 1981–2010. We forecast every 2 weeks, resulting in 26 times forecast for each year. The forecast skill for annual mean or seasonal mean can be calculated by averaging the associated period.

RESULTS

Figure 1A shows that the average prediction skill is 0.11 for all target dates, and the forecast skills vary from 2011 to 2016. The prediction skill for 2012 is highest with a value near 0.2, and it is around 0.15 for 2011 and 2016. The forecast skill for 2014, however, is −0.027, the lowest one among 6 years in the model. The 6 years can be divided into high-skill years, including 2011, 2012, 2013, and 2016, and low-skill years including 2014 and 2015.

There are also seasonal differences in forecasting skills (**Figure 1B**). To be specific, the skills of winter and spring are higher than the annual average, especially that the winter skill is the highest and exceeds 0.21. On the contrary, the summer forecast skill is the lowest and near zero, and the skill of the autumn season is also lower than the annual average. The result shows that the model is poor in forecasting precipitation in

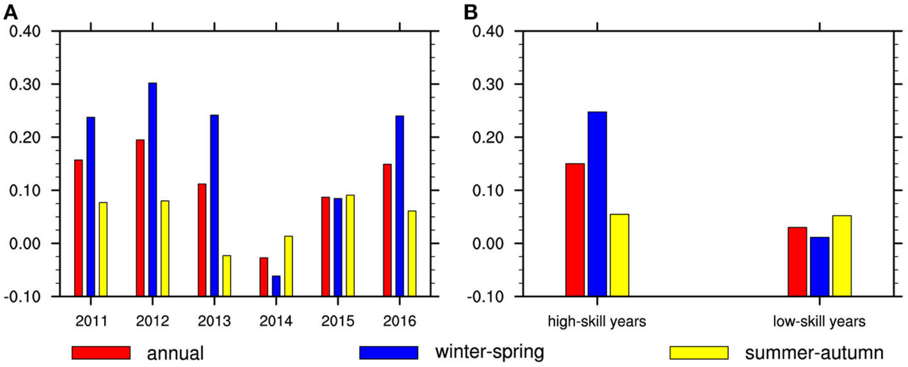

FIGURE 2 | The prediction skill of **(A)** annual average (red bar), winter–spring season (blue bar), and summer–autumn (yellow bar) for each year of 2011–2016 and of **(B)** annual average (red bar), winter–spring season (blue bar), and summer–autumn (yellow bar) for high-skill years and low-skill years, respectively.

summer and autumn seasons. As a result, the authors divide the four seasons into two types according to the annual mean values of the forecast skills, one type with winter and spring called Win-Spr, whose prediction skills are above the annual average, and the other type is to add summer and autumn together called Sum-Aut. **Figure 2B** shows that the prediction skills of Win-Spr are much higher than those of Sum-Aut in high-skill years. But in low-skill years, the skills of Win-Spr are lower than those of Sum-Aut. Moreover, not only the skills of Sum-Aut are <0.1 but also the changes are small during 2011–2016 (**Figure 2A**). In contrast, the Win-Spr prediction skills are high. Whether it is in the high-skill years or the low-skill years, the skills of Sum-Aut are nearly equal (**Figure 2B**). As for Win-Spr, the skill is very high in the high-skill years, but the skill in the low-skill years is lower than that of Sum-Aut. In summary, the annual average skill depends on that in Win-Spr, and the forecast model has good effect on winter and spring, compared with that on summer and autumn.

The authors put 21 candidate factors into MultiLLR model in the precipitation prediction task for weeks 3–4. The MultiLLR model chooses relevant features automatically from the 21 candidate factors for different target dates to improve the pertinence. According to the inclusion frequency of 21 candidate factors shown in **Figure 3**, different factors are selected with different frequencies, and the average is about 30 times. "Ones" that represent intercept term is the most frequently selected factor of them and has been used 66 times, followed by pressure (pres) and phase of MJO as the second and third, respectively. The selection frequency of temperature anomaly (tmp2m), which is the lowest, is only 7 times. Pressure and MJO are the most important physical factors in all 21 indexes for weeks 3–4 precipitation forecasting in China, inconsistent with many previous findings (He et al., 2011; Neena et al., 2014; Yao et al., 2015). Since MJO is a major source of intraseasonal predictability (Neena et al., 2014), Yao et al. (2015) found that the MJO makes effects on part of the variability of precipitation during November–March in South China, and as for the rest part which has nothing with MJO, and "cold surge" indicated by pressure at surface plays an important role. MJO is also found to be related to the subseasonal variability of precipitation over East Asian (He et al., 2011).

Figure 4 shows the distribution of ISV activity, represented by the variance of forecast and observed precipitation for four patterns. The strong ISV activity is located over the Yangtze River and Southeastern China in the Win-Spr season and expands to Central China, Northern China, and Northeast China in the Sum-Aut season (Liu et al., 2020). The model for the forecast of ISV activity performs better in winter and spring of high-skill years, which is reflected in the forecast of value and range for the ISV activity over China, including strong ISV activity over the Yangtze River and Southeastern China. In the Win-Spr season of low-skill years, the prediction of strong ISV activity value is much weaker than the observed. The forecast ability of ISV activity in the Sum-Aut season of high-skill years is similar to that of low-skill years. Specifically, forecast patterns show weak ISV activity over Northern China and Northeast China in the Sum-Aut season, inconsistent with the observations. The predicted ISV activity of Win-Spr is better than that of Sum-Aut, consistent with the higher prediction skill of Win-Spr than Sum-Aut.

According to the earlier classification, the seasonal mean forecasted pattern is near to negative anomalies, which show that the MultiLLR model mainly predicts a drought pattern for China precipitation no matter which season and year, except Win-Spr of high-skill years (**Figure 5**). **Figure 5** means the seasonal mean of the predicted precipitation, not ISV, which indicates the average statement of the forecast. The observed seasonal mean precipitation of years with higher forecast skills is less than that of lower skills. For summer and autumn seasons, the positive anomalies of the observed truths are hard to be predicted whether in the high-skill years or low-skill years, which is consistent with the low prediction skills of summer and autumn mentioned above. Comparing the forecast results of summer with those of autumn, the forecasted pattern of Win-Spr can resolve the distribution of drought and flood in certain parts of China.

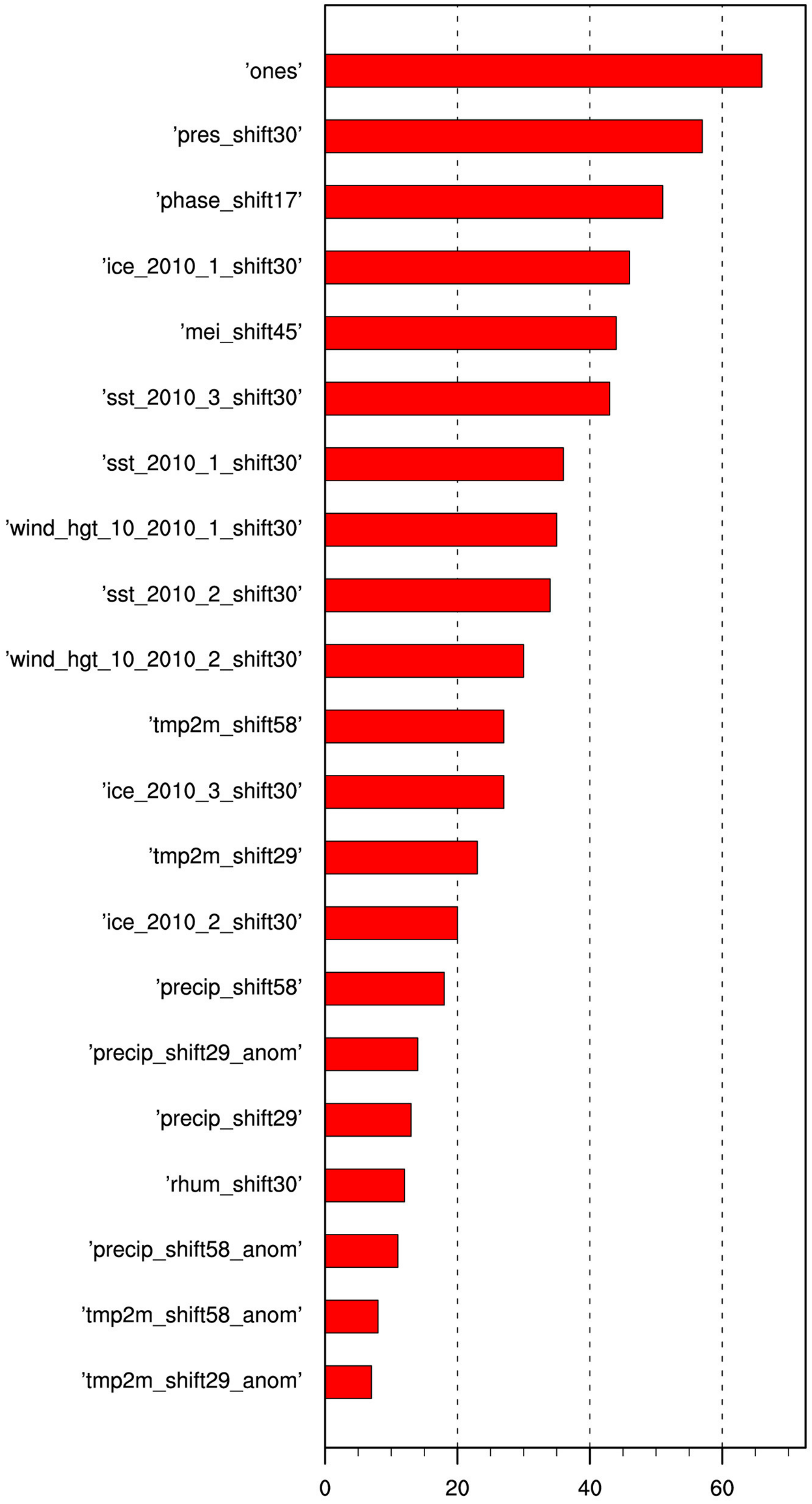

FIGURE 3 | Candidate factors inclusion frequencies selected by local linear regression with multitask feature selection (MultiLLR) models for all target dates during 2011–2016.

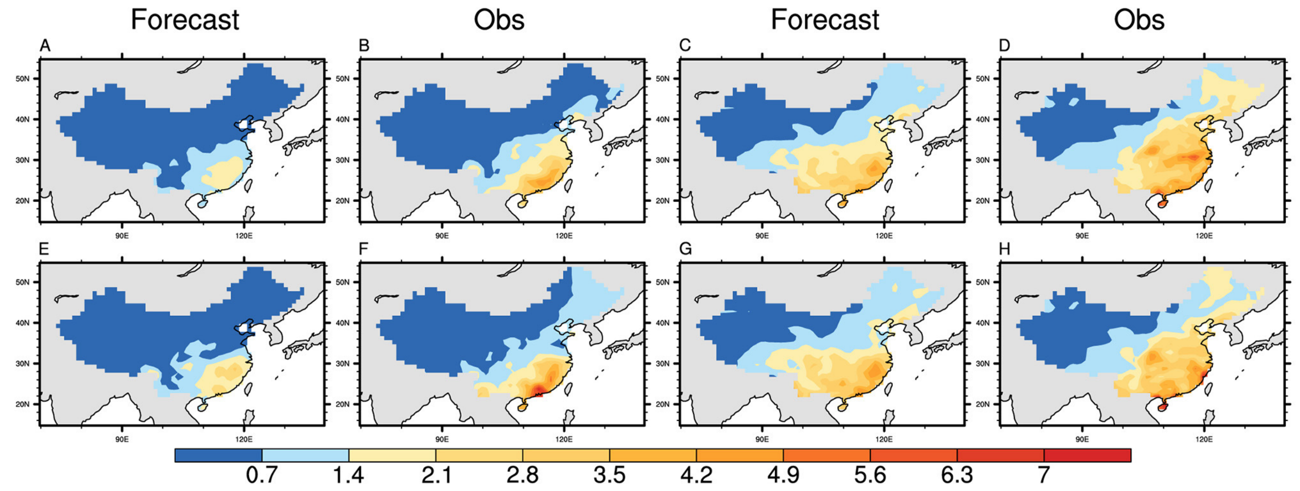

FIGURE 4 | Standard deviation of MultiLLR model predicted and observed precipitation (mm/day) of Win-Spr **(A,B,E,F)** and Sum-Aut season **(C,D,G,H)** in the high-skill years (up panels) and low-skill years (low panels), the first and third columns represent the forecast, and the second and fourth columns represent the observation values.

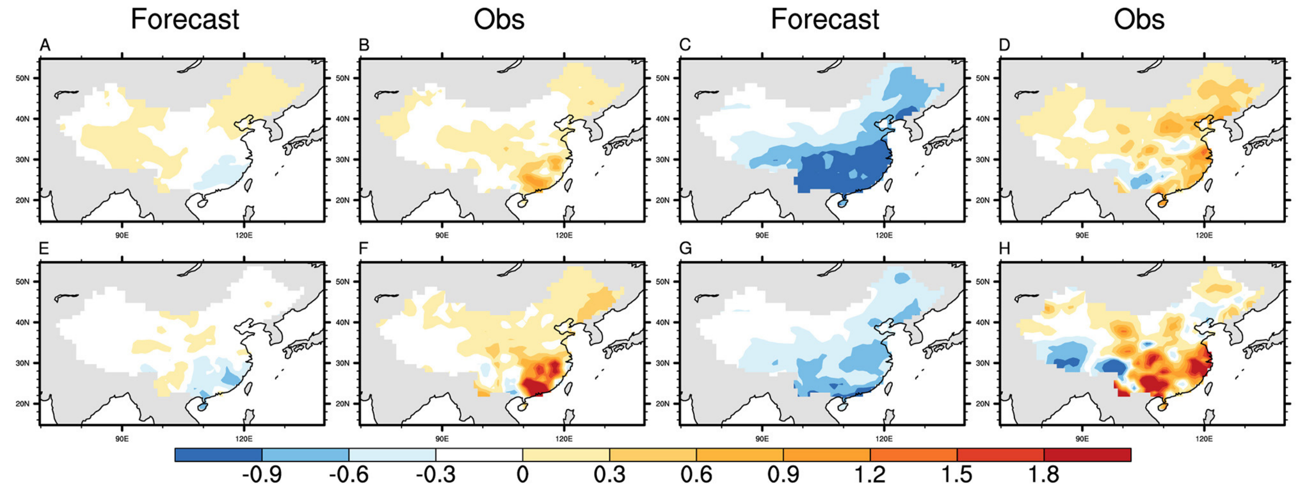

FIGURE 5 | Seasonal-mean MultiLLR model prediction and observations (mm/day) of Win-Spr **(A,B,E,F)** and Sum-Aut **(C,D,G,H)** seasons in the high-skill years (up panels) and low-skill years (low panels). The first and third columns represent the forecast, and the second and fourth columns represent the observation.

Furthermore, in high-skill years, the model forecast results were consistent with precipitation truth values, except for Southeastern China. But in the low-skill years, the forecast results of Win-Spr were worse than those in high-skill years. As for the seasonal mean precipitation pattern in Southeastern China, the model can hardly predict the distribution with 21 candidate factors.

Arctic Oscillation and the East Asian monsoon affect rainfall in China through changing the southern branch trough (SBT) and Middle East jet stream (MEJS) over the Bay of Bengal, and northward moisture transport and convergence, respectively (Ding et al., 2008; Mao et al., 2011). Many studies show that WNPSH is related to the subseasonal forecast of rainfall over China. The WNPSH has an important impact on the precipitation over Eastern China (Xiao-Xia et al., 2010), and the enhancement and location of the WNPSH were associated with two dominant subseasonal variation modes of the summer rainfall over the Yangtze River (Yang et al., 2010). Moreover, El Niño and La Niña cause the asymmetry of southern China rainfall anomalies in the winter half year, mainly through the intraseasonal oscillation of the WNPSH in lower troposphere (Zhang et al., 2015). Based on MultiLLR model with the 21 candidate factors mentioned earlier, the authors added WNPM index, two WNPSH indexes and AO index, which were notably

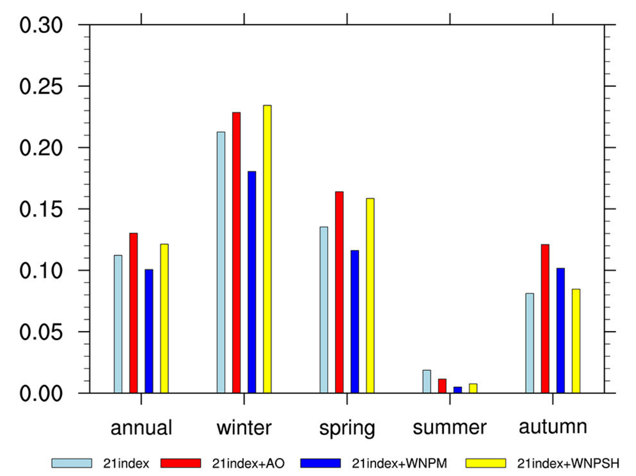

FIGURE 6 | The prediction skill of annual average, winter season, spring season, summer, and autumn season of 2011–2016 for 21 index model (light blue bar), 21 index+AO model (red bar), 21 index+WNPM model (blue bar), and 21 index+WNPSH model (yellow bar).

related to rainfall in China, into the MultiLLR model to improve the subseasonal China precipitation forecast skills, namely, 21 index+AO model, 21 index+WNPM model, and 21 index+WNPSH model. It is encouraging that the model including the new factor improves the rainfall forecast skill, especially the forecast skills of 21 index+AO model is 0.13, 16.1% more than that of the 21 index model, and AO is used 36 times. Also, the predication skill is improved, due to WNPSH index being added to the 21 index model. WNPSH1 and WNPSH2, which describe WNPSH in two ways, were selected 31 times and 35 times, respectively. After adding WNPM, the forecasting skill is reduced to 0.1 during 2011–2016. This means that AO and WNPSH physical factors contribute to the forecast skills of China precipitation, but WNPM is a negative contribution factor. **Figure 6** shows that the performance of forecasting skills improvement varies in each season. As for 21 index+AO model, all seasons forecast skills have improved except for the summer season, and the autumn forecast skill improves by the maximum extent among the four seasons by 49.1%, from 0.081 to 0.121. The 21 index+WNPSH model results of rainfall forecast skill in four seasons are consistent with those of the 21 index+AO model, but only improved in a slight way. In the winter, the 21 index+WNPSH model improves by the maximum extent. On the contrary, the 21 index+WNPM model only improves the autumn forecast skill. In summary, the comparison of the three newly added factors shows that AO is most conducive in improving the forecasting skills for MultiLLR model with the 21 candidate factors, followed by WNPSH. Moreover, WNPM is a negative factor in the MultiLLR model for subseasonal forecasting of China precipitation due to the annual average forecast skill of 0.1, less than that of the 21 index model, despite that it increases the autumn forecast skill. In a summary, the inclusion of AO mainly improves the prediction skill of spring and autumn, while the WNPSH mainly works to improve that of winter. The skill of summer, however, is weakened by the inclusion of these teleconnection factors.

This study not only evaluates the performances of MultiLLR models with different candidate predictors mentioned above, but also makes a comparison with the dynamical Climate Forecasting System (CFSv2) model. The forecast skill of CFSv2 is 0.11, compared to which the empirical model with 21 index+AO has a little better skill of 0.13. The ensemble model combining the 21 index+AO model and the CFSv2 by the same weight presents a much better skill of 0.16, and the skill improvement from 0.11 to 0.16 is above 80% confidence level, more than one standard deviation which has some reference significance. This shows that the MultiLLR model, a new statistical model, is useful to improve the subseasonal precipitation predication of China.

Also, authors try to improve the MultiLLR model by implementing the AutoKNN method proposed by Hwang et al. (2019), a local linear regression with the precipitation of 20 historical dates when the precipitation is the highest similarity to that of the target date. The negative skill of the AutoKNN model shows that subseasonal forecasting of China precipitation is hard from historical precipitation.

SUMMARY

Due to unique local weather conditions and climate circulations, subseasonal forecast of precipitation 2 weeks to 2 months in advance remains full of challenges. This study takes advantage of the local linear regression with multitask feature selection model with 21 candidate factors in the precipitation prediction task for weeks 3–4 to predict the precipitation of China in the ensuing 2 weeks. The result shows that the average prediction skill is 0.11, and the skills for four seasons vary from each other. To be specific, the forecast skill of winter is the highest, more than 0.21, and the summer forecast skill is near zero. In general, the skills of winter and spring are much higher than those of summer and autumn (**Figure 1**). This means that the model is poor in forecasting precipitation in summer and autumn. Consistent with the results of the forecast skills are that the predicted ISV activity of Win-Spr is better than that of Sum-Aut. And the model can hardly predict the seasonal mean precipitation pattern in Southeastern China with 21 candidate factors.

Besides, on the basis of MultiLLR model with 21 candidate factors, the additional physical factors AO and WNPSH are helpful to improve the forecasting skills, especially in winter, spring, and autumn. In contrast, WNPM is a useless factor for China precipitation generally in the MultiLLR model. Therefore, it is necessary that AO and WNPSH are to be added into MultiLLR model as candidate factors to improve the prediction ability of subseasonal forecasting of China precipitation. Moreover, when authors combine the MultiLLR model and CFSv2 model by the same weight, the forecast skills improved from 0.11 to 0.16. This result shows that the MultiLLR model, a new statistical model, improves the accuracy of the dynamical CFSv2 model for the subseasonal forecasting of China precipitation.

In this study, we make a first try on the subseasonal prediction of China precipitation using a simple machine learning method. In the MultiLLR, only the local regression has been used, limiting the forecast skill. More suitable methods should be tested in the future.

DATA AVAILABILITY STATEMENT

The original contributions presented in the study are included in the article/supplementary material, further inquiries can be directed to the corresponding author/s.

AUTHOR CONTRIBUTIONS

ZY and FL designed the experiments. CW, ZJ, and ZY prepared the data and performed the experiments. CW led the writing of the manuscript. All authors discussed the analysis and results and contributed to the manuscript.

FUNDING

This work was supported by the Guangdong Major Project of Basic and Applied Basic Research (2020B0301030004), and the Natural Science Foundation of China (41975107).

REFERENCES

Baldwin, M. P. (2003). Stratospheric memory and skill of extended-range weather forecasts. *Science* 301, 636–640. doi: 10.1126/science.1087143

Black, J., Johnson, N. C., Baxter, S., Feldstein, S. B., Harnos, D. S., and L' Heureux, M. L. (2017). The predictors and forecast skill of northern hemisphere teleconnection patterns for lead times of 3-4 weeks. *Month. Weather Rev.* 145, 2855–2877. doi: 10.1175/MWR-D-16-0394.1

Cai, W., Li, K., Liao, H., Wang, H., and Yu, L. (2017). Weather conditions conducive to Beijing severe haze more frequent under climate change. *Nat. Clim. Change* 7, 257–262. doi: 10.1038/nclimate3249

Cohen, J., Coumou, D., Hwang, J., Mackey, L., Orenstein, P., Totz, S., et al. (2019). S2S reboot: An argument for greater inclusion of machine learning in subseasonal to seasonal forecasts. *Wiley Interdiscip. Rev. Clim. Change* 10:e00567. doi: 10.1002/wcc.567

Ding, Y., Wang, Z., and Sun, Y. (2008). Inter-decadal variation of the summer precipitation in East China and its association with decreasing Asian summer monsoon. Part I: observed evidences. *Int. J. Climatol.* 28, 1139–1161. doi: 10.1002/joc.1615

He, J., Lin, H., and Wu, Z. (2011). Another look at influences of the Madden-Julian oscillation on the winter time East Asian weather. *J. Geophys. Res.* 116:D03109. doi: 10.1029/2010JD014787

Holland, M. M., Bailey, D. A., and Vavrus, S. (2011). Inherent sea ice predictability in the rapidly changing Arctic environment of the community climate system model version 3. *Clim. Dyn.* 36, 1239–1253. doi: 10.1007/s00382-010-0792-4

Hwang, J., Orenstein, P., Cohen, J., Pfeiffer, K., and Mackey, L. (2019). "Improving subseasonal forecasting in the western U.S. with machine learning," in *The 25th ACM SIGKDD Conference on Knowledge Discovery and Data Mining (KDD'19), August 4-8, Anchorage* (New York, NY: ACM). doi: 10.1145/3292500.3330674

Kalnay, E., Kanamitsu, M., Kistler, R., Collins, W., Deaven, D., Gandin, L., et al. (1996). The NCEP/NCAR 40-year reanalysis project. *Bull. Am. Meteorol. Soc.* 77, 437–472. doi: 10.1175/1520-0477(1996)077<0437:TNYRP>2.0.CO;2

Koster, R. D., Mahanama, S. P. P., Yamada, T. J., Balsamo, G., Berg, A. A., Boisserie, M., et al. (2010). The contribution of land surface initialization to subseasonal forecast skill. *Geophys. Res. Lett.* 37, 489–496. doi: 10.1029/2009GL041677

Li, S., and Robertson, A. W. (2015). Evaluation of submonthly precipitation forecast skill from global ensemble prediction systems. *Month. Weather Rev.* 143, 2871–2889. doi: 10.1175/MWR-D-14-00277.1

Liang, P., and Lin, H. (2018). Sub-seasonal prediction over East Asia during boreal summer using the ECCC monthly forecasting system. *Clim. Dyn.* 50, 1007–1022. doi: 10.1007/s00382-017-3658-1

Liu, F., Ouyang, Y., Wang, B., Yang, J., Ling, J., and Hsu, P. C. (2020). Seasonal evolution of the intraseasonal variability of China summer precipitation. *Clim. Dyn.* 54, 4641–4655. doi: 10.1007/s00382-020-05251-0

Liu, Y., Racah, E., Correa, J., Khosrowshahi, A., Lavers, D., Kunkel, K., et al. (2016). Application of deep convolutional neural networks for detecting extreme weather in climate datasets. *arXiv [Preprint]. arXiv:1605.01156*. doi: 10.475/123_4

Lu, R. (2002). Indices of the summertime Western North Pacific subtropical high. *Adv. Atmos. Sci.* 19, 1004–1028. doi: 10.1007/s00376-002-0061-5

Mao, R., Gong, D. Y., Yang, J., and Bao, J. D. (2011). Linkage between the arctic oscillation and winter extreme precipitation over Central-Southern China. *Clim. Res.* 50, 187–201. doi: 10.3354/cr01041

Matthews, T. K., Wilby, R. L., and Murphy, C. (2017). Communicating the deadly consequences of global warming for human heat stress. *Proc. Natl. Acad. Sci. U.S.A.* 114, 3861–3866. doi: 10.1073/pnas.1617526114

McGovern, A., Gagne, D. J., Williams, J. K., Brown, R. A., and Basara, J. B. (2014). Enhancing understanding and improving prediction of severe weather through spatiotemporal relational learning. *Mach. Learn.* 95, 27–50. doi: 10.1007/s10994-013-5343-x

Neena, J. M., Lee, J. Y., Waliser, D., Wang, B., and Jiang, X. (2014). Predictability of the Madden-Julian oscillation in the intraseasonal variability hindcast experiment (ISVHE). *J. Clim.* 27, 4531–4543. doi: 10.1175/JCLI-D-13-00624.1

Qiu, M., Zhao, P., Zhang, K., Huang, J., Shi, X., Wang, X., et al. (2017). "A short-term rainfall prediction model using multi-task convolutional neural networks," in *Data Mining (ICDM), IEEE International Conference on IEEE* (New Orleans, LA), 395–404. doi: 10.1109/ICDM.2017.49

Robertson, A. W., Kumar, A., Pea, M., and Vitart, F. (2015). Improving and promoting subseasonal to seasonal prediction. *Bull. Am. Meteorol. Soc.* 96, ES49–ES53. doi: 10.1175/BAMS-D-14-00139.1

Shi, X., Chen, Z., Wang, H., Yeung, D. Y., Wong, W. K., and Woo, W. C. (2015). Convolutional LSTM network: a machine learning approach for precipitation nowcasting. *Adv. Neural Inform. Process. Syst.* 28, 802–810. doi: 10.1007/978-3-319-21233-3_6

Sobolowski, S., Gong, G., and Ting, M. (2010). Modeled climate state and dynamic responses to anomalous North American snow cover. *J. Clim.* 23, 785–799. doi: 10.1175/2009JCLI3219.1

Strobach, E., and Bel, G. (2016). Decadal climate predictions using sequential learning algorithms. *J. Clim.* 29, 3787–3809. doi: 10.1175/JCLI-D-15-0648.1

Vitart, F., Ardilouze, C., Bonet, A., Brookshaw, A., Chen, M., Codorean, C., et al. (2017). The Subseasonal to Seasonal (S2S) prediction project database. *Bull. Am. Meteorol. Soc.* 98, 163–173. doi: 10.1175/BAMS-D-16-0017.1

Vitart, F., Robertson, A. W., and Anderson, D. L. T. (2012). Subseasonal to seasonal prediction project: bridging the gap between weather and climate. *Bull. World Meteorol. Organ.* 61, 23–28. doi: 10.1029/2018JD029375

Waliser, D. E., Lau, K. M., Stern, W., and Jones, C. (2003). Potential predictability of the Madden-Julian oscillation, *Bull. Am. Meteorol. Soc.* 84, 33–50. doi: 10.1175/BAMS-84-1-33

Wang, B., and Fan, Z. (1999). Choice of South Asian summer monsoon indices. *Bull. Amer. Meteor. Soc.* 80, 629–638. doi: 10.1175/1520-0477(1999)080<0629:COSASM>2.0.CO;2

Wang, B., Wu, R., and Lau, K. M. (2001). Interannual variability of Asian summer monsoon: Contrast between the Indian and western North Pacific-East Asian monsoons. *J. Clim.* 14, 4073–4090. doi: 10.1175/1520-0442(2001)014<4073:IVOTAS>2.0.CO;2

Woolnough, S. J., Vitart, F. and Balmaseda, M. A. (2007). The role of the ocean in the Madden-Julian Oscillation: implications for the MJO prediction. *Quart. J. Meteor. Soc.* 133, 117–128. doi: 10.1002/qj.4

Wu, J., and Gao, X. (2013). A gridded daily observation dataset over China region and comparison with the other datasets. *Chin. J. Geophys.* 56, 1102–1111. doi: 10.6038/cjg20130406

Xiao-Xia, C., Zheng-Guo, S., and Wan-Li, L. (2010). Relationships between Western Pacific subtropical high and seasonal precipitation in Eastern China. *Meteorol. Res.* 1, 81–86.

Yang, J., Wang, B., and Qing, B. (2010). Biweekly and 21–30-Day Variations of the Subtropical summer monsoon rainfall over the lower reach of the Yangtze river basin. *J. Clim*. 23, 1145–1159. doi: 10.1175/2009JCLI3005.1

Yao, Y., Lin H., and Wu, Q. (2015). Subseasonal variability of precipitation in China during boreal winter. *J. Clim.* 28, 6548–6559. doi: 10.1175/JCLI-D-15-0033.1

Zhang, R. H., Li, T. R., Wen, M., and Liu, L. K. (2015). Role of intraseasonal oscillation in asymmetric impacts of El Niño and La Niña on the rainfall over Southern China in boreal winter. *Clim. Dyn.* 45, 559–567. doi: 10.1007/s00382-014-2207-4

Zhu, Z., and Li, T. (2017). The statistical extended-range (10–30 day) forecast of summer rainfall anomalies over the entire China. *Clim. Dyn.* 48, 209–224. doi: 10.1007/s00382-016-3070-2

Conflict of Interest: ZY is employed by the company Baidu Inc.

The remaining authors declare that the research was conducted in the absence of any commercial or financial relationships that could be construed as a potential conflict of interest.

frontiers in Earth Science

ORIGINAL RESEARCH
published: 19 May 2021
doi: 10.3389/feart.2021.673943

Responses of Heat Stress to Temperature and Humidity Changes Due to Anthropogenic Heating and Urban Expansion in South and North China

Shuai Yang[1,2]*, Shuwen Li[1], Bin Chen[2]*, Zeming Xie[3,4] and Jing Peng[5]

[1] Laboratory of Cloud-Precipitation Physics and Severe Storms, Institute of Atmospheric Physics, Chinese Academy of Sciences, Beijing, China, [2] State Key Laboratory of Severe Weather, Chinese Academy of Meteorological Sciences, Beijing, China, [3] Key Laboratory of Land Surface Process and Climate Change in Cold and Arid Regions, Northwest Institute of Eco-Environment and Resources, Chinese Academy of Sciences, Lanzhou, China, [4] University of Chinese Academy of Sciences, Beijing, China, [5] Key Laboratory of Regional Climate-Environment for Temperate East Asia, Institute of Atmospheric Physics, Chinese Academy of Sciences, Beijing, China

OPEN ACCESS

Edited by:
Ming Luo,
Sun Yat-sen University, China

Reviewed by:
Jianping Tang,
Nanjing University, China
Jiachuan Yang,
Hong Kong University of Science and Technology, Hong Kong

****Correspondence:***
Shuai Yang
ys_ys@126.com
Bin Chen
chenbin@cma.gov.cn

Specialty section:
This article was submitted to Atmospheric Science, a section of the journal Frontiers in Earth Science

Received: *28 February 2021*
Accepted: *14 April 2021*
Published: *19 May 2021*

Citation:
Yang S, Li S, Chen B, Xie Z and Peng J (2021) Responses of Heat Stress to Temperature and Humidity Changes Due to Anthropogenic Heating and Urban Expansion in South and North China. Front. Earth Sci. 9:673943. doi: 10.3389/feart.2021.673943

Due to global warming and human activities, heat stress (HS) has become a frequent extreme weather event around the world, especially in megacities. This study aims to quantify the responses of urban HS (UHS) to anthropogenic heat (AH) emission and its antrophogenic sensible heat (ASH)/anthropogenic latent heat (ALH) components and increase in the size of cities in the south and north China for the 2019 summer based on observations and numerical simulations. AH release could aggravate UHS drastically, producing maximal increment in moist entropy (an effective HS metric) above 1 and 2 K over the south and north high-density urban regions mainly through ALH. In contrast, future urban expansion leads to an increase in HS coverage, and it has a larger impact on UHS intensity change (6 and 2 K in south and north China) relative to AH. The city radius of 60 km is a possible threshold to plan to city sprawl. Above that city size, the HS intensity change due to urban expansion tends to slow down in the north and inhibit in the south, and about one-third of the urban regions might be hit by extreme heat stress (EHS), reaching maximal hit ratio. Furthermore, changes in warmest EHS events are more associated with high humidity change responses, irrespective of cities being in the north or south of China, which support the idea that humidity change is the primary driving factor of EHS occurrence. The results of this study serve for effective urban planning and future decision making.

Keywords: heat stress, anthropogenic heating, urban expansion, temperature change, humidity change

INTRODUCTION

In the context of global warming, the probability, intensity, and duration of heat stress (HS) have been increasing around the world (Lee and Min, 2018; Wang et al., 2020), especially in megacities. Different from a common heat wave with high temperature, heat stress is characterized as being an extremely hot and humid environment, and it is known in China as “sauna weather”. It usually lasts for several days to a week, causing illness or even death. In addition, stable atmospheric circulation and sinking motion prevent the dispersal of pollutants during an HS period. Therefore, health problems associated with HS have attracted widespread attention (Weatherly and Rosenbaum, 2017; Napoli et al., 2019; Zander et al., 2019).

Heat stress, especially an extreme heat stress (EHS) event, usually occurs locally. The driving factors [e.g., natural factors, such as high temperatures, humidity, and solar radiation, and human activities, such as urban heat island (UHI) effect, anthropogenic heat (AH), etc.] and physical mechanisms are very different among regions (Seneviratne et al., 2012; Fischer and Knutti, 2013; Ohashi et al., 2014; Steinweg and Gutowski, 2015; Lee and Min, 2018; Lorenz et al., 2019). Furthermore, the commonly used heat stress metrics (Steadman, 1994; Willett and Sherwood, 2012; Buzan et al., 2015), such as apparent temperature and wet bulb globe temperature (WBGT), are functions of both temperature and humidity. Thus, HS change is determined by the coaction of temperature and humidity changes, which further increases the complexity of HS variation. Therefore, region-scale studies are fundamentally required to project future changes in extreme events and to assess the dependence of HS or EHS on temperature and humidity changes (Napoli et al., 2019; Lutsko, 2021).

As typically vulnerable regions in the south and north China, Pearl River Delta (PRD) and Beijing–TianJin–Heibei (JJJ) city clusters have experienced an increase in the number of heat stress events, leading to negative social influences, economic loss, and great risk in human health (Ohashi et al., 2014; Hass et al., 2016; Xie et al., 2016, 2017; Wang et al., 2020). Rapid urbanization and economic development bring about land use changes and explosive growth in both population and overloaded energy expenditures. The frequent HS events might be associated with the UHI effect because of urban expansion and excessive AH emission from human activities (Sun et al., 2016; Yang W. et al., 2017; Yang X. et al., 2017; Luo and Lau, 2018; Ye et al., 2018; Wang et al., 2019).

The UHI effect and its relationship with heatwave have been identified from a climatological perspective by previous research studies (Feng et al., 2012; Yang L. et al., 2014; Chen et al., 2016; Xie et al., 2016, 2017; Ramamurthy and Bou-Zeid, 2017), but for region-scale HS events, the UHI effect generated by urban sprawl tends to be accompanied with urban dry island (UDI). They play the opposite roles on HS change by increasing temperature but decreasing humidity. So in the future, how does continuous urban expansion impact HS change after neutralization of the positive and negative contributions of rise in temperature and decrease in humidity to HS? In the south and north China, to which factor is the occurrence of extreme urban heat stress events more sensitive, temperature change or humidity change?

In addition, the extent of AH emission is synchronously increasing because of the excessive release of waste heat from human activities. Waste heat is released to an urban canopy mainly by means of transportation and industries in the form of anthropogenic sensible heat (ASH), or through sprinkling on roads and in parks, irrigations, etc., as anthropogenic latent heat (ALH) (Sugawara and Narita, 2008; Allen et al., 2011; Yang et al., 2015). As an important heat source for urban surface energy balance (Offerle et al., 2005; Smith et al., 2009; Iamarino et al., 2012), AH could impact HS through varied urban thermal environments (Yang S. et al., 2014; Nie et al., 2017). For instance, based on numerical simulation conducted from December 1, 2006 to December 31, 2008, AH release produced 0.66°C warming in summer over the Yangtze River Delta (Feng et al., 2012), so as to be a powerful inducing factor of UHI (e.g., Chen et al., 2008, 2016; Feng et al., 2012; Nie et al., 2017; Zhang et al., 2016, 2017a). The daily average contribution ratio of AH to UHI intensity in Hangzhou city of Zhejiang province in China is 43.6 and 54.5% in summer and winter, respectively (Chen et al., 2009). In the PRD region, the proportion is even higher for certain cases, reaching up to 74% of total UHI intensity estimated by an averaged 2-m temperature difference from an 8-day numerical simulation (Zhang et al., 2016). Thus, it follows that AH and HS might change urban meteorology by aggravating UHI via directly enhanced upward heat flux (Ichinose et al., 1999; Narumi et al., 2009; Feng et al., 2012; Nie et al., 2017). Over two target regions in the south and north China, how are the responses of HS to temperature and humidity changes due to anthropogenic heat and its components (ASH and ALH) quantified?

Therefore, the goals of this study are as follows: (1) to determine the impacts of AH and its components on the pattern and diurnal variation feature of heat stress; (2) to evaluate the future HS evolution with an increase in the size of south and north cities of China; and (3) by separating the contributions of temperature and humidity changes to EHS change, to evaluate their relative significance on EHS occurrence. To address these goals, this study is arranged as follows: in Section "Model, Data, Experiment Design, and Methodology," the models, data, and experiment design will be introduced. By invoking high-resolution numerical simulations and performing sensitive experiments, the influences of AH and increase in city size on HS over south and north cities will be explored in Section "Results." Then, we will focus on EHS to determine the primary driving factor for its occurrence by weighting temperature change and humidity change more heavily. A summary will be given in the last section.

MODEL, DATA, EXPERIMENT DESIGN, AND METHODOLOGY

Model

In this study, the WRF model (V4.1.5) with an embedded single-layer urban canopy model (SLUCM) was used to conduct numerical simulations (Skamarock et al., 2019). The coupled model was able to capture the complex interaction between urban land surface characteristics and atmospheric processes. Thus, we took the urban canopy effect into full consideration, and the coupled SLUCM-WRF model system was employed during the simulation.

The main run parameters of the WRF numerical model and UCM parameters are listed in **Tables 1**, **2**, where the parameters refer to the geometric features of Chinese cities (Zhang et al.,

TABLE 1 | The main parameters used in the WRF model setup.

Model parameters	D01	D02/D03	D04/D05
Horizontal resolution (km)	9 km	3 km	1 km
Grids number	324 × 383	249 × 231	390 × 372
Vertical level	51	51	51
Time step (s)	54	18	6
Cumulus parameterization	Kain-Fritsch (Kain, 2004)	None	None
Microphysical scheme	Kessler (Kessler, 1969)		
Planetary boundary scheme	MYJ (Mesinger, 1993; Janjic, 1994)		
Long wave transfer scheme	RRTM (Iacono et al., 2008)		
Short wave transfer scheme	RRTM (Iacono et al., 2008)		
Land-surface model	Noah (Tewari et al., 2004)	Noah (Tewari et al., 2004)	Noah(S)/Noah-MP(N) (Niu et al., 2011; Yang et al., 2011)
Urban canopy model	SLUCM (Kusaka et al., 2001; Chen et al., 2011)		

TABLE 2 | Urban canopy parameters used in this study.

ZR	CAPR	CAPB	CAPG	AKSR	AKSB	AKSG	ALB	EPSB	EPSG
15 / 10 / 5	1.19	1.19	1.49	0.8	0.88	0.67	0.09	0.92	0.96

Where the parameters refer to the geometric features of Chinese cities (Zhang et al., 2017b), with ZR (m) representing building height in high-/medium-/low-density urban areas; CAPR/CAPB/CAPG ($10^6 Jm^{-3}K^{-1}$), heat capacity of roof/building wall/ ground (road); ALB (%), surface albedo; AKSR/AKSB/AKSG ($J \cdot m^{-1} \cdot s^{-1} \cdot K^{-1}$), thermal conductivity of roof/building wall/ ground (road); and EPSB/EPSG, surface emissivity of building wall/ ground (road).

2017b). Five nested domains are shown in **Figure 1a**. The vertical grid contains 51 non-uniformed full sigma levels from the surface to 50 hPa, with 16 of these levels below 1 km. Thus, we obtained a fine vertical resolution within the planetary boundary layer (PBL). The integration started at 00UTC 23 and lasted for 6 days. The first 24 h was used as a spin-up time and was not included in subsequent analyses. The model outputs with 1 h interval from the innermost D04 and D05 domains (covering PRD and JJJ, respectively, typical of south and north city clusters) were utilized as two target regions for comparative analyses.

Data

Metrological Data

In this study, multi-metrological data support observation analysis and numerical simulation were performed. The European Center for Medium-Range Weather Forecast (ECMWF) ERA5 hourly reanalysis data, with a spatial resolution of 0.25 degrees and 37 pressure levels vertically extending from 1,000 to 1 hPa, were used to drive the WRF simulation as initial and boundary conditions. Also, from the ERA5 data, we described the general synoptic situation during a heat stress episode. The humidity and temperature profiles of the PRD and JJJ target regions were depicted from upper-air sounding observation. Surface automatic weather station (AWS) observations were performed to implement model verifications.

Land Use Data and Impervious Surface Map

We adopted the Moderate-resolution Imaging Spectroradiometer (MODIS) land use/land cover data from 2019 (**Figures 1b,c**). In addition, taking the heterogeneity of urban land cover into account, we further classified urban land use (**Figures 1b,c**) into high-/medium-/low-density types (**Figures 1f,g**), retrieved according to the percentage of impervious area. Herein, we took the percentage thresholds of 80 and 50% to identify high-/medium-/low- density urban areas and referred to Tewari et al. (2007) and Zhang et al. (2017b). To test inversion validity, global 30m impervious surface maps, amplified in the PRD and JJJ regions (**Figures 1d,e**), were also plotted. They were derived from multisource and multitemporal remote sensing datasets with the Google Earth Engine platform developed by Zhang et al. (2020). By contrast, the high-intensity urban areas, as shown in **Figures 1f,g**, matched well with impervious surface-dominant regions (**Figures 1d,e**).

Anthropogenic Heat Emission

The importance of AH in changing the near-ground energy balance as a heat source has been recognized (Oke, 1988; Grimmond, 1992; Sailor, 2011; Sailor et al., 2015; Chrysoulakis et al., 2016). AH is wasted heat in the form of sensible and latent heat due to human activities, and is released to an urban canopy (Yang et al., 2015; Yang W. et al., 2017). However, most studies have assumed that anthropogenic heat is sensible in nature without accounting for the latent heat component. Several studies have suggested that water vapor emission by cooling systems constitutes a substantial portion of latent heat flux in urban areas (Sailor et al., 2007; Miao and Chen, 2014), and this flux was shown to exceed 500 W m^{-2}over central Tokyo in summer (Moriwaki et al., 2008).

In the current WRF-SLUCM system, both the ASH and ALH components of AH are considered. We adopted local AH releases (**Table 3**) over Chinese cities (Miao and Chen, 2014; Yang et al., 2015; Chew et al., 2021; Peng et al., 2021), replacing the default value modeled in WRF to improve HS simulation. The diurnal cycles of ASH and ALH (W m^{-2}) in high-, medium- and low-density cities were added into the model by diurnal profiles coefficient (shown in **Figures 1g,i**) acting on the AH values shown in **Table 3**. Two peaks of ASH

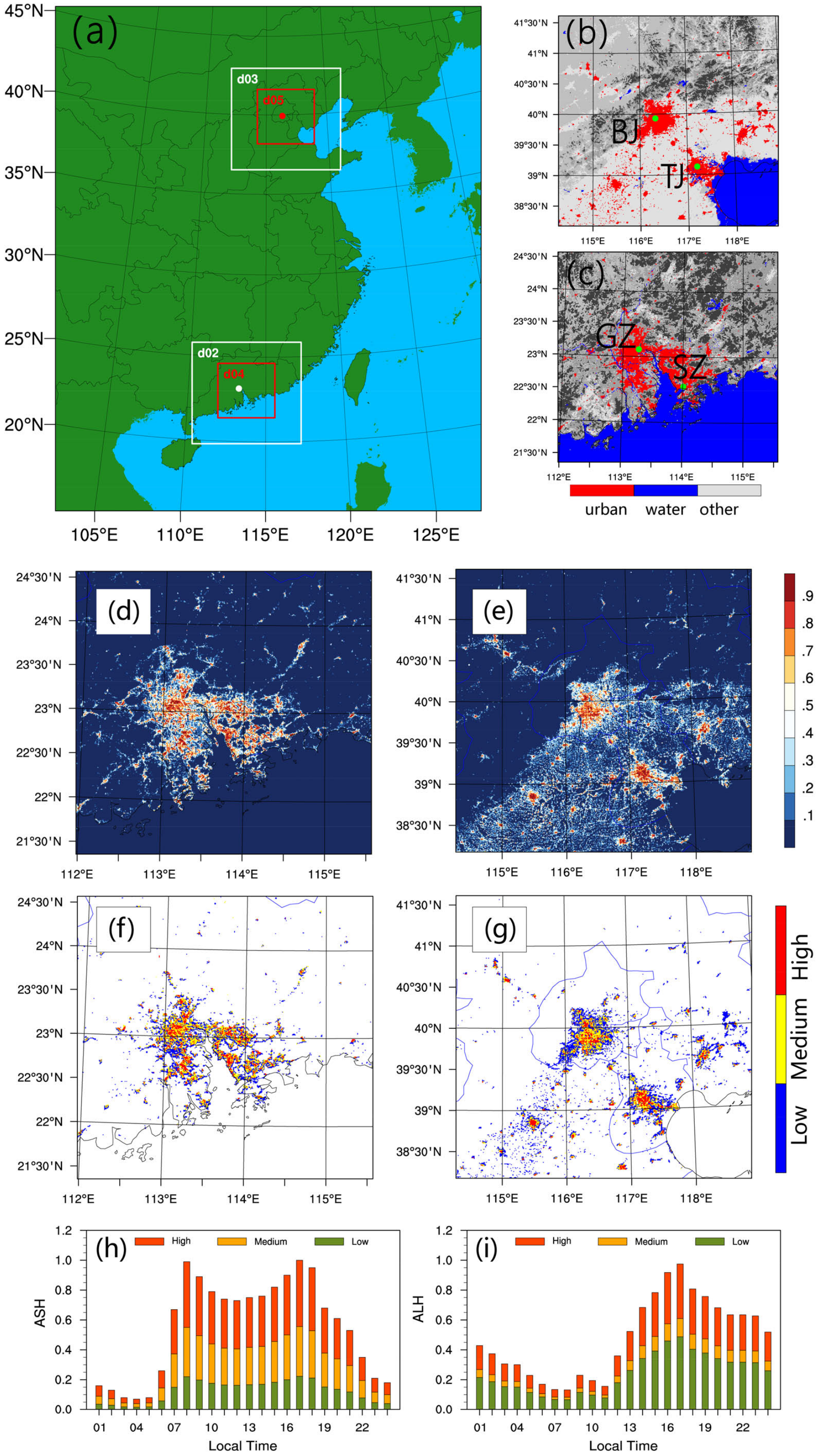

FIGURE 1 | (a) The nested simulation domains; **(b)** land cover for JJJ, and **(c)** PRD city cluster regions (red) in 2019, Beijing (BJ), Tianjin (TJ), Guangzhou (GZ), and Shenzhen (SZ) cities are marked; **(d,e)** the impervious surface ratio maps; **(f,g)**, the high-, medium-, and low-density cities retrieved from impervious surface ratio for PRD (left) and JJJ (right). In panels **(b,c)**, the black shaded regions show the terrain north of PRD and northwest of JJJ, while red, blue, and gray indicate urban, water body and other land uses. In panels **(f-g)**, red, yellow, and blue denote high-, medium-, and low-density cities. The diurnal cycle coefficients of panels **(h)** ASH and **(i)** ALH in high-, medium-, and low-density cities. By acting on AH values in **Table 3**, these coefficients are used to produce gridded ASH and ALH (W m^{-2}) values in high-, medium-, and low-density cities, characterized by diurnal variation, to be added into the model.

TABLE 3 | ASH and ALH releases in high-/medium-/low-density urban areas used in this study. The diurnal cycles of ASH and ALH (W m^{-2}) profiles in high-, medium- and low-density cities refer to **Figures 1g,i**.

	High-density urban	Medium-density urban	Low-density urban	References
ASH_South	131.6	96.3	52.7	Yang et al., 2015; Peng et al., 2021
ALH_South	85	60	30	Chew et al., 2021
ASH_North	88	48.9	19.6	Yang et al., 2015; Peng et al., 2021
ALH_North	120	75	60	Miao and Chen, 2014; Yang et al., 2015

have coincided with local rush hours (8–9 and 17–18 LST), consistent with the default profile in the model and the bimodal mode of diurnal ASH profiles over the south and north Chinese cities (Wang and Wang, 2011; Wang et al., 2016). While the ALH profile was derived by combining Beijing-325 m weather tower observation analysis with land surface model (Miao and Chen, 2014), the diurnal variation of ALH flux followed the schedule of human activity and was relatively independent of season (Moriwaki et al., 2008). Both ASH and ALH were gradually strengthened on the heels of an increase in city density. Thereinto, the ASH flux in south cities exceeded the maximal value in Guangzhou (approximately 50 $W{\cdot}m^{-2}$), which has been recently estimated by Zhu et al. (2017).

Experiment Design

We conducted numerical experiments in two groups (**Table 4**) to quantify how heat stress responds to AH release and increases in city size. By evaluating the contributions of temperature and humidity changes to HS change, the attribution to HS change was further dissected.

In the first group, we conducted four sets of experiments, which were named as Real, no ASH, no ALH, and no AH. All runs took the high-/medium-/low-density urban types of the current land cover into account. Meanwhile, reasonable AH ejections (including both ASH and ALH releases) were coupled into WRF by the SLUCM for the Real run. Then ASH run, ALH run, or both (i.e., total AH) were set to zero in turn to perform other simulations. By contrasting each run with Real run, we quantified the response of HS to each contributor. Additionally, the occurrence probabilities of EHSs in various-type urban regions were explored under different AH release scenarios.

We conducted the second group experiment to focus on how a gradual increase in city size influences heat stress intensity by utilizing the Real atmosphere idealized land-surface (RAIL) method (Schmid and Niyogi, 2013). We also probe into that, the varied HS with urban expansion is mainly determined by which driving factor, temperature change or humidity change. For the two target regions, Guangzhou (GZ) and Shenzhen (SZ) in the PRD region and Beijing (BJ) and Tianjin (TJ) in the JJJ region were selected to represent inland and coastal cities in south and north China (**Figures 1b,c**). In the Ideal run, urban land uses are replaced by the homogeneous crop land surface (i.e., the nearby rural land cover type), to remove the influence of urban land cover. Then, cities of 30, 40, 50, 60, 70, and 80 km radii (centered by green dots in **Figures 1b,c**) are designed to represent the process of urban expansions in the present and future. Refer to Schmid and Niyogi (2013) in which cities of different radii with the simplified, homogeneous land surface are designed to represent current and future city scenarios. The experiment results were used to perform comparative HS studies among inland and coastal cities in the south and north China.

Methods to Evaluate Temperature–Humidity Dependence for Heat Stress

Moist Enthalpy and Moist Entropy

Due to the high-temperature and high-humidity features of heat stress weather, two moisture-thermal energy metrics (Lutsko, 2021), moist enthalpy ($H = C_p T + Lq_v$) and moist entropy ($S = C_p \ln \theta_e$) were introduced to differentiate the different characteristics during a heat stress episode in the PRD and JJJ city clusters. They included both temperature and humidity factors. And we are easily to separate temperature change from humidity change based on moist entropy or moist enthalpy formula, to evaluate their respective contributions to heat stress variation.

Moist entropy and moist enthalpy are classic thermodynamic variables in meteorology. Despite not being frequently used for heat stress compared to other several commonly used metrics, their application potentials as HS metrics and clear advantages in dynamics attract us to use them as indicators to discuss HS in this study. Note that in this study we did not attempt to determine the best way to measure heat stress. Rather, we examined whether moist enthalpy and entropy could be evaluative metrics to demonstrate an HS episode besides the three other widely used HS metrics. (1) By contrast between them and other commonly used HS indicators, we will evaluate the validities of moist entropy and moist enthalpy as metrics to characterize HS evolution to further prove their application potentials for HS weather. (2) They are classic thermodynamic and dynamic variables in meteorology. Taking moist entropy as an example, it has conservation property for a moistly adiabatic and frictionless atmosphere. Thus, it could be used as a mass surface or a tracer to demonstrate the convergence and dispersion of high-temperature and high-humidity atmosphere, so as to illustrate the genesis and diffusion of HS weather. In this regard, it is convenient to extend dynamically to further give mechanism responsible for HS weather and as a predicative factor in our follow-up study. (3) It is easy to separate the contributions of humidity change from temperature change by taking the differential operator on the moist entropy formula. Thus, by calculating and comparing the magnitudes of temperature and humidity changes, which one is the primary driver of the moist entropy fractional change will be judged. The entire separation and comparison do not depend on some subjective and empirical parameters, such as clothing index, exposure index, medical discomfort index, etc. This is easy

TABLE 4 | Experiment design and description in section "Experiment Design."

Experiment groups	Experiment names	Descriptions
Group 1: AH experiment	Real	Real land cover with high-, medium-, low- density urban types is used, and UCM model is coupled. Both ASH and ALH releases are considered.
	No ASH	The same as Real, except that ASH release is set to zero.
	No ALH	The same as Real, except no ALH.
	No AH	The same as Real, except that neither ASH nor ALH is considered.
Group 2: City size experiment	Ideal	Urban land use is replaced by homogeneous crop land surface to remove the influence of urban land cover.
	Ideal_R30, Ideal_R40, Ideal_R50, Ideal_R60, Ideal_R70, Ideal_R80	Cities of 30, 40, 50, 60, 70 and 80 km radii, centered at BJ, TJ, GZ, and SZ (green dots in **Figures 1b,c**) are designed to represent the process of urban expansions in the present and future.

to implement based on observations and numerical model. In terms of these, in this study, we mainly used moist enthalpy and especially moist entropy as indicators to discuss heat stress:

Where T and q_v are absolute temperatures and specific humidity, C_p is the specific heat of dry air at constant pressure p. L is latent heat of vaporization and $\theta_e = \theta \exp(\frac{Lq_v}{C_p T_L})$ is equivalent potential temperature (Holton and Hakim, 2013). Herein, T_L is the temperature at the lifting condensation level.

Methods to Separate Temperature–Humidity Contribution to Heat Stress

By taking the differential operator on the θ_e formula, we have $\frac{1}{\theta_e}\nabla\theta_e \doteq \frac{1}{\theta}\nabla\theta + \frac{1}{C_p T}\nabla(Lq_v)$ [Eq. (1)], wherein the relation $O(\frac{1}{T}\nabla T) \ll O(\frac{1}{q_v}\nabla q_v)$ is used after analyzing the order of magnitude (Yang S. et al., 2014). In the near-surface level, surface pressure change is small, therefore fractional change in potential temperature ($\Delta\theta$) is roughly equal to fractional change in temperature ($L/C_p \Delta q_v$) in Eq. (1). Thus, by calculating and comparing the magnitudes of $\Delta\theta$ and $L/C_p \Delta q_v$, which one (temperature or humidity change) is the primary driver of the θ_e fractional change will be judged.

Other Metrics to Evaluate Heat Stress Weather

Furthermore, additional several commonly used heat stress metrics (Steadman, 1994; Willett and Sherwood, 2012; Buzan et al., 2015), such as Humidex to compute the "feels-like" temperature for humans ($Humidex = T_c + \frac{5}{9}(e - 10)$), apparent temperature (AT, where $AT = T_c + 0.33e - 0.7u_{10m} - 4$), simplified SWBGT, where ($SWBGT = 0.56T_c + 0.393e + 3.94$), were adopted to strengthen the validity of moist enthalpy and moist entropy as metrics to characterize heat stress events, where Tc and e are air temperature and vapor pressure in units of degrees Celsius and hPa, u_{10m} is the 10-m speed wind, and e is calculated by relative humidity and saturated vapor pressure.

RESULTS

Model Validation

Figures 2A–H compare the simulated (red) 2-m air temperature (**Figures 2A–D**) and relative humidity (**Figures 2E–H**) with observations (blue) derived from multi-stations over the region of the four cities. All these observations are from the national surface AWSs system network, with station locations shown in **Figure 3**.

According to the criterion of heat stress weather issued by China Meteorological Administration, a 4-day episode in PRD (01 LST 25-00 LST 29, i.e., 17 UTC 24-16 UTC 28) and a 2-day episode (01 LST 27-00 LST 29, i.e., 17 UTC 26-16 UTC 28) in JJJ are selected (framed by green boxes in **Figures 2A–H**) as examples to perform a comparative study for typical summer urban heat stress between the south and north cities of China. They generally satisfy the HS criterion that daily maximum temperature is more than 32°C. Meanwhile, the mean daily relative humidity (RH) is not less than 60%, and the weather process lasts at least 2 days.

The model performs well in reproducing the diurnal cycles (**Figure 2**) and spatial distributions (**Figure 3**) of near-surface air temperature and humidity during heat stress episodes (within green boxes), two key factors to evaluate heat stress intensity. It is remarkable that the simulated and observed diurnal peaks of temperature and humidity show a good agreement, despite slightly lower humidity simulations (**Figures 2E-H**). By comparing the observations between south and north cities (**Figures 2**, **3**), higher humidity (e.g., nearly 100% in GZ) and relatively lower temperature (∼about 2–4°C difference) present in south (e.g., temperatures of GZ and SZ exceed 36 and 34°C, while maximal temperatures of BJ and TJ reach up to 38 and 37°C, respectively). From simulations, the comparative results among south and north cities are also reasonable, which have similar tendency with observations.

The root-mean-square error for all stations over the GZ, SZ, BJ, and TJ city regions are shown in **Table 5**. Overall, the simulation is improved by adding AH release (cf. Real and no AH runs in **Table 5**) and is comparable with previous studies (Meir et al., 2013; Ramamurthy and Bou-Zeid, 2017), which is directly attributable to the upward AH flux into UCM model. A certain degree of improvement presents, as ASH or ALH is considered alone (by comparing no AH with no ASH or no ALH run), but the improvement is most pronounced when both factors are considered.

The general synoptic situation during the heat stress episode is briefly described. In the near-surface level, weak southerly (with region-mean intensity of wind speed less than 2 ms^{-1}) prevails in PRD, bringing moisture from the ocean to the target region (not shown). In the JJJ region, southerly dominates Beijing, leading to positive temperature advection

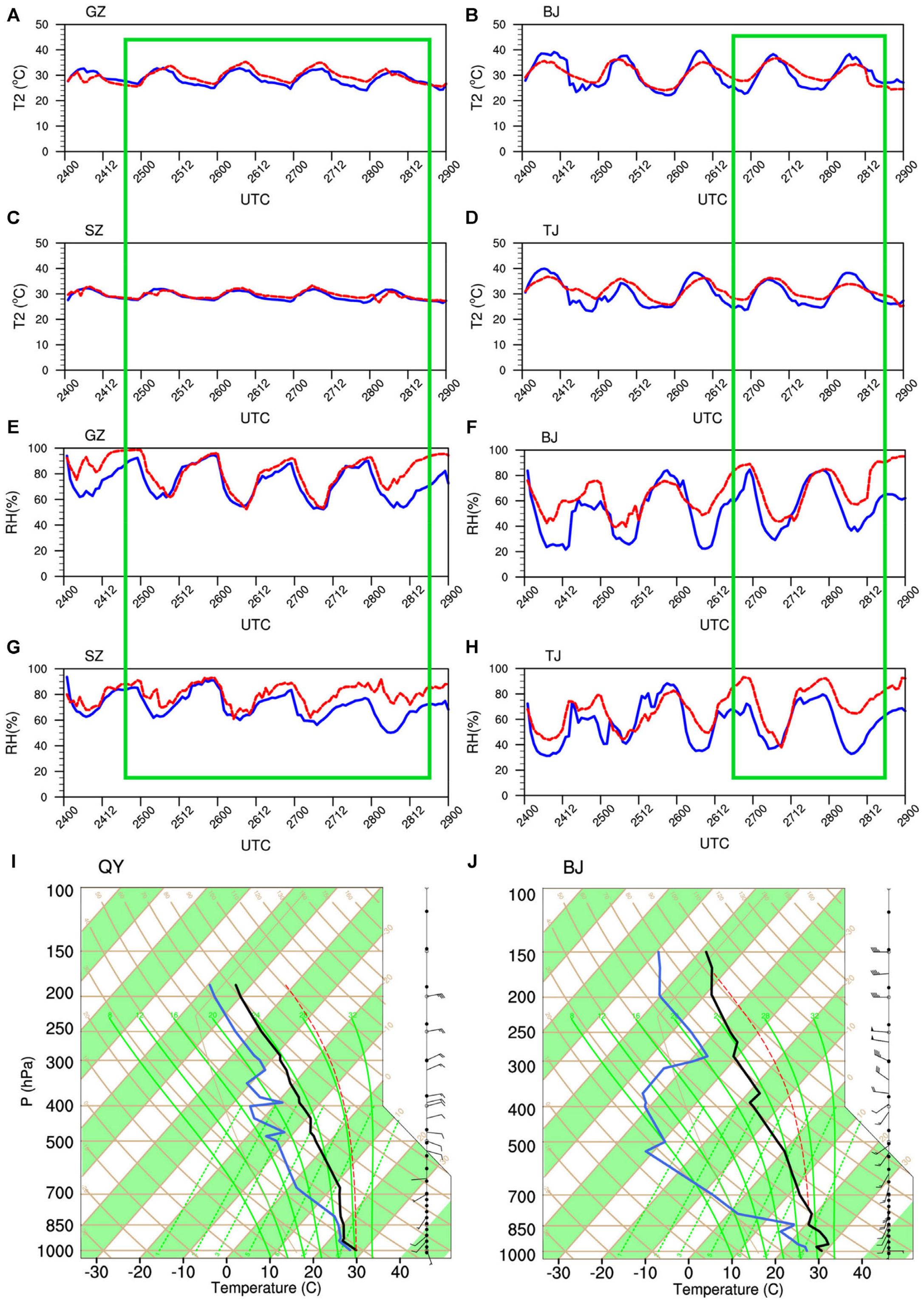

FIGURE 2 | (A–H) Observed (red) and simulated (blue) 2-m air temperature (°C) and relative humidity (%). The green frames show the heat stress episodes in south and north cities. Sounding plots in panels **(I)** Qingyuan (QY) and **(J)** Beijing (BJ) stations, denote observations in south and north, with black and blue curves representing temperature and dew point, respectively.

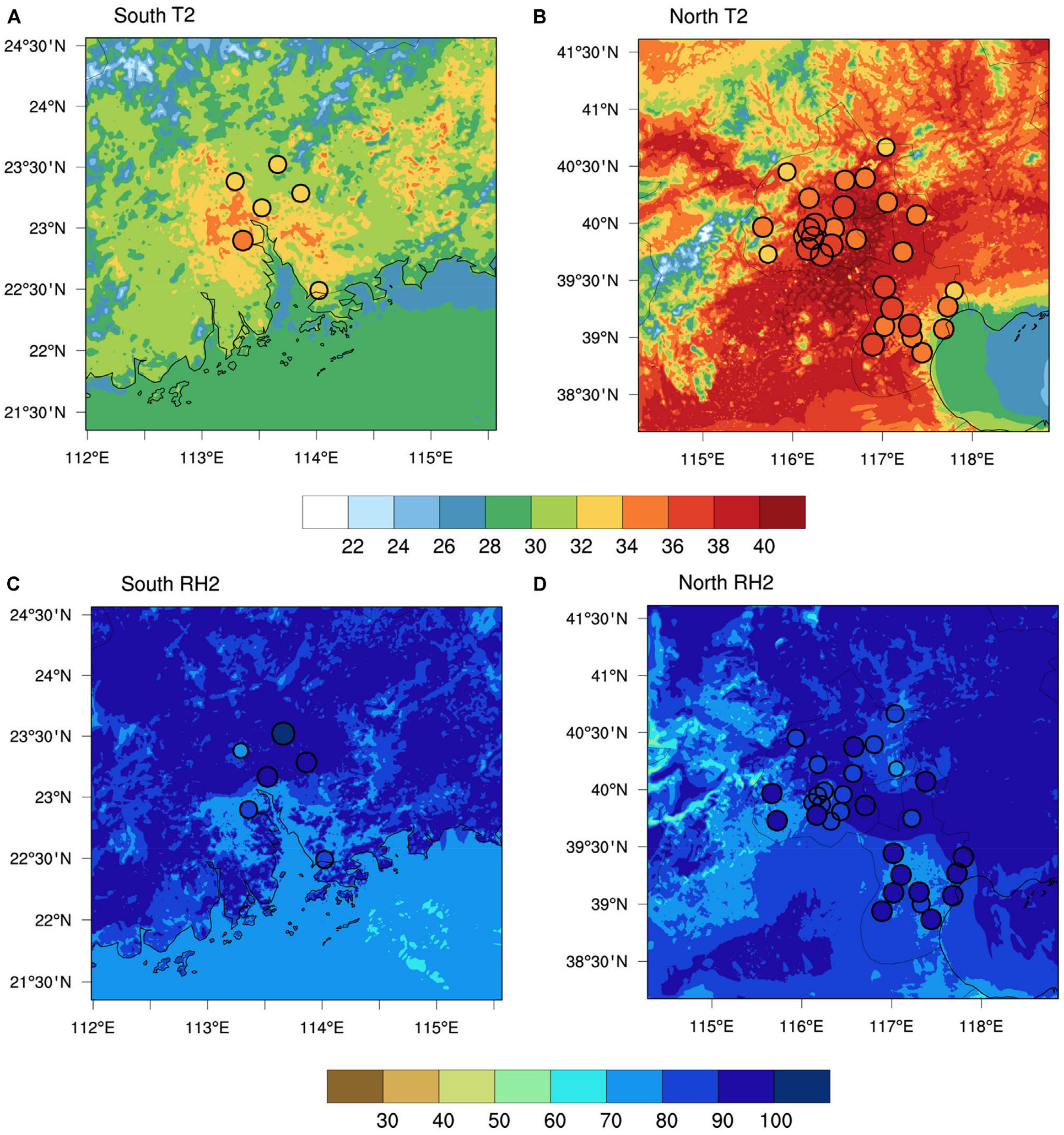

FIGURE 3 | (A–D) The spatial charts of observed (shaded circles) and simulated (shaded) 2-m air temperature (°C) at 05 UTC and relative humidity (%) at 21 UTC 27. All these observations are from the national surface AWS system network, with station locations shown by circles. Where the shaded circles have sizes proportional to temperature and humidity (cf. the color scales below **A-D**).

TABLE 5 | Root-mean-square errors of simulated air temperature (°C) for all stations over various city regions.

Experiments	Guangzhou (GZ)	Shenzhen (SZ)	Beijing (BJ)	Tianjin (TJ)
Real	1.75	1.02	3.01	2.61
No ASH	2	1.1	3.1	2.7
No ALH	1.77	1.03	3.04	2.65
No AH	1.98	1.1	3.13	2.73

from south China; while easterly presents in coastal Tianjin, convenient to moisture transport from eastern ocean to JJJ. We also address the synoptic chart extending upward into the troposphere. A deep-layer high-pressure system caused by the in-phase superposition of middle-level subtropical high and low-level ridges, sinking motion, and weak southerly or easterly near surface, coacton HS weather. From the observed sounding plots (**Figures 2I,J**), stable stratification

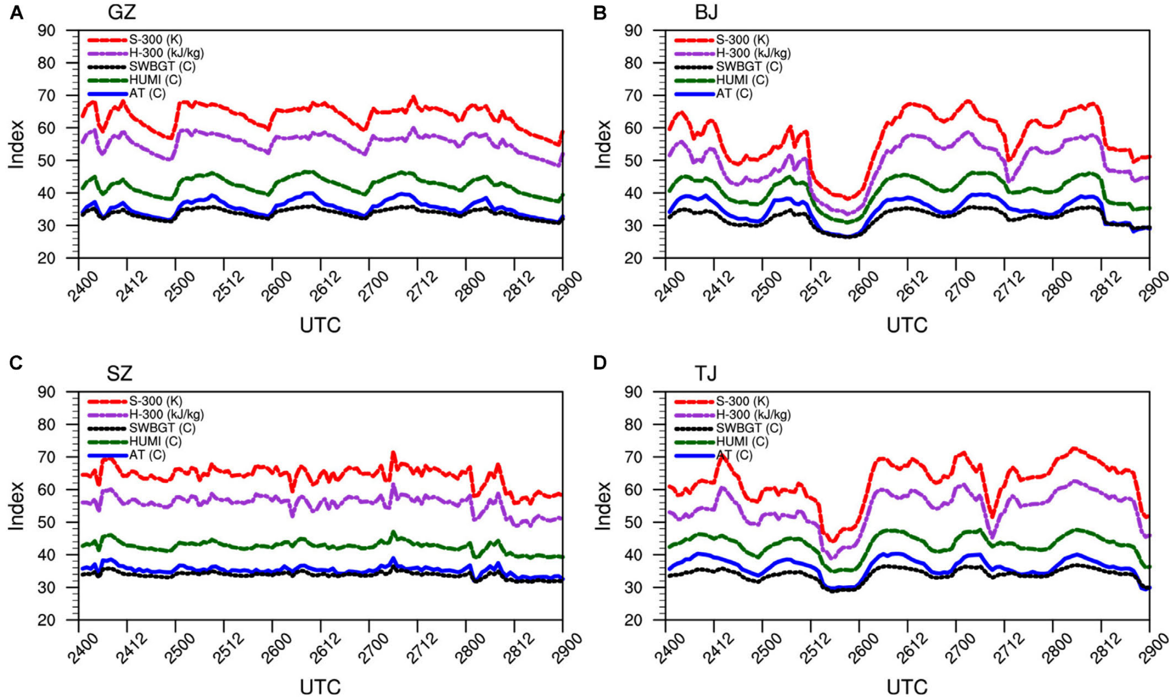

FIGURE 4 | (A–D) Curves of five metrics to evaluate heat stress intensity evolution over GZ, SZ, BJ, and TJ city regions based on multi-station observations. Five metrics are apparent temperature (blue), Humidex (green), and simplified wet bulb globe temperature (black) (°C), moist enthalpy (*H*, purple) (K J/kg), and moist entropy (*S*, red) (K), respectively, where *H* and *S* minus 300 K in magnitude, to be comparable with other metrics.

(black curve, denoted by temperature) inhibits vertical mixing under the boundary layer, which plays a key role in the formation of HS. High dew point (blue curve) indicates high humidity, especially in the south (**Figure 2I**), and a high-humidity pattern stretches up toward the whole troposphere, manifesting as approached temperature and dew point profiles. In the north (**Figure 2J**), large humidity presents in a low level. It decreases swiftly above 800 hPa, characterized by abruptly depressed dew point. All these provide favorable environments to HS weather.

Heat Stress Metrics

Several metrics are utilized to demonstrate the heat stress evolution, as shown in **Figure 4**. First, three commonly used heat stress metrics (Steadman, 1994; Willett and Sherwood, 2012; Buzan et al., 2015), AT, Humidex, and SWBGT (blue, green, and black curves in **Figure 4**), could effectively define the heat stress periods in the south and north cities (see the green boxes as shown in **Figure 2**) and reflect the HS characteristics of high temperature and high humidity. Second, moist enthalpy and moist entropy (*H* and *S*, purple and red curves in **Figure 4**), recently utilized by Lutsko (2021), are evaluative metrics to heat stress, since their evolution follow similar tendencies with other three metrics, except that they have larger value (∼370 K of moist entropy) in magnitude relative to AT, Humidex, and SWBGT (∼50°C below). In addition, consistent with SWBGM and AT, moist entropy and moist enthalpy over BJ and TJ in north China (**Figures 4B,D**) show more obvious diurnal variations compared with HS over GZ and SZ in south China (**Figures 4A,C**). Note that albeit there are strong HS signals in BJ for the 3rd day (01 LST 26-00 LST 27, i.e., 17UTC 25-16UTC 26), which is derived from little higher simulations for T2 and RH (**Figures 2B,F**). Since the observed daily mean humidity does not reach the HS criterion, we mainly concern the latter 2 days as HS episode in northern cities. The peak of HS present in the afternoon and early midnight (about 370 K for moist entropy, at about 06-12UTC) in north, while it takes on generally hot and moist in the south. For instance, the curves of moist entropy in GZ and SZ (**Figures 4A,C**) have less fluctuation than those in north cities (**Figures 4B,D**), maintaining a mean value above 360 K, which accords with our common sense and physical feelings.

Note that we do not attempt to determine the best way to measure heat stress here. Rather, we examine whether moist enthalpy and entropy could be evaluative metrics to demonstrate an HS episode, besides the other three widely used HS metrics. By contrast among metrics, we strengthen the validities of moist entropy and moist enthalpy as metrics to characterize HS evolution. The heat stress illustrates more extreme intensity and diurnal cycle in the north than in the south, for inland than for coastal cities. Of more importance is that it is easy to separate the key factors from each other (temperature and humidity herein) to drive heat stress change based on the moist entropy or moist enthalpy formula themselves. Therefore, we mainly utilize moist entropy or moist enthalpy as metrics to investigate the response of heat stress to AH and increase in city

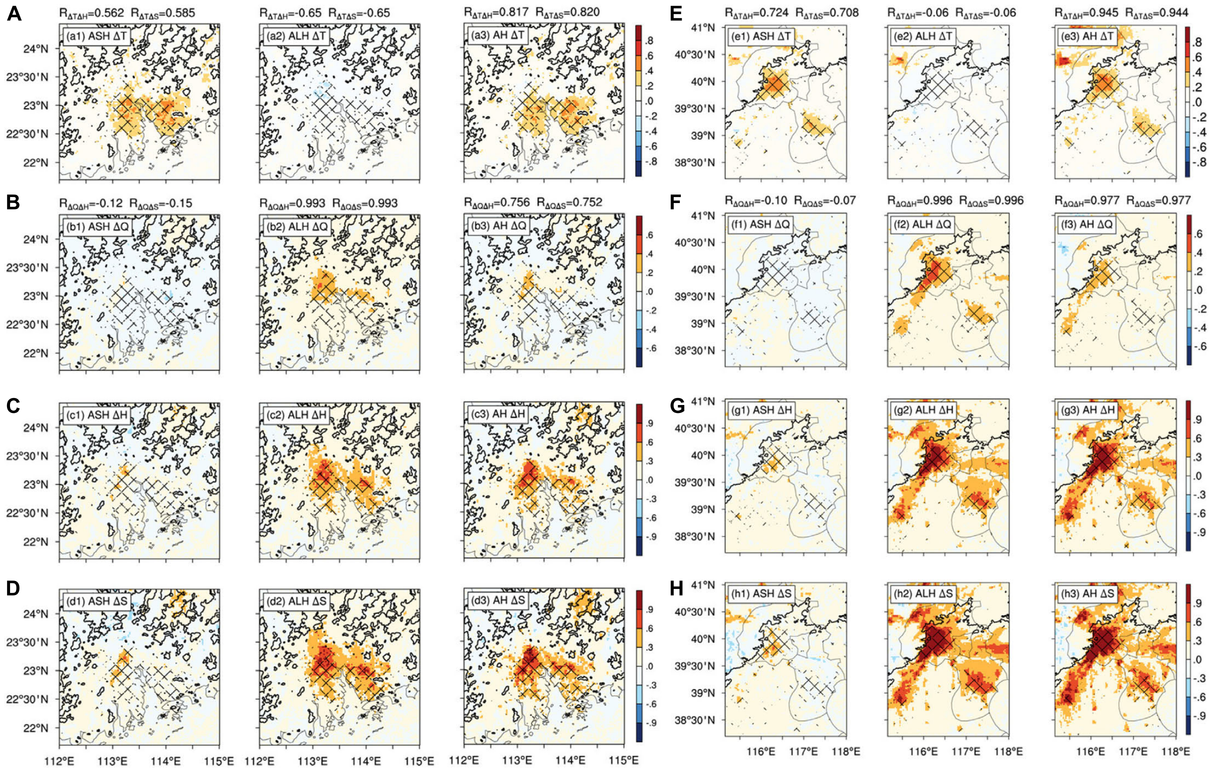

FIGURE 5 | The spatial distribution of moist enthalpy and moist entropy changes (Δ*H* and Δ*S*) and their pattern correlations with temperature and humidity change (Δ*T* and Δ*Q*) for group 1 experiment (**Table 2**), taking account of the impact of AH and its components, and *R* at the top of each panel denotes the correlation coefficient between its two subscript variables. By taking the difference between Real run and the other three runs, we quantify the sole influence of ASH (Real–no ASH), ALH (Real–no ALH), and AH (Real–no AH) in south **(A–D)** and north **(E–H)**, where gridding by slash line represents urban region.

size, and to explain the attribution to HS change by separating the contributions of temperature and humidity changes in the subsequent analyses.

Impact of AH on HS

Pattern

Figure 5 shows the spatial distributions of moist entropy and moist enthalpy changes (ΔH and ΔS) due to AH and its components, and their pattern correlations with temperature and humidity changes (ΔT and ΔQ) for the group 1 experiment (**Table 4**). Variable R at the top of each panel denotes the correlation coefficient between its two subscript variables. By taking the difference between Real run and the other three runs, we quantify the sole influence of ASH (Real-no ASH), ALH (Real-no ALH), and AH (Real-no AH) in the south (**Figures 5A–D**) and north (**Figures 5E–H**), where gridding by slash line represents the urban region.

From **Figures 5a1–d1**, the ASH effect leads to UHI (**Figure 5a1**) and UDI (**Figure 5b1**). However, their combination produces intensified urban heat stress (**Figures 5c1,d1**). In contrast to ASH, ALH (**Figures 5a2–d2**) has cooling (**Figure 5a2**) and humidifying (**Figure 5b2**) roles over the urban regions, which even produces more intense HS (**Figures 5c2,d2**) relative to the ASH effect (**Figures 5c1,d1**). Considering both components of AH (**Figures 5a3–d3**), AH makes the air over the urban region become hot (**Figure 5a3**) and moist (**Figure 5b3**) after neutralizing the contrary contributions of ASH (**Figures 5a1,a2**) and ALH (**Figures 5b1,b2**) effects on ΔT and ΔQ, which largely exacerbates heat stress (**Figures 5c3,d3**).This kind of aggravation of HS is particularly evident over the urban region (**Figures 5c3,d3**). The strong signals of positive ΔH and ΔS nearly outline the urban region. Comparing ASH (**Figures 5c1,d1**), ALH (**Figures 5c2,d2**), and AH effects (**Figures 5c3,d3**), the ALH accounts for larger proportion of total AH to strengthening HS.

In north cities (**Figures 5E–H**), the case is similar to that in south cities (**Figures 5A–D**), except for enhanced HS induced by stronger ASH effect (cf. **Figures 5c1,d1,g1,h1**), which produces stronger UHI in north than in south (cf. **Figures 5a3,e3**). In short, compared with the ASH component (**Figures 5c1,d1,g1,h1**) among total AH (**Figures 5c3,d3,g3,h3**), ALH (**Figures 5c2,d2,g2,h2**) has more significant impact on HS change. However, the contribution of ASH to HS change increases in north (**Figures 5g1,h1**), relative to that in south cities (**Figures 5c1,d1**).

As for spatial distribution, moist entropy and moist enthalpy present similar patterns of HS growth due to the AH effect over the urban regions (cf. **Figures 5c3,d3,g3,h3**). Both temperature and humidity changes have better pattern correlation with HS change in the north. For example, the correlation coefficients $R_{\Delta T\Delta S}$ ($/R_{\Delta Q\Delta S}$) between $\Delta T(/\Delta Q)$ and moist entropy change (ΔS) reaches up to 0.944(/0.977) for the AH effect experiment (**Figures 5e3,f3**), indicative of strong dependence of HS change on both temperature and humidity change in the north. While in the south, the spatial pattern of HS change due to AH release is determined mostly by the coverage of UHI ($R_{\Delta T\Delta S} = 0.820$), relative to humidity change distribution ($R_{\Delta Q\Delta S} = 0.752$).

Diurnal Variation Features

In consideration of clear diurnal cycles of ASH and ALH profiles (**Figures 1h,i**), diurnal variation features of how heat stress intensity responds to AH and its components are also demonstrated (**Figures 6A–I**), indicated by both heat stress metrics (**Figures 6G–I**) and temperature–humidity meteorological variables (**Figures 6A–F**). From **Figure 5**, the spatial patterns of ΔH and ΔS give strong signals in GZ and BJ (**Figures 5c3,d3,g3,h3**), indicative of a remarkable HS response to the AH effect. Thus, as typical cities in the south and north, GZ and BJ are chosen to illustrate the diurnal variation features of HS response to AH release.

Impacts of AH on meteorological variables are investigated first. Near-surface air temperature and humidity changes are plotted, as shown in **Figures 6A–F**, to explain the attributions to HS change (**Figures 6G–I**). Consistent with previous studies (e.g., Nie et al., 2017; Li et al., 2018), ASH heats the atmosphere by 0.2–1.2°C (**Figures 6A1,A2**), more pronounced in BJ than in GZ, with two peaks matching the ASH profile, as shown in **Figure 1h**, while ALH slightly cools T over the urban regions during daytime (**Figures 6B1,B2**), associated with human activities. Irrigated parks, greenbelt, highway sprinkling operation generate cooling but comparatively little (0.2°C). After partly offsetting between ASH and the ALH effect, ASH among total AH contributes most of urban heating. Consequently, UHI is determined mainly by ASH rather than ALH. Its peak reaches 0.6°C in south and 1.1°C in north cities (**Figures 6C1,C2**), with increased heating as the density of urbanization increases (e.g., mean $\Delta T > 0.5$°C between high- and low-density cities in BJ).

As for humidity change due to AH and its components (**Figures 6D-F**), UDI from ASH through decreased ΔQ_v (**Figures 6D1,D2**) is partly neutralized by the humidifying effect from ALH (**Figures 6E1,E2**). The ASH dries air, responsible for $\Delta Q_v < 0$, as shown in **Figures 6D1,D2**; while the ALH moistens air, directly leading to $\Delta Q_v > 0$, as shown in **Figures 6E1,E2**, which is consistent with the spatial pattern, as shown in **Figures 5b1,b2,f1,f2**. The changes in ΔQ_v as shown in **Figures 6F1,F2**, can be explained *via* a combination of ASH and ALH effects on humidity change. In brief, the $\Delta Q_v > 0$ tendency maintains for the diurnal cycle in GZ, and the curve has two peaks (**Figure 6F1**). One happens during nighttime because of decreased evaporation loss, and then humidity decreases with sunrise. The other presents in the afternoon because of ALH from irrigation and watering park, etc. However, the $\Delta Q_v > 0$ trend is broken down in the afternoon in BJ (**Figure 6F2**), even if the ALH peak synchronously presents in the afternoon (**Figure 1i**). Under higher-temperature conditions in the north, dramatic evaporation dries down the near-surface moisture, responsible for the afternoon humidity deficit (**Figure 6F2**).

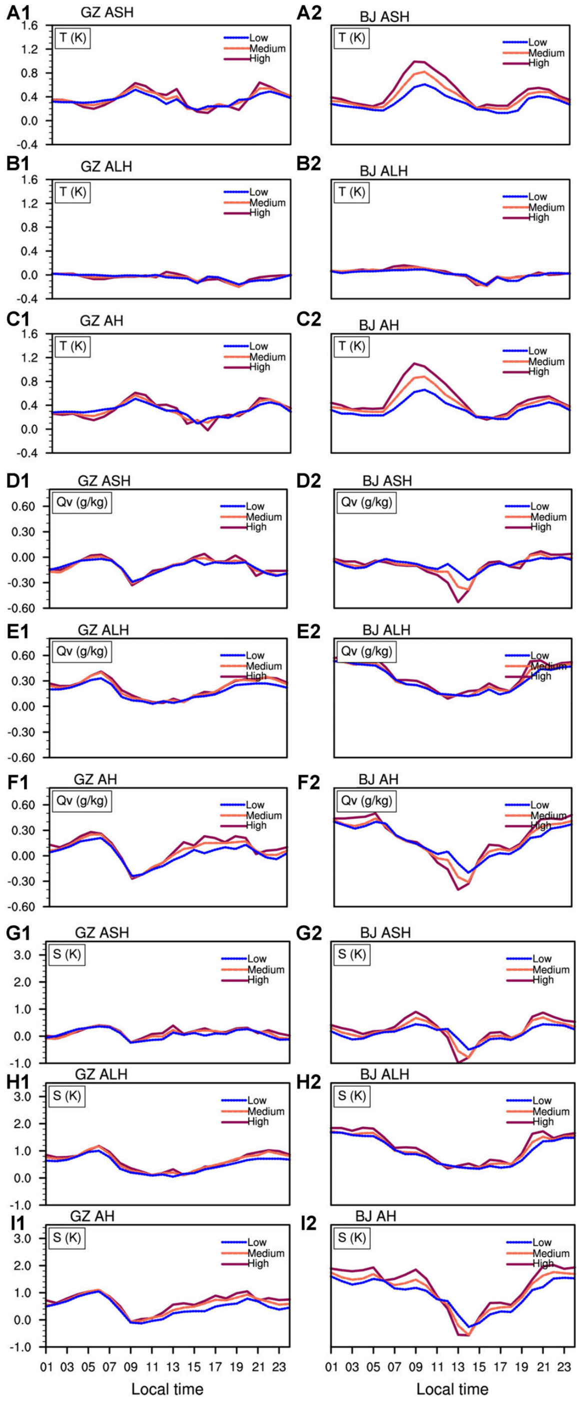

FIGURE 6 | (A-I) The diurnal variations of temperature (K), humidity (g/kg), moist entropy (K) in high-/medium-/low-density urban areas (dark red/light red/blue) due to ASH, ALH, AH release. The curves denote the difference fields between Real run and other experiments (refer to Group 1 experiment in **Table 4**). Left and right panels are GZ and BJ, respectively.

The impact of AH on heat stress metrics are analyzed and shown in **Figures 6G–I**. Since the impact of three AH releases' strategies on the pattern (cf. **Figures 4C,D**, or cf. **Figures 4G,H**) and diurnal cycle of moist enthalpy (not shown) resemble those of moist entropy (**Figures 6G–I**), we examine moist entropy as an example (**Figures 6G–I**).

The AH effect has a substantial impact on the heat stress index. Both ASH and ALH (**Figures 6G,H**) could aggravate the HS (**Figure 6I**), with a maximal increment of moist entropy about 1 K at 06/20 LST in GZ and 09/21 LST in BJ. Furthermore, the magnitude of the HS index increases with the density of urbanization. In contrast of south and north HS, there is a larger diurnal variation in BJ (**Figure 6I2**), even decreased HS between 12 and 16LST. It means that sprinkling water on the road under high-temperature conditions (**Figure 6C2**) might alleviate HS in north cities. The additional irrigation increases the amount of moisture in the air. A large amount of evaporation takes away excessive heat, reducing near-surface temperature and therefore alleviating HS. In contrast, it does not work to sprinkle water on roads or gardens in southern cities, from the positive contributions of both ASH and ALH (**Figures 6G1,H1**) to HS aggravation (**Figure 6I1**).

Impact of City Size on HS

Pattern

Figure 7 shows the spatial distributions of HS changes (ΔH and ΔS) due to an increase in city size and their pattern correlations (R) with temperature and humidity changes (ΔT and ΔQ) for the group 2 experiment in **Table 4**. By taking the difference between Ideal run and the other six simulations with varied city radii from 30 to 80 km, we evaluate HS scenarios in present and future in south (**Figures 7A–D**) and north (**Figures 7E–H**), wherein slash line regions indicate urban coverage.

From **Figures 7A–D**, UHI and UDI are remarkable over the urban regions. ΔT and ΔQ are almost in opposite-phase distributions. The coverage of UHI and UDI presents a dramatic extension with the expansion of the city, as shown in **Figures 7a1–a6, b1–b6**. After neutralizing the contrary contributions of UHI (**Figures 7a1–a6**) and UDI (**Figures 7b1–b6**) effects, we depict the HS evolution with urban sprawl (**Figures 7c1–c6,d1–d6**). It can be seen that the extension of HS coverage is also pronounced as an urban area grows. Strong HS covers an urban region well, except to the northeast of the PRD region, because of downwind heat accumulation by thermal advection originating from upstream urban. However, the enhancement of HS intensity is not as significant as that of UHI because of anti-phase synchronous growths of positive/negative contribution of UHI/ UDI to HS. In contrast, the case in north cities (**Figures 7E–H**) is similar to that in the south (**Figures 7A–D**), except for intensified HS induced by stronger UHI (cf. **Figures 7A,E**) and weaker UDI (cf. **Figures 7B,F**) in the north.

Also, from the spatial distribution, temperature change has a large pattern correlation coefficient with HS change, about 0.9 for ΔT and ΔS in the north (**Figure 7E**) and >0.6 in the south (**Figure 7A**). However, the correlation coefficients between humidity change and moist entropy change $R_{\Delta Q \Delta S}$ is small (<0.3) (**Figures 7B,F**). It indicates strong dependence of the HS pattern on temperature change due to urban expansion. If we build megacities, the temperature change will be the primary control on the spatial pattern of HS.

Intensity Change

The histograms in **Figure 8** show intensity changes in UHI (yellow histogram), UDI (blue histogram), and UHS (grown curve) under $R1$–$R6$ city size scenarios in BJ, TJ, GZ, and SZ. Thereinto, we take the daily maximum of urban region averaged temperature rise and moisture depict relative to Ideal run without the city as UHI and UDI, and the maximal equivalent potential temperature change is adopted to estimate the UHS change.

We use the temperature-humidity separation method introduced in section "Methods to Separate Temperature–Humidity Contribution to Heat Stress" to assess the relative significance of temperature and humidity changes (UHI and UDI effects) on UHS change, by weighting $\Delta\theta$ and $L/C_p \Delta q_v$ more heavily (**Figures 8A–D**). Note that the coefficient L/C_p is added into the moisture change factor, so as to produce comparable order of magnitude and equivalent unit to temperature change.

The heat stress change in south and north cities becomes complex via the combined effects of temperature and humidity changes due to urban sprawl. The UHS maintains less variation in the south in the progress of urban expansion, because of nearly simultaneous growth of the out-of-phase contributions due to UHI and UDI effects (**Figures 8A,B**). However, UHS experiences slow enhancements with the increase in city sizes in north cities (**Figures 8C,D**), mostly driven by the UHI effect. Thus, temperature change dominates the HS change due to urban expansion in north, but both temperature and humidity changes contribute equivalently to HS in the south. As expected, the contrast of environmental conditions between south and north China supports the above conclusion. It is generally wet and hot in the south, which produces large contributions of both temperature and humidity to the HS weather: while in the north, it is hotter but not as wet as in the south (**Figure 2**), so the temperature change dominates intensity evolution of HS. In contrast, stronger UHS change on account of increased urban area happens in the north, with a larger peak (~6 K) relative to that in the south (~2 K), and stronger HS presents over inland BJ/GZ than in coastal TJ/SZ. Also, note that the intensified HS over TJ (**Figure 8D**) and a little weakened HS over SZ (**Figure 8B**) due to growing city radius are associated with the urban sprawl toward inland and coastal areas. Therefore, it is more prone to severe UHS risk if we build megacities in the north in the future.

Extreme Heat Stress

Threshold of Extreme Heat Stress

To explore the EHS events, we try to derive a local threshold based on the statistical distribution mode of extreme heat stress metric, equivalent potential temperature herein. Referring to the CFAD (contoured frequency by altitude diagram) method widely applied to convective burst definition (Yuter and HouzeJr., 1995; Rogers, 2010; Heng et al., 2020), we examine the distribution pattern of equivalent potential temperature by using contoured frequency by latitude diagram (CFLD) (**Figure 9**).

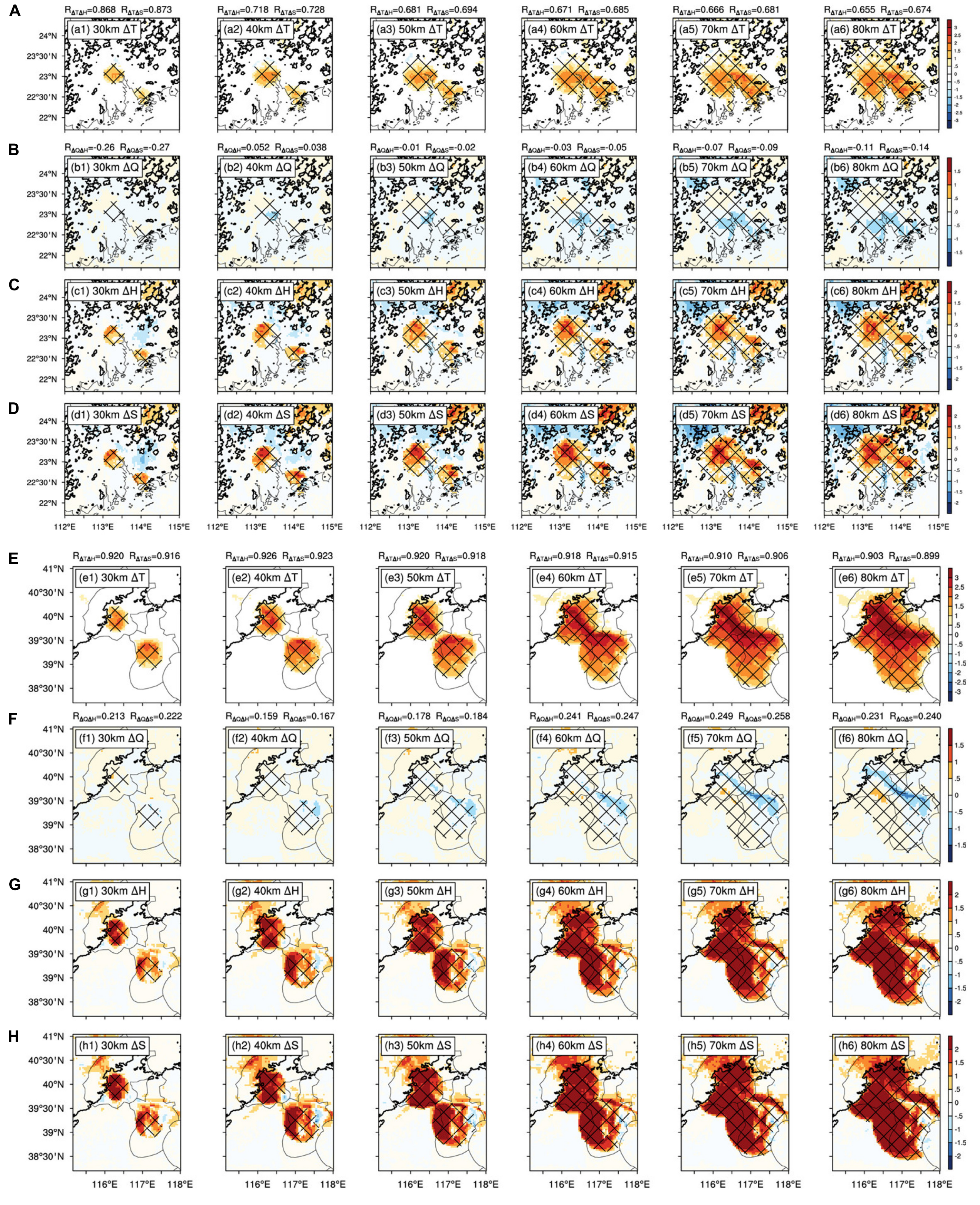

FIGURE 7 | (A-H) The same as **Figure 5** but for group 2 experiment in **Table 4** by taking account of the impact of increasing city size from *R* = 30 to 80 km.

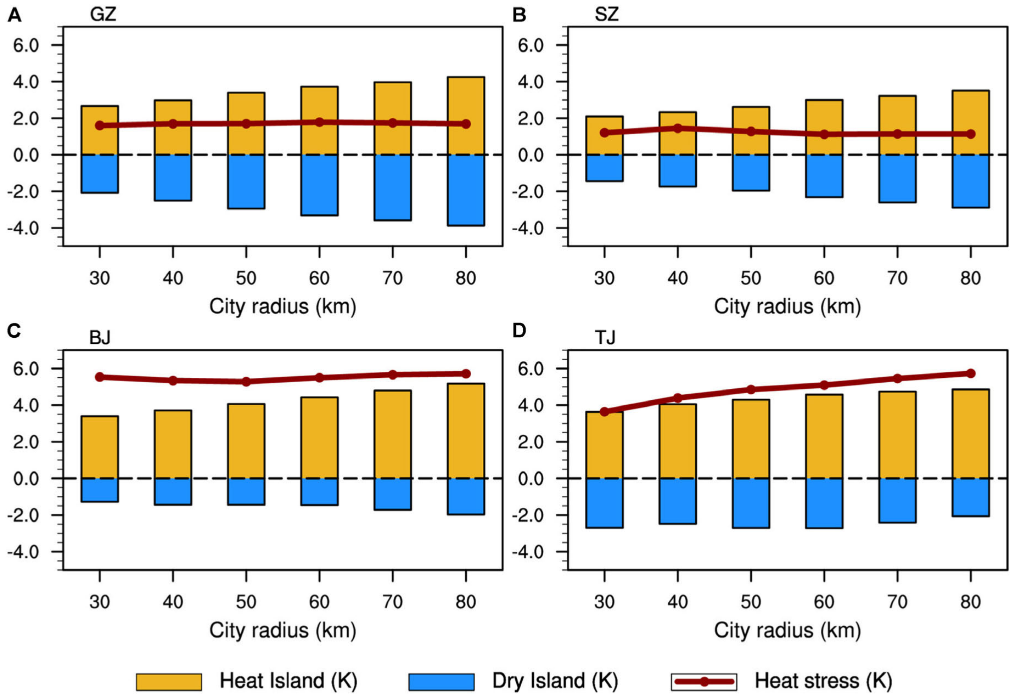

FIGURE 8 | (A-D) Daily maximum of region-averaged urban heat island effect (Δθ, K, yellow histogram), urban dry island effect (moisture depict in K, $L/C_p\,\Delta q_v$, blue histogram), and urban heat stress change ($\Delta\theta_e$, K, grown curve) under *R*1–*R*6 (*R* = 30–80 km) city size scenarios in BJ, TJ, GZ, and SZ city regions. The fractional changes (Δθ, $L/C_p\,\Delta q_v$, $\Delta\theta_e$) are taken as difference between the *R*1–*R*6 experiment and Ideal run without city (refer to Group 2 experiment in **Table 4**).

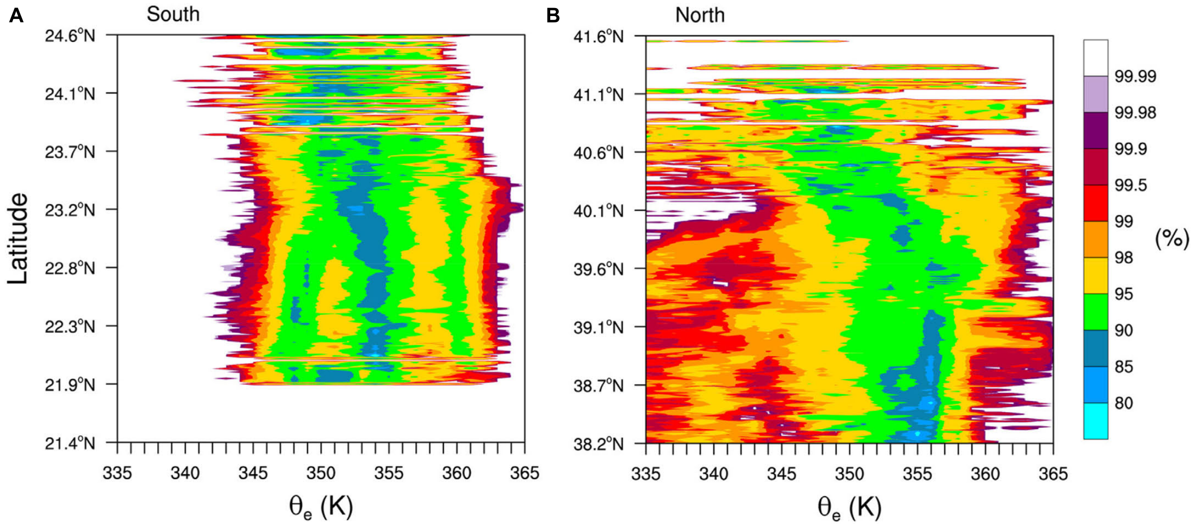

FIGURE 9 | The contoured frequency by latitude diagram distribution of equivalent potential temperature (K) **(A)** in south and **(B)** in north.

It shows the CFLDs of the simulated equivalent potential temperature binned every 1 K at various latitudes within the PRD (**Figure 9A**) and JJJ (**Figure 9B**) regions based on Real run, where blank area represents sea or other non-urban land covers. By comparative analyses of the south and north cities (**Figures 9A,B**), the frequency distribution of equivalent potential temperature is relatively spatially homogeneous in the whole PRD region (21.9–23.7°N). All θ_e values concentrate within 343–363 K irrespective of varied latitude (**Figure 9A**), with peak θ_e (98th percentile, refer to Lutsko, 2021) of 362 K, while the frequency distribution of θ_e experiences dramatic amplification and is characterized by a broader mode (varied between 335 and 365 K) in JJJ, with peak θ_e (still 98th percentile) growing mainly from 359 to 362 K with latitude (**Figure 9B**). To be convenient to perform comparisons among various cities, we need to develop a common, unified

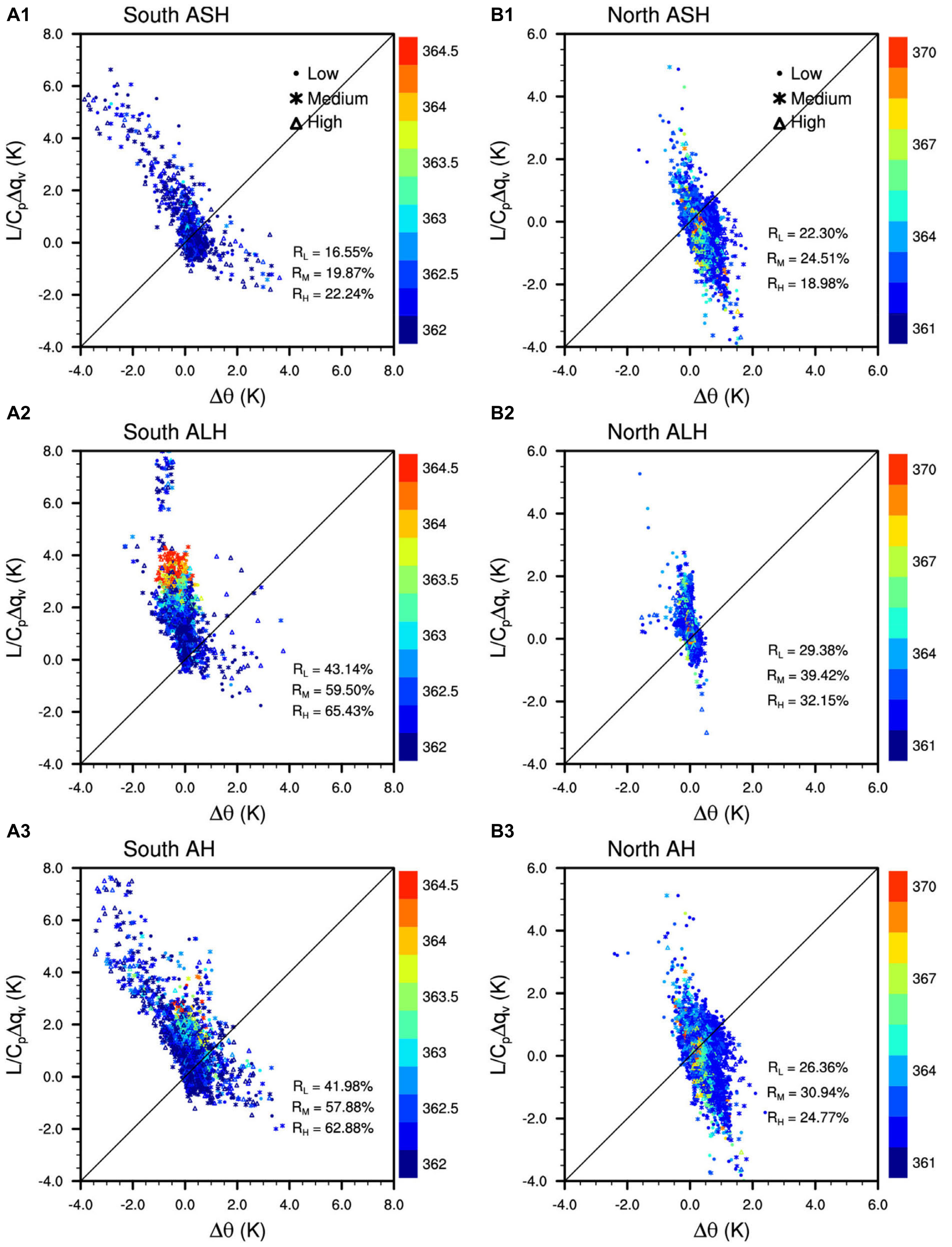

FIGURE 10 | (A,B) Scatter plots of changes in humidity ($L/C_p\Delta q_v$, K) versus changes in temperature ($\Delta\theta$, K) associated with extreme heat stress (98th percentile θ_e) events for the ASH, ALH, and AH runs. The triangle, star, and dot represent high-/medium-/low- density urban areas, colored by their associated θ_e value. Left and right panels denote south and north urban regions, respectively.

standard to feature an EHS episode based on the statistical distribution of equivalent potential temperature in our target regions. It seems that 362 K is suitable to the extreme heat stress definition derived from θ_e statistics. Therefore, this criterion is attempted to analyze the EHS episode in the following section.

Temperature–Humidity Dependence

Figures 10, **11** are the scatter plots of $\Delta\theta$ (abscissa) and $L/C_p\Delta q_v$ (ordinate) associated with EHS, which is used to study the relative importance of fractional changes in temperature and humidity on EHS occurrence under various AH release (**Figure 10**) and city size scenarios (**Figure 11**). By weighting

$\Delta\theta$ and $L/C_p\Delta q_v$ more heavily, we estimate which factor is the primary driver of EHS occurrence. Also shown is the θ_e value in high-/medium-/low-density urban regions (color triangle, star, dot in **Figure 10**) and cities with increasing size (color dot in **Figure 11**). It provides another way to estimate the sensitivity of EHS dependence on temperature–humidity change due to AH and increased city size by comparing whether the relative spread degree of EHS points is towards the abscissa or ordinate variables. The R value inset in each panel represents the hit ratio of EHS among total grids over the urban regions, with subscripts L, M, and H denoting low-/medium-/high-density city types.

From **Figure 10**, the spread in humidity changes is larger than the spread in temperature changes in southern cities, irrespective of ALH, ASH, or AH run (**Figures 10A1–A3**), which signifies humidity change is the primary driving factor of EHS events in the south. In the north, the spread in humidity changes is larger/less than the spread in temperature changes in ALH/ASH run (**Figures 10B1,B2**), which implies humidity/temperature change is the primary driving factor of EHS events under an ALH/ASH release scenario. For AH simulation (**Figure 10B3**), the spread degrees in both factors are comparable, which means the occurrence of EHS is sensitive to both temperature and humidity increase over the north cities. In contrast, the hit ratios of EHS in high-/medium-/low-density urban are different. For the present urban land cover, considering various urban types and AH emission, above 50% (/a quarter of) south (/north) urban region is hit by EHS (**Figures 10A3,B3**), and EHS tends to occur in high-density urban regions in south, followed by medium-density urban regions (e.g., for AH run, as shown in **Figure 10A3**, $R_H = 62.88\%$, $R_M = 57.88\%$, and $R_L = 41.98\%$, indicating that 62.88% of the high-density urban regions is hit by EHS). However, EHS is more easily to happen in medium-density urban regions in all of the simulation experiments for north cities (e.g., for ASH, ALH, and AH runs, R_M = 24.51, 39.42, and 30.94%, respectively).

As a city will expand dramatically in the future (**Figure 11**, and for group 2 experiment in **Table 4**), about one-third of the urban regions might be hit by EHS, with a wider scope of influence in the south than in the north (R = 28.13–40.48% in the south from **Figures 11A1–A6**, R = 24.80–37.87% in the north from **Figures 11B1–B6**). In addition, a larger extremum (with $\theta_e > 376$ K) happens in northern cities, relative to that in the south ($\theta_e \sim 366$ K). Furthermore, changes in the very warmest θ_e events are associated with large Δq_v responses in north cities (**Figures 11B1–B6**). In the south (**Figures 11A1–A6**), EHS is sensitive to both temperature and humidity changes for smaller cities (**Figures 11A1,A2**), but the shift is to be determined by larger Δq_v in the larger cities of the future (**Figures 11A3–A6**). For the EHS events in megacities in the south (**Figures 11A3–A6**), the specific humidity response is again the leading factor driving EHS occurrence in response to city size change. Therefore, constraining the probability of occurrence and regional distribution of EHS events largely comes down to constraining the humidity change associated with these events, particularly in a megalopolis or a city cluster in the future.

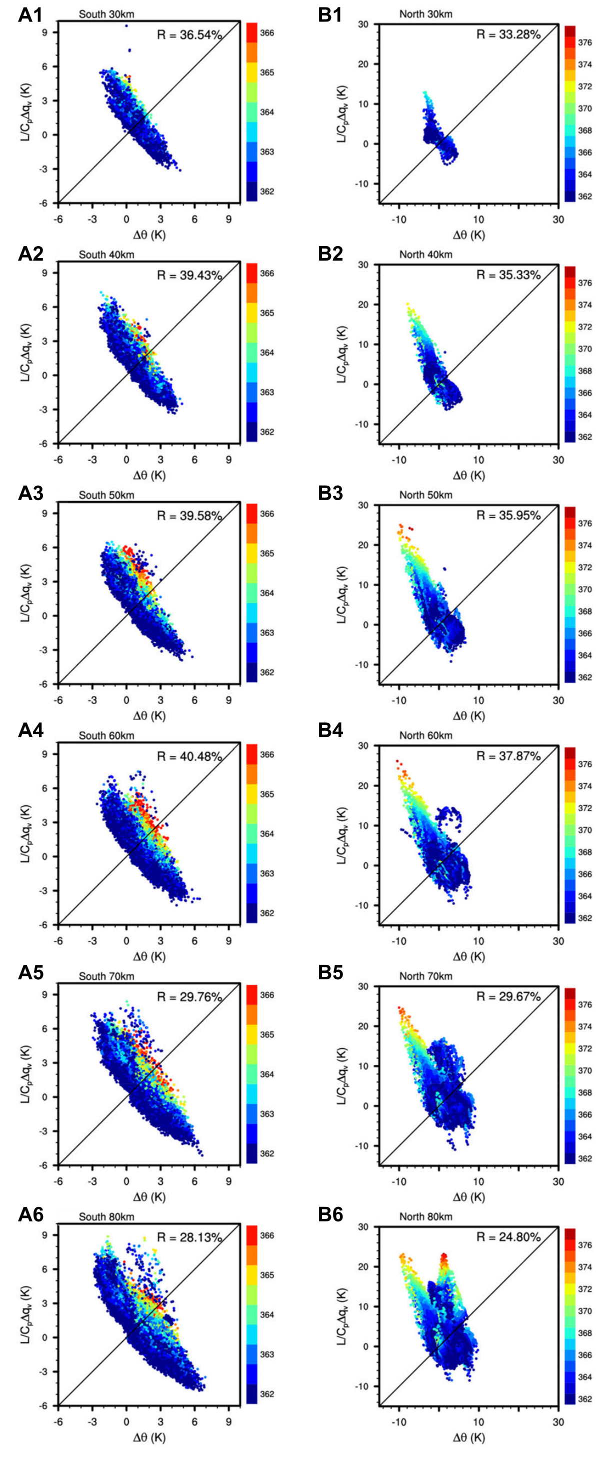

FIGURE 11 | (A,B) The same as **Figure 10** but for different city size (*R*1–*R*6) runs.

CONCLUSION AND DISCUSSION

The impacts of anthropogenic heat emission and increase in city size on urban heat stress and extreme heat stress are investigated based on numerical simulation by utilizing the coupled SLUCM-WRF model system. As effective HS metrics, moist enthalpy and moist entropy are used to evaluate the HS response to AH and urban expansion and explain the attribution to HS change by separating the contributions of temperature change from humidity change. Several main conclusions are summarized as follows.

Anthropogenic heat release could aggravate UHS drastically. It produces a maximal increment of moist entropy (an effective HS metric), above 1 and 2 K over south and north high-density urban regions, mainly through ALH. HS change shows a more prominent diurnal variation in the north than in the south, in high-density than in low-density urban regions. Despite the diurnal cycle of temperature/humidity rise due to ASH/ALH generally matching the ASH/ALH profile, HS change does not strictly obey the diurnal variation rule of any one single factor. It depends on the combined effect of both, indicative of the complexity of HS research. Note that there are slightly decreased HS between 12 and 16LST in the north in AH run, mainly by the ALH effect. It means that sprinkling water on roads under high-temperature conditions might alleviate HS in north cities. In contrast, it does not work to sprinkle water on roads or gardens in south cities, because of the positive contributions of both ASH and ALH to HS aggravation.

Urban expansion leads to an increase in HS coverage, and it has a larger impact on UHS intensity change (6 and 2 K in south and north) relative to AH. The city radius of 60 km is a possible threshold to plan to city sprawl. Above that city size, the HS intensity change due to urban expansion tends to slow down in the north and inhibit in the south (**Figure 8**), and about one-third of the urban regions might be hit by extreme heat stress (EHS), reaching maximal hit ratio (**Figure 11**). Stronger intensities of HS present over inland than in coastal cities. Therefore, it is more prone to severe UHS risk if we build megacities in the north in the future.

Furthermore, changes in warmest EHS events are more associated with high humidity change responses, irrespective of cities being in north or south of China, which supports the idea that humidity change is the primary driving factor of EHS occurrence. Therefore, constraining the occurrence probability and regional distribution of EHS events largely comes down to constraining the humidity change associated with these events, particularly in a megalopolis or a city cluster in the future.

In comparison to previous studies, Ramamurthy and Bou-Zeid (2017) performed a comparative analysis of heat waves over multiple cities. They found that UHI intensity is proportional to the physical size of the city. Based on this study, we quantify how the increase in city size impacts a heat stress episode and derive the threshold mentioned above in which this kind of influence will be slowed down. Yang et al. (2019) pointed out that urbanization increases thermal discomfort hours by 27% during summer over the urban areas of the Yangtze River Delta in East China, and that the contribution of AH to the increase in total discomfort hours is almost equal to that due to urban land use change. Our results reveal a stronger response of HS to urban expansion relative to AH in south and north cities in China. Furthermore, we demonstrate the influence path of AH on HS, mainly via its latent component but not the traditional anthropogenic sensible component. Certainly, updated numerical model setup, local UCM parameter, and densely gridded ASH and ALH data are expected to further simulate HS, and more thermodynamic and dynamic aspects based on conserved moist entropy are needed in the next study to reveal the mechanism responsible for the genesis and dispersion of HS.

DATA AVAILABILITY STATEMENT

The original contributions presented in the study are included in the article/supplementary material, further inquiries can be directed to the corresponding author/s.

AUTHOR CONTRIBUTIONS

SY and BC designed the research and led the writing of the manuscript. SL prepared all figures. ZX and JP performed the part data analysis. All authors discussed the results and commented on the manuscript.

FUNDING

The authors were supported by the National Natural Science Foundation of China (Grant Nos. 41875079 and 91937301), the Open Research Program of the State Key Laboratory of Severe Weather, Chinese Academy of Meteorological Sciences (2019LASW-A04), the National Key Research and Development Program on Monitoring, Early Warning and Prevention of Major Natural Disaster (2018YFC1506001), the Second Tibetan Plateau Comprehensive Scientific Expedition and Research Program (2019QZKK0105), and the S&T Development Fund of CAMS (2020KJ017).

REFERENCES

Allen, L., Lindberg, F., and Grimmond, C. S. B. (2011). Global to city scale urban anthropogenic heat flux: model and variability. *Int. J. Climatol.* 31, 1990–2005. doi: 10.1002/joc.2210

Buzan, J. R., Oleson, K., and Huber, M. (2015). Implementation and comparison of a suite of heat stress metrics within the Community Land Model version 4.5. *Geosci. Model Dev.* 8, 151–170. doi: 10.5194/gmd-8-151-2015

Chen, F., Kusaka, H., Bornstain, R., Ching, J., Grimmond, C. S. B., Grossman-Clarke, S., et al. (2011). The integrated WRF/urban modeling system: development, evaluation, and applications to urban environmental problems. *Int. J. Climatol.* 31, 273–288. doi: 10.1002/joc.2158

Chen, F., Yang, X., and Wu, J. (2016). Simulation of the urban climate in a Chinese megacity with spatially heterogeneous anthropogenic heat data. *J. Geophys. Res. Atmosph.* 121, 5193–5212. doi: 10.1002/2015jd024642

Chen, Y., Jiang, W. M., Zhang, N., He, X. F., and Zhou, R. W. (2008). Numerical simulation of the anthropogenic heat effect on urban boundary layer structure. *Theoret. Appl. Climatol.* 97, 123–134. doi: 10.1007/s00704-008-0054-0

Chen, Y., Jiang, W. M., Zhang, N., He, X. F., and Zhou, R. W. (2009). Numerical simulation of the anthropogenic heat effect on urban boundary layer structure. *Theor. Appl. Climatol.* 97, 123–134.

Chew, L. W., Liu, X., Li, X. X., and Norford, L. K. (2021). Interaction between heat wave and urban heat island: a case study in a tropical coastal city, Singapore. *Atmosph. Res.* 247:105134.

Chrysoulakis, N., Heldens, W., Gastellu-Etchegorry, J. P., Grimmond, S., Feigenwinter, C., Lindberg, F., et al. (2016). A novel approach for anthropogenic heat flux estimation from space IEEE International Geoscience & Remote Sensing Symposium. *IEEE* 2016, 6774–6777.

Feng, J.-M., Wang, Y.-L., Ma, Z.-G., and Liu, Y.-H. (2012). Simulating the regional impacts of urbanization and anthropogenic heat release on climate across China. *J. Clim.* 25, 7187–7203. doi: 10.1175/jcli-d-11-00333.1

Fischer, E. M., and Knutti, R. (2013). Robust projections of combined humidity and temperature extremes. *Nat. Climate Change* 3, 126–130. doi: 10.1038/nclimate1682

Grimmond, C. S. B. (1992). The suburban energy balance: methodological considerations and results for a midlatitude west coast city under winter and spring conditions. *Int. J. Climatol.* 12, 481–497.

Hass, A. L., Ellis, K. N., Mason, L. R., Hathaway, J. M., and Howe, D. A. (2016). Heat and humidity in the city: Neighborhood heat index variability in a mid-sized city in the southeastern United States. *Int. J. Environ. Res. Public Health* 13, 1–19. doi: 10.3390/ijerph1301010117

Heng, J., Yang, S., Gong, Y. F., Gu, J. F., and Liu, H. W. (2020). Characteristics of the convective bursts and their relationship with the rapid intensification of Super Typhoon Maria (2018). *Atmosph. Ocean. Sci. Lett.* 13, 146–154. doi: 10.1080/16742834.2020.1719009

Holton, J. R., and Hakim, G. J. (2013). *An Introduction to Dynamic Meteorology*, 5th Edn. Cambridge, MA: Academic Press.

Iacono, M. J., Delamere, J. S., Mlawer, E. J., Shephard, M. W., Clough, S. A., and Collins, W. D. (2008). Radiative forcing by long–lived greenhouse gases: calculations with the AER radiative transfer models. *J. Geophys. Res.* 113, D13103. doi: 10.1029/2008JD009944

Iamarino, M., Beevers, S., and Grimmond, C. S. B. (2012). High-resolution (space, time) anthropogenic heat emissions: London 1970–2025. *Int. J. Climatol.* 32, 1754–1767. doi: 10.1002/Joc.2390

Ichinose, T., Shimodozono, K., and Hanaki, K. (1999). Impact of anthropogenic heat on urban climate in Tokyo. *Atmos. Environ.* 33, 3897–3909. doi: 10.1016/S1352-2310(99)00132-6

Janjic, Z. I. (1994). The step-mountain eta coordinate model: further developments of the convection, viscous sublayer, and turbulence closure schemes. *Month. Weather Rev.* 122, 927–945.

Kain, J. S. (2004). The Kain-Fritsch convective parameterization: an update. *J. Appl. Meteor.* 43, 170–181. doi: 10.1175/1520-0450

Kessler, E. (1969). On the distribution and continuity of water substance in atmoshperic circulations. *Meteor.Monogr* 32:84. doi: 10.1007/978-1-935704-36-2_1

Kusaka, H., Kondo, H., Kikegawa, Y., and Kimura, F. (2001). A simple single-layer urban canopy model for atmospheric models: comparison with multi-layer and slab models. *Bound. Layer Meteorol.* 101, 329–358.

Lee, S. M., and Min, S. K. (2018). Heat stress changes over East Asia under 1.5° and 2.0°C global warming targets. *J. Clim.* 31, 2819–2831. doi: 10.1175/JCLI-D-17-0449.1

Li, S. W., Yang, S., and Liu, H. W. (2018). Sensitivity of warm-sector heavy precipitation to the impact of anthropogenic heating in South China. *Atmos. Oceanic. Sci. Lett.* 11, 236–245. doi: 10.1080/16742834.2018.1469952

Lorenz, R., Stalhandske, Z., and Fischer, E. M. (2019). Detection of a climate change signal in extreme heat, heat stress, and cold in Europe from observations. *Geophys. Res. Lett.* 46, 8363–8374. doi: 10.1029/2019GL082062

Luo, M., and Lau, N. C. (2018). Increasing heat stress in urban areas of eastern China: acceleration by urbanization. *Geophys. Res. Lett.* 45, 1360–1369. doi: 10.1029/2018GL080306

Lutsko, N. J. (2021). The relative contributions of temperature and moisture to heat stress changes under warming. *J. Clim.* 34, 901–917. doi: 10.1175/JCLI-D-20-0262.1

Meir, T., Orton, P., Pullen, J., Holt, T., Thompson, W., and Arend, M. (2013). Forecasting the New York City urban heat island and sea breeze during extreme heat events. *Weather Forecast*. 28, 1460–1477.

Mesinger, F. (1993). *Forecasting Upper Tropospheric Turbulence Within the Framework of the Mellor-Yamada 2.5 Closure. Research Activities in Atmospheric and Oceanic Modelling*. CAS/JSC WGNE Reper No. 18, Geneva: WMO, 28–24.

Miao, S. G., and Chen, F. (2014). Enhanced modeling of latent heat flux from urban surfaces in the Noah/single-layer urban canopy coupled model. *Sci. China Earth Sci.* 57, 2408–2416. doi: 10.1007/s11430-014-4829-0

Moriwaki, R., Kanda, M., Senoo, H., Hagishima, A., and Kinouchi, T. (2008). Anthropogenic water vapor emissions in Tokyo. *Water Resour Res.* 44, W11424.

Napoli, C. D., Pappenberger, F., and Cloke, H. (2019). Verfication of heat stress thresholds for a helth-based heat wave definition. *J. Appl. Meteorol. Climatol.* 58, 1177–1194.

Narumi, D., Kondo, A., and Shimoda, Y. (2009). Effects of anthropogenic heat release upon the urban climate in a Japanese megacity. *Environ. Res.* 109, 421–431. doi: 10.1016/j.envres.2009.02.013

Nie, W., Zaitchik, B. F., Ni, G., and Sun, T. (2017). Impacts of anthropogenic heat on summertime rainfall in Beijing. *J. Hydrometeorol.* 18, 693–712. doi: 10.1175/JHM-D-16-0173.1

Niu, G. Y., Yang, Z. L., Mitchell, K. E., Chen, F., Michael, B., Barlage, M., et al. (2011). The community Noah land surface model with multiparameterization options (Noah–MP): 1. Model description and evaluation with local–scale measurements. *J. Geophys. Res.* 116:D12109. doi: 10.1029/2010JD015139

Offerle, B., Grimmond, C. S. B., and Fortuniak, K. (2005). Heat storage and anthropogenic heat flux in relation to the energy balance of a central European city centre. *Int. J. Climatol.* 25, 1405–1419. doi: 10.1002/Joc.1198

Ohashi, Y., Kikegawa, Y., Ihara, T., and Sugiyama, N. (2014). Numerical simulations of outdoor heat stress index and heat disorder risk in the 23 wards of Tokyo. *J. Appl. Meteorol. Climatol.* 53, 583–597. doi: 10.1175/JAMC-D-13-0127.1

Oke, T. R. (1988). The urban energy balance. *Prog. Phys. Geog.* 12:471–508.

Peng, T., Sun, C., Feng, S., Zhang, Y., and Fan, F. (2021). Temporal and spatial variation of anthropogenic heat in the central urban area: a case study of Guangzhou, China. *ISPRS Int. J. Geo Inf.* 10:160. doi: 10.3390/ijgi10030160

Ramamurthy, P., and Bou-Zeid, E. (2017). Heatwaves and urban heat islands: a comparative analysis of multiple cities. *J.Geophys.Res.Atmos*. 122, 168–178. doi: 10.1002/2016JD025357

Rogers, R. (2010). Convective-scale structure and evolution during a high-resolution simulation of tropical cyclone rapid intensification. *J. Atmosph. Sci.* 67, 44–70. doi: 10.1175/2009jas3122.1

Sailor, D. J. (2011). A review of methods for estimating anthropogenic heat and moisture emissions in the urban environment. *Int. J. Climatol.* 31, 189–199. doi: 10.1002/joc.2106

Sailor, D. J., Brooks, A., Hart, M., and Heiple, S. (2007). "A bottom-up approach for estimating latent and sensible heat emissions from anthropogenic sources," in *Seventh Symposium on the Urban Environment, San Diego, California, 10-13 September 2007*, Yokohama.

Sailor, D. J., Georgescu, M., Milne, J. M., and Hart, M. A. (2015). Development of a national anthropogenic heating database with an extrapolation for international cities. *Atmos. Environ.* 118, 7–18. doi: 10.1016/j.atmosenv.2015.07.016

Schmid, P. E., and Niyogi, D. (2013). Impact of city size on precipitation-modifying potential. *Geophys. Res. Lett.* 40, 5263–5267. doi: 10.1002/grl.50656

Seneviratne, S. I., Nicholls, N., Easterling, D., Goodess, C. M., Kanae, S., Kossin, J., et al. (2012). "Changes in climate extremes and their impacts on the natural physical environment," in *Managing the Risks of Extreme Events and Disasters to Advance Climate Change Adaptation. A Special Report of Working Groups I and II of the Intergovernmental Panel on Climate Change (IPCC)*, eds C. B. Field, V. Barros, T. F. Stocker, D. Qin, D. J. Dokken, K. L. Ebi, et al. (Cambridge: Cambridge University Press), 109–230.

Skamarock, W. C., Klemp, J. B., Dudhia, J., Gill, D. O., Liu, Z. W., Berner, J., et al. (2019). *A Description of the Advanced Research WRF Version 4.*

NCAR Tech. Note NCAR/TN-556+STR. Boulder, CO: University Corporation for Atmospheric Research, 145. doi: 10.5065/1dfh-6p97

Smith, C., Lindley, S., and Levermore, G. (2009). Estimating spatial and temporal patterns of urban anthropogenic heat fluxes for UK cities: the case of Manchester. *Theor. Appl. Climatol.* 98, 19–35. doi: 10.1007/s00704-008-0086-5

Steadman, R. G. (1994). Norms of apparent temperature in Australia. *Aust. Met. Mag.* 43, 1–16.

Steinweg, C., and Gutowski, W. (2015). Projected changes in Greater St.Louis summer heat stress in NARCCAP simulations. *Weather Climate Soc.* 7, 159–168. doi: 10.1175/WCAS-D-14-00041.1

Sugawara, H., and Narita, K.-I. (2008). Roughness length for heat over an urban canopy. *Theoret. Appl. Climatol.* 95, 291–299. doi: 10.1007/s00704-008-0007-7

Sun, Y., Zhang, X., Ren, G., Zwiers, F. W., and Hu, T. (2016). Contribution of urbanization to warming in China. *Nat. Clim. Change* 6, 706–709. doi: 10.1038/nclimate2956

Tewari, M., Chen, F., Wang, W., Dudhia, J., LeMone, M. A., Mitchell, K., et al. (2004). "Implementation and verification of the unified NOAH land surface model in the WRF model," in *Proceedings of the 20th Conference on Weather Analysis and Forecasting/16th Conference on Numerical Weather Prediction*, Seattle, WA, 11–15.

Tewari, M., Chen, F., Kusaka, H., and Miao, S. (2007). *Coupled WRF/Unified Noah/Urban-Canopy Modeling System.*

Wang, J., Chen, Y., Tett, S., Yan, Z. W., Zhai, P. M., Feng, J. M., et al. (2020). Anthropogenically-driven increases in the risks of summertime compound hot extremes. *Nat. Commun.* 11:528. doi: 10.1038/s41467-019-14233-8

Wang, Y. N., Chen, T. T., and Sun, R. H. (2016). Assessing the spatiotemporal characteristics of anthropogenic heat in Beijing. *China Environ. Sci. (in Chinese)* 36, 2178–2185.

Wang, Y., Chen, L., Song, Z., Huang, Z., Ge, E., Lin, L., et al. (2019). Human-perceived temperature changes over South China: long-term trends and urbanization effects. *Atmosph. Res.* 215, 116–127. doi: 10.1016/j.atmosres.2018.09.006

Wang, Z. M., and Wang, X. M. (2011). Estimation and sensitivity test of anthropogenic heat flux in Guangzhou. *J. Meteorol. Sci.* 31, 422–430.

Weatherly, M., and Rosenbaum, J. W. (2017). Future projections of fire-risk indices for the continuous United States. *J. Appl. Meteorol. Climatol.* 56, 863–876. doi: 10.1175/JAMC-D-16-0068.1

Willett, K. M., and Sherwood, S. (2012). Exceedance of heat index thresholds for 15 regions under a warming climate using the wet-bulb globe temperature. *Int. J. Climatol.* 32, 161–177. doi: 10.1002/joc.2257

Xie, M., Shu, L., Wang, T. J., Liu, Q., Gao, D., Li, S., et al. (2017). Natural emissions under future climate condition and their effects on surface ozone in the Yangtze River Delta region *China Atmosph. Environ.* 150, 162–180. doi: 10.1016/j.atmosenv.2016.11.053

Xie, M., Zhu, K. G., Wang, T. J., Feng, W., Gao, D., Li, M. M., et al. (2016). Changes in regional meteorology induced by anthropogenic heat and their impacts on air quality in South China. *Atmos. Chem. Phys* 16, 15011–15031. doi: 10.5194/acp-16-15011-2016

Yang, J. C., Wang, Z. H., Chen, F., Miao, S. G., Tewari, M., Voogt, J. A., et al. (2015). Enhancing hydrologic modelling in the coupled weather research and forecasting–urban modelling system. *Bound. Layer Meteorol.* 155, 87–109. doi: 10.1007/s10546-014-9991-6

Yang, L., Tian, F., Smith, J. A., and Hu, H. (2014). Urban signatures in the spatial clustering of summer heavy rainfall events over the Beijing metropolitan region. *J. Geophys. Res. Atmosph.* 119, 1203–1217. doi: 10.1002/2013jd020762

Yang, S., Gao, S. T., and Lu, C. G. (2014). A generalized frontogenesis function and its application. *Adv. Atmos. Sci.* 31, 1065–1078. doi: 10.1007/s00376-014-3228-y

Yang, W., Luan, Y., Liu, X., Yu, X., Miao, L., and Cui, X. (2017). A new global anthropogenic heat estimation based on high-resolution nighttime light data. *Sci. Data.* 4:170116. doi: 10.1038/sdata.2017.116

Yang, X., Leung, L. R., Zhong, S., Qian, Y., Zhao, C., et al. (2019). Modeling the impacts of urbanization on summer thermal comfort: the role of urban land use and anthropogenic heat. *J. Geophys. Res. Atmosph.* 124, 6681–6697. doi: 10.1029/2018JD029829

Yang, X., Leung, R. L., Zhao, N., Zhao, C., Qian, Y., Hu, K., et al. (2017). Contribution of urbanization to the increase of extreme heat events in an urban agglomeration in East China. *Geophys. Res. Lett.* 44, 6940–6950. doi: 10.1002/2017GL074084

Yang, Z. L., Niu, G. Y., Mitchell, K. E., Chen, F., Ek, M. B., Barlage, M., et al. (2011). The community Noah land surface model with multiparameterization options (Noah–MP): 2. Evaluation over global river basins. *J. Geophys. Res.* 116:D12110. doi: 10.1029/2010JD015140

Ye, H., Huang, Z., Huang, L., Lin, L., and Luo, M. (2018). Effects of urbanization on increasing heat risks in South China. *Int. J. Climatol.* 38, 5551–5562. doi: 10.1002/joc.5747

Yuter, S. E., and Houze, R. A. Jr. (1995). Three-dimensional kinematic and microphysical evolution of Florida Cumulonimbus. Part II: frequency distributions of vertical velocity, reflectivity, and differential reflectivity. *Monthly Weath. Rev.* 123, 1941–1963.

Zander, K. K., Moss, S., and Garnett, S. T. (2019). Climate change-related heat stress and subjective well-being in Australia. *Weather Clim. Soc.* 11, 505–520. doi: 10.1175/18-WCAS-D-0074.1

Zhang, N., Wang, X., Chen, Y., Dai, W., and Wang, X. (2016). Numerical simulations on influence of urban land cover expansion and anthropogenic heat release on urban meteorological environment in Pearl River Delta. *Theoret. Appl. Climatol.* 126, 469–479. doi: 10.1007/s00704-015-1601-0

Zhang, X., Liu, L., Wu, C., Chen, X., Gao, Y., Xie, S., et al. (2020). Development of a global 30m impervious surface map using multisource and multitemporal remote sensing datasets with the Google Earth Engine platform. *Earth Syst. Sci. Data* 12, 1625–1648. doi: 10.5194/essd-12-1625-2020

Zhang, Y. Z., Miao, S. G., Dai, Y. J., and Bornstein, R. (2017a). Numerical simulation of urban land surface effects on summer convective rainfall under different UHI intensity in Beijing. *J. Geophys. Res. Atmos* 122, 7851–7868. doi: 10.1002/2017JD026614

Zhang, Y. Z., Miao, S. G., Li, Q. C., and Dai, Y. J. (2017b). Numerical simulation of the impact of urban underlying surface on fog in Beijing. *Chinese J. Geophys. (in Chinese)* 60, 22–36. doi: 10.6038/cjp20170103

Zhu, K., Zhao, W., Xie, M., Zhu, X., Li, M., and Feng, W. (2017). Characteristics of human thermal emission in South China." [In Chinese.]. *J. Ecol. Rural Environ.* 33, 201–206.

Conflict of Interest: The authors declare that the research was conducted in the absence of any commercial or financial relationships that could be construed as a potential conflict of interest.

frontiers in Earth Science

ORIGINAL RESEARCH
published: 09 June 2021
doi: 10.3389/feart.2021.673786

Synergistic Influence of Local Climate Zones and Wind Speeds on the Urban Heat Island and Heat Waves in the Megacity of Beijing, China

Lian Zong[1], Shuhong Liu[1], Yuanjian Yang[1]*, Guoyu Ren[2,3], Miao Yu[4], Yanhao Zhang[1] and Yubin Li[1]

[1]Collaborative Innovation Centre on Forecast and Evaluation of Meteorological Disasters, School of Atmospheric Physics, Nanjing University of Information Science and Technology, Nanjing, China, [2]Department of Atmospheric Science, School of Environmental Studies, China University of Geosciences, Wuhan, China, [3]Laboratory for Climate Studies, National Climate Center, China Meteorological Administration, Beijing, China, [4]Chinese Academy of Meteorological Sciences, China Meteorological Administration, Beijing, China

Large-scale modifications to urban underlying surfaces owing to rapid urbanization have led to stronger urban heat island (UHI) effects and more frequent urban heat wave (HW) events. Based on observations of automatic weather stations in Beijing during the summers of 2014–2020, we studied the interaction between HW events and the UHI effect. Results showed that the UHI intensity (UHII) was significantly aggravated (by 0.55˚C) during HW periods compared to non-heat wave (NHW) periods. Considering the strong impact of unfavorable weather conditions and altered land use on the urban thermal environment, we evaluated the modulation of HW events and the UHI effect by wind speed and local climatic zones (LCZs). Wind speeds in urban areas were weakened due to the obstruction of dense high-rise buildings, which favored the occurrence of HW events. In detail, 35 HW events occurred over the LCZ1 of a dense high-rise building area under low wind speed conditions, which was much higher than that in other LCZ types and under high wind speed conditions (< 30 HW events). The latent heat flux in rural areas has increased more due to the presence of sufficient water availability and more vegetation, while the increase in heat flux in urban areas is mainly in the form of sensible heat flux, resulting in stronger UHI effect during HW periods. Compared to NHW periods, lower boundary layer and wind speed in the HW events weakened the convective mixing of air, further expanding the temperature gap between urban and rural areas. Note that LCZP type with its high-density vegetation and water bodies in the urban park area generally exhibited, was found to have a mitigating effect on the UHI, whilst at the same time increasing the frequency and duration of HW events during HW periods. Synergies between HWs and the UHI amplify both the spatial and temporal coverage of high-temperature events, which in turn exposes urban residents to additional heat stress and seriously threatens their health. The findings have important implications for HWs and UHII forecasts, as well as for scientific guidance on decision-making to improve the thermal environment and to adjust the energy structure.

Keywords: urban heat island, heat wave events, local climatic zones, wind speed, urbanization

Edited by:
Wei Zhang,
Utah State University, United States

Reviewed by:
Yunfei Li,
Potsdam Institute for Climate Impact Research (PIK), Germany
XianXiang Li,
Sun Yat-Sen University, China

****Correspondence:***
Yuanjian Yang
yyj1985@mail.ustc.edu.cn

Specialty section:
This article was submitted to Interdisciplinary Climate Studies, a section of the journal Frontiers in Earth Science

Received: *28 February 2021*
Accepted: *25 May 2021*
Published: *09 June 2021*

Citation:
Zong L, Liu S, Yang Y, Ren G, Yu M, Zhang Y and Li Y (2021) Synergistic Influence of Local Climate Zones and Wind Speeds on the Urban Heat Island and Heat Waves in the Megacity of Beijing, China. Front. Earth Sci. 9:673786. doi: 10.3389/feart.2021.673786

INTRODUCTION

Economies around the world are developing rapidly with global economic integration. Meanwhile, the processes of urbanization and industrialization are also accelerating year by year. Due to increases in population density, immense changes in land use, increases in anthropogenic heat emissions, and reduced green space have led to strong urban heat island (UHI) effects (Yang et al., 2016; Li et al., 2020). This phenomenon, manifested by enhanced air/surface temperature in urban areas compared to their rural surrounding areas (Oke and Maxwell, 1975; Roth, 2007), is one of the key characteristics of urban climates. The UHI effect has become one of the primary factors affecting the urban ecological environment, with important impacts on extreme climate events, human health, and economic losses (Ren, 2015; Rizwan et al., 2008; Yang et al., 2019; Luo and Lau, 2018; Luo and Lau, 2019).

As the capital of China, Beijing is one of the fastest developing metropolizes in recent decades. A significant UHI phenomenon has been induced in Beijing by its rapid urbanization in the past few decades (Liu et al., 2007; Zheng et al., 2018; Yang et al., 2020b). Liu et al. (2007) studied the interannual variation of the near-surface UHI intensity (UHII) during 1977–2000 in Beijing and found that the temperature rise in urban areas was greater than in rural areas. Based on long-term temperature observations from 1967 to 2016, Huang and Lu (2018) reported that the UHII had increased significantly, with a growth rate of about 0.29°C/10a, in those 50 years. Many studies have also pointed out that, usually, the UHII in Beijing is stronger in winter and weaker in summer (Xie et al., 2006; Yang et al., 2013); while in terms of daily variation, it tends to be stronger at night than during the day (Ren et al., 2007; Huang and Lu, 2018).

In the context of global warming, extreme high-temperature events are increasing in both frequency and duration (Meehl and Tebaldi, 2004; Yang et al., 2017; Lehner et al., 2018). The superimposed effect of heat waves (HWs) and UHIs causes more days and areas to experience high-temperature events, which poses a serious threat to the health of urban dwellers owing to intensified and prolonged heat exposure (Tan et al., 2010; Chew et al., 2021). Li et al. (2015) revealed that the UHII is enhanced during HW periods compared to non-HW (NHW) periods in Beijing. Also, consistent synergies between UHIs and HWs have been reported in western Sydney (Khan et al., 2020), Seoul (Ngarambe et al., 2020), Singapore (Mughal et al., 2020), and Rome (Zinzi et al., 2020). Regarding the factors modulating UHIs and HWs, they are complex and vary both spatially and temporally, but can broadly be categorized into natural-type factors (local topography, synoptic weather, meteorological factors such as wind speed, cloud cover, relative humidity, etc.) and anthropogenic-type factors (i.e., anthropogenic activities such as emissions of anthropogenic heat and aerosols, as well as land use/land cover changes related to rapid urbanization, etc.) (Li et al., 2015; Ngarambe et al., 2020; Zinzi et al., 2020). To some extent, buildings, the surface composition, and pavements also affect the exchanges of heat in cities (Shahidan et al., 2012; Wong et al., 2017; He, 2019). Therefore, the synergies between UHIs and HWs are highly localized. In most previous studies, the air temperature at a single urban site has been used to represent the air temperature of an entire city. Clearly, this is flawed, as the temperature at a meteorological station can only represent the temperature of its immediate surroundings, and different meteorological stations in large cities might differ completely in terms of their underlying surface types. Therefore, it is difficult to make generalizations on this basis.

Accordingly, in this study, we took local climate zones [LCZs—a new and systematic classification of field sites for heat island studies (Stewart and Oke, 2012)] around the selected automatic weather stations into account. Besides, we also considered the impact of wind speed, since it has a certain heat dissipation effect on different building structures and urban forms (Uehara et al., 2000; Wang Q. et al., 2020). Based on the data from the selected automatic weather stations in Beijing during the summer seasons of 2014–2020, we explored how LCZs, together with wind speed, modulate the UHI and HWs in Beijing.

DATA AND METHODS

Summertime hourly meteorological data (surface air temperature and wind speed) during 2014–2020, for 10 urban sites and 7 rural sites, were retrieved from automatic weather stations in Beijing (http://data.cma.cn/en). As the capital of China, Beijing has experienced large-scale and rapid changes to its urban environment in the past few decades, with the urban space having expanded mainly in suburban areas in the most recent decade (Li et al., 2021). Therefore, an important selection criterion was applied in that, during the study period (2014–2020), urban stations had to be within the urban center (considered here as within or near the Fifth Ring Road), and rural stations had to be far away from major construction areas (**Figure 1**; **Table 1**). The selection of urban and rural stations refers to the method of previous studies (Yang et al., 2013; Shi et al., 2015; Shi et al., 2021). The method described by Xu et al. (2013) was used for quality control and homogenization of the daily meteorological data.

In this study, we defined UHII as the difference between the surface air temperature at each urban site and the surface air temperature averaged over rural sites. Countries and regions around the world adopt different methods to study high-temperature HW events, and the standards for defining high-temperature HWs also vary greatly. HW events are usually identified as cases in which the daily maximum temperature reaches or exceeds a certain threshold for several consecutive days. The threshold for high temperature can be a relative value or an absolute threshold (Ngarambe et al., 2020). In this paper, an HW event is defined as when the daily maximum temperature exceeds 35°C for three consecutive days or more, as described by Yao et al. (2020).

To explore the potential impact of urban forms and land-cover types on the interaction between the UHI and HWs, we obtained the LCZ category of each reference station based on the LCZ dataset produced by the Institute of Urban Meteorology, China

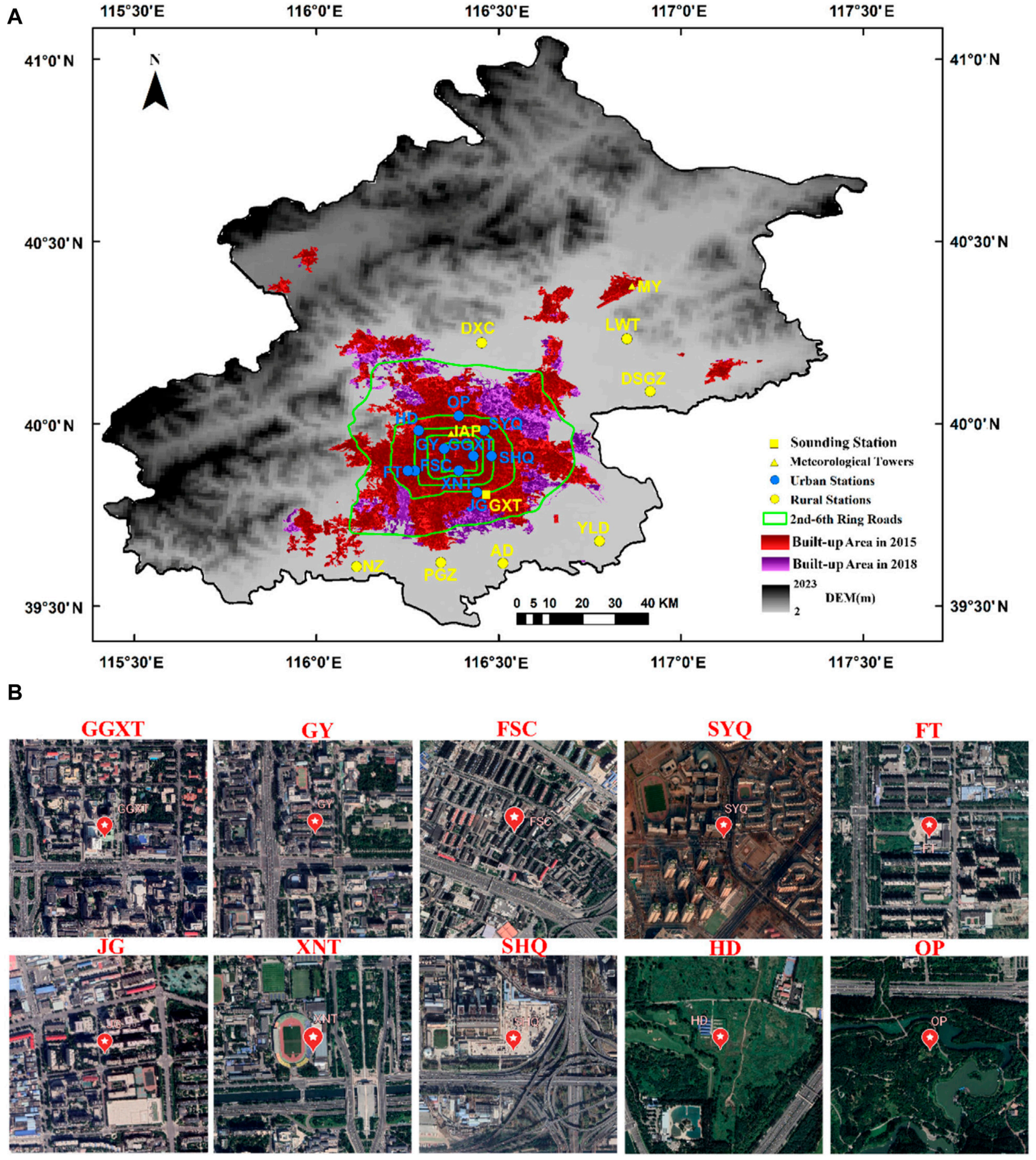

FIGURE 1 | (A) Geographical locations of reference stations within the boundaries of Beijing. **(B)** Google Earth images of urban stations. The built-up areas data can be accessed at https://zenodo.org/record/4034161#.YFc56driuUl.

Meteorological Administration, Beijing. The fine-scale underlying surface data were derived in SAGA GIS by a random forest classification of the Landsat eight satellite data in 2018 according to the workflow provided by the World Urban Database and Access Portal Tools. This LCZ dataset for Beijing consists of 17 LCZ types with significant differences based on the characteristics of the underlying surface of the urban climate proposed in previous studies (Stewart and Oke, 2012; Stewart et al., 2014). In particular, owing to the rapid urbanization of the city, we defined a special category, LCZH, to classify regions

TABLE 1 | Geographical locations of the reference stations.

Station	Lon (°E)	Lat (°N)	Site type	Local climate zone
LWT	116.85	40.23	Rural	LCZA
AD	116.51	39.61	Rural	LCZB
DXC	116.45	40.22	Rural	LCZC
YLD	116.78	39.67	Rural	LCZC
PGZ	116.34	39.61	Rural	LCZC
DSGZ	116.92	40.08	Rural	LCZD
NZ	116.11	39.6	Rural	LCZD
GGXT	116.43	39.91	Urban	LCZ1
GY	116.35	39.93	Urban	LCZ1
FSC	116.27	39.87	Urban	LCZ2
SYQ	116.46	39.98	Urban	LCZ2
FT	116.25	39.87	Urban	LCZ4
JG	116.44	39.81	Urban	LCZ4
XNT	116.39	39.87	Urban	LCZ5
SHQ	116.48	39.91	Urban	LCZ5
HD	116.28	39.98	Urban	LCZP
OP	116.39	40.02	Urban	LCZP

composed of a large number of construction areas. Exploring the thermal environment of urban green spaces as well can help to get a better understanding of their contribution to urban environment and a more comprehensive view on urban thermal environment. Therefore, we also defined the underlying surface of the green space and forest park in the urban as a new type of LCZP to distinguish between the greenery within and outside city. We chose the five most common categories of LCZ (i.e., LCZ1, LCZ2, LCZ4, LCZ5, and LCZP) in the Beijing urban area. Two urban stations for each chosen LCZ were selected in this study (see **Figure 1** and **Table 1** for their geographical locations). To ensure that the impact of urbanization changes on the reference stations was minimized, an important criterion was employed in that urban stations had to be within or near the 5th Ring Road and remote from LCZH. It is important to emphasize that green space was found in both urban and rural areas, and they had similar underlying surface structures, but a major difference between them was that urban LCZP was mostly forest parkland in the urban center, and there were still urban buildings around it, while the rural green space was far away from urban built-up areas and the thermal impact of human activities was smaller. It is worth noting that this provides strong evidence that green space and vegetation in the city help to effectively alleviate the UHI effect (Doick et al., 2014; Zhou et al., 2019).

Besides, we also referred to observational heat flux data during an HW event (2016.07.09–2016.07.11) and an NHW event (2016.07.06–2016.07.08) at an urban site (Institute of Atmospheric Physics Tower, IAP, at 47 m) and rural site (Miyun Tower, MY, at 36 m) (specific locations are shown in **Figure 1A**). Similarly, sounding profiles at 0800, 1400, and 2000 LST at Guanxiangtai (GXT) station (see **Figure 1A**) during this period were used to calculate the boundary layer height (BLH). Furthermore, to study the potential effect of wind speeds on the UHI and HWs, wind speeds were classified into three categories [low (0–0.74 m/s), medium (0.75–1.44 m/s) and high (1.45–11.7 m/s)] using the *k*-means clustering algorithm. Finally, we employed analysis of variance (ANOVA) tests to assess the UHII differences under different wind speed and LCZ categories, and the statistical significance was tested at a 0.001 confidence level.

RESULTS

UHII Differences Between HW and NHW Periods

Figure 2 shows that the summer UHII in Beijing was strong at night and in the early morning, and weak during the daytime in 2014–2020, which is similar to the results of previous studies (Xie et al., 2006; Liu et al., 2007; Yang et al., 2013). In general, the diurnal variation of summer UHII displays a U-shaped fluctuation. The 7-years average UHII during HW and NHW periods ranged from 0.55 to 2.53°C and from 0.28 to 1.72°C, respectively. Overall, the average UHII during HW periods was larger than that during NHW periods. Moreover, the impact of urbanization on HW events cannot be ignored. With the acceleration of urbanization, urban and suburban stations have experienced varying degrees of warming, which has not only led to a more extensive UHI effect, but also caused more HW events with long durations in urban areas compared to rural areas (Tan et al., 2010; see also **Supplementary Figure S1**).

In addition, the diurnal cycles of maximum UHII among all urban stations are also shown, to detect the relationship between hourly maximum UHII and HW events (**Supplementary Figure S2**). Similarly, the average maximum UHII during HW periods was stronger than during NHW periods. To further analyze the difference in UHII between HW and NHW periods, we calculated ΔUHII as the UHII during HW periods minus the UHII during NHW periods, and the diurnal variation of ΔUHII is shown in **Figure 3**. The ΔUHII reached up to 1.77 and 1.67°C in 2015 and 2020, respectively. While ΔUHII usually reached a minimum at 0900 and 1800 LST, the peak often occurred at noon or at midnight. The diurnal variation of ΔUHII roughly followed a “W” shape. In general, the diurnal variation of ΔmaxUHII is consistent with that of ΔUHII, and are mainly modulated by anthropogenic heat emissions, aerosols, atmospheric circulation, etc. (Zheng et al., 2018; Zheng et al., 2020; Yang et al., 2020a). The HW–NHW differences in UHII suggest that UHII can be amplified by HW events, and then the enhancement of UHII can feed back positively to HWs (Luo and Lau, 2018; Ngarambe et al., 2020).

Modulation of HWs and UHII by Wind Speed

To assess the influence of wind speed on HWs and UHII, we applied *k*-means clustering to the wind speed data and divided the results into three categories—namely, high, medium, and low. The numbers of HW events under these different wind speed categories for each urban station are shown in **Figure 4** (see also **Supplementary Figure S3** for the durations of HW events under different wind speed categories for each urban station). Under high wind speeds, the highest number of HW events (6) was at station SYQ, out of a total of 19 HW days. The number of occurrences of HW events at GGXT, HD, and OP was 0. During medium wind speed periods, 5 out of 10 urban stations

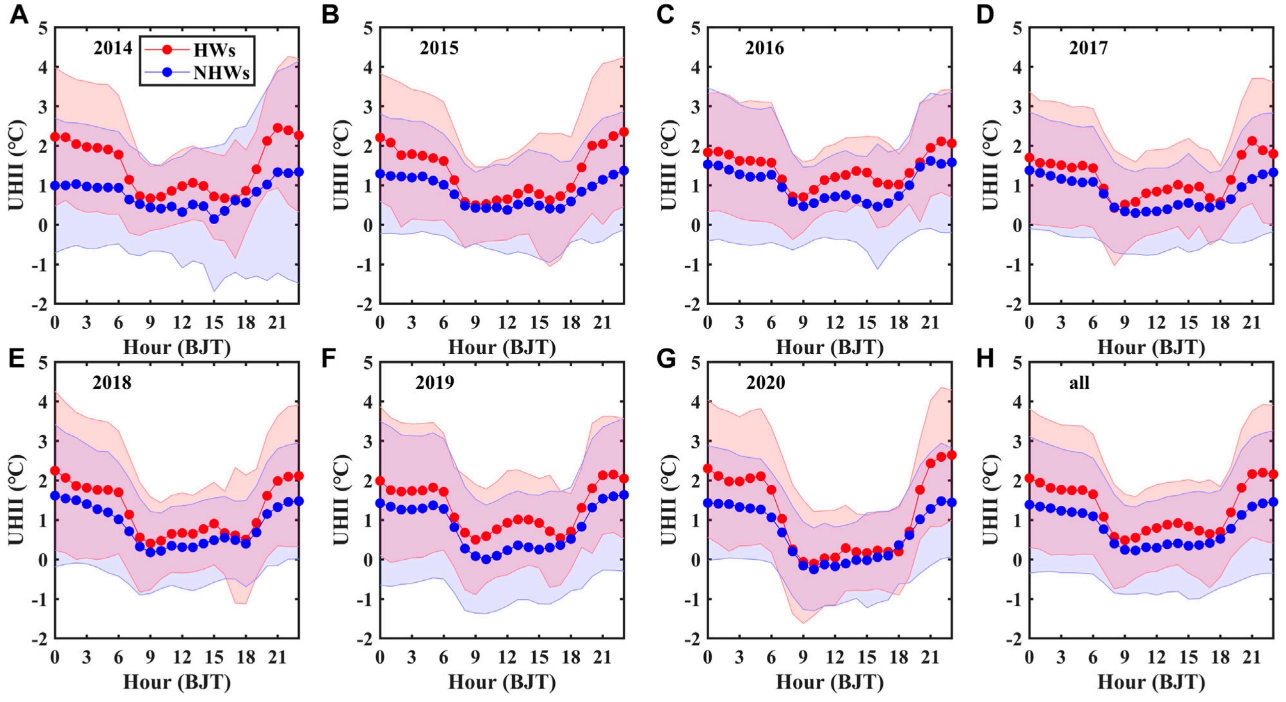

FIGURE 2 | Diurnal variation of UHII between HW and NHW periods during summertime (June–August) 2014–2020. HW and NHW periods are indicated by red and blue, respectively. Lines denote average UHII values and shaded areas present the standard deviation of the average UHII values according to all urban reference stations.

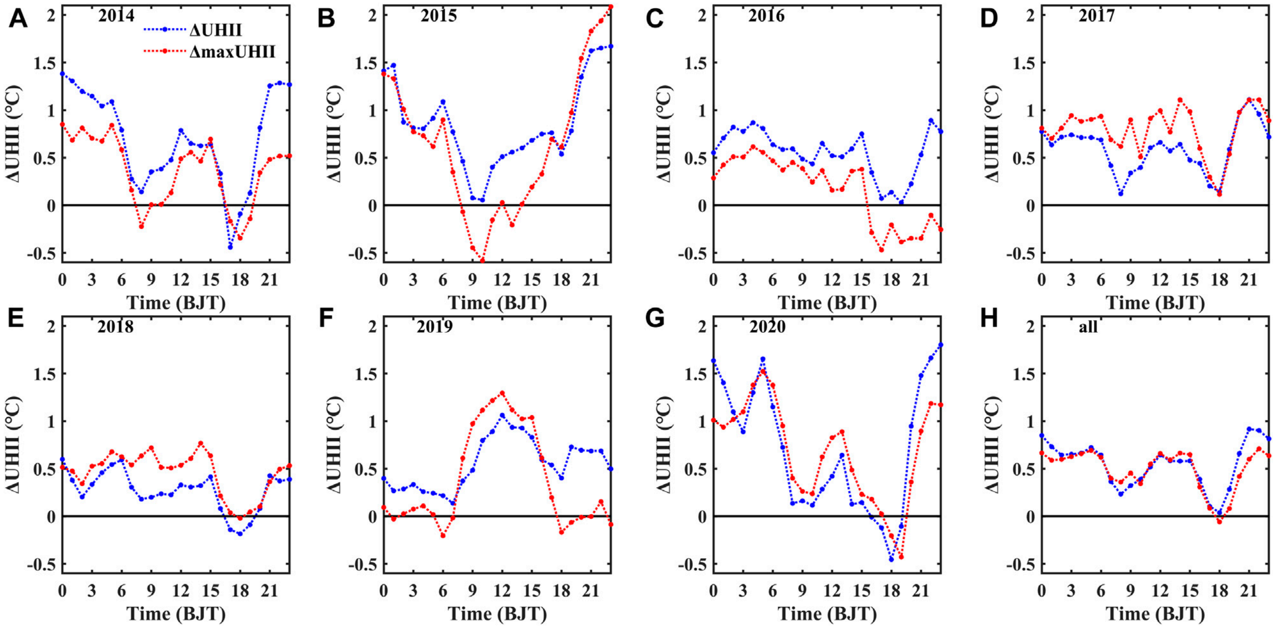

FIGURE 3 | Diurnal differences in UHII between HW and NHW periods during summertime (June–August) 2014–2020. Red lines present average maximum UHII values, and blue lines present average UHII values according to all urban reference stations.

experienced more than 10 HW events, the average duration of which was more than 35 days. SHQ had 20 HW events (72 days). As for periods of low wind speed, the number of HW events at GGXT (25) was much higher than at other stations, and much longer (average of 109 days). At many stations, there were fewer HW events under low wind speeds, which may have been due to

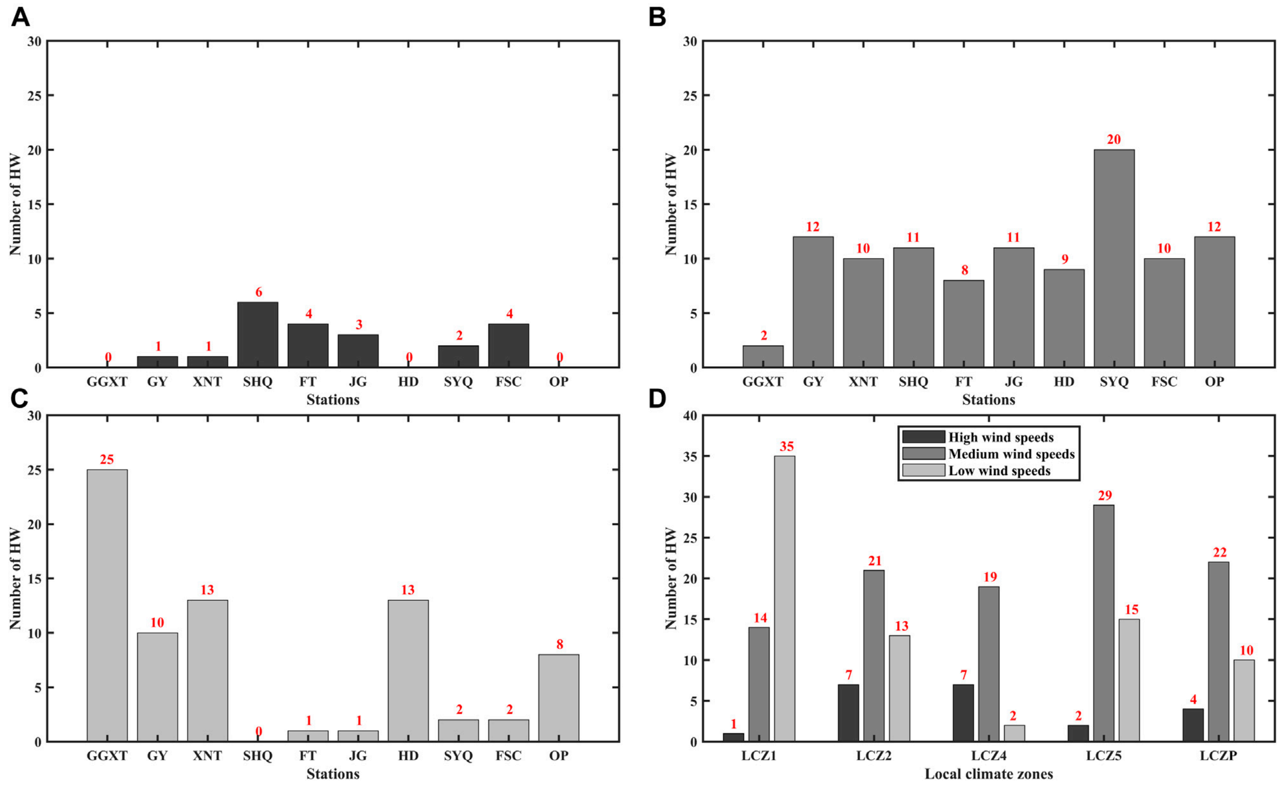

FIGURE 4 | Number of HW events under different wind speed conditions at each urban station during 2014–2020: **(A)** high wind speeds; **(B)** medium wind speeds; **(C)** low wind speeds; **(D)** wind speeds per LCZ.

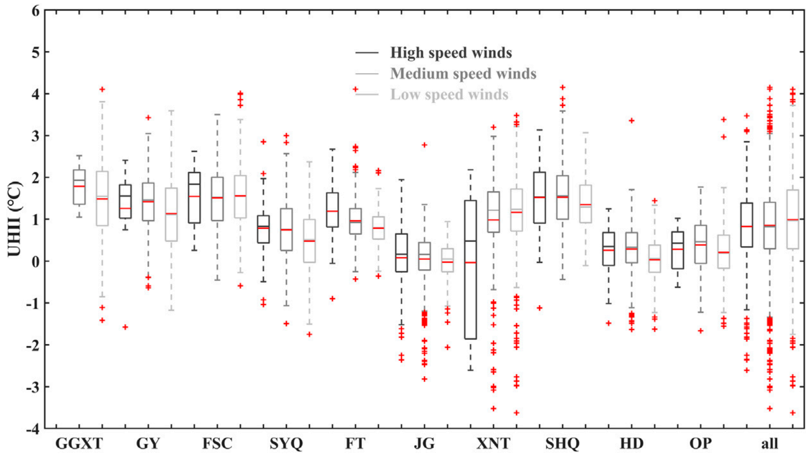

FIGURE 5 | Box-and-whisker plots of the UHII values under different wind speed conditions at each urban station during 2014–2020. In the plots, the central box represents the values from the lower to upper quartile (25th to 75th percentile). The vertical line extends from the maximum to the minimum value. The middle black solid line represents the median, the middle red solid line represents the average, and the red plus signs represent outliers.

the smaller threshold difference between the low and medium wind speed categories.

Figure 5 depicts the UHII values under for each urban station and all urban stations under different wind speed categories. The average UHII value under high, medium and low wind speed was 0.82, 0.85 and 0.99°C, respectively. Based on ANOVA, the average UHII difference of the three wind speed groups was statistically significant, with $F\,(6418) = 18.46$ and $p < 0.001$. Under high wind

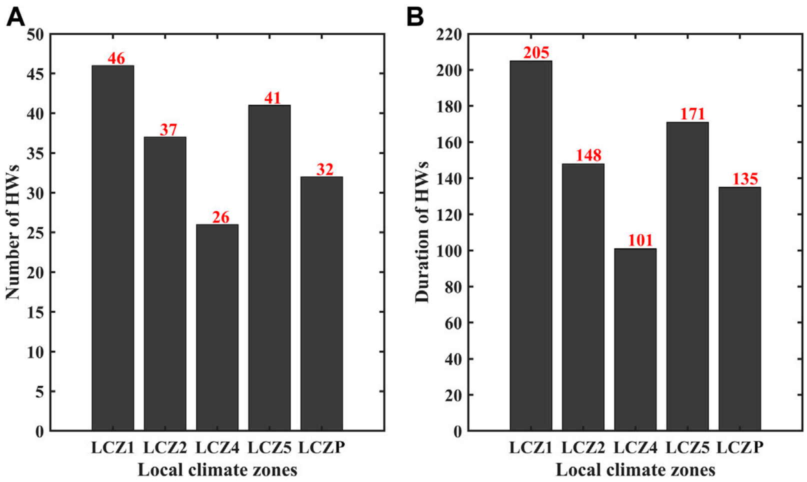

FIGURE 6 | Number and duration of HW events under each LCZ.

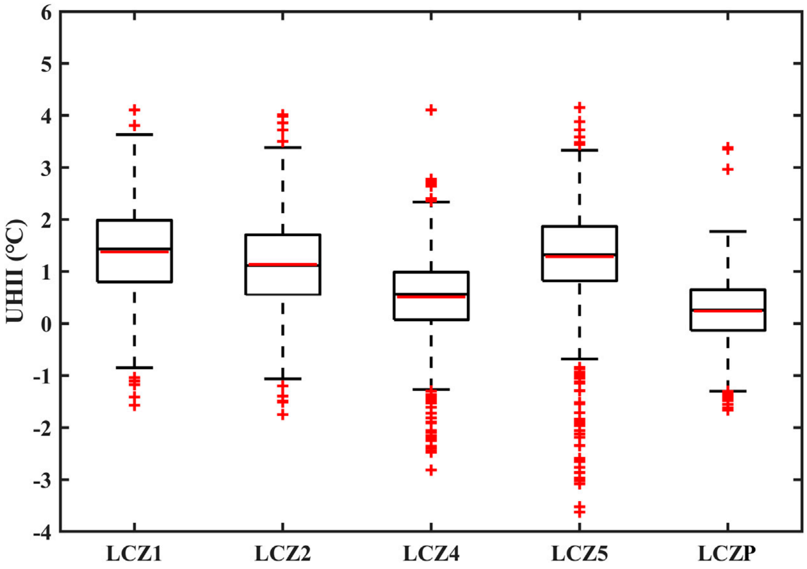

FIGURE 7 | Box-and-whisker plots of the UHII values under each LCZ.

speeds, the UHIIs of SYQ, FT and SHQ were significantly higher than at other stations. This may have been due to the low number of wind speed samples at these stations; plus, even those samples classified into the high wind speed category were closer to the lower bound of the qualifying range.

Modulations of HWs and UHII by the LCZs

To explore how the LCZs modulate HW events and UHI effects, we quantified the HW events and UHII values under each LCZ category. Two urban stations for each category of LCZ were included, and the specific LCZ types of each urban station can be seen in **Table 1**. It is worth mentioning that LCZ1 stands for a dense high-rise building area, and LCZ2 for a dense middle-rise building area, LCZ4 for an open high-rise building area, LCZ5 for an open mid-rise building area, and LCZP for a sparse tree area.

As shown in **Figure 6**, in the 7 years of the study period, there were 46, 37, 26, 41 and 32 HW events in LCZ1, LCZ2, LCZ4, LCZ5, and LCZP, with durations of 205, 148, 101, 171, and 135 days, respectively. It is clear that the number and duration of HW events under LCZ1, LCZ2, and LCZ4 was significantly decreasing. It strongly proves that the LCZs have a very positive regulatory effect on HW events. In dense high-rise-building areas, HW events occur more frequently and last longer. Compared with LCZ1 and LCZ2, LCZ4, LCZ5, and LCZP have a lower building density and a relatively small building height to width ratio, which may reduce the duration and frequency of HW events (Ngarambe et al., 2020).

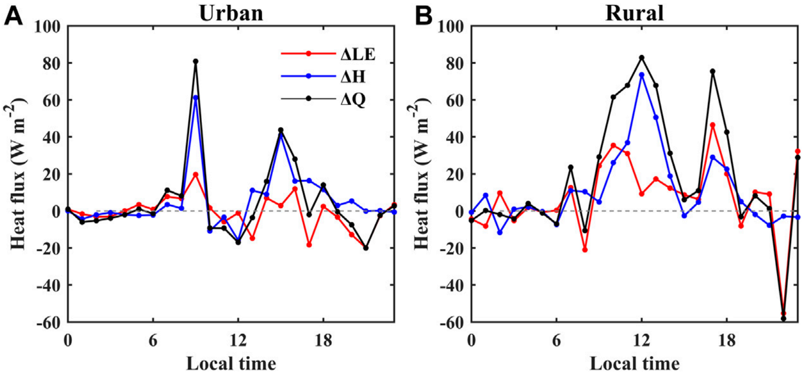

FIGURE 8 | The differences of heat flux at urban station (IAP) and rural station (MY) between HW days (2016.07.06–2016.07.08) and NHW days (2016.07.09–2016.07.11). LE: latent heat flux, H: sensible heat flux, to calculate Q as LE + H, $\Delta LE = LE_{HWS}-LE_{NHWS}$, $\Delta H = H_{HWS}-H_{NHWS}$, $\Delta Q = Q_{HWS}-Q_{NHWS}$.

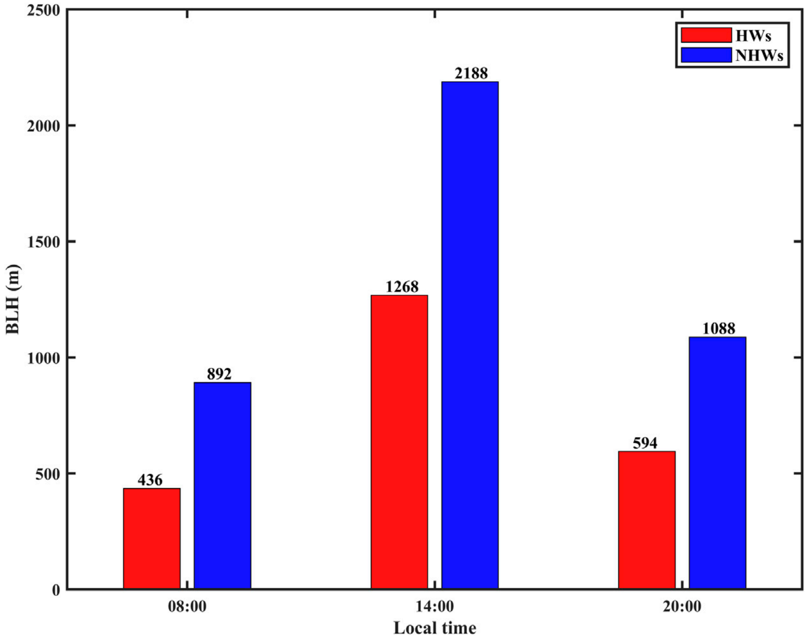

FIGURE 9 | The averaged BLH during a case for 2016.07.06–2016.07.11, included both HW days (2016.07.06–2016.07.08) and NHW days (2016.07.09–2016.07.11).

Surprisingly, the number of HW events in LCZ5 was higher than in LCZ2 and LCZ4. Why this was the case is further discussed in the next section.

Furthermore, ANOVA was employed to test the differences in the UHII levels under the five LCZs, giving a result of F (6423) = 498.64 and $p < 0.001$. The UHII levels under the five LCZs varied significantly. The largest mean UHII value was found in LCZ1, which was 1.38°C. The average UHII of LCZ2, LCZ4, LCZ5, and LCZP was 1.14, 0.51, 1.28 and 0.29°C, respectively. The UHII under LCZ1, LCZ2, LCZ4, and LCZP depended strongly on the characteristics of the underlying surface. Similar to what was found for HW events, the UHII under LCZ5 was also higher than under LCZ2 and LCZ4 (**Figure 7**).

DISCUSSION

In *UHII Differences Between HW and NHW Periods* we analyzed the daily variation of UHII during HW and NHW periods in the summers of 2014–2020. The difference between them was also calculated. We found that the UHII during HW periods was significantly stronger than during NHW periods. This means that, compared to NHW periods, the urban heat during HW periods increased more than in rural areas, resulting in a stronger UHI effect. In general, the surface receives more shortwave and longwave radiation during HW periods than NHW periods (**Supplementary Figure S5**; Hong et al., 2018). Additionally, the latent heat flux in rural areas has increased more due to the

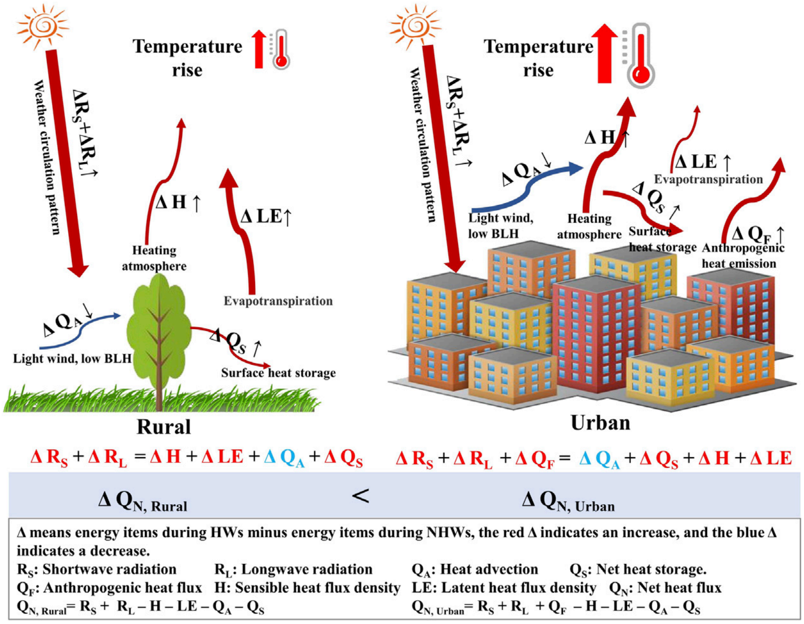

FIGURE 10 | Schematics of mechanisms of HW events enhancing UHI effect.

presence of sufficient water availability and more vegetation, while the increase in heat flux in urban areas is mainly in the form of sensible heat flux (Li et al., 2015; Zheng et al., 2018; see also **Figure 8**, and **Supplementary Figure S6**). Coupled with the high-pressure controlled during the HW period, the downdraft restrained the boundary layer development (Tressol et al., 2008). Similarly, relative to the NHW period, lower BLH during the HW period was observed in the present work (**Figure 9**), which was not conducive to convective mixing. Moreover, due to the unique underlying city canopy-layer structure with good thermal conductivity and large heat capacity (Stewart and Oke, 2012; Ren, 2015; Wang L. et al., 2020), the increase in net heat flux was more over urban areas than rural areas (i.e., $\Delta Q_{N,\ Rural} < \Delta Q_{N,\ Urban}$ in **Figure 10**), resulting in stronger UHI effect during HW periods. In addition, the demand for water and electricity for heatstroke prevention and cooling during HW periods has soared, which may increase anthropogenic heat emissions in the urban. As a result, the temperature of dry air in urban areas will rise more than humid air in rural areas, causing a wider temperature gap between urban and rural areas under HW conditions. In general, the schematics of mechanisms of HW events enhancing UHI effect can be summarized in **Figure 10**. In the present work, the daily variation of ΔUHII between HW and NHW periods roughly followed a W-shaped curve, with the troughs appearing at 0800 and 1800 LST. Interestingly, at around 1800 LST, the interaction between HWs and UHII was almost negligible (ΔUHII between HW and NHW periods was zero or close to zero). As shown in **Figure 8**, the difference in radiation flux between HW and NHW periods, both in urban and rural areas, was also approximately zero, resulting in little difference in the temperature increase between urban and rural areas.

Moreover, in view of the impact of weather conditions and land-use characteristics on the urban thermal environment, we evaluated the influences of wind speed and LCZs on HW events and UHII. It was found that, when the surface temperature increases rapidly and the horizontal wind speed is low, this is conducive to the formation of HW events with a high-pressure anticyclone controlled by a prevailing downdraft and stable atmosphere (Tressol et al., 2008). Wind speed plays an important role in local heat exchange (Tong and Leung, 2012), wherein reduced horizontal advection cooling could promote an increased UHII (**Figure 5** indicates that UHII under low wind speeds was higher than under medium or high wind speeds). The characteristics of surface land use and the spatial configuration of urban buildings are also likely to be responsible for enhancing the UHII during HW periods. Bare soil and vegetation in rural areas might favor soil evapotranspirative cooling. On the contrary, less water content due to pavements and buildings restrains evapotranspiration in urban areas. As a result, there will be a greater frequency of HW events and a stronger UHI effect in dense high-rise-building areas such as LCZ1, LCZ2, LCZ4, LCZ5, etc. However, in the present study, the results for LCZ5 conflicted with this assertion. In this respect, it should be noted that XNT is located close to the Beijing South Second Ring Road, and SHQ is near the East Fourth Ring Road, close to the most complex overpass in Beijing (**Figure 1B**). Vast heat emissions caused by traffic may therefore have been partly responsible for high-temperature events and strong UHI effects under LCZ5.

Note that LCZP experienced many more and longer HWs than other LCZs. Usually, LCZP is composed of low-density plants, and its vegetation and green spaces alleviate the overall UHII considerably owing to higher rates of evaporation causing surface cooling (Doick et al., 2014; Zhou et al., 2019). However,

TABLE 2 | Two-way analysis of variance between wind speed and LCZs to UHII.

Source	Sum Sq	d.f	Mean Sq	*F*	Prob>*F*
WS	1.01	2	0.505	0.79	0.3755
LCZ	458.71	4	114.677	178.35	0
WS*LCZ	10.56	8	10.56	16.42	0
Error	4121.49	6410	0.643		
Total	5514.08	6424			

numerous studies have established that cooler surfaces caused by a higher proportion of green space and associated additional irrigation increased the risk from HW events over the North China Plain (Kang and Eltahir, 2018; Krakauer et al., 2020). In this study, the LCZP at OP station, with high-density vegetation and water bodies, was similar to an irrigation area. In the early stage of an HW event, due to the evapotranspiration of water bodies and vegetation, a large amount of heat is stored, and then this enormous quantity of heat might be emitted into the air in the form of sensible heat (**Figure 8**), resulting in a sharp rise in temperature (Stap et al., 2014; Teuling et al., 2010). The evaporation of vegetation and water effectively suppresses the increase in the surrounding air temperature during the initial period. However, this process will eventually accelerate the consumption of soil moisture, and then dissipate more heat to the air, leading to increased temperature, especially in HW periods with strong solar radiation. In addition, Zhao et al. (2014) observed that the cooling efficiency of UHIs was reduced by 58% in humid areas with more vegetation, and Feinberg (2021) believed that, in this case, water vapor, as a greenhouse gas, can double the direct radiative forcing to heat the air. As a result, it is more conducive to increasing the occurrence of HW events. Although the effects of vegetation and water bodies on the process of radiation transmission are highly complex, we observed two opposite effects on the urban thermal environment. On the one hand, in general, green space and water bodies in the urban area had a mitigating effect on the UHI phenomenon. On the other hand, during HW periods, they also increased the frequency and duration of HW events. Elucidating the physical mechanism involved here is worthy of further study *via* numerical experiments.

There was a clear correlation between wind speed and the LCZ categories, and this is because wind speed may be weakened due to the obstruction of dense high-rise buildings (the distributions of wind speed under different LCZ categories are shown in **Supplementary Figure S4**). Therefore, HW events and UHI effects are regulated by LCZs in combination with wind speed. **Table 2** shows the influence of wind speed and LCZs on UHII *via* two-way ANOVA. It is clear that, under the interactive effect of wind speed and LCZs, the average UHII difference was significant [F (8) = 16.42, p < 0.001]. This is robust proof of a co-regulatory effect of LCZ type and wind speed on UHII, and that the LCZ is more sensitive to the regulation of UHII. In addition, **Figures 4D, 11** present the number of HW events and the distribution of UHII under different wind speed periods for each LCZ, which to some extent can separate the effects from wind speed and LZCs. When considering the impact of LCZs only on HW events, there were clear gaps in the frequency and duration of HW events under different LCZs. It shows that, under a specific wind speed category, HW events in dense high-rise-building areas have a higher frequency and longer duration. High-frequency and long-duration HW events are more likely to happen under lower wind speeds in a certain LCZ area.

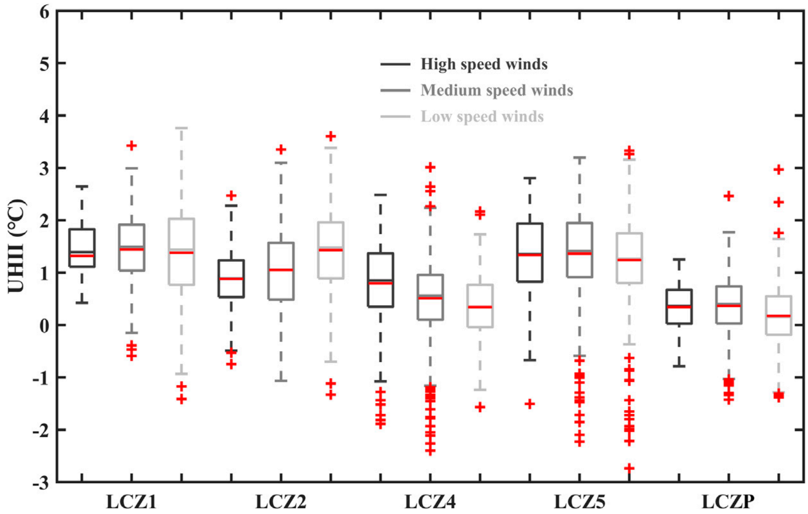

FIGURE 11 | Box-and-whisker plots of the UHII values under different wind speed categories in each LCZ.

Our work still has a few limitations. For example, relative humidity, cloud cover, precipitation, and other meteorological factors also have an impact on the UHI effect, which may affect the interaction between HWs and UHII. In addition, the atmospheric circulation situation, anthropogenic heat emissions, and the impact of aerosols on the balance of surface radiation are other potential influencing factors of HW events and UHI effects (Li et al., 2015; Yang et al., 2020b; Ngarambe et al., 2020; Zinzi et al., 2020). Therefore, future studies should also consider these factors to explore their influences on HW events and the UHI effect.

CONCLUSION

Based on the observations of automatic weather stations in Beijing during the summers of 2014–2020, the joint effects of wind speed and LCZs on urban extreme high-temperature events and the UHI effect were explored. Results showed that UHII was significantly aggravated during HW periods compared to NHW periods. Wind speeds in urban areas were weakened due to the obstruction of dense high-rise buildings, which favored the occurrence of HW events. During HW periods, both rural and urban surfaces received more shortwave and longwave radiation, resulting in increased heat storage. The latent heat flux in rural areas has increased more due to the presence of sufficient water availability and more vegetation, while the increase in heat flux in urban areas is mainly in the form of sensible heat flux. Moreover, due to city canopy-layer structure with good thermal conductivity and large heat capacity, the increase in net heat flux was more over urban areas than rural areas, resulting in stronger UHI effect during HW periods. Lower boundary layer and wind speed in the HW events have weakened the convective mixing of air, which would further expand the temperature gap between urban and rural areas, compared to NHW periods. Meanwhile, LCZP in the urban park area, with its water bodies and vegetation, was found to play unique roles in HWs and UHII as follows: On the one hand, in general, green space and water bodies in urban areas can have a mitigating effect on the UHI phenomenon. On the other hand, during HW periods, they can also increase the frequency and duration of HW events.

In general, synergies between HWs and UHI amplify both the spatial and temporal coverage of high-temperature events, which in turn exposes urban residents to additional heat stress and seriously threatens their health. The present work can lend support to the prediction of extreme high-temperature events and UHI effects in megacities like Beijing. Our findings have important implications for HWs and UHII forecasts, as well as for scientific guidance on decision-making to improve the thermal environment and to adjust the energy structure.

DATA AVAILABILITY STATEMENT

The original contributions presented in the study are included in the article/**Supplementary Material**, further inquiries can be directed to the corresponding author.

AUTHOR CONTRIBUTIONS

Conceptualization, YY; methodology, LZ and YY; software, LZ and SL; formal analysis, LZ, SL, and YY; data curation, LZ, YZ, and MY; writing—original draft preparation, LZ; writing—review and editing, LZ, MY, YL, GR, and YY; supervision, YY; funding acquisition, YY. All authors have read and agreed to the published version of the manuscript.

FUNDING

This study was supported by the National Natural Science Foundation of China (42061134009, 42075072, and 41575010) and the Beijing Natural Science Foundation (8202022 and 8171002).

ACKNOWLEDGMENTS

The authors also thank the Meteorological Information Centre of the China Meteorological Administration for providing meteorological data (http://data.cma.cn/site/index.html)

SUPPLEMENTARY MATERIAL

The Supplementary Material for this article can be found online at: https://www.frontiersin.org/articles/10.3389/feart.2021.673786/full#supplementary-material

REFERENCES

Chew, L. W., Liu, X., Li, X. X., and Norford, L. K. (2021). Interaction Between Heat Wave and Urban Heat Island: A Case Study in a Tropical Coastal City, Singapore. *Atmos. Res.* 247, 105134. doi:10.1016/j.atmosres.2020.105134

Doick, K. J., Peace, A., and Hutchings, T. R. (2014). The Role of One Large Greenspace in Mitigating London's Nocturnal Urban Heat Island. *Sci. Total Environ.* 493, 662–671. doi:10.1016/j.scitotenv.2014.06.048

Feinberg, A. (2021). Urban Heat Island Local GHG Water-Vapor Feedback Concerns Requiring Albedo Management. *ResearchGate*. doi:10.13140/RG.2.2.20529.81766/5

He, B.-J. (2019). Towards the Next Generation of green Building for Urban Heat Island Mitigation: Zero UHI Impact Building. *Sustainable Cities Soc.* 50 (di), 101647. doi:10.1016/j.scs.2019.101647

Hong, J.-S., Yeh, S.-W., and Seo, K.-H. (2018). Diagnosing Physical Mechanisms Leading to Pure Heat Waves versus Pure Tropical Nights over the Korean Peninsula. *J. Geophys. Res. Atmos.* 123 (14), 7149–7160. doi:10.1029/2018JD028360

Huang, Q. F., and Lu, Y. Q. (2018). Long-term Trend of Urban Heat Island Intensity and Climatological Affecting Mechanism in Beijing City. *Sci. Geogr. Sin.* 38 (10), 1715–1723. doi:10.13249/j.cnki.sgs.2018.10.016

Kang, S., and Eltahir, E. A. B. (2018). North China Plain Threatened by Deadly Heatwaves Due to Climate Change and Irrigation. *Nat. Commun.* 9 (1), 1–9. doi:10.1038/s41467-018-05252-y

Khan, H. S., Paolini, R., Santamouris, M., and Caccetta, P. (2020). Exploring the Synergies between Urban Overheating and Heatwaves (HWS) in Western Sydney. *Energies* 13 (2), 470. doi:10.3390/en13020470

Krakauer, N. Y., Cook, B. I., and Puma, M. J. (2020). Effect of Irrigation on Humid Heat Extremes. *Environ. Res. Lett.* 15 (9), 094010. doi:10.1088/1748-9326/ab9ecf

Lehner, F., Deser, C., and Sanderson, B. M. (2018). Future Risk of Record-Breaking Summer Temperatures and its Mitigation. *Climatic Change* 146 (3–4), 363–375. doi:10.1007/s10584-016-1616-2

Li, D., Sun, T., Liu, M., Yang, L., Wang, L., and Gao, Z. (2015). Contrasting Responses of Urban and Rural Surface Energy Budgets to Heat Waves Explain Synergies between Urban Heat Islands and Heat Waves. *Environ. Res. Lett.* 10 (5), 054009–054010. doi:10.1088/1748-9326/10/5/054009

Li, Y., Schubert, S., Kropp, J. P., and Rybski, D. (2020). On the Influence of Density and Morphology on the Urban Heat Island Intensity. *Nat. Commun.* 11, 2647. doi:10.1038/s41467-020-16461-9

Li, Y., Ye, H., Sun, X., Zheng, J., and Meng, D. (2021). Coupling Analysis of the Thermal Landscape and Environmental Carrying Capacity of Urban Expansion in Beijing (China) over the Past 35 Years. *Sustainability* 13, 584. doi:10.3390/su13020584

Liu, W., Ji, C., Zhong, J., Jiang, X., and Zheng, Z. (2007). Temporal Characteristics of the Beijing Urban Heat Island. *Theor. Appl. Climatol.* 87 (1–4), 213–221. doi:10.1007/s00704-005-0192-6

Luo, M., and Lau, N.-C. (2018). Increasing Heat Stress in Urban Areas of Eastern China: Acceleration by Urbanization. *Geophys. Res. Lett.* 45 (23), 13060–13069. doi:10.1029/2018gl080306

Luo, M., and Lau, N.-C. (2019). Urban Expansion and Drying Climate in an Urban Agglomeration of east China. *Geophys. Res. Lett.* 46 (2), 6868–6877. doi:10.1029/2019gl082736

Meehl, G. A., and Tebaldi, C. (2004). More Intense, More Frequent, and Longer Lasting Heat Waves in the 21st Century. *Science* 305, 994–997. doi:10.1126/science.1098704

Mughal, M. O., Li, X., and Norford, L. K. (2020). Urban Climate Urban Heat Island Mitigation in Singapore: Evaluation Using WRF / Multilayer Urban Canopy Model and Local Climate Zones. *Urban Clim.* 34, 100714. doi:10.1016/j.uclim.2020.100714

Ngarambe, J., Nganyiyimana, J., Kim, I., Santamouris, M., and Yun, G. Y. (2020). Synergies between Urban Heat Island and Heat Waves in Seoul: The Role of Wind Speed and Land Use Characteristics. *PLoS One* 15 (12), e0243571. doi:10.1371/journal.pone.0243571

Oke, T. R., and Maxwell, G. B. (1975). Urban Heat Island Dynamics in Montreal and Vancouver. *Atmos. Environ. (1967)* 9 (2), 191–200. doi:10.1016/0004-6981(75)90067-0

Ren, G.-Y. (2015). Urbanization as a Major Driver of Urban Climate Change. *Adv. Clim. Change Res.* 6 (1), 1–6. doi:10.1016/j.accre.2015.08.003

Ren, G. Y., Chu, Z. Y., Chen, Z. H., and Ren, Y. Y. (2007). Implications of Temporal Change in Urban Heat Island Intensity Observed at Beijing and Wuhan Stations. *Geophys. Res. Lett.* 34 (5), 1–5. doi:10.1029/2006GL027927

Rizwan, A. M., Dennis, L. Y. C., and Liu, C. (2008). A Review on the Generation, Determination and Mitigation of Urban Heat Island. *J. Environ. Sci.* 20 (1), 120–128. doi:10.1016/S1001-0742(08)60019-4

Roth, M. (2007). Review of Urban Climate Research in (Sub)tropical Regions. *Int. J. Climatol.* 27, 1859–1873. doi:10.1002/joc.1591

Shahidan, M. F., Jones, P. J., Gwilliam, J., and Salleh, E. (2012). An Evaluation of Outdoor and Building Environment Cooling Achieved through Combination Modification of Trees with Ground Materials. *Building Environ.* 58, 245–257. doi:10.1016/j.buildenv.2012.07.012

Shi, T., Huang, Y., Sun, D., Lu, G., and Yang, Y. (2021). A New Method for Correcting Urbanization-Induced Bias in Surface Air Temperature Observations: Insights From Comparative Site-Relocation Data. *Front. Environ. Sci.* 9, 625418. doi:10.3389/fenvs.2021.625418

Shi, T., Huang, Y., Wang, H., Shi, C.-E., and Yang, Y.-J. (2015). Influence of Urbanization on the thermal Environment of Meteorological Station: Satellite Observed Evidence. *Adv. Clim. Change Res.* 6, 715. doi:10.1016/j.accre.2015.07.001

Stap, L. B., Van Den Hurk, B. J. J. M., Van Heerwaarden, C. C., and Neggers, R. A. J. (2014). Modeled Contrast in the Response of the Surface Energy Balance to Heat Waves for forest and Grassland. *J. Hydrometeorol.* 15 (3), 973–989. doi:10.1175/JHM-D-13-029.1

Stewart, I. D., Oke, T. R., and Krayenhoff, E. S. (2014). Evaluation of the 'local Climate Zone' Scheme Using Temperature Observations and Model Simulations. *Int. J. Climatol.* 34 (4), 1062–1080. doi:10.1002/joc.3746

Stewart, I. D., and Oke, T. R. (2012). Local Climate Zones for Urban Temperature Studies. *Bull. Am. Meteorol. Soc.* 93 (12), 1879–1900. doi:10.1175/BAMS-D-11-00019.1

Tan, J., Zheng, Y., Tang, X., Guo, C., Li, L., Song, G., et al. (2010). The Urban Heat Island and its Impact on Heat Waves and Human Health in Shanghai. *Int. J. Biometeorol.* 54 (1), 75–84. doi:10.1007/s00484-009-0256-x

Teuling, A. J., Seneviratne, S. I., Stöckli, R., Reichstein, M., Moors, E., Ciais, P., et al. (2010). Contrasting Response of European forest and Grassland Energy Exchange to Heatwaves. *Nat. Geosci* 3 (10), 722–727. doi:10.1038/ngeo950

Tong, N. Y. O., and Leung, D. Y. C. (2012). Effects of Building Aspect Ratio, Diurnal Heating Scenario, and Wind Speed on Reactive Pollutant Dispersion in Urban Street Canyons. *J. Environ. Sci.* 24 (12), 2091–2103. doi:10.1016/S1001-0742(11)60971-6

Tressol, M., Ordonez, C., Zbinden, R., Brioude, J., Thouret, V., Mari, C., et al. (2008). Air Pollution during the 2003 European Heat Wave as Seen by MOZAIC Airliners. *Atmos. Chem. Phys.* 8 (8), 2133–2150. doi:10.5194/acp-8-2133-2008

Uehara, K., Murakami, S., Oikawa, S., and Wakamatsu, S. (2000). Wind Tunnel Experiments on How thermal Stratification Affects Flow in and above Urban Street Canyons. *Atmos. Environ.* 34 (10), 1553–1562. doi:10.1016/S1352-2310(99)00410-0

Wang, L., Fan, S., Hu, F., Miao, S., Yang, A., Li, Y., et al. (2020). Vertical Gradient Variations in Radiation Budget and Heat Fluxes in the Urban Boundary Layer: A Comparison Study between Polluted and Clean Air Episodes in Beijing during Winter. *J. Geophys. Res. Atmos.* 125. doi:10.1029/2020JD032478

Wang, Q., Hang, J., Fan, Y., and Li, Y. (2020). Urban Plume Characteristics under Various Wind Speed, Heat Flux, and Stratification Conditions. *Atmos. Environ.* 239 (3), 117774. doi:10.1016/j.atmosenv.2020.117774

Wong, L. P., Alias, H., Aghamohammadi, N., Aghazadeh, S., and Nik Sulaiman, N. M. (2017). Urban Heat Island Experience, Control Measures and Health Impact: A Survey Among Working Community in the City of Kuala Lumpur. *Sustainable Cities Soc.* 35, 660–668. doi:10.1016/j.scs.2017.09.026

Xie, Z., Cui, J. L., Chen, D. G., and Hu, B. K. (2006). The Annual, Seasonal and Monthly Characteristics of Diurnal Variation of Urban Heat Island Intensity in Beijing. *Clim. Environ. Res.* 11 (1), 69–75. (in Chinese).

Xu, W., Li, Q., Wang, X. L., Yang, S., Cao, L., and Feng, Y. (2013). Homogenization of Chinese Daily Surface Air Temperatures and Analysis of Trends in the Extreme Temperature Indices. *J. Geophys. Res. Atmos.* 118 (17), 9708–9720. doi:10.1002/jgrd.50791

Yang, J., Hu, L., and Wang, C. (2019). Population Dynamics Modify Urban Residents' Exposure to Extreme Temperatures across the United States. *Sci. Adv.* 5 (12), eaay3452. doi:10.1126/sciadv.aay3452

Yang, J., Wang, Z. H., and Kaloush, K. E. (2016). Effect of Pavement thermal Properties on Mitigating Urban Heat Islands: A Multi-Scale Modeling Case Study in Phoenix. *Building Environ.* 108 (11), 110–121. doi:10.1016/j.buildenv.2016.08.021

Yang, P., Ren, G., and Liu, W. (2013). Spatial and Temporal Characteristics of Beijing Urban Heat Island Intensity. *J. Appl. Meteorol. Climatol.* 52 (8), 1803–1816. doi:10.1175/JAMC-D-12-0125.1

Yang, X., Leung, L. R., Zhao, N., Zhao, C., Qian, Y., Hu, K., et al. (2017). Contribution of Urbanization to the Increase of Extreme Heat Events in an Urban Agglomeration in east China. *Geophys. Res. Lett.* 44 (13), 6940–6950. doi:10.1002/2017gl074084

Yang, Y., Fan, S., Wang, L., Gao, Z., Zhang, Y., Zou, H., et al. (2020a). Diurnal Evolution of the Wintertime Boundary Layer in Urban Beijing, China: Insights from Doppler Lidar and a 325-m Meteorological Tower. *Remote Sensing* 12, 3935. doi:10.3390/rs12233935

Yang, Y., Zheng, Z., Yim, S. Y. L., Roth, M., Ren, G., Gao, Z., et al. (2020b). PM 2.5 Pollution Modulates Wintertime Urban Heat Island Intensity in the Beijing-Tianjin-Hebei Megalopolis, China. *Geophys. Res. Lett.* 47 (1), 1–12. doi:10.1029/2019GL084288

Yao, J., Sun, X., Tang, J., Ji, Y., Xu, Y., and Yang, X.-Q. (2020). Summer Regional Pentad Heat Wave in Eastern China and Their Possible Causes. *Front. Earth Sci.* 8 (11), 511. doi:10.3389/feart.2020.598027

Zhao, L., Lee, X., Smith, R. B., and Oleson, K. (2014). Strong Contributions of Local Background Climate to Urban Heat Islands. *Nature* 511 (7508), 216–219. doi:10.1038/nature13462

Zheng, Z., Ren, G., Wang, H., Dou, J., Gao, Z., Duan, C., et al. (2018). Relationship between Fine-Particle Pollution and the Urban Heat Island in Beijing, China: Observational Evidence. *Boundary-layer Meteorol.* 169 (1), 93–113. doi:10.1007/s10546-018-0362-6

Zheng, Z., Zhao, C., Lolli, S., Wang, X., Wang, Y., Ma, X., et al. (2020). Diurnal Variation of Summer Precipitation Modulated by Air Pollution: Observational Evidences in the Beijing Metropolitan Area. *Environ. Res. Lett.* 15, 094053. doi:10.1088/1748-9326/ab99fc

Zhou, W., Shen, X., Cao, F., and Sun, Y. (2019). Effects of Area and Shape of Greenspace on Urban Cooling in Nanjing, China. *J. Urban Plan. Dev.* 145 (4), 04019016. doi:10.1061/(asce)up.1943-5444.0000520

Zinzi, M., Agnoli, S., Burattini, C., and Mattoni, B. (2020). On the thermal Response of Buildings under the Synergic Effect of Heat Waves and Urban Heat Island. *Solar Energy* 211 (10), 1270–1282. doi:10.1016/j.solener.2020.10.050

Conflict of Interest: The authors declare that the research was conducted in the absence of any commercial or financial relationships that could be construed as a potential conflict of interest.

frontiers
in Earth Science

ORIGINAL RESEARCH
published: 16 June 2021
doi: 10.3389/feart.2021.636777

Increasing Compound Heat and Precipitation Extremes Elevated by Urbanization in South China

Sijia Wu[1], Ting On Chan[1], Wei Zhang[2], Guicai Ning[3], Peng Wang[1], Xuelin Tong[1], Feng Xu[1], Hao Tian[1], Yu Han[1], Yongquan Zhao[4]* and Ming Luo[1,3]*

[1]School of Geography and Planning, and Guangdong Key Laboratory for Urbanization and Geo-simulation, Sun Yat-sen University, Guangzhou, China, [2]IIHR-Hydroscience and Engineering, The University of Iowa, Iowa City, IA, United States, [3]Institute of Environment, Energy and Sustainability, The Chinese University of Hong Kong, Sha Tin, China, [4]Department of Geography, The Ohio State University, Columbus, OH, United States

Compared with individual events, compound weather and climate extremes may impose more serious influences on natural systems and human society, especially in populated areas. In this study, we examine the changes in the compound precipitation events that follow extremely hot weather within several days during 1961–2017 in South China by taking the Guangdong Province as an example. Additionally, we assess the impacts of urbanization on these changes. It is found that extreme precipitation events in Guangdong are often preceded by hot weather, with an average fraction of 28.25%. The fraction of such compound events is even larger in more populated and urbanized areas such as the Pearl River Delta (PRD) region. Moreover, our results reveal significant increases in the frequency and fraction of the compound extreme heat and precipitation events. These increases are especially stronger in more developed areas (e.g., PRD), and their increasing trends tend to accelerate in recent decades. Furthermore, the local urbanization contributes to 40.91 and 49.38% of the increases in the frequency and fraction of the compound events, respectively. Our findings provide scientific references for policy-makers and urban planners to mitigate the influences of the compound heat and precipitation extremes by considering their increasing risks under the context of global climate change and local urbanization.

Keywords: compound events, extreme precipitation, heatwave, urbanization effects, long-term trend, climate change, South China

Edited by:
Tomas Halenka,
Charles University, Czechia

Reviewed by:
Xuchao Yang,
Zhejiang University, China
Xuezhi Tan,
Sun Yat-Sen University, China

****Correspondence:***
Yongquan Zhao
yqzhao@link.cuhk.edu.hk
Ming Luo
luo.ming@hotmail.com

Specialty section:
This article was submitted to Interdisciplinary Climate Studies, a section of the journal Frontiers in Earth Science

Received: *02 December 2020*
Accepted: *31 May 2021*
Published: *16 June 2021*

Citation:
Wu S, Chan TO, Zhang W, Ning G, Wang P, Tong X, Xu F, Tian H, Han Y, Zhao Y and Luo M (2021) Increasing Compound Heat and Precipitation Extremes Elevated by Urbanization in South China.
Front. Earth Sci. 9:636777.
doi: 10.3389/feart.2021.636777

INTRODUCTION

Global warming increases the occurrence probability of climate extremes in worldwide ranges, and these climate events seriously impact human communities and the natural environment (IPCC, 2014; World Economic Forum, 2019). For example, heatwaves and heavy precipitation are more harmful to human health (Matthies and Menne, 2009; Lin et al., 2015), agriculture (Wreford and Adger, 2010; Sun et al., 2014), economy (Kjellstrom, 2015; Zhang et al., 2017b), and public infrastructure (McEvoy et al., 2012). For instance, heatwaves increased the death rate by 2,300 folds (136,000 deaths) from 2001 to 2010, compared with the last decade of the 20th century (World Meteorological Organization, 2013). Additionally, precipitation extremes resulted in the devastating floods in the Yangtze River of China in 1998, which caused thousands of deaths and missing country-wide (Orsolini et al., 2015). Furthermore, these resultant influences of climate extremes have been proved to be exacerbated due to global warming (Liu et al., 2020a; Perkins-Kirkpatrick and Lewis, 2020).

Extreme climate and weather events often occur simultaneously or sequentially within a short period of time, known as compound events (Leonard et al., 2014). As a combination of two or more extremes (e.g., preconditioned heat and subsequent extreme precipitation), compound events often result in larger impacts than individual events (Zscheischler et al., 2018; Weber et al., 2020). Moreover, the hazards resulting from interacted climate extremes may further intensify the magnitude and severity of the risks caused by individual events (Leonard et al., 2014; Alizadeh et al., 2020). For instance, the compound high-temperature and severe precipitation events have vital effects on plants during the growing season (Madden and Williams, 1978). A compound event with low temperatures, strong wind, and following extreme precipitation in Queensland of Australia caused the deaths of half a million cattle (Cowan et al., 2019). While most existing studies paid much attention to individual events, few focused on compound events with magnified impacts compared to the individual events (Weber et al., 2020).

In addition to global warming, local urbanization significantly affects changes in regional weather and climate extremes. During the urbanization process, land use/land cover (LULC) changes such as the transformation from vegetation to impervious surfaces accelerate the variations in surface temperature and increase the frequency and duration of severe precipitation events (Pielke Sr et al., 2011; Sun et al., 2019; Lin et al., 2020). Furthermore, LULC changes affect the original energy balance generating a prominent phenomenon, i.e., urban heat island (UHI), making urban areas warmer than surrounding rural areas (Oke, 1982; Zhou et al., 2004; Jones et al., 2008; Luo and Lau, 2018). Urbanization and the associated UHI can deteriorate extreme heat and heavy precipitation events under a warming climate (Stone, 2012; Oleson et al., 2015; Yu and Liu, 2015; Zhang et al., 2018). For instance, Luo and Lau (2018) estimated that urbanization accounted for nearly 30% of the increases in average extreme heat stress in the urban areas of eastern China. The rising numbers of heatwaves may increase mortality in urban regions (Li et al., 2013; Mishra et al., 2015). Liang and Ding (2017) found that urbanization is conducive to enhance the frequency and intensity of heavy precipitation events on urban stations, thus further increasing the total precipitation. Although previous studies have linked increasing extreme events to urbanization and its associated UHI effects (Yang et al., 2017a; Luo and Lau, 2017), the possible physical mechanisms underlying these linkages have not been revealed and warrant further investigations.

China has been experiencing rapid urbanization since the 1970s, and its urban population proportion increased from 18.4 to 58.52% during 1961–2017 (National Bureau of Statistics of China, 2018). Under global climate change and rapid region urbanization in China, the characteristics in terms of frequency, duration, and intensity of extreme weather and climate events have been drastically intensified in most parts of China (Ren and Zhou, 2014; Yang et al., 2017b; Sun et al., 2019). For example, Ren and Zhou (2014) estimated that urbanization contributed to 37.8% for tropical nights and 12.8% for summer days in China during 1961–2008. In particular, Yang et al. (2017b) suggested that urbanization accounts for more than one-third of the increase of the intensity of heat extremes in East China, and urbanization tends to have stronger effects on cold and warm nights than the daytime extremes in this region (Sun et al., 2019). These effects are especially stronger in urbanized and populated areas, such as the Beijing-Tianjin-Hebei (BTH), the Yangtze River Delta (YRD), and the Pearl River Delta (PRD) region (Zhang et al., 2017a; Peng et al., 2017). As one of the most populated and urbanized areas, South China suffers from the impacts brought by both frequent extreme hot weather and intense precipitation events (Wang et al., 2019), which pose remarkable impacts on public health in this area. Nevertheless, the temporal and spatial changes in compound heat and extreme precipitation in South China, along with the possible effects of urbanization on these changes have not been reported in the literature.

In this study, therefore, we investigate the changes in sequentially compound precipitation events with preconditioned hot weather in South China, and evaluate the contribution of local urbanization to these changes. The remainder of this paper is structured as follows. Section *Materials and Methods* introduces the study area, data, and methods. The examinations of the changes of compound events and urbanization effects are presented in Section *Results*. Section *Conclusion and Discussions* summarizes the main findings of this study.

MATERIALS AND METHODS

Study Area

In this research, we examine the changes in compound extreme heat and precipitation events in South China, by taking Guangdong Province as an example since it possesses the densest population and is the most urbanized province in South China. It is characterized by a subtropical monsoon climate with hot-humid summer and cool-dry winter. Guangdong has experienced rapid urbanization and industrialization since the commence of China's economic reform and opening-up policy (Xiong et al., 2012). Among all provincial units of China, Guangdong has been holding the largest Gross Domestic Product (GDP) since 1989. Its urbanization level reached 69.85% in 2017. Of Guangdong, the PRD region (as denoted by the red boundary in **Figure 1**) exhibits the highest urbanization level of 85.29% and the largest population density (Statistics Bureau of Guangdong Province, 2017). Moreover, this area has been severely suffering from dramatic increases in extreme weather and climate events over the past decades (Chen et al., 2015; Lin et al., 2019).

Data

In this study, the compound extreme heat and precipitation events are derived from daily maximum temperature (T_{max}) and daily precipitation. Observations recorded at 86 meteorological stations in Guangdong from 1961 to 2017 are

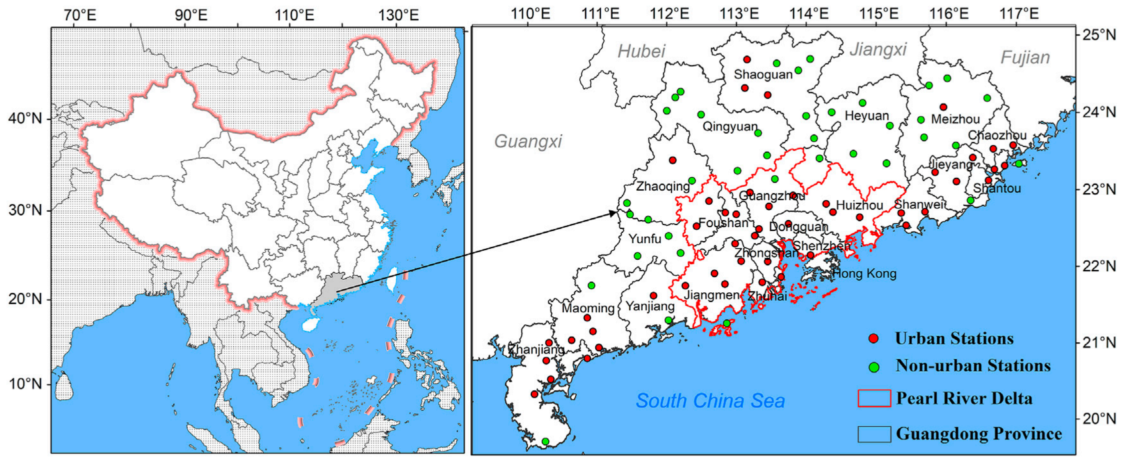

FIGURE 1 | Locations of the meteorological stations in Guangdong Province of South China. Urban and non-urban stations are marked as red and green dots, respectively. PRD is marked by the red boundary.

obtained from the China Meteorological Data Service Center (http://data.cma.cn). The raw data have been homogenized using a statistical approach proposed by Xu et al. (2013). Their temporal inhomogeneity has been evaluated by the Easterling-Peterson method (Li et al., 2004; You et al., 2010). In this study, stations with ≥3 missing days in any month from June to August are excluded.

Definition of Compound Events

Compound events are defined as comprising a combination of two or more different extremes occurring coincidentally or sequentially within a certain period of time (Mueller and Seneviratne, 2012; AghaKouchak et al., 2014; Leonard et al., 2014; Wahl et al., 2015). These extremes are considered contributing to complex interactions of multiple hazards such as widespread wildfires (Witte et al., 2011), large-scale air pollution (Konovalov et al., 2011) to human society/ecosystems (Weber et al., 2020). In this study, compound heat and precipitation extremes are defined for each station individually. An extreme precipitation event is first detected when daily precipitation is larger than the 90th percentile value for all rainy days (≥0.1 mm) in the summers of the reference period of 1961–1990. Then the compound event is counted if the extreme precipitation event is preceded by an extreme heat event within three days. Here, a heat event is defined when daily T_{max} is larger than the 90th percentile of the reference period. To quantify the compound events, we adopt a probabilistic metric by using the fraction of the compound events accounting for all extreme precipitation events in a calendar year.

Statistical Methods

In order to evaluate the possible influences of urbanization on compound events, we classify all meteorological stations into urban and non-urban types, as suggested by previous studies (Mishra et al., 2015; Luo and Lau, 2018; Wang et al., 2019). Stations are tagged as urban type if they are located in urban areas or urban buffers of 25 km that have a population more than 250,000; otherwise, they are classified as non-urban type. The urban area extents are derived from the DeLorme World Base Map dataset (https://www.baruch.cuny.edu/confluence/display/geoportal/ESRI+International+Data), which has been validated by the urban extents extracted from Moderate Resolution Imaging Spectroradiometer (MODIS) satellite data (Mishra et al., 2015).

The urbanization effects are quantified by calculating the differences in the trends between the urban and non-urban series (Ren and Zhou, 2014; Luo and Lau, 2019b). The urban (non-urban) series of the frequency and fraction of compound events are obtained by averaging all urban (non-urban) stations. The secular trend of the series of compound events is estimated by the conventional linear regression, and its significance is evaluated by the modified nonparametric Mann-Kendall (mMK) test. The mMK method considers the autocorrelation in the time series to provide an unbiased evaluation of the trend (Hamed and Rao, 1998). It has been widely used in hydrological and climatological studies (e.g., Luo and Lau (2019a); Sa'adi et al. (2019))

RESULTS

Climatology of Compound Events

Based on the above definition, we search for the compound events at all stations from 1961 to 2017, and obtain the multi-year mean frequency and fraction of these events. As shown in **Figure 2**, compound events with extreme precipitation and hot days have occurred in all parts of Guangdong. On average, 28.25% of extreme precipitation events are preceded by a heat extreme within three days, and the study area experiences 1.26 compound events per year. The frequency and fraction of compound events demonstrate obvious spatial variations across the study area. Specifically, compound events are more prominent in densely populated and highly urbanized areas such as PRD, in which the highest frequency and fraction of compound events are observed. The PRD region has 1.49 compound events per year, and 31.81% of its precipitation

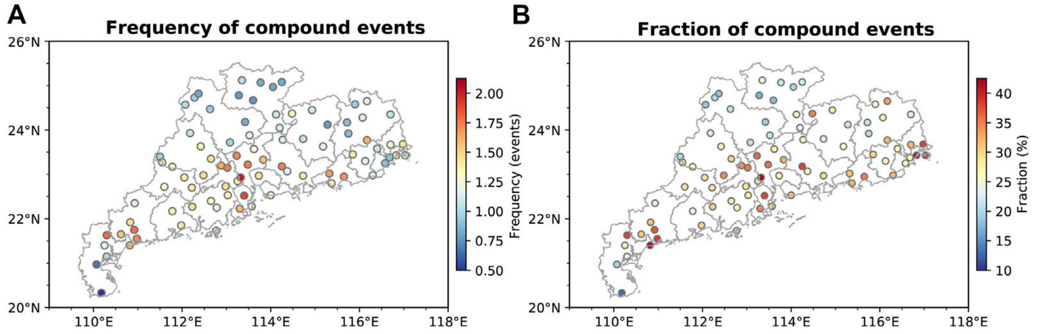

FIGURE 2 | Spatial distribution of mean **(A)** frequency and **(B)** fraction of compound events in Guangdong Province from 1961 to 2017.

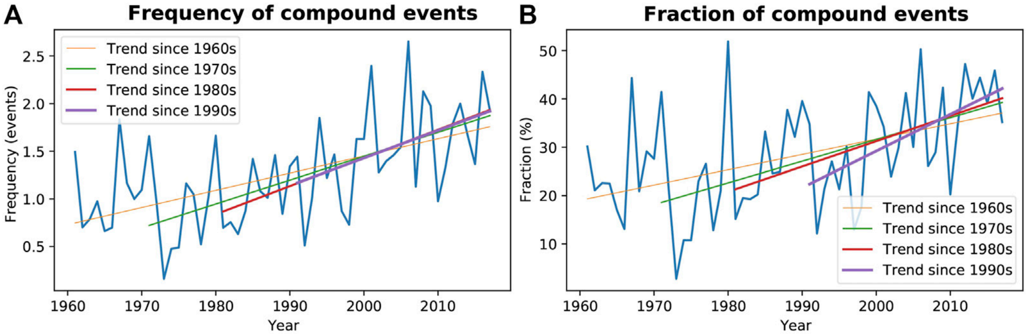

FIGURE 3 | Time series of regional mean **(A)** frequency and **(B)** fraction of compound events in Guangdong Province from 1961 to 2017. Straight lines denote the corresponding linear trends in different subperiods.

extremes occur following a previous extreme heat day within a short period. The larger (smaller) frequency and fraction in more (less) urbanized areas indicate that local urbanization may increase the occurrence of compound events.

Nearly all stations have experienced the compound events (with the frequency of compound events > 0). This result is in accordance with the findings of Hao et al. (2013) that heat and precipitation extremes have co-occurred in the high latitudes and tropical regions. The spatial variations of the compound heat and extreme precipitation events are highly consistent with the distribution of the urban and non-urban stations, i.e., compound events tend to occur more frequently at the urban than non-urban stations.

Spatial and Temporal Changes of Compound Events

To understand the temporal evolution of compound events, we calculate the regional mean frequency and fraction of compound events by averaging all stations (**Figure 3**). Both the frequency and fraction show dramatic increasing trends, i.e., statistically significant at the 0.05 level. The regional mean frequency of compound events has increased by 0.18 events per decade, and the fraction has risen by 3.17% per decade over the study period. It indicates that the probability of extreme precipitation events following a heat event tends to increase.

It is also shown in **Figure 3** that the increasing trends of the compound frequency and fraction tend to be accelerated since the 1960s. The magnitudes of the trends are 0.25 and 4.49% per decade during 1971–2017 for the frequency and fraction of compound events, respectively. These trend magnitudes become larger during 1981–2017, i.e., 0.30 and 5.23%, respectively. The trends remain significant and continue to increase till at least the 1990s, since which the frequency and fraction increased by 0.29 and 7.60%, respectively. These results suggest that the increasing speed of the proportion of extreme precipitation that follows a heat event has elevated.

Figure 4 depicts the spatial distribution of the secular trends of the frequency and fraction of compound events at the individual station during 1961–2017. Compound events exhibit increasing tendencies in measure of frequency (fraction) since the 1960s at nearly all stations, of which 55.81% (56.98%) are significant at the 0.05 level. The upward trends show regional disparities with stronger magnitude in more populated and urbanized areas and weaker in less developed regions. In particular, the PRD region with the densest population and highest urbanization level has the most substantial increasing tendency, whereas other less urbanized areas such as the northern parts of Guangdong possess relatively weaker trends. These features indicate that the residents living in PRD are facing intensifying threats induced by compound heat-precipitation events. More substantial intensification of compound events in faster-

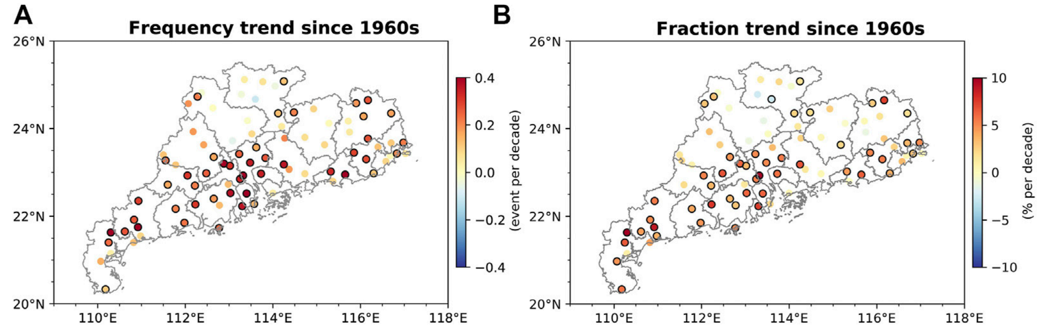

FIGURE 4 | Spatial distribution of the trends in the **(A)** frequency and **(B)** fraction of compound events in Guangdong Province from 1961 to 2017. The black circle indicates significance at the 0.05 level.

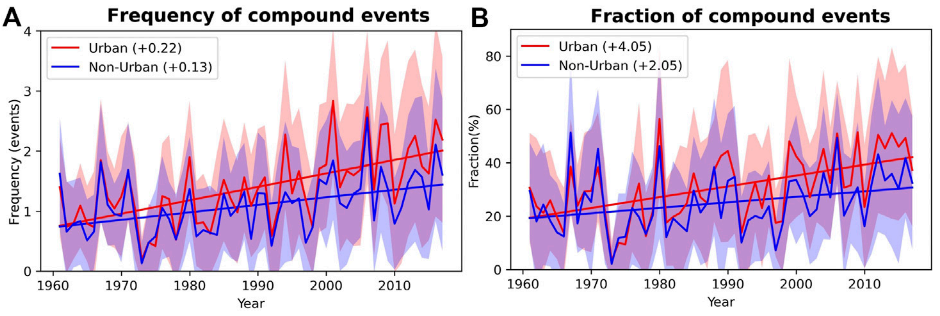

FIGURE 5 | Time series of regional annual mean **(A)** frequency and **(B)** fraction of compound events from 1961 to 2017 for urban (red) and non-urban (blue) stations. The pink (cyan) shading indicates the mean ± standard deviation of frequency and fraction of compound events for urban (rural) stations. The straight lines indicate their corresponding linear trends (unit: event per decade and % per decade for the frequency and fraction, respectively).

urbanized areas implies that the urbanization process possibly plays an important role in accelerating this phenomenon.

The trends of compound heat-precipitation events revealed above are consistent with the findings of Scherrer et al. (2016) in such a way that the increasing trends of hot days and heavy precipitation were found in warmer places. Hao et al. (2013) used the Coupled Model Intercomparison Project phase 5 (CMIP5) climate model to simulate concurrent wet and warm events, and demonstrated that those events increased significantly in high-latitude and tropical regions (Hao et al., 2013). The reason for the increasing trend of compound events in South China is likely that the preconditioned extreme hot weather with higher temperature leads to increased higher evaporation rates and vapor content, thus accelerating the hydrological cycle under the context of global warming (Menzel and Bürger, 2002). Moreover, the preceded heat can enhance the moisture flux and the convective available potential energy (CAPE) and thereby provide a suitable environment for extreme precipitation and flooding in several subsequent days (Zhang and Villarini, 2020). In our study, we also find that the upward trends of frequency and fraction of the compound climate events in South China became even steeper from 1990 to 2017. A possible reason for the acceleration since the 1990s is that the increased Tibetan Plateau snow cover and sea surface temperature in the equatorial Indian Ocean boosted the precipitation in South China (Wu et al., 2010).

Urbanization Effects and Contribution

To quantify the impacts of urbanization on the increases in the frequency and fraction of compound events, all stations are categorized into urban and non-urban types (**Figure 1**), and we calculate the annual mean values for the two types of stations from 1961 to 2017 (see **Figure 5**). Both the urban and non-urban areas exhibit rising trends in terms of the compound frequency and fraction. It is noteworthy that the urban stations (as shown in pink shading) exhibit even steeper trends than those in the non-urban areas (as shown in cyan shading), demonstrating a remarkable contribution of urbanization. The frequency (fraction) of compound events in the urban and non-urban areas increased by 0.22 events (4.05%) and 0.13 events (2.05%) per decade, respectively. The differences in the trend between the urban and non-urban regions are 0.09 events for the compound frequency and 2.00% for the compound fraction. Since possible influences by other impact factors such as global warming and large-scale circulations are comparable at the local scale, the differences between trends for the urban and non-urban regions mainly result from local urbanization. Accordingly, we estimate that urbanization accounts for 40.91% (49.38%) of the total increasing trend in the frequency (fraction) of the compound events in the urban region.

These results indicate that the urbanization process tends to exert intensifying impacts on compound heat-precipitation events. Previous studies such as Chen et al. (2015); Wang et al. (2018) found that the PRD region experienced much stronger precipitation compared to its surrounding rural areas and attributed this difference to urbanization. Other studies have also confirmed that urbanization can affect extreme precipitation by influencing UHI (Oke, 1982; Dixon and Mote, 2003), urban canopy (Miao et al., 2009), and urban aerosols (Han and Baik, 2008). Specifically, UHI effects can be enhanced by the increases in anthropogenic heat release, as suggested in many modeling studies by the Weather Research and Forecasting (WRF) model coupled with the Urban Canopy Model (UCM) (Feng et al., 2012; Chen et al., 2014; Yang et al., 2019). The urban development enhances the total thermal discomfort hours by 27% in the urban core areas of YRD, and anthropogenic heat release and urban land use change contribute nearly equally to this change (Yang et al., 2019). Warmer temperature in urban areas enhances the disturbance above the ground and strengthens the upward motion and convective activities (Collier, 2006). Moreover, urban canopy disturbs the water vapor and energy balance in urban boundary layers and impacts heavy convective precipitation by increasing the surface roughness, which reduces surface wind, bifurcates the approaching moist air mass upward, and then aggregates them in the downwind of urban areas (Cotton and Pielke, 2007; Zhang et al., 2014). Additionally, extreme precipitation is contributed by the interactions of urban aerosols with radiation and clouds (Liu et al., 2020b). Urban aerosols absorb and scatter solar radiation to generate condensation nuclei, which can influence deep convection and hence precipitation (Li et al., 2011; Liu et al., 2020b). Consequently, via these processes, the local urbanization provides favorable conditions for extreme compound heat and precipitation events.

CONCLUSION AND DISCUSSIONS

In this study, we investigate the changes in sequentially compound extreme heat and precipitation events during 1961–2017 in South China and quantify the contribution of urbanization to the long-term changes of this type of extreme weather for the first time. Our results indicate that extreme precipitation events in South China are often preceded by hot weather within three days, and demonstrate that the local urbanization exerts significant impacts on this compound extremes event.

The compound heat and precipitation extremes occur frequently in South China and they are more frequent in more populated and urbanized regions such as PRD. The increases in the frequency and fraction of the compound events are observed almost everywhere in Guangdong, especially in the PRD region. Similarly, Zhang and Villarini (2020) found that compound heat stress and flooding extremes in the central United States become more frequent, and these increasing compound events may lead to greater societal and economic impacts. In our research, we demonstrate that the increasing trends of compound heat and precipitation extremes in China also tend to accelerate in recent decades. This result is also consistent with the study by Scherrer et al. (2016), who found increasing trends in hot temperature and heavy precipitation extremes in Switzerland, while the upward trends of compound heat-precipitation events have not been linked to human activities such as urbanization. These studies collectively suggest that compound heat-precipitation events have increased in many parts of the world, posing increasing threats to human society and the natural environments. A better understanding of such events is urgently warranted and thus of great significance to improve the forecast, prediction and mitigation of the compound weather and climate disasters.

Previous studies have shown that urban expansion plays an important role in extreme precipitation, and urbanization contributes to nearly 50% of the increase in the heatwave frequency in the PRD region of South China (Luo and Lau, 2017; Wang et al., 2018). However, these studies only considered individual extreme events, without examining the extreme events that occur simultaneously or sequentially within a short period of time. Our present study provides the first examination of the changes in compound heat-precipitation events in South China and quantifies the urbanization effects on these changes by classifying the stations into urban and non-urban ones. Chen et al. (2021) has studied another type of compound event, i.e., sequential flood-heatwave events across China, and found that anthropogenic forcings contributed greatly to these compound extremes. Nevertheless, to what degree local urbanization influences the compound events has not been evaluated and needs to be further investigated.

In this study, we estimate that the contributions of urbanization to the increases in the frequency and fraction of compound heat-precipitation events are 40.91% and 49.38%, respectively. It is noteworthy that the frequency and fraction of compound event in urban areas increase more steeply than in non-urban areas. Our results demonstrate a prominent urbanization contribution by local human activities to these compound events. Local urbanization contributes to nearly half of the increases in the frequency and fraction of compound events. It is thus suggested that future mitigations to climate change and disasters should take more consideration of urban planning and the increasing threats by compound weather and climate extremes.

Additionally, previous observational and modeling studies revealed various mechanisms underlying the urbanization effects on regional or local climate change, such as UHI (Dixon and Mote, 2003; Chen et al., 2014), urban canopy (Miao et al., 2009; Chen et al., 2011), and urban aerosol effects (Han and Baik, 2008; Jin et al., 2010). Many studies have used WRF model simulations to qualify the urbanization effects on climate (Feng et al., 2012; Yang et al., 2014; Zhang et al., 2018; Yang et al., 2019). This modeling approach may broaden our understanding of the mechanisms of compound events and the urbanization effects. In our future work, we shall use climate modeling to conduct a deeper investigation of the processes associated with the compound heat-precipitation events and reveal the mechanisms underlying the urbanization effects on these events. It is also of great interest to examine how these compound event will change in the future under different scenarios of emission and socio-economic development, i.e., via analyzing the projections of phase six of the Coupled Model Intercomparison Project (CMIP6). Moreover, as it remains unclear how compound heat-precipitation events changed in other climate regimes beyond South China, compound extremes in other urbanized and populated areas of China such as YRD and BTH also warrant investigations.

DATA AVAILABILITY STATEMENT

The original contributions presented in the study are included in the article/Supplementary Material, further inquiries can be directed to the corresponding authors.

AUTHOR CONTRIBUTIONS

YZ and ML design the research. SW and ML conduct the analysis. All authors discuss the results and edit and review the manuscript.

FUNDING

This study was supported by the National Key R&D Program of China (2019YFC1510400) and National Natural Science Foundation of China (41871029). The appointment of ML at Sun Yat-sen University is partially supported by the Pearl River Talent Recruitment Program of Guangdong Province, China (2017GC010634).

REFERENCES

AghaKouchak, A., Cheng, L., Mazdiyasni, O., and Farahmand, A. (2014). Global Warming and Changes in Risk of Concurrent Climate Extremes: Insights from the 2014 California Drought. *Geophys. Res. Lett.* 41 (24), 8847–8852. doi:10.1002/2014GL062308

Alizadeh, M. R., Adamowski, J., Nikoo, M. R., AghaKouchak, A., Dennison, P., and Sadegh, M. (2020). A century of Observations Reveals Increasing Likelihood of continental-scale Compound Dry-Hot Extremes. *Sci. Adv.* 6 (39), eaaz4571. doi:10.1126/sciadv.aaz4571

Chen, F., Kusaka, H., Bornstein, R., Ching, J., Grimmond, C. S. B., Grossman-Clarke, S., et al. (2011). The Integrated WRF/urban Modelling System: Development, Evaluation, and Applications to Urban Environmental Problems. *Int. J. Climatol.* 31 (2), 273–288. doi:10.1002/joc.2158

Chen, F., Yang, X., and Zhu, W. (2014). WRF Simulations of Urban Heat Island under Hot-Weather Synoptic Conditions: the Case Study of Hangzhou City, China. *Atmos. Res.* 138 (1), 364–377. doi:10.1016/j.atmosres.2013.12.005

Chen, S., Li, W.-B., Du, Y.-D., Mao, C.-Y., and Zhang, L. (2015). Urbanization Effect on Precipitation over the Pearl River Delta Based on CMORPH Data. *Adv. Clim. Change Res.* 6 (1), 16–22. doi:10.1016/j.accre.2015.08.002

Chen, Y., Liao, Z., Shi, Y., Tian, Y., and Zhai, P. (2021). Detectable Increases in Sequential Flood-Heatwave Events across China during 1961-2018. *Geophys. Res. Lett.* 48 (6), e2021GL092549. doi:10.1029/2021GL092549

Collier, C. G. (2006). The Impact of Urban Areas on Weather. *Q. J. R. Meteorol. Soc.* 132 (614), 1–25. doi:10.1256/qj.05.199

Cotton, W. R., and Pielke, R. A. S. (2007). *Human Impacts on Weather and Climate*. Cambridge: Cambridge University Press. doi:10.1017/CBO9780511808319

Cowan, T., Wheeler, M. C., Alves, O., Narsey, S., de Burgh-Day, C., Griffiths, M., et al. (2019). Forecasting the Extreme Rainfall, Low Temperatures, and strong Winds Associated with the Northern Queensland Floods of February 2019. *Weather Clim. Extremes* 26, 100232. doi:10.1016/j.wace.2019.100232

Dixon, P. G., and Mote, T. L. (2003). Patterns and Causes of Atlanta's Urban Heat Island–Initiated Precipitation. *J. Appl. Meteorology* 42 (9), 1273–1284. doi:10.1175/1520-0450(2003)042<1273:PACOAU>2.0.CO;2

Feng, J.-M., Wang, Y.-L., Ma, Z.-G., and Liu, Y.-H. (2012). Simulating the Regional Impacts of Urbanization and Anthropogenic Heat Release on Climate across China. *J. Clim.* 25 (20), 7187–7203. doi:10.1175/JCLI-D-11-00333.1

Hamed, K. H., and Ramachandra Rao, A. (1998). A Modified Mann-Kendall Trend Test for Autocorrelated Data. *J. Hydrol.* 204 (1), 182–196. doi:10.1016/S0022-1694(97)00125-X

Han, J.-Y., and Baik, J.-J. (2008). A Theoretical and Numerical Study of Urban Heat Island-Induced Circulation and Convection. *J. Atmos. Sci.* 65 (6), 1859–1877. doi:10.1175/2007JAS2326.1

Hao, Z., AghaKouchak, A., and Phillips, T. J. (2013). Changes in Concurrent Monthly Precipitation and Temperature Extremes. *Environ. Res. Lett.* 8 (3), 034014. doi:10.1088/1748-9326/8/3/034014

IPCC (2014). *Climate Change 2014: Impacts, Adaptation, and Vulnerability. Part A: Global and Sectoral Aspects. Contribution of Working Group II to the Fifth Assessment Report of the Intergovernmental Panel on Climate Change*. Cambridge, UK and New York, USA: Cambridge University Press.

Jin, M., Shepherd, J. M., and Zheng, W. (2010). Urban Surface Temperature Reduction via the Urban Aerosol Direct Effect: a Remote Sensing and WRF Model Sensitivity Study. *Adv. Meteorology* 2010 (2), 1–14. doi:10.1155/2010/681587

Jones, P. D., Lister, D. H., and Li, Q. (2008). Urbanization Effects in Large-Scale Temperature Records, with an Emphasis on China. *J. Geophys. Res.* 113 (D16), D16122. doi:10.1029/2008JD009916

Kjellstrom, T. (2015). Impact of Climate Conditions on Occupational Health and Related Economic Losses. *Asia Pac. J. Public Health* 28 (2_Suppl. l), 28S–37S. doi:10.1177/1010539514568711

Konovalov, I. B., Beekmann, M., Kuznetsova, I. N., Yurova, A., and Zvyagintsev, A. M. (2011). Atmospheric Impacts of the 2010 Russian Wildfires: Integrating Modelling and Measurements of the Extreme Air Pollution Episode in the Moscow Megacity Region. *Atmos. Chem. Phys. Discuss.* 11 (4), 12141–12205. doi:10.5194/acpd-11-12141-2011

Leonard, M., Westra, S., Phatak, A., Lambert, M., van den Hurk, B., McInnes, K., et al. (2014). A Compound Event Framework for Understanding Extreme Impacts. *Wires Clim. Change* 5 (1), 113–128. doi:10.1002/wcc.252

Li, Q., Liu, X., Zhang, H., Thomas C., P., and David R., E. (2004). Detecting and Adjusting Temporal Inhomogeneity in Chinese Mean Surface Air Temperature Data. *Adv. Atmos. Sci.* 21 (2), 260–268. doi:10.1007/BF02915712

Li, T., Horton, R. M., and Kinney, P. L. (2013). Projections of Seasonal Patterns in Temperature- Related Deaths for Manhattan, New York. *Nat. Clim Change* 3 (8), 717–721. doi:10.1038/nclimate1902

Li, Z., Niu, F., Fan, J., Liu, Y., Rosenfeld, D., and Ding, Y. (2011). Long-term Impacts of Aerosols on the Vertical Development of Clouds and Precipitation. *Nat. Geosci*. 4 (12), 888–894. doi:10.1038/ngeo1313

Liang, P., and Ding, Y. (2017). The Long-Term Variation of Extreme Heavy Precipitation and its Link to Urbanization Effects in Shanghai during 1916-2014. *Adv. Atmos. Sci.* 34 (3), 321–334. doi:10.1007/s00376-016-6120-0

Lin, L., Gao, T., Luo, M., Ge, E., Yang, Y., Liu, Z., et al. (2020). Contribution of Urbanization to the Changes in Extreme Climate Events in Urban Agglomerations across China. *Sci. Total Environ.* 744, 140264. doi:10.1016/j.scitotenv.2020.140264

Lin, L., Luo, M., Chan, T. O., Ge, E., Liu, X., Zhao, Y., et al. (2019). Effects of Urbanization on winter Wind Chill Conditions over China. *Sci. Total Environ.* 688, 389–397. doi:10.1016/j.scitotenv.2019.06.145

Lin, Y., Zhao, M., and Zhang, M. (2015). Tropical Cyclone Rainfall Area Controlled by Relative Sea Surface Temperature. *Nat. Commun.* 6 (1), 6591. doi:10.1038/ncomms7591

Liu, B., Tan, X., Gan, T. Y., Chen, X., Lin, K., Lu, M., et al. (2020a). Global Atmospheric Moisture Transport Associated with Precipitation Extremes: Mechanisms and Climate Change Impacts. *WIREs Water* 7 (2), e1412. doi:10.1002/wat2.1412

Liu, Z., Ming, Y., Zhao, C., Lau, N. C., Guo, J., Bollasina, M., et al. (2020b). Contribution of Local and Remote Anthropogenic Aerosols to a Record-Breaking Torrential Rainfall Event in Guangdong Province, China. *Atmos. Chem. Phys.* 20 (1), 223–241. doi:10.5194/acp-20-223-2020

Luo, M., and Lau, N.-C. (2019a). Characteristics of Summer Heat Stress in China during 1979–2014: Climatology and Long-Term Trends. *Clim. Dyn.* 53 (9-10), 5375–5388. doi:10.1007/s00382-019-04871-5

Luo, M., and Lau, N.-C. (2017). Heat Waves in Southern China: Synoptic Behavior, Long-Term Change, and Urbanization Effects. *J. Clim.* 30 (2), 703–720. doi:10.1175/JCLI-D-16-0269.1

Luo, M., and Lau, N. C. (2018). Increasing Heat Stress in Urban Areas of Eastern China: Acceleration by Urbanization. *Geophys. Res. Lett.* 45 (23), 13060–13069. doi:10.1029/2018GL080306

Luo, M., and Lau, N. C. (2019b). Urban Expansion and Drying Climate in an Urban Agglomeration of east China. *Geophys. Res. Lett.* 46 (12), 6868–6877. doi:10.1029/2019GL082736

Madden, R. A., and Williams, J. (1978). The Correlation between Temperature and Precipitation in the United States and Europe. *Monthly Weather Rev.* 106 (1), 142–147. doi:10.1175/1520-0493(1978)106<0142:TCBTAP>2.0.CO;2

Matthies, F., and Menne, B. (2009). Prevention and Management of Health Hazards Related to Heatwaves. *Int. J. Circumpolar Health* 68 (1), 8–12. doi:10.3402/ijch.v68i1.18293

McEvoy, D., Ahmed, I., and Mullett, J. (2012). The Impact of the 2009 Heat Wave on Melbourne's Critical Infrastructure. *Local Environ.* 17 (8), 783–796. doi:10.1080/13549839.2012.678320

Menzel, L., and Bürger, G. (2002). Climate Change Scenarios and Runoff Response in the Mulde Catchment (Southern Elbe, Germany). *J. Hydrol.* 267 (1-2), 53–64. doi:10.1016/S0022-1694(02)00139-7

Miao, S., Chen, F., Lemone, M. A., Tewari, M., Li, Q., and Wang, Y. (2009). An Observational and Modeling Study of Characteristics of Urban Heat Island and Boundary Layer Structures in Beijing. *J. Appl. Meteorology Climatology* 48 (3), 484–501. doi:10.1175/2008JAMC1909.1

Mishra, V., Ganguly, A. R., Nijssen, B., and Lettenmaier, D. P. (2015). Changes in Observed Climate Extremes in Global Urban Areas. *Environ. Res. Lett.* 10 (2), 024005. doi:10.1088/1748-9326/10/2/024005

Mueller, B., and Seneviratne, S. I. (2012). Hot Days Induced by Precipitation Deficits at the Global Scale. *Proc. Natl. Acad. Sci.* 109 (31), 12398–12403. doi:10.1073/pnas.1204330109

National Bureau of Statistics of China (2018). *China Statistical Yearbook 2017*. Beijing: China Statistics Press.

Oke, T. (1982). The Energetic Basic of the Urban Heat Island. *Q. J. R. Meteorol. Soc.* 108 (455), 1–24. doi:10.1002/qj.4971084550210.1256/smsqj.45501

Oleson, K. W., Monaghan, A., Wilhelmi, O., Barlage, M., Brunsell, N., Feddema, J., et al. (2015). Interactions between Urbanization, Heat Stress, and Climate Change. *Climatic Change* 129 (3), 525–541. doi:10.1007/s10584-013-0936-8

World Meteorological Organization (2013). "The Global Climate 2001-2010: a Decade of Climate Extremes," Editor W. M. Organization, Geneva Switzerland: World Meteorological Organization.

Orsolini, Y. J., Zhang, L., Peters, D. H. W., Fraedrich, K., Zhu, X., Schneidereit, A., et al. (2015). Extreme Precipitation Events over north China in August 2010 and Their Link to Eastward-propagating Wave-trains across Eurasia: Observations and Monthly Forecasting. *Q.J.R. Meteorol. Soc.* 141 (693), 3097–3105. doi:10.1002/qj.2594

Peng, X., She, Q., Long, L., Liu, M., Xu, Q., Zhang, J., et al. (2017). Long-term Trend in Ground-Based Air Temperature and its Responses to Atmospheric Circulation and Anthropogenic Activity in the Yangtze River Delta, China. *Atmos. Res.* 195, 20–30. doi:10.1016/j.atmosres.2017.05.013

Perkins-Kirkpatrick, S. E., and Lewis, S. C. (2020). Increasing Trends in Regional Heatwaves. *Nat. Commun.* 11 (1), 3357. doi:10.1038/s41467-020-16970-7

Pielke, R. A., Pitman, A., Niyogi, D., Mahmood, R., McAlpine, C., Hossain, F., et al. (2011). Land Use/land Cover Changes and Climate: Modeling Analysis and Observational Evidence. *Wires Clim. Change* 2 (6), 828–850. doi:10.1002/wcc.144

Ren, G., and Zhou, Y. (2014). Urbanization Effect on Trends of Extreme Temperature Indices of National Stations over mainland China, 1961-2008. *J. Clim.* 27 (6), 2340–2360. doi:10.1175/JCLI-D-13-00393.1

Sa'adi, Z., Shahid, S., Ismail, T., Chung, E.-S., and Wang, X. (2019). Trends Analysis of Rainfall and Rainfall Extremes in Sarawak, Malaysia Using Modified Mann–Kendall Test. *Meteorology Atmos. Phys.* 131 (3), 263–277. doi:10.1007/s00703-017-0564-3

Scherrer, S. C., Fischer, E. M., Posselt, R., Liniger, M. A., Croci-Maspoli, M., and Knutti, R. (2016). Emerging Trends in Heavy Precipitation and Hot Temperature Extremes in Switzerland. *J. Geophys. Res. Atmos.* 121 (6), 2626–2637. doi:10.1002/2015JD024634

Statistics Bureau of Guangdong Province (2017). *Guangdong Statistical Yearbook*. Beijing, China: China Statistics Press.

Stone, B. (2012). *The City and the Coming Climate: Climate Change in the Places We liveCivil Engineering*. New York City: Cambridge University Press. doi:10.1017/cbo9781139061353

Sun, Y., Hu, T., Zhang, X., Li, C., Lu, C., Ren, G., et al. (2019). Contribution of Global Warming and Urbanization to Changes in Temperature Extremes in Eastern China. *Geophys. Res. Lett.* 46 (20), 11426–11434. doi:10.1029/2019GL084281

Sun, Y., Zhang, X., Zwiers, F. W., Song, L., Wan, H., Hu, T., et al. (2014). Rapid Increase in the Risk of Extreme Summer Heat in Eastern China. *Nat. Clim Change* 4 (12), 1082–1085. doi:10.1038/nclimate2410

Wahl, T., Jain, S., Bender, J., Meyers, S. D., and Luther, M. E. (2015). Increasing Risk of Compound Flooding from Storm Surge and Rainfall for Major US Cities. *Nat. Clim Change* 5 (12), 1093–1097. doi:10.1038/nclimate2736

Wang, D., Wang, D., Qi, X., Liu, L., and Wang, X. (2018). Use of High-Resolution Precipitation Observations in Quantifying the Effect of Urban Extent on Precipitation Characteristics for Different Climate Conditions over the Pearl River Delta, China. *Atmos. Sci. Lett.* 19 (6), e820. doi:10.1002/asl.820

Wang, Y., Chen, L., Song, Z., Huang, Z., Ge, E., Lin, L., et al. (2019). Human-perceived Temperature Changes over South China: Long-Term Trends and Urbanization Effects. *Atmos. Res.* 215, 116–127. doi:10.1016/j.atmosres.2018.09.006

Weber, T., Bowyer, P., Rechid, D., Pfeifer, S., Raffaele, F., Remedio, A. R., et al. (2020). Analysis of Compound Climate Extremes and Exposed Population in Africa under Two Different Emission Scenarios. *Earth's Future* 8 (9), e2019EF001473. doi:10.1029/2019ef001473

Witte, J. C., Douglass, A. R., Da Silva, A., Torres, O., Levy, R. C., and Duncan, B. N. (2011). NASA A-Train and Terra Observations of the 2010 Russian Wildfires. *Atmos. Chem. Phys. Discuss.* 11 (17), 19113–19142. doi:10.5194/acpd-11-19113-2011

World Economic Forum (2019). *The Global Risks Report 2019. 14th Edition*, Geneva Switzerland: World Economic Forum.

Wreford, A., and Adger, W. N. (2010). Adaptation in Agriculture: Historic Effects of Heat Waves and Droughts on UK Agriculture. *Int. J. Agric. Sustainability* 8 (4), 278–289. doi:10.3763/ijas.2010.0482

Wu, R., Wen, Z., Yang, S., and Li, Y. (2010). An Interdecadal Change in Southern China Summer Rainfall Around 1992/93. *J. Clim.* 23 (9), 2389–2403. doi:10.1175/2009JCLI3336.1

Xiong, Y., Huang, S., Chen, F., Ye, H., Wang, C., and Zhu, C. (2012). The Impacts of Rapid Urbanization on the thermal Environment: a Remote Sensing Study of Guangzhou, South China. *Remote Sensing* 4 (7), 2033–2056. doi:10.3390/rs4072033

Xu, W., Li, Q., Wang, X. L., Yang, S., Cao, L., and Feng, Y. (2013). Homogenization of Chinese Daily Surface Air Temperatures and Analysis of Trends in the Extreme Temperature Indices. *J. Geophys. Res. Atmos.* 118 (17), 9708–9720. doi:10.1002/jgrd.50791

Yang, B., Yang, X., Leung, L. R., Zhong, S., Qian, Y., Zhao, C., et al. (2019). Modeling the Impacts of Urbanization on Summer thermal comfort: the Role of Urban Land Use and Anthropogenic Heat. *J. Geophys. Res. Atmos.* 124 (13), 6681–6697. doi:10.1029/2018JD029829

Yang, L., Smith, J. A., Baeck, M. L., Bou-Zeid, E., Jessup, S. M., Tian, F., et al. (2014). Impact of Urbanization on Heavy Convective Precipitation under Strong Large-Scale Forcing: A Case Study over the Milwaukee-Lake Michigan Region. *J. Hydrometeorology* 15 (1), 261–278. doi:10.1175/JHM-D-13-020.1

Yang, P., Ren, G., and Yan, P. (2017a). Evidence for a strong Association of Short-Duration Intense Rainfall with Urbanization in the Beijing Urban Area. *J. Clim.* 30 (15), 5851–5870. doi:10.1175/JCLI-D-16-0671.1

Yang, X., Ruby Leung, L., Zhao, N., Zhao, C., Qian, Y., Hu, K., et al. (2017b). Contribution of Urbanization to the Increase of Extreme Heat Events in an Urban Agglomeration in east China. *Geophys. Res. Lett.* 44 (13), 6940–6950. doi:10.1002/2017GL074084

You, Q., Kang, S., Pepin, N., Flügel, W.-A., Sanchez-Lorenzo, A., Yan, Y., et al. (2010). Climate Warming and Associated Changes in Atmospheric Circulation in the Eastern and central Tibetan Plateau from a Homogenized Dataset. *Glob. Planet. Change* 72 (1), 11–24. doi:10.1016/j.gloplacha.2010.04.003

Yu, M., and Liu, Y. (2015). The Possible Impact of Urbanization on a Heavy Rainfall Event in Beijing. *J. Geophys. Res. Atmos.* 120 (16), 8132–8143. doi:10.1002/2015JD023336

Zhang, J., Song, X., Wang, G., He, R., and Wang, X. (2014). Development and Challenges of Urban Hydrology in a Changing Environment: I: Hydrological Response to Urbanization. *Adv. Water Sci.* 25 (4), 594–605. doi:10.14042/j.cnki.32.1309.2014.04.020

Zhang, L., Zhang, Z., Wang, C., Zhou, M., and Yin, P. (2017a). Different Mortality Effects of Extreme Temperature Stress in Three Large City Clusters of Northern and Southern China. *Int. J. Disaster Risk Sci.* 8 (4), 445–456. doi:10.1007/s13753-017-0149-2

Zhang, Q., Gu, X., Li, J., Shi, P., and Singh, V. P. (2018b). The Impact of Tropical Cyclones on Extreme Precipitation over Coastal and Inland Areas of China and its Association to ENSO. *J. Clim.* 31 (5), 1865–1880. doi:10.1175/JCLI-D-17-0474.1

Zhang, W., and Villarini, G. (2020). Deadly Compound Heat Stress-Flooding Hazard across the Central United States. *Geophys. Res. Lett.* 47 (15), e2020GL089185. doi:10.1029/2020GL089185

Zhang, W., Villarini, G., Vecchi, G. A., and Smith, J. A. (2018). Urbanization Exacerbated the Rainfall and Flooding Caused by hurricane Harvey in Houston. *Nature* 563 (7731), 384–388. doi:10.1038/s41586-018-0676-z

Zhou, L., Dickinson, R. E., Tian, Y., Fang, J., Li, Q., Kaufmann, R. K., et al. (2004). Evidence for a Significant Urbanization Effect on Climate in China. *Proc. Natl. Acad. Sci.* 101 (26), 9540–9544. doi:10.1073/pnas.0400357101

Zscheischler, J., Westra, S., van den Hurk, B. J. J. M., Seneviratne, S. I., Ward, P. J., Pitman, A., et al. (2018). Future Climate Risk from Compound Events. *Nat. Clim Change* 8 (6), 469–477. doi:10.1038/s41558-018-0156-3

Conflict of Interest: The authors declare that the research was conducted in the absence of any commercial or financial relationships that could be construed as a potential conflict of interest.

The reviewer (XT) declared a shared affiliation with several of the authors, (ML, YH, HT, FX, XT, PW, TC, SW), to the handling editor at time of review.

frontiers in Earth Science

ORIGINAL RESEARCH
published: 20 July 2021
doi: 10.3389/feart.2021.660359

Evolution of Frequency and Intensity of Concurrent Heavy Precipitation and Storm Surge at the Global Scale: Implications for Compound Floods

Yangchen Lai[1,2,3,4], *Qingquan Li*[1]*, *Jianfeng Li*[2,3,4]*, *Qiming Zhou*[2,4], *Xinchang Zhang*[5] *and Guofeng Wu*[1]

[1]MNR Key Laboratory for Geo-Environmental Monitoring of Great Bay Area, Shenzhen University, Shenzhen, China, [2]The Centre for Geo-computation Studies and Department of Geography, Hong Kong Baptist University, Hong Kong, China, [3]Guangdong-Hong Kong Joint Laboratory for Water Security, Hong Kong, China, [4]Institute for Research and Continuing Education, Hong Kong Baptist University, Shenzhen, China, [5]School of Geography and Remote Sensing, Guangzhou University, Guangzhou, China

Compound flood raised from the concurrent heavy precipitation and storm surge receives increasing attention because of its potential threat to coastal areas. Analyzing the past changes in the characteristics of compound flood events is critical to understand the changing flood risks associated with the combination of multiple drivers/hazards. Here, we examined the evolution of the compound flood days (defined as days of concurrent extreme precipitation and extreme storm surge exceeding the 90th percentiles) based on the observed precipitation and storm surge data across the globe. Results show that the annual number of compound flood days increased significantly by 1–4 per decade ($\alpha = 0.1$) on the east coast of the US and northern Europe, while the annual number of compound flood days decreased significantly in southern Europe and Japan. The increasing trends in precipitation under extreme storm surge and storm surge under extreme precipitation were found extensively across the world except in Japan, suggesting that more intense precipitation appeared when extreme storm surges occurred, and higher storm surge emerged when extreme precipitation occurred. Comparatively, the global fractional contributions of storm surge (i.e., 65%) on changes in compound flood days were higher than that of precipitation (i.e., 35%), demonstrating that storm surge was more likely to dominate the changes in the number of compound flood days. This study presents the spatial and temporal characteristics of the compound flood events at the global scale, which helps better understanding the compound floods and provides scientific references for flood risk management and an indispensable foundation for further studies.

Keywords: compound flood, extreme precipitation, storm surge, interannual variability, climate change

Edited by:
Abdou Khouakhi,
Cranfield University, United Kingdom

Reviewed by:
Chen Wei-Bo,
National Science and Technology Center for Disaster Reduction (NCDR), Taiwan
Md Mamunur Rashid,
University of Central Florida, United States
Dirk Eilander,
Deltares, Netherlands

***Correspondence:**
Qingquan Li
liqq@szu.edu.cn
Jianfeng Li
jianfengli@hkbu.edu.hk

Specialty section:
This article was submitted to Geohazards and Georisks, a section of the journal Frontiers in Earth Science

Received: *29 January 2021*
Accepted: *07 July 2021*
Published: *20 July 2021*

Citation:
Lai Y, Li Q, Li J, Zhou Q, Zhang X and Wu G (2021) Evolution of Frequency and Intensity of Concurrent Heavy Precipitation and Storm Surge at the Global Scale: Implications for Compound Floods. Front. Earth Sci. 9:660359. doi: 10.3389/feart.2021.660359

INTRODUCTION

Floods can be classified into three types according to different triggering mechanisms: 1) fluvial floods caused by precipitation over an extended period (riverine floods); 2) pluvial floods due to high-intensity and short-duration rainstorms (waterlogging floods); and 3) coastal floods resulting from the extreme sea levels associated with storm surge and high tides (Huntingford et al., 2014). Different types of floods can co-occur in certain weather conditions, for example, the concurrence of heavy rainfall and storm surge caused by tropical cyclones (Wahl et al., 2015; Ikeuchi et al., 2017; Lai et al., 2020). These combinations of two or more different floods are referred to as compound floods.

Compound floods are highly risky because the interplay among multiple extremes can exacerbate the adverse impacts (Intergovernmental Panel on Climate Change, 2012; Leonard et al., 2014; Zscheischler et al., 2018; Raymond et al., 2020). For their privilege of proximity to the sea, coastal areas are usually the most densely populated and economically developed areas of a country, and they are also the most vulnerable regions to the risk of compound floods from heavy precipitation and storm surge exactly because of the high population and property density as well as the special location (Chan et al., 2012; Neumann et al., 2015). For examples, Hurricane Harvey in 2017 caused heavy rainfall exceeding 1,000 mm and extreme storm surge higher than 1.8 m (Emanuel, 2017; Zhang et al., 2018a); and severe flooding was developed from the storm surge and rainfall during super typhoon Hato in Macau, 2017 (Hong Kong Observatory, 2017; Wang et al., 2019). These two compound floods led to record-breaking economic damages and life losses (Hong Kong Observatory, 2017; Klotzbach et al., 2018). Given the substantial damage caused by compound floods, a better understanding of the characteristics and driven mechanisms of compound floods is urgently needed.

Even though compound floods can occur coincidently, the dependence among different types of floods has been widely evidenced. For examples, Svensson and Jones (2002), Svensson and Jones (2004) analyzed the dependence among precipitation, river flow, and storm surge; Zheng et al. (2013) identified the significant dependence between precipitation and storm surge along the coastlines of Australia; and at the global scale, Ward et al. (2018) assessed the dependence between high sea level and high river discharge in most areas across the globe. The correlations among precipitation, river flow, and storm surge are determined by various factors such as meteorological conditions and regional topography. For example, the compound floods from heavy precipitation and storm surge can occur in certain weather conditions. In general, the weather conditions associated with compound floods are characterized by deep low pressure, cyclonic winds, and high precipitable water content, which can be found in storm systems (Wahl et al., 2015; Bevacqua et al., 2019). Therefore, storms (including tropical cyclones and extratropical cyclones) are one of the most important triggers of compound floods from heavy rainfall and storm surge (Wahl et al., 2015; Booth et al., 2016; Ikeuchi et al., 2017). The meteorological forcings-caused correlation between precipitation and storm surge can be identified between stations hundreds of kilometers far away (Zheng et al., 2013). The regional topography can also significantly impact the correlation among precipitation, river flow, and storm surge. For instance, the strong dependence between precipitation and storm surge is more likely to be found in hilly coastal areas, and the dependence between storm surge and river flow will be stronger in the steep catchments because of the shorter time required by peak flow to reach the estuary (Svensson and Jones, 2002; Svensson and Jones, 2004).

It's vital to take account of the dependencies among different floods when assessing the compound flood risk because ignoring these dependencies would result in considerable underestimation of compound flood risk. By constructing the joint distribution, previous studies have assessed the potential risk of compound floods from precipitation, river discharge, and storm surge at the regional and global scale (e.g., Moftakhari et al., 2007; Moftakhari et al., 2019; Lian et al., 2013; Van Den Hurk et al., 2015; Wahl et al., 2015; Bevacqua et al., 2017, Bevacqua et al., 2019; Bevacqua et al., 2020a; Bevacqua et al., 2020b; Xu et al., 2019; Couasnon et al., 2020). The regional studies on evaluation of compound flood risks were mainly concentrated on the US and Europe, where the tide gauges are densely distributed and have the best data completeness in a longer period (e.g., Moftakhari et al., 2007; Wahl et al., 2015; Bevacqua et al., 2017, 2019). Besides, some studies assessed the risk of compound floods using hydrodynamic models (e.g., Lian et al., 2013; Ikeuchi et al., 2017; Moftakhari et al., 2019; Gori et al., 2020; Jane et al., 2020; Khanam et al., 2021). These studies, better considered the interactions between flood drivers and localized features, however, were limited to analysis of regional compound flood cases. Constrained by the available data, the global-scale studies based on long-term observations are rare. However, a number of global studies have recently emerged benefitting from the development of simulated storm surge data (Bevacqua et al., 2020a; Bevacqua et al., 2020b; Couasnon et al., 2020; Ridder et al., 2020). These studies provided valuable information of compound floods in the areas where observations were absent (e.g., the coastal area of South America and Africa) but contained substantial uncertainties. Furthermore, Bevacqua et al. (2019), Bevacqua et al. (2020b) projected that driven by the changes in extreme precipitation and meteorological tide under the high emissions scenario, the compound flood risks would increase generally by >25% by the end of this century. These studies have well assessed the risk of compound floods; however, rare studies illustrated the evolutions of occurrences of compound floods based on long-term observations.

In this study, the evolutions in concurrences of heavy precipitation and extreme storm surge were analyzed based on the observed precipitation and storm surge data across the globe. The main research questions we aimed to address are as follows: 1) How's the spatial distribution of compound floods? Which areas of the world are the most susceptible to compound floods? In which season do most compound floods occur? 2) What is the interannual variability of compound floods in past decades? And how're the contributions of precipitation and storm surge to the interannual variability? 3) What could be the meteorological drivers causing the changes in compound floods? The answers are critical to understanding the changing compound flood risks, and serves as a scientific reference for flood risk management and an indispensable foundation for further studies.

DATA AND METHODS

Data

The compound floods from heavy precipitation and extreme storm surge were analyzed based on the observed precipitation

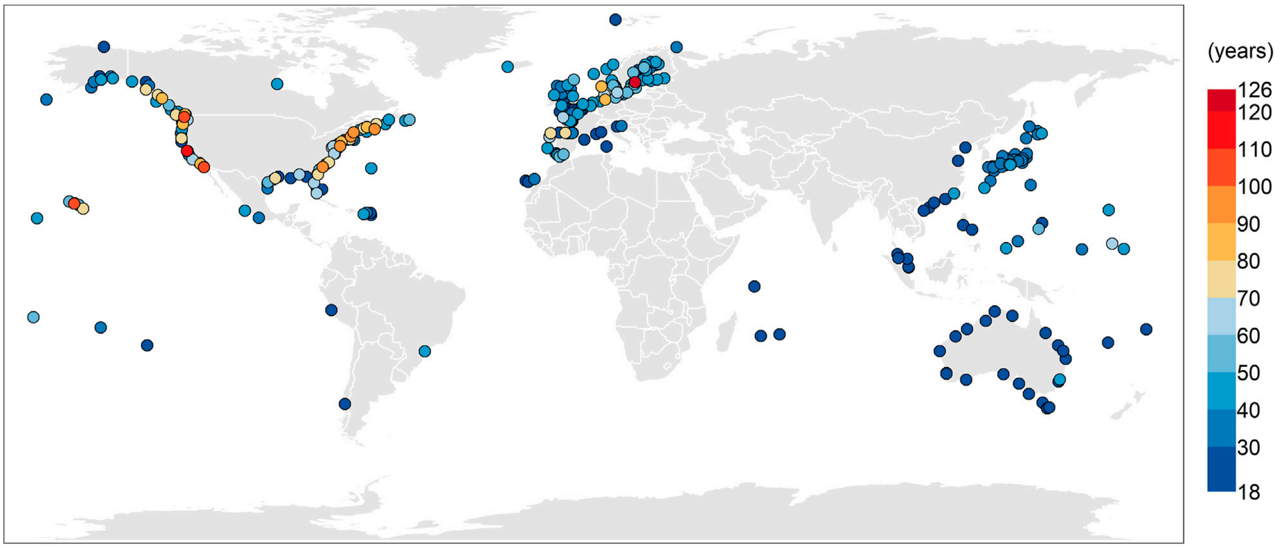

FIGURE 1 | Locations of tide gauges and the number of overlapping years. Only tide gauges with ≥18 overlapping years were used in this study.

and storm surge data. The observed hourly sea level data were obtained from the Global Extreme Sea Level Analysis version 2 (GESLA-2, https://www.gesla.org/; Woodworth et al., 2016). The observed sea level consists of mean sea level, astronomical tides, and non-tidal residual (i.e., storm surge and waves), in which the astronomical tides are caused by the gravitational effects of the moon and the sun, while the storm surge and waves are meteorological phenomena driven by atmospheric pressure and wind (Karim and Minura, 2008; Vousdoukas et al., 2018). Even though the actual water levels causing coastal flood can be estimated as the superpositions of extreme storm surge and astronomical high tides (Bevacqua et al., 2019; Yu et al., 2019), the astronomical tides are not likely to have relationships with meteorologically driven factors such as storm surge and precipitation. Therefore, we used the non-tidal residual to represent the storm surge to better investigate the meteorological drivers that cause the changes in compound floods as many previous studies did (e.g., Bevacqua et al., 2020a, Bevacqua et al., 2020b; Couasnon et al., 2020; Ridder et al., 2020; Wahl et al., 2015; Zheng et al., 2013). To extract the storm surge component, we applied a tidal harmonic analysis (T-tide; Pawlowicz et al., 2002) to analyze the observed sea level of each year to remove the impact of mean sea level rise. Hence, hourly storm surge data was converted to daily time series by extracting the daily maxima.

Daily precipitation data of more than 4,900 stations with the record lengths varying from 18 to 126 years were obtained from the Global Historical Climatology Network (GHCN-Daily, https://www.ncdc.noaa.gov/ghcn-daily-description; Menne et al., 2012). For each tide gauge, the average precipitation of all stations within a radius of 25 km from the tide gauge was used (Wahl et al., 2015). In the case there was no precipitation station within 25 km from the tide gauge, the search radius was expanded to 50 km. The years with >25% missing days were discarded. To assess whether the choice of precipitation average method would affect our analysis, the results based on precipitation calculated by inverse distance weighted method are shown in **Supplementary Material**. Only the tide gauges with record lengths >18 years over 1979–2014 were considered. 314 tide gauges were selected, and they are mainly located along the coasts of North America, Europe, Australia, East Asia, and Southeast Asia (**Figure 1**). The atmospheric variables used to analyze the weather conditions associated with compound floods included sea level pressure, three-dimension winds, and precipitable water content at $2.5^\circ \times 2.5^\circ$ spatial resolution during 1948–2014, and they were obtained from NCEP/NCAR reanalysis dataset (https://www.esrl.noaa.gov/psd/data/gridded/data.ncep.reanalysis.html; Kalnay et al., 1996).

Methods

There is no consistent mathematical definition of compound floods, and a widely used definition is based on the annual maxima. For example, Wahl et al. (2015) identified the compound floods from the time series of annual maxima of one variable (e.g., precipitation) and the corresponding block maxima of the other variable (e.g., storm surge). The sample size of compound floods based on this method is small because only one data pair is sampled for each year and each location, which is not ideal for the following statistical analyses of changes in compound floods. An alternative method to define compound floods is based on the peak-over-threshold method, in which, compound floods are usually defined as the co-occurrences of univariate extremes (e.g., extreme precipitation and extreme storm surge) exceeding a given percentile (Bevacqua et al., 2019; Bevacqua et al., 2020b). One advantage of this method is that more compound flood days could be sampled. In this study, the 90th percentiles were used to identify extreme precipitation/storm surge, and compound floods were defined as the co-occurrence of both extreme precipitation and extreme storm surge exceeding the percentiles. Here, the storm surge and precipitation data at the same calendar day were paired without consideration of time lag, and each day with precipitation and storm surge exceeding the threshold was taken as a compound flood day. The number of compound flood days was defined as an index to investigate the evolution of the days of concurrent heavy precipitation and storm surge. Indices based on similar definitions (e.g., number of days with precipitation >75th, 95th, and 99th percentiles) have been widely used in previous studies to detect the changes in extreme events (Fatichi and Caporali, 2009; Li et al., 2013; Zhang et al., 2013).

One drawback of defining compound flood days using the peak-over-threshold method is that the threshold exceedances may occur successively during extreme weather systems (e.g., tropical cyclones), thus not fully respect the independence assumption (Fatichi and Caporali, 2009). However, since the objective of this study is to assess whether the number of compound flood days is changing instead of evaluating the changes in the return period of compound flood events, the dependence between some compound flood days should not substantially affect our results of the trend detection (Fatichi and Caporali, 2009). Besides, a compound flood event that lasts longer might lead to greater damage than that lasts shorter. An increase in compound flood days implies more frequent compound flood events and/or longer durations of compound flood events. In either case, the potential risk of compound floods increases, and vice versa.

Even though using a lower threshold (i.e., 90th percentile) implies that the concurrent extreme precipitation and extreme storm surge may not lead actual compound floods, but it can ensure that enough compound flood days could be sampled to conduct a more robust analysis. The 90th percentile was widely used as a threshold to define flood events in previous studies (Gemmer et al., 2011; Iannuccilli et al., 2021; Li et al., 2015; Muis et al., 2018; Zhang et al., 2013). Besides, whether an actual flood occurs or not highly depends on localized characteristics such as topography, land use, regional climate, and their interactions (Bevacqua et al., 2020a; Hendry et al., 2019). In this case, we limited our analysis to the compound flood potentials (i.e., probability of occurrences) rather than the actual compound flood to better understanding their changes. To evaluate whether the choice of threshold would affect the analysis, the results with thresholds of 85th and 95th percentiles are shown in **Supplementary Material**. Considering the non-stationary statistics of hydrometeorological variables under climate change, the probability distribution of a hydrometeorological variable might change over time and hence the statistics of a period can not reflect those of another period (Gu et al., 2017; Milly et al., 2008; She et al., 2015). If we estimate the percentile threshold based on the data in a long period, the statistics of the variable may have altered in the study period (for example, the percentile in an earlier sub-period may be different from that in a later sub-period). To mitigate the impact of non-stationarity, the percentiles of precipitation/storm surge at all stations were estimated based on the daily time series from 1979 to 2014. This approach is the same as that used in many previous studies about climate extremes (You et al., 2011; Zhai et al., 2005; Zhang et al., 2005). For example, the Expert Team on Climate Change Detection and Indices (ETCCDI; https://www.wcrp-climate.org/etccdi) includes a number of climate extreme indices based on percentile thresholds (Li et al., 2013; Kurniadi et al., 2021). The percentile threshold is calculated from the fixed period of 1961–1990 in ETCCDI (Zhang et al., 2011). For instance, R95pTOT is defined as annual total precipitation when daily precipitation exceeds the 95th percentile in the 1961–1990 period (Dong et al., 2021). The 95th percentile threshold estimated in 1961–1990 is used to identify climate extremes in the past (e.g., before 1961) and the future (e.g., the 21st century).

The precipitation under extreme storm surge (i.e., precipitation of days with storm surge exceeding the 90th percentile) and storm surge under extreme precipitation (i.e., the storm surge of days with precipitation exceeding the 90th percentile) were analyzed to investigate the relationship between changes in compound floods, precipitation and storm surge. According to our definition of compound floods, the intensity of compound floods is determined by the intensity of precipitation and storm surge height. With this understanding, the changes in precipitation under extreme storm surge and the changes in storm surge under extreme precipitation reflect the changes in the intensity of compound floods. That is, given one of the two variables (e.g., precipitation as an example) exceeds the threshold, the increase (or decrease) in the other variable (e.g., storm surge) indicates the increase (or decrease) in the intensity of a potential compound event. Once the storm surge exceeds the threshold, it is considered a compound flood in this study. Therefore, the changes in the intensity of compound floods can be reflected in terms of 1) the changes of precipitation under extreme storm surge, and 2) the changes of storm surge under extreme precipitation.

The contributions of changes in precipitation and storm surge to the changes in the number of compound flood days were determined by the multivariate regression methodology. This method has been applied in the attribution analysis of changes in soil moisture (Zhang et al., 2018b). The regression equation is written as:

$$CF' = a \times P + b \times S + \varepsilon, \tag{1}$$

where CF' is the number of compound flood days predicted; P and S represent the precipitation under extreme storm surge, and storm surge under extreme precipitation, respectively; a and b are regression coefficients, and ε is a constant intercept coefficient. Therefore, the annual number of compound flood days is jointly affected by precipitation and storm surge, and the changes in the number of compound flood days, $\Delta CF'$, can be estimated by:

$$\Delta CF' = a \times \Delta P + b \times \Delta S, \tag{2}$$

where ΔP and ΔS are the changes in precipitation under extreme storm surge, and storm surge under extreme precipitation, respectively. The contributions of precipitation under extreme storm surge, and storm surge under extreme precipitation to the number of compound flood days can be calculated as:

$$\begin{cases} CP = \dfrac{(a \times \Delta P)}{\Delta CF'} \times 100\% \\ CS = \dfrac{(b \times \Delta S)}{\Delta CF'} \times 100\% \end{cases}, \tag{3}$$

where *CP* and *CS* represent the contributions of precipitation under extreme storm surge, and storm surge under extreme precipitation to the number of compound flood days, respectively. Since the trends of the annual number of compound flood days can be positive or negative, so do the contributions. To facilitate the comparison of contributions of precipitation and storm surge, we transferred the contributions into fractional contributions through:

$$\begin{cases} CP' = \dfrac{|CP|}{|CP| + |CS|} \times 100\% \\ CS' = \dfrac{|CS|}{|CP| + |CS|} \times 100\% \end{cases}, \tag{4}$$

where CP' and CS' represent the fractional contributions of precipitation under extreme storm surge, and storm surge under extreme precipitation to the number of compound flood days, respectively.

To reveal the drivers associated with the changes in compound floods, the meteorological variables (i.e., precipitable water content, vertical wind shear, sea level pressure, and near-land wind speed) associated with extreme precipitation and extreme storm surge (i.e., >90th percentiles) in three tide gauges (i.e., New York, NY in the US, Honmoku in Japan, and Tregde in Europe) were analyzed. These three tide gauges were selected based on three criteria: 1) the tide gauges should distribute in different parts of the world for the analysis of spatial variations; 2) the tide gauges should have longer data record years for more robust trend analysis; 3) the changes in compound flood days are significant at the selected tide gauges, and at least one significant trend can be detected in time series of precipitation and storm surge. For each tide gauge, the precipitable water content and vertical wind shear (calculated as the wind difference between 850 hPa and 200 hPa levels; Chen et al., 2006; Chen et al., 2011; Zhang et al., 2018c) during extreme storm surge events were extracted and averaged by year to examine their relationships with changes in precipitation under extreme storm surge, while sea level pressure and near-land wind speed (i.e., wind speed at the 0.995 sigma level) during extreme precipitation events were extracted and averaged by year to examine their relationships with the changes in storm surge under extreme precipitation. It shall be noted that our analysis on meteorological variables was based on extreme events from 1948 to 2014 because NCEP/NCAR reanalysis dataset is not available before this period. The trends in compound floods between the periods of 1948–2014 and 1979–2014 were analyzed and shown in the **Supplementary Material**.

The trend of time series was detected using the Modified Mann-Kendall test, which is a nonparametric trend detection method that considers autocorrelation in time series (Hamed and Ramachandra Rao, 1998). A trend was taken as a significant trend when the *p*-value is < 0.1 (i.e., $a = 0.1$). Sen's slope method was used to estimate the magnitude of the trend of time series (Sen, 1968).

RESULTS

Spatial Pattern and Seasonal Variation of Compound Floods

As shown in **Figure 2**, we examined the annual number of compound flood days with extreme precipitation and extreme storm surge exceeding the 90th percentiles. In southern Europe, the west and northeast coast of the US, and northern Japan, the compound floods occurred most frequently (i.e., >12 per year), followed by the east and southeast of the US, northern Europe, western Australia, and Japan, where experienced average 8–12 compound flood days per year. The co-occurrences of extreme precipitation and storm surge can happen by chance or because of the dependence between univariate extreme events driven by associated meteorological systems. If the precipitation and storm surge are independent of each other, the expected annual number of co-occurrences of precipitation and storm surge exceeding the 90th percentile should be $0.1 \times 0.1 \times 365 = 3.65$. However, the actual number of compound flood days in reality is affected by various factors such as the dependence between precipitation and storm surge and autocorrelation of time series (Martius et al., 2016). The observed annual number of compound flood days in 305 out of 314 tide gauges was higher than 3.65, which means that not all compound floods occurred by chance, and the extra compound flood days were very likely to be associated with the dependence between precipitation and storm surge (Zheng et al., 2013; Couasnon et al., 2020). Besides, the dependence between precipitation and storm surge at regional and global scales has been reported in many previous studies (e.g., Zheng et al., 2013; Wahl et al., 2015; Bevacqua et al., 2019; Bevacqua et al., 2020a). For example, Bevacqua et al. (2020a) calculated Kendall's *t* correlation between precipitation and storm surge and found a stronger correlation between precipitation and storm surge on the coast of the US, western Europe, East Asia, and Australia. This spatial pattern generally coincides with that of the annual number of compound flood days, which further proves the relationship between compound floods and dependence. From these results, the hotspots of compound floods, including the coast of the US, southern Europe, East Asia, and Australia, were identified. The identified hotspots of compound floods are consistent with that of studies that using reanalysis data (Bevacqua et al., 2020a; Couasnon et al., 2020). These areas involve many socio-economically important regions, such as Europe, the coast of the US, and southeastern China, which hold densely distributed populations and properties and thus exposed to compound flood hazards. When using the 85th and 95th percentiles to identify the compound flood events, or examining the trends between different periods (i.e., 1948–2014 and 1979–2014), the

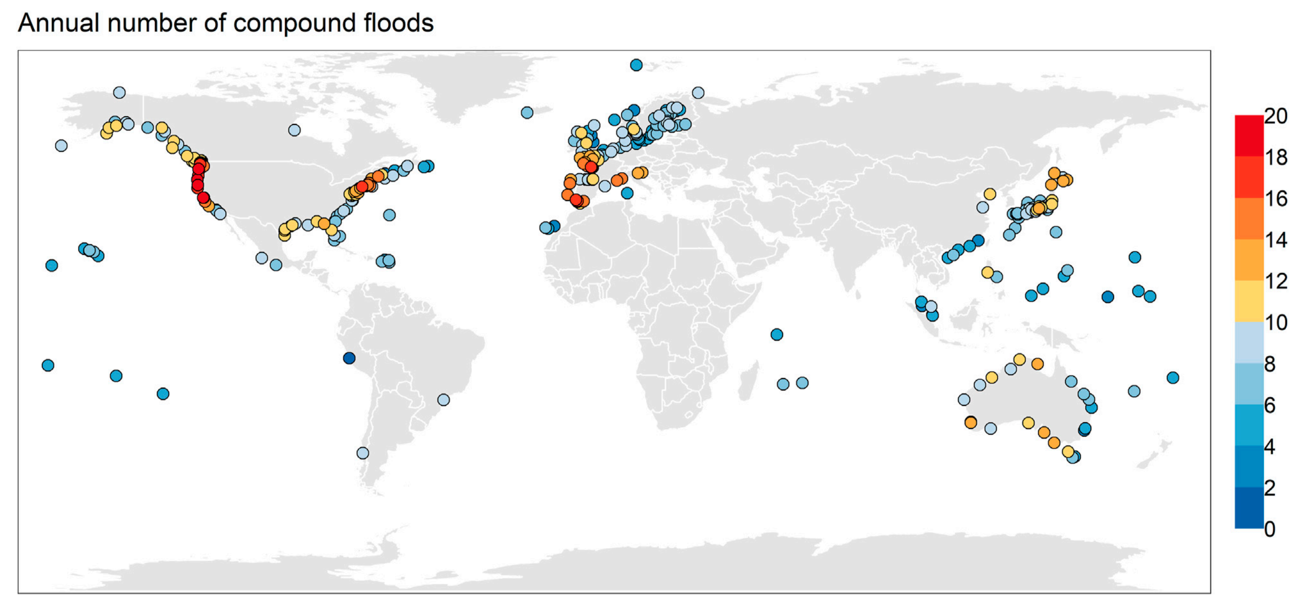

FIGURE 2 | The annual number of compound flood days. Compound flood days are the days with extreme precipitation and extreme storm surge exceeding the 90th percentile values.

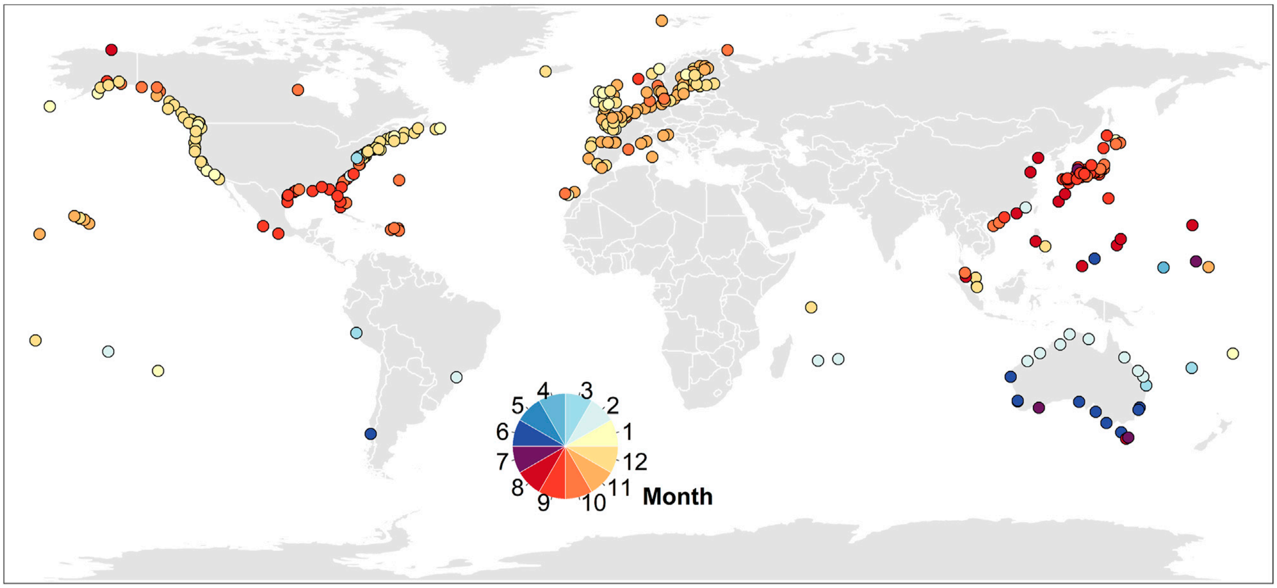

FIGURE 3 | The month with the most frequent concurrences of extreme precipitation and extreme storm surge exceeding the 90th percentile values.

spatial distributions of compound floods showed very similar patterns with those based on the 90th percentile and all available data (**Supplementary Figures S1, S5, S8**).

Figure 3 shows the months in which compound floods occurred most frequently to illustrate the seasonal variation of compound floods. In Europe, the west coast of North America, and northeast of the US, compound floods tended to occur in November and December, while in the southeast coast of the US, and East Asia, the peak season of compound floods was September. In the Southern Hemisphere, the peak season of compound floods in southern Australia is June, while this was February in northern Australia. In the areas affected by tropical cyclones such as East Asia, the southeast coast of the US, and northern Australia (Walsh et al., 2016; Khouakhi et al., 2017), the occurrences of compound floods were affected by tropical cyclone activities (Wahl et al., 2015; Ikeuchi et al., 2017;

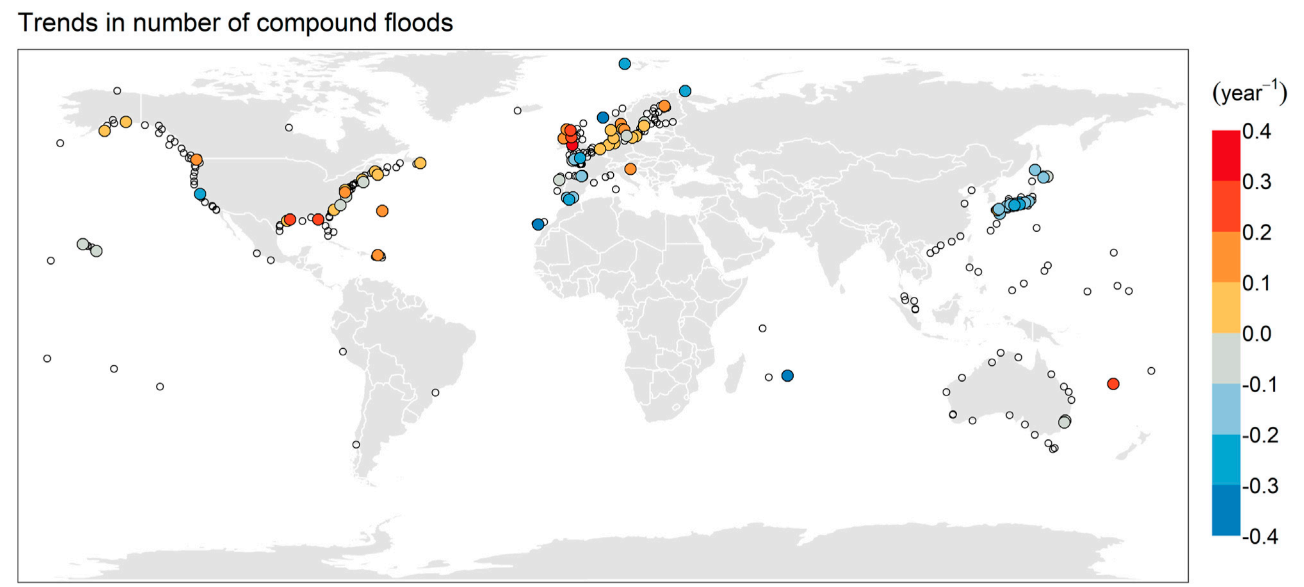

FIGURE 4 | Trends in the annual number of compound flood days. Compound flood days are the days with extreme precipitation and extreme storm surge exceeding the 90th percentile values. Open circles denote the trends are insignificant (α = 0.1).

Xu et al., 2018), and therefore the peak seasons of compound floods were concentrated on tropical cyclone seasons (i.e., July–September in the North Hemisphere, and December–February in the South Hemisphere). In mid and high-latitude areas, the compound floods tended to occur during winter (i.e., November–January in North Hemisphere, and June–July in South Hemisphere).

Trends in Frequency and Intensity of Concurrences of Heavy Precipitation and Storm Surge

Figure 4 shows the trends in the annual number of compound flood days across the globe. The largest increasing trend was found in the UK, where the number of compound flood days increased by > 2 days per decade. Besides, in northwestern Europe and the east coast of the US, the annual number of compound flood days increased with a magnitude of 1–3 days per decade, implicating increasing compound flood risks in these areas. In contrast, the number of compound flood days decreased significantly in some tide gauges of southwestern Europe and Japan. The changes in the annual number of compound flood days were not significant (i.e., $p > 0.1$) in most locations of the east coast of North America, South America, Australia, and Southeast China. Noted that these changes in compound flood days were estimated based on record lengths varying by tide gauge (**Figure 1**). When constraining the study period as 1948–2014 or 1979–2014, the spatial patterns of changes in compound flood days are similar (**Supplementary Figures S6, S9**).

To investigate the evolution of the intensity of compound floods, we examined the changes in precipitation under extreme storm surge and the changes in storm surge under extreme precipitation. **Figure 5A** shows that precipitation under extreme storm surge increased significantly on the coast of North America, Europe, the east coast of Japan, and some locations of northern Australia, indicating the elevating probability of occurrences of heavy rainfall when extreme storm surges occurred. The changes in storm surge under extreme precipitation showed greater regional variation. On the west and northeast coast of the US and Japan, the storm surge under extreme precipitation decreased slightly (i.e., <4 mm/year), while on the southeast coast of the US and Europe, storm surge under extreme precipitation showed an increasing trend (**Figure 5B**). We examined the sensitivity of these results to the choice of thresholds (i.e., 85th and 95th percentile values. The spatial patterns of changes are consistent with those using the threshold of 90th percentile even though the magnitudes of changes and number of significant trends might be different (**Supplementary Figures S2–S4**). When conducting these analyses in different periods (i.e., 1948–2014 and 1979–2014), the results are similar except that the storm surge under extreme precipitation showed increasing trends on the northeast coast of the US during 1979–2014, while decreasing trends were detected in this area during the long period (e.g., 1948–2014; **Supplementary Figures S7, S10**).

Comparing the spatial patterns of changes in compound floods, precipitation under extreme storm surge, and storm surge under extreme precipitation (**Figures 4, 5**), it can be found that, on the west coast of the US where the precipitation increased but the storm surge decreased, the changes in the number of compound flood days were not obvious; in northwestern Europe, both precipitation under extreme storm surge and storm surge under extreme precipitation showed increasing trends, thus the number of compound flood days increased most substantially. In contrast, in Japan, where the precipitation showed different directions in

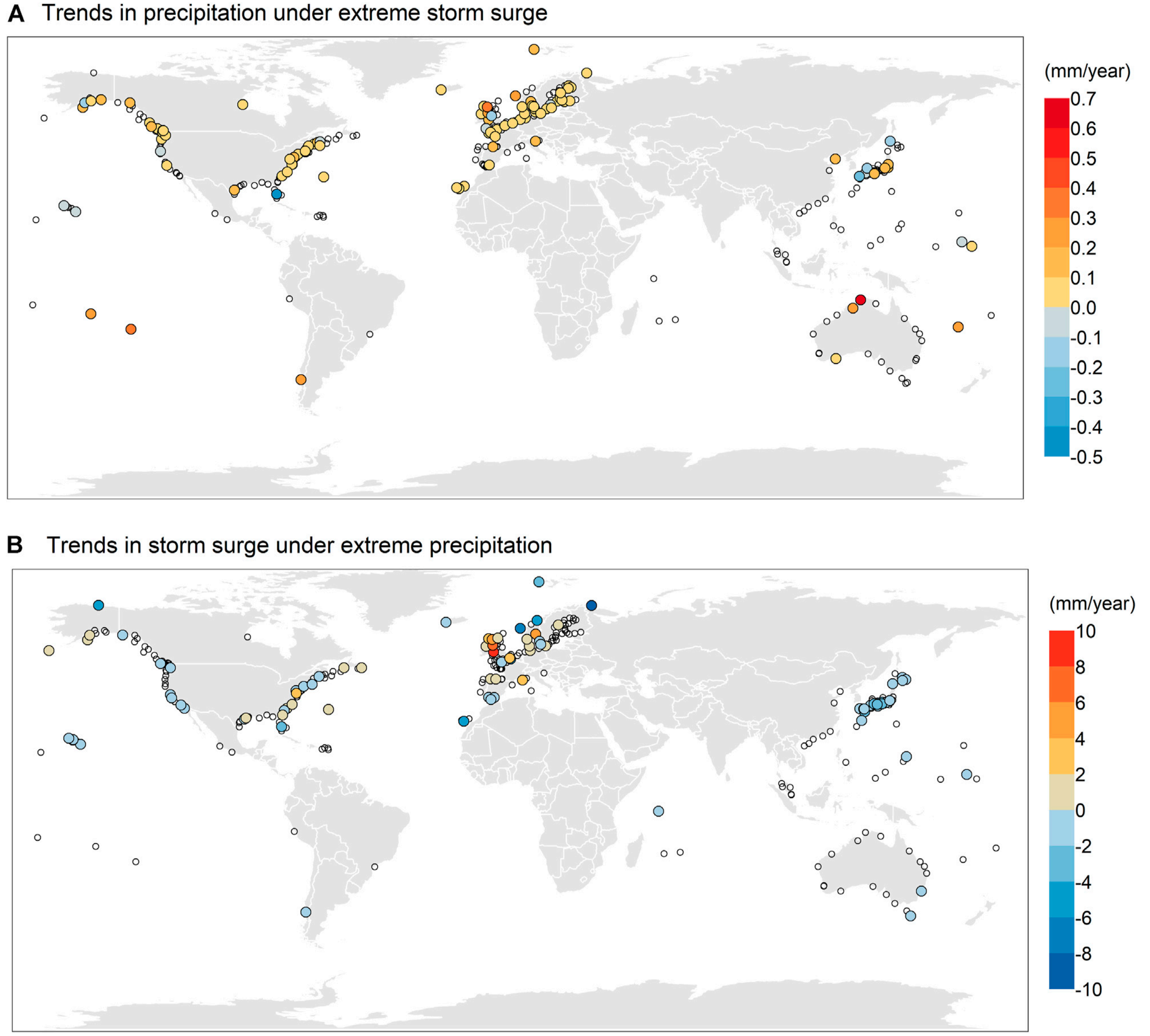

FIGURE 5 | Trends in **(A)** precipitation under extreme storm surge (i.e., >90th percentile); and **(B)** storm surge under extreme precipitation (i.e., >90th percentile). Open circles denote the insignificant trends (α = 0.1).

different areas (i.e., negative trends on the west coast and positive trends on the east coast) while the storm surge showed significant decreasing trends across the country, the number of compound flood days also decreased significantly. Comparatively, the spatial distribution of changes in storm surge under extreme precipitation matched better with that of changes in compound floods, implicating that the changes in storm surge were more likely to dominate the changes in compound floods.

To justify this inference, the fractional contributions of precipitation under extreme storm surge, and storm surge under extreme precipitation were calculated based on the multivariate regression methodology. As shown in **Figure 6A**, the changes in precipitation under extreme storm surge contributed to more than 50% of changes in compound floods in northern Europe (mainly on the coast of the North Sea and Baltic Sea) and tide gauges on the east coast of the US and southern Australia, indicating the changes in precipitation dominated the changes in compound floods in these areas. By contrast, in the other areas including the west coast of the US, western and southern Europe, Japan, northern Australia, and also some tide gauge on the east coast of the US, the fractional contribution of changes in storm surge under extreme precipitation exceeded 50%, demonstrating the dominate role of storm surge in affecting the number of compound flood days (**Figure 6B**). The average contributions of precipitation and storm surge across the globe were 35 and 65%, respectively.

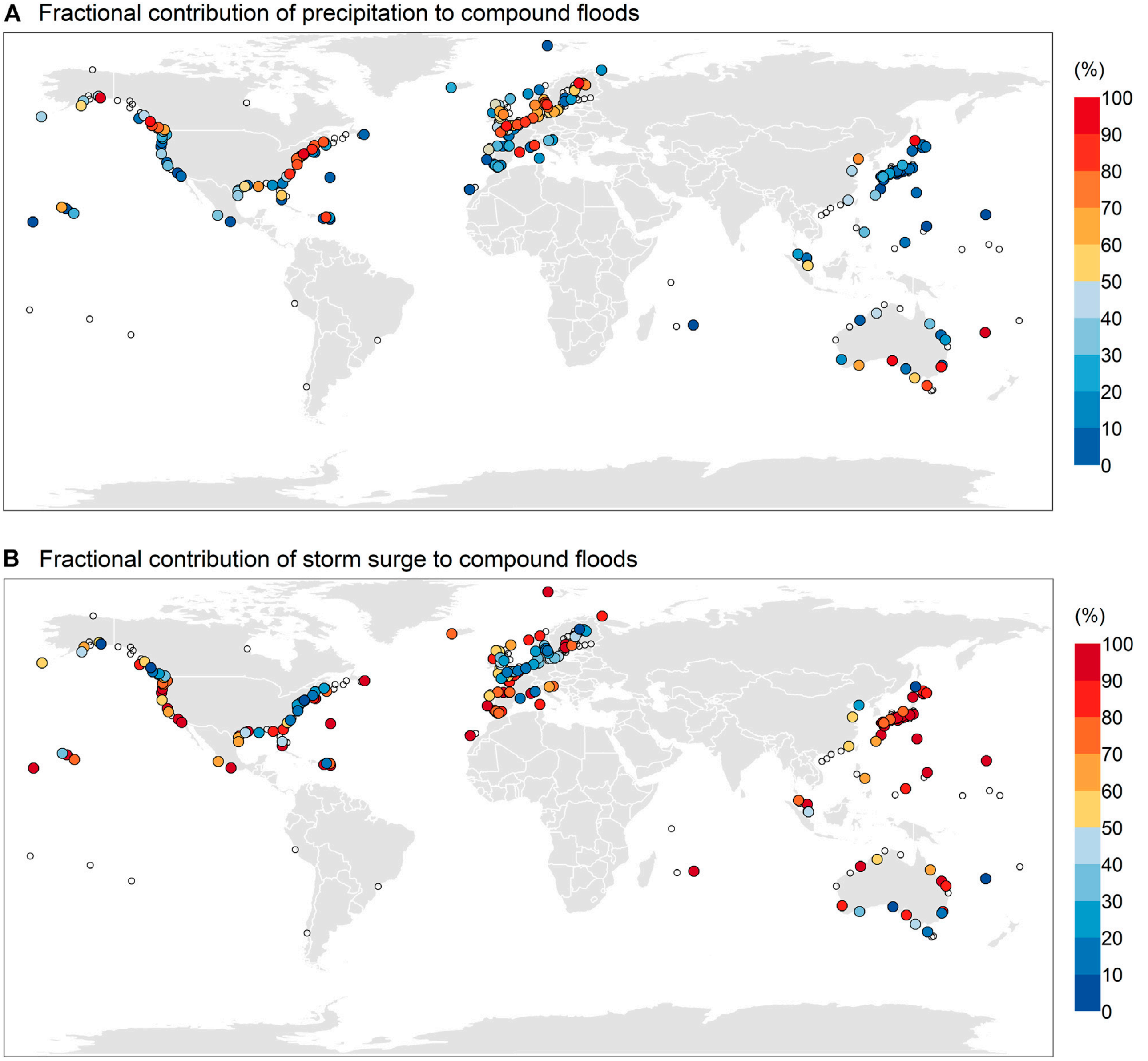

FIGURE 6 | Fractional contribution of **(A)** changes in precipitation and **(B)** storm surge to the changes in number of compound flood days. Open circles denote that the Sen's slope of the number of compound flood days is 0.

These results further prove our inference that changes in storm surge were more likely to dominate the changes in compound floods.

Changes in Meteorological Variables Associated With Precipitation Under Extreme Storm Surge and Storm Surge Under Extreme Precipitation

The meteorological variables including precipitable water content, vertical wind shear, sea level pressure, and near-land wind speed associated with extreme precipitation and extreme storm surge (i.e., >90th percentiles) in three tide gauges (i.e., New York, NY, Honmoku, and Tregde) were analyzed to explore the meteorological drivers associated with changes in the compound floods. Before evaluating the changes in meteorological variables, the time series of the annual number of compound flood days, precipitation under extreme storm surge, and storm surge under extreme precipitation in tide gauges New York, NY, Honmoku, and Tregde were analyzed for more details (**Figures 7**, **8**). In New York, NY, the annual number of compound flood days showed an insignificant increasing trend during the long period between 1921 and 2014, while the significant slight increasing trend was detected in the shorter period between 1948 and 2014 (**Figure 7A**). In Honmoku, the number of compound flood days significantly decreased by 40% during 1961–2006

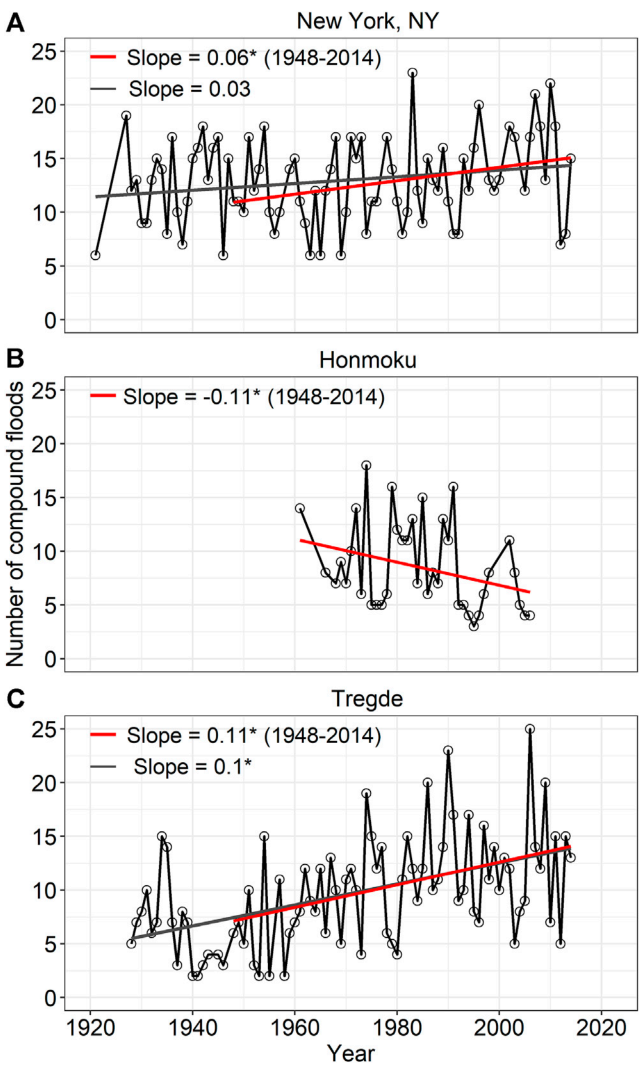

FIGURE 7 | Temporal evolution of the annual number of compound flood days in tide gauge **(A)** New York, NY, **(B)** Honmoku, and **(C)** Tregde. The black straight line in **(A)** and **(C)** indicates the trend of the complete time series. The red straight line indicates the trend of the time series during 1948–2014. The Sen's slopes were estimated. Significant trends are identified by an asterisk (α = 0.1).

(**Figure 7B**). In contrast, the number of compound flood days increased by 153% during 1928–2014 in Tregde, and this percentage is 97% for the shorter period from 1948 to 2014 (**Figure 7C**). The results of changes in the number of compound flood days were also supported by the changes in precipitation under extreme storm surge and storm surge under extreme precipitation. In New York, NY, the precipitation under extreme storm surge increased significantly in both longer and shorter periods, which contributed to more than 90% of the changes in the number of compound flood days (**Table 1**). The storm surge under extreme precipitation showed no obvious trend and contributed less to the increase of compound floods (**Figures 8A,B**). In Honmoku, the changes in precipitation under extreme storm surge were not significant, but the storm surge under extreme precipitation decreased by 26%, which was responsible for the increase in the number of compound flood days (**Figures 8C,D**; **Table 1**). For the tide gauge Tregde, both precipitation under extreme storm surge and storm surge under extreme precipitation showed significant increasing trends (**Figures 8E,F**), indicating more intense precipitation when extreme storm surge events occurred, and higher storm surge during extreme precipitation events. The fractional contributions of precipitation and storm surge in Tregde are 62.7 and 37.3%, respectively (**Table 1**).

The changes in precipitable water content and vertical wind shear on the days of extreme storm surge were estimated to investigate their relationships with changes in precipitation under extreme storm surge. The precipitable water content measures the amount of available moisture in the atmosphere, which is closely related to precipitation (Dong et al., 2019; Kunkel et al., 2020). Vertical wind shear measures the changes of winds with height, which relates to convective activity (Tramblay et al., 2020). Vertical wind shear has different impacts on different types of storms: an environment of weak vertical wind shear favors the genesis and maintenance of tropical cyclones (Frank and Ritchie, 2001; Wong and Chan, 2004), while significant vertical wind shear is required for the development of extratropical cyclones (Lim and Simmonds, 2007; Ynase and Niino, 2015; Ynase and Niino, 2019). In New York, NY, the precipitable water content around the New York showed an insignificant trend, while the vertical wind shear was stronger at the north of New York, NY, and weaker in the south of New York, NY (**Figures 9A,D**). The weaker vertical wind shear over the sea to the southeast of New York, NY allowed the tropical cyclones to sustain for a longer duration and move to the midlatitudes, and the increased vertical wind shear at higher latitude areas is likely a signature of the extratropical transition processes of tropical cyclones (Liu et al., 2017; Towey et al., 2018; Evans and Hart, 2003). The more frequent cyclone activities imply more precipitation events, which is consistent with the observed increasing trend of precipitation under extreme storm surge during the period from 1948 to 2014 in New York, NY. In Honmoku, the precipitable water content decreased significantly, which was consistent with the decreasing trend of precipitation under extreme storm surge (**Figure 9B**). The vertical wind shear showed an increasing but insignificant trend (**Figure 9E**). Considering that Honmoku is frequently affected by tropical cyclones (e.g., tropical cyclones contribute to 40–65% of extreme precipitation in Japan; Khouakhi et al., 2017), the increased vertical wind shear might apply an adverse impact on the strength maintenance of tropical cyclones and cause a shorter duration of tropical cyclones over this region. In Tregde, the changes in precipitable water content were insignificant, while the vertical wind shear showed increasing trends over most of western Europe, implicating the enhanced convective activity in this region (**Figures 9C,F**). Furthermore, the increased vertical wind shear in higher latitude might contribute to the development of extratropical cyclones, which is an important driver of heavy rainfall and extreme storm surge in Europe (Hawcroft et al., 2012; Hawcroft et al., 2018; Weisse et al., 2012; Pinto et al., 2014). In this case, the increase in

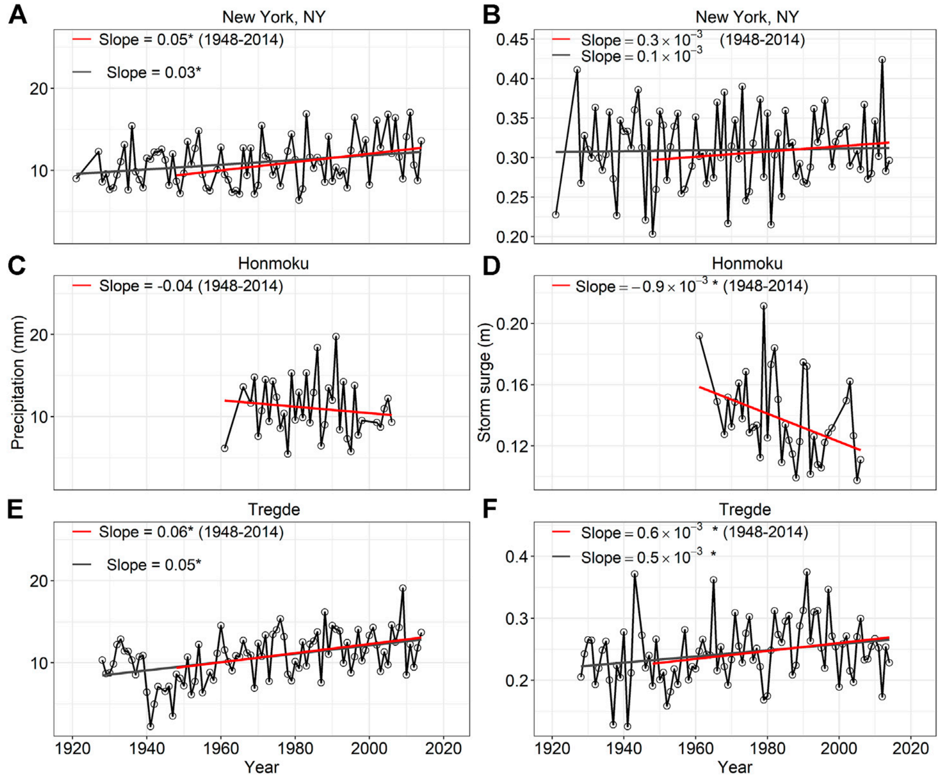

FIGURE 8 | Temporal evolution of **(A, C, E)** precipitation under extreme storm surge, and **(B, D, F)** storm surge under extreme precipitation in tide gauge **(A, B)** New York, NY **(C, D)** Honmoku, and **(E, F)** Tregde. The black straight line in **(A)** and **(C)** indicates the trend of the complete time series. The red straight line indicates the trend of the time series during 1948–2014. The Sen's slopes were estimated. Significant trends were identified by an asterisk (α = 0.1).

TABLE 1 | Statistics of compound floods, precipitation and storm surge between 1948 and 2014.

Tide gauge	New York, NY	Honmoku	Tregde
Trends of compound flood days (year^{-1})	0.06*	−0.11*	0.11*
Trends of precipitation (mm/year)	0.05*	−0.04	0.06*
Trends of storm surge (10^{-3} m/year)	0.3	−0.9*	0.6*
Contribution of precipitation (%)	94.8	9.3	62.7
Contribution of storm surge (%)	5.2	90.7	37.3

The asterisks (*) denote significant trends (α = 0.1).

precipitation under extreme storm surge might be related to the increase of vertical wind shear.

The sea level pressure and near-land wind speed on the days of extreme precipitation were analyzed to examine their relationships with storm surge under extreme precipitation. Results showed that the changes in sea level pressure around the New York, NY were not significant (**Figure 10A**), while the wind over the waterside of New York, NY increased significantly, which can cause higher wind waves (**Figure 10D**). In Honmoku, the sea level pressure increased over large areas of the Western North Pacific (**Figure 10B**). The increasing trend over large areas helps little in increasing the pressure gradient, thus may not help increase the storm surge. What's more, the winds were weaker over the near-coast sea area, which is unfavorable for the generation of wind waves (**Figure 10E**). In Tregde, the sea level pressure decreased over the north of the location of interest, but increased over the other side (**Figure 10C**). This change increased the pressure gradient, resulting in higher storm surges. At the same time, the significant intensifying winds over western Europe also contributed to the increase of wind waves under extreme precipitation (**Figure 10F**).

DISCUSSIONS

In this study, we analyzed the evolution of precipitation under extreme storm surge and storm surge under extreme precipitation to attribute the changes in compound floods. According to the

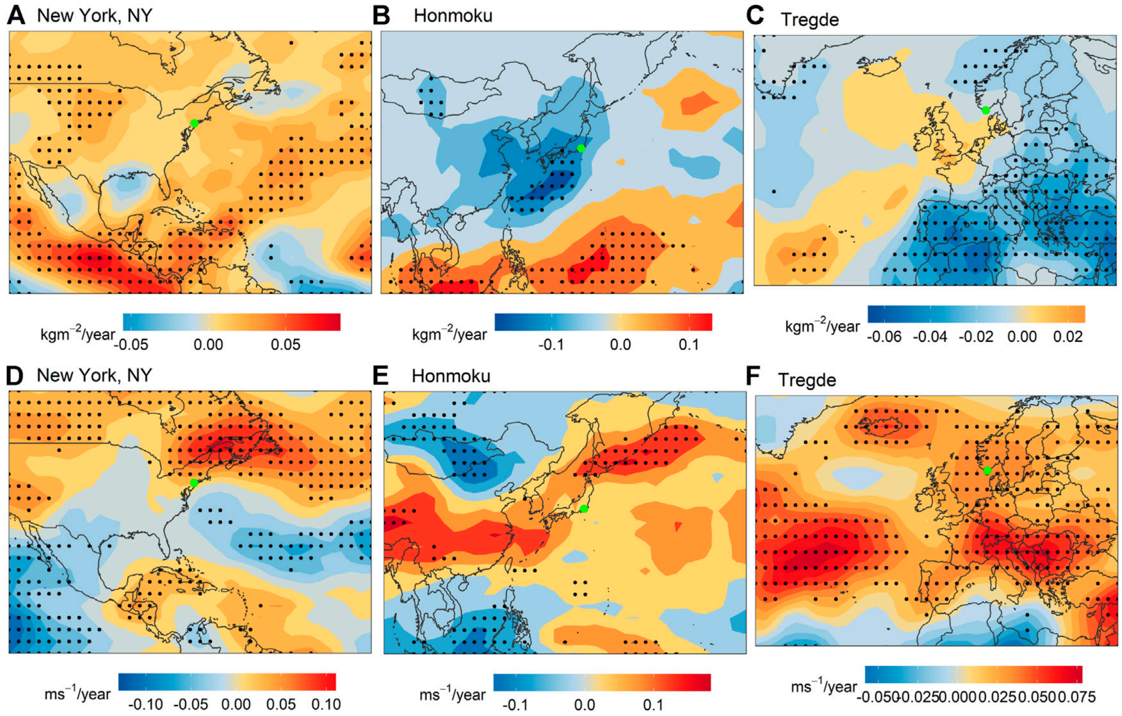

FIGURE 9 | Trends in **(A–C)** precipitable water contents (kgm^{-2}/year) and **(D–F)** vertical wind shear (ms^{-1}/year) during precipitation under extreme storm surge in tide gauge New York, NY **(A, D)**, Honmoku **(B, E)**, and Tregde **(C, F)**. Locations of the tide gauges interested are denoted by the green spots. Stippled regions represent areas with significant trends ($\alpha = 0.1$).

definitions provided in Intergovernmental Panel on Climate Change, 2012, compound events can be two or more extreme events occurring simultaneously (i.e., compound floods defined in this study), and the combinations of events, that alone are not extreme, leading to an extreme impact. For floods events, the compound floods can be combinations of 1) extreme precipitation and extreme storm surge (i.e., compound floods defined in this study), 2) extreme storm surge and precipitation that can produce runoff and thus increase water level at the estuary, and 3) extreme precipitation and storm surge that may be not extreme but great enough to block or slow down the drainage (Wahl et al., 2015; Zscheischler et al., 2018). In this case, the precipitation under extreme storm surge contains the second type of compound flood events, and the third type of compound floods was included in the storm surge under extreme precipitation. The increasing trends in precipitation under extreme storm surge across the worlds can be interpreted in two aspects: 1) As the precipitation increasing, the probability of concurrence of extreme precipitation and extreme storm surge is higher than before (i.e., more precipitation under extreme storm surge reaches extreme levels). 2) Given an extreme storm surge event, the precipitation is more intense (not has to be extreme), therefore its interplay with storm surge is more probable to exacerbate the adverse impact. This interpretation also applies to storm surge under extreme precipitation. From this perspective, analyzing the precipitation under extreme storm surge and storm surge under extreme precipitation could provide more information than analyzing the precipitation and storm surge directly.

Even though compound floods are receiving more and more attention, rare studies have analyzed the inter-annual changes in compound floods during past decades based on observational data. At the regional scale, Wahl et al. (2015) examined the enhanced dependence between precipitation and storm surge, and reported the increasing trends in compound flood risk in past decades along the coast of the US. At the global scale, our study analyzed the trends in compound floods, precipitation under extreme storm surge, and storm surge under extreme precipitation based on observations, and found the significant increasing trends in compound flood risk over Europe and the US in past decades. These findings are critical to better understand the changing compound flood risk, and provide important references for the evaluation of the simulation-based studies. For example, Bevacqua et al. (2019), Bevacqua et al. (2020b) projected the higher probability of occurrence of compound floods from precipitation and storm surge across the globe under a high emission scenario in the future, which means the increasing trends identified in this study are probable to continue in the future. However, in Japan, where the compound floods and storm surge under extreme precipitation decreased significantly from 1961 to 2006, the return periods of compound floods were projected to shorten by >60% under a high emissions scenario (Bevacqua et al., 2020b). The mechanisms behind this transition from the downward trend in the past to the upward trend in the

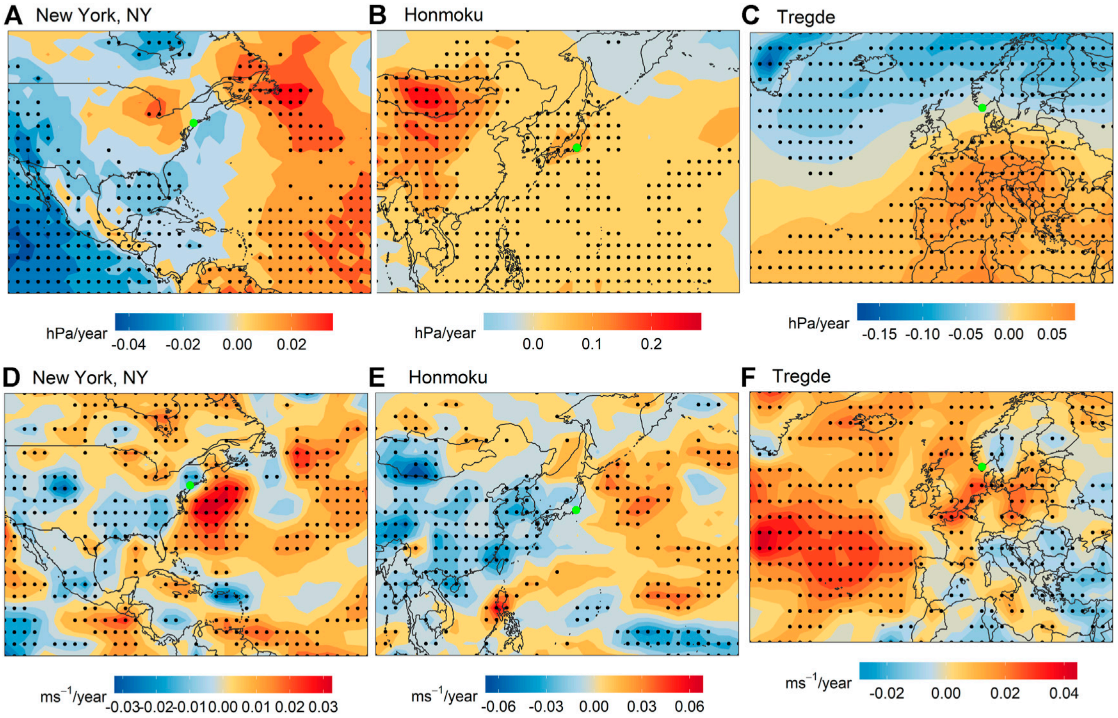

FIGURE 10 | Trends in **(A–C)** sea level pressure (hPa/year) and **(D–F)** wind speed (ms^{-1}/year) during storm surge under extreme precipitation in tide gauge New York, NY **(A, D)**, Honmoku **(B, E)**, and Tregde **(C, F)**. Locations of the tide gauges interested are denoted by the green spots. Stippled regions represent areas with significant trends ($\alpha = 0.1$).

future are worth exploring. Considering the relatively short record lengths of observational data in this region and the large uncertainties of simulation-based studies, further studies are needed to examine the characteristics of compound flood events in Japan.

The results of compound floods from heavy precipitation and extreme storm surge exceeding the 90th percentiles were discussed in this study. The compound floods exceeding the 85th percentiles and 95th percentiles were analyzed and were shown in the SI (**Supplementary Figures S1–S4**). Compared the changes in the annual number of compound flood days of different intensities, we found that the direction of trends (i.e., increase or decrease) was consistent between compound floods of different intensities, but the lower the threshold, the more stations showing significant trends (**Figure 4** and **Supplementary Figure S2**). This phenomenon could also be found in the changes in precipitation under extreme precipitation (**Figure 5A** and **Supplementary Figure S3**). For storm surge under extreme precipitation, the spatial pattern of changes in storm surge under extreme precipitation exceeding the 85th percentiles was almost the same as that of exceeding the 90th percentiles. However, the changes in storm surge under extreme precipitation turned from negative to positive in some stations on the coast of the US when the thresholds elevated from 85th to 95th percentiles (**Figure 5B** and **Supplementary Figure S4**), indicating the higher storm surge occurred during the most extreme precipitation events. In general, the spatial patterns of changes in compound floods, precipitation under extreme storm surge, and storm surge under extreme precipitation defined by 85th and 95th percentiles were very similar, except that when using the higher threshold (i.e., the 95th percentile), less significant trends could be detected because less extreme events could be identified when using the higher threshold. However, if the threshold is set too low, there is a risk of failing in capturing the change signal of the most extreme event. Results of the sensitivity analyses show that the spatial and temporal characteristics of compound floods are similar when using the inverse distance weighted method to calculate the average precipitation (**Supplementary Figures S11–S13**).

Previous studies found that the weather conditions associated with compound floods were characterized by the deep low-pressure system, cyclonic winds, and high precipitable water contents (Wahl et al., 2015; Bevacqua et al., 2019). We also analyzed these meteorological variables to explain the changes in precipitation under extreme storm surge and storm surge under extreme precipitation. Results found that the changes in storm surge under precipitation in three locations (i.e., New York, NY, Honmoku, and Tregde) could be well explained by the changes in sea level pressure and near-land wind speed. The physical mechanisms that impact the precipitation under extreme storm surge might be more complex. The changes in precipitable water content could not explain all the changes in precipitation under extreme storm surge. For example, in Tregde, the precipitable water content showed no significant trends, while the precipitation under extreme storm surge here increased significantly by 51%. Therefore, there might be some other factors causing the increase in precipitation. We further analyzed the vertical wind shear. Results showed that the increased vertical wind shear might reflect the enhanced convective activity in Europe, which might be related to the increased precipitation under extreme storm surge. But the impact of vertical wind shear should be identified carefully because of its complex effect on storms. Storms such as tropical cyclones and extratropical cyclones are accompanied by low-pressure, cyclonic wind, and abundant moisture transportation, and thus usually cause compound floods. Further studies focused on the impact of storm activities on compound floods will be helpful to better understand the characteristics of compound floods.

In this study, we used the non-tidal residual to represent the meteorologically driven coastal flood without consideration of the storm-tide interaction, which might cause uncertainties in the results. Many studies have pointed out that the storm-tide interaction can not be neglected when estimating the extreme sea levels, because the storm-tide interaction could modulate the actual highest water level (Horsburgh and Wilson, 2007; Zhang et al., 2010; Mawdsley and Haigh, 2016; Williams et al., 2016; Arns et al., 2020). When neglecting the storm-tide interaction, the storm surge was assumed to be independent of the water level, which is not true because the observed highest storm surge was found to be more likely to occur at mid- or low-tides rather than at the high-tides (Horsburgh and Wilson, 2007). If neglecting the non-linear storm-tide interaction, the extreme sea level would be overestimated by 30% (Arns et al., 2020). However, since the storm-tide interaction is highly affected by local features such as locations, topography, oscillations, tide ranges, etc., it shows less robust correlation with tidal levels or tidal contributions and varies greatly across different regions of the world (Zhang et al., 2010; Arns et al., 2020). In general, it has been identified that the storm-tide interaction is strongest on the east coast of the US, western Europe, northern Australia, and Japan (Mawdsley and Haigh, 2016; Arns et al., 2020). Even though we are aware of the important role of storm-tidal interaction in modulating the estimation of coastal floods, it is still uncertain that what method can be used to take care of storm-tide interaction efficiently when assessing the coastal flood. Some previous studies have tried to use skew surge, which is the difference between the maximum total water level and maximum predicted tidal level within a tidal cycle, to represent the coastal floods, and suggested the independence between skew surge and tide (Mawdsley and Haigh, 2016; Williams et al., 2016). However, a more recent statistical method-based study assessed the non-linear storm-tide interaction and found that both non-tidal residuals and skew surges associated with the highest water levels were significantly dependent on tide (Arns et al., 2020). Besides, since the skew surge is an integrated measure calculated within tidal cycles, it runs the risk of losing information of changes in water levels driven by meteorological factors (Mawdsley and Haigh, 2016; Williams et al., 2016). For example, Mawdsley and Haigh (2016) mentioned that the skew surge failed in capturing extreme storm surge caused by tropical cyclones. Therefore, we studied the compound floods based on the traditional non-tidal residual in this study. Although the uncertainties remain, we would like to highlight the contribution of our results on revealing the evolutions of compound floods potential from heavy precipitation and storm surge driven by meteorological systems based on historical observations.

CONCLUSION

In this study, the spatial and temporal characteristics of concurrences of precipitation and storm surge were examined based on observed storm surge and precipitation with the longest overlapping record of >120 years. First, the spatial distribution and seasonal variation of concurrent extreme precipitation and storm surge were presented. Then the trends in compound floods, precipitation under extreme storm surge, and storm surge under extreme precipitation were estimated to illustrate the long-term changes in compound floods. Last, the changes in weather conditions associated with precipitation under extreme storm surge, and storm surge under extreme precipitation in three tide gauges were analyzed to investigate the possible mechanisms associated with the changes in compound floods. Our main findings include:

1) The areas including southern Europe, the west and northeast coast of the US, and northern Japan experienced >12 compound flood days per year, followed by the east and southeast of the US, northern Europe, western Australia, and Japan, where experienced average of 8–12 compound flood days per year. The seasonal variation analysis showed that in the south and east coast of the US, the north of South America, East Asia, and northern Australia, most of the compound floods occurred during tropical cyclones seasons (i.e., July–September in North Hemisphere and December–February in South Hemisphere), while in mid and high-latitude areas (i.e., the north of North America, Europe, the south of South America and southern Australia), most occurrences of compound floods concentrated on the winter (i.e., November–January in North Hemisphere and June–August in South Hemisphere).
2) Our results on evolutions of frequency of compound flood days showed an increasing trend in compound flood risk in most areas across the globe except Japan. Europe experienced the most substantial increase in compound flood days (i.e., increased by > 2 days per decade), followed by the east coast of the US (i.e., increased by 1–3 days per decade). Increased precipitation under extreme storm surge could be identified in North America, Europe, and Australia, indicating more intense precipitation under extreme storm surge events. The changes in storm surge under extreme precipitation showed larger regional variation. The significant increasing trends could be found in Europe, the east coast of the US, while decrease trends were mainly found in Japan and the west coast of the US. This result was consistent with the changes in the annual number of

compound flood days. The contribution analysis indicated that except in northern Europe and some tide gauges on the east coast of the US and southern Australia, the fractional contribution of storm surge on the changes in the number of compound flood days exceeded 50% in most areas across the globe, which demonstrated that the changes in storm surge were more likely to dominate the changes in compound floods.

3) The analyses on meteorological variables suggested that the changes in storm surge under extreme precipitation were likely driven by changes in sea level pressure and near-land winds, while the changes in precipitation under extreme storm surge were associated with the changes in precipitable water content and the convective activity.

This study presented the spatial distribution and seasonal variation of compound floods from precipitation and storm surge, estimated the changes in compound floods, precipitation under extreme storm surge, and storm surge under extreme precipitation across the globe. These analyses were based on the observed precipitation and storm surge data with the longest record lengths of 126 years, which can provide useful information for better understanding the evolution in compound floods, and serve as scientific references in flood risk management and climate change adaptation strategy design.

DATA AVAILABILITY STATEMENT

Publicly available datasets were analyzed in this study. This data can be found here: The daily precipitation data from Global Historical Climatology Network (GHCN-Daily) is available at https://www.ncdc.noaa.gov/ghcn-daily-description. The hourly sea level from the Global Extreme Sea Level Analysis version 2 (GESLA-2) can be obtained from https://www.gesla.org/. The NCEP/NCAR reanalysis dataset can be obtained from https://psl.noaa.gov/data/gridded/data.ncep.reanalysis.html.

AUTHOR CONTRIBUTIONS

QL, JL, and YL designed study; YL and JL performed research; YL, QL, JL, QZ, XZ, GW analyzed and wrote the paper.

FUNDING

The work described in this paper was supported by grants from the National Key R&D Program of China (Project No. 2019YFC1510400), Natural Science Foundation of China (NSFC) General Program (41971386), the Research Grants Council of the Hong Kong Special Administrative Region, China (HKBU12303517, HKBU12302518, and 12301820), and Guangdong-Hong Kong Joint Laboratory for Water Security (2020B1212030005).

SUPPLEMENTARY MATERIAL

The Supplementary Material for this article can be found online at: https://www.frontiersin.org/articles/10.3389/feart.2021.660359/full#supplementary-material

REFERENCES

Arns, A., Wahl, T., Wolff, C., Vafeidis, A. T., Haigh, I. D., Woodworth, P., et al. (2020). Non-linear Interaction Modulates Global Extreme Sea Levels, Coastal Flood Exposure, and Impacts. *Nat. Commun.* 11 (1), 1–9. doi:10.1038/s41467-020-15752-5

Bevacqua, E., Maraun, D., Hobæk Haff, I., Widmann, M., and Vrac, M. (2017). Multivariate Statistical Modelling of Compound Events via Pair-Copula Constructions: Analysis of Floods in Ravenna (Italy). *Hydrol. Earth Syst. Sci.* 21 (6), 2701–2723. doi:10.5194/hess-21-2701-2017

Bevacqua, E., Maraun, D., Vousdoukas, M. I., Voukouvalas, E., Vrac, M., Mentaschi, L., et al. (2019). Higher Probability of Compound Flooding from Precipitation and Storm Surge in Europe under Anthropogenic Climate Change. *Sci. Adv.* 5 (9), 5531. doi:10.1126/sciadv.aaw5531

Bevacqua, E., Vousdoukas, M. I., Shepherd, T. G., and Vrac, M. (2020a). Brief Communication: The Role of Using Precipitation or River Discharge Data when Assessing Global Coastal Compound Flooding. *Nat. Hazards Earth Syst. Sci.* 20 (6), 1765–1782. doi:10.5194/nhess-20-1765-2020

Bevacqua, E., Vousdoukas, M. I., Zappa, G., Hodges, K., Shepherd, T. G., Maraun, D., et al. (2020b). More Meteorological Events that Drive Compound Coastal Flooding Are Projected under Climate Change. *Commun. Earth Environ.* 1 (1). doi:10.1038/s43247-020-00044-z

Booth, J. F., Rieder, H. E., and Kushnir, Y. (2016). Comparing hurricane and Extratropical Storm Surge for the Mid-Atlantic and Northeast Coast of the United States for 1979-2013. *Environ. Res. Lett.* 11 (9). doi:10.1088/1748-9326/11/9/094004

Intergovernmental Panel on Climate Change (2012). "Changes in Climate Extremes and Their Impacts on the Natural Physical Environment," in *Managing the Risks of Extreme Events and Disasters to Advance Climate Change Adaptation*. C. B. Field, V. Barros, T. F. Stocker, D. Qin, D. Jon Dokken, K. L. Ebi, et al. (Cambridge, UK, and New York, NY, USA: Cambridge University Press), 109–230.

Chan, F. K. S., Mitchell, G., Adekola, O., and McDonald, A. (2012). Flood Risk in Asia's Urban Mega-Deltas. *Environ. Urbanization Asia* 3 (1), 41–61. doi:10.1177/097542531200300103

Couasnon, A., Eilander, D., Muis, S., Veldkamp, T. I. E., Haigh, I. D., Wahl, T., et al. (2020). Measuring Compound Flood Potential from River Discharge and Storm Surge Extremes at the Global Scale. *Nat. Hazards Earth Syst. Sci.* 20 (2), 489–504. doi:10.5194/nhess-20-489-2020

Dong, S., Sun, Y., Li, C., Zhang, X., Min, S.-K., and Kim, Y.-H. (2021). Attribution of Extreme Precipitation with Updated Observations and CMIP6 Simulations. *J. Clim.* 34 (3), 871–881. doi:10.1175/jcli-d-19-1017.1

Dong, W., Lin, Y., Wright, J. S., Xie, Y., Yin, X., and Guo, J. (2019). Precipitable Water and CAPE Dependence of Rainfall Intensities in China. *Clim. Dyn.* 52 (5–6), 3357–3368. doi:10.1007/s00382-018-4327-8

Emanuel, K. (2017). Assessing the Present and Future Probability of Hurricane Harvey's Rainfall. *Proc. Natl. Acad. Sci. USA* 114 (48), 12681–12684. doi:10.1073/pnas.1716222114

Evans, J. L., and Hart, R. E. (2003). Objective Indicators of the Life Cycle Evolution of Extratropical Transition for Atlantic Tropical Cyclones. *Mon. Wea. Rev.* 131 (5), 909–925. doi:10.1175/1520-0493(2003)131<0909:oiotlc>2.0.co;2

Fatichi, S., and Caporali, E. (2009). A Comprehensive Analysis of Changes in Precipitation Regime in Tuscany. *Int. J. Climatol.* 29 (13), 1883–1893. doi:10.1002/joc.1921

Frank, W. M., and Ritchie, E. A. (2001). Effects of Vertical Wind Shear on the Intensity and Structure of Numerically Simulated Hurricanes. *Mon. Wea. Rev.* 129 (9), 2249–2269. doi:10.1175/1520-0493(2001)129<2249:eovwso>2.0.co;2

Gemmer, M., Fischer, T., Jiang, T., Su, B., and Liu, L. L. (2011). Trends in Precipitation Extremes in the Zhujiang River basin, South China. *J. Clim.* 24 (3), 750–761. doi:10.1175/2010jcli3717.1

Gori, A., Lin, N., and Xi, D. (2020). Tropical Cyclone Compound Flood Hazard Assessment: From Investigating Drivers to Quantifying Extreme Water Levels. *Earth's Future* 8 (12). doi:10.1029/2020ef001660

Gu, X., Zhang, Q., Singh, V. P., and Shi, P. (2017). Nonstationarity in Timing of Extreme Precipitation across China and Impact of Tropical Cyclones. *Glob. Planet. Change* 149, 153–165. doi:10.1016/j.gloplacha.2016.12.019

Hamed, K. H., and Ramachandra Rao, A. (1998). A Modified Mann-Kendall Trend Test for Autocorrelated Data. *J. Hydrol.* 204 (1–4), 182–196. doi:10.1016/s0022-1694(97)00125-x

Hawcroft, M. K., Shaffrey, L. C., Hodges, K. I., and Dacre, H. F. (2012). How Much Northern Hemisphere Precipitation Is Associated with Extratropical Cyclones?. *Geophys. Res. Lett.* 39 (24), 1–6. doi:10.1029/2012gl053866

Hawcroft, M., Walsh, E., Hodges, K., and Zappa, G. (2018). Significantly Increased Extreme Precipitation Expected in Europe and North America from Extratropical Cyclones. *Environ. Res. Lett.* 13 (12), 124006. doi:10.1088/1748-9326/aaed59

Hendry, A., Haigh, I. D., Nicholls, R. J., Winter, H., Neal, R., Wahl, T., et al. (2019). Assessing the Characteristics and Drivers of Compound Flooding Events Around the UK Coast. *Hydrol. Earth Syst. Sci.* 23 (7), 3117–3139. doi:10.5194/hess-23-3117-2019

Hong Kong Observatory (2017).. Super Typhoon Hato (1713) 20 to 24 August 2017. Retrieved September 24, 2020, from Available at: https://www.weather.gov.hk/informtc/hato17/report.html.

Horsburgh, K. J., and Wilson, C. (2007). Tide-surge Interaction and its Role in the Distribution of Surge Residuals in the North Sea. *J. Geophys. Res. Oceans* 112 (8), 1–13. doi:10.1029/2006jc004033

Huntingford, C., Marsh, T., Scaife, A. A., Kendon, E. J., Hannaford, J., Kay, A. L., et al. (2014). Potential Influences on the United Kingdom's Floods of winter 2013/14. *Nat. Clim Change* 4 (9), 769–777. doi:10.1038/nclimate2314

Iannuccilli, M., Bartolini, G., Betti, G., Crisci, A., Grifoni, D., Gozzini, B., et al. (2021). Extreme Precipitation Events and Their Relationships with Circulation Types in Italy. *Int. J. Climatol*, 1–25. doi:10.1002/joc.7109

Ikeuchi, H., Hirabayashi, Y., Yamazaki, D., Muis, S., Ward, P. J., Winsemius, H. C., et al. (2017). Compound Simulation of Fluvial Floods and Storm Surges in a Global Coupled River-Coast Flood Model: Model Development and its Application to 2007 Cyclone Sidr in Bangladesh. *J. Adv. Model. Earth Syst.* 9 (4), 1847–1862. doi:10.1002/2017ms000943

Jane, R., Cadavid, L., Obeysekera, J., and Wahl, T. (2020). Multivariate Statistical Modelling of the Drivers of Compound Flood Events in South Florida. *Nat. Hazards Earth Syst. Sci.* 20 (10), 2681–2699. doi:10.5194/nhess-20-2681-2020

Kalnay, E., Kanamitsu, M., Kistler, R., Collins, W., Deaven, D., Gandin, L., et al. (1996). The NCEP/NCAR 40-year Reanalysis Project. *Bull. Amer. Meteorol. Soc.* 77 (3), 437–471. doi:10.1175/1520-0477(1996)077<0437:tnyrp>2.0.co;2

Karim, M., and Mimura, N. (2008). Impacts of Climate Change and Sea-Level Rise on Cyclonic Storm Surge Floods in Bangladesh. *Glob. Environ. Change* 18 (3), 490–500. doi:10.1016/j.gloenvcha.2008.05.002

Khanam, M., Sofia, G., Koukoula, M., Lazin, R., Nikolopoulos, E. I., Shen, X., et al. (2021). Impact of Compound Flood Event on Coastal Critical Infrastructures Considering Current and Future Climate. *Nat. Hazards Earth Syst. Sci.* 21 (2), 587–605. doi:10.5194/nhess-21-587-2021

Khouakhi, A., Villarini, G., and Vecchi, G. A. (2017). Contribution of Tropical Cyclones to Rainfall at the Global Scale. *J. Clim.* 30 (1), 359–372. doi:10.1175/jcli-d-16-0298.1

Klotzbach, P. J., Bowen, S. G., Pielke, R., and Bell, M. (2018). Continental U.S. Hurricane Landfall Frequency and Associated Damage: Observations and Future Risks. *Bull. Am. Meteorol. Soc.* 99 (7), 1359–1376. doi:10.1175/bams-d-17-0184.1

Kunkel, K. E., Karl, T. R., Squires, M. F., Yin, X., Stegall, S. T., and Easterling, D. R. (2020). Precipitation Extremes: Trends and Relationships with Average Precipitation and Precipitable Water in the Contiguous United States. *J. Appl. Meteorology Climatology* 59 (1), 125–142. doi:10.1175/jamc-d-19-0185.1

Kurniadi, A., Weller, E., Min, S. K., and Seong, M. G. (2021). Independent ENSO and IOD Impacts on Rainfall Extremes over Indonesia. *Int. J. Climatol* 41 (6), 3640–3656. doi:10.1002/joc.7040

Lai, Y., Li, J., Gu, X., Chen, Y. D., Kong, D., Gan, T. Y., et al. (2020). Greater Flood Risks in Response to Slowdown of Tropical Cyclones over the Coast of China. *Proc. Natl. Acad. Sci. USA* 117 (26), 14751–14755. doi:10.1073/pnas.1918987117

Leonard, M., Westra, S., Phatak, A., Lambert, M., van den Hurk, B., Mcinnes, K., et al. (2014). A Compound Event Framework for Understanding Extreme Impacts. *Wires Clim. Change* 5 (1), 113–128. doi:10.1002/wcc.252

Li, J., Zhang, Q., Chen, Y. D., and Singh, V. P. (2015). Future Joint Probability Behaviors of Precipitation Extremes across China: Spatiotemporal Patterns and Implications for Flood and Drought Hazards. *Glob. Planet. Change* 124, 107–122. doi:10.1016/j.gloplacha.2014.11.012

Li, J., Zhang, Q., Chen, Y. D., and Singh, V. P. (2013). GCMs-Based Spatiotemporal Evolution of Climate Extremes during the 21stcentury in China. *J. Geophys. Res. Atmos.* 118 (19), 11017–11035. doi:10.1002/jgrd.50851

Lian, J. J., Xu, K., and Ma, C. (2013). Joint Impact of Rainfall and Tidal Level on Flood Risk in a Coastal City with a Complex River Network: A Case Study of Fuzhou City, China. *Hydrol. Earth Syst. Sci.* 17 (2), 679–689. doi:10.5194/hess-17-679-2013

Lim, E.-P., and Simmonds, I. (2007). Southern Hemisphere winter Extratropical Cyclone Characteristics and Vertical Organization Observed with the ERA-40 Data in 1979-2001. *J. Clim.* 20 (11), 2675–2690. doi:10.1175/jcli4135.1

Liu, M., Vecchi, G. A., Smith, J. A., and Murakami, H. (2017). The Present-Day Simulation and Twenty-First-century Projection of the Climatology of Extratropical Transition in the North Atlantic. *J. Clim.* 30 (8), 2739–2756. doi:10.1175/jcli-d-16-0352.1

Mawdsley, R. J., and Haigh, I. D. (2016). Spatial and Temporal Variability and Long-Term Trends in Skew Surges Globally. *Front. Mar. Sci.* 3, 1–17. doi:10.3389/fmars.2016.00029

Menne, M. J., Durre, I., Vose, R. S., Gleason, B. E., and Houston, T. G. (2012). An Overview of the Global Historical Climatology Network-Daily Database. *J. Atmos. Oceanic Tech.* 29 (7), 897–910. doi:10.1175/jtech-d-11-00103.1

Milly, P. C. D., Betancourt, J., Falkenmark, M., Hirsch, R. M., Kundzewicz, Z. W., Lettenmaier, D. P., et al. (2008). Stationarity Is Dead: Whither Water Management?. *Science* 319 (5863), 573–574. doi:10.1126/science.1151915

Moftakhari, H. R., Salvadori, G., AghaKouchak, A., Sanders, B. F., and Matthew, R. A. (2017). Compounding Effects of Sea Level Rise and Fluvial Flooding. *Proc. Natl. Acad. Sci. USA* 114 (37), 9785–9790. doi:10.1073/pnas.1620325114

Moftakhari, H., Schubert, J. E., AghaKouchak, A., Matthew, R. A., and Sanders, B. F. (2019). Linking Statistical and Hydrodynamic Modeling for Compound Flood hazard Assessment in Tidal Channels and Estuaries. *Adv. Water Resour.* 128, 28–38. doi:10.1016/j.advwatres.2019.04.009

Muis, S., Haigh, I. D., Guimarães Nobre, G., Aerts, J. C. J. H., and Ward, P. J. (2018). Influence of El Niño-Southern Oscillation on Global Coastal Flooding. *Earth's Future* 6 (9), 1311–1322. doi:10.1029/2018ef000909

Neumann, B., Vafeidis, A. T., Zimmermann, J., and Nicholls, R. J. (2015). Future Coastal Population Growth and Exposure to Sea-Level Rise and Coastal Flooding - A Global Assessment. *PLoS ONE* 10 (3). doi:10.1371/journal.pone.0118571

Pawlowicz, R., Beardsley, B., and Lentz, S. (2002). Classical Tidal Harmonic Analysis Including Error Estimates in MATLAB Using T_TIDE. *Comput. Geosciences* 28 (8), 929–937. doi:10.1016/s0098-3004(02)00013-4

Pinto, J. G., Gómara, I., Masato, G., Dacre, H. F., Woollings, T., and Caballero, R. (2014). Large-scale Dynamics Associated with Clustering of Extratropical Cyclones Affecting Western Europe. *J. Geophys. Res. Atmos.* 119 (24), 13704–13719. doi:10.1002/2014jd022305

Raymond, C., Horton, R. M., Zscheischler, J., Martius, O., AghaKouchak, A., Balch, J., et al. (2020). Understanding and Managing Connected Extreme Events. *Nat. Clim. Chang.* 10 (7), 611–621. doi:10.1038/s41558-020-0790-4

Ridder, N. N., Pitman, A. J., Westra, S., Ukkola, A., Hong, X. Do., Bador, M., et al. (2020). Global Hotspots for the Occurrence of Compound Events. *Nat. Commun.* 11 (1), 1–10. doi:10.1038/s41467-020-20502-8

Sen, P. K. (1968). Estimates of the Regression Coefficient Based on Kendall's Tau. *J. Am. Stat. Assoc.* 63 (3), 1379–1389. doi:10.1080/01621459.1968.10480934

She, D., Shao, Q., Xia, J., Taylor, J. A., Zhang, Y., Zhang, L., et al. (2015). Investigating the Variation and Non-stationarity in Precipitation Extremes Based on the Concept of Event-Based Extreme Precipitation. *J. Hydrol.* 530, 785–798. doi:10.1016/j.jhydrol.2015.10.029

Svensson, C., and Jones, D. A. (2002). Dependence between Extreme Sea Surge, River Flow and Precipitation in Eastern Britain. *Int. J. Climatol.* 22 (10), 1149–1168. doi:10.1002/joc.794

Svensson, C., and Jones, D. A. (2004). Dependence between Sea Surge, River Flow and Precipitation in South and West Britain. *Hydrol. Earth Syst. Sci.* 8 (5), 973–992. doi:10.5194/hess-8-973-2004

Towey, K. L., Booth, J. F., Frei, A., and Sinclair, M. R. (2018). Track and Circulation Analysis of Tropical and Extratropical Cyclones that Cause strong Precipitation and Streamflow Events in the New York City Watershed. *J. Hydrometeorology* 19 (6), 1027–1042. doi:10.1175/jhm-d-17-0199.1

Tramblay, Y., Villarini, G., and Zhang, W. (2020). Observed Changes in Flood hazard in Africa. *Environ. Res. Lett.* 15 (10), 1040b5. doi:10.1088/1748-9326/abb90b

Van Den Hurk, B., Van Meijgaard, E., De Valk, P., Van Heeringen, K.-J., and Gooijer, J. (2015). Analysis of a Compounding Surge and Precipitation Event in the Netherlands. *Environ. Res. Lett.* 10 (3), 035001. doi:10.1088/1748-9326/10/3/035001

Vousdoukas, M. I., Mentaschi, L., Voukouvalas, E., Verlaan, M., Jevrejeva, S., Jackson, L. P., et al. (2018). Global Probabilistic Projections of Extreme Sea Levels Show Intensification of Coastal Flood hazard. *Nat. Commun.* 9 (1), 2360. doi:10.1038/s41467-018-04692-w

Wahl, T., Jain, S., Bender, J., Meyers, S. D., and Luther, M. E. (2015). Increasing Risk of Compound Flooding from Storm Surge and Rainfall for Major US Cities. *Nat. Clim Change* 5 (12), 1093–1097. doi:10.1038/nclimate2736

Walsh, K. J. E., McBride, J. L., Klotzbach, P. J., Balachandran, S., Camargo, S. J., Holland, G., et al. (2016). Tropical Cyclones and Climate Change. *Wires Clim. Change* 7 (1), 65–89. doi:10.1002/wcc.371

Wang, Q., Xu, Y., Wei, N., Wang, S., and Hu, H. (2019). Forecast and Service Performance on Rapidly Intensification Process of Typhoons Rammasun (2014) and Hato (2017). *Trop. Cyclone Res. Rev.* 8 (1), 18–26. doi:10.1016/j.tcrr.2019.07.002

Ward, P. J., Couasnon, A., Eilander, D., Haigh, I. D., Hendry, A., Muis, S., et al. (2018). Dependence between High Sea-Level and High River Discharge Increases Flood hazard in Global Deltas and Estuaries. *Environ. Res. Lett.* 13 (8). doi:10.1088/1748-9326/aad400

Weisse, R., von Storch, H., Niemeyer, H. D., and Knaack, H. (2012). Changing North Sea Storm Surge Climate: An Increasing hazard?. *Ocean Coastal Manag.* 68, 58–68. doi:10.1016/j.ocecoaman.2011.09.005

Williams, J., Horsburgh, K. J., Williams, J. A., and Proctor, R. N. F. (2016). Tide and Skew Surge independence: New Insights for Flood Risk. *Geophys. Res. Lett.* 43 (12), 6410–6417. doi:10.1002/2016gl069522

Wong, M. L. M., and Chan, J. C. L. (2004). Tropical Cyclone Intensity in Vertical Wind Shear. *J. Atmos. Sci.* 61 (15), 1859–1876. doi:10.1175/1520-0469(2004)061<1859:tciivw>2.0.co;2

Woodworth, P. L., Hunter, J. R., Marcos, M., Caldwell, P., Menéndez, M., and Haigh, I. (2016). Towards a Global Higher-Frequency Sea Level Dataset. *Geosci. Data J.* 3 (2), 50–59. doi:10.1002/gdj3.42

Xu, H., Xu, K., Bin, L., Lian, J., and Ma, C. (2018). Joint Risk of Rainfall and Storm Surges during Typhoons in a Coastal City of Haidian Island, China. *Int. J. Environ. Res. Public Health* 15 (7). doi:10.3390/ijerph15071377

Xu, H., Xu, K., Lian, J., and Ma, C. (2019). Compound Effects of Rainfall and Storm Tides on Coastal Flooding Risk. *Stoch Environ. Res. Risk Assess.* 33 (7), 1249–1261. doi:10.1007/s00477-019-01695-x

Yanase, W., and Niino, H. (2015). Idealized Numerical Experiments on Cyclone Development in the Tropical, Subtropical, and Extratropical Environments. *J. Atmos. Sci.* 72 (9), 3699–3714. doi:10.1175/jas-d-15-0051.1

Yanase, W., and Niino, H. (2019). Parameter Sweep Experiments on a Spectrum of Cyclones with Diabatic and Baroclinic Processes. *J. Atmos. Sci.* 76 (7), 1917–1935. doi:10.1175/jas-d-18-0232.1

You, Q., Kang, S., Aguilar, E., Pepin, N., Flügel, W.-A., Yan, Y., et al. (2011). Changes in Daily Climate Extremes in China and Their Connection to the Large Scale Atmospheric Circulation during 1961-2003. *Clim. Dyn.* 36 (11–12), 2399–2417. doi:10.1007/s00382-009-0735-0

Yu, Y. C., Chen, H., Shih, H. J., Chang, C. H., Hsiao, S. C., Chen, W. B., et al. (2019). Assessing the Potential Highest Storm Tide hazard in Taiwan Based on 40-year Historical Typhoon Surge Hindcasting. *Atmosphere* 10 (6). doi:10.3390/atmos10060346

Zhai, P., Zhang, X., Wan, H., and Pan, X. (2005). Trends in Total Precipitation and Frequency of Daily Precipitation Extremes over China. *J. Clim.* 18 (7), 1096–1108. doi:10.1175/jcli-3318.1

Zhang, Q., Li, J., Gu, X., and Shi, P. (2018b). Is the Pearl River basin, China, Drying or Wetting? Seasonal Variations, Causes and Implications. *Glob. Planet. Change* 166, 48–61. doi:10.1016/j.gloplacha.2018.04.005

Zhang, Q., Li, J., Singh, V. P., and Xu, C.-Y. (2013). Copula-based Spatio-Temporal Patterns of Precipitation Extremes in China. *Int. J. Climatol.* 33 (5), 1140–1152. doi:10.1002/joc.3499

Zhang, W., Vecchi, G. A., Murakami, H., Villarini, G., Delworth, T. L., Yang, X., et al. (2018a). Dominant Role of Atlantic Multidecadal Oscillation in the Recent Decadal Changes in Western North Pacific Tropical Cyclone Activity. *Geophys. Res. Lett.* 45 (1), 354–362. doi:10.1002/2017gl076397

Zhang, W., Villarini, G., Vecchi, G. A., and Smith, J. A. (2018c). Urbanization Exacerbated the Rainfall and Flooding Caused by hurricane Harvey in Houston. *Nature* 563 (7731), 384–388. doi:10.1038/s41586-018-0676-z

Zhang, W. Z., Shi, F., Hong, H. S., Shang, S. P., and Kirby, J. T. (2010). Tide-surge Interaction Intensified by the Taiwan Strait. *J. Geophys. Res. Oceans* 115 (6), 1–17. doi:10.1029/2009jc005762

Zhang, X., Aguilar, E., Sensoy, S., Melkonyan, H., Tagiyeva, U., Ahmed, N., et al. (2005). Trends in Middle East Climate Extreme Indices from 1950 to 2003. *J. Geophys. Res. Atmospheres* 110 (22), 1–12. doi:10.1029/2005jd006181

Zhang, X., Alexander, L., Hegerl, G. C., Jones, P., Tank, A. K., Peterson, T. C., et al. (2011). Indices for Monitoring Changes in Extremes Based on Daily Temperature and Precipitation Data. *Wires Clim. Change* 2 (6), 851–870. doi:10.1002/wcc.147

Zheng, F., Westra, S., and Sisson, S. A. (2013). Quantifying the Dependence between Extreme Rainfall and Storm Surge in the Coastal Zone. *J. Hydrol.* 505, 172–187. doi:10.1016/j.jhydrol.2013.09.054

Zscheischler, J., Westra, S., Van Den Hurk, B. J. J. M., Seneviratne, S. I., Ward, P. J., Pitman, A., et al. (2018). Future Climate Risk from Compound Events. *Nat. Clim Change* 8 (6), 469–477. doi:10.1038/s41558-018-0156-3

Conflict of Interest: The authors declare that the research was conducted in the absence of any commercial or financial relationships that could be construed as a potential conflict of interest.

frontiers in Earth Science

ORIGINAL RESEARCH
published: 26 July 2021
doi: 10.3389/feart.2021.674037

Intensified Moisture Sources of Heavy Precipitation Events Contributed to Interannual Trend in Precipitation Over the Three-Rivers-Headwater Region in China

Ruiyu Zhao, Bin Chen and Xiangde Xu*

State Key Laboratory of Severe Weather, Chinese Academy of Meteorological Sciences, Beijing, China

Evidence has indicated an overall wetting trend over the Three-Rivers Headwater Region (TRHR) in the recent decades, whereas the possible mechanisms for this change remain unclear. Detecting the main moisture source regions of the water vapor and its increasing trend over this region could help understand the long-term precipitation change. Based on the gauge-based precipitation observation analysis, we find that the heavy precipitation events act as the main contributor to the interannual increasing trend of summer precipitation over the TRHR. A Lagrangian moisture tracking methodology is then utilized to identify the main moisture source of water vapor over the target region for the boreal summer period of 1980–2017, with focus particularly on exploring its change associated with the interannual trend of precipitation. On an average, the moisture sources for the target regions cover vast regions, including the west and northwest of the Tibetan Plateau by the westerlies, the southwest by the Indian summer monsoon, and the adjacent regions associated with the local recycling. However, the increased interannual precipitation trend over the TRHR could be largely attributed to the enhanced moisture sources from the neighboring northeastern areas of the targeted region, particularly associated with the heavy precipitation events. The increased water vapor transport from the neighboring areas of the TRHR potentially related to the enhanced local hydrological recycling over these regions plays a first leading role in the recent precipitation increase over the TRHR.

Keywords: heavy precipitation, interannual trend, Three-Rivers headwater region, moisture sources, climate change

Edited by:
Ming Luo,
Sun Yat-Sen University, China

Reviewed by:
Ronald Kwan Kit Li,
The Chinese University of Hong Kong, China
Qiang Liu,
Beijing Normal University, China

****Correspondence:***
Bin Chen
chenbin@cma.gov.cn

Specialty section:
This article was submitted to Atmospheric Science, a section of the journal Frontiers in Earth Science

Received: *28 February 2021*
Accepted: *25 May 2021*
Published: *26 July 2021*

Citation:
Zhao R, Chen B and Xu X (2021) Intensified Moisture Sources of Heavy Precipitation Events Contributed to Interannual Trend in Precipitation Over the Three-Rivers-Headwater Region in China.
Front. Earth Sci. 9:674037.
doi: 10.3389/feart.2021.674037

INTRODUCTION

The Three-Rivers Headwater Region (TRHR), located at the high-altitude region of the Tibetan Plateau (TP), acts as the "Asian water tower" (Immerzeel et al., 2010; Xu et al., 2014; Yao et al., 2017), which supplies considerable water for many Asian major rivers, including the Yellow, Yangtze, and Lantscang (as shown in **Figure 1A**). The TRHR is considered to be more vulnerable to extreme weather events since it is under the influences of the South Asian monsoon, East Asian monsoon, and mid-latitude westerlies (Xi et al., 2018; Sun et al., 2019).

During the past decades, the whole TRHR was getting wetter under the global climate change (Li et al., 2010; Gao et al., 2014). The annual precipitation overall shows an increasing trend, even though

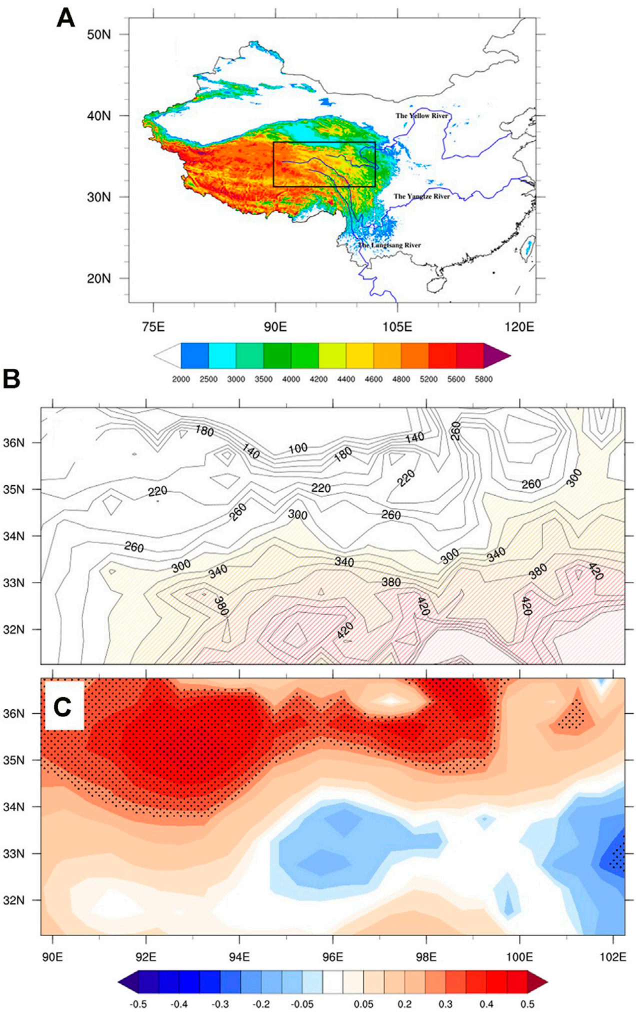

FIGURE 1 | (A) The topographical distribution (color shaded, unit in m) with the height exceeding 2000 m. **(B)** The climatology of the summer seasonal mean (June, July, and August) precipitation during the period of 1980–2017 over the TRHR (unit in mm). The shaded area represents precipitation exceeding 330 mm; **(C)** The trend of annual summer precipitation over the TRHR calculated from the gauge-based precipitation from 1980 to 2017 (unit in mm yr^{-1}). The observed station precipitation data are based on the gridded daily precipitation observation data with a spatial resolution of $0.25^\circ \times 0.25^\circ$.

the precipitation in the TRHR exhibits spatial heterogeneity (Liang et al., 2013; Yi et al., 2013; Tong et al., 2014; Sun et al., 2018). In this context, the exploration of the nature of long-term trend and reasons behind increasing precipitation over the TRHR has become a hotspot of the academic community because of its societal ramifications (Yang et al., 2014; Wang et al., 2018; Gao et al., 2019).

Generally, a large amount of water vapor supply has been regarded as a priority for precipitation formation (Gimeno et al., 2012; Wang et al., 2018). Knowledge about the origin of water vapor that produces the rainfall over a target region could promote a better understanding of the long-term precipitation trend (Stohl and James 2004; Gimeno et al., 2012; Wang et al., 2018). It can be speculated that the increased precipitation in the TRHR could be associated with more water vapor supply, from either the internal sources or external moisture origins (Gao et al., 2014). The identification of the moisture origins in the TRHR and its change thereby merit further exploration.

Based on the above consideration, two questions will be discussed in this study: 1) What is the relative importance of different categories of precipitation that contributed to the long-term changes of summer precipitation over the TRHR? 2) What is the relationship between the change in moisture sources and the interannual trend of summer precipitation in the TRHR?

DATA AND METHODS

Data

The daily observed rainfall data with a spatial resolution of $0.25^\circ \times 0.25^\circ$ across mainland China are derived from more than 2,400 gauge stations by the National Meteorological Information Center of the China Meteorological Administration (NMIC/CMA). These observed precipitation data have been extensively utilized to explore the characteristics of the precipitation multi-scale spatiotemporal variation over the vast East Asian monsoon region (Shen et al., 2010; Zhang et al., 2021).

To conduct the Lagrangian modeling, the European Center for Medium-Range Weather Forecasts reanalysis (ERA)–Interim data are adopted as the meteorological fields to force the Lagrangian model. The meteorological fields contained in the ERA-Interim data are in the 60 hybrid model levels from the surface layer to 0.1 hPa, at a spatial resolution of $0.75^\circ \times 0.75^\circ$ and 6-hour time step. Further details of ERA-Interim can be found in the reference section (Dee et al., 2011).

Lagrangian Model and its Configuration

The FLEXPART model (FLEXIBLE PARTicle dispersion model) version V9.0 was used to carry out the multiyear simulations to produce the datasets for further moisture source diagnosis. This Lagrangian model has been widely utilized for a large amount of research on air mass and water vapor transport, particularly for the identification of moisture sources (Sodemann et al., 2008; Drumond et al., 2011; Drumond et al., 2019; Gimeno et al., 2012; Sun and Wang, 2014).

To start with, the model divides the whole column atmosphere over the Asian monsoon region (−15–60°N and 0–160°E) into approximately 2 million air parcels of constant mass (roughly equals $1.12 \times 1{,}012$ kg), which are advected freely by the three-dimensional winds during the simulation. The model integrates from 15 April to 15 September for each boreal summer. Eventually, a 6-hourly Lagrangian simulation output dataset, including three-dimensional positions, specific humidity, and temperature, is then constructed for each air parcel for the period of 1980–2017.

Method for Water Vapor Source Diagnosis

Considering that the high values of long-term summer precipitation trend are mainly located in the northwestern TRHR (**Figure 1C**), the target region is defined as the area

TABLE 1 | Definition of extreme precipitation indices.

Extreme precipitation index	Abbreviation	Definition	Unit
Simple daily intensity index	SDII	Intensity of daily precipitation (PR) on wet days	mm
Highest 1 day precipitation amount	RX1day	Maximum amount of precipitation on a single day	mm
Precipitation fraction due to very wet days	R95pTOT	Percentage of total precipitation from amount on very wet days when PR> 95th percentile of precipitation	%
Precipitation fraction due to extremely wet days	R99pTOT	Percentage of total precipitation from amount on extremely wet days when PR> 99th percentile of precipitation	%
Heavy precipitation days	R10 mm	Count of days when PR ≥ 10 mm	days
Very heavy precipitation days	R20 mm	Count of days when PR ≥ 20 mm	days
Consecutive dry days	CDD	Longest number of consecutive days with PR< 1 mm	days
Consecutive wet days	CWD	Longest number of consecutive days with PR ≥ 1mm	days

within 32.5°N–36°N and 80.5°E–92.5°E. To estimate the source of the water vapor, all air parcels that reached the target region in each time interval (6 h) during the modeling period are first selected and then tracked backward in time of 10 days, which approximately equals to the residence time of the water vapor in the atmosphere (Numaguti, 1999). A database of trajectories entering into this target region is then constructed first. Thus, the changes in the specific humidity (q) along each air particle within the time step (*t*) can be expressed as e–p = m (dq/dt), where m is the mass of the individual air particle and (e–p) is the evaporation-minus-precipitation. By adding (e–p) for all the particles over the entire atmospheric column for all the resident air parcels, we obtained the surface fresh water flux (E–P), where E and P are the rates of evaporation and precipitation, respectively. We track (E–P) from the target region backwards in time along the trajectories. The sources of water vapor are recognized as the regions in which the evaporation exceeds the precipitation, that is, (E–P)> 0. Then, the moisture source fields from all backward air parcels are linearly interpolated to a regular grid with 1.0° × 1.0° spatial resolution. Eventually, the climatology of well-resolved 6-hourly trajectory-based moisture uptake fields for the TRHR is constructed.

Definition of Extreme Precipitation Indices

In this study, eight extreme precipitation indices of ETCCDI (Expert Team on Climate Change Detection and Indices) were selected to characterize the precipitation anomalies over the TRHR (**Table 1**), which are defined and utilized commonly as the precipitation indices to study the extreme precipitation events (Karl, 1999; Peterson et al., 2001; Sillmann et al., 2013).

RESULTS AND DISCUSSION

The Interannual Trend of Summer Precipitation Over the TRHR

The climatological seasonal mean of summer precipitation over the TRHR calculated from the NMIC/CMA dataset for the period of 1980–2017 is shown in **Figure 1B**. It is not surprising that the distributions of the precipitation are less spatially uniform over this region due to its large spatial extent of a high-elevation terrain. The values of precipitation decrease from the southeast to northwest over the TRHR. This spatial pattern of summer rainfall reflects that the precipitation over the TRHR is mainly modulated by the water vapor conveyed by the low-latitudinal atmospheric flows associated with the Indian and Eastern Asian summer monsoon (Yao et al., 2013; Pan et al., 2018; Lai et al., 2021).

The corresponding interannual trend of precipitation over the TRHR is shown in **Figure 1C**. It is worth noting that a wide range of the south–southeast TRHR shows a negative trend, indicating that precipitation over these regions decreased for the past decades. However, the TRHR shows a general wetting trend, with the positive values mainly located north of 34°N, particularly in the northwestern TRHR, illustrating a significant increase in precipitation. Taking the TRHR as a whole region, the summer precipitation over the target region is increased due to the contribution from the northwestern part (as shown in **Figure 1C**, black dots). This interannual precipitation trend of the "south-drier and north-wetter" spatial pattern is consistent with the wetting trend in the TRHR, which have been demonstrated in previous studies, for example, by Yi et al. (2013) and Liu et al. (2019).

The Association of Interannual Trend With the Precipitation Intensity Anomalies

To further understand the characteristics of interannual trend of precipitation over the TRHR, we computed the time series of the extreme precipitation indices for the period of 1980–2017, together with the corresponding interannual precipitation (**Figure 2**). In general, most indices exhibited an increasing trend during the past decades. There are six indices (SDII, RX1day, R99Ptot, R10mm, R20mm, and CWD), which agree with the variation of regional summer precipitation in the TRHR on an interannual scale, with the correlation coefficient between each index and regional average precipitation being 0.658, 0.543, 0.628, 0.814, 0.628, and 0.549, respectively. Note that the variation of consecutive dry days (CDDs), which exhibits a small decreasing trend, is obviously in contrary to the variation of summer precipitation. This result is similar to the work by Xi et al. (2018), in which they argued that the consecutive dry days in the TRHR have been declining significantly in the past 50 years, with a decadal variability of 4.5 days per 10 years.

It is noteworthy that, on the interannual scale, the daily intensity index (SDII), precipitation fraction due to extremely

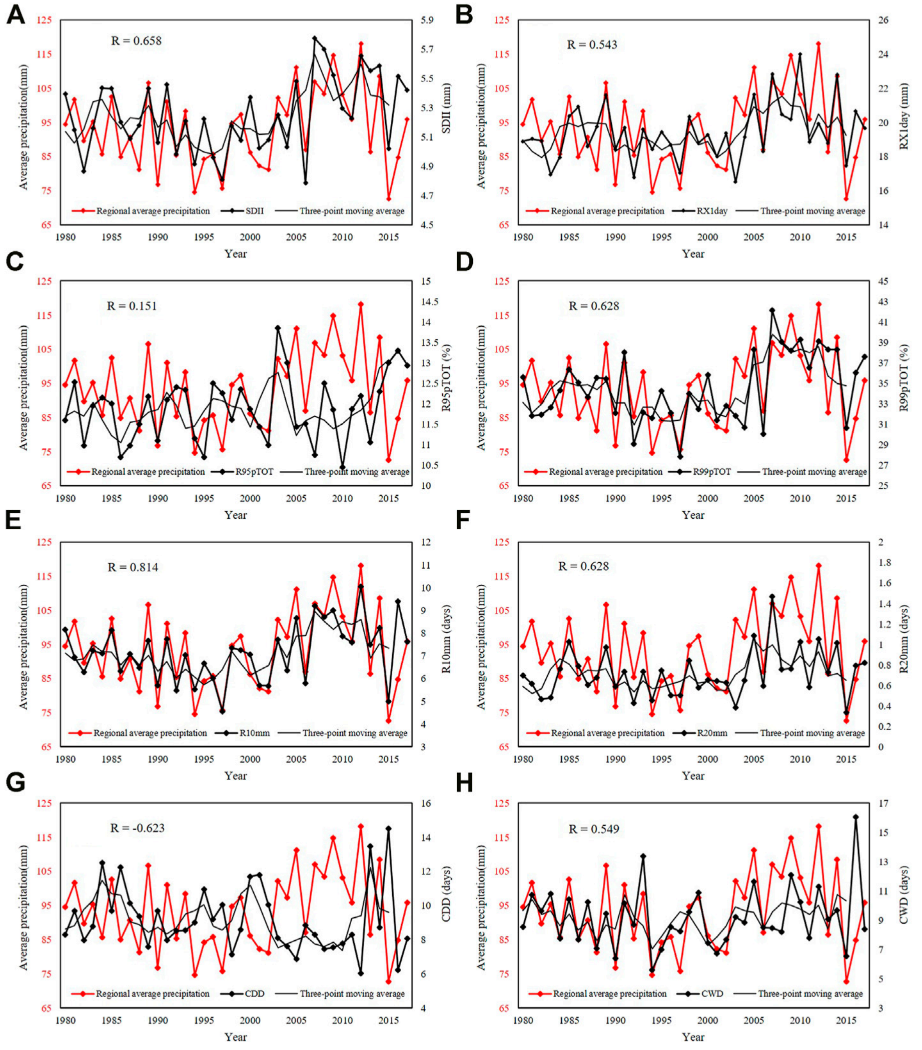

FIGURE 2 | The interannual variation of the eight extreme precipitation indices **(A)** SDII; **(B)** RX1 days; **(C)** R95dTOT; **(D)** R99pTOT; **(E)** R10mm; **(F)** R20mm; **(G)** CDD; and **(H)** CWD; the meaning of abbreviation for the six indices is shown in **Table 1**, together with the regional mean precipitation over the TRHR. The correlation coefficient between each index and the regional average precipitation is shown in the left corner, and seven indices have passed the 0.05 significance level except for the precipitation fraction due to wet days (R95pTOT).

wet days (R99pTOT), and very heavy precipitation days (R20mm) are closely correlated with the summer rainfall, with the correlation coefficients being 0.658, 0.628, and 0.628 (**Figures 2A,D,F**), respectively. In particular, the correlation coefficient between the heavy precipitation days and the summer mean precipitation in the TRHR reaches the highest value of 0.814 (**Figure 2E**). These results indicate that the interannual trend of summer precipitation over the TRHR may be related to the variation in the intensity and frequency of heavy and extreme precipitation events. In other words, the increase in the heavy and extreme heavy precipitation is potentially playing a critical role in the increasing summer mean rainfall.

To further demonstrate the impacts of changes in the intensity of precipitation events on the interannual trend of summer precipitation, we divided the precipitation events into four categories based on their daily values, namely, drizzle, little rain, moderate rain, and heavy rain (**Table 2**). We calculated the correlation coefficient, on the interannual scale, between the precipitation days of each category and the summer mean precipitation over the TRHR. Note that the annual precipitation is only positively correlated with days of heavy rain ($PR \geq 9$ mm) that occurred with a correlation coefficient reaching 0.547 but negatively correlated with other categories of

TABLE 2 | Correlation coefficient between precipitation intensity and the four categories of precipitation events on the interannual scale.

Range of rainfall	Precipitation type	Correlation coefficient
$1\text{ mm} < PR < 2\text{ mm}$	Drizzle	−0.58
2 mmPR<4 mm	Little rain	−0.537
4 mmPR<6 mm	Moderate rain	−0.383
$PR \geq 9$mm	Heavy rain	0.547

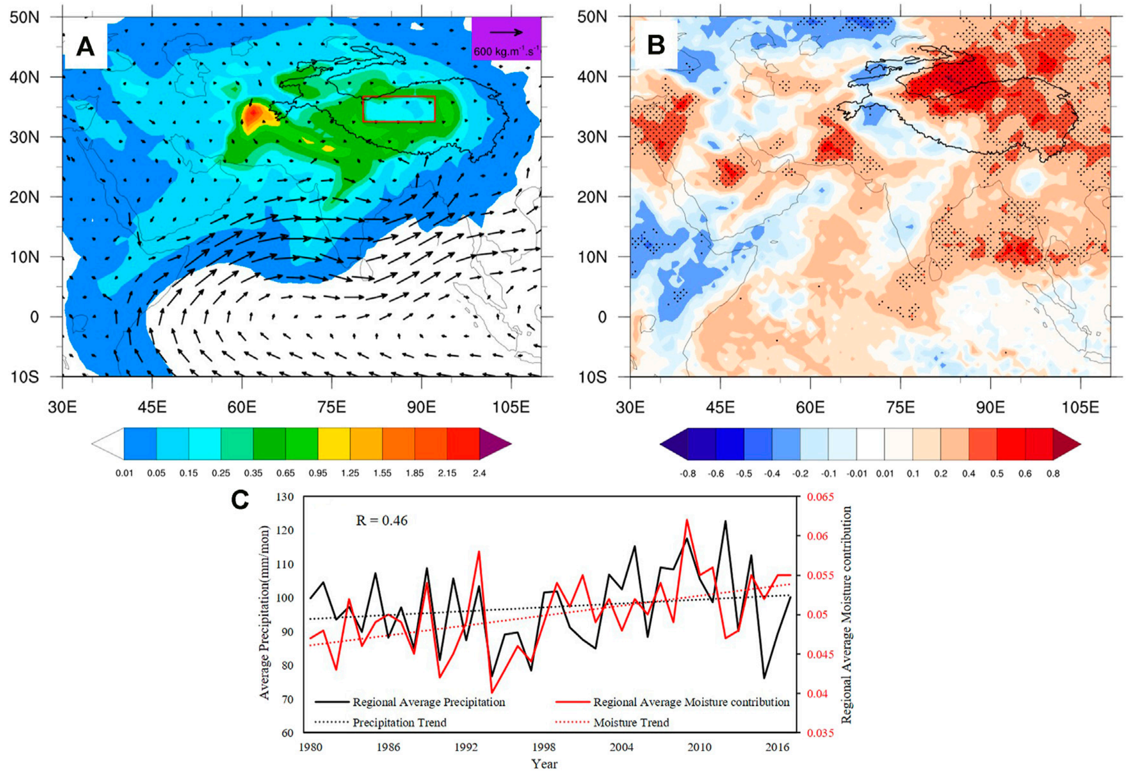

FIGURE 3 | (A) Horizontal spatial distribution of the climatological (1980–2017) integrated moisture source contribution, that is, the Lagrangian E-P diagnosed (E - P)> 0 of days 1–10 for the TRHR (units: millimeter per day). The vector indicates the vertically integrated water vapor flux derived from the ERA-Interim (JJA, 1980–2017, vector, in kgm^{-1} s^{-1}). The target region for the water sources diagnosis is defined as the continental areas within the red rectangular box (32.5°N–36°N and 80.5°E–92.5°E. **(B)** The interannual trend of the moisture contribution in the THRR for the period of 1980–2017. The dotted areas indicated the regions that exceeded the 0.05 significance level with the Student's t test. **(C)** Time series of interannual regional average moisture sources (red) and the regional average summer mean precipitation (black) in the TRHR. The dot lines indicate the long-term trend, respectively.

precipitation events. This result further suggests that the increase in heavy rainfall may be the main cause for the increasing interannual trend of precipitation over the TRHR, while light or moderate precipitation events play a minor role (**Supplementary Figure S1**). Combined with the results of the correlation coefficient of extreme precipitation indices above, the increase in the summer mean rainfall in the TRHR is largely dominated by the change of heavy precipitation events, which are reflected both in the increase of heavy precipitation days and the enhancement of precipitation intensity. These results would be further evidenced in the following section.

Summer Seasonal Mean of Evaporative Moisture Sources and its Long-Term Trend

Figure 3A exhibits the climatology of the summer seasonal mean moisture uptakes, that is, integrated (E - P)> 0 of days 1–10, together with the vertically integrated water vapor flux (vector). This result shows the average of all gains of moisture over the previous 10 days prior to reaching the TRHR. It can be found that those regions with the largest values, that is, the most influential moisture origins are largely located in India and its northwestern areas. This result partly agrees with previous researches by Sun and Wang (2014) and Chen et al. (2016), indicating that the moisture contribution from the adjacent regions could play a critical role in the water vapor supply and the remote moisture uptake from oceanic areas could be precipitated out during their period of transport. The regions over the Arabian Sea, the northern India, and even the tropical Indian Ocean are ranked as the second moisture source. It can be deduced that this spatial pattern of the moisture sources is consistent with the pattern of water vapor transport (**Figure 3A**, vector), indicating that the atmospheric vapor reaching the TRHR is mainly shaped by the Indian summer monsoon and the westerlies (Yao et al., 2013; Pan et al., 2018).

Note that the objective of this study was to identify the moisture sources of external water vapor reaching the TRHR; thus, only those air parcels penetrating the target region in each time interval (6 h) during the boreal summer are selected and then were tracked backward for 10 days to diagnose the moisture sources, which gave rise to a sharp discontinuity of moisture sources contribution at the edges of the target region box. However, a fraction of selected air parcels could return and reside in the target region by backward tracking, due to the influence of complicated local atmospheric circulations. These multi-boundary–crossing air parcels with increased humidity will

TABLE 3 | Determination of five precipitation types.

Threshold	<5th	(10th, 30th)	(40th, 60th)	(70th,95th)	>99th
Precipitation	PR < 0.44 mm	(0.64 mm,1.65 mm)	(2.26 mm,3.58 mm)	(4.36 mm,7.29 mm)	PR > 9.25 mm
Type	Dry	Light	Moderate	Heavy	Extremely heavy

result in the target region itself as a contributor, but with less significance.

The variation of the regional summer precipitation and moisture contribution represents a good consistency on the interannual scale (**Figure 3C**). Both the precipitation and moisture contribution show a similar trend, with turning points from decreasing to increasing occurring in the middle and late 1990s (1995). The Pearson correlation coefficient is 0.46, with a significance level above 0.05. This result shows that the moisture contribution for the precipitation could capture the variation of precipitation, which in turn indicates that the exploration on the variability of moisture sources could reveal the underlying mechanism of the regional precipitation evolution.

The interannual trend of moisture sources over the TRHR is illustrated in **Figure 3B**, with the dotted areas indicating the regions with a trend exceeding the 0.05 significance level with the Student's t test. The areas with positive values cover vast regions, including but not limited to southern Asia, the Arabian Sea, the Bay of Bengal, the northern India, and the vast areas of the Indian Ocean. However, the region that exhibits a significant increase in the trend is mainly centered on the adjacent regions to the TRHR itself, where contributions from the targeted west–northeastern TRHR increased the most in intensity.

Above results emphasize the importance of the local water vapor recycling, particularly in the surrounding area on the northwest side of the TRHR and the Tibetan Plateau. It has been evidenced that the strengthening of the local water vapor recycling process may correlate with the evapotranspiration over the TRHR, which in turn facilitated the growth of vegetation (Gan et al., 2020). Studies have further pointed out that the enhancement of the westerlies over the mid-latitude may be one reason for the continuous increase in moisture around the northwestern side of the plateau (Liao et al., 2018). Thus, we can deduce that the neighboring west–northeastern region supplies a large amount of extra moisture for increased precipitation, with the increased moisture contribution from the ocean playing a secondary role, although the water vapor from this region has a strong correlation with the interannual variation of precipitation in the TRHR (Chen et al., 2012; Zhang et al., 2019).

Interannual Trend Comparison for Different Categories of Precipitation Events

We have demonstrated that the interannual trend of summer rainfall over the TRHR could be largely attributed to the enhancement of the heavy and extreme precipitation events, both in frequency and intensity. However, a question remains to be elucidated: Do the areas with larger values of the interannual trend for the moisture contribution for summer mean precipitation coincide spatially with that for the heavy precipitation events?

To address this question, we utilized different percentiles as thresholds to categorize the precipitation events based on the daily observed regional precipitation. The details on the threshold selection and their corresponding magnitude of daily rainfall are listed in **Table 3**. The moisture sources for the different category precipitation events are calculated individually (Figure not shown). The moisture sources for the different category precipitation events show a similar spatial pattern, which is analogous to that for the summer mean precipitation, with a large amount of moisture originating from the vaster regions, such as the Central Asia, Indian Peninsula, the Bay of Bengal, and to the northwest of target region. However, differences exist among the different types of precipitation events. For example, the cross-equatorial moisture transport from the Indian Ocean is getting more significant for the heavy and extreme, comparing to the light and moderate (shown in **Supplementary Figure S2**). Further examination of the differences in the moisture sources for five categories of precipitation is beyond the scope of the present study.

Figure 4 shows the interannual trend of the moisture contribution, which is the same as **Figure 3B**, but corresponds to the five predefined category precipitation events. Obviously, the spatial distributions of the interannual trend for the moisture uptake vary significantly among the five categories of precipitation events. For the dry days, the long-term trend is less significant. For other types of precipitation events (i.e., the light, moderate, heavy, and extremely heavy), the interannual trend gets higher and higher. With the strength of precipitation intensity, the moisture contribution from the remote moisture sources originating from the tropical to subtropical Arabian Sea corridor gets more significant, which means that the external regions as the moisture uptake fields play an important role in the enhancement of rainfall. However, when we compare the results shown in **Figure 3B** to that in **Figure 4**, it is easy to find that the spatial pattern of the interannual trend in the moisture contribution by the heavy rainfall events coincides roughly with that for the overall moisture contribution, with the majority of the positive high-value areas centered over the areas neighboring the TRHR, including the northeastern and western parts of the Tibetan Plateau. This result affirms again that the heavy but not the extreme rainfall events play a first leading role in the increased interannual trend in the summer mean precipitation in the target region.

For a specific region, the trend of the moisture uptakes contribution to the rainfall events could be impacted by two factors: 1) the increases in large-scale water vapor transport and 2) the enhancement of local evaporation over the source origins (Gimeno et al., 2012). As shown in **Figure 4**, except for the relatively

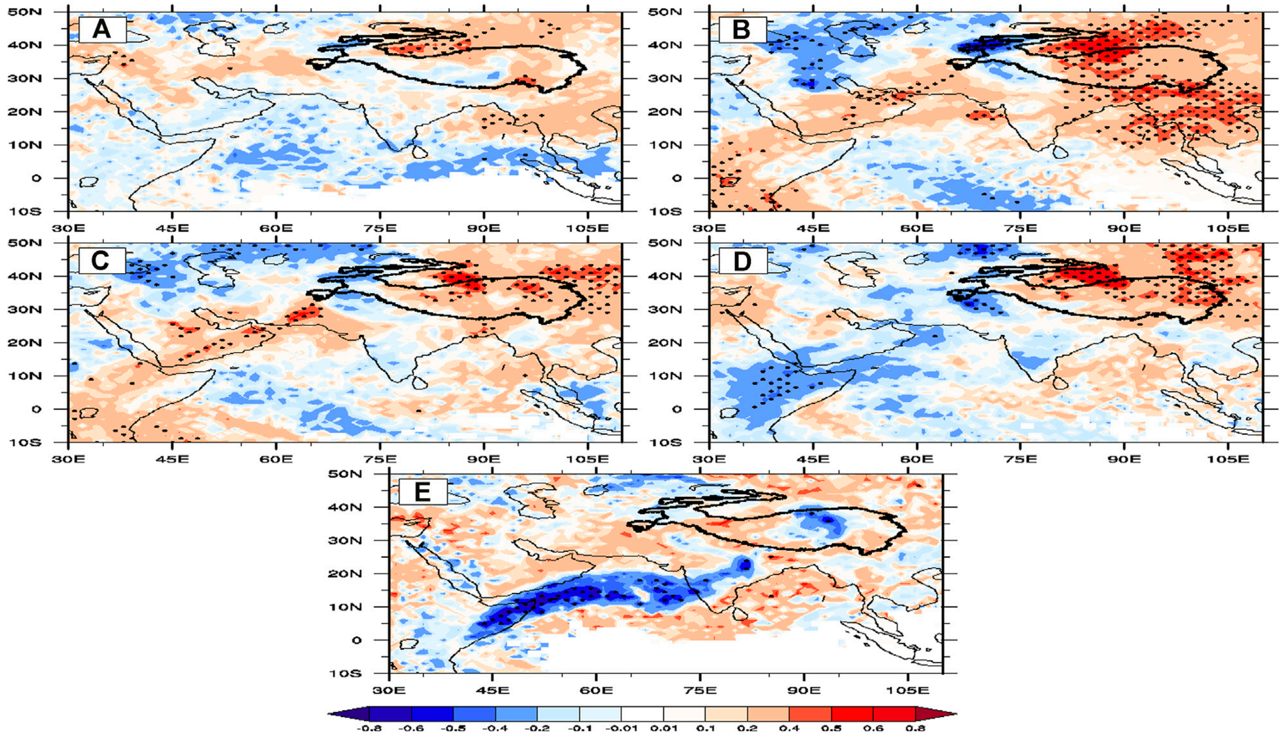

FIGURE 4 | Distribution for the interannual trend of the Lagrangian E-P diagnosed moisture sources contribution of the five category precipitation events for **(A)** dry, **(B)** light, **(C)** moderate, **(D)** heavy, and **(E)** extremely heavy, respectively. The dotted regions are significant at the 95% confidence level.

small contribution from the remote moisture sources, the increase of water vapor for the heavy rainfall events from the adjacent northwestern land areas are particularly significant, indicating the importance of the local recycling process of the plateau itself to the interannual trend of heavy precipitation over the TRHR.

CONCLUSION

During the recent decades, the Three-Rivers Headwater Region (TRHR) experiences an overall wetting trend, whereas the reasons it behind remain elusive. In order to shed some light on this issue, we examined the association of interannual trend of the summer mean precipitation with the anomalies in the intensity of precipitation. We also identified the remote evaporative moisture uptakes contributed to the rainfall over the TRHR during a summer period of 38 years (1980–2017), with focus particularly on the association of moisture sources with the variability in precipitation intensity. The main results of the present study could be summarized as follows:

1) The results show that the TRHR has been getting wetter during the recent decades, especially with the obvious increasing precipitation in the northwest of the TRHR. The interannual variation of the observed summer precipitation agrees well with the integrated diagnosed moisture sources, indicating that the changes of precipitation could be well captured by the moisture sources.
2) The moisture sources for the TRHR cover vast regions, including but not limited to the west and northwest of the Tibetan Plateau by the westerlies, and that from the southwest by the Indian summer monsoon. Compared to the contribution of oceanic moisture sources, the terrestrial moisture supply is more important. Also, the increased interannual precipitation trend over the TRHR could be largely attributed to the enhanced moisture sources from the neighboring northeastern areas of the target region.
3) Further analysis shows that enhanced moisture contribution highly resemble the heavy precipitation events. Thus, the enhanced water vapor transport conveyed by the heavy precipitation events from the neighboring areas of the TRHR, which is largely associated with the intensified land surface evaporation or local hydrological recycling over these regions, in combination with enhanced transport from low-latitude oceanic regions, play a critical role in supplying vapor for the recent summer rainfall increase over the TRHR.

The results of this research shed some light on the characteristics of the rainfall and underlying mechanisms associated with its interannual trend. However, due to the complexity of the land surface conditions and atmospheric circulations over the target area, the relationship between the changes in the atmospheric moisture uptakes and atmospheric circulations over the TRHR is elusive, which invites further studies.

DATA AVAILABILITY STATEMENT

The raw data supporting the conclusions of this article will be made available by the authors, without undue reservation.

AUTHOR CONTRIBUTIONS

BC designed the research. RZ and XX performed the data analysis, prepared all figures, and led the writing of the article. All the authors discussed the results and commented on the article. All authors contributed to the article and approved the submitted version.

FUNDING

This research is supported by the National Natural Science Foundation of China (Grant Nos. 91937301), the National Key Research and Development Program on Monitoring, Early Warning and Prevention of Major Natural Disaster (2018YFC1506001), S&T Development Fund of CAMS (2020KJ017 and 2021KJ021), the Open Research of the State Key Laboratory of Severe Weather, Chinese Academy of Meteorological Sciences (2019LASW-A04) and the second pilot project of the Second Tibetan Plateau Comprehensive Scientific Research Project (I07-T01-2018-06/06-JH).

SUPPLEMENTARY MATERIAL

The Supplementary Material for this article can be found online at: https://www.frontiersin.org/articles/10.3389/feart.2021.674037/full#supplementary-material

REFERENCES

Chen, B., and Xiang-De, X. (2016). Spatiotemporal Structure of the Moisture Sources Feeding Heavy Precipitation Events over the Sichuan Basin. *Int. J. Climatol* 36, 3446–3457. doi:10.1002/joc.4567

Chen, B., Xu, X.-D., Yang, S., and Zhang, W. (2012). On the Origin and Destination of Atmospheric Moisture and Air Mass over the Tibetan Plateau. *Theor. Appl. Climatol* 110 (3), 423–435. doi:10.1007/s00704-012-0641-y

Dee, D. P.Coauthors (2011). The ERA-Interim Reanalysis: Configuration and Performance of the Data Assimilation System. *Q. J. Roy Meteorol. Soc* 137, 553–597. doi:10.1002/qj.828

Drumond, A., Nieto, R., and Gimeno, L. (2011). On the Contribution of the Tropical Western Hemisphere Warm Pool Source of Moisture to the Northern Hemisphere Precipitation through a Lagrangian Approach. *J. Geophys. Res.* 116, D00Q04. doi:10.1029/2010jd015397

Drumond, A., Stojanovic, M., Nieto, R., Vicente-Serrano, S. M., and Gimeno, L. (2019). Linking Anomalous Moisture Transport and Drought Episodes in the IPCC Reference Regions. *Bull. Amer. Meteorol. Soc.* 100, 1481–1498. doi:10.1175/bams-d-18-0111.1

Gan, H. H., Jin, X. M., Zhang, X. C., and Zhu, X. Q. (2020). Temporal and Spatial Distribution of Evapotranspiration in Three-Rivers Headwater Region. *Geoscience*. doi:10.19657/j.geoscience.1000-8527.2020.075 (in chinese)

Gao, J., Yao, T., Masson-Delmotte, V., Steen-Larsen, H. C., and Wang, W. (2019). Collapsing Glaciers Threaten Asia's Water Supplies. *Nature* 565, 19–21. doi:10.1038/d41586-018-07838-4

Gao, Y., Cuo, L., and Zhang, Y. (2014). Changes in Moisture Flux over the Tibetan Plateau during 1979-2011 and Possible Mechanisms. *J. Clim.* 27, 1876–1893. doi:10.1175/JCLI-D-13-00321.1

Gimeno, L.Coauthors (2012). Oceanic and Terrestrial Sources of continental Precipitation. *Rev. Geophys.* 50 (5), 3647–3649. doi:10.1029/2012rg000389

Immerzeel, W. W., van Beek, L. P. H., and Bierkens, M. F. P. (2010). Climate Change Will Affect the Asian Water Towers. *Science* 328, 1382–1385. doi:10.1126/science.1183188

Karl, T. R., Nicholls, N., and Ghazi, A. (1999). CLIVAR/GCOS/WMO Workshop on Indices and Indicators for Climate Extremes Workshop Summary. *Climatic Change* 42 (1), 3–7. doi:10.1007/978-94-015-9265-9_2

Lai, H.-W., Chen, H. W., Kukulies, J., Ou, T., and Chen, D. (2021). Regionalization of Seasonal Precipitation over the Tibetan Plateau and Associated Large-Scale Atmospheric Systems. *J. Clim.* 34 (7), 2635–2651. doi:10.1175/jcli-d-20-0521.1

Li, L., Yang, S., Wang, Z. X., Zhu, X., and Tang, H. (2010). Evidence of Warming and Wetting Climate over the Qinghai-Tibet Plateau. *Arctic, Antarctic, Alpine Res.* 42, 449–457. doi:10.1657/1938-4246-42.4.449

Liang, L., Li, L., Liu, C., and Cuo, L. (2013). Climate Change in the Tibetan Plateau Three Rivers Source Region: 1960-2009. *Int. J. Climatol.* 33, 2900–2916. doi:10.1002/joc.3642

Liao, Q., Xiao, T. G., and Jin, R. H. (2018). Analysis on Inter-annual Variation of East Asian Subtropical Westerly Jet. *J. Chengdu Univ. Inf. Technol.* 33 (01), 68–77. doi:10.16836/j.cnki.jcuit.2018.01.013

Liu, X. Q., Wu, Z. Z., Liu, Y. S., Zhao, X. Z., Rui, Y., and Zhang, J. (2019). Spatial-temporal Characteristics of Precipitation from 1960 to 2015 in the Three River' Headstream Region, Qinghai, China. *ACTA GEOGRAPHIC SINICA* 74 (9). (In Chinese). doi:10.11821/dlxb201909008

Numaguti, A. (1999). Origin and Recycling Processes of Precipitating Water over the Eurasian Continent: Experiments Using an Atmospheric General Circulation Model. *J. Geophys. Res.* 104, 1957–1972. doi:10.1029/1998jd200026

Pan, C., Zhu, B., Gao, J., Kang, H., and Zhu, T. (2018). Quantitative Identification of Moisture Sources over the Tibetan Plateau and the Relationship between thermal Forcing and Moisture Transport. *ClimDynam*, 1–16. doi:10.1007/s00382-018-4130-6

Peterson, T. C., Folland, C., Gruza, G., Hogg, G., Mokssit, A., and Plummer, N. (2001). *Report on the Activities of the Working Group on Climate Change Detection and Related Rapporteurs 1998-2001, World Meteorological Organization Rep*. Geneva, Switzerland: WCDMP-47, WMO-TD 1071, 143.

Shen, Y., Xiong, A., Wang, Y., and Xie, P. (2010). Performance of High-Resolution Satellite Precipitation Products over China. *J. Geophys. Res.* 115, D02114. doi:10.1029/2009JD012097

Sillmann, J., Kharin, V. V., Zhang, X., Zwiers, F. W., and Bronaugh, D. (2013). Climate Extremes Indices in the CMIP5 Multimodel Ensemble: Part 1. Model Evaluation in the Present Climate. *J. Geophys. Res. Atmos.* 118, 1716–1733. doi:10.1002/jgrd.205020310.1002/jgrd.50203

Sodemann, H., Schwierz, C., and Wernli, H. (2008). Interannual Variability of Greenland winter Precipitation Sources: Lagrangian Moisture Diagnostic and North Atlantic Oscillation Influence. *J. Geophys. Res.* 113, D03107. doi:10.1029/2007jd008503

Sun, B., and Wang, H. (2019). Enhanced Connections between Summer Precipitation over the Three-River-Source Region of China and the Global Climate System. *Clim. Dyn.* 52 (5), 3471–3488. doi:10.1007/s00382-018-4326-9

Sun, B., and Wang, H. (2018). Interannual Variation of the spring and Summer Precipitation over the Three River Source Region in China and the Associated Regimes. *J. Clim.* 31, 7441–7457. doi:10.1175/JCLI-D-17-0680.1

Sun, B., and Wang, H. (2014). Moisture Sources of Semiarid Grassland in China Using the Lagrangian Particle Model FLEXPART. *J. Clim.* 27, 2457–2474. doi:10.1175/jcli-d-13-00517.1

Tong, L., Xu, X., Fu, Y., and Li, S. (2014). Wetland Changes and Their Responses to Climate Change in the "Three-River Headwaters" Region of China since the 1990s. *Energies* 7 (4), 2515–2534. doi:10.3390/en7042515

Wang, X., Pang, G., and Yang, M. (2018). Precipitation over the Tibetan Plateau during Recent Decades: a Review Based on Observations and Simulations. *Int. J. Climatol* 38, 1116–1131. doi:10.1002/joc.5246

Xi, Y., Miao, C., Wu, J., Duan, Q., Lei, X., and Li, H. (2018). Spatiotemporal Changes in Extreme Temperature and Precipitation Events in the Three-Rivers Headwater Region, china. *J. Geophys. Res. Atmos.* 123, 5827–5844. doi:10.1029/2017jd028226

Xu, X., Zhao, T., Lu, C., Guo, Y., Chen, B., Liu, R., et al. (2014). An Important Mechanism Sustaining the Atmospheric "Water tower" over the Tibetan Plateau. *Atmos. Chem. Phys.* 14, 11287–11295. doi:10.5194/acp-14-11287-2014

Yang, K., Wu, H., Qin, J., Lin, C., Tang, W., and Chen, Y. (2014). Recent Climate Changes over the Tibetan Plateau and Their Impacts on Energy and Water Cycle: A Review. *Glob. Planet. Change* 112, 79–91. doi:10.1016/j.gloplacha.2013.12.001

Yao, T. D., Xue, Y. K., Chen, D. L., Chen, F. H., Thompson, L., Cui, P., et al. (2017). Recent Third Pole's Rapid Warming Accompanies Cryospheric Melt and Water Cycle Intensification and Interactions between Monsoon and Environment: Multi-Disciplinary Approach with Observation, Modeling and Analysis. *B Am. Meteorol. Soc.* 100 (3), 423–444. doi:10.1175/bams-d-17-0057.1

Yao, T., Masson-Delmotte, V., Gao, J., Yu, W., Yang, X., Risi, C., et al. (2013). A Review of Climatic Controls on δ18O in Precipitation over the Tibetan Plateau: Observations and Simulations. *Rev. Geophys.* 51, 525–548. doi:10.1002/rog.20023

Yi, X., Li, G., and Yin, Y. (2013). Spatio-temporal Variation of Precipitation in the Three-River Headwater Region from 1961 to 2010. *J. Geogr. Sci.* 23, 447–464. doi:10.1007/s11442-013-1021-y

Zhang, L., Li, X., Zheng, D., Zhang, K., Ma, Q., Zhao, Y., et al. (2021). Merging Multiple Satellite-Based Precipitation Products and Gauge Observations Using a Novel Double Machine Learning Approach. *J. Hydrol.* 594, 125969. doi:10.1016/j.jhydrol.2021.125969

Zhang, Y., Huang, W., and Zhong, D. (2019). Major Moisture Pathways and Their Importance to Rainy Season Precipitation over the Sanjiangyuan Region of the Tibetan Plateau. *J. Clim.* 32 (20), 6837–6857. doi:10.1175/jcli-d-19-0196.1

Conflict of Interest: The authors declare that the research was conducted in the absence of any commercial or financial relationships that could be construed as a potential conflict of interest.

frontiers
in Earth Science

REVIEW
published: 13 October 2021
doi: 10.3389/feart.2021.673495

Compound Hydrometeorological Extremes: Drivers, Mechanisms and Methods

Wei Zhang[1]*, **Ming Luo**[2,3]*, **Si Gao**[4,5], **Weilin Chen**[6], **Vittal Hari**[7] **and Abdou Khouakhi**[8]

[1]Department of Plants, Soils and Climate, Utah State University, Logan, UT, United States, [2]School of Geography and Planning, Sun Yat-sen University, Guangzhou, China, [3]Guangdong Key Laboratory for Urbanization and Geo-simulation, Guangdong Provincial Engineering Research Center for Public Security and Disaster, Guangzhou, China, [4]School of Atmospheric Sciences, Sun Yat-sen University, Zhuhai, China, [5]Southern Marine Science and Engineering Guangdong Laboratory (Zhuhai), Zhuhai, China, [6]Joint International Research Laboratory of Climate and Environment Change, Collaborative Innovation Center on Forecast and Evaluation of Meteorological Disasters, Nanjing University of Information Science and Technology, Nanjing, China, [7]UFZ-Helmholtz Centre for Environmental Research, Leipzig, Germany, [8]Centre for Environmental and Agricultural Informatics, School of Water, Energy and Environment, Cranfield University, Cranfield, United Kingdom

Edited by:
Gert-Jan Steeneveld,
Wageningen University and Research,
Netherlands

Reviewed by:
Wei-Bo Chen,
National Science and Technology
Center for Disaster Reduction(NCDR),
Taiwan
George Varlas,
Hellenic Centre for Marine Research
(HCMR), Greece

***Correspondence:**
Wei Zhang
w.zhang@usu.edu
Ming Luo
luom38@mail.sysu.edu.cn

Specialty section:
This article was submitted to
Atmospheric Science,
a section of the journal
Frontiers in Earth Science

Received: 27 February 2021
Accepted: 28 September 2021
Published: 13 October 2021

Citation:
Zhang W, Luo M, Gao S, Chen W,
Hari V and Khouakhi A (2021)
Compound Hydrometeorological
Extremes: Drivers, Mechanisms
and Methods.
Front. Earth Sci. 9:673495.
doi: 10.3389/feart.2021.673495

Compound extremes pose immense challenges and hazards to communities, and this is particularly true for compound hydrometeorological extremes associated with deadly floods, surges, droughts, and heat waves. To mitigate and better adapt to compound hydrometeorological extremes, we need to better understand the state of knowledge of such extremes. Here we review the current advances in understanding compound hydrometeorological extremes: compound heat wave and drought (hot-dry), compound heat stress and extreme precipitation (hot-wet), cold-wet, cold-dry and compound flooding. We focus on the drivers of these extremes and methods used to investigate and quantify their associated risk. Overall, hot-dry compound extremes are tied to subtropical highs, blocking highs, atmospheric stagnation events, and planetary wave patterns, which are modulated by atmosphere-land feedbacks. Compared with hot-dry compound extremes, hot-wet events are less examined in the literature with most works focusing on case studies. The cold-wet compound events are commonly associated with snowfall and cold frontal systems. Although cold-dry events have been found to decrease, their underlying mechanisms require further investigation. Compound flooding encompasses storm surge and high rainfall, storm surge and sea level rise, storm surge and riverine flooding, and coastal and riverine flooding. Overall, there is a growing risk of compound flooding in the future due to changes in sea level rise, storm intensity, storm precipitation, and land-use-land-cover change. To understand processes and interactions underlying compound extremes, numerical models have been used to complement statistical modeling of the dependence between the components of compound extremes. While global climate models can simulate certain types of compound extremes, high-resolution regional models coupled with land and hydrological models are required to simulate the variability of compound extremes and to project changes in the risk of such extremes. In terms of statistical modeling of compound extremes, previous studies have used empirical approach, event coincidence analysis, multivariate distribution, the indicator approach, quantile regression and the Markov Chain method to understand the dependence, greatly advancing the state of science of compound extremes. Overall, the selection of methods depends on the type of compound extremes of interests and relevant variables.

Keywords: compound hydrometeorological extremes, hot-dry, hot-wet, storm surge, tropical cyclones, floods/droughts, cold-dry, cold-wet

INTRODUCTION

Extreme weather and climate events can have devastating consequences on human societies and the environment (Troy et al., 2015; Zscheischler et al., 2020b). A combination of extreme events can exacerbate the damages by cascading individual natural hazard (AghaKouchak et al., 2018), leading to compound events. Compound extremes events are defined as "1) two or more extreme events occurring simultaneously or successively, 2) combinations of extreme events with underlying conditions that amplify the impact of the events, or 3) combinations of events that are not themselves extremes but lead to an extreme event or impact when combined. The contributing events can be of similar (clustered multiple events) or different type(s)" (Seneviratne et al., 2012). Recently, a more general definition of compound extremes has been developed as "A compound event is an extreme impact that depends on multiple statistically dependent variables or events" (Leonard et al., 2014). Under this definition, compound events may be interpreted as extreme impacts that *depend* on multiple variables or events.

Over the past several years, major efforts have been devoted to advancing the science of compound extremes, evidenced by several review articles in the literature (Leonard et al., 2014; Hao et al., 2018; Zscheischler et al., 2018; AghaKouchak et al., 2020; Raymond et al., 2020a; Zscheischler et al., 2020a). For example, compound events have been organized into four themes: preconditioned, multivariate, temporally compounding, spatially compounding, and temporal connections (Zscheischler et al., 2020a). This structuring of compound events facilitates the unravelling of their physical mechanisms and societal impacts, marking a big step in scientific advancements. As a global investigation of compound extremes, Ridder et al. (2020) identified twenty-seven pairs of compound events (e.g., extreme precipitation and temperatures) that provide the first spatial estimates of their occurrences at the global scale.

Compound hydrometeorological extremes are the most deadly and dangerous compound events in terms of damages and impacts (Martius et al., 2016; Hao et al., 2018; Sedlmeier et al., 2018; Li et al., 2020a). Overall, compound hydrometeorological extremes may be subdivided into five categories: hot-dry (Mazdiyasni and AghaKouchak, 2015; Schumacher et al., 2019; Tavakol et al., 2020a), hot-wet (Fischer and Knutti, 2013; Russo et al., 2017; Tavakol and Rahmani, 2019a), cold-wet (Bisci et al., 2012; Hao et al., 2018; Hochman et al., 2019; De Luca et al., 2020), cold-dry (Dabhi et al., 2018; Wu Y. et al., 2021), and compound flood (e.g., storm surge and rainfall) (Wahl et al., 2015; Moftakhari et al., 2017a). First, compound hot and dry (or heat wave and drought) events have been evaluated globally and regionally (Feng et al., 2020), including Europe (Ionita et al., 2017; Liu et al., 2020), China (Chen L. et al., 2019; Kong et al., 2020; Xu et al., 2021; Yu and Zhai, 2020), Australia (Cowan et al., 2014; Herold et al., 2016), northern hemisphere (Vogel et al., 2019), the United States (Mazdiyasni and AghaKouchak, 2015; Hao et al., 2020c; Tavakol et al., 2020a), southern Africa (Hao Y. et al., 2020) and at the global scale (Zscheischler and Seneviratne, 2017; Feng et al., 2020; Wu et al., 2021). Overall, this type of compound extreme is manifested by drought, heat and aridity events in which there are usually low soil moisture, high temperature and high vapor pressure deficit (Zhou et al., 2019). Second, compound hot and wet extremes have been reported across the globe, including hot-humid events (Fischer and Knutti, 2013; Li et al., 2020; Poppick and McKinnon, 2020; Yuan et al., 2020; Luo and Lau, 2021). The main driver of this compound is that heat stress is associated with high humidity, which is conducive to precipitation. In order to better quantify the future change of precipitation extremes, dew point temperature may be used (Zhang et al., 2019b), highlighting the role of humidity in formulating the compound hot and wet extremes. For example, extreme heat stress events are followed by flooding in the central United States (Zhang and Villarini, 2020). Third, compound cold-wet extreme events were documented over the Mediterranean (Bisci et al., 2012; Hao et al., 2018; Hochman et al., 2019; De Luca et al., 2020), associated with snowfall and cold frontal systems. Fourth, compound cold-dry events have been reported across China (Miao et al., 2016; Zhou and Liu, 2018), Europe (Potopová et al., 2021) and the globe (Dabhi et al., 2018; Wu Y. et al., 2021). Fifth, compound flooding arising from storm surge and rainfall has received attention (Wahl et al., 2015; Moftakhari et al., 2017a; Paprotny et al., 2018; Bevacqua et al., 2019; Marsooli et al., 2019; Bevacqua et al., 2020; Couasnon et al., 2020; Gori et al., 2020a, 2020b). Compound floods include storm surge and heavy rainfall, storm surge and sea level rise, storm surge and high discharge, and sea level rise and river flow. Compound flooding in the coastal regions may be caused by tropical cyclones and other weather systems (e.g., frontal systems, atmospheric rivers and low-pressure systems). Associated with strong wind and torrential precipitation (Khouakhi et al., 2017; Rios Gaona et al., 2018; Zhang et al., 2018), tropical cyclones play a central role in causing compound flooding (Wahl et al., 2015; Gori et al., 2020a, 2020b). **Table 1** summarizes compound hot and dry, hot and wet, cold and dry, cold and wet and compound flooding, which fall into the four categories documented in (Zscheischler et al., 2020) (i.e., preconditioned, multivariate, temporally compounding and spatially compounding).

Despite substantial progress in understanding compound extremes, there is still no review summarizing the drivers,

TABLE 1 | Types of compound hydrometeorological extremes under the four categories documented in (Zscheischler et al., 2020). "X" represents that the compound extreme type falls into a category based on literature.

Types	Preconditioned	Multivariate	Temporally compounding	Spatially compounding
Hot and Dry	Tavakol et al. (2020a)	Wu et al. (2020)	Zhang and Villarini (2020)	Alizadeh et al. (2020)
Hot and Wet	Wang et al. (2019b)	Soneja et al. (2016)		
Cold and Dry	Miao et al. (2016)	Dabhi et al. (2018)	Hsiao et al. (2021)	
Cold and Wet	Hochman et al. (2019)	De Luca et al. (2020)		
Compound Flooding	Ridder et al. (2018)	Xu et al. (2018)		

mechanisms, and methods employed for their evaluation. A previous review article by Hao et al. (2018) did summarize advancements in the study of compound hydrometeorological extremes, but the present work, in contrast, focuses on physical mechanisms and drivers. Here, we review the status of recent scientific advancements and suggest potential future directions for studying compound extremes and extremes in general. We additionally assess recent advancements in understanding compound hydrometeorological extremes in terms of their fundamental drivers, underpinning mechanisms, and methods employed.

COMPOUND HOT AND DRY EXTREMES

Compound hot and dry extreme is among the first investigated compound hydrometeorological extremes in the literature (Chang and Wallace, 1987; Easterling et al., 2000; Ciais et al., 2005). Back to the 1980s, drought and heat wave in Kansas City have been identified to occur together, associated with circulation patterns and moisture conditions (Chang and Wallace, 1987). This type of compound is featured by two variables: temperature and precipitation, which are closely associated with one another due to the well-known thermodynamic relationship (Held and Soden, 2006). The land-atmospheric feedbacks are commonly used to interpret this compound mechanism (Miralles et al., 2019).

Overall, there are two physical mechanisms used to explain compound hot and dry extremes in the literature. The first concept is that there are persistent atmospheric circulation patterns which are responsible for both drought and heat waves (Vautard et al., 2007; Rowell, 2009; Mueller and Seneviratne, 2012; Quesada et al., 2012; Schneidereit et al., 2012; Seager and Hoerling, 2014). The large-scale circulation patterns related to drought or heat wave consist of blocking highs (Schneidereit et al., 2012; Horton et al., 2014; Dong et al., 2018; Luo et al., 2020; Luo and Lau, 2020), atmospheric stagnation events (Horton et al., 2014), planetary wave patterns (Teng et al., 2013; Screen and Simmonds, 2014; Mann et al., 2017) and subtropical highs (Luo and Lau, 2017; Zhang Y. et al., 2019; Li et al., 2019; Liu et al., 2019; Kong et al., 2020). For example, blocking highs and ridge patterns sit on the atmosphere for a long period of time, increasing temperature and evapotranspiration and suppressing precipitation (Matsueda, 2011; Schneidereit et al., 2012; Hoskins and Woollings, 2015; Dong et al., 2018; Schumacher et al., 2019). Moreover, atmospheric stagnation events not only influence temperature and precipitation—because of lack of convection and atmospheric movement and transport (Tressol et al., 2008; Zou et al., 2020)—but they can also deprive the air quality (Kerr and Waugh, 2018; Toro et al., 2019; Zou et al., 2020). Subtropical high/anticyclonic patterns are known as a strong high-pressure system that drives drought and heat waves over East Asia and North America, responsible for the compound hot-dry extreme.

n addition to large-scale circulation patterns, atmosphere-land feedbacks are also responsible for the compound heat waves and droughts (Lansu et al., 2020, 2020; Zhou et al., 2021). Overall, dry soil and plants tend to reduce evaporation, leading to dry atmospheric condition and suppressed precipitation, thereby resulting in meteorological droughts (Dickinson, 1995; Seneviratne et al., 2006). On the other hand, the reduced evapotranspiration can also be associated with more solar radiation and sensible heat that increase temperatures on the earth surface, leading to or magnifying the heat wave. The atmosphere-land feedback is known as a fundamental mechanism for interpreting compound heat wave and drought. For example, the severity of atmospheric aridity is dramatically decreased if the feedback from soil to atmosphere state does not exist (Zhou et al., 2019). Moreover, surface albedo change induced by drought conditions may also be coupled with heat waves (Eltahir, 1998). However, the impacts of albedo on the land-atmosphere coupling may be limited and secondary (Teuling and Seneviratne, 2008).

The evaporation and transpiration on land play a central role in the land-atmosphere feedback, which is influenced by changes in radiation and temperature, shapes cloud feedback and water vapor variability, and acts as a bridge between water and carbon cycles through its connection to photosynthesis. In other words, evapotranspiration modulates the surface energy partitioning by affecting key meteorological variables including air temperature and precipitation. Observing evaporation is still quite challenging and the capability of observing evaporation is limited (Wang and Dickinson, 2012). Although some evaporation data have been released over the years, these data are not directly sensed from space or *in situ*. Rather, they are produced by simple physical or statistical models (Fisher et al., 2008; Jung et al., 2010; Miralles et al., 2011; Mu et al., 2011). The evaporation is associated with land conditions and plant physiology during droughts and heat waves, potentially modulating the atmospheric boundary layer state (Betts et al., 1996;

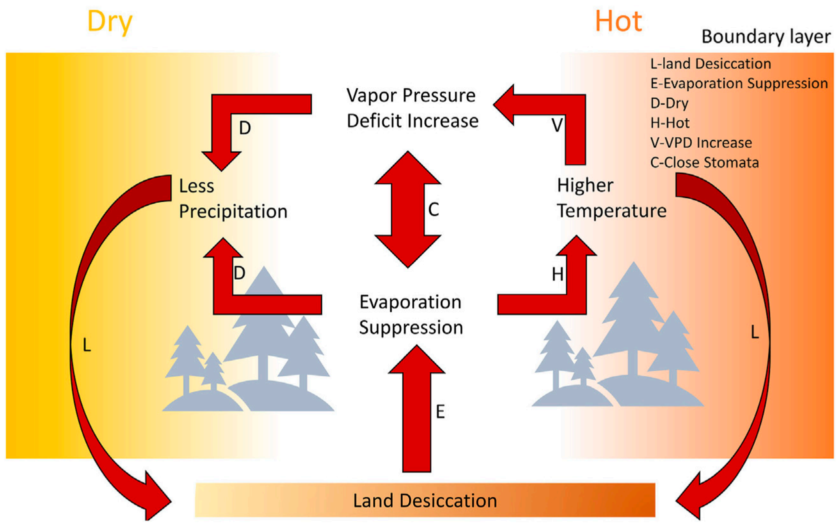

FIGURE 1 | Physical mechanisms of compound hot-dry extremes and land-atmosphere interactions. The physical mechanisms are based on previous studies on compound hot-dry extremes (e.g., Mazdiyasni and AghaKouchak, 2015; Massmann et al., 2019; Miralles et al., 2019; Schumacher et al., 2019; Tavakol et al., 2020a).

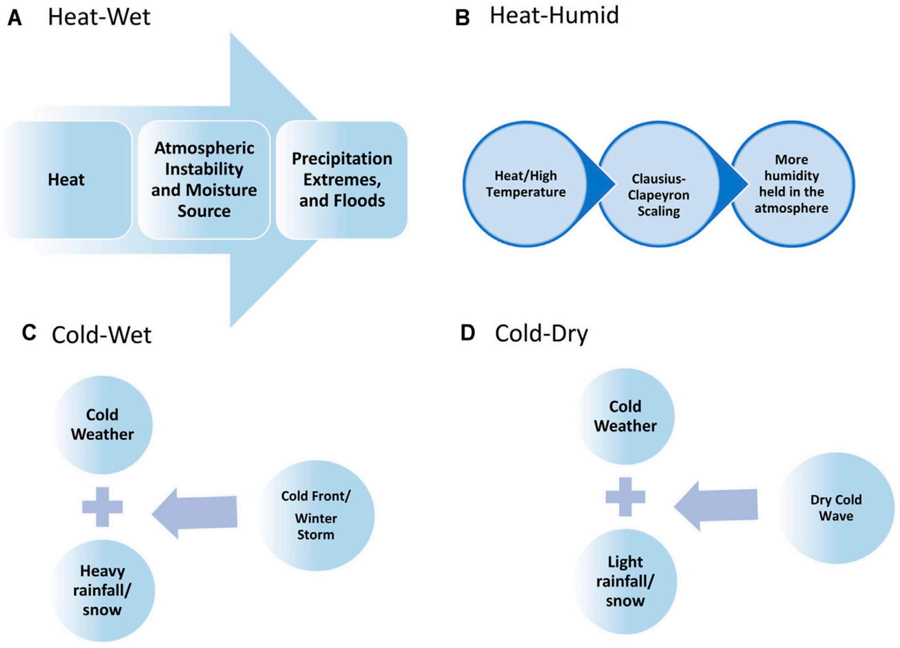

FIGURE 2 | Schematic of compound hydrometeorological extremes: **(A)** heat-wet (Soneja et al., 2016; Wang S. S.-Y. et al., 2019; Imada et al., 2019; Zhang and Villarini, 2020; Chen et al., 2021), **(B)** heat-humid extremes (Fischer and Knutti, 2013; Li et al., 2020; Poppick and McKinnon, 2020; Yuan et al., 2020), **(C)** cold-wet (Bisci et al., 2012; Hao et al., 2018; Hochman et al., 2019; De Luca et al., 2020) and **(D)** cold-dry (Dabhi et al., 2018; Wu Y. et al., 2021; Potopová et al., 2021). The Clausius-Clapeyron scaling represents the water holding capacity of the atmosphere corresponding to air temperature changes (Held and Soden, 2006).

Holtslag and Ek, 1996; Ek and Holtslag, 2004). Under increased vapor pressure deficit (VPD), plants tend to close the stomata to avoid water loss (**Figure 1**), thereby reducing evapotranspiration (Rigden and Salvucci, 2017; Massmann et al., 2019). Compound hot extremes consist of both daytime and nighttime heat extremes (Wang et al., 2020). The spatially compound dry events have been identified to cause damages to agriculture (Singh et al., 2021). The schematic of compound hot-dry extremes is illustrated from the perspective of land-atmosphere feedbacks (**Figure 1**).

COMPOUND HEAT AND WET EXTREMES

Compared with compound hot and dry extremes, compound heat and wet extremes are less explored in the literature (**Figure 2**). This type of extreme is manifested by flooding and heat wave (Soneja et al., 2016; Wang S. S.-Y. et al., 2019; Imada et al., 2019; Zhang and Villarini, 2020; Chen et al., 2021) and heat wave and humid events (Fischer and Knutti, 2013; Li et al., 2020; Poppick and McKinnon, 2020; Yuan et al., 2020). We will elaborate on these compound extremes in the following discussion.

Flooding/Precipitation and Heat Wave/Stress

This type of compound can be classified into temporal compounding (e.g., occur sequentially) (Raymond et al., 2020a; Zscheischler et al., 2020a). The compound flooding and heat waves are featured by heat waves followed by floods or vice versa. The understanding of this compound extreme is still limited and previous research has mainly focused on case studies. No theories have been proposed to formulate these compounds. There are compound summer heat and precipitation extremes reported over central Europe (Beniston, 2009; Sedlmeier et al., 2018), Spain (Morán-Tejeda et al., 2013) and China (Hao et al., 2013; Wu S. et al., 2021; Wang P. et al., 2021). Moreover, floods that follow heat waves have been identified across the central United States (Zhang and Villarini, 2020), and this compound is manifested by the fact that heat stress may set the stage for extreme precipitation and flooding due to increasing sensible heat flux and moisture convergence under extreme heat stress. Similarly, the floods followed by elevated heat have also been identified across China during 1961–2018, exhibiting an increasing trend (Chen et al., 2021). Western Japan experienced catastrophic floods followed by a record-breaking heatwave during early July 2018 (Wang S. S.-Y. et al., 2019; Imada et al., 2019) and this catastrophic compound event caused an estimated 10 billion USD in damage. Based on climate projections, this type of compound will be more frequent under global warming (Wang S. S.-Y. et al., 2019). Currently, the compound flooding and heat waves are still under investigation, and furtherunderstanding of their drivers and mechanisms is required in the near future.

Heat Wave and Humid Event

The combined humidity and temperature extremes have been discussed in the literature and identified by climate models and observations (Fischer and Knutti, 2013) and the joint behavior of temperature and humidity extremes arises from the Clausius-Clapeyron (C-C) relationship. Overall, surface humidity increases as temperatures increase over open water bodies. However, this relationship may not hold over land due to the lack of soil moisture (Fischer and Knutti, 2013). Many factors may influence the risk of such humid heat extremes, including irrigation (Lobell et al., 2008; Krakauer et al., 2020), external forcing that contains both natural (e.g., volcanic eruption) and anthropogenic (e.g., greenhouse gases) sources (Fischer and Knutti, 2013; Russo et al., 2017; Lutsko, 2021), and urbanization (Oleson et al., 2015; Luo and Lau, 2018; Wang Y. et al., 2019).

While the heat and humid events have been projected to increase under global warming (Russo et al., 2017; Byrne and O'Gorman, 2018; Chen X. et al., 2019; Tavakol and Rahmani, 2019b; Wang P. et al., 2021), the combination of heat and relative humidity in the future is still uncertain (Byrne and O'Gorman, 2018). We commonly use wet bulb temperature or apparent temperature to quantify the compound heat-humid events (Russo et al., 2017), although the wet bulb temperature exhibits nonlinear relationship between temperature and relative humidity which is magnified by an increase in temperature (Coffel et al., 2019).

COMPOUND COLD-DRY AND COLD-WET EXTREMES

Cold-wet compound extreme events have been reported over the Mediterranean (Bisci et al., 2012; Hao et al., 2018; Hochman et al., 2019; De Luca et al., 2020). The wintertime cold-wet compound events are commonly associated with snowfall and cold frontal systems. For example, the polar air outbreak associated with a cold front tends to cause heavy snowfall and rainfall. In contrast, compound cold-dry events have been found in China (Miao et al., 2016; Zhou and Liu, 2018), Europe (Potopová et al., 2021) and the globe (Dabhi et al., 2018; Wu Y. et al., 2021). Compound cold/dry and cold/wet extremes have decreased over the vast majority of the world, and are projected to be less frequent using CMIP6 model projection (Wu Y. et al., 2021).

COMPOUND FLOODING

Rising attention has been paid to compound flooding that arises from storm surge and rainfall (Wahl et al., 2015; Moftakhari et al., 2017a; Paprotny et al., 2018; Bevacqua et al., 2019; Marsooli et al., 2019; Bevacqua et al., 2020; Couasnon et al., 2020; Gori et al., 2020a, 2020b). Compound flooding includes storm surge and high rainfall, storm surge and mean sea level rise, storm surge and riverine flooding, and coastal and riverine flooding. Tropical cyclones, atmospheric rivers and extratropical cyclones play a central role in causing the compound flooding (Wahl et al., 2015; Gori et al., 2020a, 2020b) because these storms associated with strong wind are responsible for storm surge and heavy precipitation (Khouakhi and Villarini 2016a; Khouakhi et al., 2017; Rios Gaona et al., 2018; Zhang et al., 2018, 2019a; 2021) in the coastal regions (**Figure 3**). Tropical cyclones have been projected to intensify under climate change, thereby probably leading to higher storm surge (Knutson et al., 2010, 2015; Bhatia et al., 2019). Meanwhile, rainfall caused by tropical cyclones has also been projected to increase in the future (Knutson et al., 2010; Wright et al., 2015; Scoccimarro et al., 2017; Liu et al., 2018). The changes in the intensity of tropical cyclones in concert with the increase in rainfall suggest a higher future risk of compound extremes caused by storms.

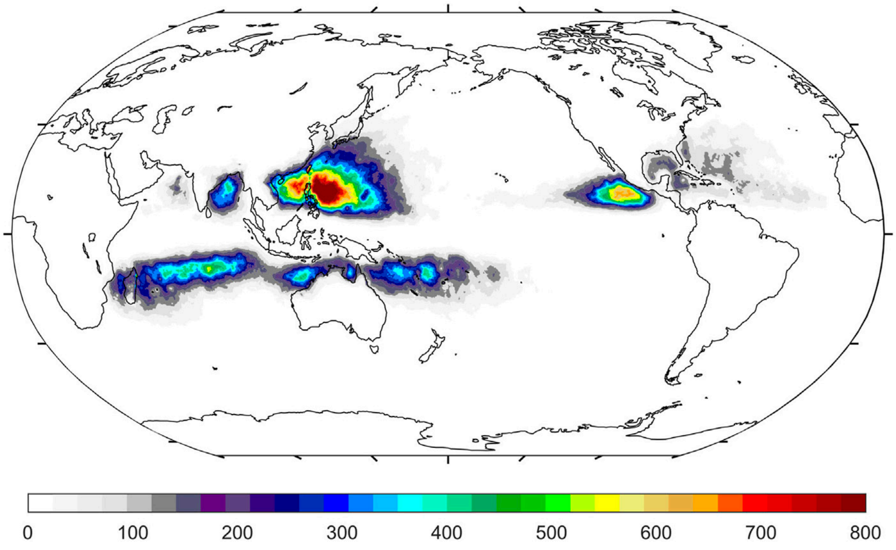

FIGURE 3 | Annual average tropical cyclone precipitation (unit: mm/year) in observations based on the International Best Track Archive for Climate Stewardship (IBTrACS; Knapp et al., 2010) dataset and the Multi-Source Weighted-Ensemble Precipitation Version 2 (MSWEP v2, Beck et al., 2017a; 2017b) precipitation data.

Storm Surge and Heavy Rainfall

Storm surge is defined as a rise in sea level during tropical/extratropical cyclones due to strong winds that force the sea water on shore (Lin and Chavas, 2012; Waliser and Guan, 2017; Veatch and Villarini, 2020), leading to coastal flooding (Khouakhi and Villarini, 2016b; Garner et al., 2017; Herdman et al., 2018; Xu et al., 2019). When storm surge is accompanied by heavy rainfall associated with tropical cyclones, the resulting damages would be exacerbated. Strong dependence has been found between extreme rainfall and storm surge in coastal regions (Zheng et al., 2013; Mohanty et al., 2020). Overall, the compound storm surge and heavy rainfall events are associated with tropical cyclones, atmospheric rivers (Lin et al., 2010a), medicanes (Amores et al., 2020; Davolio et al., 2020; Zhang et al., 2020), and extreme extratropical cyclones (Danard et al., 2004; Colle et al., 2015; Mäll et al., 2017; Lin et al., 2019).

This type of compound has also been reported in many parts of the world including the Netherlands (van den Hurk et al., 2015; Ridder et al., 2018), in coastal and estuarine regions of Australia (Wu et al., 2018), Morocco (Zellou and Rahali, 2019), the United States (Lin et al., 2010b; Gori et al., 2020a), China (Xu et al., 2018; Fang et al., 2021), Britain (Svensson and Jones, 2002, 2004), and Europe in general (Bevacqua et al., 2019). In particular, the catastrophic impacts of the compound storm surge and heavy precipitation are marked in urban watershed (Joyce et al., 2018).

The risk of compound flooding resulting from storm surge and heavy rainfall has been increasing in major coastal cities of the United States (Wahl et al., 2015). The risk of compound storm surge and heavy rainfall is projected to increase in the future (Karim and Mimura, 2008; Bevacqua et al., 2019; Bates et al., 2020; Hsiao et al., 2021). However, there are still large uncertainties in quantifying changes in the risk of compound flooding due to the insufficient skill of climate models in simulating extreme precipitation caused by storms (Zhang et al., 2019a; Roberts et al., 2020; Vannière et al., 2020). Alternatively, previous efforts have been made to develop parametric tropical cyclone rainfall models (Marks and DeMaria, 2003; Lonfat et al., 2007; Langousis and Veneziano, 2009; Zhu et al., 2013; Emanuel, 2017; Brackins and Kalyanapu, 2020; Xi et al., 2020). The parametric tropical cyclone rainfall models are listed in **Table 2**, including R-CLIPER (Marks and DeMaria, 2003; Tuleya et al., 2007), IPET (IPET 2006), PHRaM (Lonfat et al., 2007), MSR (Langousis and Veneziano, 2009), RMS (Grieser and Jewson, 2012) and TCRM (Zhu et al., 2013; Emanuel, 2017; Xi et al., 2020). The parametric models are very useful to quantify the future risk of tropical cyclone rainfall and coastal flooding (Zheng et al., 2014; Geoghegan et al., 2018).

Storm surge caused by tropical/extratropical cyclones will be exacerbated by the rise of sea level, magnifying the coastal flood hazards (Little et al., 2015; Haigh et al., 2016; Muis et al., 2016; Vousdoukas et al., 2018; Marsooli et al., 2019). Indeed, sea level rise can greatly increase the risk of coastal flooding caused by storm surge (McInnes et al., 2003; Karim and Mimura, 2008; Hallegatte et al., 2011; Tebaldi et al., 2012; Zhang et al., 2013; Arns et al., 2015).

Storm Surge and Riverine Floods

While storm surge can be compounded with extreme rainfall, it is also dangerous when storm surge is in concert with riverine flooding. Many studies have analyzed the co-occurrence of storm surge and riverine/fluvial floods (Kew et al., 2013; Klerk et al., 2015; Khanal et al., 2019), including simulations using global coupled river-coast flood model (Ikeuchi et al., 2017). The effect of compound storm surge and riverine flooding has also been examined using remote sensing technologies in western coastal Louisiana (Ramsey et al., 2011), in a tidal river in Rhode Island

TABLE 2 | Parametric models for tropical cyclone rainfall.

Parametric models	Short name	References
Rain-Climatology and Persistence	R-CLIPER	Marks and DeMaria, 2003, Tuleya et al. (2007)
Interagency Performance Evaluation Task Force	IPET	IPET, (2006)
Parametric Hurricane Rainfall Model	PHRaM	Lonfat et al. (2007)
Modified Smith for Rainfall	MSR	Langousis and Veneziano, (2009)
Risk Management Solutions, LTD.	RMS	Grieser and Jewson, (2012)
Tropical cyclone rainfall model	TCRM	Zhu et al. (2013), Emanuel. (2017)

(Teng et al., 2017), the Rhine–Meuse Delta (Klerk et al., 2015), the United Kingdom (Hendry et al., 2019), the Netherlands (Khanal et al., 2019), the USA (Dietrich et al., 2010; Couasnon et al., 2018) and Italy (Bevacqua et al., 2017). In addition to regional scale analysis of this compound extreme, some studies have examined the dependence of storm surge and extreme discharge at the global scale (Ward et al., 2018). The compound flooding is caused by the interactions between physical drivers from oceanographic, hydrological, and meteorological processes in coastal areas, leading to highly complex interplays (Couasnon et al., 2020). Overall, the compound flooding is based on their drivers, including storm surge, precipitation, and river discharges. While many compound flood events are associated with tropical cyclones, some are related to typical synoptic weather systems (Couasnon et al., 2020).

Statistical methods and coupled modeling have been used to quantify the compound storm surge and riverine flood (Dietrich et al., 2010). For example, a global river routing model forced by global hydrological models and bounded downstream by a global tide and surge model has been used to assess the effect of storm surge on riverine flood (Eilander et al., 2020). Hydrologic and hydrodynamic models are combined to assess compound flooding caused by the 2016 tropical storm Matthew (Zhang and Najafi, 2020). In addition, joint probabilities and copula have been widely used to examine the compounds (Czajkowski et al., 2013; Petroliagkis et al., 2016; Couasnon et al., 2018).

Sea Level Rise and Coastal Flooding

Sea level rise may reduce the gap between high tidal datum and flood stage, increasing the frequency of coastal flooding (Andersen and Shepherd, 2013; Kriebel and Geiman, 2014; Schindelegger et al., 2018). When riverine and coastal floods occur back-to-back, their impacts would be stronger than they happen in isolation (Ward et al., 2018, 2018). Overall, sea level rise can double the frequency of coastal flooding in the next few decades (Mousavi et al., 2011; Woodruff et al., 2013; Karegar et al., 2017; Vitousek et al., 2017). For example, due to sea level rise, there is increased coastal flooding in California (Heberger et al., 2011; Garcia and Loáiciga, 2014), Mekong Delta (Takagi et al., 2015), Italian coastal plains (Rinaldo et al., 2008; Antonioli et al., 2017), Mediterranean (Reimann et al., 2018), the US East Coast (Ezer and Atkinson, 2014; Dahl et al., 2017), Miami Beach, Florida (Wdowinski et al., 2016), Latin America (Reguero et al., 2015), China (Fang et al., 2016). Sea level rise is found to be compounded with fluvial flooding using a bivariate flood hazard assessment (Moftakhari et al., 2017a). Sea level rise can influence cyclonic storm surge floods in Bangladesh (Karim and Mimura, 2008). Future sea level rise can not only increase the probability of infrastructure failure, but it can also increase the compounding flood drivers (Moftakhari et al., 2017a). Climate change will increase the potential to cause higher frequency and magnitude of coastal flooding due to hurricane intensification and sea level rise (**Figure 4**) (Mousavi et al., 2011).

Coastal and Riverine Floods

Riverine and coastal floods characterized by the simultaneous or successive occurrence of high sea levels and high river flows can be life threatening and cause infrastructures damage (Nadal et al., 2010; Ganguli et al., 2020; Khanam et al., 2021). This type of flooding was remarkable during hurricane Harvey in Houston-Galveston Bay (Valle-Levinson et al., 2020; Huang et al., 2021b). For example, around 600 million people in coastal regions may be exposed to this type of compound flood by 2,100 (Kulp and Strauss, 2019). Over the years, the location in a river system where riverine and coastal flood drivers can contribute to the water level has been defined as the transition zone (Bilskie and Hagen, 2018). For example, the 2016 Louisiana flood was caused by excessive rainfall and coastal floods (Wang et al., 2016).

NUMERICAL MODELING

Climate models have been used to quantify compound extremes and their distributions (Sherwood, 2018; Raymond et al., 2020b; Xu et al., 2021; Yuan et al., 2020). Given the five types of compound extremes (**Table 1**), it is still quite challenging to represent the extremes in numerical models (**Table 3**). Due to the key role of land-atmosphere feedbacks in shaping the compound dry-hot events, fully-coupled models are desirable for performing simulations (Fischer et al., 2007; Stéfanon et al., 2014; Keune et al., 2016; Sillmann et al., 2017). Current numerical models have been used to simulate the compound extremes, including large eddy simulators (Cioni and Hohenegger, 2017), column models (Van Heerwaarden et al., 2010; Miralles et al., 2014), regional climate models and global climate models (Vautard et al., 2013; Chung et al., 2014; Stegehuis et al., 2015). While regional climate models are extremely useful in resolving land conditions (Fischer et al., 2007; Stéfanon et al., 2014; Keune et al., 2016; Sillmann et al., 2017), global climate models are commonly used to assess changes in land conditions on extreme weather (e.g., drought and heat wave) (Hauser et al., 2016; Kala et al., 2016; Rasmijn et al., 2018). The models in the Coupled Model

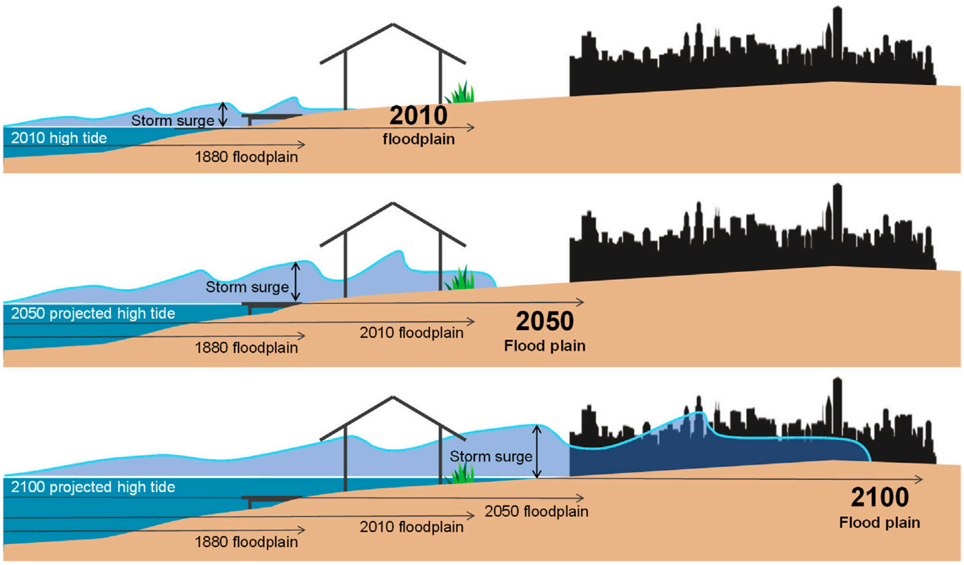

FIGURE 4 | Schematic illustrating the risk of coastal flooding under the present and future climates (Andersen and Shepherd, 2013; Kriebel and Geiman, 2014; Moftakhari et al., 2017a; Schindelegger et al., 2018).

TABLE 3 | Numerical models for studying compound extremes.

Numerical models	References	Description
Single column models	Van Heerwaarden et al., 2010 Miralles et al., 2014	A mechanistic model of the soil-water-atmosphere column
Large eddy simulators	Cioni and Hohenegger (2017)	A very high-resolution regional model (<1,000 m)
Regional climate models	Vautard et al. (2013) Chung et al. (2014) Stegehuis et al. (2015)	A high-resolution model that can simulate atmosphere-land interactions
Global climate models	Hauser et al. (2016) Kala et al. (2016) Rasmijn et al. (2018)	A model the simulates the global climate with a lower spatial resolution
Storm surge models coupled with wave model (SLOSH, ADCRIC) and hydrological models	Sebastian et al. (2014) Yin et al. (2016)	A coupled system that simulates storm surge, sea level rise, river discharge and stream flow

Intercomparison Project Phase 6 (CMIP6) exhibit some skill in simulating the co-occurrence of hot and dry compound events in North America and Europe (Ridder et al., 2021). Because the numerical models' outputs are limited by the climatological biases, univariate and multivariate bias correction methods have been used to correct the biases, and thus improving the performance and usability of the models (Maraun, 2016; Vezzoli et al., 2017; Vrac, 2018; Zscheischler et al., 2018; François et al., 2020). While univariate bias correction operates well in a single variable, multivariate bias correction methods aim to reduce biases that depend on multiple variables, which is an important feature of compound extreme events. Climate model evaluation is usually univariate without considering the multivariate nature of multiple hazards, it is thus important to evaluate the biases in the dependence between the contributing variables in climate models (Vezzoli et al., 2017). However, rare studies have evaluated the climate model multivariate representation of hazard indicators (Bevacqua et al., 2019; Villalobos-Herrera et al., 2021; Zscheischler et al., 2021).

Regional climate models also take initial and boundary conditions from the output of global climate models and can resolve small-scale processes, thereby perform well in simulating single events simulations (Fischer et al., 2007; Stéfanon et al., 2014; Keune et al., 2016; Sillmann et al., 2017). Therefore, regional climate models depend heavily on the simulation of global climate models, which are commonly used to simulate a longer simulation (e.g., years or decades) with a coarser spatial resolution (~1–2°) (Orlowsky and Seneviratne, 2013; Cook et al., 2020; Ridder et al., 2020, 2021; Ukkola et al., 2020; Vogel et al., 2020; Su et al., 2021).

Numerical models have also been used to study compound flooding. Ideally, an earth system model that resolves tropical cyclones, waves, ocean circulation, and hydrological cycle can simulate all the processes and interactions at play (Flato, 2011). However, the current generation of earth system models cannot resolve or simplify the processes responsible for the compound flooding (Meehl et al., 2020). To quantify the impacts of sea level rise on storm surge, previous studies have used three methods: numerical simulation of storm surge with sea level rise using the

TABLE 4 | Statistical methods for studying compound extremes.

Statistical methods	References	Description
Empirical Approach	Fischer and Knutti, (2013) Hao et al. (2013) Morán-Tejeda et al. (2013) Miao et al. (2016)	Count the occurrence frequency based on threshold and percentile
Event coincidence analysis	He and Sheffield, (2020) Zhang and Villarini, (2020) Chen et al. (2021)	Examine the coincidence of two events against random occurrence
Multivariate Distribution	Trepanier et al. (2017) Zscheischler and Seneviratne, (2017) Sadegh et al. (2018) Alizadeh et al. (2020) Hao et al. (2020b) Ribeiro et al. (2020a)	Examine the dependence of the two or more extremes using the joint/marginal probability
Indicator Approach	Karl et al. (1996) Gallant and Karoly, (2010) Gallant et al. (2014) Wu et al. (2020)	Combine the components of the compound extreme into an indicator
Quantile Regression	Quesada et al. (2012) Meng and Shen, (2014)	Examine the relationship between predictand and predictor, which are extremes
Markov Chain Model	Steinemann, (2003) Chowdhury et al. (2015) Sedlmeier et al. (2016)	Describe a sequence of events where the present state depends only on the antecedent state
Complex Networks	Boers et al. (2019) Nowack et al. (2020) Sun et al. (2018)	Identify interacting extreme events with a dynamic lead-lag

Sea, Lake, and Overland Surges from Hurricanes (SLOSH) model (Glahn et al., 2009) or the Advanced Circulation (ADCIRC) model (Sebastian et al., 2014; Yin et al., 2016), the simple linear addition method (Kleinosky et al., 2007; Frazier et al., 2010) and Linear addition by expansion method (McInnes et al., 2013). The storm surge model and hydrological model are forced with high-resolution climate model outputs for analyzing the joint occurrence of coastal water levels and river peaks (Ganguli et al., 2020).

STATISTICAL MODELING

Statistical models and observations have been used to investigate compound hydrological extremes. For example, a theoretical framework has been developed to examine compound extremes (Leonard et al., 2014). Recently, much attention has been paid to understand the dependence between multiple relevant variables associated with compound extremes, particularly from a statistical perspective. Overall, the statistical methods employed across the literature consist of empirical approach, event coincidence analysis (ECA), multivariate distribution, the indicator approach, quantile regression and the Markov Chain method (**Table 4**) (Hao et al., 2018).

Empirical Approach

The empirical approach is performed by counting the simultaneous or sequential frequency/occurrence of the extremes based on the definition (e.g., maxima, threshold or percentile). This approach has been used to examine the compound temperature and precipitation extremes (Fischer and Knutti, 2013; Hao et al., 2013; Morán-Tejeda et al., 2013; Miao et al., 2016, 1961–2011), air pollution and temperature extremes (Schnell and Prather, 2017), storm surge and rainfall (Wahl et al., 2015). Based on the frequency/occurrence of the compound events, the trend and change point of the time series has been commonly examined to identify temporal change patterns (Dabhi et al., 2021; Feng and Hao, 2020).

Event Coincidence Analysis

Event coincidence analysis (e.g., events synchronization) has been used to formulate and test null hypotheses on the origin of the observed relationship (Donges et al., 2016). In the analysis of temporal compound extremes (e.g., floods that follow heat stress) (Zscheischler et al., 2020a), it is important to test the null hypothesis that whether this lagged association between floods and heat stress is randomly distributed (Zhang and Villarini, 2020). This method has been used to quantify the lagged compound droughts and pluvial floods (He and Sheffield, 2020), the association between precipitation and soil moisture extremes (Sun et al., 2018), and flood-heatwave events (Chen et al., 2021).

Multivariate Distribution

As discussed before, an essential element of the compound extreme is the dependence between different drivers (Leonard et al., 2014). In order to quantify the dependence, multivariable distribution has been widely used in applications (Trepanier et al., 2017; Zscheischler and Seneviratne, 2017). The multivariate distribution has been employed to quantify the joint distribution of temperature and precipitation extremes

(Hawkes, 2008; Tebaldi and Sansó, 2009; Rodrigo, 2015; Zscheischler and Seneviratne, 2017). Different ways have been proposed to construct the multivariate distribution, including parametric distribution, copula, entropy, and nonparametric models.

Copula theory has been employed to characterize the bivariate and trivariate joint distribution and assess complex dependence structures, e.g., in the case of upper tail dependence (Bevacqua et al., 2017; Ribeiro et al., 2020b; Tavakol et al., 2020b).$C(x, y) = P(X \leq x, Y \leq y) = S(U, V; \theta)$, where θ denotes the copula parameter, X and Y are two random variables and U and V denote the marginal distribution and S is the copula. In order to better quantify the dependence, a number of copula families have been developed including extreme-value copula, archimedean copula and elliptical copula (Nelsen, 2007).

The copula models can be used to calculate the joint probability and/or bivariate return periods of compound extremes, thereby quantifying their risk (Sadegh et al., 2018; Alizadeh et al., 2020; Ribeiro et al., 2020a; Hao et al., 2020b). In addition, the copula theory has also been used in multivariate bias correction methods to adjust dependencies among variables in climate models' output (Vezzoli et al., 2017).

The multivariate distribution approach can also quantify the conditional association among different extremes. A common compound extreme (hot-dry event) is characterized by the dependence of high temperatures on precipitation deficit (Alizadeh et al., 2020; Hao et al., 2020b) due to land-atmospheric feedbacks. Different from previous methods in which the extremes were selected prior to analysis, some compound extremes may happen when not all components are defined as extreme. The conditional probability approach can solve this problem (Heffernan and Tawn, 2004; Zhang and Singh, 2007).

Indicator Approach

In defining compound extremes, it is extremely difficult to define a "threshold" for identifying extremes in a multivariate situation (Salvadori et al., 2013). The indicator approach develops an indicator based on the information of multiple variables by formulating a function F, which could be a linear combination or joint distribution of these variables.

Previous studies have developed such indicators for compound extremes (Karl et al., 1996; Gallant and Karoly, 2010; Gallant et al., 2014; Wu et al., 2020). Similar indicators have been developed to characterize drought and flood conditions (Kao and Govindaraju, 2010; Hao and AghaKouchak, 2013; Hao and Singh, 2015; Paprotny et al., 2018; Wang L. et al., 2019).

Quantile Regression, Markov chain Model and Complex Networks

The quantile regression enables the quantification of the relationship between the extremes of two variables (i.e., predictand and predictor). The quantile regression is therefore useful to study the compound extremes (e.g., drought and temperature extremes) (Quesada et al., 2012; Meng and Shen, 2014) and humidity and temperature extremes (Poppick and McKinnon, 2020; Huang et al., 2021), compound cool/dry and cool/wet events (Zhou and Liu, 2018). The Markov Chain model is another method to examine the connections between a sequence of extreme events. Previous works have used this method to examine the temporal change of drought (Steinemann, 2003) and heavy precipitation (Chowdhury et al., 2015; Sedlmeier et al., 2016). Complex networks are a powerful tool to unravel the connections between nodes of the network (Boers et al., 2019; Nowack et al., 2020). Complex networks are capable of driving the casual relationship between two or more variables (Sun et al., 2018). In addition, Bayesian network (Couasnon et al., 2018; Tilloy et al., 2019; Sanuy et al., 2020) and Artificial Neural Network (Kabir et al., 2020; Feng et al., 2021; Huang et al., 2021a) have been used to understand compound extremes (e.g., compound flooding).

CONCLUSION AND DISCUSSION

Compound hydrometeorological extremes (e.g., hot and drought compound) exert profound impacts on agriculture and water irrigation demand (Zampieri et al., 2017; Lu et al., 2018; Ribeiro et al., 2020b; Haqiqi et al., 2021; Vogel et al., 2021). For example, the compound drought and heatwave events may affect socio-ecological systems (Mukherjee et al., 2020), wildfires (Abatzoglou and Williams, 2016; AghaKouchak et al., 2020; Sutanto et al., 2020), air pollution (Tressol et al., 2008; Zhang H. et al., 2017; Wang et al., 2017; Lin et al., 2020), heat-related deaths (D'Ippoliti et al., 2010; Mitchell et al., 2016). Hot and dry weather conditions may lead to outbreaks of extreme fire due to low humidity and dry vegetation (AghaKouchak et al., 2020).

To mitigate and adapt to compound hydrometeorological extremes, we need to better understand the current state of the science of such extremes. Here, we have reviewed the current understanding of hydrometeorological extremes focusing on heat waves and drought (hot-dry events), heat stress and extreme precipitation (hot-wet events), compound flooding, dynamical models, and statistical methods.

Overall, there are two physical mechanisms used to explain compound hot and dry extreme in the literature. The first concept is that there are persistent atmospheric circulation patterns which are responsible for both drought and heat waves, and land-atmosphere feedbacks which are also responsible for the compound heat waves and droughts. Compared with compound hot and dry extremes, compound hot and wet extremes are less visited in the literature with case studies. We have summarized compound flooding events that include storm surge and high rainfall, storm surge and sea level rise, storm surge and riverine flooding, and coastal and riverine flooding. Looking ahead, there is a rising risk of compound flooding in the future because of changes in sea level rise, storm intensity and precipitation, land-use-land-cover change in the future (Slater et al., 2021).

In terms of methods, numerical modeling and statistical methods have been used to investigate compound extremes. Overall, climate models alone or coupled with land models, hydrological models, hydrodynamic models and wave models are common tools to investigate compound floods by complementing statistical modeling tools. Climate models still lack skill in simulating dynamical compound extremes, although they perform well in simulating some thermodynamic aspects. Overall, the statistical methods consist of empirical approaches, event coincidence analysis, multivariate distributions, the indicator approach, quantile regression and the Markov Chain method. These methods have greatly advanced our understanding of such extremes, providing a quantification of risk associated with the extremes. Over the decades, machine learning algorithms have advanced many research fields in recent years including climate science. However, while machine learning research has been used to examine individual extreme events (e.g. Grazzini et al., 2019; Bruneau et al., 2020; Chattopadhyay et al., 2020), work on compound extremes is still in its infancy. At the time of writing this article, there were hardly any published studies harnessing machine learning or deep learning to better understand compound hydrometeorological extremes. Therefore, machine learning and its recent algorithmic advances can provide an opportunity and a promising avenue to improve our understanding of compound extreme events.

It would be extremely valuable to build prediction systems for compound hydrometeorological extremes. Indeed, a statistical prediction system has been built to predict compound hot-dry extremes (Hao et al., 2019). Building a statistical prediction model for compound extremes requires the identification of predictors and the evaluation of the predictability of the predictors, which are still challenging tasks (Sillmann et al., 2017). Hybrid statistical-dynamical prediction systems which combine statistical modelling with outputs from dynamical climate models would be promising for predicting compound extremes. Specifically, hybrid statistical-dynamical prediction systems train the relationship between predictors and predictands based on statistical modeling and make predictions based on predictors based on dynamical models. Indeed, several hybrid prediction systems have been developed for individual extremes such as tropical cyclones in the western North Pacific and North Atlantic (Murakami et al., 2016; Zhang W. et al., 2017) and more recently for flood prediction in the USA (Slater and Villarini, 2018). Future research may use Subseasonal to Seasonal (S2S) forecasts such as the products of the North American Multi-Model Ensemble (NMME) or the C3S system of the European Centre for Medium-Range Weather Forecasts (ECMWF) and Copernicus to develop an enhanced prediction of compound extremes.

Given the strong impacts of compound extremes on society, the bottom-up approach is used to examine the compound extremes (Culley et al., 2016; Zscheischler et al., 2018), by identifying the drivers and/or hazards that lead to large impacts. This approach usually begins with a strong impact (e.g., disaster), followed by identifying underlying factors, processes or phenomena shaping the outcome. This includes identifying which factors lead to large impacts. This bottom-up approach has been widely used to study compound weather and climate events. While the bottom-up approach is relevant, the perspective of the present study lies in the physical hazards associated with compound events.

Finally, we have identified several future research directions for compound hydrometeorological extremes, including:

- projecting the risk of compound extremes for different levels of future warming (Zscheischler et al., 2018; Wang et al., 2020);
- evaluating the impacts of the compound extremes on natural and built environments (AghaKouchak et al., 2020; Zhang and Najafi, 2020);
- developing adaptation measures to the changing risk of compound extremes (Weber et al., 2020; Clarke et al., 2021);
- enhancing subseasonal-to-seasonal prediction of these extremes (Zamora et al., 2021; Zou, 2021);
- improving the representation and evaluation of compound extremes in fully-coupled climate models (Ridder et al., 2021; Zscheischler et al., 2021) and developing multivariate bias correction for these models (Vezzoli et al., 2017; Zscheischler et al., 2019);
- applying machine learning to understand these extremes (Wang L. et al., 2021; Zou, 2021).

AUTHOR CONTRIBUTIONS

WZ, SG, and ML designed the research. All the authors contribute to writing and reviewing the manuscript.

FUNDING

This study was jointly supported by the National Key R&D Program of China (2019YFC1510400), the National Natural Science Foundation of China (41871029), and the Science and Technology Program of Guangzhou (202102020489). The appointment of ML at Sun Yat-sen University is partially supported by the Pearl River Talent Recruitment Program of Guangdong Province, China (2017GC010634). WZ is supported by USDA NIFA Hatch Project (1026229), the UAES Seed Grant and the startup fund of Utah State University.

REFERENCES

Abatzoglou, J. T., and Williams, A. P. (2016). Impact of Anthropogenic Climate Change on Wildfire across Western US Forests. *Proc. Natl. Acad. Sci. USA* 113, 11770–11775. doi:10.1073/pnas.1607171113

AghaKouchak, A., Chiang, F., Huning, L. S., Love, C. A., Mallakpour, I., Mazdiyasni, O., et al. (2020). Climate Extremes and Compound Hazards in a Warming World. *Annu. Rev. Earth Planet. Sci.* 48, 519–548. doi:10.1146/annurev-earth-071719-055228

AghaKouchak, A., Huning, L. S., Chiang, F., Sadegh, M., Vahedifard, F., Mazdiyasni, O., et al. (2018). How Do Natural Hazards Cascade to Cause Disasters. 561, 458–460.

Alizadeh, M. R., Adamowski, J., Nikoo, M. R., AghaKouchak, A., Dennison, P., and Sadegh, M. (2020). A century of Observations Reveals Increasing Likelihood of continental-scale Compound Dry-Hot Extremes. *Sci. Adv.* 6. eaaz4571. doi:10.1126/sciadv.aaz4571

Amores, A., Marcos, M., Carrió, D. S., and Gómez-Pujol, L. (2020). Coastal Impacts of Storm Gloria (January 2020) over the north-western Mediterranean. *Nat. Hazards Earth Syst. Sci.* 20, 1955–1968. doi:10.5194/nhess-20-1955-2020

Andersen, T. K., and Marshall Shepherd, J. (2013). Floods in a Changing Climate. *Geogr. Compass* 7, 95–115. doi:10.1111/gec3.12025

Antonioli, F., Anzidei, M., Amorosi, A., Lo Presti, V., Mastronuzzi, G., Deiana, G., et al. (2017). Sea-level Rise and Potential Drowning of the Italian Coastal plains: Flooding Risk Scenarios for 2100. *Quat. Sci. Rev.* 158, 29–43. doi:10.1016/j.quascirev.2016.12.021

Arns, A., Wahl, T., Dangendorf, S., and Jensen, J. (2015). The Impact of Sea Level Rise on Storm Surge Water Levels in the Northern Part of the German Bight. *Coastal Eng.* 96, 118–131. doi:10.1016/j.coastaleng.2014.12.002

Bates, P. D., Quinn, N., Sampson, C., Smith, A., Wing, O., Sosa, J., et al. (2020).*Combined Modelling of US Fluvial, Pluvial and Coastal Flood hazard under Current and Future Climates*. Water Resources Research, e2020WR028673.

Beck, H. E., Van Dijk, A. I. J. M., Levizzani, V., Schellekens, J., Miralles, D. G., Martens, B., et al. (2017a). MSWEP: 3-hourly 0.25° Global Gridded Precipitation (1979-2015) by Merging Gauge, Satellite, and Reanalysis Data. *Hydrol. Earth Syst. Sci.* 21, 589–615. doi:10.5194/hess-21-589-2017

Beck, H. E., Vergopolan, N., Pan, M., Levizzani, V., van Dijk, A. I. J. M., Weedon, G. P., et al. (2017b). Global-scale Evaluation of 22 Precipitation Datasets Using Gauge Observations and Hydrological Modeling. *Hydrol. Earth Syst. Sci.* 21, 6201–6217. doi:10.5194/hess-21-6201-2017

Beniston, M. (2009). Trends in Joint Quantiles of Temperature and Precipitation in Europe since 1901 and Projected for 2100. *Geophys. Res. Lett.* 36, L07707. doi:10.1029/2008gl037119

Betts, A. K., Ball, J. H., Beljaars, A. C. M., Miller, M. J., and Viterbo, P. A. (1996). The Land Surface-Atmosphere Interaction: A Review Based on Observational and Global Modeling Perspectives. *J. Geophys. Res.* 101, 7209–7225. doi:10.1029/95jd02135

Bevacqua, E., Maraun, D., Vousdoukas, M. I., Voukouvalas, E., Vrac, M., Mentaschi, L., et al. (2019). Higher Probability of Compound Flooding from Precipitation and Storm Surge in Europe under Anthropogenic Climate Change. *Sci. Adv.* 5, eaaw5531. doi:10.1126/sciadv.aaw5531

Bevacqua, E., Vousdoukas, M. I., Zappa, G., Hodges, K., Shepherd, T. G., Maraun, D., et al. (2020). More Meteorological Events that Drive Compound Coastal Flooding Are Projected under Climate Change. *Commun. Earth Environ.* 1, 47–11. doi:10.1038/s43247-020-00044-z

Bevacqua, E., Maraun, D., Hobæk Haff, I., Widmann, M., and Vrac, M. (2017). Multivariate Statistical Modelling of Compound Events via Pair-Copula Constructions: Analysis of Floods in Ravenna (Italy). *Hydrol. Earth Syst. Sci.* 21, 2701–2723. doi:10.5194/hess-21-2701-2017

Bhatia, K. T., Vecchi, G. A., Knutson, T. R., Murakami, H., Kossin, J., Dixon, K. W., et al. (2019). Recent Increases in Tropical Cyclone Intensification Rates. *Nat. Commun.* 10, 635. doi:10.1038/s41467-019-08471-z

Bilskie, M. V., and Hagen, S. C. (2018). Defining Flood Zone Transitions in Low-Gradient Coastal Regions. *Geophys. Res. Lett.* 45, 2761–2770. doi:10.1002/2018gl077524

Bisci, C., Fazzini, M., Beltrando, G., Cardillo, A., and Romeo, V. (2012). The February 2012 Exceptional Snowfall along the Adriatic Side of Central Italy. *metz* 21, 503–508. doi:10.1127/0941-2948/2012/0536

Boers, N., Goswami, B., Rheinwalt, A., Bookhagen, B., Hoskins, B., and Kurths, J. (2019). Complex Networks Reveal Global Pattern of Extreme-Rainfall Teleconnections. *Nature* 566, 373–377. doi:10.1038/s41586-018-0872-x

Brackins, J. T., and Kalyanapu, A. J. (2020). Evaluation of Parametric Precipitation Models in Reproducing Tropical Cyclone Rainfall Patterns. *J. Hydrol.* 580, 124255. doi:10.1016/j.jhydrol.2019.124255

Bruneau, N., Polton, J., Williams, J., and Holt, J. (2020). Estimation of Global Coastal Sea Level Extremes Using Neural Networks. *Environ. Res. Lett.* 15 (7). doi:10.1088/1748-9326/ab89d6

Byrne, M. P., and O'Gorman, P. A. (2018). Trends in continental Temperature and Humidity Directly Linked to Ocean Warming. *Proc. Natl. Acad. Sci. USA* 115, 4863–4868. doi:10.1073/pnas.1722312115

Chang, F.-C., and Wallace, J. M. (1987). Meteorological Conditions during Heat Waves and Droughts in the United States Great Plains. *Mon. Wea. Rev.* 115, 1253–1269. doi:10.1175/1520-0493(1987)115<1253:mcdhwa>2.0.co;2

Chattopadhyay, A., Nabizadeh, E., and Hassanzadeh, P. (2020). Analog Forecasting of Extreme-Causing Weather Patterns Using Deep Learning. *J. Adv. Model. Earth Syst.* 12, e2019MS001958. doi:10.1029/2019MS001958

Chen, L., Chen, X., Cheng, L., Zhou, P., and Liu, Z. (2019a). Compound Hot Droughts over China: Identification, Risk Patterns and Variations. *Atmos. Res.* 227, 210–219. doi:10.1016/j.atmosres.2019.05.009

Chen, X., Li, N., Liu, J., Zhang, Z., and Liu, Y. (2019b). Global Heat Wave hazard Considering Humidity Effects during the 21st century. *Ijerph* 16, 1513. doi:10.3390/ijerph16091513

Chen, Y., Liao, Z., Shi, Y., Tian, Y., and Zhai, P. (2021). Detectable Increases in Sequential Flood-heatwave Events across China during 1961-2018. *Geophys. Res. Lett.* 48, e2021GL092549. doi:10.1029/2021gl092549

Chowdhury, Afmk., Lockart, N., Willgoose, G., Kuczera, G., Kiem, A. S., and Manage, N. P. (2015). *Modelling Daily Rainfall along the East Coast of Australia Using a Compound Distribution Markov Chain Model. In 36th Hydrology and Water Resources Symposium: The art and science of water*. Hobart, Australia: Engineers Australia, 625.

Chung, U., Gbegbelegbe, S., Shiferaw, B., Robertson, R., Yun, J. I., Tesfaye, K., et al. (2014). Modeling the Effect of a Heat Wave on maize Production in the USA and its Implications on Food Security in the Developing World. *Weather Clim. Extremes* 5-6, 67–77. doi:10.1016/j.wace.2014.07.002

Ciais, P., Reichstein, M., Viovy, N., Granier, A., Ogée, J., Allard, V., et al. (2005). Europe-wide Reduction in Primary Productivity Caused by the Heat and Drought in 2003. *Nature* 437, 529–533. doi:10.1038/nature03972

Cioni, G., and Hohenegger, C. (2017). Effect of Soil Moisture on Diurnal Convection and Precipitation in Large-Eddy Simulations. *J. Hydrometeorology* 18, 1885–1903. doi:10.1175/jhm-d-16-0241.1

Clarke, B. J., E. L. Otto, F. F., and Jones, R. G. (2021). Inventories of Extreme Weather Events and Impacts: Implications for Loss and Damage from and Adaptation to Climate Extremes. *Clim. Risk Manag.* 32, 100285. doi:10.1016/j.crm.2021.100285

Coffel, E. D., Horton, R. M., Winter, J. M., and Mankin, J. S. (2019). Nonlinear Increases in Extreme Temperatures Paradoxically Dampen Increases in Extreme Humid-Heat. *Environ. Res. Lett.* 14, 084003. doi:10.1088/1748-9326/ab28b7

Colle, B. A., Booth, J. F., and Chang, E. K. M. (2015). A Review of Historical and Future Changes of Extratropical Cyclones and Associated Impacts along the US East Coast. *Curr. Clim. Change Rep.* 1, 125–143. doi:10.1007/s40641-015-0013-7

Cook, B. I., Mankin, J. S., Marvel, K., Williams, A. P., Smerdon, J. E., and Anchukaitis, K. J. (2020). Twenty-first century Drought Projections in the CMIP6 Forcing Scenarios. *Earth's Future* 8, e2019EF001461. doi:10.1029/2019ef001461

Couasnon, A., Eilander, D., Muis, S., Veldkamp, T. I. E., Haigh, I. D., Wahl, T., et al. (2020). Measuring Compound Flood Potential from River Discharge and Storm Surge Extremes at the Global Scale. *Nat. Hazards Earth Syst. Sci.* 20, 489–504. doi:10.5194/nhess-20-489-2020

Couasnon, A., Sebastian, A., and Morales-Nápoles, O. (2018). A Copula-Based Bayesian Network for Modeling Compound Flood hazard from Riverine and Coastal Interactions at the Catchment Scale: An Application to the houston Ship Channel. *Tex. Water* 10, 1190.

Cowan, T., Purich, A., Perkins, S., Pezza, A., Boschat, G., and Sadler, K. (2014). More Frequent, Longer, and Hotter Heat Waves for Australia in the Twenty-First century. *J. Clim.* 27, 5851–5871. doi:10.1175/jcli-d-14-00092.1

Culley, S., Noble, S., Yates, A., Timbs, M., Westra, S., Maier, H. R., et al. (2016). A Bottom-Up Approach to Identifying the Maximum Operational Adaptive Capacity of Water Resource Systems to a Changing Climate. *Water Resour. Res.* 52, 6751–6768. doi:10.1002/2015wr018253

Czajkowski, J., Kunreuther, H., and Michel-Kerjan, E. (2013). Quantifying Riverine and Storm-surge Flood Risk by Single-Family Residence: Application to Texas. *Risk. Anal.* 33, 2092–2110. doi:10.1111/risa.12068

Dabhi, H., Dubrovsky, M., and Rotach, M. (2018). Simulation of Extreme Events Using a Stochastic Weather Generator in View of its Ability to deal with Compound Events. 19857.

Dabhi, H., Rotach, M. W., Dubrovský, M., and Oberguggenberger, M. (2021). Evaluation of a Stochastic Weather Generator in Simulating Univariate and Multivariate Climate Extremes in Different Climate Zones across Europe. *Meteorologische Z.* 30, 127–151. doi:10.1127/metz/2020/1021

Dahl, K. A., Fitzpatrick, M. F., and Spanger-Siegfried, E. (2017). Sea Level Rise Drives Increased Tidal Flooding Frequency at Tide Gauges along the U.S. East and Gulf Coasts: Projections for 2030 and 2045. *PloS one* 12, e0170949. doi:10.1371/journal.pone.0170949

Danard, M. B., Dube, S. K., Gönnert, G., Munroe, A., Murty, T. S., Chittibabu, P., et al. (2004). Storm Surges from Extra-tropical Cyclones. *Nat. Hazards* 32, 177–190. doi:10.1023/b:nhaz.0000031312.98231.81

Davolio, S., Della Fera, S., Laviola, S., Miglietta, M. M., and Levizzani, V. (2020). Heavy Precipitation over Italy from the Mediterranean Storm "Vaia" in October 2018: Assessing the Role of an Atmospheric River. *Monthly Weather Rev.* 148, 3571–3588. doi:10.1175/mwr-d-20-0021.1

De Luca, P., Messori, G., Faranda, D., Ward, P. J., and Coumou, D. (2020). Compound Warm-Dry and Cold-Wet Events over the Mediterranean. *Earth Syst. Dynam.* 11, 793–805. doi:10.5194/esd-11-793-2020

Dickinson, R. E. (1995). Land-atmosphere Interaction. *Rev. Geophys.* 33, 917–922. doi:10.1029/95rg00284

Dietrich, J. C., Bunya, S., Westerink, J. J., Ebersole, B. A., Smith, J. M., Atkinson, J. H., et al. (2010). A High-Resolution Coupled Riverine Flow, Tide, Wind, Wind Wave, and Storm Surge Model for Southern Louisiana and Mississippi. Part II: Synoptic Description and Analysis of Hurricanes Katrina and Rita. *Monthly Weather Rev.* 138, 378–404. doi:10.1175/2009mwr2907.1

D'Ippoliti, D., Michelozzi, P., Marino, C., de'Donato, F., Menne, B., Katsouyanni, K., et al. (2010). The Impact of Heat Waves on Mortality in 9 European Cities: Results from the EuroHEAT Project. *Environ. Health* 9, 1–9.

Dong, L., Mitra, C., Greer, S., and Burt, E. (2018). The Dynamical Linkage of Atmospheric Blocking to Drought, Heatwave and Urban Heat Island in southeastern US: A Multi-Scale Case Study. *Atmosphere* 9, 33. doi:10.3390/atmos9010033

Donges, J. F., Schleussner, C.-F., Siegmund, J. F., and Donner, R. V. (2016). Event Coincidence Analysis for Quantifying Statistical Interrelationships between Event Time Series. *Eur. Phys. J. Spec. Top.* 225, 471–487. doi:10.1140/epjst/e2015-50233-y

Easterling, D. R., Meehl, G. A., Parmesan, C., Changnon, S. A., Karl, T. R., and Mearns, L. O. (2000). Climate Extremes: Observations, Modeling, and Impacts. *Science* 289, 2068–2074. doi:10.1126/science.289.5487.2068

Eilander, D., Couasnon, A., Ikeuchi, H., Muis, S., Yamazaki, D., Winsemius, H. C., et al. (2020). The Effect of Surge on Riverine Flood hazard and Impact in Deltas Globally. *Environ. Res. Lett.* 15, 104007. doi:10.1088/1748-9326/ab8ca6

Ek, M. B., and Holtslag, A. A. M. (2004). Influence of Soil Moisture on Boundary Layer Cloud Development. *J. Hydrometeor* 5, 86–99. doi:10.1175/1525-7541(2004)005<0086:iosmob>2.0.co;2

Eltahir, E. A. B. (1998). A Soil Moisture-Rainfall Feedback Mechanism: 1. Theory and Observations. *Water Resour. Res.* 34, 765–776. doi:10.1029/97wr03499

Emanuel, K. (2017). Assessing the Present and Future Probability of Hurricane Harvey's Rainfall. *Proc. Natl. Acad. Sci. USA* 114, 12681–12684. doi:10.1073/pnas.1716222114

Ezer, T., and Atkinson, L. P. (2014). Accelerated Flooding along the U.S. East Coast: On the Impact of Sea-level Rise, Tides, Storms, the Gulf Stream, and the North Atlantic Oscillations. *Earth's Future* 2, 362–382. doi:10.1002/2014ef000252

Fang, J., Wahl, T., Fang, J., Sun, X., Kong, F., and Liu, M. (Forthcoming 2020). Compound Flood Potential from Storm Surge and Heavy Precipitation in Coastal China. *Hydrol. Earth Syst. Sci. Discuss.*

Fang, Y., Yin, J., and Wu, B. (2016). Flooding Risk Assessment of Coastal Tourist Attractions Affected by Sea Level Rise and Storm Surge: a Case Study in Zhejiang Province, China. *Nat. Hazards* 84, 611–624. doi:10.1007/s11069-016-2444-4

Feng, S., and Hao, Z. (2020). Quantifying Likelihoods of Extreme Occurrences Causing maize Yield Reduction at the Global Scale. *Sci. Total Environ.* 704, 135250. doi:10.1016/j.scitotenv.2019.135250

Feng, S., Wu, X., Hao, Z., Hao, Y., Zhang, X., and Hao, F. (2020). A Database for Characteristics and Variations of Global Compound Dry and Hot Events. *Weather Clim. Extremes* 30, 100299. doi:10.1016/j.wace.2020.100299

Feng, Y., Maulik, R., Wang, J., Balaprakash, P., Huang, W., Rao, V., et al. (2021). Characterization of Extremes and Compound Impacts: Applications of Machine Learning and Interpretable Neural Networks. *AI4ESP*. doi:10.2172/1769686

Fischer, E. M., and Knutti, R. (2013). Robust Projections of Combined Humidity and Temperature Extremes. *Nat. Clim Change* 3, 126–130. doi:10.1038/nclimate1682

Fischer, E. M., Seneviratne, S. I., Vidale, P. L., Lüthi, D., and Schär, C. (2007). Soil Moisture-Atmosphere Interactions during the 2003 European Summer Heat Wave. *J. Clim.* 20, 5081–5099. doi:10.1175/jcli4288.1

Fisher, J. B., Tu, K. P., and Baldocchi, D. D. (2008). Global Estimates of the Land-Atmosphere Water Flux Based on Monthly AVHRR and ISLSCP-II Data, Validated at 16 FLUXNET Sites. *Remote Sensing Environ.* 112, 901–919. doi:10.1016/j.rse.2007.06.025

Flato, G. M. (2011). Earth System Models: an Overview. *Wires Clim. Change* 2, 783–800. doi:10.1002/wcc.148

François, B., Vrac, M., Cannon, A. J., Robin, Y., and Allard, D. (2020). Multivariate Bias Corrections of Climate Simulations: Which Benefits for Which Losses. *Earth Syst. Dynam.* 11, 537–562. doi:10.5194/esd-11-537-2020

Frazier, T. G., Wood, N., Yarnal, B., and Bauer, D. H. (2010). Influence of Potential Sea Level Rise on Societal Vulnerability to hurricane Storm-Surge Hazards, Sarasota County, Florida. *Appl. Geogr.* 30, 490–505. doi:10.1016/j.apgeog.2010.05.005

Gallant, A. J. E., and Karoly, D. J. (2010). A Combined Climate Extremes index for the Australian Region. *J. Clim.* 23, 6153–6165. doi:10.1175/2010jcli3791.1

Gallant, A. J. E., Karoly, D. J., and Gleason, K. L. (2014). Consistent Trends in a Modified Climate Extremes index in the United States, Europe, and Australia. *J. Clim.* 27, 1379–1394. doi:10.1175/jcli-d-12-00783.1

Ganguli, P., Paprotny, D., Hasan, M., Güntner, A., and Merz, B. (2020). Projected Changes in Compound Flood hazard from Riverine and Coastal Floods in Northwestern Europe. *Earth's Future* 8, e2020EF001752. doi:10.1029/2020ef001752

Garcia, E. S., and Loáiciga, H. A. (2014). Sea-level Rise and Flooding in Coastal Riverine Flood plains. *Hydrological Sci. J.* 59, 204–220. doi:10.1080/02626667.2013.798660

Garner, A. J., Mann, M. E., Emanuel, K. A., Kopp, R. E., Lin, N., Alley, R. B., et al. (2017). Impact of Climate Change on New York City's Coastal Flood hazard: Increasing Flood Heights from the Preindustrial to 2300 CE. *Proc. Natl. Acad. Sci. USA* 114, 11861–11866. doi:10.1073/pnas.1703568114

Geoghegan, K. M., Fitzpatrick, P., Kolar, R. L., and Dresback, K. M. (2018). Evaluation of a Synthetic Rainfall Model, P-CLIPER, for Use in Coastal Flood Modeling. *Nat. Hazards* 92, 699–726. doi:10.1007/s11069-018-3220-4

Glahn, B., Taylor, A., Kurkowski, N., and Shaffer, W. A. (2009). The Role of the SLOSH Model in National Weather Service Storm Surge Forecasting. *Natl. Weather Dig.* 33, 3–14.

Gori, A., Lin, N., and Smith, J. (2020a). Assessing Compound Flooding from Landfalling Tropical Cyclones on the North Carolina Coast. *Water Resour. Res.* 56, e2019WR026788. doi:10.1029/2019wr026788

Gori, A., Lin, N., and Xi, D. (2020b). Tropical Cyclone Compound Flood hazard Assessment: from Investigating Drivers to Quantifying Extreme Water Levels. *Earth's Future* 8, e2020EF001660. doi:10.1029/2020ef001660

Grazzini, F., Craig, G. C., Keil, C., Antolini, G., and Pavan, V. (2019). Extreme Precipitation Events over Northern Italy. Part I: A Systematic Classification with Machine-learning Techniques. *Q. J. R. Meteorol. Soc.* 146, 69–85. doi:10.1002/qj.3635

Grieser, J., and Jewson, S. (2012). The RMS TC-Rain Model. *metz* 21, 79–88. doi:10.1127/0941-2948/2012/0265

Haigh, I. D., Wadey, M. P., Wahl, T., Ozsoy, O., Nicholls, R. J., Brown, J. M., et al. (2016). Spatial and Temporal Analysis of Extreme Sea Level and Storm Surge Events Around the Coastline of the UK. *Sci. Data* 3, 160107–160114. doi:10.1038/sdata.2016.107

Hallegatte, S., Ranger, N., Mestre, O., Dumas, P., Corfee-Morlot, J., Herweijer, C., et al. (2011). Assessing Climate Change Impacts, Sea Level Rise and Storm Surge Risk in Port Cities: a Case Study on Copenhagen. *Climatic Change* 104, 113–137. doi:10.1007/s10584-010-9978-3

Hao, Y., Hao, Z., Feng, S., Zhang, X., and Hao, F. (2020a). Response of Vegetation to El Niño-Southern Oscillation (ENSO) via Compound Dry and Hot Events in Southern Africa. *Glob. Planet. Change* 195, 103358. doi:10.1016/j.gloplacha.2020.103358

Hao, Z., and AghaKouchak, A. (2013). Multivariate Standardized Drought Index: A Parametric Multi-index Model. *Adv. Water Resour.* 57, 12–18. doi:10.1016/j.advwatres.2013.03.009

Hao, Z., AghaKouchak, A., and Phillips, T. J. (2013). Changes in Concurrent Monthly Precipitation and Temperature Extremes. *Environ. Res. Lett.* 8, 034014. doi:10.1088/1748-9326/8/3/034014

Hao, Z., Hao, F., Singh, V. P., Ouyang, W., Zhang, X., and Zhang, S. (2020b). A Joint Extreme index for Compound Droughts and Hot Extremes. *Theor. Appl. Climatol* 142, 321–328. doi:10.1007/s00704-020-03317-x

Hao, Z., Hao, F., Xia, Y., Singh, V. P., and Zhang, X. (2019). A Monitoring and Prediction System for Compound Dry and Hot Events. *Environ. Res. Lett.* 14, 114034. doi:10.1088/1748-9326/ab4df5

Hao, Z., Li, W., Singh, V. P., Xia, Y., Zhang, X., and Hao, F. (2020c). Impact of Dependence Changes on the Likelihood of Hot Extremes under Drought Conditions in the United States. *J. Hydrol.* 581, 124410. doi:10.1016/j.jhydrol.2019.124410

Hao, Z., Singh, V., and Hao, F. (2018). Compound Extremes in Hydroclimatology: a Review. *Water* 10, 718. doi:10.3390/w10060718

Hao, Z., and Singh, V. P. (2015). Drought Characterization from a Multivariate Perspective: A Review. *J. Hydrol.* 527, 668–678. doi:10.1016/j.jhydrol.2015.05.031

Haqiqi, I., Grogan, D. S., Hertel, T. W., and Schlenker, W. (2021). Quantifying the Impacts of Compound Extremes on Agriculture. *Hydrol. Earth Syst. Sci.* 25, 551–564. doi:10.5194/hess-25-551-2021

Hauser, M., Orth, R., and Seneviratne, S. I. (2016). Role of Soil Moisture versus Recent Climate Change for the 2010 Heat Wave in Western Russia. *Geophys. Res. Lett.* 43, 2819–2826. doi:10.1002/2016gl068036

Hawkes, P. J. (2008). Joint Probability Analysis for Estimation of Extremes. *J. Hydraulic Res.* 46, 246–256. doi:10.1080/00221686.2008.9521958

He, X., and Sheffield, J. (2020). Lagged Compound Occurrence of Droughts and Pluvials Globally over the Past Seven Decades. *Geophys. Res. Lett.* 47, e2020GL087924. doi:10.1029/2020gl087924

Heberger, M., Cooley, H., Herrera, P., Gleick, P. H., and Moore, E. (2011). Potential Impacts of Increased Coastal Flooding in California Due to Sea-Level Rise. *Climatic Change* 109, 229–249. doi:10.1007/s10584-011-0308-1

Heffernan, J. E., and Tawn, J. A. (2004). A Conditional Approach for Multivariate Extreme Values (With Discussion). *J. R. Stat. Soc B* 66, 497–546. doi:10.1111/j.1467-9868.2004.02050.x

Held, I. M., and Soden, B. J. (2006). Robust Responses of the Hydrological Cycle to Global Warming. *J. Clim.* 19, 5686–5699. doi:10.1175/jcli3990.1

Hendry, A., Haigh, I. D., Nicholls, R. J., Winter, H., Neal, R., Wahl, T., et al. (2019). Assessing the Characteristics and Drivers of Compound Flooding Events Around the UK Coast. *Hydrol. Earth Syst. Sci.* 23, 3117–3139. doi:10.5194/hess-23-3117-2019

Herdman, L., Erikson, L., and Barnard, P. (2018). Storm Surge Propagation and Flooding in Small Tidal Rivers during Events of Mixed Coastal and Fluvial Influence. *Jmse* 6, 158. doi:10.3390/jmse6040158

Herold, N., Kala, J., and Alexander, L. V. (2016). The Influence of Soil Moisture Deficits on Australian Heatwaves. *Environ. Res. Lett.* 11, 064003. doi:10.1088/1748-9326/11/6/064003

Hochman, A., Alpert, P., Harpaz, T., Saaroni, H., and Messori, G. (2019). A New Dynamical Systems Perspective on Atmospheric Predictability: Eastern Mediterranean Weather Regimes as a Case Study. *Sci. Adv.* 5, eaau0936. doi:10.1126/sciadv.aau0936

Holtslag, A. A. M., and Ek, M. (1996). Simulation of Surface Fluxes and Boundary Layer Development over the pine forest in HAPEX-MOBILHY. *J. Appl. Meteorol.* 35, 202–213. doi:10.1175/1520-0450(1996)035<0202:sosfab>2.0.co;2

Horton, D. E., Skinner, C. B., Singh, D., and Diffenbaugh, N. S. (2014). Occurrence and Persistence of Future Atmospheric Stagnation Events. *Nat. Clim Change* 4, 698–703. doi:10.1038/nclimate2272

Hoskins, B., and Woollings, T. (2015). Persistent Extratropical Regimes and Climate Extremes. *Curr. Clim. Change Rep.* 1, 115–124. doi:10.1007/s40641-015-0020-8

Hsiao, S.-C., Chiang, W.-S., Jang, J.-H., Wu, H.-L., Lu, W.-S., Chen, W.-B., et al. (2021). Flood Risk Influenced by the Compound Effect of Storm Surge and Rainfall under Climate Change for Low-Lying Coastal Areas. *Sci. Total Environ.* 764, 144439. doi:10.1016/j.scitotenv.2020.144439

Huang, W. K., Monahan, A. H., and Zwiers, F. W. (2021a). Estimating Concurrent Climate Extremes: A Conditional Approach. *Weather Clim. Extremes* 33, 100332. doi:10.1016/j.wace.2021.100332

Huang, W., Ye, F., Zhang, Y. J., Park, K., Du, J., Moghimi, S., et al. (2021b). Compounding Factors for Extreme Flooding Around Galveston Bay during Hurricane Harvey. *Ocean Model.* 158, 101735. doi:10.1016/j.ocemod.2020.101735

Ikeuchi, H., Hirabayashi, Y., Yamazaki, D., Muis, S., Ward, P. J., Winsemius, H. C., et al. (2017). Compound Simulation of Fluvial Floods and Storm Surges in a Global Coupled River-Coast Flood Model: Model Development and its Application to 2007 Cyclone Sidr in Bangladesh. *J. Adv. Model. Earth Syst.* 9, 1847–1862. doi:10.1002/2017ms000943

Imada, Y., Watanabe, M., Kawase, H., Shiogama, H., and Arai, M. (2019). The July 2018 High Temperature Event in Japan Could Not Have Happened without Human-Induced Global Warming. *SOLA*, 15A, 8–12. doi:10.2151/sola.15a-002

Interagency Performance Evaluation Task Force (IPET), 2006. "Performance Evaluation of the New Orleans and Southeast Louisiana Hurricane Protection System Draft Final Report of the Interagency Performance Evaluation Task Force Volume VIII – Engineering and Operational Risk and Reliability Analysis".

Ionita, M., Tallaksen, L. M., Kingston, D. G., Stagge, J. H., Laaha, G., Van Lanen, H. A. J., et al. (2017). The European 2015 Drought from a Climatological Perspective. *Hydrol. Earth Syst. Sci.* 21, 1397–1419. doi:10.5194/hess-21-1397-2017

Joyce, J., Chang, N.-B., Harji, R., Ruppert, T., and Singhofen, P. (2018). Cascade Impact of hurricane Movement, Storm Tidal Surge, Sea Level Rise and Precipitation Variability on Flood Assessment in a Coastal Urban Watershed. *Clim. Dyn.* 51, 383–409. doi:10.1007/s00382-017-3930-4

Jung, M., Reichstein, M., Ciais, P., Seneviratne, S. I., Sheffield, J., Goulden, M. L., et al. (2010). Recent Decline in the Global Land Evapotranspiration Trend Due to Limited Moisture Supply. *Nature* 467, 951–954. doi:10.1038/nature09396

Kabir, S., Patidar, S., Xia, X., Liang, Q., Neal, J., and Pender, G. (2020). A Deep Convolutional Neural Network Model for Rapid Prediction of Fluvial Flood Inundation. *J. Hydrol.* 590, 125481. doi:10.1016/j.jhydrol.2020.125481

Kala, J., De Kauwe, M. G., Pitman, A. J., Medlyn, B. E., Wang, Y.-P., Lorenz, R., et al. (2016). Impact of the Representation of Stomatal Conductance on Model Projections of Heatwave Intensity. *Sci. Rep.* 6, 1–7. doi:10.1038/srep23418

Kao, S.-C., and Govindaraju, R. S. (2010). A Copula-Based Joint Deficit index for Droughts. *J. Hydrol.* 380, 121–134. doi:10.1016/j.jhydrol.2009.10.029

Karegar, M. A., Dixon, T. H., Malservisi, R., Kusche, J., and Engelhart, S. E. (2017). Nuisance Flooding and Relative Sea-Level Rise: The Importance of Present-Day Land Motion. *Sci. Rep.* 7, 11197–11199. doi:10.1038/s41598-017-11544-y

Karim, M., and Mimura, N. (2008). Impacts of Climate Change and Sea-Level Rise on Cyclonic Storm Surge Floods in Bangladesh. *Glob. Environ. Change* 18, 490–500. doi:10.1016/j.gloenvcha.2008.05.002

Karl, T. R., Knight, R. W., Easterling, D. R., and Quayle, R. G. (1996). Indices of Climate Change for the United States. *Bull. Amer. Meteorol. Soc.* 77, 279–292. doi:10.1175/1520-0477(1996)077<0279:ioccft>2.0.co;2

Kerr, G. H., and Waugh, D. W. (2018). Connections between Summer Air Pollution and Stagnation. *Environ. Res. Lett.* 13, 084001. doi:10.1088/1748-9326/aad2e2

Keune, J., Gasper, F., Goergen, K., Hense, A., Shrestha, P., Sulis, M., et al. (2016). Studying the Influence of Groundwater Representations on Land Surface-atmosphere Feedbacks during the European Heat Wave in 2003. *J. Geophys. Res. Atmospheres* 121 (13), 301–313. doi:10.1002/2016jd025426

Kew, S. F., Selten, F. M., Lenderink, G., and Hazeleger, W. (2013). The Simultaneous Occurrence of Surge and Discharge Extremes for the Rhine delta. *Nat. Hazards Earth Syst. Sci.* 13, 2017–2029. doi:10.5194/nhess-13-2017-2013

Khanal, S., Ridder, N., de Vries, H., Terink, W., and van den Hurk, B. (2019). Storm Surge and Extreme River Discharge: a Compound Event Analysis Using Ensemble Impact Modeling. *Front. Earth Sci.* 7, 224. doi:10.3389/feart.2019.00224

Khanam, M., Sofia, G., Koukoula, M., Lazin, R., Nikolopoulos, E. I., Shen, X., et al. (2021). Impact of Compound Flood Event on Coastal Critical Infrastructures Considering Current and Future Climate. *Nat. Hazards Earth Syst. Sci.* 21, 587–605. doi:10.5194/nhess-21-587-2021

Khouakhi, A., and Villarini, G. (2016a). Attribution of Annual Maximum Sea Levels to Tropical Cyclones at the Global Scale. *Int. J. Climatol.* 37, 540–547. doi:10.1002/joc.4704

Khouakhi, A., and Villarini, G. (2016b). On the Relationship between Atmospheric Rivers and High Sea Water Levels along the U.S. West Coast. *Geophys. Res. Lett.* 43, 8815–8822. doi:10.1002/2016gl070086

Khouakhi, A., Villarini, G., and Vecchi, G. A. (2017). Contribution of Tropical Cyclones to Rainfall at the Global Scale. *J. Clim.* 30, 359–372. doi:10.1175/jcli-d-16-0298.1

Kleinosky, L. R., Yarnal, B., and Fisher, A. (2007). Vulnerability of Hampton Roads, Virginia to Storm-Surge Flooding and Sea-Level Rise. *Nat. Hazards* 40, 43–70. doi:10.1007/s11069-006-0004-z

Klerk, W. J., Winsemius, H. C., Van Verseveld, W. J., Bakker, A. M. R., and Diermanse, F. L. M. (2015). The Co-incidence of Storm Surges and Extreme Discharges within the Rhine-Meuse Delta. *Environ. Res. Lett.* 10, 035005. doi:10.1088/1748-9326/10/3/035005

Knapp, K. R., Kruk, M. C., Levinson, D. H., Diamond, H. J., and Neumann, C. J. (2010). The International Best Track Archive for Climate Stewardship (IBTrACS). *Bull. Amer. Meteorol. Soc.* 91, 363–376. doi:10.1175/2009bams2755.1

Knutson, T. R., McBride, J. L., Chan, J., Emanuel, K., Holland, G., Landsea, C., et al. (2010). Tropical Cyclones and Climate Change. *Nat. Geosci* 3, 157–163. doi:10.1038/ngeo779

Knutson, T. R., Sirutis, J. J., Zhao, M., Tuleya, R. E., Bender, M., Vecchi, G. A., et al. (2015). Global Projections of Intense Tropical Cyclone Activity for the Late Twenty-First Century from Dynamical Downscaling of CMIP5/RCP4.5 Scenarios. *J. Clim.* 28, 7203–7224. doi:10.1175/jcli-d-15-0129.1

Kong, Q., Guerreiro, S. B., Blenkinsop, S., Li, X.-F., and Fowler, H. J. (2020). Increases in Summertime Concurrent Drought and Heatwave in Eastern China. *Weather Clim. Extremes* 28, 100242. doi:10.1016/j.wace.2019.100242

Krakauer, N. Y., Cook, B. I., and Puma, M. J. (2020). Effect of Irrigation on Humid Heat Extremes. *Environ. Res. Lett.* 15, 094010. doi:10.1088/1748-9326/ab9ecf

Kriebel, D. L., and Geiman, J. D. (2014). A Coastal Flood Stage to Define Existing and Future Sea-Level Hazards. *J. Coastal Res.* 297, 1017–1024. doi:10.2112/jcoastres-d-13-00068.1

Kulp, S. A., and Strauss, B. H. (2019). New Elevation Data Triple Estimates of Global Vulnerability to Sea-Level Rise and Coastal Flooding. *Nat. Commun.* 10, 4844. doi:10.1038/s41467-019-12808-z

Langousis, A., and Veneziano, D. (2009). Theoretical Model of Rainfall in Tropical Cyclones for the Assessment of Long-term Risk. *J. Geophys. Res. Atmospheres* 114. doi:10.1029/2008jd010080

Lansu, E. M., van Heerwaarden, C. C., Stegehuis, A. I., and Teuling, A. J. (2020). Atmospheric Aridity and Apparent Soil Moisture Drought in European forest during Heat Waves. *Geophys. Res. Lett.* 47, e2020GL087091. doi:10.1029/2020gl087091

Leonard, M., Westra, S., Phatak, A., Lambert, M., van den Hurk, B., McInnes, K., et al. (2014a). A Compound Event Framework for Understanding Extreme Impacts. *Wires Clim. Change* 5, 113–128. doi:10.1002/wcc.252

Li, D., Yuan, J., and Kopp, R. E. (2020). Escalating Global Exposure to Compound Heat-Humidity Extremes with Warming. *Environ. Res. Lett.* 15, 064003. doi:10.1088/1748-9326/ab7d04

Li, M., Yao, Y., Luo, D., and Zhong, L. (2019). The Linkage of the Large-Scale Circulation Pattern to a Long-Lived Heatwave over Mideastern China in 2018. *Atmosphere* 10, 89. doi:10.3390/atmos10020089

Lin, M., Horowitz, L. W., Xie, Y., Paulot, F., Malyshev, S., Shevliakova, E., et al. (2020). Vegetation Feedbacks during Drought Exacerbate Ozone Air Pollution Extremes in Europe. *Nat. Clim. Chang.* 10, 444–451. doi:10.1038/s41558-020-0743-y

Lin, N., and Chavas, D. (2012). On hurricane Parametric Wind and Applications in Storm Surge Modeling. *J. Geophys. Res. Atmospheres* 117. doi:10.1029/2011jd017126

Lin, N., Emanuel, K. A., Smith, J. A., and Vanmarcke, E. (2010a). Risk Assessment of hurricane Storm Surge for New York City. *J. Geophys. Res. Atmospheres* 115. doi:10.1029/2009jd013630

Lin, N., Marsooli, R., and Colle, B. A. (2019). Storm Surge Return Levels Induced by Mid-to-late-twenty-first-century Extratropical Cyclones in the Northeastern United States. *Climatic change* 154, 143–158. doi:10.1007/s10584-019-02431-8

Lin, N., Smith, J. A., Villarini, G., Marchok, T. P., and Baeck, M. L. (2010b). Modeling Extreme Rainfall, Winds, and Surge from Hurricane Isabel (2003). *Weather Forecast.* 25, 1342–1361. doi:10.1175/2010waf2222349.1

Little, C. M., Horton, R. M., Kopp, R. E., Oppenheimer, M., Vecchi, G. A., and Villarini, G. (2015). Joint Projections of US East Coast Sea Level and Storm Surge. *Nat. Clim Change* 5, 1114–1120. doi:10.1038/nclimate2801

Liu, M., Vecchi, G. A., Smith, J. A., and Murakami, H. (2018). Projection of Landfalling-Tropical Cyclone Rainfall in the Eastern United States under Anthropogenic Warming. *J. Clim.* 31, 7269–7286. doi:10.1175/jcli-d-17-0747.1

Liu, Q., Zhou, T., Mao, H., and Fu, C. (2019). Decadal Variations in the Relationship between the Western Pacific Subtropical High and Summer Heat Waves in East China. *J. Clim.* 32, 1627–1640. doi:10.1175/jcli-d-18-0093.1

Liu, X., He, B., Guo, L., Huang, L., and Chen, D. (2020). Similarities and Differences in the Mechanisms Causing the European Summer Heatwaves in 2003, 2010, and 2018. *Earth's Future* 8, e2019EF001386. doi:10.1029/2019ef001386

Lobell, D. B., Bonfils, C. J., Kueppers, L. M., and Snyder, M. A. (2008). Irrigation Cooling Effect on Temperature and Heat index Extremes. *Geophys. Res. Lett.* 35. doi:10.1029/2008gl034145

Lonfat, M., Rogers, R., Marchok, T., and Marks, F. D., Jr (2007). A Parametric Model for Predicting hurricane Rainfall. *Monthly Weather Rev.* 135, 3086–3097. doi:10.1175/mwr3433.1

Lu, Y., Hu, H., Li, C., and Tian, F. (2018). Increasing Compound Events of Extreme Hot and Dry Days during Growing Seasons of Wheat and maize in China. *Sci. Rep.* 8, 16700–16708. doi:10.1038/s41598-018-34215-y

Luo, M., and Lau, N.-C. (2017). Heat Waves in Southern China: Synoptic Behavior, Long-Term Change, and Urbanization Effects. *J. Clim.* 30, 703–720. doi:10.1175/jcli-d-16-0269.1

Luo, M., and Lau, N.-C. (2018). Increasing Heat Stress in Urban Areas of Eastern China: Acceleration by Urbanization. *Geophys. Res. Lett.* 45, 13060–13069. doi:10.1029/2018gl080306

Luo, M., and Lau, N.-C. (2021). *Increasing Human-Perceived Heat Stress Risks Exacerbated by Urbanization in China: A Comparative Study Based on Multiple Metrics*. Earth's Future 9, e2020EF001848. doi:10.1029/2020EF001848

Luo, M., and Lau, N.-C. (2020). Summer Heat Extremes in Northern Continents Linked to Developing ENSO Events. *Environ. Res. Lett.* 15, 074042. doi:10.1088/1748-9326/ab7d07

Luo, M., Ning, G., Xu, F., Wang, S., Liu, Z., and Yang, Y. (2020). Observed Heatwave Changes in Arid Northwest China: Physical Mechanism and Long-Term Trend. *Atmos. Res.* 242, 105009. doi:10.1016/j.atmosres.2020.105009

Lutsko, N. J. (2021). The Relative Contributions of Temperature and Moisture to Heat Stress Changes under Warming. *J. Clim.* 34, 901–917. doi:10.1175/jcli-d-20-0262.1

Mäll, M., Suursaar, Ü., Nakamura, R., and Shibayama, T. (2017). Modelling a Storm Surge under Future Climate Scenarios: Case Study of Extratropical Cyclone Gudrun (2005). *Nat. Hazards* 89, 1119–1144. doi:10.1007/s11069-017-3011-3

Mann, M. E., Rahmstorf, S., Kornhuber, K., Steinman, B. A., Miller, S. K., and Coumou, D. (2017). Influence of Anthropogenic Climate Change on Planetary Wave Resonance and Extreme Weather Events. *Scientific Rep.* 7, 1–12. doi:10.1038/srep45242

Maraun, D. (2016). Bias Correcting Climate Change Simulations - a Critical Review. *Curr. Clim. Change Rep.* 2, 211–220. doi:10.1007/s40641-016-0050-x

Marks, F. D., and DeMaria, M. (2003). Development of a Tropical Cyclone Rainfall Climatology and Persistence (R-CLIPER) Model. Technical report, NOAA/OAR/AOML/HurricaneResearch Division.

Marsooli, R., Lin, N., Emanuel, K., and Feng, K. (2019). Climate Change Exacerbates hurricane Flood Hazards along US Atlantic and Gulf Coasts in Spatially Varying Patterns. *Nat. Commun.* 10, 3785–3789. doi:10.1038/s41467-019-11755-z

Martius, O., Pfahl, S., and Chevalier, C. (2016). A Global Quantification of Compound Precipitation and Wind Extremes. *Geophys. Res. Lett.* 43, 7709–7717. doi:10.1002/2016gl070017

Massmann, A., Gentine, P., and Lin, C. (2019). When Does Vapor Pressure Deficit Drive or Reduce Evapotranspiration. *J. Adv. Model. Earth Syst.* 11, 3305–3320. doi:10.1029/2019ms001790

Matsueda, M. (2011). Predictability of Euro-Russian Blocking in Summer of 2010. *Geophys. Res. Lett.* 38. doi:10.1029/2010gl046557

Mazdiyasni, O., and AghaKouchak, A. (2015). Substantial Increase in Concurrent Droughts and Heatwaves in the United States. *Proc. Natl. Acad. Sci. USA* 112, 11484–11489. doi:10.1073/pnas.1422945112

McInnes, K. L., Macadam, I., Hubbert, G., and O'Grady, J. (2013). An Assessment of Current and Future Vulnerability to Coastal Inundation Due to Sea-Level Extremes in Victoria, Southeast Australia. *Int. J. Climatol.* 33, 33–47. doi:10.1002/joc.3405

McInnes, K. L., Walsh, K. J. E., Hubbert, G. D., and Beer, T. (2003). Impact of Sea-Level Rise and Storm Surges on a Coastal Community. *Nat. Hazards* 30, 187–207. doi:10.1023/a:1026118417752

Meehl, G. A., Senior, C. A., Eyring, V., Flato, G., Lamarque, J.-F., Stouffer, R. J., et al. (2020). Context for Interpreting Equilibrium Climate Sensitivity and Transient Climate Response from the CMIP6 Earth System Models. *Sci. Adv.* 6, eaba1981. doi:10.1126/sciadv.aba1981

Meng, L., and Shen, Y. (2014). On the Relationship of Soil Moisture and Extreme Temperatures in East China. *Earth Interactions* 18, 1–20. doi:10.1175/2013ei000551.1

Miao, C., Sun, Q., Duan, Q., and Wang, Y. (2016). Joint Analysis of Changes in Temperature and Precipitation on the Loess Plateau during the Period 1961-2011. *Clim. Dyn.* 47, 3221–3234. doi:10.1007/s00382-016-3022-x

Miralles, D. G., Gentine, P., Seneviratne, S. I., and Teuling, A. J. (2019). Land-atmospheric Feedbacks during Droughts and Heatwaves: State of the Science and Current Challenges. *Ann. N.Y. Acad. Sci.* 1436, 19–35. doi:10.1111/nyas.13912

Miralles, D. G., Holmes, T. R. H., De Jeu, R. A. M., Gash, J. H., Meesters, A. G. C. A., and Dolman, A. J. (2011). Global Land-Surface Evaporation Estimated from Satellite-Based Observations. *Hydrol. Earth Syst. Sci.* 15, 453–469. doi:10.5194/hess-15-453-2011

Miralles, D. G., Teuling, A. J., Van Heerwaarden, C. C., and Vilà-Guerau de Arellano, J. (2014). Mega-heatwave Temperatures Due to Combined Soil Desiccation and Atmospheric Heat Accumulation. *Nat. Geosci* 7, 345–349. doi:10.1038/ngeo2141

Mitchell, D., Heaviside, C., Vardoulakis, S., Huntingford, C., Masato, G., P Guillod, B., et al. (2016). Attributing Human Mortality during Extreme Heat Waves to Anthropogenic Climate Change. *Environ. Res. Lett.* 11, 074006. doi:10.1088/1748-9326/11/7/074006

Moftakhari, H. R., Salvadori, G., AghaKouchak, A., Sanders, B. F., and Matthew, R. A. (2017a). Compounding Effects of Sea Level Rise and Fluvial Flooding. *Proc. Natl. Acad. Sci. USA* 114, 9785–9790. doi:10.1073/pnas.1620325114

Mohanty, M. P., Sherly, M. A., Ghosh, S., and Karmakar, S. (2020). Tide-rainfall Flood Quotient: an Incisive Measure of Comprehending a Region's Response to Storm-Tide and Pluvial Flooding. *Environ. Res. Lett.* 15, 064029. doi:10.1088/1748-9326/ab8092

Morán-Tejeda, E., Herrera, S., Ignacio López-Moreno, J., Revuelto, J., Lehmann, A., and Beniston, M. (2013). Evolution and Frequency (1970-2007) of Combined Temperature-Precipitation Modes in the Spanish Mountains and Sensitivity of Snow Cover. *Reg. Environ. Change* 13, 873–885. doi:10.1007/s10113-012-0380-8

Mousavi, M. E., Irish, J. L., Frey, A. E., Olivera, F., and Edge, B. L. (2011). Global Warming and Hurricanes: the Potential Impact of hurricane Intensification and Sea Level Rise on Coastal Flooding. *Climatic Change* 104, 575–597. doi:10.1007/s10584-009-9790-0

Mu, Q., Zhao, M., and Running, S. W. (2011). Improvements to a MODIS Global Terrestrial Evapotranspiration Algorithm. *Remote sensing Environ.* 115, 1781–1800. doi:10.1016/j.rse.2011.02.019

Mueller, B., and Seneviratne, S. I. (2012). Hot Days Induced by Precipitation Deficits at the Global Scale. *Proc. Natl. Acad. Sci.* 109, 12398–12403. doi:10.1073/pnas.1204330109

Muis, S., Verlaan, M., Winsemius, H. C., Aerts, J. C. J. H., and Ward, P. J. (2016). A Global Reanalysis of Storm Surges and Extreme Sea Levels. *Nat. Commun.* 7, 11969. doi:10.1038/ncomms11969

Mukherjee, S., Ashfaq, M., and Mishra, A. K. (2020). Compound Drought and Heatwaves at a Global Scale: The Role of Natural Climate Variability-associated Synoptic Patterns and Land-surface Energy Budget Anomalies. *J. Geophys. Res. Atmospheres* 125, e2019JD031943. doi:10.1029/2019jd031943

Murakami, H., Villarini, G., Vecchi, G. A., Zhang, W., and Gudgel, R. (2016). Statistical-Dynamical Seasonal Forecast of North Atlantic and U.S. Landfalling Tropical Cyclones Using the High-Resolution GFDL FLOR Coupled Model. *Monthly Weather Rev.* 144, 2101–2123. doi:10.1175/mwr-d-15-0308.1

Nadal, N. C., Zapata, R. E., Pagán, I., López, R., and Agudelo, J. (2010). Building Damage Due to Riverine and Coastal Floods. *J. Water Resour. Plann. Manage.* 136, 327–336. doi:10.1061/(asce)wr.1943-5452.0000036

Nelsen, R. B. (2007). *An Introduction to Copulas*. Springer Science & Business Media.

Nowack, P., Runge, J., Eyring, V., and Haigh, J. D. (2020). Causal Networks for Climate Model Evaluation and Constrained Projections. *Nat. Commun.* 11, 1–11. doi:10.1038/s41467-020-15195-y

Oleson, K. W., Monaghan, A., Wilhelmi, O., Barlage, M., Brunsell, N., Feddema, J., et al. (2015). Interactions between Urbanization, Heat Stress, and Climate Change. *Climatic Change* 129, 525–541. doi:10.1007/s10584-013-0936-8

Orlowsky, B., and Seneviratne, S. I. (2013). Elusive Drought: Uncertainty in Observed Trends and Short- and Long-Term CMIP5 Projections. *Hydrol. Earth Syst. Sci.* 17, 1765–1781. doi:10.5194/hess-17-1765-2013

Paprotny, D., Vousdoukas, M. I., Morales-Nápoles, O., Jonkman, S. N., and Feyen, L. (2018). Compound Flood Potential in Europe. *Hydrol. Earth Syst. Sci. Discuss.* 1–34.

Petroliagkis, T. I., Voukouvalas, E., Disperati, J., and Bidlot, J. (2016). *Joint Probabilities of Storm Surge, Significant Wave Height and River Discharge Components of Coastal Flooding Events*. Italia: European Commission-JRC Technical Reports. Available at: http://bookshop.europa.eu/en/joint-probabilities-of-storm-surge-significant-wave-height-and-river-discharge-components-of-coastal-flooding-eventspbLBNA27824.

Poppick, A., and McKinnon, K. A. (2020). Observation-based Simulations of Humidity and Temperature Using Quantile Regression. *J. Clim.* 33, 10691–10706. doi:10.1175/jcli-d-20-0403.1

Potopová, V., Lhotka, O., Možný, M., and Musiolková, M. (2021). Vulnerability of Hop-Yields Due to Compound Drought and Heat Events over European Key-Hop Regions. *Int. J. Climatology* 41, E2136–E2158. doi:10.1002/joc.6836

Quesada, B., Vautard, R., Yiou, P., Hirschi, M., and Seneviratne, S. I. (2012). Asymmetric European Summer Heat Predictability from Wet and Dry Southern winters and Springs. *Nat. Clim Change* 2, 736–741. doi:10.1038/nclimate1536

Ramsey, E., Lu, Z., Suzuoki, Y., Rangoonwala, A., and Werle, D. (2011). Monitoring Duration and Extent of Storm-Surge and Flooding in Western Coastal Louisiana Marshes with Envisat ASAR Data. *IEEE J. Sel. Top. Appl. Earth Observations Remote Sensing* 4, 387–399. doi:10.1109/jstars.2010.2096201

Rasmijn, L. M., Van der Schrier, G., Bintanja, R., Barkmeijer, J., Sterl, A., and Hazeleger, W. (2018). Future Equivalent of 2010 Russian Heatwave Intensified by Weakening Soil Moisture Constraints. *Nat. Clim Change* 8, 381–385. doi:10.1038/s41558-018-0114-0

Raymond, C., Horton, R. M., Zscheischler, J., Martius, O., AghaKouchak, A., Balch, J., et al. (2020a). Understanding and Managing Connected Extreme Events. *Nat. Clim. Chang.* 10, 611–621. doi:10.1038/s41558-020-0790-4

Raymond, C., Matthews, T., and Horton, R. M. (2020b). The Emergence of Heat and Humidity Too Severe for Human Tolerance. *Sci. Adv.* 6, eaaw1838. doi:10.1126/sciadv.aaw1838

Reguero, B. G., Losada, I. J., Díaz-Simal, P., Méndez, F. J., and Beck, M. W. (2015). Effects of Climate Change on Exposure to Coastal Flooding in Latin America and the Caribbean. *PLoS One* 10, e0133409. doi:10.1371/journal.pone.0133409

Reimann, L., Vafeidis, A. T., Brown, S., Hinkel, J., and Tol, R. S. (2018). Mediterranean UNESCO World Heritage at Risk from Coastal Flooding and Erosion Due to Sea-Level Rise. *Nat. Commun.* 9, 1–11. doi:10.1038/s41467-018-06645-9

Ribeiro, A. F. S., Russo, A., Gouveia, C. M., Páscoa, P., and Zscheischler, J. (2020b). Risk of Crop Failure Due to Compound Dry and Hot Extremes Estimated with Nested Copulas. *Biogeosciences* 17, 4815–4830. doi:10.5194/bg-17-4815-2020

Ribeiro, A. F. S., Russo, A., Gouveia, C. M., and Pires, C. A. L. (2020a). Drought-related Hot Summers: A Joint Probability Analysis in the Iberian Peninsula. *Weather Clim. Extremes* 30, 100279. doi:10.1016/j.wace.2020.100279

Ridder, N., de Vries, H., and Drijfhout, S. (2018). The Role of Atmospheric Rivers in Compound Events Consisting of Heavy Precipitation and High Storm Surges along the Dutch Coast. *Nat. Hazards Earth Syst. Sci.* 18, 3311–3326. doi:10.5194/nhess-18-3311-2018

Ridder, N. N., Pitman, A. J., and Ukkola, A. M. (2021). Do CMIP6 Climate Models Simulate Global or Regional Compound Events Skillfully. *Geophys. Res. Lett.* 48, e2020GL091152. doi:10.1029/2020gl091152

Ridder, N. N., Pitman, A. J., Westra, S., Ukkola, A., Do, H. X., Bador, M., et al. (2020). Global Hotspots for the Occurrence of Compound Events. *Nat. Commun.* 11, 5956. doi:10.1038/s41467-020-19639-3

Rigden, A. J., and Salvucci, G. D. (2017). Stomatal Response to Humidity and CO 2 Implicated in Recent Decline in US Evaporation. *Glob. Change Biol.* 23, 1140–1151. doi:10.1111/gcb.13439

Rinaldo, A., Nicotina, L., Alessi Celegon, E., Beraldin, F., Botter, G., Carniello, L., et al. (2008). Sea Level Rise, Hydrologic Runoff, and the Flooding of Venice. *Water Resour. Res.* 44. doi:10.1029/2008wr007195

Rios Gaona, M. F., Villarini, G., Zhang, W., and Vecchi, G. A. (2018). The Added Value of IMERG in Characterizing Rainfall in Tropical Cyclones. *Atmos. Res.* 209, 95–102. doi:10.1016/j.atmosres.2018.03.008

Roberts, M. J., Camp, J., Seddon, J., Vidale, P. L., Hodges, K., Vannière, B., et al. (2020). Projected Future Changes in Tropical Cyclones Using the CMIP6 HighResMIP Multimodel Ensemble. *Geophys. Res. Lett.* 47, e2020GL088662. doi:10.1029/2020GL088662

Rodrigo, F. S. (2015). On the Covariability of Seasonal Temperature and Precipitation in Spain, 1956-2005. *Int. J. Climatol.* 35, 3362–3370. doi:10.1002/joc.4214

Rowell, D. P. (2009). Projected Midlatitude continental Summer Drying: North America versus Europe. *J. Clim.* 22, 2813–2833. doi:10.1175/2008jcli2713.1

Russo, S., Sillmann, J., and Sterl, A. (2017). Humid Heat Waves at Different Warming Levels. *Sci. Rep.* 7, 7477–7. doi:10.1038/s41598-017-07536-7

Sadegh, M., Moftakhari, H., Gupta, H. V., Ragno, E., Mazdiyasni, O., Sanders, B., et al. (2018). Multihazard Scenarios for Analysis of Compound Extreme Events. *Geophys. Res. Lett.* 45, 5470–5480. doi:10.1029/2018gl077317

Salvadori, G., Durante, F., and De Michele, C. (2013). Multivariate Return Period Calculation via Survival Functions. *Water Resour. Res.* 49, 2308–2311. doi:10.1002/wrcr.20204

Sanuy, M., Rigo, T., Jiménez, J. A., and Llasat, M. C. (2020). Classifying Compound Coastal Storm and Heavy Rainfall Events in the north-western Spanish Mediterranean. *Hydrol. Earth Syst. Sci. Discuss.* 1–24.

Schindelegger, M., Green, J. A. M., Wilmes, S. B., and Haigh, I. D. (2018). Can We Model the Effect of Observed Sea Level Rise on Tides. *J. Geophys. Res. Oceans* 123, 4593–4609. doi:10.1029/2018jc013959

Schneidereit, A., Schubert, S., Vargin, P., Lunkeit, F., Zhu, X., Peters, D. H. W., et al. (2012). Large-scale Flow and the Long-Lasting Blocking High over Russia: Summer 2010. *Monthly Weather Rev.* 140, 2967–2981. doi:10.1175/mwr-d-11-00249.1

Schnell, J. L., and Prather, M. J. (2017). Co-occurrence of Extremes in Surface Ozone, Particulate Matter, and Temperature over Eastern North America. *Proc. Natl. Acad. Sci. USA* 114, 2854–2859. doi:10.1073/pnas.1614453114

Schumacher, D. L., Keune, J., Van Heerwaarden, C. C., Vilà-Guerau de Arellano, J., Teuling, A. J., and Miralles, D. G. (2019). Amplification of Mega-Heatwaves through Heat Torrents Fuelled by Upwind Drought. *Nat. Geosci.* 12, 712–717. doi:10.1038/s41561-019-0431-6

Scoccimarro, E., Villarini, G., Gualdi, S., Navarra, A., Vecchi, G., Walsh, K., et al. (2017).Tropical Cyclone Rainfall Changes in a Warmer Climate. In Hurricanes and Climate Change. Springer, 243–255. doi:10.1007/978-3-319-47594-3_10

Screen, J. A., and Simmonds, I. (2014). Amplified Mid-latitude Planetary Waves Favour Particular Regional Weather Extremes. *Nat. Clim Change* 4, 704–709. doi:10.1038/nclimate2271

Seager, R., and Hoerling, M. (2014). Atmosphere and Ocean Origins of North American Droughts*. *J. Clim.* 27, 4581–4606. doi:10.1175/jcli-d-13-00329.1

Sebastian, A., Proft, J., Dietrich, J. C., Du, W., Bedient, P. B., and Dawson, C. N. (2014). Characterizing hurricane Storm Surge Behavior in Galveston Bay Using the SWAN+ADCIRC Model. *Coastal Eng.* 88, 171–181. doi:10.1016/j.coastaleng.2014.03.002

Sedlmeier, K., Feldmann, H., and Schädler, G. (2018). Compound Summer Temperature and Precipitation Extremes over central Europe. *Theor. Appl. Climatol* 131, 1493–1501. doi:10.1007/s00704-017-2061-5

Sedlmeier, K., Mieruch, S., Schädler, G., and Kottmeier, C. (2016). Compound Extremes in a Changing Climate - a Markov Chain Approach. *Nonlin. Process. Geophys.* 23, 375–390. doi:10.5194/npg-23-375-2016

Seneviratne, S. I., Lüthi, D., Litschi, M., and Schär, C. (2006). Land-atmosphere Coupling and Climate Change in Europe. *Nature* 443, 205–209. doi:10.1038/nature05095

Seneviratne, S., Nicholls, N., Easterling, D., Goodess, C., Kanae, S., Kossin, J., et al. (2012). Changes in Climate Extremes and Their Impacts on the Natural Physical Environment.

Sherwood, S. C. (2018). How Important Is Humidity in Heat Stress. *J. Geophys. Res. Atmospheres* 123 (11), 808–811. doi:10.1029/2018jd028969

Sillmann, J., Thorarinsdottir, T., Keenlyside, N., Schaller, N., Alexander, L. V., Hegerl, G., et al. (2017). Understanding, Modeling and Predicting Weather and Climate Extremes: Challenges and Opportunities. *Weather Clim. Extremes* 18, 65–74. doi:10.1016/j.wace.2017.10.003

Singh, J., Ashfaq, M., Skinner, C. B., Anderson, W. B., and Singh, D. (2021). Amplified Risk of Spatially Compounding Droughts during Co-occurrences of Modes of Natural Ocean Variability. *npj Clim. Atmos. Sci.* 4, 1–14. doi:10.1038/s41612-021-00161-2

Slater, L. J., Anderson, B., Buechel, M., Dadson, S., Han, S., Harrigan, S., et al. (2021). Nonstationary Weather and Water Extremes: a Review of Methods for Their Detection, Attribution, and Management. *Hydrol. Earth Syst. Sci.*, 1–54. doi:10.5194/hess-25-3897-2021

Slater, L. J., and Villarini, G. (2018). Enhancing the Predictability of Seasonal Streamflow with a Statistical-Dynamical Approach. *Geophys. Res. Lett.* 45 (13), 6504–6513. doi:10.1029/2018gl077945

Soneja, S., Jiang, C., Fisher, J., Upperman, C. R., Mitchell, C., and Sapkota, A. (2016). Exposure to Extreme Heat and Precipitation Events Associated with Increased Risk of Hospitalization for Asthma in Maryland, U.S.A. *Environ. Health* 15, 57–7. doi:10.1186/s12940-016-0142-z

Stéfanon, M., Drobinski, P., D'Andrea, F., Lebeaupin-Brossier, C., and Bastin, S. (2014). Soil Moisture-Temperature Feedbacks at Meso-Scale during Summer Heat Waves over Western Europe. *Clim. Dyn.* 42, 1309–1324. doi:10.1007/s00382-013-1794-9

Stegehuis, A. I., Vautard, R., Ciais, P., Teuling, A. J., Miralles, D. G., and Wild, M. (2015). An Observation-Constrained Multi-Physics WRF Ensemble for Simulating European Mega Heat Waves. *Geosci. Model. Dev.* 8, 2285–2298. doi:10.5194/gmd-8-2285-2015

Steinemann, A. (2003). Drought Indicators and Triggers: a Stochastic Approach to Evaluation. *J. Am. Water Resour. Assoc* 39, 1217–1233. doi:10.1111/j.1752-1688.2003.tb03704.x

Su, B., Huang, J., Mondal, S. K., Zhai, J., Wang, Y., Wen, S., et al. (2021). Insight from CMIP6 SSP-RCP Scenarios for Future Drought Characteristics in China. *Atmos. Res.* 250, 105375. doi:10.1016/j.atmosres.2020.105375

Sun, A. Y., Xia, Y., Caldwell, T. G., and Hao, Z. (2018). Patterns of Precipitation and Soil Moisture Extremes in Texas, US: A Complex Network Analysis. *Adv. Water Resour.* 112, 203–213. doi:10.1016/j.advwatres.2017.12.019

Sutanto, S. J., Vitolo, C., Di Napoli, C., D'Andrea, M., and Van Lanen, H. A. J. (2020). Heatwaves, Droughts, and Fires: Exploring Compound and Cascading Dry Hazards at the Pan-European Scale. *Environ. Int.* 134, 105276. doi:10.1016/j.envint.2019.105276

Svensson, C., and Jones, D. A. (2002). Dependence between Extreme Sea Surge, River Flow and Precipitation in Eastern Britain. *Int. J. Climatol.* 22, 1149–1168. doi:10.1002/joc.794

Svensson, C., and Jones, D. A. (2004). Dependence between Sea Surge, River Flow and Precipitation in South and West Britain. *Hydrol. Earth Syst. Sci.* 8, 973–992. doi:10.5194/hess-8-973-2004

Takagi, H., Ty, T. V., Thao, N. D., and Esteban, M. (2015). Ocean Tides and the Influence of Sea-Level Rise on Floods in Urban Areas of the Mekong Delta. *J. Flood Risk Manage.* 8, 292–300. doi:10.1111/jfr3.12094

Tavakol, A., and Rahmani, V. (2019a).Changes in the Frequency of Hot, Humid Conditions in the Mississippi River Basin. In 2019 ASABE Annual International Meeting, 1. American Society of Agricultural and Biological Engineers. doi:10.13031/aim.201901502

Tavakol, A., and Rahmani, V. (2019b). *Changes in the Frequency of Hot, Humid Conditions in the Mississippi River Basin*. ASABE Paper No. 1901502, 1. St. Joseph, MI: ASABE. doi:10.13031/aim.201901502

Tavakol, A., Rahmani, V., and Harrington, J., Jr (2020a). Evaluation of Hot Temperature Extremes and Heat Waves in the Mississippi River Basin. *Atmos. Res.* 239, 104907. doi:10.1016/j.atmosres.2020.104907

Tavakol, A., Rahmani, V., and Harrington Jr., J., Jr (2020b). Probability of Compound Climate Extremes in a Changing Climate: a Copula-Based Study of Hot, Dry, and Windy Events in the central United States. *Environ. Res. Lett.* 15, 104058. doi:10.1088/1748-9326/abb1ef

Tebaldi, C., and Sansó, B. (2009). Joint Projections of Temperature and Precipitation Change from Multiple Climate Models: a Hierarchical Bayesian Approach. *J. R. Stat. Soc. Ser. A (Statistics Society)* 172, 83–106. doi:10.1111/j.1467-985x.2008.00545.x

Tebaldi, C., Strauss, B. H., and Zervas, C. E. (2012). Modelling Sea Level Rise Impacts on Storm Surges along US Coasts. *Environ. Res. Lett.* 7, 014032. doi:10.1088/1748-9326/7/1/014032

Teng, F., Shen, Q., Huang, W., Ginis, I., and Cai, Y. (2017). Characteristics of River Flood and Storm Surge Interactions in a Tidal River in Rhode Island, USA. *Proced. IUTAM* 25, 60–64. doi:10.1016/j.piutam.2017.09.009

Teng, H., Branstator, G., Wang, H., Meehl, G. A., and Washington, W. M. (2013). Probability of US Heat Waves Affected by a Subseasonal Planetary Wave Pattern. *Nat. Geosci* 6, 1056–1061. doi:10.1038/ngeo1988

Teuling, A. J., and Seneviratne, S. I. (2008). Contrasting Spectral Changes Limit Albedo Impact on Land-atmosphere Coupling during the 2003 European Heat Wave. *Geophys. Res. Lett.* 35. doi:10.1029/2007gl032778

Tilloy, A., Malamud, B. D., Winter, H., and Joly-Laugel, A. (2019). A Review of Quantification Methodologies for Multi-hazard Interrelationships. *Earth-Science Rev.* 196, 102881. doi:10.1016/j.earscirev.2019.102881

Toro A, R., Kvakić, M., Klaić, Z. B., Koračin, D., Morales S, R. G. E., and Leiva G, M. A. (2019). Exploring Atmospheric Stagnation during a Severe Particulate Matter Air Pollution Episode over Complex Terrain in Santiago, Chile. *Environ. Pollut.* 244, 705–714. doi:10.1016/j.envpol.2018.10.067

Trepanier, J. C., Yuan, J., and Jagger, T. H. (2017). The Combined Risk of Extreme Tropical Cyclone Winds and Storm Surges along the U.S. Gulf of Mexico Coast. *J. Geophys. Res. Atmos.* 122, 3299–3316. doi:10.1002/2016jd026180

Tressol, M., Ordonez, C., Zbinden, R., Brioude, J., Thouret, V., Mari, C., et al. (2008). Air Pollution during the 2003 European Heat Wave as Seen by MOZAIC Airliners. *Atmos. Chem. Phys.* 8, 2133–2150. doi:10.5194/acp-8-2133-2008

Troy, T. J., Kipgen, C., and Pal, I. (2015). The Impact of Climate Extremes and Irrigation on US Crop Yields. *Environ. Res. Lett.* 10, 054013. doi:10.1088/1748-9326/10/5/054013

Tuleya, R. E., DeMaria, M., and Kuligowski, R. J. (2007). Evaluation of GFDL and Simple Statistical Model Rainfall Forecasts for U.S. Landfalling Tropical Storms. *Weather Forecast.* 22, 56–70. doi:10.1175/waf972.1

Ukkola, A. M., De Kauwe, M. G., Roderick, M. L., Abramowitz, G., and Pitman, A. J. (2020). Robust Future Changes in Meteorological Drought in CMIP6 Projections Despite Uncertainty in Precipitation. *Geophys. Res. Lett.* 47, e2020GL087820. doi:10.1029/2020gl087820

Valle-Levinson, A., Olabarrieta, M., and Heilman, L. (2020). Compound Flooding in Houston-Galveston Bay during Hurricane Harvey. *Sci. Total Environ.* 747, 141272. doi:10.1016/j.scitotenv.2020.141272

van den Hurk, B., van Meijgaard, E., de Valk, P., van Heeringen, K.-J., and Gooijer, J. (2015). Analysis of a Compounding Surge and Precipitation Event in the Netherlands. *Environ. Res. Lett.* 10, 035001. doi:10.1088/1748-9326/10/3/035001

Van Heerwaarden, C. C., Vilà-Guerau de Arellano, J., Gounou, A., Guichard, F., and Couvreux, F. (2010). Understanding the Daily Cycle of Evapotranspiration: A Method to Quantify the Influence of Forcings and Feedbacks. *J. Hydrometeorology* 11, 1405–1422. doi:10.1175/2010jhm1272.1

Vannière, B., Roberts, M., Vidale, P. L., Hodges, K., Demory, M.-E., Caron, L.-P., et al. (2020). The Moisture Budget of Tropical Cyclones in HighResMIP Models: Large-Scale Environmental Balance and Sensitivity to Horizontal Resolution. *J. Clim.* 33, 8457–8474. doi:10.1175/jcli-d-19-0999.1

Vautard, R., Gobiet, A., Jacob, D., Belda, M., Colette, A., Déqué, M., et al. (2013). The Simulation of European Heat Waves from an Ensemble of Regional Climate Models within the EURO-CORDEX Project. *Clim. Dyn.* 41, 2555–2575. doi:10.1007/s00382-013-1714-z

Vautard, R., Yiou, P., D'andrea, F., De Noblet, N., Viovy, N., Cassou, C., et al. (2007). Summertime European Heat and Drought Waves Induced by Wintertime Mediterranean Rainfall Deficit. *Geophys. Res. Lett.* 34. doi:10.1029/2006gl028001

Veatch, W., and Villarini, G. (2020). Modeling the Seasonality of Extreme Coastal Water Levels with Mixtures of Circular Probability Density Functions. *Theor. Appl. Climatol* 140, 1199–1206. doi:10.1007/s00704-020-03143-1

Vezzoli, R., Salvadori, G., and De Michele, C. (2017). A Distributional Multivariate Approach for Assessing Performance of Climate-Hydrology Models. *Sci. Rep.* 7, 12071. doi:10.1038/s41598-017-12343-1

Villalobos-Herrera, R., Bevacqua, E., Ribeiro, A. F. S., Auld, G., Crocetti, L., Mircheva, B., et al. (2021). Towards a Compound-Event-Oriented Climate Model Evaluation: a Decomposition of the Underlying Biases in Multivariate Fire and Heat Stress Hazards. *Nat. Hazards Earth Syst. Sci.* 21, 1867–1885. doi:10.5194/nhess-21-1867-2021

Vitousek, S., Barnard, P. L., Fletcher, C. H., Frazer, N., Erikson, L., and Storlazzi, C. D. (2017). Doubling of Coastal Flooding Frequency within Decades Due to Sea-Level Rise. *Sci. Rep.* 7, 1399–9. doi:10.1038/s41598-017-01362-7

Vogel, J., Rivoire, P., Deidda, C., Rahimi, L., Sauter, C. A., Tschumi, E., et al. (2021). Identifying Meteorological Drivers of Extreme Impacts: an Application to Simulated Crop Yields. *Earth Syst. Dynam.* 12, 151–172. doi:10.5194/esd-12-151-2021

Vogel, M. M., Hauser, M., and Seneviratne, S. I. (2020b). Projected Changes in Hot, Dry and Wet Extreme Events' Clusters in CMIP6 Multi-Model Ensemble. *Environ. Res. Lett.* 15, 094021. doi:10.1088/1748-9326/ab90a7

Vogel, M. M., Zscheischler, J., Wartenburger, R., Dee, D., and Seneviratne, S. I. (2019). Concurrent 2018 Hot Extremes across Northern Hemisphere Due to Human-Induced Climate Change. *Earth's Future* 7, 692–703. doi:10.1029/2019ef001189

Vousdoukas, M. I., Mentaschi, L., Voukouvalas, E., Verlaan, M., Jevrejeva, S., Jackson, L. P., et al. (2018). Global Probabilistic Projections of Extreme Sea Levels Show Intensification of Coastal Flood hazard. *Nat. Commun.* 9, 1–12. doi:10.1038/s41467-018-04692-w

Vrac, M. (2018). Multivariate Bias Adjustment of High-Dimensional Climate Simulations: the Rank Resampling for Distributions and Dependences (R2D2) Bias Correction. *Hydrol. Earth Syst. Sci.* 22, 3175–3196. doi:10.5194/hess-22-3175-2018

Wahl, T., Jain, S., Bender, J., Meyers, S. D., and Luther, M. E. (2015). Increasing Risk of Compound Flooding from Storm Surge and Rainfall for Major US Cities. *Nat. Clim Change* 5, 1093–1097. doi:10.1038/nclimate2736

Waliser, D., and Guan, B. (2017). Extreme Winds and Precipitation during Landfall of Atmospheric Rivers. *Nat. Geosci* 10, 179–183. doi:10.1038/ngeo2894

Wang, J., Chen, Y., Tett, S. F. B., Yan, Z., Zhai, P., Feng, J., et al. (2020). Anthropogenically-driven Increases in the Risks of Summertime Compound Hot Extremes. *Nat. Commun.* 11, 528. doi:10.1038/s41467-019-14233-8

Wang, K., and Dickinson, R. E. (2012). A Review of Global Terrestrial Evapotranspiration: Observation, Modeling, Climatology, and Climatic Variability. *Rev. Geophys.* 50. doi:10.1029/2011rg000373

Wang, L., Yu, H., Yang, M., Yang, R., Gao, R., and Wang, Y. (2019a). A Drought index: The Standardized Precipitation Evapotranspiration Runoff index. *J. Hydrol.* 571, 651–668. doi:10.1016/j.jhydrol.2019.02.023

Wang, L., Zhao, Q., Gao, S., Zhang, W., and Feng, L. (2021). A New Extreme Detection Method for Remote Compound Extremes in Southeast China. *Front. Earth Sci.* 9. doi:10.3389/feart.2021.630192

Wang, P., Yang, Y., Tang, J., Leung, L. R., and Liao, H. (2021). Intensified Humid Heat Events under Global Warming. *Geophys. Res. Lett.* 48, e2020GL091462. doi:10.1029/2020gl091462

Wang, S.-Y. S., Zhao, L., and Gillies, R. R. (2016). Synoptic and Quantitative Attributions of the Extreme Precipitation Leading to the August 2016 Louisiana Flood. *Geophys. Res. Lett.* 43 (11), 805–811. doi:10.1002/2016gl071460

Wang, S. S.-Y., Kim, H., Coumou, D., Yoon, J.-H., Zhao, L., and Gillies, R. R. (2019b). Consecutive Extreme Flooding and Heat Wave in Japan: Are They Becoming a Norm. *Atmos. Sci. Lett.* 20, e933. doi:10.1002/asl.933

Wang, Y., Chen, L., Song, Z., Huang, Z., Ge, E., Lin, L., et al. (2019c). Human-perceived Temperature Changes over South China: Long-Term Trends and Urbanization Effects. *Atmos. Res.* 215, 116–127. doi:10.1016/j.atmosres.2018.09.006

Wang, Y., Xie, Y., Dong, W., Ming, Y., Wang, J., and Shen, L. (2017). Adverse Effects of Increasing Drought on Air Quality via Natural Processes. *Atmos. Chem. Phys.* 17, 12827–12843. doi:10.5194/acp-17-12827-2017

Ward, P. J., Couasnon, A., Eilander, D., Haigh, I. D., Hendry, A., Muis, S., et al. (2018). Dependence between High Sea-Level and High River Discharge Increases Flood hazard in Global Deltas and Estuaries. *Environ. Res. Lett.* 13, 084012. doi:10.1088/1748-9326/aad400

Wdowinski, S., Bray, R., Kirtman, B. P., and Wu, Z. (2016). Increasing Flooding hazard in Coastal Communities Due to Rising Sea Level: Case Study of Miami Beach, Florida. *Ocean Coastal Manag.* 126, 1–8. doi:10.1016/j.ocecoaman.2016.03.002

Weber, T., Bowyer, P., Rechid, D., Pfeifer, S., Raffaele, F., Remedio, A. R., et al. (2020). Analysis of Compound Climate Extremes and Exposed Population in Africa under Two Different Emission Scenarios. *Earth's Future* 8, e2019EF001473. doi:10.1029/2019EF001473

Woodruff, J. D., Irish, J. L., and Camargo, S. J. (2013). Coastal Flooding by Tropical Cyclones and Sea-Level Rise. *Nature* 504, 44–52. doi:10.1038/nature12855

Wright, D. B., Knutson, T. R., and Smith, J. A. (2015). Regional Climate Model Projections of Rainfall from U.S. Landfalling Tropical Cyclones. *Clim. Dyn.* 45, 3365–3379. doi:10.1007/s00382-015-2544-y

Wu, S., Chan, T. O., Zhang, W., Ning, G., Wang, P., Tong, X., et al. (2021a). Increasing Compound Heat and Precipitation Extremes Elevated by Urbanization in South China. *Front. Earth Sci.* 9. doi:10.3389/feart.2021.636777

Wu, W., McInnes, K., O'Grady, J., Hoeke, R., Leonard, M., and Westra, S. (2018). Mapping Dependence between Extreme Rainfall and Storm Surge. *J. Geophys. Res. Oceans* 123, 2461–2474. doi:10.1002/2017jc013472

Wu, X., Hao, Z., Tang, Q., Singh, V. P., Zhang, X., and Hao, F. (2021). Projected Increase in Compound Dry and Hot Events over Global Land Areas. *Int. J. Climatol* 41, 393–403. doi:10.1002/joc.6626

Wu, X., Hao, Z., Zhang, X., Li, C., and Hao, F. (2020). Evaluation of Severity Changes of Compound Dry and Hot Events in China Based on a Multivariate Multi-index Approach. *J. Hydrol.* 583, 124580. doi:10.1016/j.jhydrol.2020.124580

Wu, Y., Miao, C., Sun, Y., AghaKouchak, A., Shen, C., and Fan, X. (2021b). Global Observations and CMIP6 Simulations of Compound Extremes of Monthly Temperature and Precipitation. *GeoHealth* 5, e2021GH000390. doi:10.1029/2021GH000390

Xi, D., Lin, N., and Smith, J. (2020). Evaluation of a Physics-Based Tropical Cyclone Rainfall Model for Risk Assessment. *J. Hydrometeorology* 21, 2197–2218. doi:10.1175/jhm-d-20-0035.1

Xu, F., Chan, T. O., and Luo, M. (2021). Different Changes in Dry and Humid Heat Waves over China. *Int. J. Climatol* 41, 1369–1382. doi:10.1002/joc.6815

Xu, H., Xu, K., Bin, L., Lian, J., and Ma, C. (2018). Joint Risk of Rainfall and Storm Surges during Typhoons in a Coastal City of Haidian Island, China. *Ijerph* 15, 1377. doi:10.3390/ijerph15071377

Xu, H., Xu, K., Lian, J., and Ma, C. (2019). Compound Effects of Rainfall and Storm Tides on Coastal Flooding Risk. *Stoch Environ. Res. Risk Assess.* 33, 1249–1261. doi:10.1007/s00477-019-01695-x

Yin, J., Lin, N., and Yu, D. (2016). Coupled Modeling of Storm Surge and Coastal Inundation: A Case Study in New York City during Hurricane Sandy. *Water Resour. Res.* 52, 8685–8699. doi:10.1002/2016wr019102

Yu, R., and Zhai, P. (2020). Changes in Compound Drought and Hot Extreme Events in Summer over Populated Eastern China. *Weather Clim. Extremes* 30, 100295. doi:10.1016/j.wace.2020.100295

Yuan, J., Stein, M. L., and Kopp, R. E. (2020). The Evolving Distribution of Relative Humidity Conditional upon Daily Maximum Temperature in a Warming Climate. *J. Geophys. Res. Atmospheres* 125, e2019JD032100. doi:10.1029/2019jd032100

Zamora, R. A., Zaitchik, B. F., Rodell, M., Getirana, A., Kumar, S., Arsenault, K., et al. (2021). Contribution of Meteorological Downscaling to Skill and Precision of Seasonal Drought Forecasts. *J. Hydrometeorology* 1. doi:10.1175/jhm-d-20-0259.1

Zampieri, M., Ceglar, A., Dentener, F., and Toreti, A. (2017). Wheat Yield Loss Attributable to Heat Waves, Drought and Water Excess at the Global, National and Subnational Scales. *Environ. Res. Lett.* 12, 064008. doi:10.1088/1748-9326/aa723b

Zellou, B., and Rahali, H. (2019). Assessment of the Joint Impact of Extreme Rainfall and Storm Surge on the Risk of Flooding in a Coastal Area. *J. Hydrol.* 569, 647–665. doi:10.1016/j.jhydrol.2018.12.028

Zhang, H., Wang, Y., Park, T.-W., and Deng, Y. (2017a). Quantifying the Relationship between Extreme Air Pollution Events and Extreme Weather Events. *Atmos. Res.* 188, 64–79. doi:10.1016/j.atmosres.2016.11.010

Zhang, K., Li, Y., Liu, H., Xu, H., and Shen, J. (2013). Comparison of Three Methods for Estimating the Sea Level Rise Effect on Storm Surge Flooding. *Climatic Change* 118, 487–500. doi:10.1007/s10584-012-0645-8

Zhang, L., and Singh, V. P. (2007). Bivariate Rainfall Frequency Distributions Using Archimedean Copulas. *J. Hydrol.* 332, 93–109. doi:10.1016/j.jhydrol.2006.06.033

Zhang, W., Vecchi, G. A., Villarini, G., Murakami, H., Gudgel, R., and Yang, X. (2017b). Statistical-Dynamical Seasonal Forecast of Western North Pacific and East Asia Landfalling Tropical Cyclones Using the GFDL FLOR Coupled Climate Model. *J. Clim.* 30, 2209–2232. doi:10.1175/jcli-d-16-0487.1

Zhang, W., and Villarini, G. (2020). Deadly Compound Heat Stress-flooding hazard across the central United States. *Geophys. Res. Lett.* 47, e2020GL089185. doi:10.1029/2020gl089185

Zhang, W., Villarini, G., Scoccimarro, E., and Napolitano, F. (2020). Examining the Precipitation Associated with Medicanes in the High-resolution ERA-5 Reanalysis Data. *Int. J. Climatology*.

Zhang, W., Villarini, G., Scoccimarro, E., Roberts, M., Vidale, P. L., Vanniere, B., et al. (2021). Tropical Cyclone Precipitation in the HighResMIP Atmosphere-Only Experiments of the PRIMAVERA Project. *Clim. Dyn.* 57, 253–273. doi:10.1007/s00382-021-05707-x

Zhang, W., Villarini, G., Vecchi, G. A., and Murakami, H. (2019a). Rainfall from Tropical Cyclones: High-Resolution Simulations and Seasonal Forecasts. *Clim. Dyn.* 52, 5269–5289. doi:10.1007/s00382-018-4446-2

Zhang, W., Villarini, G., Vecchi, G. A., and Smith, J. A. (2018). Urbanization Exacerbated the Rainfall and Flooding Caused by hurricane Harvey in Houston. *Nature* 563, 384–388. doi:10.1038/s41586-018-0676-z

Zhang, W., Villarini, G., and Wehner, M. (2019b). Contrasting the Responses of Extreme Precipitation to Changes in Surface Air and Dew point Temperatures. *Climatic Change* 154, 257–271. doi:10.1007/s10584-019-02415-8

Zhang, Y., and Najafi, M. R. (2020). Probabilistic Numerical Modeling of Compound Flooding Caused by Tropical Storm Matthew over a Data-Scarce Coastal Environment. *Water Resour. Res.* 56, e2020WR028565. doi:10.1029/2020wr028565

Zhang, Y., You, Q., Mao, G., Chen, C., and Ye, Z. (2019c). Short-term Concurrent Drought and Heatwave Frequency with 1.5 and 2.0 °C Global Warming in Humid Subtropical Basins: a Case Study in the Gan River Basin, China. *Clim. Dyn.* 52, 4621–4641. doi:10.1007/s00382-018-4398-6

Zheng, F., Westra, S., Leonard, M., and Sisson, S. A. (2014). Modeling Dependence between Extreme Rainfall and Storm Surge to Estimate Coastal Flooding Risk. *Water Resour. Res.* 50, 2050–2071. doi:10.1002/2013wr014616

Zheng, F., Westra, S., and Sisson, S. A. (2013). Quantifying the Dependence between Extreme Rainfall and Storm Surge in the Coastal Zone. *J. Hydrol.* 505, 172–187. doi:10.1016/j.jhydrol.2013.09.054

Zhou, P., and Liu, Z. (2018). Likelihood of Concurrent Climate Extremes and Variations over China. *Environ. Res. Lett.* 13, 094023. doi:10.1088/1748-9326/aade9e

Zhou, S., Williams, A. P., Berg, A. M., Cook, B. I., Zhang, Y., Hagemann, S., et al. (2019). Land-atmosphere Feedbacks Exacerbate Concurrent Soil Drought and Atmospheric Aridity. *Proc. Natl. Acad. Sci. USA* 116, 18848–18853. doi:10.1073/pnas.1904955116

Zhou, S., Williams, A. P., Lintner, B. R., Berg, A. M., Zhang, Y., Keenan, T. F., et al. (2021). Soil Moisture–Atmosphere Feedbacks Mitigate Declining Water Availability in Drylands. *Nat. Clim. Change*, 1–7.

Zhu, L., Quiring, S. M., and Emanuel, K. A. (2013). Estimating Tropical Cyclone Precipitation Risk in Texas. *Geophys. Res. Lett.* 40, 6225–6230. doi:10.1002/2013gl058284

Zou, Y. (2021). *Hybridizing Machine Learning and Physically-Based Earth System Models to Improve Prediction of Multivariate Extreme Events (AI Exploration of Wildland Fire Prediction).* Oak Ridge, TN (United States): Oak Ridge National Lab. ORNL.

Zou, Y., Wang, Y., Xie, Z., Wang, H., and Rasch, P. J. (2020). Atmospheric Teleconnection Processes Linking winter Air Stagnation and Haze Extremes in China with Regional Arctic Sea Ice Decline. *Atmos. Chem. Phys.* 20, 4999–5017. doi:10.5194/acp-20-4999-2020

Zscheischler, J., Fischer, E. M., and Lange, S. (2019). The Effect of Univariate Bias Adjustment on Multivariate hazard Estimates. *Earth Syst. Dynam.* 10, 31–43. doi:10.5194/esd-10-31-2019

Zscheischler, J., Martius, O., Westra, S., Bevacqua, E., Raymond, C., Horton, R. M., et al. (2020a). A Typology of Compound Weather and Climate Events. *Nat. Rev. Earth Environ.* 1, 333–347. doi:10.1038/s43017-020-0060-z

Zscheischler, J., Naveau, P., Martius, O., Engelke, S., and Raible, C. C. (2021). Evaluating the Dependence Structure of Compound Precipitation and Wind Speed Extremes. *Earth Syst. Dynam.* 12, 1–16. doi:10.5194/esd-12-1-2021

Zscheischler, J., and Seneviratne, S. I. (2017). Dependence of Drivers Affects Risks Associated with Compound Events. *Sci. Adv.* 3, e1700263. doi:10.1126/sciadv.1700263

Zscheischler, J., van den Hurk, B., Ward, P. J., and Westra, S. (2020b). "Multivariate Extremes and Compound Events," in *In Climate Extremes and Their Implications for Impact and Risk Assessment*. Editors J. Sillmann, S. Sippel, and S. Russo (Elsevier), 59–76. doi:10.1016/b978-0-12-814895-2.00004-5

Zscheischler, J., Westra, S., Van Den Hurk, B. J. J. M., Seneviratne, S. I., Ward, P. J., Pitman, A., et al. (2018). Future Climate Risk from Compound Events. *Nat. Clim Change* 8, 469–477. doi:10.1038/s41558-018-0156-3

Conflict of Interest: The authors declare that the research was conducted in the absence of any commercial or financial relationships that could be construed as a potential conflict of interest.

Advantages of publishing in Frontiers

OPEN ACCESS

Articles are free to read
for greatest visibility
and readership

FAST PUBLICATION

Around 90 days
from submission
to decision

HIGH QUALITY PEER-REVIEW

Rigorous, collaborative,
and constructive
peer-review

TRANSPARENT PEER-REVIEW

Editors and reviewers
acknowledged by name
on published articles

Frontiers
Avenue du Tribunal-Fédéral 34
1005 Lausanne | Switzerland

Visit us: www.frontiersin.org
Contact us: frontiersin.org/about/contact

REPRODUCIBILITY OF RESEARCH

Support open data
and methods to enhance
research reproducibility

DIGITAL PUBLISHING

Articles designed
for optimal readership
across devices

FOLLOW US

@frontiersin

IMPACT METRICS

Advanced article metrics
track visibility across
digital media

EXTENSIVE PROMOTION

Marketing
and promotion
of impactful research

LOOP RESEARCH NETWORK

Our network
increases your
article's readership